Trachette L. Jackson *Editor*

Modeling Tumor Vasculature

Molecular, Cellular, and Tissue Level Aspects and Implications

Springer

Modeling Tumor Vasculature

Trachette L. Jackson
Editor

Modeling Tumor Vasculature

Molecular, Cellular, and Tissue Level Aspects and Implications

Foreword by Luisa Iruela-Arispe, Ph.D.

Department of Molecular, Cell, and Developmental Biology, University of California, Los Angeles, California

Springer

Editor
Trachette L. Jackson
Department of Mathematics
University of Michigan
Ann Arbor, MI 48109
USA
tjacks@umich.edu

ISBN 978-1-4614-0051-6 e-ISBN 978-1-4614-0052-3
DOI 10.1007/978-1-4614-0052-3
Springer New York Dordrecht Heidelberg London

Library of Congress Control Number: 2011935359

Foreword

Modeling Tumor Vasculature: Molecular, Cellular, and Tissue Level Aspects and Implications

The formation of blood vessels requires an elaborate coordination between cell proliferation, migration, differentiation, and heterotypic cell–cell interactions. The process is essential for mammalian development and plays a critical role in homeostasis, tissue repair, and in the outcome of many pathologies. In fact, modulation of vascular growth has been a target for therapeutic intervention in cancer, retinopathies, cardiac disease, arthritis, and skin diseases. Therefore, a clear understanding of how vessels expand, differentiate, and anastomose to form interactive networks can offer the potential for intervention in situations where enhancement or suppression of vascular growth becomes necessary.

A major limitation in understanding angiogenesis, however, centers on the complexity of interplaying signaling pathways, cell types, and extracellular matrix components. Albeit cumbersome, the complete integration of these pathways is essential for therapeutic exploration, as blockade of one pathway imposes a wide range of consequences to other pathways. This is where mathematical modeling becomes an outstanding and necessary tool for the concrete advancement of angiogenesis research in medical applications.

Computational models of angiogenesis have enabled us to quantify, predict, and mimic in silico discrete stages of the vasculogenic process. While the field is still in its infancy, the expectation is that computational mathematical imaging models will pave the way for future therapeutic exploration, enabling predictability of outcomes that could help in restricting experimental questions. Towards this goal, interdisciplinary interactions with experimentalists and integrative multiscale models of in vivo angiogenesis will be essential. As the evolution of the discipline lands itself to sophisticated, accurate, and efficient means of analyszing parameters in angiogenesis, one can foresee a nearby future when cell biologists will first "run" their experiments on the computer and only later verify the predictions at the bench.

Los Angeles, California, USA — Luisa Iruela-Arispe

Contents

Contributors

Tomás Alarcón Centre de Recerca Matemàtica, Campus de Bellaterra, Bellaterra, Barcelona, Spain, tomasalarc@gmail.com

Alexander R.A. Anderson H. Lee Moffitt Cancer Center and Research Institute, Tampa, FL, USA, Alexander.Anderson@moffitt.org

Amy L. Bauer Los Alamos National Laboratory, Theoretical Biology and Biophysics Group, Theoretical Division, Los Alamos, NM, USA, albauer@lanl.gov

Michael Bergdorf Chair of Computational Science, ETH Zurich, Switzerland, bergdorf@inf.ethz.ch

Mark A.J. Chaplain University of Dundee, Dundee, Scotland, Chaplain@maths.dundee.ac.uk

Arnaud Chauvière Department of Pathology, University of New Mexico, Albuquerque, NM, USA, achauviere@salud.unm.edu

Vittorio Cristini Department of Pathology and Department of Chemical and Biomedical, Engineering, University of New Mexico, Albuquerque, NM, USA, vcristini@salud.unm.edu

Michael Dupin Massachusetts General Hospital and Harvard Medical School, Charlestown, MA, USA, mdupin@steele.mgh.harvard.edu

Feilim Mac Gabhann Institute for Computational Medicine and Department of Biomedical Engineering, Johns Hopkins University, Baltimore, MD, USA, feilim@jhu.edu

J. De Groot Department of Neuro-Oncology, Cancer Medicine, The University of Texas M. D. Anderson Cancer Center, Houston, TX, USA, jdegroot@mdanderson.org

Haralambos Hatzikirou Department of Pathology, University of New Mexico, Albuquerque, NM, USA, hhatzikirou@salud.unm.edu

Trachette Levon Jackson Department of Mathematics, University of Michigan, Ann Arbor, MI, USA, tjacks@umich.edu

Harsh Vardhan Jain Mathematical Biosciences Institute, The Ohio State University, Columbus, OH, USA, hjain@mbi.osu.edu

Yi Jiang Theoretical Division, Los Alamos National Laboratory, Los Alamos, NM, USA, jiang@lanl.gov, yijianglanl@gmail.com

Walid Kamoun Massachusetts General Hospital and Harvard Medical School, Charlestown, MA, USA, walid@steele.mgh.harvard.edu

Petros Koumoutsakos Chair of Computational Science, ETH Zurich, Switzerland, petros@inf.ethz.ch

Quan Long Brunel Brunel Institute for Bioengineering, Brunel University, Uxbridge, Middlesex, UK, quan.long@brunel.ac.uk

John Lowengrub Department of Mathematics, The University of California at Irvine, Irvine, CA, USA, lowengrb@math.uci.edu

Stephen McDougall Heriot-Watt University, Edinburgh, Scotland, Steve.McDougall@pet.hw.ac.uk

Florian Milde Chair of Computational Science, ETH Zurich, Switzerland, mildef@inf.ethz.ch

Lance L. Munn Massachusetts General Hospital and Harvard Medical School, Charlestown, MA USA, lance@steele.mgh.harvard.edu;

Karen M. Page Department of Mathematics, University College London, Gower Street, London, UK, kpage@math.ucl.ac.uk

Aleksander S. Popel Department of Biomedical Engineering, Johns Hopkins University School of Medicine, Baltimore, MD, USA, apopel@jhu.edu

Heiko Rieger Theoretische Physik, Saarland University, Saarbrucken, Germany, h.rieger@mx.uni-saarland.de

Thimo Rohlf Epigenomics Project, Genopole, Evry and MPI-MIS, ISSB, Genopole Campus 1, Genavenir, France, rohlf@mis.mpg.de

Marianne O. Stefanini Department of Biomedical Engineering, Johns Hopkins University School of Medicine, Baltimore, MD, USA, stefanini@jhmi.edu

James Alex Tyrrell Massachusetts General Hospital and Harvard Medical School, Charlestown, MA, USA, lance@steele.mgh.harvard.edu

Michael Welter Theoretische Physik, Saarland University, Saarbrucken, Germany, mwelter@lusi.uni-sb.de

Jie Wu School of Naval Architecture, Ocean and Civil Engineering, Shanghai Jiaotong University, Shanghai, Peoples Republic of China, janny_wujie@yahoo.com.cn

Shi-xiong Xu Department of Mechanics and Engineering Science, Fudan University, Shanghai, Peoples Republic of China, xusx_fd@yahoo.com.cn

Xiaoming Zheng Department of Mathematics, Central Michigan University, Mount Pleasant, MI, USA, xzheng@cmich.edu

Part I
Cell Signaling and Molecular Aspects of Tumor Blood Vessel Formation

Chapter 1
Mathematical Modeling of the VEGF Receptor

Tomás Alarcón and Karen M. Page

1 Introduction

Angiogenesis is the process whereby new blood vessels are generated from the existing vasculature in response to substances secreted and released by the surrounding tissues. These substances are special types of cytokines called growth factors (GFs). Endothelial cells (ECs) possess surface receptors specific for each of these growth factors. There are many such growth factors and cell surface receptors involved in angiogenesis, but there is a particularly important one, VEGF, as the VEGF receptor (VEGFR) is expressed only by ECs. Angiogenesis can occur in a variety of biological settings both normal and pathological, ranging from wound healing to cancer.

The onset of angiogenesis is controlled by the so-called angiogenic switch. The usual picture of the angiogenic switch is a scale measuring the levels of angiogenic factors and anti-angiogenic substances. When the former are found in excess of the latter, angiogenesis is triggered (Berger and Benjamin 2003).

Here, we argue that this image of the angiogenic switch might be incomplete. The VEGFR is a receptor tyrosine kinase (RTK). Within their cytoplasmic domains, RTKs have regions which, upon phosphorylation, exhibit tyrosine kinase activity. Activation of these regions, however, occurs only upon receptor oligomerisation (Alberts et al. 2002; Helmreich 2001). Most GF molecules are multivalent ligands, i.e. one molecule of GF has more than one receptor binding domain and therefore it can engage in binding with as many

T. Alarcón (✉)
Centre de Recerca Matemàtica, Campus de Bellaterra, Edifici C, 08193 Bellaterra, Barcelona, Spain
e-mail: tomasalarc@gmail.com

K.M. Page
Department of Mathematics, University College London, Gower Street, London, WC1E 6BT, UK
e-mail: kpage@math.ucl.ac.uk

T.L. Jackson (ed.), *Modeling Tumor Vasculature: Molecular, Cellular, and Tissue Level Aspects and Implications*, DOI 10.1007/978-1-4614-0052-3_1,

receptors as it possesses binding regions. Mathematical models of multivalent ligand/multivalent receptor systems have been formulated and analysed (see Posner et al. 1995; Woolf and Linderman 2004; Lauffenburger and Linderman 1993 and references therein). One remarkable property exhibited by these models concerns the behaviour of the response curve (which, roughly speaking, represents the probability of a cell within a population to respond to a given concentration of ligand). Whereas the response curve for receptors that do not depend on receptor oligomerisation for activation (e.g. G protein-linked receptors) is monotonic, saturating for high ligand concentration, the response curve for multivalent ligand/multivalent receptors is bell-shaped: cellular responses are inactivated at high concentrations of ligand. With the help of the models presented here, we aim to discuss the implications of this property of RTKs in relation to the onset of angiogenesis and antiangiogenic therapy.

In spite of the initial enthusiasm raised by antiangiogenic therapy, the actual results obtained on patients in clinical practice have been poor and its impact on the life expectancy of cancer patients has been very disappointing, in particular when the antiangiogenic drugs were used alone (see the review by Jain 2005 and references therein). This lack of results, especially in contrast with the success registered on laboratory animals, has been puzzling. A commonly adopted explanation for such a failure is that, whereas antiangiogenic drugs can kill many cancer cells, they do not eradicate the tumour completely and the remaining tumour cells will eventually trigger angiogenesis anew (Hempton 2005). One of our aims is to use our models to try to produce plausible explanations of this failure.

Tumour vasculature, whether tumour vessels are the product of tumour-induced angiogenesis or they are native vessels of the host which have been engulfed by the growing tumour mass, presents many structural abnormalities in comparison to its normal counterpart (Jain 2005). An example of such de-regulation is an overexpression of the VEGF surface receptor (Cross et al. 2003; Ferrara 2002). Further evidence for this can be found in experiments carried out on retinal microvascular ECs under stimulation with estrogen (Suzuma et al. 1999). Estrogen is known to promote proliferation of some types of breast cancer cells (Amlal et al. 2006) and, therefore, it is plausible that the same mechanism upregulates VEGFR. Moreover, recent experiments by Zhang et al. (2005) show that the platelet-derived growth factor (PDGF) receptor, a system analogous to the VEGFR in every significant aspect, is upregulated in ECs of hepatocellular carcinoma. In this paper, we aim to study the effect of overexpression of surface VEGFR on antiangiogenic therapy. We consider two possible mechanisms for overexpression of surface VEGFR, namely increased rate of VEGFR synthesis (Suzuma et al. 1999; Zhang et al. 2005) and downregulation of receptor endocytosis (Polo et al. 2004).

The models presented here are formulated in terms of Markov processes and analysed by means of a Wenzel-Kramer-Brillouin (WKB) approximation of the Master Equation (Kitahara 1973; Kubo et al. 1973). Our models include ligand/receptor binding, ligand-induced receptor dimerisation, receptor internalization and binding of enzymes carrying SH2 domains (e.g. members of the Src tyrosine kinase family) to activated (dimerised) receptors. This last process constitutes the

earliest event in RTK-activation induced signalling. Our analysis allows us to discern the contribution of each of these processes to the overall behaviour of the VEGFR system as well as to assess plausible roles of each of them in resistance to antiangiogenic therapy in solid tumours.

There are several recent studies of models of GF/RTK ligation dynamics. Mac Gabham and Popel (2004) study a model of competitive binding of VEGF and placental growth factor (PlGF) to VEGFR. There is some evidence of synergy (i.e. enhancement of cell response) between PlGF and VEGF in pathological situations. The mathematical models presented by Mac Gabham and Popel (2004) help to elucidate the mechanisms of this synergy. Their models take into account receptor internalization but do not account for VEGFR dimerisation. Mac Gabham and Popel (2005a) have studied the system VEGF/VEGF receptor 2/neuropilin-1. Both VEGF receptor 2 (VEGFR2) and neuropilin-1 (NRP1) are found on the surface of endothelial cells. They do not interact directly but can be cross-linked by a VEGF isoform which has binding sites for both VEGFR2 and NRP1. This model considers cross-linking between VEGFR2 and NRP1 but does not account for either receptor internalization or VEGFR dimerisation.

A model of the PDGF/PDGF receptor (PDGFR) has been proposed by Park et al. (2003). This model incorporates some early events in the signalling cascade triggered by PDGF/PDGFR binding, including phosphoinositide2 in Alarcón and Page (2007)-kinase-dependent activation of Akt. The authors also incorporate an alternative model for receptor dimerisation in which dimerisation is mediated by receptor domains which are only active or exposed when the receptors are bound, forming a sort of "pre-dimer". Ligand and receptor are supposed to associate and dissociate rapidly. The dissociation of one of the ligands from its receptor within a pre-dimer leads to the formation of a stable dimerised complex. The model presented by Park et al. (2003) exhibits good agreement with experimental data.

Mac Gabham and Popel (2005b) have proposed a stochastic analysis of VEGF binding to cell surface receptors. In physiological circumstances, VEGF is usually found in very low concentrations, typically of the order of the picomolar. These concentrations imply less than one ligand molecule in each cubic micron of fluid. Such low concentrations lead them to consider the validity of the *excess of ligand* assumption (Sulzer et al. 1996) and the effects of the fluctuations in cellular response, especially in a scenario in which response is threshold triggered. They find agreement between stochastic and determinitic models in the range of VEGF concentrations handled in in vitro experiments (of the order of the nanomolar), but argue that in in vivo situations the effects of fluctuations might be more important.

This paper is organised as follows. Section 2 is devoted to giving details of our model formulation and a brief summary of the necessary biological background. In Sect. 2 in Alarcón and Page (2007), the stochastic models formulated in Sect. 2 are analysed by means of an asymptotic analysis (a generalisation to arbitrary dimension of the work by Kubo et al. (1973)). This analysis produces a set of ordinary differential equations for the first and second moments which are then solved numerically. Section 2 in Alarcón and Page (2007) also contains details of the estimation of parameter values. In Sect. 4, we present numerical simulations of

the response of our models to antiangiogenic therapy, assuming both a physiological and a pathological scenario, the latter one characterised by overexpression of surface receptors by inhibition of endocytosis. Another possible source of overexpression of receptors is upregulation of receptor synthesis. This situation is analysed in Sect. 5. Section 6 presents an analysis of the fluctuations. Finally, in Sect. 7 we summarise and discuss our results.

2 Biological Background and Model Formulation

Here we briefly summarise the biological background necessary to understand how our models are set up and then we discuss our model formulation.

2.1 Biological Background

VEGF denotes a large family of dimeric glycoproteins which consists of five mammalian and one virus-encoded members. VEGF-A was the first member to be discovered and has been shown to be involved in a large number of processes, with both physiological and pathological functions. VEGF-A, in turn, is expressed as four isoforms of different lengths. The shortest of them (VEGF-A_{121}, 121 aminoacids long) differs from the other three in its lack of ability to bind to the extracellular matrix (ECM) and, therefore, it diffuses freely (Hicklin and Ellis 2005).

Regarding the VEGF receptors, there are three different types VEGFR-1, -2 and -3.[1] ECs in tumour blood vessels express mostly VEGFR-2, although VEGFR-1 and -3 might also be expressed. In physiological conditions, the vascular endothelium expresses VEGFR-1 and -2 whereas the lymphatic endothelium expresses VEGFR-2 and -3 (Cross et al. 2003). Of the two receptors expressed on ECs, only VEGFR-2 seems to contribute to intracellular signalling, with the function of VEGFR-1 most likely being sequestering (excess) VEGF (Cross et al. 2003).

In order to keep our model as simple as possible and stay focused on the study of how ligand/receptor binding dynamics affect the early events of the VEGF binding-induced signalling cascade, we concentrate on the effects of diffusible VEGF-A, VEGF-A_{121} and its binding to VEGFR-2. This particular system appears to make a major contribution to tumour-induced angiogenesis. Thus, hereafter, for simplicity in the notation, the system VEGF-A_{121}/VEGFR-2 will be referred to simply as VEGF/VEGFR.

In the case of the VEGF/VEGFR system, the ligand (VEGF molecule) is bivalent and the receptor (VEGFR) is monovalent, meaning that one VEGF molecule binds two VEGFRs, while each VEGFR can bind a single VEGF molecule.

[1] These three types of VEGFR are surface receptors. There is also a soluble form of VEGFR-1.

This property provides a mechanism for RTK activation, which is elusive from a purely structural perspective: receptors are oligomerised (in the particular case of the VEGFR, dimerised) upon ligand binding. The receptors within the oligomer are brought into close proximity which leads to receptor *cross-phosphorylation* (Alberts et al. 2002). Cross-phosphorylation yields attachment of phosphate to the tyrosine kinase domains within the cytoplasmic tail of the RTKs, providing high-affinity docking sites for selected substrates to bind. These substrates, usually members of the Src family of tyrosine kinases, carry the src-homology 2 (SH2) domain, which has high specifity for the phosphorylated domains within the RTKs, and are themselves tyrosine kinases activated by binding to phosphorylated RTKs. These are the earlier events in the signalling cascade triggered by GF/RTK binding. Activated SH2-carrying kinases relay the signal on to other tyrosine kinases which lead to activation of the corresponding pathways and the alteration of cell behaviour.

Each VEGF receptor has two kinase domains. We consider that each of these has only one tyrosine residue that is cross-phosphorylated under ligand induced dimerisation, thus providing four high-affinity docking sites for SH2 domains (Cross et al. 2003). Actually, dimerised receptors exhibit more than four possible docking sites (6 or more according to Cross et al. 2003). We have made this approximation in order to keep the model as simple as possible. Later, we comment on the effects of this approximation.

According to Sawyer (1998), there are basically two types of SH2-bearing tyrosine kinase: those carrying only one SH2 domain, hereafter to be referred to as *SH2 monomers*, and those carrying two SH2 domains (eg ZAP70 or PI3K). In this paper, only the former ones are considered.

2.2 Model Formulation

The stochastic models we analyse in this paper are specified in terms of three quantities, namely the state vector $\mathbf{X}$ whose components are the number of molecules of each of the species involved, the probability per unit time corresponding to each of the reactions involved in the process being modeled, W_i and the corresponding vector $\mathbf{r}_i$. The components of $\mathbf{r}_i$ are the increments in the number of molecules when the ith reaction occurs. To summarise, the occurrence of the ith reaction induces the change in the state vector $\mathbf{X} \to \mathbf{X} + \mathbf{r}_i$ and occurs with probability proportional to W_i. The system is then described by the probability density of the system being in state $\mathbf{X}$ at time t, $\Psi(\mathbf{X}, t)$, whose dynamics is given by the Master Equation:

$$\frac{\partial \Psi(\mathbf{X}, t)}{\partial t} = \sum_{\mathbf{r}} (W(\mathbf{X} - \mathbf{r}, \mathbf{r}, t)\Psi(\mathbf{X} - \mathbf{r}, t) - W(\mathbf{X}, \mathbf{r}, t)\Psi(\mathbf{X}, t)) . \tag{1.1}$$

Next, we present a description of the three models to be analysed.

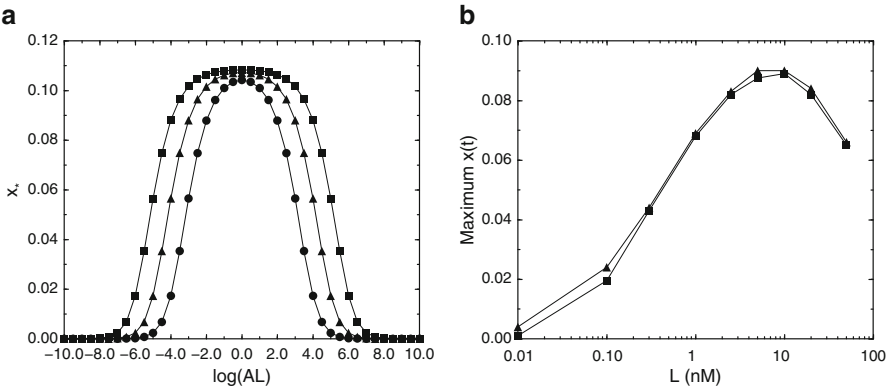

Fig. 1.1 Panel (**a**) shows the steady-state value of dimerised receptor, x_*, for Model 1 as a function of the dimensionless quantity AL for different values of the dimensionless quantity k_{on}^x. Parameter values have been taken from Table 1.1. Key: *squares* $k_{\text{on}}^x = 4.6{\times}10^3\ \text{s}^{-1}$, *triangles* $k_{\text{on}}^x = 4.6{\times}10^2\ \text{s}^{-1}$, *circles* $k_{\text{on}}^x = 4.6 \times 10^1\ \text{s}^{-1}$. Panel (**b**) shows simulation results corresponding to Model 2 in Alarcón and Page (2007) and 4 (with $k_s = 9 \times 10^{-5}\ \text{s}^{-1}$). The *squares* (Model 3) and *triangles* (Model 4) in this plot show the maximum values achieved by the proportion of surface dimers as a function of ligand concentration when the models were simulated until $t = 1.2$, i.e. 20 min in dimensional terms. Other parameter values are taken form Table 1.1

2.3 Receptor Binding Model

We use a version of the stochastic model for multivalent ligand-induced receptor oligomerisation developed in Alarcón and Page (2006). Here, the model corresponds to a bivalent ligand and a univalent receptor, which corresponds to the case of the VEGF/VEGFR system. The stochastic dynamics of this model is summarised in Table 1.1 in Alarcón and Page (2007), where the precise forms of the transition rates for the different events involved in the ligand–receptor binding model are given, and depicted in Fig. 1.1 in Alarcón and Page (2007), where the different reactions involved in the ligand/receptor binding are represented schematically. In Fig. 1.1 in Alarcón and Page (2007), U is the number of unbound receptors, B is the number of bound receptors and X is the number of dimers ($U + B + 2X = N_{\text{R}}$, with N_{R} is the number of surface receptors). In Table 1.1 in Alarcón and Page (2007), $u \equiv U/N$, $b \equiv B/N$ and $x \equiv X/N$.[2] Here $N = N_S + N_{\text{R}}$ is the total number of molecules in our simulation. N_S is the number of SH2-carrying enzymes (see Table 1.1). L is the concentration (in moles/litre) of free ligand, which is assumed to be constant, i.e. ligand is supplied at a rate that matches its rate of binding at the surface of the cells.

[2]Throughout the paper, we use the same covention: an upper-case letter represents numbers of molecules of a given type, whereas the corresponding lower-case letter represents the proportion of molecules of that particular kind with respect to the total number of molecules. An exception to this rule is L, whose meaning is explained in the text.

Table 1.1 Parameter values for the VEGF receptor models

Parameter	Value (units)	Source
k_{on}	10^7 ($M^{-1}\times s^{-1}$)	
k_{off}	10^{-3} (s^{-1})	Mac Gabham and Popel (2004)
$A = k_{on}/k_{off}$	10^{10} (M^{-1})	Cross et al. (2003)
k^x_{on}	4.6×10^3 (1/s)	Alarcón and Page (2007)
k^x_{off}	10^{-3} (1/s)	Alarcón and Page (2007)
$A_x = k^x_{on}/k^x_{off}$	4.6×10^6 (none)	Alarcón and Page (2007)
Δ	2.5 (nm)	Alarcón and Page (2007)
Cell surface (S_c)	1,000 (μm^2)	Mac Gabham and Popel (2004)
Cell volume (V_c)	2,974 (μm^3)	Mac Gabham and Popel (2004)
Number of receptors (N_R)	50,000	Mac Gabham and Popel (2004)
Receptor surface density ($\rho = N_R/S_c$)	50 (μm^{-2})	
k^s_{on}	10^8 ($M^{-1}\times s^{-1}$)	Felder et al. (1993)
k^s_{off}	10^{-1} (s^{-1})	Felder et al. (1993)
Number of SH2 monomers (N_S)	1,80,000	Alarcón and Page (2007)
k^{nd}_{in}	5×10^{-4} (s^{-1})	Mac Gabham and Popel (2004)
k^{d}_{in}	5×10^{-3} (s^{-1})	Mac Gabham and Popel (2004)
k_{re}	9.7×10^{-4} (s^{-1})	Lauffenburger and Linderman (1993)
k_d	3.7×10^{-3} (s^{-1})	Lauffenburger and Linderman (1993)
k_s	9×10^{-5} (min^{-1})	Alarcón and Page (2007)

The actual model (i.e. transition rates for each reaction and the corresponding vectors $\mathbf{r}_i$) used for receptor binding is summarised in Table 1.1 in Alarcón and Page (2007) and Fig. 1.1 in Alarcón and Page (2007). This model will be hereafter referred to as Model 1. The transition rate corresponding to reaction $\mathbf{r}_3$ (k^x_{eff} in Fig. 1.1 in Alarcón and Page (2007)) needs further clarification (Alarcón and Page 2006). The transition rate for this reaction, which corresponds to the formation of a dimer, is obtained as the product of two factors: the rate of binding between an unbound receptor and a ligand–receptor heterodimer and the probability of finding another receptor within a characteristic distance Δ of the ligand–receptor heterodimer. The latter is given by $\pi\Delta^2\rho$, with $\rho = N/4\pi R^2$ being the surface density of receptors on the cell surface and R, the average radius of an EC.

2.4 SH2 Binding to Dimerised Receptors

We consider that each VEGF receptor provides two high-affinity docking sites for tyrosine kinases carrying SH2 domains upon ligand-induced dimerisation, thus providing four high-affinity docking sites for SH2 domains.

In Fig. 1.2 in Alarcón and Page (2007) and Table in Alarcón and Page (2007), $S_F \equiv N_S - S$ stands for the number of free SH2 domains, i.e. those that are not bound to dimerised receptor. S is the number of bound SH2 domains. X is the total

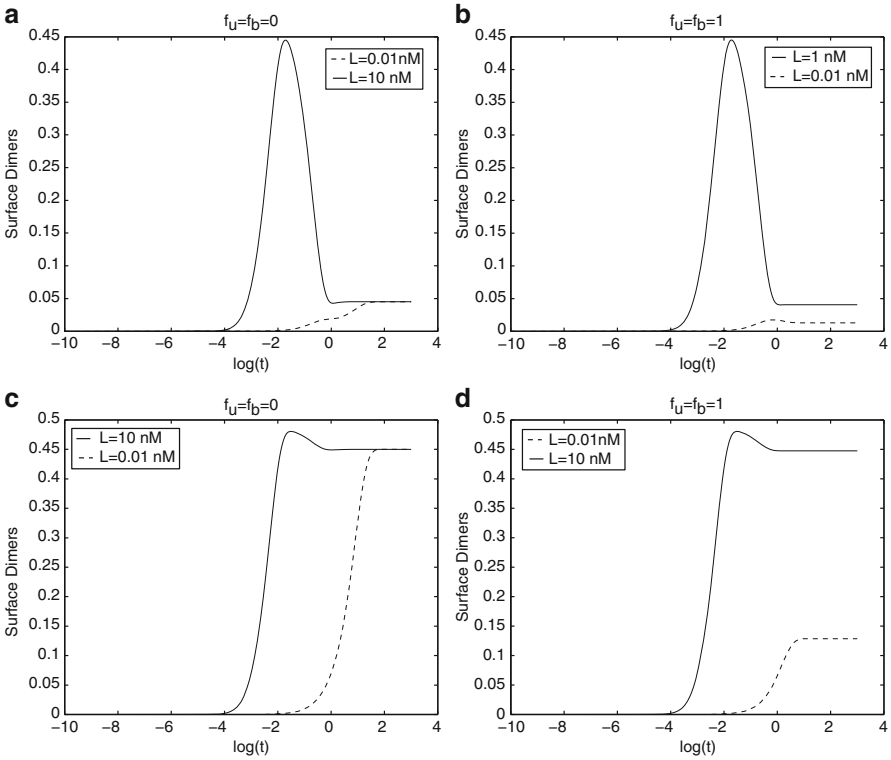

Fig. 1.2 Simulation results corresponding to (1.30)–(1.37). This plot shows the time course of the proportion of surface dimers, $x(t)$. *Solid lines* correspond to $L = 10$ nM and *dashed lines* to $L = 0.01$ nM. $K_{\rm cl}(y) = k^x_{\rm on}\pi\Delta^2 N_{\rm R}\frac{y}{S_c}$. $K_s(x) = k_s$. (**a**) $k_s = 4.5\times10^{-4}$ s^{-1} and $f_u = f_b = 0$. (**b**) $k_s = 4.5\times10^{-4}$ s^{-1} and $f_u = f_b = 1$. (**c**) $k_s = 4.5\times10^{-3}$ s^{-1} and $f_u = f_b = 0$. (**d**) $k_s = 4.5\times10^{-3}$ s^{-1} and $f_u = f_b = 1$. Other parameter values taken from Table 1.1

number of dimers, X_1 is the number of dimers bound to a single SH2 domain, X_2 is the number of dimers bound to two SH2 domains, X_3 is the number of dimers bound to three SH2 domains, X_4 is the number of dimers bound to four. X_0 is defined as the number of "free" (i.e. not bound to SH2) receptor dimers. Taking into account these definitions, it is straightforward to see that $S \equiv X_1 + 2X_2 + 3X_3 + 4X_4$ and $X_0 \equiv X - X_1 - X_2 - X_3 - X_4$.

The rate constants $k^s_{{\rm eff}i}$, $i = 1,..,4$ that appear in Fig.1.2 in Alarcón and Page (2007) need further clarification. According to Table in Alarcón and Page (2007), $k^s_{{\rm eff}i} = (4-(i-1))\frac{k^s_{\rm on}}{V_c N_A}$. $k^s_{\rm on}$ is the binding rate of a SH2 domain to a phosphotyrosine residue on a receptor dimer (see Table 1.1). Because this constant is given in M^{-1}s^{-1}, we need to use the factor $V_c N_A$, where V_c is the volume of an EC and $N_{\rm A}$ is Avogadro's number, to convert to appropriate units. The factor $4-(i-1)$ corresponds to the number of free docking sites that are left on the receptor dimer.

The model summarised in Table in Alarcón and Page (2007) will be hereafter referred to as Model 2.

2.5 *Endocytosis of Surface Receptors*

We introduce a third element in our model, namely, receptor internalization (Teis and Huber 2003). Receptor tyrosine kinases undergo clearance from the surface upon ligand-mediated activation (i.e. dimerisation) in a very efficient manner. Inactivated receptors (i.e. unbound and non-dimerised bound receptors) also undergo internalization.

Receptor endocytosis is a complex process involving a sophisticated network of protein interactions of which not all the details are known. As we intend to produce a simple model of receptor endocytosis capturing its essential features, we only give a very brief and incomplete summary of the biology of receptor internalization. The reader is referred to Helmreich (2001) and Teis and Huber (2003) for more detailed reviews.

Both inactive (i.e. non-dimerised) RTKs and RTK dimers undergo internalization by essentially the same mechanism.[3] The first step is the formation of a structure called a clathrin-coated pit around the RTK dimer. This pit eventually pinches off the membrane forming a vesicle containing the RTK dimer. Once these vesicles are formed, the RTKs enter the so-called early endosome. Although the mechanism of early RTK internalization is the same for both non-dimerised and dimerised receptors, the rate of endocytosis of the latter is much in excess of the former. This indicates that a protein network regulating endocytosis is upregulated upon RTK dimerisation (Teis and Huber 2003).

After entering the early endosome, dimer and non-dimer RTKs follow different pathways. Non-dimer RTKs are rapidly recycled to the membrane (we will assume that they do so as unbound receptors). However, most of the dimerised RTKs are transported to the so-called late endosomes, from where they pass into the lysosomes, where they undergo degradation (Teis and Huber 2003).

As the total number of cell surface receptors seems to stay constant, parallel to endocytosis, RTK production must be sustained by the cell at some given rate (Lauffenburger and Linderman 1993).

Further to these assumptions, we make the hypothesis that somewhere down the endocytic pathway, the SH2-carrying enzymes potentially attached to RTK dimers are detached and released into the cytoplasm. This assumption allows us to ensure that the total number of SH2 domains stays constant. A further simplifying assumption will be that the rate of internalization and degradation for dimerised receptors is independent of the number of SH2 domains bound to their active sites. We also assume that unbound RTKs and non-dimerised ligand/receptor complexes are internalized and recycled back to the membrane at the same rate.

Our stochastic model is inspired by a model by Lauffenburger and Linderman (1993). Our model, however, contains some simplifications with respect to

[3] Teis and Huber (2003) distinguish between *active* and *inactive* RTKs. We will assume that "active" refers to dimerised receptors, which seems to be pretty clear from the context, and that "inactive" refers to both unbound receptors and non-dimerised ligand/receptor complexes.

Table 1.2 Reaction probability per unit time, $W_i \equiv W(\mathbf{X}, \mathbf{r}_i, t)$, $i = 1, .., 12$. $\mathbf{r}_i = (r_{iu}, r_{ib}, r_{ix}, r_{ix_1}, r_{ix_2}, r_{ix_3}, r_{ix_4}, r_{iu^i}, r_{ib^i}, r_{ix^i}, r_{ix_1^i}, r_{ix_2^i}, r_{ix_3^i}, r_{ix_4^i})$

Reaction probability p.u.t	$\mathbf{r}_i$	Reaction
$W_1 = k_{\text{on}} L N u$	$(-1, 1, 0, 0, 0, 0, 0, 0, 0, 0, 0, 0, 0, 0)$	Receptor binding
$W_2 = k_{\text{off}} N b$	$(1, -1, 0, 0, 0, 0, 0, 0, 0, 0, 0, 0, 0, 0)$	Receptor dissociation
$W_3 = k_{\text{on}}^x N \pi \Delta^2 \rho u b$	$(-1, -1, 1, 0, 0, 0, 0, 0, 0, 0, 0, 0, 0, 0)$	Dimer formation
$W_4 = k_{\text{off}}^x N x_0$	$(1, 1, -1, 0, 0, 0, 0, 0, 0, 0, 0, 0, 0, 0)$	Dimer dissociation
$W_5 = 4 \frac{k_{\text{on}}^s}{V_c N_A} N x_0 \left(\frac{N_S}{N} - s\right)$	$(0, 0, 0, 1, 0, 0, 0, 0, 0, 0, 0, 0, 0, 0)$	SH2 binding
$W_6 = 3 \frac{k_{\text{on}}^s}{V_c N_A} N x_1 \left(\frac{N_S}{N} - s\right)$	$(0, 0, 0, -1, 1, 0, 0, 0, 0, 0, 0, 0, 0, 0)$	SH2 binding
$W_7 = 2 \frac{k_{\text{on}}^s}{V_c N_A} N x_2 \left(\frac{N_S}{N} - s\right)$	$(0, 0, 0, 0, -1, 1, 0, 0, 0, 0, 0, 0, 0, 0)$	SH2 binding
$W_8 = \frac{k_{\text{on}}^s}{V_c N_A} N x_3 \left(\frac{N_S}{N} - s\right)$	$(0, 0, 0, 0, 0, -1, 1, 0, 0, 0, 0, 0, 0, 0)$	SH2 binding
$W_9 = k_{\text{off}}^s N x_1$	$(0, 0, 0, -1, 0, 0, 0, 0, 0, 0, 0, 0, 0, 0)$	SH2 dissociation
$W_{10} = 2 k_{\text{off}}^s N x_2$	$(0, 0, 0, 1, -1, 0, 0, 0, 0, 0, 0, 0, 0, 0)$	SH2 dissociation
$W_{11} = 3 k_{\text{off}}^s N x_3$	$(0, 0, 0, 0, 1, -1, 0, 0, 0, 0, 0, 0, 0, 0)$	SH2 dissociation
$W_{12} = 4 k_{\text{off}}^s N x_4$	$(0, 0, 0, 0, 0, 1, -1, 0, 0, 0, 0, 0, 0, 0)$	SH2 dissociation
$W_{13} = k_{\text{in}}^{\text{nd}} N u$	$(-1, 0, 0, 0, 0, 0, 0, 1, 0, 0, 0, 0, 0, 0)$	Internalization
$W_{14} = k_{\text{in}}^{\text{nd}} N b$	$(0, -1, 0, 0, 0, 0, 0, 0, 1, 0, 0, 0, 0, 0)$	Internalization
$W_{15} = k_{\text{in}}^{\text{d}} N x$	$(0, 0, -1, 0, 0, 0, 0, 0, 0, 1, 0, 0, 0, 0)$	Internalization
$W_{16} = k_{\text{in}}^{\text{d}} N x_1$	$(0, 0, 0, -1, 0, 0, 0, 0, 0, 0, 1, 0, 0, 0)$	Internalization
$W_{17} = k_{\text{in}}^{\text{d}} N x_2$	$(0, 0, 0, 0, -1, 0, 0, 0, 0, 0, 0, 1, 0, 0)$	Internalization
$W_{18} = k_{\text{in}}^{\text{d}} N x_3$	$(0, 0, 0, 0, 0, -1, 0, 0, 0, 0, 0, 0, 1, 0)$	Internalization
$W_{19} = k_{\text{in}}^{\text{d}} N x_4$	$(0, 0, 0, 0, 0, 0, -1, 0, 0, 0, 0, 0, 0, 1)$	Internalization
$W_{20} = k_{\text{re}} N u^i$	$(1, 0, 0, 0, 0, 0, 0, -1, 0, 0, 0, 0, 0, 0)$	Non-dimer recycling
$W_{21} = k_{\text{re}} N b^i$	$(1, 0, 0, 0, 0, 0, 0, 0, -1, 0, 0, 0, 0, 0)$	Non-dimer recycling
$W_{22} = k_d N x^i$	$(2, 0, 0, 0, 0, 0, 0, 0, 0, -1, 0, 0, 0, 0)$	Degradation
$W_{23} = k_d N x_1^i$	$(2, 0, 0, 0, 0, 0, 0, 0, 0, 0, -1, 0, 0, 0)$	Degradation
$W_{24} = k_d N x_2^i$	$(2, 0, 0, 0, 0, 0, 0, 0, 0, 0, 0, -1, 0, 0)$	Degradation
$W_{25} = k_d N x_3^i$	$(2, 0, 0, 0, 0, 0, 0, 0, 0, 0, 0, 0, -1, 0)$	Degradation
$W_{26} = k_d N x_4^i$	$(2, 0, 0, 0, 0, 0, 0, 0, 0, 0, 0, 0, 0, -1)$	Degradation

In this Table N refers to the number of receptors plus the number of proteins carrying a SH2 domain. N_{A} is Avogadro's number. We assume that each receptor dimer carries four phosphorylated tyrosines to which two SH2 domains can bind. See Table 1.1 for a summary of parameter values

Lauffenburger and Linderman (1993). We will assume that all the internalized RTK dimers go to degradation in the lysosomes (without considering the two intermediate compartments described earlier) and that only unbound RTKs and non-dimerised ligand/receptor complexes undergo recycling. We further assume that none of these pass into the lysosome and that they are not degraded. Moreover, we assume that the rate at which receptors are synthesized is such that receptor degradation is exactly balanced by receptor synthesis. This assumption is introduced in order to have a constant number of "particles" in our model. This assumption could be relaxed by considering N_{R} as a random variable included in the model rather than as a model parameter.

In Table 1.2, the variables bearing the superindex "i" are the *internalized* counterparts of the *surface* variables, which bear no index. The physical meaning of the "surface" variables is the same as in Model 2. For example, X_1 is the number

of surface dimers bound to a single SH2 domain, whereas X_1^i is the number of internalized dimers bound to a single SH2 domain. The total number of bound SH2 dimers is now $S \equiv X_1 + X_1^i + 2(X_2 + X_2^i) + 3(X_3 + X_3^i) + 4(X_4 + X_4^i)$.

The model summarised in Table 1.2 will be hereafter referred to as Model 3. Models 1 and 2 are considered as sub-models of Model 3.

3 Model Analysis: WKB Approximation

The methodology we use to analyse the models presented in Sect. 2, originally proposed within the field of chemical physics, is due to Van Kampen (1992) and Kubo et al. (1973).[4] This technique essentially consists of extending the form of the equilibrium probability density to a non-equilibrium setting. In thermodynamic systems, the equilibrium probability density is given by:

$$\Psi_e(\mathbf{X}) = C \exp(-\Phi_e(\mathbf{X})), \tag{1.2}$$

where C is the normalization constant, $\mathbf{X}$ a set of extensive variables, whose values determine the state of the system and the function $\Phi_e(\mathbf{X})$ has the properties of a thermodynamic potential, i.e. is a homogeneous function:

$$\Phi_e(\mathbf{X}) = N\phi_e(\mathbf{x}); \ \mathbf{x} = \frac{\mathbf{X}}{N}, \tag{1.3}$$

where N is the size of the system which, for example, can correspond to the number of particles. From these two equations, we can see that $\Psi_e(\mathbf{X})$ is the probability density for fluctuations of the macroscopic extensive variables $\mathbf{X}$ with respect to the equilibrium state, as $\Psi_e(\mathbf{X})$ is a Boltzmann-like function, i.e. the exponential of an homogeneous function which plays the role of thermodynamic potential.

Kubo et al. (1973) have proved that, under the appropriate scaling substitution, the time-dependent solution of the ME can be approximated by a function of the same form as its equilibrium solution (1.2), namely, the exponential of a homogeneous function, which we call S, of $\mathbf{X}$:

$$\Psi(\mathbf{X}, t) = C \exp(-S(\mathbf{X}, t)) = C \exp(-Ns(\mathbf{x}, t)). \tag{1.4}$$

Intuitively, the accuracy of this approximation can be assessed in terms of the comparison between the characteristic time scale associated with the disturbance that drives the system out of equilibrium and the time scale of the phenomena occurring locally in the system. If the former is much shorter than the latter (which

[4]Within the statistical physics community, this approximation is often referred to as the *eikonal* approximation.

usually happens in weak noise limits), the system may be considered locally in equilibrium. From a more rigorous point of view, Van Kampen (1992) have shown that the extensive variables exhibit the following asymptotic behaviour

$$\mathbf{X}(t) = \langle \mathbf{X}(t) \rangle + \boldsymbol{\xi}(t) N^{1/2} \text{for} N \gg 1, \tag{1.5}$$

where $\langle \mathbf{X}(t) \rangle$ is the solution of the macroscopic equations, i.e. the average value of X and $\boldsymbol{\xi}$ is a Gaussian random variable. This equation reveals that out of equilibrium the fluctuations of an extensive Markovian variable around its mean value depend on the volume in the same way as in equilibrium. Thus, this fact justifies the substitution of (1.4).

Let us consider a system whose stochastic dynamics is described by the ME:

$$\frac{\partial \Psi(\mathbf{X}, t)}{\partial t} = \sum_{\mathbf{r}} \left(W(\mathbf{X} - \mathbf{r}, \mathbf{r}, t) \Psi(\mathbf{X} - \mathbf{r}, t) - W(\mathbf{X}, \mathbf{r}, t) \Psi(\mathbf{X}, t) \right). \tag{1.6}$$

Kubo et al. (1973) have shown that the transition rates $W(\mathbf{X}, \mathbf{r}, t)$ must be homogeneous functions of $\mathbf{X}$ to obtain a solution of the ME of the form of (1.4):

$$W(\mathbf{X}, \mathbf{r}, t) \; = \; N a(\mathbf{x}, \mathbf{r}, t). \tag{1.7}$$

Accordingly, the probability of a given reaction to occur within an infinitesimal interval of time is proportional to the size of the system and is determined only by the state of the system, represented by the set of intensive variables $\mathbf{x}$. The following definition:

$$\psi(\mathbf{x}, t) \; = \; N \Psi(\mathbf{X}, t), \tag{1.8}$$

together with (1.7), enables us to write the ME (1.6) in WKB form:

$$\frac{1}{N} \frac{\partial \psi(\mathbf{x}, t)}{\partial t} \; = \; \sum_{\mathbf{r}} \left(\mathrm{e}^{-\frac{\mathbf{r}}{N} \cdot \frac{\partial}{\partial \mathbf{x}}} - 1 \right) a(\mathbf{x}, \mathbf{r}, t) \psi(\mathbf{x}, t), \tag{1.9}$$

where we have used that $\mathrm{e}^{-\mathbf{r} \cdot \frac{\partial}{\partial \mathbf{x}}}$ is the generator of the translations in the space of states of the system.

For arbitrary n, the scaling substitution for the cumulants of the probability distribution (for example: $(q_1)_i \; = \; \langle x_i \rangle$; $(q_2)_{ij} \; = \; \langle x_i x_j \rangle - \langle x_i \rangle \langle x_j \rangle$ and so on) $q_n(t) = \epsilon^{n-1} q_{n1}(t) + \epsilon^n q_{n2}(t) + O(\epsilon^{n+1})$ yields a consistent expansion leading to balanced equations for the cumulants $q_n(t)$. Eventually, this leads to the following equation for the leading order term for $q_1(t)$:

$$\dot{q}_{11}(t) = \sum_{\mathbf{r}} \mathbf{r} \frac{1}{(2\pi)^d} \int_{-\infty}^{\infty} \mathrm{d}\mathbf{v} \, \mathrm{e}^{-i \mathbf{v} \cdot q_{11}} w(\mathbf{v}, \mathbf{r}, t) = \mathtt{c}(q_{11}, t), \tag{1.10}$$

where $w(\mathbf{v}, \mathbf{r}, t)$ is the Fourier transform of $a(\mathbf{x}, \mathbf{r}, t)$ and the quantity $\mathsf{c}(q_{11}, t)$ is defined by:

$$\mathsf{c}(q_{11}, t) = \sum_{\mathbf{r}} \mathbf{r}\, a(q_{11}(t), \mathbf{r}, t). \tag{1.11}$$

Note that this is the result predicted by the Law of Mass Action. Likewise, the equation for the cumulants of order 2 is given by:

$$\dot{\mathsf{Q}}_{ij}(t) = \sum_{k} \left(\mathsf{Q}_{ik} \frac{\partial \mathsf{c}_j(q_{11}, t)}{\partial q_{11k}} + \frac{\partial \mathsf{c}_i(q_{11}, t)}{\partial q_{11k}} \mathsf{Q}_{kj} \right) + \sum_{\mathbf{r}} r_i r_j a(q_{11}, \mathbf{r}, t), \tag{1.12}$$

where $\mathsf{Q}_{ij} \equiv (q_{21})_{ij}$ and the first term on the right-hand side has been symmetrised (q_{21} is a symmetrical matrix). Equations (1.10) and (1.12) are our final result and constitute the generalisation to arbitrary dimension of the results obtained by Kubo et al. (1973).[5] A detailed proof of these results is given in the supplementary material that accompanies this paper. This supplementary material includes also an alternative derivation using stochastic calculus rather than assymptotic methods.

3.1 Evolution Equations for the VEGFR Model

The results obtained in Sect. 3 are valid in general, as long as the transition rates in the ME fulfil the homogeneity condition stated by (1.7). In this Section we apply these results to the particular case of Model 3 described in Sect. 2, i.e. we use (1.10) and (1.12) to formulate the systems of ODEs for the leading order contributions to the first and second cumulants (i.e. the first and second moments, respectively). Model 3 is the most general of the three described in Sect. 2. Models 1 and 2 can be obtained as particular cases of Model 3 as detailed later.

The conservation laws $u + u^i + b + b^i + 2\sum_j (x_j + x_j^i) = n_R$ and $s_{\mathrm{F}} = n_s - s_B$ (s_{F} standing for the fraction of unbound SH2 domains) are used and the quantities $N \equiv N_{\mathrm{R}} + N_S$, $n_R \equiv N_{\mathrm{R}}/N$ and $n_s \equiv N_s/N$, $s_B = x_1 + 2x_2 + 3x_3 + 4x_4$ have been defined. L stands for the concentration of ligand, in this particular case VEGF. We assume the so-called *excess of ligand* regime, namely, the concentration of (free) ligand is not affected by binding (Sulzer et al. 1996). $N(t = 0) = 2.3 \cdot 10^5$ (see Table 1.1). The evolution equations corresponding to Model 2 can be obtained from (1.13)–(1.26) by setting $k_{\mathrm{in}}^{\mathrm{nd}} = 0$, $k_{\mathrm{in}}^{\mathrm{d}} = 0$, $k_{\mathrm{re}} = 0$, $k_d = 0$, and $k_s = 0$. The equations for Model 1 are (1.13)–(1.14) with $k_{\mathrm{in}}^{\mathrm{nd}} = 0$, $k_{\mathrm{re}} = 0$ and $k_s = 0$.

By substituting the corresponding values of $a(\mathbf{x}, \mathbf{r}, t)$ and $\mathbf{r}$ from Model 3 Table 1.1 in Alarcón and Page (2007) into (1.10) we obtain:

[5] Kubo et al. (1973) states the multidimensional result without a proof.

$$\frac{\mathrm{d}u}{\mathrm{d}t} = k_{\mathrm{off}} b - k_{\mathrm{on}} L u + k^x_{\mathrm{off}} x_0 - k^x_{\mathrm{on}} \pi \Delta^2 \rho u b - k^{\mathrm{nd}}_{\mathrm{in}} u$$
$$+ k_{\mathrm{re}}(u^i + b^i) + 2k_d(x^i_0 + x^i_1 + x^i_2 + x^i_3 + x^i_4) \tag{1.13}$$

$$\frac{\mathrm{d}b}{\mathrm{d}t} = k_{\mathrm{on}} L u + k^x_{\mathrm{off}} x_0 - k_{\mathrm{off}} b - k^x_{\mathrm{on}} \pi \Delta^2 \rho u b - k^{\mathrm{nd}}_{\mathrm{in}} b \tag{1.14}$$

$$\frac{\mathrm{d}x_0}{\mathrm{d}t} = -k^x_{\mathrm{off}} x_0 + k^x_{\mathrm{on}} \pi \Delta^2 \rho u b + k^s_{\mathrm{off}} x_1 - k^{\mathrm{d}}_{\mathrm{in}} x_0 - \frac{4k^s_{\mathrm{on}}}{V_c N_A} x_0 s_{\mathrm{F}} \tag{1.15}$$

$$\frac{\mathrm{d}x_1}{\mathrm{d}t} = \frac{4k^s_{\mathrm{on}}}{V_c N_A} x_0 s_{\mathrm{F}} - k^s_{\mathrm{off}} x_1 + 2k^s_{\mathrm{off}} x_2 - k^{\mathrm{d}}_{\mathrm{in}} x_1 - \frac{3k^s_{\mathrm{on}}}{V_c N_A} x_1 s_f \tag{1.16}$$

$$\frac{\mathrm{d}x_2}{\mathrm{d}t} = \frac{3k^s_{\mathrm{on}}}{V_c N_A} x_1 s_f - 2k^s_{\mathrm{off}} x_2 + 3k^s_{\mathrm{off}} x_3 - k^{\mathrm{d}}_{\mathrm{in}} x_2 - \frac{2k^s_{\mathrm{on}}}{V_c N_A} x_2 s_{\mathrm{F}} \tag{1.17}$$

$$\frac{\mathrm{d}x_3}{\mathrm{d}t} = \frac{2k^s_{\mathrm{on}}}{V_c N_A} x_2 s_{\mathrm{F}} - 3k^s_{\mathrm{off}} x_3 + 4k^s_{\mathrm{off}} x_4 - k^{\mathrm{d}}_{\mathrm{in}} x_3 - \frac{k^s_{\mathrm{on}}}{V_c N_A} x_3 s_{\mathrm{F}} \tag{1.18}$$

$$\frac{\mathrm{d}x_4}{\mathrm{d}t} = \frac{k^s_{\mathrm{on}}}{V_c N_A} x_3 s_{\mathrm{F}} - 4k^s_{\mathrm{off}} x_4 - k^{\mathrm{d}}_{\mathrm{in}} x_4 \tag{1.19}$$

$$\frac{\mathrm{d}u^i}{\mathrm{d}t} = k^{\mathrm{nd}}_{\mathrm{in}} u - k_{\mathrm{re}} u^i \tag{1.20}$$

$$\frac{\mathrm{d}b^i}{\mathrm{d}t} = k^{\mathrm{nd}}_{\mathrm{in}} b - k_{\mathrm{re}} b^i \tag{1.21}$$

$$\frac{\mathrm{d}x^i_0}{\mathrm{d}t} = k^{\mathrm{d}}_{\mathrm{in}} x_0 - k_d x^i_0 \tag{1.22}$$

$$\frac{\mathrm{d}x^i_1}{\mathrm{d}t} = k^{\mathrm{d}}_{\mathrm{in}} x_1 - k_d x^i_1 \tag{1.23}$$

$$\frac{\mathrm{d}x^i_2}{\mathrm{d}t} = k^{\mathrm{d}}_{\mathrm{in}} x_2 - k_d x^i_2 \tag{1.24}$$

$$\frac{\mathrm{d}x^i_3}{\mathrm{d}t} = k^{\mathrm{d}}_{\mathrm{in}} x_3 - k_d x^i_3 \tag{1.25}$$

$$\frac{\mathrm{d}x^i_4}{\mathrm{d}t} = k^{\mathrm{d}}_{\mathrm{in}} x_4 - k_d x^i_4. \tag{1.26}$$

Likewise, a system of ODEs can be written for $q_{21}(t)$. This quantity is a symmetric 13×13[6] matrix and, therefore, has 91 independent components. Hence, the corresponding ODE system has 91 equations. Furthermore, this system of 91

[6]The system (1.13)–(1.26) has 14 equations but the conservation law $u + u^i + b + b^i + 2\sum_j (x_j + x^i_j) = n_R$ allows us to reduce the dimensionality of the system by one unit.

ODEs is coupled to (1.13)–(1.26).[7] As a result, a full analysis of the fluctuations for the proposed model implies a system of 104 ODEs. In general, for a system with dimension d, the system of ODEs determining the dynamics of the first- and second-order cumulants at leading order has $d(d+3)/2$ equations. In fact, this is the most serious shortcoming of the method presented here: the size of the resulting system of ODEs makes the analysis painstaking, even for modestly complex models like the one given in Table in Alarcón and Page (2007). With some degree of uncertainty in the parameter values and 104 equations, further simplification seems necessary. Consequently, only the behaviour of the mean value of the full model of Table in Alarcón and Page (2007) ((1.13)–(1.26)) is analysed. However, if we restrict ourselves to the receptor model described in Table 1.1 in Alarcón and Page (2007), we obtain a system that we can easily handle.

Using (1.12) and Table 1.1 in Alarcón and Page (2007), the equations for the fluctuations of u and b corresponding to the receptor model read:

$$\begin{aligned}\frac{\mathrm{d}\mathsf{Q}_{11}}{\mathrm{d}t} &= -\left(k_{\mathrm{on}}L + k^x_{\mathrm{off}} + k^x_{\mathrm{on}}\pi\Delta^2\rho b\right)\mathsf{Q}_{11}\\ &\quad + \left(k_{\mathrm{off}} - k^x_{\mathrm{off}} - k^x_{\mathrm{on}}\pi\Delta^2\rho u\right)\mathsf{Q}_{12}\\ &\quad + \left(k_{\mathrm{on}}Lu + k_{\mathrm{off}}b + k^x_{\mathrm{on}}\pi\Delta^2\rho ub\right.\\ &\qquad \left. + k^x_{\mathrm{off}}(n_r - u - b)\right) \qquad (1.27)\\ \frac{\mathrm{d}\mathsf{Q}_{22}}{\mathrm{d}t} &= -\left(k_{\mathrm{off}} + k^x_{\mathrm{off}} + k^x_{\mathrm{on}}\pi\Delta^2\rho u\right)\mathsf{Q}_{22}\\ &\quad + \left(k_{\mathrm{on}}L - k^x_{\mathrm{off}} - k^x_{\mathrm{on}}\pi\Delta^2\rho b\right)\mathsf{Q}_{12}\\ &\quad + \left(k_{\mathrm{on}}Lu + k_{\mathrm{off}}b + k^x_{\mathrm{on}}\pi\Delta^2\rho ub\right.\\ &\qquad \left. + k^x_{\mathrm{off}}(n_r - u - b)\right) \qquad (1.28)\\ \frac{\mathrm{d}\mathsf{Q}_{12}}{\mathrm{d}t} &= -\left(k_{\mathrm{on}}L + k^x_{\mathrm{off}} + k^x_{\mathrm{on}}\pi\Delta^2\rho b\right))\mathsf{Q}_{11}\\ &\quad - \left(k_{\mathrm{off}} + k^x_{\mathrm{off}} + k^x_{\mathrm{on}}\pi\Delta^2\rho u\right)\mathsf{Q}_{22}\\ &\quad - \left(AL + k_{\mathrm{off}} + k^x_{\mathrm{off}}\right.\\ &\qquad \left. + k^x_{\mathrm{on}}\pi\Delta^2\rho(u+b)\right)\mathsf{Q}_{12}\\ &\quad + \left(-k_{\mathrm{on}}Lu - k_{\mathrm{off}}b + k^x_{\mathrm{on}}\pi\Delta^2\rho ub\right.\\ &\qquad \left. + k^x_{\mathrm{off}}(n_r - u - b)\right) \qquad (1.29)\end{aligned}$$

[7] In fact, this method produces a hierarchy of "kinetic" equations where the cumulants of order n depend on the all the cumulants of order up to $n-1$.

where $\mathsf{Q}_{ij} = \mathsf{Q}_{ji}$. Q_{11} and Q_{22} correspond to the variance of u and b, respectively. These equations are to be solved together with (1.13) and (1.14) with $k_{\text{in}}^{\text{nd}} = 0$, $k_{\text{re}} = 0$ and $k_s = 0$. Using the conservation law $x = (n_R - u - b)/2$, we obtain the following expression for the variance of x, Q_{33}, in terms of the dependent variables of (1.27)–(1.29): $Q_{33} = (Q_{11} + Q_{22} + 2Q_{12})/4$.

It is important to bear in mind that, whilst the dynamics of the mean value of the variables corresponding to the receptor model (u, b and x) is unaffected by the dynamics of the intracellular SH2 domains, the dynamics of the fluctuations (q_{21}) of the receptor variables depends on fluctuations and mean values of SH2 variables. Therefore, whereas our restricted analysis may provide useful insights, its conclusions should not be applied to the dynamics of the fluctuations of the whole system.

4 Perfect and Imperfect Adaptation

Growth factors (GFs) are extracellular signalling molecules that bind a type of surface receptors called receptor tyrosine kinases (RTKs). Upon receptor binding, these molecules stimulate cell growth and differentiation. Most growth factors, however, can also induce a variety of other cellular responses depending on the particular context and the cell type they are acting on Alberts et al. (2002), Helmreich (2001). The wide range of cellular responses in addition to growth and differentiation goes from cell division to chemotactic behaviour. Growth factor signalling is also instrumental for activation of survival pathways in many types of cells (Alberts et al. 2002).

Many GFs have been shown to have chemotactic effects on different types of cells. Some examples are the vascular endothelial growth factor (VEGF) (Terranova et al. 1985; Lash et al. 2003), platelet-derived growth factor (PDGF) (Grotendorst et al. 1982; Klominek et al. 1998; Shneider and Haugh 2005), hepatocyte growth factor (Ebens et al. 1996; Ohshima et al. 2001), nerve growth factor (Sawada et al. 2000) and transforming growth factor $\beta 1$ (Reibman et al. 1991) among others.

A common feature of chemotactic (or, more precisely, chemokinetic) systems is their ability to, upon stimulation with a chemotactic ligand, adapt or desensitise after a short excitation transient. This means that the cell response terminates regardless of the presence of the ligand: after the initial excitation in response to the ligand the system relaxes to a "background" state which is independent of the concentration of ligand. Only a change in ligand concentration will induce a new cellular response (resensitation), which will eventually decay again (Knox et al. 1986; Tyson et al. 2003). This behaviour has been demonstrated experimentally in chemotactic bacteria (Alon et al. 1999) and several theoretical models have been proposed (Spiro et al. 1997; Yi et al. 2000). A model that appears to reproduce the chemotactic behaviour of some eukaryotic cells (amoebae and neutrophils) has been recently proposed which also accounts for excitation and perfect adaptation (Levchenko and Iglesias 2002). Although perfect adaptation is regarded as an

important componentin gradient-sensing systems, recent experiments combined with mathematical modeling (Shneider and Haugh 2005) have shown that the chemotactic response of fibroblasts to gradients of PDGF does not involve perfect adaptation. Shneider and Haugh (2005) have rather shown that fibroblasts exhibit transient activation of the PDGF receptors (i.e. an activation peak in response to stimulation with PDGF followed by a relaxation to a steady state value) but not perfect adaptation.

On the other hand, other cell responses such as differentiation are better described in terms of a *switch-like* behaviour in which the response is activated and sustained over time (Marshall 1995). Furthermore, GF-induced proliferation seems to be triggered by a transient activation without perfect adaptation (Marshall 1995).

The question arises as to how a single system (i.e. the GF/RTK system) is able to produce such different cell responses as chemotaxis (perfect adaptation), proliferation (transient response without perfect adaptation) and differentiation (sustained activation), as there seems to be no specific pathway for each of these responses. Our aim in this paper is to formulate a simple mathematical model that accounts for the basic mechanisms involved in the onset of GF-induced signalling (GF-induced dimerisation, receptor endocytosis and receptor synthesis and degradation) and can explain the three different cell behaviours described earlier. We will show that downregulation of internalised receptor degradation leads to perfect adaptation whereas upregulation of either receptor synthesis or internalised receptor degradation produces a sustained response. Similar results have been reported by Vilar et al. (2006) in a different context.

4.1 The Model

The model (Model 4) we consider to study how different cellular responses can be elicited by the same sensory system is a sub-model of Model 3, where we consider ligand binding and receptor endocytosis and recycling.

We further assume that all the internalised RTK dimers, x_i, are degraded in the lysosomes (without considering the two intermediate compartments described in the Introduction). We will also assume that no internalised dimers are recycled back to the surface. We also assume that a fraction of inactive receptors, f_u and f_b for unbound and GF/RTK complexes, respectively, passes into the lysosome for degradation, whereas the rest is recycled and sent back to the cell surface, $1-f_u$ and $1-f_b$ for unbound and GF/RTK complexes, respectively (Lauffenburger and Linderman 1993). All the receptors sent to the lysosomes are assumed to be degraded at the same rate, k_d.

Receptor synthesis is assumed to produce receptors that are incorporated in the surface, increasing u at a rate $K_s(x)$. Different models for $K_s(x)$ are considered and discussed in Sect. 4.2.

The corresponding ODE system for the evolution of our model is given by:

$$\frac{\mathrm{d}u}{\mathrm{d}t} = k_{\mathrm{off}}b - k_{\mathrm{on}}Lu + k^{x}_{\mathrm{off}}x - K_{\mathrm{cl}}(y_s)ub - k^{\mathrm{nd}}_{\mathrm{in}}u + k^{u}_{\mathrm{re}}u_{\mathrm{re}} + k^{b}_{\mathrm{re}}b_{\mathrm{re}} + K_s(x) \tag{1.30}$$

$$\frac{\mathrm{d}b}{\mathrm{d}t} = k_{\mathrm{on}}Lu + k^{x}_{\mathrm{off}}x - k_{\mathrm{off}}b - K_{\mathrm{cl}}(y_s)ub - k^{\mathrm{nd}}_{\mathrm{in}}b \tag{1.31}$$

$$\frac{\mathrm{d}x}{\mathrm{d}t} = -k^{x}_{\mathrm{off}}x + K_{\mathrm{cl}}(y_s)ub - k^{\mathrm{d}}_{\mathrm{in}}x \tag{1.32}$$

$$\frac{\mathrm{d}u_{\mathrm{re}}}{\mathrm{d}t} = k^{\mathrm{nd}}_{\mathrm{in}}(1-f_u)u - k^{u}_{\mathrm{re}}u_{\mathrm{re}} \tag{1.33}$$

$$\frac{\mathrm{d}u_{md}}{\mathrm{d}t} = k^{\mathrm{nd}}_{\mathrm{in}}f_u u - k^{u}_{d}u_{md} \tag{1.34}$$

$$\frac{\mathrm{d}b_{\mathrm{re}}}{\mathrm{d}t} = k^{\mathrm{nd}}_{\mathrm{in}}(1-f_b)b - k^{b}_{\mathrm{re}}b_{\mathrm{re}} \tag{1.35}$$

$$\frac{\mathrm{d}b_{md}}{\mathrm{d}t} = k^{\mathrm{nd}}_{\mathrm{in}}f_b b - k^{b}_{d}b_{md} \tag{1.36}$$

$$\frac{\mathrm{d}x_i}{\mathrm{d}t} = k^{\mathrm{d}}_{\mathrm{in}}x - k^{x}_{d}x_i \tag{1.37}$$

$$y(t) = u(t) + b(t) + 2x(t) + u_{\mathrm{re}}(t) + u_{md}(t) + b_{\mathrm{re}}(t) + b_{md} + 2x_i(t). \tag{1.38}$$

where $y_s = u + b + 2x$ is the proportion of surface receptors.

4.2 Models of Dimer-Formation Rate and Receptor Synthesis

We consider a number of different models for the rate of formation of receptor dimers out of an unbound RTK and a GF/RTK complex. In particular, we consider three different models: density-limited model (Alarcón and Page 2007), diffusion-limited (Lauffenburger and Linderman 1993) and, for comparison, $K_{\mathrm{cl}}(y_s) =$ constant. The models we use and the corresponding expressions for $K_{\mathrm{cl}}(y_s)$ are summarised in Table 1.3.

All these models have been considered in detail somewhere else and, consequently, we only give here a general summary.

The density-limited model considers that the *intrinsic* cross-linking rate needs to be corrected by a factor which depends on the probability of finding an unbound RTK within a distance Δ of a GTK/RTK complex, which is proportional to the surface density of RTK and the surface of a region of radius Δ. The expression given in Table 1.3 follows immediately (see Alarcón and Page 2007 for more details).

Table 1.3 Different scenarios considered in the present work

Models for $K_{\mathrm{cl}}(y)$		
Density-limited model	$K_{\mathrm{cl}}(y_s) = k_{\mathrm{on}}^x \pi \Delta^2 N_{\mathrm{R}} \frac{y_s}{S_c}$	Alarcón and Page (2007)
Diffusion-limited model	$K_{\mathrm{cl}}(y_s) = \left(\frac{\ln(r_0/2\Delta)}{2\pi D} + \frac{1}{k_{\mathrm{on}}^x} \right)^{-1}$	Lauffenburger and Linderman (1993)
Constant	$K_{\mathrm{cl}}(y_s) = \overline{k}_{\mathrm{on}}^x$	–
Models for $K_s(x)$		
Constant	$K_s(x) = k_s$	Alarcón and Page (2007)
Receptor activation-dependent model	$K_s(x) = k_s \frac{x}{x_h + x}$	–

In this Table $r_0 = (S_c/\pi N_R y_s)^{1/2}$ (see Lauffenburger and Linderman (1993) for a full account) and $y_s = u + b + 2x$, i.e. the proportion of receptors on the surface of the cell

The diffusion-limited model is the result of assuming that the unbound receptors diffuse with respect to a given bound receptor and that when they are close enough, at a distance $r = \Delta$, they bound to each other at a rate k_{on}^x. This condition is mathematically imposed as a boundary condition on the stationary diffusion problem. To close the problem properly, a second boundary condition that prescribes a *bulk* the concentration of unbound receptors at $r = r_0$ is imposed. The parameter r_0 is one half of the average distance between receptors and is given by $r_0 = (S_c/\pi N_R y_s)^{1/2}$. The reader is referred to Lauffenburger and Linderman (1993) for a detailed account.

4.3 Parameter Values

The parameter values used in our simulations are summarised in Table 1.1. Estimation of the parameter values corresponding to the ligand binding and receptor dimerisation has been described in detail in Alarcón and Page (2007). Regarding the parameter values of the part of the model corresponding to receptor internalisation and synthesis, a detailed discussion follows.

The processes of endocytosis, recycling and degradation of surface receptors have been analysed in order to elucidate whether this processes depend on receptor occupancy, in other words whether they are affected by the receptors being free or bound to a GF molecule, or kinase activity (Mitchell et al. 2004; Wiley 1991).

Endocytosis appears to be dependent on kinase activity, rather than purely on receptor occupancy. Wiley (1991) found that active receptors are internalised at a rate about ten times higher than free or bound but inactive receptors. Hence, in our model, the internalisation rates of non-dimerised receptors, i.e. unbound and GF/RTK complexes, are assumed to be equal, $k_{\mathrm{in}}^{\mathrm{nd}}$. According to the values given in Table 1.1, the internalisation rate of dimerised (active) receptors, $k_{\mathrm{in}}^{\mathrm{d}}$, is ten times bigger than $k_{\mathrm{in}}^{\mathrm{nd}}$.

Recycling of internalised receptors is thought to be independent of receptor status and, therefore, we assume that all the receptors are recycled at the same rate, $k_{\mathrm{re}}^{u} = k_{\mathrm{re}}^{b} = k_{\mathrm{re}}$, regardless of receptor type (Mitchell et al. 2004; Wiley 1991).

The situation with respect to receptor degradation rates seems to be less clear. Whereas there is some consensus with respect the two previous points, the behaviour of receptor degradation has been observed to differ in different experimental situations. For example, whilst (Mitchell et al. 2004) find that receptors in the TGF-β/TIR1/TIR2 system are degraded at the same rate regardless of receptor occupation, Wiley (1991) report that receptor degradation depends on receptor occupation but not on kinase activity: degradation is accelerated upon receptor binding in a kinase-activity independent way. Here, we assume that $k_d^x = k_d^u = k_d^b = k_d$ (see Table 1.1).

Regarding the rate of receptor synthesis, we have followed the same procedure as in Alarcón and Page (2007), namely, we fix all the other parameter values and then fit the value of k_s to obtain a sensible total receptor number (of the order of 10^4) for experimentally achievable GF concentrations (between $L = 0.01$ nM and $L = 10$ nM). The result is the value given in Table 1.1.

5 Results: Anti-VEGF Therapy

We now proceed to summarise our main results for the models presented in the previous sections. We start by presenting our modeling results for the analysis regarding anit-angiogenic therapy using Models 1, 2, and 3 in Alarcón and Page (2007). We then move on to present our results regarding perfect adaptation behaviour of the VEGFR system.

5.1 Receptor Dimerisation Induces Non-monotonic Response Functions

Response functions characterise the cellular response to stimulation with a given concentration of ligand, VEGF in our case. Depending on the model, they can be given in terms of the steady state of dimerised receptors (Sulzer et al. 1996) or in terms of the peak values of receptor activation (Park et al. 2003). A property that Models 2 and 3 in Alarcón and Page (2007) inherit from Model 1 is that fact that the corresponding response functions are not monotonic. The leading order equations in the WKB approximation for Model 1 are given in terms of dimensionless quantities (see Alarcón and Page 2007) read:

$$\begin{aligned}
\frac{\mathrm{d}u}{\mathrm{d}t} &= b - ALu + \frac{k_{\mathrm{off}}^x}{2}(n_R - u - b) - k_{\mathrm{on}}^x \pi \Delta^2 \rho u b \\
\frac{\mathrm{d}b}{\mathrm{d}t} &= ALu + \frac{k_{\mathrm{off}}^x}{2}(n_R - u - b) - b - k_{\mathrm{on}}^x \pi \Delta^2 \rho u b
\end{aligned} \tag{1.39}$$

which in steady state correspond to:

$$b_* - \mathrm{AL}u_* = 0 \tag{1.40}$$

$$n_R - (1 + \mathrm{AL})u_* - 2A_x AL\pi\Delta^2\rho u_*^2 = 0. \tag{1.41}$$

We can see that if $AL \gg 1$ then $u_* = O(\epsilon)$ and $b_* = n_R - O(\epsilon)$ with $\epsilon = (\mathrm{AL})^{-1}$. If $AL \ll 1$, $u_* = n_R - O(\epsilon)$ and $b_* = O(\epsilon)$ with $\epsilon = AL$. In both cases the number of dimerised receptors is so small that it is impossible for the cell to produce a response. Equations (1.40) and (1.41) yield the following solution for the steady state of the receptor model:

$$u_* = \frac{-(1 + \mathrm{AL}) + \sqrt{(1 + \mathrm{AL})^2 + 8n_R A_x AL\pi\Delta^2\rho}}{4A_x AL\pi\Delta^2\rho} \tag{1.42}$$

$$b_* = \mathrm{AL}u_* \tag{1.43}$$

$$x_* = \frac{1}{2}(n_R - (1 + \mathrm{AL})u_*). \tag{1.44}$$

The corresponding response curve $x_*(\mathrm{AL})$ (Sulzer et al. 1996) is shown in Fig. 1.1a, where we can appreciate that it is bell-shaped (in log(AL)) rather monotonously growing.

Models 2 and 3 in Alarcón and Page (2007), of which Model 1 is a sub-model, have a much more complex dynamics than the latter and they are not amenable to such straightforward analysis. However, when we look at their characteristic response curves in terms of the height of corresponding activation peaks as a function of AL (Fig. 1.1b), we observe that it exhibits a non-monotonic behaviour inherited from Model 1. In other words, in either model large concentrations of VEGF inhibit cellular response. Although the experimental evidence for such behaviour may not be extensive, the work by Cai et al. (2006) appears to point in that direction, Cai et al. (see Fig. 5c of Cai et al. (2006)) have found that the proliferative activity induced by VEGF on retinal microvascular ECs is a bimodal function of the concentration of VEGF. Thus, both experiments and theory point to an inhibition of the cellular response for high ligand concentration, although our models do not predict the bimodal response curve found by Cai et al. (2006).

This property of the function response of the VEGF receptor has obvious consequences on anti-VEGF therapies: reducing the (effective) concentration of VEGF may not yield the expected result, i.e. a reduction on EC response, as this appears not to exhibit a non-monotonous dependence on ligand concentration.

5.2 *The Dynamical Behaviour of the VEGFR Strongly Depends on Ligand Concentration*

Another factor that may affect the effectiveness of anti-VEGF therapies is related to how the *relaxation time*, τ, i.e. the time the system takes to settle down to a

close-to-equilibrium state, depends on log(AL), the relaxation process being faster for larger values of log(AL). Two illustrative examples of this are shown in Fig. 8 in Alarcón and Page (2007). (a) and (b) for $\log(\mathrm{AL}) = -3$ and $\log(\mathrm{AL}) = 1$, respectively.

From these numerical results and the model equations we can see that $\tau(L) \simeq O(\mathrm{AL})^{-1}$. This implies that, in the pathological situation this model is aimed to reproduce, the stationary response of the system for $L = 10^{-7}$ M has the same intensity as that for $L = 10^{-13}$ M, but whereas in the former case this response built up in a time of the order of $\tau(L = 10^{-7}) \simeq 10^{-3}$, in the later the time required is $\tau(L = 10^{-13}) \simeq 10^{3}$, which in dimensional terms corresponds to 0.0167 min and 16667 min, respectively. The reader should note that values of $L = 10^{-7}$ M (100 nM) for the VEGF concentration are possibly unrealistic as such high concentrations are unlikely to be found in either physiological or pathological circumstances. We are only using these extreme values here to illustrate our point.

5.3 Upregulation of VEGFR Expression Contributes to Resistance to Anti-VEGF Therapy

An observation with respect to the physiological situation described by Model 3 is that blocking receptor endocytosis appears to induce an important change in the dynamical behaviour of the system. Whilst Model 3 supports a scenario in which there is a fast, transient (a peak in receptor) activation followed by a decay to a stationary state, Model 2 suggests that, in the pathological setting, the response is slow and sustained.

This observation may have deep therapeutic significance. We have run simulations of anti-VEGF therapy to compare the responses of the physiological (Model 3) with the pathological (Model 2) situations. As in Sect. 4.1 we have performed simulations in which at some point during the evolution of the system the concentration of VEGF has been reduced from $L = 10^{-8}$ M (10 nM) to $L = 10^{-11}$ (0.01 nM) as shown in Fig. 9 in Alarcón and Page (2007). From the results shown in Alarcón and Page (2007), we observe that this therapeutic intervention, in spite of reducing the concentration of VEGF by three orders of magnitude, has had virtually no effect on the peak or steady state of the surface dimers or bound SH2 in the pathological system. Moreover, we find that the anti-VEGF therapy does much worse in the pathological than in the physiological case. A far more efficient clearance of active VEGF by the anti-VEGF drug is needed in order to produce better outcomes.

Furthermore, as the dynamics of the system has been slowed down by three orders of magnitude (from time scales of the order of magnitude of minutes to hours or days) by the reduction of ligand concentration, even if a decrease in the angiogenic activity is initially observed, angiogenic activity could resume simply because VEGF clearance by the drug was not effective enough due to inefficient VEGF clearance by the anti-VEGF agent.

From this discussion we can infer that the therapeutic outcome of an anti-VEGF drug could be improved by some strategy aimed to narrow the width of the bell-shaped stationary response curve. Results shown in Alarcón and Page (2007) show that decreasing the value of the dimerisation rate k_{on}^{x} yields such an effect. Simulation results of simultaneously reducing L and k_{on}^{x} are presented in Alarcón and Page (2007) where a substantial improvement in anti-VEGF performance when k_{on}^{x} is reduced.

6 Results: Perfect and Imperfect Adaptation

6.1 Downregulation of Inactivated Receptor Degradation Yields Perfect Adaptation

In a previous work, we have shown that absence of internalisation (and net receptor production) leads to a situation in which the stationary value of surface dimers, x_*, has a bell-shaped dependence on log(AL) (Alarcón and Page 2007), and, consequently, the corresponding system does not exhibit perfect adaptation. On the other hand, removal of the ligand-induced cross-linking from the model leads to a linear system that lacks the necessary feed-backs to produce perfect adaptation behaviour (Tyson et al. 2003). In such cases, additional elements need to be introduced in the model pathway to reproduce such behaviour (Levchenko and Iglesias 2002).

These results indicate that up- or down-regulation of the different processes involved in our model for RTK activation, i.e. receptor dimerisation, synthesis, internalisation and degradation, may lead to different dynamical behaviours corresponding to different cellular responses.

In fact, our model for RTK activation exhibits different dynamical behaviour depending on the strength of the degradation of inactive receptors. Figure 1.2 shows that upon downregulation of the degradation rate of the inactive receptors the system exhibits perfect adaptation. Otherwise, the system exhibits transient activation, i.e. a peak of activity followed by a relaxation to a steady state activation, but not perfect adaptation: the steady state value is now a function of L (see Fig. 1.2a, b).

Furthermore, the perfect adaptation behaviour observed when degradation of the inactive receptors is negligible compared to the degradation rate of active receptors is a fairly robust feature of the model with respect to model details and parameter values. To assess this issue, we analyse the steady state behaviour of (1.30)–(1.36) with $f_u = f_b = 0$:

$$k_{\text{off}}b - k_{\text{on}}Lu + k_{\text{off}}^{x}x - K_{\text{cl}}(y)ub - k_{\text{in}}^{\text{nd}}u + k_{\text{re}}^{u}u_{\text{re}} + k_{\text{re}}^{b}b_{\text{re}} + K_s(x) = 0 \quad (1.45)$$

$$k_{\text{on}}Lu + k_{\text{off}}^{x}x - k_{\text{off}}b - K_{\text{cl}}(y)ub - k_{\text{in}}^{\text{nd}}b = 0 \quad (1.46)$$

$$K_{\text{cl}}(y)ub - k_{\text{off}}^{x}x - k_{\text{in}}^{\text{d}}x = 0 \quad (1.47)$$

$$k_{\text{in}}^{\text{nd}} u - k_{\text{re}}^{u} u_{\text{re}} = 0 \tag{1.48}$$

$$k_{\text{in}}^{\text{nd}} b - k_{\text{re}}^{b} b_{\text{re}} = 0 \tag{1.49}$$

$$k_{\text{in}}^{\text{d}} x - k_{d}^{x} x_i = 0 \tag{1.50}$$

$$y = u + b + 2x + u_{\text{re}} + b_{\text{re}} + 2x_i\,. \tag{1.51}$$

We have use that for $f_u = f_b = 0\, u_{md} = b_{md} = 0$. Adding up (1.45) and (1.46), we obtain:

$$2k_{\text{off}}^{x} x - 2K_{\text{cl}}(y) ub - k_{\text{in}}^{\text{nd}}(u + b) + k_{\text{re}}^{u} u_{\text{re}} + k_{\text{re}}^{b} b_{\text{re}} + K_s(x) = 0. \tag{1.52}$$

Likewise, adding up (1.48) and (1.49) leads to:

$$k_{\text{in}}^{\text{nd}}(u + b) - k_{\text{re}}^{u} u_{\text{re}} - k_{\text{re}}^{b} b_{\text{re}} = 0 \tag{1.53}$$

which, in combination with (1.50), leads to:

$$2k_{\text{off}}^{x} x - 2K_{\text{cl}}(y) ub + K_s(x) = 0. \tag{1.54}$$

Equations (1.47) and (1.54) lead to:

$$x = \frac{K_s(x)}{2k_{\text{in}}^{d}}, \tag{1.55}$$

Thus, we conclude that, as long as the function $K_s(x)$ is such that (1.54) has a positive root, the steady state value of x will not depend on L providing the system with perfect adaptation behaviour. A feature of the system that this analysis puts forward is the independence of the perfect adaptation behaviour with respect to K_{cl}, as illustrated in the numerical simulations presented in Fig. 1.3c, d, where we have solved our model equations for constant degradation rate and constant and diffusion-limited dimerisation rate.

These analytical results are illustrated by the simulations shown in Fig. 1.3, which shows results corresponding to numerical solution of (1.30)–(1.37) with $K_{\text{cl}}(y) = k_{\text{on}}^{x} \pi \Delta^2 N_R y / S_c$ and different assumptions for receptor synthesis. We observe that both excitation and perfect adaptation are robust to changes in the model for receptor synthesis. There are however some features of the dynamics of the system that are sensitive to the value of x_h (see Table 1.3). If this parameter is chosen to be $x_h > 0.05$, receptor synthesis is not able to sustain a reasonable number of receptors on the cell surface, i.e. $y(t)$ decays towards zero (results not shown).

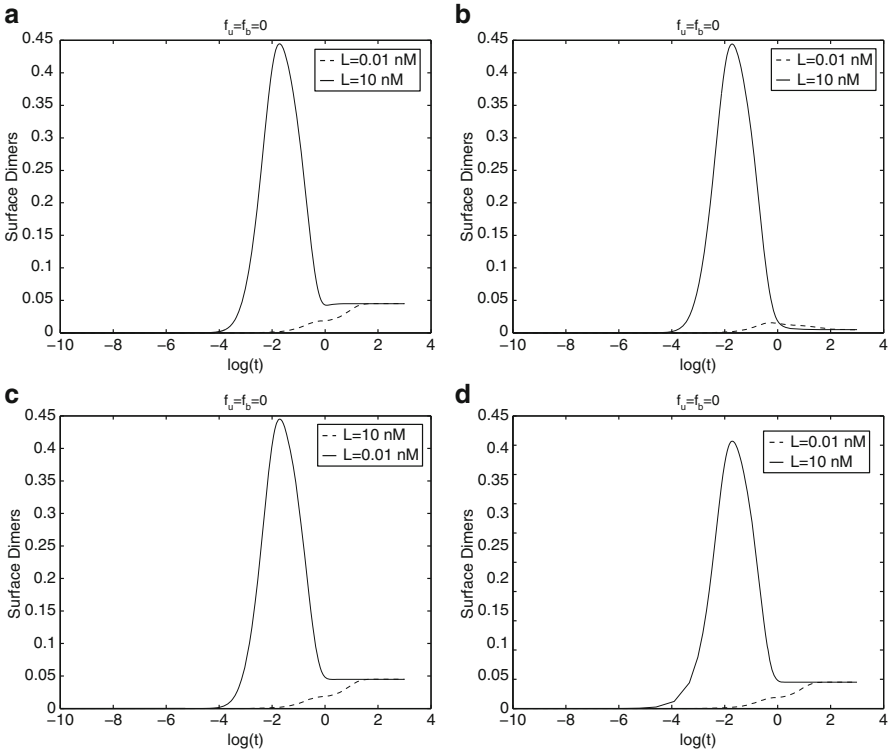

Fig. 1.3 Analysis of the robustness of the perfect adaptation behaviour. Plots (**a**) and (**b**) show simulation results corresponding to (1.30)–(1.37) with $f_u = f_b = 0$. These plots show the time course of the proportion of surface dimers, $x(t)$, with $K_{\mathrm{cl}}(y) = k_{\mathrm{on}}^x \pi \Delta^2 N_{\mathrm{R}} \frac{y}{S_c}$ for different models of receptor synthesis. (**a**) $K_s(x) = k_s$. (**b**) $K_s(x) = k_s \frac{x}{x_h + x}$ with $x_h = 0.02$. Plots (**c**) and (**d**) show simulation results corresponding to (1.30)–(1.37) with $f_u = f_b = 0$. These plots show the time course of the proportion of surface dimers, $x(t)$, with $K_s(y) = k_s$ for different models of receptor dimerisation. (**a**) $K_{\mathrm{cl}}(y_s) = \overline{k}_{\mathrm{on}}^x = 4.6 \cdot 10^3$. (bf b) $K_{\mathrm{cl}}(y) = \left(\frac{\ln(b/2\Delta)}{2\pi D} + \frac{1}{k_{\mathrm{on}}^x} \right)^{-1}$. According to Lauffenburger and Linderman (1993), $D = 10^{-9}$ cm^2/seg. For all the panels shown in this figure $k_d^x = k_d$. Key: *solid line* corresponds to $L = 10$ nM and *dashed line* to $L = 0.01$ nM. Parameter values taken from Table 1.1

6.2 *Upregulation of Receptor Synthesis Leads to Sustained Cellular Response*

In the previous section we have shown that our model predicts that downregulation of degradation of inactivated receptors leads to perfect adaptation in the RTK system. Perfect adaptation involves, in addition to a relaxation to a steady state condition which is independent of the stimulus, a transient peak of activation whose height is a function of the concentration of signalling molecule. This leads to an

scenario in which the response is triggered by the activation reaching a threshold level. The response is switched off when the activation level falls below threshold.

However, there are other situations in which the cellular response is triggered only when activation by the signalling molecule is sustained over time rather than by a transient excitation (Tyson et al. 2003; Marshall 1995). The results shown in Fig. 1.3 indicate that upregulation of receptor synthesis leads to a sustained RTK activation in response to stimulation with growth factor. We can see from Fig. 1.3b, d, and f that as the rate of receptor synthesis grows the transient response is substituted by a sustained one.

6.3 Comparison to Other Models Incorporating Receptor Dimerisation

In Sect. 6.1 we have proved that our results regarding the emergence of perfect adaptation upon downregulation of degradation of inactive RTKs is robust with respect to most of the model details. In this section we take this one step forward and prove that the mentioned results are, in fact, robust to the actual mechanism for receptor dimerisation and activation.

Park et al. (2003) have proposed an alternative model of receptor dimerisation which has been adapted by Shneider and Haugh (2005) to study the chemotactic response of fibroblasts to PDGF gradients. This model assumes a different mechanism for receptor dimerisation. They assume that the rate-limiting process is the association of two PDGF/PDGFR complexes. When this complex dimer has formed one of them releases its PDGF molecule, thus forming an active receptor dimer. This last process is assumed to be very fast. We refer the reader to the on-line supplementary material of Park et al. (2003) and Shneider and Haugh (2005) for a thorough derivation of their model.

The corresponding model, in the notation used by Shneider and Haugh (2005), is given by:

$$\frac{\mathrm{d}R}{\mathrm{d}t} = k_r C_1 - k_f L R - k_t R + k_{-x} C_2 + V_s \tag{1.56}$$

$$\frac{\mathrm{d}C_1}{\mathrm{d}t} = k_f L R - k_r C_1 - k_t C_1 + k_{-x} C_2 - 2k_x C_1^2 \tag{1.57}$$

$$\frac{\mathrm{d}C_2}{\mathrm{d}t} = k_x C_1^2 - (k_{-x} + k_e) C_2 \,, \tag{1.58}$$

where R is the concentration of free receptors, C_1 the concentration of PDGF/PDGFR complexes, C_2 the concentration of active receptor dimers, k_f and k_r are the binding and unbinding rates, respectively, k_t the rate of degradation of free and PDGF-bound receptors and k_x and k_{-x} are the dimer formation and dissociation rates, respectively.

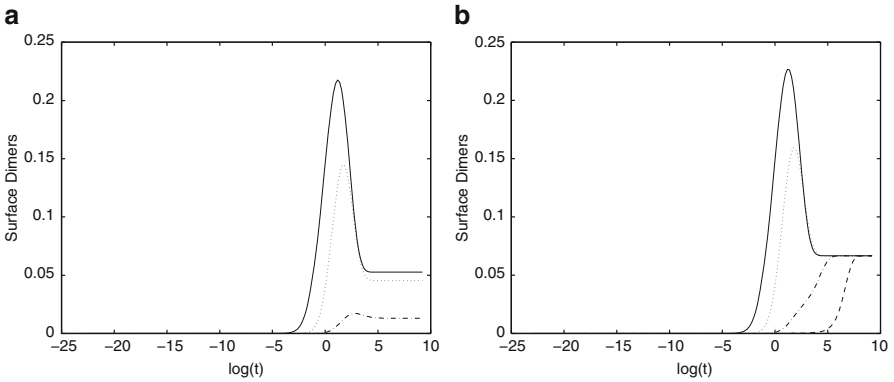

Fig. 1.4 Simulation results corresponding to (1.55)–(1.57) (Shneider and Haugh 2005). This plot shows the time course of the proportion of surface dimers, $C_2(t)$. Key: *solid line* corresponds to $L = 10$ nM, *dotted line* to $L = 1$ nM, *dot-dashed line* to $L = 0.1$ nM, and *dashed line* to $L = 0.01$ nM. Plot (**a**) corresponds to $k_t = 0.02$ min^{-1} (Shneider and Haugh 2005), whereas plot (**b**) corresponds to $k_t = 0$. Other parameter values are taken from Shneider and Haugh (2005): $k_f/k_r = 1.5$ min^{-1}nM^{-1}, $k_r = 1$ min^{-1}, $k_x = 0.3$ min^{-1}, $k_{-x} = 0.07$ min^{-1}, $k_e = 0.3$ min^{-1}, $V_s = 0.02$ min^{-1}

Figure 1.4 shows simulation results corresponding to (1.56)–(1.58) with ($k_t \neq 0$) and without ($k_t = 0$) inactive receptor degradation. The remaining parameter values are given by Shneider and Haugh (2005). We see that whereas for $k_t \neq 0$, the system exhibits a transient activation with relaxation to a steady state that depends on L, when $k_t = 0$ the system exhibits perfect adaptation. In fact, a steady state analysis with $k_t = 0$ reveals that $C_2 = V_s/2k_e$ which is independent of the concentration of growth factor.

Thus, in spite of incorporating a totally different model of activation by dimerisation, the behaviour of this model upon downregulation of inactive receptor degradation is the same as the behaviour of our model. This property, therefore, appears to be a general feature of receptor models incorporating activation by dimerisation, regardless of the particular activation mechanism involved.

7 Discussion

We have proposed a model for the ligation of the VEGF receptor by VEGF ligands which includes receptor dimerisation, endocytosis of surface VEGFR and the early events in the corresponding signalling cascade following cross-phosphorylation of dimerised receptors. The model is formulated as continuous-time Markov process and analysed using a WKB approximation on the corresponding Master Equation. Our aim is to address two different issues, namely how the dynamics of the VEGFR response may affect the outcome of anti-VEGF therapy and what mechanisms are

likely to be involved in the triggering of different cellular responses by a single sensory system (in this case, the VEGF receptor).

Concerning the former, our analysis shows that factors such as the bell-shaped curve response induced by receptor dimerisation upon ligand binding and the increased sensitivity to low VEGF concentrations due to up-regulation of surface VEGFR have a negative effect on the efficiency of anti-VEGF therapies. Bell-shaped response curves or, more generally, non-monotonic response curves (see Fig. 1.1) have the implication that, rather paradoxically, a decrease in the concentration of available ligand (VEGF) may lead to an increase in the potency of the cellular response triggered by the VEGFR reaction to the remaining ligand. On the other hand, over-expression of surface VEGFR, as observed in the endothelial cells of tumour vessels, increases their sensitivity to low levels of VEGF, thus compromising the efficiency of anti-VEGF.

We have analysed the effects of overexpression of surface receptors, including its potential effects on response to anti-VEGF treatment. We have first studied the effect of receptor overexpression by inhibition of endocytosis (Model 3).

A second way of achieving overexpression of surface receptors is by upregulation of receptor synthesis. This scenario cannot be studied within the framework of our stochastic models, as our model formulation requires a system with a constant number of particles. Instead, we have formulated a deterministic model based on the Law of Mass Action that allows us to study this situation (Model 4). The physiological scenario, characterised by the value of the rate of receptor synthesis corresponding to this model, yields a dynamical behaviour similar to the one exhibited by Model 3: an initial transient activation followed by a relaxation to a steady state. However, there is an important difference with respect to Model 3, namely, Model 4 shows perfect adaptation to the VEGF concentration. Within the framework of Model 4, the pathological case is characterised by an increased rate of receptor synthesis.

The main result of our analysis is that both mechanisms of overexpression of surface receptors lead to a substantially increased resistance to treatment with an anti-VEGF drug. In both cases the dynamical mechanism appears to be similar: the transient activation exhibited by the physiological case is replaced by a slower and more sustained response. Moreover, in both cases there is an increased sensitivity to low values of the concentration of VEGF. Model 2 exhibits close-to-full activation for concentrations as low as 10^{-5} nM (see Fig. 7 in Alarcón and Page 2007), whereas physiological activation occurs in the proximity of 1 nM (see Fig. 1.4b in Alarcón and Page (2007) and Park et al. (2003)).

In the case of Model 4, increasing the rate of receptor synthesis to pathological levels leads to a larger steady-state activation value than the one observed for physiological receptor synthesis, which means that the angiogenic response may not be shut down after the initial transient is over.

A feature that Models 2, 3 and 4 inherit from Model 1 is the inhibition of the cell response for high ligand concentrations. Although the experimental evidence for such behaviour may not be extensive, the work by Cai et al. (2006) appears to point in that direction. Figure 18b in Alarcón and Page (2007) shows their

experimental results (data extracted from Fig. 5c of Cai et al. (2006)), in which the proliferative activity induced by VEGF on retinal microvascular ECs is measured with respect to the activity of unstimulated cells. Figure 1.1b shows the peak of activated (dimerised) surface receptors as a function of L for Models 3 and 4 (in physiological conditions). We can see that both experiments and theory point to an inhibition of the cellular response for high ligand concentration. However, our models do not predict the bimodal response curve found by Cai et al. (2006).

Regarding the eliciting of different cell responses by the VEGFR, our model suggests that regulation of the rates receptor synthesis and degradation are involved in switching from transient cellular response to sustained cellular response to VEGFR ligation by VEGF ligand molecules. As these two types of response curves are usually associated with different cellular responses, we argue the regulation of these processes is involved in switching from one type of response to the other. We also show that the VEGFR system is capable of perfect adaptation, a behaviour typically associated with chemotactic response. Similar results have been obtained by Vilar et al. (2006) in the context of the TGF-β receptor.

The aim of this paper is to formulate a model which helps to understand a fundamental question in cell biology, namely, how stimulation with growth factor molecules leads to substantially different cell responses without the existence of response-specific pathways (Marshall 1995).

We have proposed a simple model of a receptor tyrosine kinase such as the VEGFR, in which the basic ingredients of its dynamics (ligand binding, growth factor-induced dimerisation (activation), internalisation and synthesis) have been included. We have shown that this simple model accounts for different patterns of receptor tyrosine kinase patterns, namely, sustained activation, transient activation and perfect adaptation.

A paradigmatic and much studied system is the cell line PC12 and its response to NGF and EGF (see Marshall 1995; Vaudry et al. 2000 and references therein). Upon stimulation with NGF, PC12 cells undergo differentiation. In contrast, stimulation of PC12 cells with EGF leads to proliferation. Moreover, activation of both NGFR and EGFR converge to and are mediated by activation of the extracellular-signal-regulated kinase (ERK) (Sasagawa et al. 2005). Although, as pointed out by Marshall (1995), there are no great qualitative difference between the transduction events that lead to proliferation and differentiation, there are important quantitative difference between them: whilst NGF induces sustained ERK activation, EGF produces transient ERK activation. These results are further confirmed by experiments in which mutant PC12 cells unable of differentiating exhibit transient ERK activation upon NGF stimulation (Yaka et al. 1998).

In the context of our model results, the results reported by Traverse et al. (1994) and Schelessinger and Bar-Sagi (1995) are particularly interesting. Traverse et al. (1994) present results according to which overexpression of EGFR leads to sustained ERK activation, producing differentiation. In turn, in PC12 lines that do not respond to NGF as a differentiation signal, NGFR is downregulated, ERK activation is transient and the response is to stimulation with NEGF is proliferation (Schelessinger and Bar-Sagi 1995).

Our model results are in agreement with these experimental results, as we predict that overexpression of RTKs leads to sustained activation and, on the contrary, downregulation of RTK synthesis yields transient activation.

Another main result presented here concerns the possibility of inducing perfect adaptation by downregulation of inactive receptor degradation. There is extensive evidence for the chemotactic response many growth factors induce in a wide variety of cells. However, recent studies carried out by Shneider and Haugh (2005) appear to indicate that perfect adaptation is not necessary for chemotactic behaviour. Shneider and Haugh (2005) have carried out experiments with fibroblasts exposed to a gradient of PDGF, showing that, whilst fibroblasts migrate up the PDGF concentration gradient, they do not exhibit perfect adaptation. Shneider and Haugh (2005) highlight some differences between fibroblasts and other eukaryotic cells, such as neutrophils, which exhibit both chemotactic and perfect adaptation behaviour. They found that fibroblasts exhibit a much narrower range of chemoattractant concentrations to which they respond efficiently. Fibroblasts also need much steeper gradients than neutrophils. Hence, it seems that perfect adaptation is necessary for increasing efficiency of the chemotactic response although this response can be induced without perfect adaptation. If this is actually the case, this provides a way to verify our predictions: downregulating inactive receptor degradation should lead to a more efficient chemotactic response in fibroblasts, as this would induce a perfectly adapted response.

Our model provides a framework in which we can study the different cellular responses induced by a single sensorial system (i.e. GF/RTK). Our model predicts that pathways controlling receptor synthesis and degradation may be instrumental for controlling the cellular response, through either transient or sustained signals, to a given signalling cue in a particular cellular context.

The scope of the models presented here may be considered as limited because they do not include some of the complexities involved in the VEGFR sensory system. For example, we have considered only one ligand and one receptor type, which is likely to constitute an over-simplification as it has been shown that different tyrosine kinases can be phosphorylated upon receptor activation, each of them capable of initiating different signalling pathways (Shibuya and Claesson-Welsh 2006). Heterodimerisation, i.e. dimerisation of receptors of different types, contributes to increase the complexity of signalling because the phosphorylation profile on each receptor depends upon its partner receptor in the dimer (Dixelius et al. 2003), as does multiplicity of ligands: different ligands activate different sets of tyrosine sites within the receptors (Autiero et al. 2003). All these different patterns of receptor activation affect and modify cellular response. However, since this scenario implies that the regulation of the level of each receptor is a critical parameter to control receptor signalling, mechanisms and behaviours such as those shown in Sect. 6 will still be useful to understand the different patterns of cell response. Additionally, our models focus on general mechanisms which allow us to identify generic biophysical mechanisms which will apply to models including a more detailed description of the patterns of phosphorylation of the tyrosine sites in active receptors.

References

Alarcón, T. and Page, K.M. (2006). *Stochastic models of receptor oligomerisation by bivalent ligand*. J. R. Soc. Interface. **3**, 545-559.

Alarcón, T. and Page, K.M. (2007). *Mathematical models of the VEGF receptor and its role in cancer therapy*. J. R. Soc. Interface. **4**, 283-304.

Autiero, M., Waltenberg, J., Communi, D., Kranz, A., Moons, L., Lambrechts, D., Kroll, J., Plaisance, S., De Mol, M. Bono, F., Kilche, S., Fellbrich, G., Ballmer-Hofer, K., Maglione, D., Mayer-Beyrle, U., Dewerchin, M., Dombrowski, S., Stanimirovic, D., Van Hummelen, P., Heio, C., Hicklin, D.J., Persico, G., Herbert, J.M., Shibuya, M., Collen, D., Conway E.M., Carmeliet, P. (2003). *Role of PIGF in the intra- and inter-molecular cross-talk between the VEGF receptor Flt1 and Flk1*. Nat. Med. **9**. 936-943.

Alberts, B., Johnson, A., Lewis, J., Raff, M., Roberts, K., Walter, P. (2002). *Molecular biology of the cell*. Garland Publishing, New York, NY (USA).

Alon, U., M.G. Surette, N. Barkai, S. Leibler. (1999). *Robustness in bacterial chemotaxis.* Nature. **347**, 168-171.

Amlal, H., Faroqui, S., Balasubramaniam, A., and Sheriff, S. (2006). *Estrogen up-regulates neuropeptide YY1 receptor expression in a human breast cancer cell line*. Cancer Res. **66**, 3706-3714.

Berger, G., and Benjamin, L.E. (2003). *Tumorigenesis and the angiogenic switch.* Nature Rev. Cancer. **3**, 401-410.

Cai, J., Jians, W.G., Ahmed, A. and Bulton, M. (2006). *Vascular endothelial growth factor induced cells proliferation is regulated by interaction between VEGFR-s, SH-PTP1 and eNOS*. Microvasc. Res. **71**, 20-31.

Cross, M.J., Dixelius, J., Matsumoto, T., and Claesson-Welsh, L. (2003). *VEGF-receptor signal transduction.* Trends Biochem. Sci. **28**, 488-494.

Dixelius, J., Makinen, T., Wirzenius, M., Karkkainen, M.J., Wernstedt, C., Alitalo, K., Claesson-Welsh, L. (2003). *Ligand-induced vascular endothelial growth factor receptor-3 (VEGFR-3) heterodimerisation with VEGFR-2 in primary lymphatic endothelial cells regulates tyrosine phosphorylation sites*. J. Biol. Chem. **278**, 40973-40979.

Ebens, A., K. Brose, E.D. Leonardo, M.G. Hanson, F. Bladt, C. Birchmeier, B.A. Barres, M. TessierLavigne. (1996). *Hepatocyte growth factor scatter factor is an axonal chemoattractant and a neurotrophic factor for spinal motor neurons* . Neuron. **17**, 1157-1172.

Felder, S., Zhou, M., Hu, P., Urena, J., Ullrich, A., Chaudhuri, M., White, M., Shoelson, S.E., and Schlessinger, J. (1993). *SH2 domains exhibit high affinity binding to tyrosine-phosphorylated peptides yet al.so exhibit rapid dissociation and exchange.* Mol. Cell. Biol. **13**, 1449-1455.

Ferrara, N. (2002). *Role of vascular endothelial growth factor in physiologic and pathologic angiogenesis: therapeutic implications*. Semin. Oncol. **29** (6 Suppl. 16), 10-14.

Grotendorst, G.R., Chang, T., Seppa, H.E., Kleinman, H.K., and Martin, G.R. (1982). *Platelet-derived growth factor is a chemoattractant for vascular smooth muscle cells*. J. Cell Physiol. **113**, 261-266.

Hampton, T. (2005). *Antiangiogenic therapy a two-trick pony?* JAMA. **293**, 1051.

Helmreich, E.J.M. (2001). *The biochemistry of cell signalling*. Oxford University Press, New York, NY (USA).

Hicklin, D.J., and Ellis, L.M. (2005). *Role of the vascular endothelial growth factor pathway in tumor growth and angiogenesis*. J. Clin. Oncol. **23**, 1011-1027.

Holash, J., Wiegand, S.J., Yancopoulos, G.D. (1999). *New model of tumor angiogenesis: dynamic balance between vessel regression and growth mediated by angiopoietins and VEGF*. Oncogene. **18**, 5356-5362.

Jain, R. (2005). *Normalization of tumour vasculature: an emerging concept in antiangiogenic therapy* Science. **307**, 58-62.

Kitahara, K. (1973). *The Hamilton-Jacobi equation approach to fluctuation phenomena* Adv. Chem. Phy. **29**, 85-111.

Klominek, J., Baskin, B., and Hauzenberger, D. (1998). *Platelet-derived growth factor (PDGF) BB acts as a chemoattractant for human malignant mesothelioma cells via PDGF receptor β-integrin α3β1 interaction.* Clin. Exp. Metastasis. **16**, 529-539.

Knox, B.E., P.N. Devreotes, A. Goldbeter, L.A. Segel. (1986). *A molecular mechanism for sensory adaptation based on ligand-induced receptor modification* Proc. Nat. Acad. Sci. **83**, 2345-2349.

Kubo, R., Matsuo, K., and Kitahara, K. (1973). *Fluctuation and relaxation of macrovariables* J. Stat. Phys. **9**, 51-96.

Lauffenburger, D.A., and Linderman, J.J. (1993). *Receptors: models for binding, trafficking, and signalling.* Oxford University Press, New York, (USA).

Lash, G.E., A.Y. Warren, S. Underwood, P.N. Baker. (2003). *Vascular endothelial growth factor is a chemoattractant for trophoblast cells*. Placenta. **24**, 549-556.

Levchenko, A., P.A. Iglesias. (2002). *Models of eukaryotic gradient sensing: application to chemotaxis of amoebae and neutrophils*. Biophys. J. **82**, 50-63.

Mac Gabham, F., and Popel, A.S. (2004). *Model of competitive binding of vascular endothelial growth factor and placental growth factor to VEGF receptors on endothelial cells.* Am. J. Physiol. Heart Circ. Physiol. **286**, H153-H164.

Mac Gabham, F., and Popel, A.S. (2005a). *Differential binding of VEGF isoforms to VEGF receptor 2 in the presence of neuropilin-1: a computational model*. Am. J. Physiol. Heart Circ. Physiol. **288**, H2851-H2860.

Mac Gabham, F., and Popel, A.S. (2005b). *Monte Carlo simulations of VEGF binding to cell surface receptors in vitro*. Biochim. Biophys. Acta – Mol. Cell Res. **1746**, 95-107.

Marshall, C.J. (1995). *Specifity of receptor tyrosine kinase signaling: transient versus sustained extracellular signal-regulated kinase activation*. Cell. **80**, 179-185.

Mitchell, H., A. Chowdhury, R.E. Pagano, E.B. Leof. (2004). *Ligand-dependent and -independent tranforming growth factor-β receptor recycling regulated by clathrin-mediated endocytosis and Rab11*. Mol. Biol. Cell. **15**, 4166-4178.

Ohshima, M., Y. Noguchi, Y. Ito, M. Maeno, K. Otsuka. (2001). *Hepatocyte growth factor secreted by periodontal ligament and gingival fibroblasts is a major chemoattractant for gingival epithelial cells*. J. Periodontal Res. **36**, 377-383.

Park, C.H, Schneider, I.C., and Maugh, J.M. (2003). *Kinetic analysis of platelet-derived growth factor receptor/phosphoinositide 3-kinase/Akt signalling in fibroblast*. J. Biol. Chem. **278**, 37064-37072.

Polo, S., Pece, S., and Di Fiore, P.P. (2004). *Endocytosis and cancer*. Curr. Opin. Cell Biol. **16**, 156-161.

Posner, R.G., Wofsy, C., and Goldstein, B. (1995). *The kinetics of bivalent ligand-bivalent receptor aggregation: Ring formation and the breakdown of equivalent site approximation* Math. Biosciences. **126**, 171-190.

Reibman, J., S. Meixler, T.C. Lee, L.I. Gold, B.N. Cronstein, K.A. Haines, S.L. Kolasinski, G. Weissmann. (1991). *Transforming growth factor β1, a potent chemoattractant for human neutrophils, bypasses classic signal-transduction pathways*. Proc. Nat. Acad. Sci. **88**, 6805-6809.

Sasagawa, S., Y. Ozaki, K. Fujita, S. Kuroda. (2005). *Prediction and validation of the distinct dynamics of transient and sustained ERK activation*. Nature Cell Biol. **7**, 365-373.

Sawada, J., A. Itakura, A. Tanaka, T. Furusaka, H. Matsuda. (2000). *Nerve growth factor functions as a chemoattractant for mast cells through both mitogen-activated protein kinase and phosphatidylinositol 3-kinase signaling pathways*. Blood. **95**, 2052-2058.

Sawyer, T.K. (1998). *Src homology-2 domains: Structure, mechanisms and drug discovery*. Biopolymers. **47** 243-261.

Schlesinger, J., D. Bar-Sagi. (1995). *Activation of Ras and other signalling pathways by tyrosine kinase receptors*. In Symposia on Quantitative Biology: Molecular Genetics and Biology. (Cold Spring Harbor Laboratory Press, Cold Spring Harbor, USA).

Schneider, I.C., J.M. Haugh. (2005). *Quantitative elucidation of a distinct spatial gradient-sensing mechanism in fibroblasts*. J. Cell Biol. **171**, 883-892.

Shibuya, M., Claesson-Welsh, L. (2006). *Signal transduction by VEGF receptors in regulation of angiogenesis and lymphoangiogenesis.* Exp. Cell Res. **312**, 549-560.

Spiro, P.A., J.S. Parkinson, H.G. Othmer. (1997). *A model for excitation and adaptation in bacterial chemotaxis*. Proc. Nat. Acad. Sci. **94**, 7263-7268.

Sulzer, B., De Boer, R.J., and Perelson, A.S. (1996). *Cross-linking reconsidered: binding and cross-linking fields and the cellular response*. Biophys. J. **70**, 1154-1168.

Suzuma, I., Mandai, M., Takagi, H., Suzuma, K., Otani, A., Oh, H., Kobayashi, K., and Honda, Y. (1999). *17 β-estradiol increases VEGF receptor-2 and promotes DNA synthesis in retinal microvascular endothelial cells*. Invest. Ophth. Vis. Sci. **40**, 2122-2129.

Teis, D., and Huber, L.A. (2003). *The odd couple: signal transduction and endocytosis*. Cell. Mol. Life Sci. **60**, 2020-2033.

Terranova, V.P., DiFlorio, R., Lyall, R.M., Hic, S., Friesel, R., and Maciag, T. (1985). *Human endothelial cells are chemotactic to endothelial cell growth factor and heparin*. J. Cell Biol. **101**, 2330-2334.

Traverse, S., K. Seedorf, H. Patterson, C.J. Marshall, P. Cohen, A. Ullrich. (1994). *EGF triggers neuronal differentiation of PC12 cells that overexpress EGF receptor*. Curr. Biol. **4**, 694-701.

Tyson, J.J., Chen, K.C., and Novak, B. (2003). *Sniffers, buzzers, toggles and blinkers: dynamics and signalling pathways in the cell*. Curr. Opin. Cell Biol. **15**, 221-231.

Van Kampen, N. (1992). *Stochastic processes in physics and chemistry*. North-Holland, Amsterdam.

Vaudry, D., P.J.S. Stork, P. Lazarovici, L.E. Eiden. (2002). *Signalling pathways for PC12 cell differentiation: making the right connections*. Science. **296**, 1648-1649.

Vilar, J.M.G. , Jansen, R., and Sander, C. (2006). *Signal processing in the TGF-β superfamily ligand receptor network*. PLOS Comput. Biol. **2**, 36-45.

Wiley, H.S., J.J. Herbst, B.J. Walsh, D.A. Lauffenburger, M.G. Rosenfeld. (1991). *The role of receptor tyrosine kinase activity in endocytosis, compartmentation and down-regulation of the epidermal growth factor receptor*. J. Biol. Chem. **266**, 11083-11094.

Woolf, P.J., and Linderman, J.J. (2004). *An algebra of dimerisation and its implications for G-protein coupled receptor*. J. theor. Biol. **229**, 157-168.

Yaka, R., A. Gamliel, D. Gurwitz, R. Stein. (1998). *NGF induces transient but not sustained activation of ERK in PC12 mutant cells incapable of differentiating*. J. Cell. Biochem. **70**, 425-432.

Yi, T.-M., Y. Huang, M.I. Simon, J. Doyle. (2000). *Robust perfect adaptation in bacterial chemotaxis through integral feedback control*. Proc. Nat. Acad. Sci. **97**, 4649-4653.

Ti Zhang, Hui-Chuan Sun, Yang Xu, Ke-Zhi Zhang, Lu Wang, Lun-Xiu Qin, Wei-Zhong Wu, Yin-Kun Liu, Sheng-Long Ye, and Zhao-You Tang. (2005). *Overexpression of PDGF Receptor α in endothelial cells of hepatocellular carcinoma associated with metastatic potential*. Clin Cancer Res. **11**, 8557-8563.

Chapter 2
Simulating Therapeutics Using Multiscale Models of the VEGF Receptor System in Cancer

Feilim Mac Gabhann, Marianne O. Stefanini, and Aleksander S. Popel

1 Angiogenesis as a Therapeutic Target in Cancer

Exploration of antiangiogenic cancer therapeutics began when Dr. Judah Folkman postulated that tumors must depend on angiogenesis (neovascularization) for their growth and metastasis, and therefore that angiogenesis is a therapeutic target (Folkman 1971). His pioneering research paved the way to the discoveries of the primary angiogenic cytokine, Vascular Endothelial Growth Factor (VEGF) (Dvorak 2006; Leung et al. 1989), and subsequent development of therapeutic agents targeting VEGF and its receptors (Gaur et al. 2009; Mac Gabhann and Popel 2008). In the last two decades numerous other molecular families have been identified and extensively studied as potential targets for antiangiogenic therapeutics including: integrins; angiopoietins; the delta-notch system; semaphorins; ephrins; platelet-derived growth factors (PDGF); hepatocyte growth factor (HGF); transforming growth factor beta (TGFβ); matrix metalloproteinases (MMP); and the transcription factors, hypoxia-inducible factors (HIF). These are variously involved in initiation, propagation, or stabilization of sprouting angiogenic neovessels. Many of these families interact with one another directly or at the level of intracellular signaling, and thus quantitative systems biology approaches are required to unravel this complexity and to design novel approaches to antiangiogenic therapeutics.

In this chapter we will outline approaches to multiscale molecular-detailed computational modeling of the VEGF family, with particular emphasis on

F. Mac Gabhann
Institute for Computational Medicine and Department of Biomedical Engineering, Johns Hopkins University, Baltimore, MD 21218, USA
e-mail: feilim@jhu.edu

M.O. Stefanini • A.S. Popel (✉)
Department of Biomedical Engineering, Johns Hopkins University School of Medicine, Baltimore, MD 21205, USA
e-mail: stefanini@jhmi.edu; apopel@jhu.edu

T.L. Jackson (ed.), *Modeling Tumor Vasculature: Molecular, Cellular, and Tissue Level Aspects and Implications*, DOI 10.1007/978-1-4614-0052-3_2,

pharmacokinetic-pharmacodynamic (PK/PD) modeling of current or potential therapeutic interventions. At the molecular and cellular scales, we use a biophysically accurate kinetic model of ligand–receptor interactions and/or intracellular signaling. Models of other molecular families important for angiogenesis have also been formulated and can be incorporated into integrative models: fibroblast growth factor-2 (Filion and Popel 2004; Forsten-Williams et al. 2008); MMPs (Karagiannis and Popel 2004; Karagiannis and Popel 2006; Vempati et al. 2007); PDGF (Park et al. 2003); and HIF1α (Qutub and Popel 2008). Along with these molecular and kinetic details, multiscale models also incorporate cellular and tissue information, to simulate molecular trafficking and tissue responses to drugs. Combined molecular-cellular models have sought to delineate the role of the Delta-Notch family in endothelial tip cells and stalk cells in the development of nascent capillary sprouts (Bentley et al. 2008, 2009). At the tissue scale, models have been developed to simulate the processes of growing vasculature; the vessels may be treated as discrete objects (Bauer et al. 2007; Owen et al. 2009; Sun et al. 2005; Milde et al. 2008; Qutub and Popel 2009; Das et al. 2010; Macklin et al. 2009), or as a continuum in terms of vascular density (Levine et al. 2001). Molecular-detailed and integrative models of angiogenesis have been reviewed in (Owen et al. 2009; Macklin et al. 2009; Anderson and Quaranta 2008; Byrne 2010; Chaplain et al. 2006; Qutub and Popel 2009; Frieboes et al. 2010; Peirce 2008; Stefanini et al. 2011). Some of these models describe not only the vasculature but also the growing tumor, which further increases the level of complexity. In assembling these multiscale models, processes at different scales may be simulated using different modeling methodologies; ordinary differential equations (ODEs), partial differential equations (PDEs), stochastic Monte Carlo simulations, and agent-based modeling (ABM) are all used as appropriate; examples are given later.

Systems biology, and specifically computational modeling and simulations, is becoming mainstream in drug discovery (Laubenbacher et al. 2009). There are several examples of pharmacokinetic and pharmacodynamic computational predictions from angiogenesis models. A PDE-based continuum model that describes temporal and spatial aspects of endothelial cell migration, proliferation, apoptosis and cell–cell contact, as well as tumor cell cycle was applied to model endostatin gene therapy (Billy et al. 2009). A compartment ODE-based model was formulated to describe temporal variation of spatially-averaged vessel density, growth, maturation, and regression, as well as tumor growth (Arakelyan et al. 2003); the model was applied to simulate administration of a chemotherapeutic drug in combination with an antiangiogenic drug bevacizumab, a monoclonal antibody to VEGF (Gorelik et al. 2008). A model with a similar structure was applied to study a combination of chemotherapeutic and antiangiogenic agents (d'Onofrio and Gandolfi 2010). A single-compartment ODE-based model describing ligand–receptor interactions for VEGF isoforms and their receptors simulated administration of agents disrupting the association of VEGF receptor-2 (VEGFR2) with neuropilin-1 (NRP1) (Mac Gabhann and Popel 2006). A multi-compartment model describing VEGF transport among blood, tumor, and normal tissue compartments simulated bevacizumab

administration, as a single bolus or metronomic treatment (Stefanini et al. 2011). An ODE-based signal transduction model of Bcl-2 protein downstream from VEGFR2 made predictions for inhibition of Bcl-2 by a small-molecule inhibitor (Jain et al. 2009).

Complementing experimental studies of important molecular factors and cellular and tissue processes in tumor angiogenesis, multiscale mathematical modeling is prepared to move toward translational applications, such as antiangiogenic drug discovery and development. The models can be used to analyze the results of clinical trials and application of approved antiangiogenic agents as a monotherapy or in combination with other agents (antiangiogenic or chemotherapeutic), and also to design novel therapeutics.

2 The VEGF Receptor System

The VEGF family in humans includes five genes encoding cell-secreted protein ligands: VEGF-A, -B, -C, -D, and placental growth factor (PlGF), comprising important cytokines involved in angiogenesis and lymphangiogenesis (Ferrara et al. 2004; Takahashi and Shibuya 2005). VEGF-A is commonly referred to as VEGF; this convention is used later. VEGF has been shown to have several effects on the vasculature. For example, VEGF increase is often correlated with vascular density, vessel tortuosity, and increased microvascular permeability (Lee et al. 2005; Nagy et al. 2009; Nagy et al. 2007). Human VEGF family mRNA splice variants give rise to VEGF isoforms including: $VEGF_{121}$, $VEGF_{145}$, $VEGF_{165}$, $VEGF_{183}$, $VEGF_{189}$, $VEGF_{206}$, $VEGF\text{-}B_{167}$, $VEGF\text{-}B_{186}$ (Robinson and Stringer 2001). The VEGF family of ligands has multiple cell-membrane receptors: homodimers of VEGFR1 (Flt-1), VEGFR2 (Flk-1 or KDR), and VEGFR3 (Flt-4); the heterodimers VEGFR1/2 and VEGFR2/3; and the coreceptors neuropilin-1 (NRP1) and neuropilin-2 (NRP2) (Ferrara et al. 2003). Soluble (nonmembrane-based) forms of these receptors, such as sFlt-1, also bind VEGF isoforms.

The set of exons encoding each VEGF isoform determines the specific binding of that isoform to the receptors (Fig. 2.1a). For example, $VEGF_{165}$, which contains exon 7, can bind to NRP1, and bridge VEGFR2 and NRP1 (Soker et al. 2002). $VEGF_{121}$ does not contain exon 7 and was thought not to be able to bind NRP1 (Neufeld et al. 2002; Pan et al. 2007). Recently, however, it was experimentally shown that, although unable to bridge VEFGR2 and NRP1, $VEGF_{121}$ does bind NRP1 (Pan et al. 2007). NRP1 also serves as a receptor to PlGF-2 and $VEGF_{145}$, while NRP2 serves as a receptor to $VEGF_{165}$, PlGF-2, $VEGF_{145}$, and VEGF-C (Neufeld et al. 2002; Gluzman-Poltorak et al. 2000). Both NRP1 and NRP2 are thought to enhance $VEGF_{121}$-stimulated signal transduction by the VEGFR-2 receptor (Pan et al. 2007; Shraga-Heled et al. 2007). Because of its involvement in cancer, neuropilin receptors are potential targets for antiangiogenic treatments (Geretti and Klagsbrun 2007).

As with neuropilins, class 3 semaphorins (SEMA3) were originally discovered for their involvement in the nervous system but have shown promising results

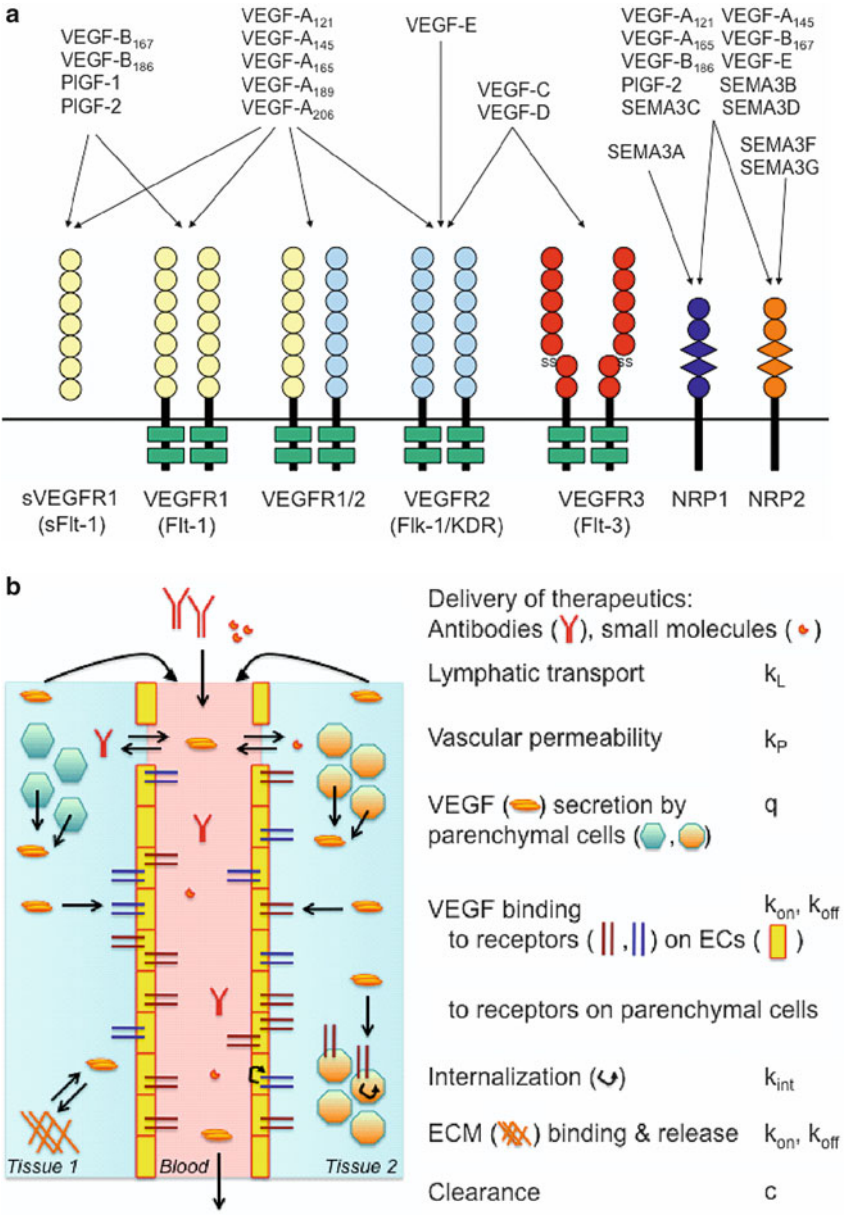

Fig. 2.1 Schematics of the VEGF-VEGFR interactions and pharmacokinetic-pharmacodynamic (PK/PD) models. (**a**) At the heart of the coupled-ODE model is a reconstruction of the kinetic interaction network between the various VEGF ligands and their receptors. Simulating the pharmacodynamics of VEGF-targeting agents requires including the interactions of the agent with these VEGF and VEGFR molecules. (**b**) The pharmacokinetic model includes the transport of VEGF, and any therapeutics for testing, within and between compartments (tissues). We combine this model with the kinetics of VEGF (**a**) and pharmacodynamics of therapeutic agents

in tumor angiogenesis (Gaur et al. 2009; Geretti et al. 2008; Rizzolio and Tamagnone 2007). The inhibitory effects of SEMA3 may be due to competitive binding to VEGF receptors and coreceptors. SEMA3A binds to NRP1, whereas SEMA3F and SEMA3G bind to NRP2. Other members (SEMA3B, SEMA3C, SEMA3D) bind to both neuropilins. Because of this competition with VEGF isoforms, exogenously administered class 3 semaphorins could serve as potential anti-VEGF therapy.

3 Multiscale Models of the VEGF Receptor System

In order to look at tumor angiogenesis and the effects of different angiogenic targets, multiscale computational models have been developed. These models are classified in two categories: spatial and nonspatial (compartment) models.

Spatial multiscale models focus on the spatial VEGF distribution within tissues and how the tumor microenvironment plays a role in drug delivery; they include diffusion and possibly convection terms for diffusible VEGF ligands and therapeutic molecules (Qutub et al. 2010; Wu et al. 2009). Matrix metalloproteinases (MMPs) are key factors in the matrix degradation, facilitate the tip cell migration into the tissue, and cleave VEGF molecules into smaller isoforms. Some spatial models therefore include the interactions between VEGF and MMPs (Small et al. 2008; Vempati et al. 2010).

In compartment models, each compartment can represent a tissue volume, an organ or an organ system; compartments are characterized by their total volume, the volumes and surface areas of the cell types that comprise the tissue, the vascular volume, and the concentrations of the molecules of interest. An ensemble of these compartments can therefore model an organ system or the whole body, and are thus more suitable for a pharmacokinetic-pharmacodynamic approach, applied to the human body or to animal disease models with species-specific parameters.

As an example, a compartmental model was used to investigate VEGF distribution in the whole body in healthy subjects and cancer patients. This design was motivated by a meta-analysis that showed that VEGF concentration was several-fold higher in cancer patients as compared to healthy subjects on average (Kut et al. 2007). This model was a necessary step for simulating the administration of antiangiogenic drugs. The model is divided into: the vascular system; the tissue of interest (in this case, a tumor; in the case of peripheral arterial disease, ischemic calf muscle); and the rest of the body (Fig. 2.1b, Stefanini et al. 2011; Wu et al. 2009; Stefanini et al. 2008). The models retain tissue characteristics (cell geometry, basement membranes, extra-cellular matrix). The molecular interaction of VEGF with its receptors, as described earlier, as well as VEGF secretion, receptor internalization, and binding to the extracellular matrix are included. Diffusible molecules travel between the compartments via microvascular permeability and lymphatic drainage and are cleared from the system by plasma clearance (Fig. 2.1b). Ligands in the system, such as VEGF, are described by nonlinear ODEs in the form:

$$\frac{\mathrm{d}[V_i]_N}{\mathrm{d}t} = q_i^N + \sum_j \left(k_{\mathrm{off},VR}[V_i R_j]_N - k_{\mathrm{on},V,R}[V_i]_N[R_j]_N\right) + \sum_j \left(k_{\mathrm{off},VM}[V_i M_j]_N - k_{\mathrm{on},V,M}[V_i]_N[M_j]_N\right) + \frac{S_{NB}}{U_N}\left(k_{pV}^{BN}\frac{[V_i]_B}{K_{AV,B}} - k_{pV}^{NB}\frac{[V_i]_N}{K_{AV,N}}\right) - \frac{k_L}{U_N}\frac{[V_i]_N}{K_{AV,N}}. \tag{2.1}$$

On the right-hand side, q represents the secretion of VEGF isoform i by the parenchymal cells in the normal tissue compartment (denoted N); the second and third terms are the binding interactions of VEGF with receptors (R) or matrix components (M); the fourth and fifth terms correspond to intercompartmental transport (microvascular permeability and lymphatic drainage, respectively) between the tissue (N) and the blood (B). $K_{AV,i}$ represents the ratio of the fluid volume accessible to VEGF and the total volume of the same tissue U_i, while S_{NB} represents the tissue–blood interface area. The kinetic parameters k_{off}, k_{on}, k_{pV}^{BN} ,and k_L are the dissociation and association rates of VEGF with the receptors or the matrix components, the microvascular permeability rate for VEGF (from the blood B to the tissue N) and the lymphatic drainage rate of VEGF, respectively. A similar equation governs the temporal variation of the VEGF concentration in the tumor (denoted T), with the additional assumption that the lymph flow rate is assumed to be negligible in this compartment, as tumor lymphatics are thought not to properly function because of the interstitial pressure exerted on the vessels (Fukumura and Jain 2007; Jain and Fenton 2002; Ji 2006). Thus, the equation reads:

$$\frac{\mathrm{d}[V_i]_T}{\mathrm{d}t} = q_i^T + \sum_j \left(k_{\mathrm{off},VR}[V_i R_j]_T - k_{\mathrm{on},V,R}[V_i]_T[R_j]_T\right) + \sum_j \left(k_{\mathrm{off},VM}[V_i M_j]_T - k_{\mathrm{on},V,M}[V_i]_T[M_j]_T\right) + \frac{S_{TB}}{U_T}\left(k_{pV}^{BT}\frac{[V_i]_B}{K_{AV,B}} - k_{pV}^{TB}\frac{[V_i]_T}{K_{AV,T}}\right). \tag{2.2}$$

Finally, the blood communicates with both other compartments and the temporal variation of plasma VEGF concentration is governed by:

$$\frac{\mathrm{d}[V_i]_B}{\mathrm{d}t} = -c_V[V_i]_B + \frac{S_{NB}}{U_B}\left(k_{pV}^{NB}\frac{[V_i]_N}{K_{AV,N}} - k_{pV}^{BN}\frac{U_B}{U_p}[V_i]_B\right) + \frac{k_L}{U_B}\frac{[V_i]_N}{K_{AV,N}} + \frac{S_{TB}}{U_B}\left(k_{pV}^{TB}\frac{[V_i]_T}{K_{AV,T}} - k_{pV}^{BT}\frac{U_B}{U_p}[V_i]_B\right), \tag{2.3}$$

where c_V represents the clearance of VEGF from the plasma, and U_p is the volume of plasma.

The earlier equations are replicated for each of the isoforms of VEGF included in the model, with isoform-specific parameters for binding and transport. The addition of therapeutic molecules (such as antibodies to VEGF – see Sect. 4) requires additional equations to describe transport of those proteins, and terms describing the interaction of these proteins with VEGF isoforms are added to the VEGF equations.

4 Targeting VEGF Ligands

Several molecules targeting VEGF and its receptor tyrosine kinases have been under development in the past decade (Hsu and Wakelee 2009). These drugs may be antibodies, short peptides, fusion proteins, or small molecules and they vary in isoform specificity.

We have extended our compartment model for VEGF outlined earlier by adding equations describing the kinetics and transport of a VEGF-sequestering agent A in the blood, normal and tumor tissue compartments; e.g., in the blood compartment (Stefanini et al. 2011):

$$\frac{\mathrm{d}[A]_B}{\mathrm{d}t} = q_A - c_A[A]_B + \sum_i \left(k_{\mathrm{off},VA}[V_i A]_B - k_{\mathrm{on},V,A}[V_i]_B[A]_B\right) - k_{pV}^{BN}\frac{S_{NB}}{U_p}[A]_B + \left(\frac{k_L + k_{pV}^{NB}S_{NB}}{U_B}\right)\frac{[A]_N}{K_{AV,N}} - k_{pV}^{BT}\frac{S_{TB}}{U_p}[A]_B + k_{pV}^{TB}\frac{S_{TB}}{U_B}\frac{[A]_T}{K_{AV,T}}. \quad (2.4)$$

VEGF-sequestering molecules include humanized monoclonal antibodies (such as bevacizumab or HuMV833), and fusion proteins (such as aflibercept, a fusion of VEGF-binding domains of VEGFR1 and VEGFR2; Holash et al. 2002; Tew et al. 2010; Lockhart et al. 2010; Jayson et al. 2005; Jayson et al. 2002).

Using parameters specific for bevacizumab, Fig. 2.2 illustrates predictions of the computational model for the response of VEGF in plasma and tumor interstitium following drug infusion. Tumor VEGF concentrations do not appear to decline if the bevacizumab is restricted to the plasma. In addition, free VEGF concentration in plasma is predicted to decrease if the anti-VEGF agent is confined in the blood but will increase if the anti-VEGF agent extravasates into the tissue interstitium in accordance with its molecular-weight dependent permeability (Fig. 2.2b). This last result is in agreement with observations in several clinical studies (Gordon et al. 2001; Segerstrom et al. 2006; Willett et al. 2005; Yang et al. 2003) These simulations also reveal that one of the modes of action of the anti-VEGF agent is to deplete the tumor interstitium of free VEGF concentration.

While most antiangiogenic therapies target one or multiple isoforms of VEGF-A, evidence is mounting that other ligands of the VEGF family may also be useful targets (Fischer et al. 2008). PlGF-2 ligates and activates VEGFR1 but not VEGFR2 (Fig. 2.1a), and appears to be pro-angiogenic and synergistic with VEGF-A (Autiero et al. 2003). An antibody to mouse PlGF-2 was reported to decrease

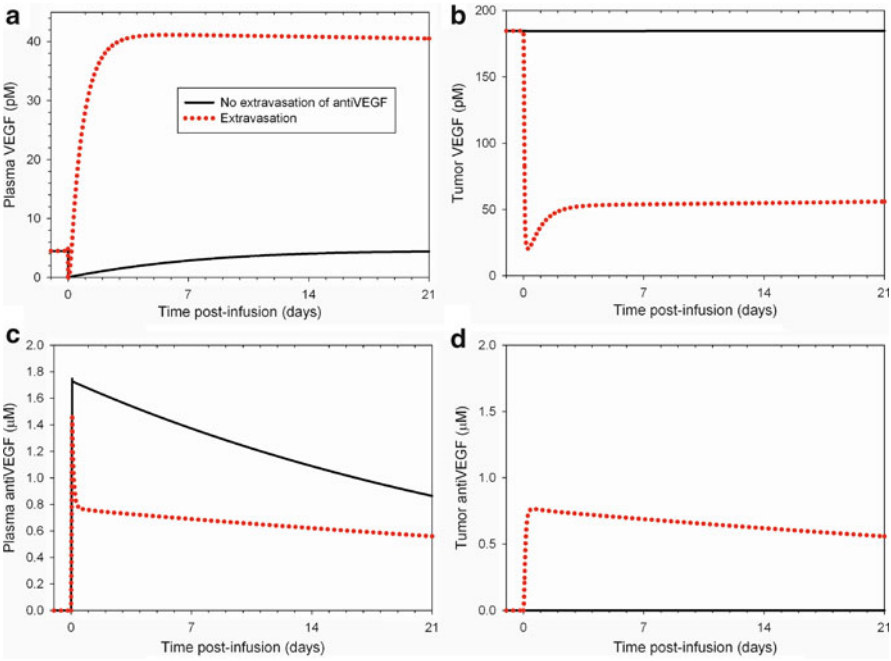

Fig. 2.2 Simulations of antiVEGF treatment: transport and effect on VEGF. The impact on VEGF in the plasma (**a**) or in the interstitial space of a tumor (**b**) of infusing a VEGF-sequestering agent depends on the ability of that agent to extravasate (**c**–**d**). Extravasation (*red lines*) is required for decrease in VEGF within the tissue, but not in the blood. The decrease in the tissue is also long-lasting, despite a rebound of VEGF in the blood. Simulations based on three-compartment model of VEGF transport (Stefanini et al. 2011)

the growth and metastasis of certain pancreatic, colon, and melanoma syngeneic tumors, and enhanced response to anti-VEGFR2 antibodies (Fischer et al. 2007). However, different PlGF-2 antibodies with similar characteristics were reported to fail to reduce growth and inhibit angiogenesis in many tumors, including some of the same tumor lines tested for the first antibody (Bais et al. 2010). Further studies with additional anti-PlGF antibodies reported significant differences among these molecules in the inhibition of neovascularization (Van de Veire et al. 2010). This variability in response between groups of investigators may reflect the complexity in controlling the VEGF system in vivo, with subtle changes in approach resulting in altered efficacy. Computational modeling of these individual antibodies may allow for effective therapeutic design. In single-compartment simulations, the expression of either PlGF isoform can impact the efficacy of VEGF-targeted therapy (Fig. 2.3a), while inhibition of both VEGF and PlGF is dependent on the local receptor expression profile (Fig. 2.3a, b). An antibody to VEGF-B, which like PlGF binds VEGFR1 but not VEGFR2, has also been shown to regress neovascular growth in corneal models (Zhang et al. 2009). None of the anti-PlGF or anti-VEGF-B antibodies has yet entered human clinical trials.

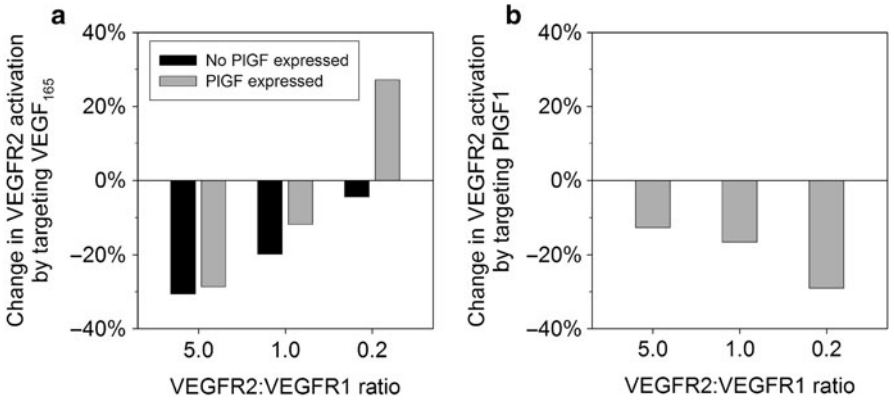

Fig. 2.3 Simulations of therapies targeting VEGF ligands. (**a**) The ability of anti-VEGF targeting agents to alter VEGFR2 activation depends on the relative expression of receptors and of competing ligands, such as PlGF. (**b**) Anti-PlGF targeting has a different dependence on receptor expression. Simulations based on steady inhibition of the ligands in a single-compartment model

5 Targeting VEGF Receptors

The ability of VEGF to initiate and sustain angiogenesis signaling is mediated by binding to VEGFRs, and VEGFR targeting is a possible route for anti-angiogenic therapies (Lyons et al. 2010; Shibuya 2006; Shibuya and Claesson-Welsh 2006). Such therapeutic interventions can also be described by computational models. Equations governing VEGF receptors already utilized in the developed models are of the form:

$$\frac{\mathrm{d}[R_j]_N}{\mathrm{d}t} = s_{Rj} - k_{\mathrm{int},R}[R_j]_N + \sum_i \left(k_{\mathrm{off},VR}[V_i R_j]_N - k_{\mathrm{on},V,R}[V_i]_N[R_j]_N\right) + \sum_{k\neq j}\left(k_{\mathrm{dissoc},RjRk}[R_j R_k]_N - k_{c,Rj,Rk}[R_j]_N[R_k]_N\right), \tag{2.5}$$

where s_R and k_{int} represent the insertion and internalization rates of the receptor R_j. The second term illustrates the binding of VEGF to VEGF receptors and the third term corresponds to the coupling of neuropilins and VEGFRs. Incorporating anti-VEGFR antibodies A into these equations requires additional terms:

$$\frac{\mathrm{d}[R_j]_N}{\mathrm{d}t} = s_{Rj} - k_{\mathrm{int},R}[R_j]_N + \sum_i \left(k_{\mathrm{off},VR}[V_i R_j]_N - k_{\mathrm{on},V,R}[V_i]_N[R_j]_N\right) + k_{\mathrm{off},AR}[AR_j]_N - k_{\mathrm{on},V,A}[A]_N[R_j]_N + \sum_{k\neq j}\left(k_{\mathrm{dissoc},RjRk}[R_j R_k]_N - k_{c,Rj,Rk}[R_j]_N[R_k]_N\right). \tag{2.6}$$

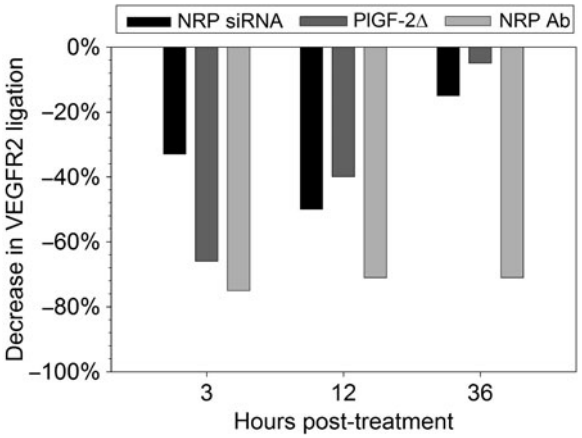

Fig. 2.4 Targeting neuropilin to inhibit VEGFR2 signaling. Three methods for targeting neuropilin – decreasing expression with siRNA (NRP siRNA), blocking VEGF-NRP binding with a fragment of PlGF (PlGF-2Δ), or blocking VEGFR-NRP coupling with a NRP antibody (NRP Ab), differ significantly in their ability to create and sustain VEGFR2 inhibition. Simulations based on single-compartment model (Mac Gabhann and Popel 2006)

Most antibodies and short-peptide drugs compete with ligands for the ligand-binding site on VEGFR1 (Schwartz et al. 2010; Wu et al. 2006; Hattori et al. 2002), VEGFR2 (Youssoufian et al. 2007; Witte et al. 1998; Krupitskaya and Wakelee 2009; Spratlin et al. 2010), or NRP1 (von Wronski et al. 2006; Barr et al. 2005). Some interfere with the coupling reaction or dimerization (Mac Gabhann and Popel 2006; Kolodkin et al. 1997); these behaviors are incorporated into the equations for the antibody and for the antibody–receptor complex.

Thus, an antibody to the VEGF-binding domain of NRP competes with (and has a similar mathematical formulation to) a VEGF isoform; while an antibody to the NRP dimerization domain does not compete with ligand binding, but creates an antibody–NRP complex that has different VEGFR-coupling characteristics. The outcomes of these approaches are quite different, as shown in Fig. 2.4 for neuropilin-targeting drugs; blocking VEGF binding displaces VEGF from neuropilin to the other VEGF receptors, while blocking coupling allows the internalization of VEGF by neuropilin without the involvement of VEGFRs, thus decreasing overall VEGF binding to VEGFRs (Mac Gabhann and Popel 2006).

Tyrosine kinase inhibitors (TKIs) are small molecule ATP competitors, less specific than antibodies, inhibiting signaling of several VEGFRs and related receptors. In the mathematical models, small molecules such as TKIs are transported differently to proteins due to their ability to cross cell membranes, and their binding does not interfere with ligand binding.

Neuropilin or the VEGFRs are expressed on the tumor cells themselves in several cancers (Ellis 2006). Thus a NRP-targeting drug can result in inhibition of NRP on both endothelial cells and tumor cells, a potentially beneficial impact; however it

reduces the impact of the inhibitor on the endothelial cell specifically, thus blunting any vascular-specific effects. Mathematically, the expression of VEGF receptors on parenchymal or other cells is incorporated as a distinct receptor population that competes for the binding of interstitial VEGF and other ligands or inhibitors (Fig. 2.1b).

6 Lymphangiogenesis, Angiogenesis, and Targeting VEGFR3

VEGF receptors are present on the endothelial cells lining both blood vessels and lymphatic vessels (Xu et al. 2010). VEGFR3 has been used as a marker for lymphatic vessels, however recent evidence supports expression of both VEGFR2 and VEGFR3 on both vascular and lymphatic cells (Nilsson et al. 2010; Nilsson et al. 2004; Dixelius et al. 2003), and blockade of VEGFR3 has been reported to reduce neovascularization in embryoid body models of vascular development in vitro (Nilsson et al. 2010). A VEGFR3 antibody is in development for oncology applications, possibly in combination with anti-VEGFR2 antibodies, along with a diabody of anti-VEGFR2 and anti-VEGFR3 molecules (Jimenez et al. 2005). Neuropilin may also be involved in VEGFR3 signaling, increasing the complexity further (Xu et al. 2010).

VEGFR3 blockade also inhibits the lymphangiogenesis (Bock et al. 2008; Tammela and Alitalo 2010) that contributes to tumor growth and metastasis. The ability to inhibit both blood and lymphatic vascular formation and the fact that expression of VEGFR3 appears to be specifically associated with active angiogenic sprouts (Nilsson et al. 2010; Tammela et al. 2008), make it a useful target for pathological growth.

The impact of VEGFR3 on angiogenesis appears to be via VEGFR2/VEGFR3 heterodimers (Nilsson et al. 2010), which demonstrate different phosphorylation profiles than VEGFR2 homodimers. Mathematically, dimerization of VEGFRs has been modeled using surface-restricted receptor-coupling (Mac Gabhann and Popel 2007), as described earlier for the neuropilin-VEGFR interactions; activation of VEGFRs requires VEGF to bind two receptor monomers simultaneously. The expression of VEGFR3 on both vascular and lymphatic endothelial cells can be modeled as described earlier for parenchymal expression of receptors; the two receptor populations will compete for binding of ligands and antibodies. Therapies targeting VEGFR3 can therefore be included similarly to those targeting other receptors.

7 DLL4-NOTCH

VEGF receptors are internalized, recycled, degraded, and new receptors inserted into the membrane continuously. The expression of VEGFR1, 2, and 3 is an opportunity for external control of the system by therapeutics, and is controlled both

by VEGF signaling itself within a single cell, and by a cell–cell communication mechanism mediated by Dll4 and Notch (Jakobsson et al. 2009); typically, this permits the repression of VEGFRs on neighboring cells to suppress close sprouting (Tammela et al. 2008; Suchting et al. 2007), and inhibition of this Dll4 axis has been shown to inhibit tumor growth (Noguera-Troise et al. 2006; Ridgway et al. 2006). Simulation of this dynamic control requires the first term in (2.5) to be dependent on the activation of receptors on adjacent cells (with or without explicit simulation of the Dll4-Notch interaction). Models of these dynamics can result in realistic sprout simulation (Bentley et al. 2008, 2009; Qutub and Popel 2009), allowing molecules that interfere with VEGFR production to be simulated.

8 Conclusion and Future Studies

We have systematically outlined existing and prospective mathematical models to describe the VEGF family. We included both compartment and spatial models that describe VEGF ligands and their receptors and some of the important molecules that are associated with this family. Multiple extracellular and intracellular molecular interactions define a complex web that will increasingly require the power of systems biology (computational models, bioinformatics, high-throughput experiments) to unravel this complexity and to predict therapeutic approaches that can successfully control the behavior of the system (Laubenbacher et al. 2009; Edelman et al. 2010). Important translational information can be derived from compartment models in which various pharmacological agents targeting angiogenic factors are introduced. The agents can be small molecules, peptides, oligonucleotides, or macromolecules; the targets can be growth factors, cell-membrane or intracellular receptors, enzymes, signaling molecules, or genetic elements. In parallel with these developments, complex spatial models of vascular and tumor growth will continue to evolve. Significant progress has already been achieved, but emerging temporal and spatial data from animal models and humans using different imaging methodologies should contribute significantly to the progress. ABM appears to be an appropriate methodology, combined with PDE-based methods. Integrative models of this kind describe the phenomena at multiple scales and comprise models that can be formulated autonomously (e.g., ligand–receptor interactions; transcriptional control of angiogenic genes; cell proliferation, migration, and apoptosis; oxygen transport, blood flow; capillary sprout formation; microvascular network maturation; antiangiogenic drug pharmacokinetics) and then combined computationally as interacting modules (Qutub 2009). To incorporate an increasing number of modules, likely from different laboratories, a computational systems biology infrastructure is required, e.g., markup languages to formulate models in standardized form, model repositories, parameter databases, and effective simulation tools such as for ABM and PDEs (Popel and Hunter 2009). These developments addressing the complexity of the disease at the multiple levels, from gene to organism, will eventually lead to novel effective agents and procedures for cancer therapeutics.

References

Anderson, A.R. and V. Quaranta, *Integrative mathematical oncology*. Nat Rev Cancer, 2008. **8**(3): p. 227–34.

Arakelyan, L., et al., *Multi-scale analysis of angiogenic dynamics and therapy*. In Cancer modeling and simulation, ed. L. Preziosi. 2003, LLC (UK): CRC Press. 185–219.

Autiero, M., et al., *Role of PlGF in the intra- and intermolecular cross talk between the VEGF receptors Flt1 and Flk1*. Nat Med, 2003. **9**(7): p. 936–43.

Bais, C., et al., *PlGF blockade does not inhibit angiogenesis during primary tumor growth*. Cell, 2010. **141**(1): p. 166–77.

Barr, M.P., et al., *A peptide corresponding to the neuropilin-1-binding site on VEGF(165) induces apoptosis of neuropilin-1-expressing breast tumour cells*. Br J Cancer, 2005. **92**(2): p. 328–33.

Bauer, A.L., T.L. Jackson, and Y. Jiang, *A cell-based model exhibiting branching and anastomosis during tumor-induced angiogenesis*. Biophys J, 2007. **92**(9): p. 3105–21.

Bentley, K., H. Gerhardt, and P.A. Bates, *Agent-based simulation of notch-mediated tip cell selection in angiogenic sprout initialisation*. J Theor Biol, 2008. **250**(1): p. 25–36.

Bentley, K., et al., *Tipping the balance: robustness of tip cell selection, migration and fusion in angiogenesis*. PLoS Comput Biol, 2009. **5**(10): e1000549.

Billy, F., et al., *A pharmacologically based multiscale mathematical model of angiogenesis and its use in investigating the efficacy of a new cancer treatment strategy*. J Theor Biol, 2009. **260**(4): p. 545–62.

Bock, F., et al., *Blockade of VEGFR3-signalling specifically inhibits lymphangiogenesis in inflammatory corneal neovascularisation*. Graefes Arch Clin Exp Ophthalmol, 2008. **246**(1): p. 115–9.

Byrne, H.M., *Dissecting cancer through mathematics: from the cell to the animal model*. Nat Rev Cancer, 2010. **10**(3): p. 221–30.

Chaplain, M.A., S.R. McDougall, and A.R. Anderson, *Mathematical modeling of tumor-induced angiogenesis*. Annu Rev Biomed Eng, 2006. **8**: p. 233–57.

Das, A., et al., *A hybrid continuum-discrete modeling approach to predict and control angiogenesis: analysis of combinatorial growth factor and matrix effects on vessel-sprouting morphology*. Philos Transact A Math Phys Eng Sci, 2010. **368**(1921): p. 2937–60.

Dixelius, J., et al., *Ligand-induced vascular endothelial growth factor receptor-3 (VEGFR-3) heterodimerization with VEGFR-2 in primary lymphatic endothelial cells regulates tyrosine phosphorylation sites*. J Biol Chem, 2003. **278**(42): p. 40973–9.

d'Onofrio, A. and A. Gandolfi, *Chemotherapy of vascularised tumours: role of vessel density and the effect of vascular "pruning"*. J Theor Biol, 2010. **264**(2): p. 253–65.

Dvorak, H.F., *Discovery of vascular permeability factor (VPF)*. Exp Cell Res, 2006. **312**(5): p. 522–6.

Edelman, L.B., J.A. Eddy, and N.D. Price, *In silico models of cancer*. Wiley Interdisciplinary Reviews: Systems Biology and Medicine, 2010. **2**(4): p. 438–9.

Ellis, L.M., *The role of neuropilins in cancer*. Mol Cancer Ther, 2006. **5**(5): p. 1099–107.

Ferrara, N., H.P. Gerber, and J. LeCouter, *The biology of VEGF and its receptors*. Nat Med, 2003. **9**(6): p. 669–76.

Ferrara, N., *Vascular endothelial growth factor: basic science and clinical progress*. Endocr Rev, 2004. **25**(4): p. 581–611.

Filion, R.J. and A.S. Popel, *A reaction-diffusion model of basic fibroblast growth factor interactions with cell surface receptors*. Ann Biomed Eng, 2004. **32**(5): p. 645–63.

Fischer, C., et al., *Anti-PlGF inhibits growth of VEGF(R)-inhibitor-resistant tumors without affecting healthy vessels*. Cell, 2007. **131**(3): p. 463–75.

Fischer, C., et al., *FLT1 and its ligands VEGFB and PlGF: drug targets for anti-angiogenic therapy?* Nat Rev Cancer, 2008. **8**(12): p. 942–56.

Folkman, J., *Tumor angiogenesis: therapeutic implications*. N Engl J Med, 1971. **285**(21): p. 1182–6.

Forsten-Williams, K., et al., *Control of growth factor networks by heparan sulfate proteoglycans*. Ann Biomed Eng, 2008. **36**(12): p. 2134–48.

Frieboes, H.B., et al., *Three-dimensional multispecies nonlinear tumor growth-II: Tumor invasion and angiogenesis*. J Theor Biol, 2010. **264**(4): p. 1254–78.

Fukumura, D. and R.K. Jain, *Tumor microenvironment abnormalities: causes, consequences, and strategies to normalize*. J Cell Biochem, 2007. **101**(4): p. 937–49.

Gaur, P., et al., *Role of class 3 semaphorins and their receptors in tumor growth and angiogenesis*. Clin Cancer Res, 2009. **15**(22): p. 6763–70.

Gaur, P., et al., *Targeting tumor angiogenesis*. Semin Oncol, 2009. **36**(2 Suppl 1): p. S12–9.

Geretti, E. and M. Klagsbrun, *Neuropilins: novel targets for anti-angiogenesis therapies*. Cell Adh Migr, 2007. **1**(2): p. 56–61.

Geretti, E., A. Shimizu, and M. Klagsbrun, *Neuropilin structure governs VEGF and semaphorin binding and regulates angiogenesis*. Angiogenesis, 2008. **11**(1): p. 31–9.

Gluzman-Poltorak, Z., et al., *Neuropilin-2 is a receptor for the vascular endothelial growth factor (VEGF) forms VEGF-145 and VEGF-165*. J Biol Chem, 2000. **275**(24): p. 18040–5.

Gordon, M.S., et al., *Phase I safety and pharmacokinetic study of recombinant human anti-vascular endothelial growth factor in patients with advanced cancer*. J Clin Oncol, 2001. **19**(3): p. 843–50.

Gorelik, B., et al., *Efficacy of weekly docetaxel and bevacizumab in mesenchymal chondrosarcoma: a new theranostic method combining xenografted biopsies with a mathematical model*. Cancer Res, 2008. **68**(21): p. 9033–40.

Hattori, K., et al., *Placental growth factor reconstitutes hematopoiesis by recruiting VEGFR1(+) stem cells from bone-marrow microenvironment*. Nat Med, 2002. **8**(8): p. 841–9.

Holash, J., et al., *VEGF-Trap: a VEGF blocker with potent antitumor effects*. Proc Natl Acad Sci U S A, 2002. **99**(17): p. 11393–8.

Hsu, J.Y. and H.A. Wakelee, *Monoclonal antibodies targeting vascular endothelial growth factor: current status and future challenges in cancer therapy*. BioDrugs, 2009. **23**(5): p. 289–304.

Jain, R.K. and B.T. Fenton, *Intratumoral lymphatic vessels: a case of mistaken identity or malfunction?* J Natl Cancer Inst, 2002. **94**(6): p. 417–21.

Jain, H.V., J.E. Nor, and T.L. Jackson, *Quantification of endothelial cell-targeted anti-Bcl-2 therapy and its suppression of tumor growth and vascularization*. Mol Cancer Ther, 2009. **8**(10): p. 2926–36.

Jakobsson, L., K. Bentley, and H. Gerhardt, *VEGFRs and Notch: a dynamic collaboration in vascular patterning*. Biochem Soc Trans, 2009. **37**(Pt 6): p. 1233–6.

Jayson, G.C., et al., *Molecular imaging and biological evaluation of HuMV833 anti-VEGF antibody: implications for trial design of antiangiogenic antibodies*. J Natl Cancer Inst, 2002. **94**(19): p. 1484–93.

Jayson, G.C., et al., *Phase I investigation of recombinant anti-human vascular endothelial growth factor antibody in patients with advanced cancer*. Eur J Cancer, 2005. **41**(4): p. 555–63.

Ji, R.C., *Lymphatic endothelial cells, tumor lymphangiogenesis and metastasis: New insights into intratumoral and peritumoral lymphatics*. Cancer Metastasis Rev, 2006. **25**(4): p. 677–94.

Jimenez, X., et al., *A recombinant, fully human, bispecific antibody neutralizes the biological activities mediated by both vascular endothelial growth factor receptors 2 and 3*. Mol Cancer Ther, 2005. **4**(3): p. 427–34.

Karagiannis, E.D. and A.S. Popel, *A theoretical model of type I collagen proteolysis by matrix metalloproteinase (MMP) 2 and membrane type 1 MMP in the presence of tissue inhibitor of metalloproteinase 2*. J Biol Chem, 2004. **279**(37): p. 39105–14.

Karagiannis, E.D. and A.S. Popel, *Distinct modes of collagen type I proteolysis by matrix metalloproteinase (MMP) 2 and membrane type I MMP during the migration of a tip endothelial cell: insights from a computational model*. J Theor Biol, 2006. **238**(1): p. 124–45.

Kolodkin, A.L., et al., *Neuropilin is a semaphorin III receptor*. Cell, 1997. **90**(4): p. 753–62.

Krupitskaya, Y. and H.A. Wakelee, *Ramucirumab, a fully human mAb to the transmembrane signaling tyrosine kinase VEGFR-2 for the potential treatment of cancer*. Curr Opin Investig Drugs, 2009. **10**(6): p. 597–605.

Kut, C., F. Mac Gabhann, and A.S. Popel, *Where is VEGF in the body? A meta-analysis of VEGF distribution in cancer*. Br J Cancer, 2007. **97**(7): p. 978–85.

Laubenbacher, R., et al., *A systems biology view of cancer*. Biochim Biophys Acta, 2009. **1796**(2): p. 129–39.

Lee, Y.C., *The involvement of VEGF in endothelial permeability: a target for anti-inflammatory therapy*. Curr Opin Investig Drugs, 2005. **6**(11): p. 1124–30.

Leung, D.W., et al., *Vascular endothelial growth factor is a secreted angiogenic mitogen*. Science, 1989. **246**(4935): p. 1306–9.

Levine, H.A., et al., *Mathematical modeling of capillary formation and development in tumor angiogenesis: penetration into the stroma*. Bull Math Biol, 2001. **63**(5): p. 801–63.

Lockhart, A.C., et al., *Phase I study of intravenous vascular endothelial growth factor trap, aflibercept, in patients with advanced solid tumors*. J Clin Oncol, 2010. **28**(2): p. 207–14.

Lyons, J.M., 3rd, et al., *The role of VEGF pathways in human physiologic and pathologic angiogenesis*. J Surg Res, 2010. **159**(1): p. 517–27.

Mac Gabhann, F. and A.S. Popel, *Systems biology of vascular endothelial growth factors*. Microcirculation, 2008. **15**(8): p. 715–38.

Mac Gabhann, F. and A.S. Popel, *Targeting neuropilin-1 to inhibit VEGF signaling in cancer: Comparison of therapeutic approaches*. PLoS Comput Biol, 2006. **2**(12): p. e180.

Mac Gabhann, F. and A.S. Popel, *Dimerization of VEGF receptors and implications for signal transduction: a computational study*. Biophys Chem, 2007. **128**(2–3): p. 125–39.

Macklin, P., et al., *Multiscale modeling and nonlinear simulation of vascular tumour growth*. J Math Biol, 2009. *58*(4–5): p. 765–98.

Milde, F., M. Bergdorf, and P. Koumoutsakos, *A hybrid model for three-dimensional simulations of sprouting angiogenesis*. Biophys J, 2008. **95**(7): p. 3146–60.

Nagy, J.A., et al., *Why are tumour blood vessels abnormal and why is it important to know?* Br J Cancer, 2009. **100**(6): p. 865–9.

Nagy, J.A., A.M. Dvorak, and H.F. Dvorak, *VEGF-A and the induction of pathological angiogenesis*. Annu Rev Pathol, 2007. **2**: p. 251–75.

Neufeld, G., O. Kessler, and Y. Herzog, *The interaction of Neuropilin-1 and Neuropilin-2 with tyrosine-kinase receptors for VEGF*. Adv Exp Med Biol, 2002. **515**: p. 81–90.

Nilsson, I., et al., *VEGF receptor 2/-3 heterodimers detected in situ by proximity ligation on angiogenic sprouts*. EMBO J, 2010. **29**(8): p. 1377–88.

Nilsson, I., et al., *Vascular endothelial growth factor receptor-3 in hypoxia-induced vascular development*. Faseb J, 2004. **18**(13): p. 1507–15.

Noguera-Troise, I., et al., *Blockade of Dll4 inhibits tumour growth by promoting non-productive angiogenesis*. Nature, 2006. **444**(7122): p. 1032–7.

Owen, M.R., et al.,*Angiogenesis and vascular remodelling in normal and cancerous tissues*. J Math Biol, 2009. **58**(4–5): p. 689–721.

Pan, Q., et al., *Neuropilin-1 binds to VEGF121 and regulates endothelial cell migration and sprouting*. J Biol Chem, 2007. **282**(33): p. 24049–56.

Park, C.S., I.C. Schneider, and J.M. Haugh, *Kinetic analysis of platelet-derived growth factor receptor/phosphoinositide 3-kinase/Akt signaling in fibroblasts*. J Biol Chem, 2003. **278**(39): p. 37064–72.

Peirce, S.M., *Computational and mathematical modeling of angiogenesis*. Microcirculation, 2008. **15**(8): p. 739–51.

Popel, A.S. and P.J. Hunter, *Systems biology and Physiome projects*. Wiley Interdisciplinary Reviews: Systems Biology and Medicine, 2009. **1**: p. 153–8.

Qutub, A.A. and A.S. Popel, *Reactive oxygen species regulate hypoxia-inducible factor 1alpha differentially in cancer and ischemia*. Mol Cell Biol, 2008. **28**(16): p. 5106–19.

Qutub, A.A. and A.S. Popel, *Elongation, proliferation & migration differentiate endothelial cell phenotypes and determine capillary sprouting*. BMC Syst Biol, 2009. **3**: 13.

Qutub, A.A., et al., *Multiscale models of angiogenesis*. IEEE Eng Med Biol Mag, 2009. **28**(2): p. 14–31.

Qutub, A.A., et al., *In silico modeling of angiogenesis at multiple scales: From nanoscale to organ system, in Multiscale Modeling of Particle Interactions: Applications in Biology and Nanotechnology*, M.R. King and D.J. Gee, Editors. 2010, Wiley. p. 287–320.

Ridgway, J., et al., *Inhibition of Dll4 signalling inhibits tumour growth by deregulating angiogenesis*. Nature, 2006. **444**(7122): p. 1083–7.

Rizzolio, S. and L. Tamagnone, *Semaphorin signals on the road to cancer invasion and metastasis*. Cell Adh Migr, 2007. **1**(2): p. 62–8.

Robinson, C.J. and S.E. Stringer, *The splice variants of vascular endothelial growth factor (VEGF) and their receptors*. J Cell Sci, 2001. **114**(Pt 5): p. 853–65.

Schwartz, J.D., et al., *Vascular endothelial growth factor receptor-1 in human cancer: concise review and rationale for development of IMC-18F1 (Human antibody targeting vascular endothelial growth factor receptor-1)*. Cancer, 2010. **116**(4 Suppl): p. 1027–32.

Segerstrom, L., et al., *The anti-VEGF antibody bevacizumab potently reduces the growth rate of high-risk neuroblastoma xenografts*. Pediatr Res, 2006. **60**(5): p. 576–81.

Shibuya, M., *Differential roles of vascular endothelial growth factor receptor-1 and receptor-2 in angiogenesis*. J Biochem Mol Biol, 2006. **39**(5): p. 469–78.

Shibuya, M. and L. Claesson-Welsh, *Signal transduction by VEGF receptors in regulation of angiogenesis and lymphangiogenesis*. Exp Cell Res, 2006. **312**(5): p. 549–60.

Shraga-Heled, N., et al., *Neuropilin-1 and neuropilin-2 enhance VEGF121 stimulated signal transduction by the VEGFR-2 receptor*. FASEB J, 2007. **21**(3): p. 915–26.

Small, A.R., et al., *Spatial distribution of VEGF isoforms and chemotactic signals in the vicinity of a tumor*. J Theor Biol, 2008. **252**(4): p. 593–607.

Soker, S., et al., *VEGF165 mediates formation of complexes containing VEGFR-2 and neuropilin-1 that enhance VEGF165-receptor binding*. J Cell Biochem, 2002. **85**(2): p. 357–68.

Spratlin, J.L., et al., *Phase I pharmacologic and biologic study of ramucirumab (IMC-1121B), a fully human immunoglobulin G1 monoclonal antibody targeting the vascular endothelial growth factor receptor-2*. J Clin Oncol, 2010. **28**(5): p. 780–7.

Stefanini, M.O., et al., *A compartment model of VEGF distribution in blood, healthy and diseased tissues*. BMC Syst Biol, 2008. **2**: 77.

Stefanini, M.O., et al., *The increase of plasma vascular endothelial growth factor following the intravenous administration of bevacizumab predicted by a pharmacokinetic model*. Cancer Res, 2010. **70**(23): 9886–94.

Stefanini, M.O., et al., *Computational models of VEGF-associated angiogenic processes in cancer*. Math Med Biol, 2011, to appear.

Suchting, S., et al., *The Notch ligand Delta-like 4 negatively regulates endothelial tip cell formation and vessel branching*. Proc Natl Acad Sci U S A, 2007. **104**(9): p. 3225–30.

Sun, S., et al., *A deterministic model of growth factor-induced angiogenesis*. Bull Math Biol, 2005. **67**(2): p. 313–37.

Takahashi, H. and M. Shibuya, *The vascular endothelial growth factor (VEGF)/VEGF receptor system and its role under physiological and pathological conditions*. Clin Sci (Lond), 2005. **109**(3): p. 227–41.

Tammela, T., et al., *Blocking VEGFR-3 suppresses angiogenic sprouting and vascular network formation*. Nature, 2008. **454**(7204): p. 656–60.

Tammela, T. and K. Alitalo, *Lymphangiogenesis: Molecular mechanisms and future promise*. Cell, 2010. **140**(4): p. 460–76.

Tew, W.P., et al., *Phase 1 study of aflibercept administered subcutaneously to patients with advanced solid tumors*. Clin Cancer Res, 2010. **16**(1): p. 358–66.

Van de Veire, S., et al., *Further pharmacological and genetic evidence for the efficacy of PlGF inhibition in cancer and eye disease*. Cell, 2010. **141**(1): p. 178–90.

von Wronski, M.A., et al., *Tuftsin binds neuropilin-1 through a sequence similar to that encoded by exon 8 of vascular endothelial growth factor*. J Biol Chem, 2006. **281**(9): p. 5702–10.

Vempati, P., E.D. Karagiannis, and A.S. Popel, *A biochemical model of matrix metalloproteinase 9 activation and inhibition*. J Biol Chem, 2007. **282**(52): p. 37585–96.

Vempati, P., F. Mac Gabhann, and A.S. Popel, *Quantifying the proteolytic release of extracellular matrix-sequestered VEGF with a computational model*. PLoS One, 2010. **5**(7): e11860.

Witte, L., et al., *Monoclonal antibodies targeting the VEGF receptor-2 (Flk1/KDR) as an anti-angiogenic therapeutic strategy*. Cancer Metastasis Rev, 1998. **17**(2): p. 155–61.

Wu, Y., et al., *Anti-vascular endothelial growth factor receptor-1 antagonist antibody as a therapeutic agent for cancer*. Clin Cancer Res, 2006. **12**(21): p. 6573–84.

Wu, F.T., et al., *Modeling of growth factor-receptor systems from molecular-level protein interaction networks to whole-body compartment models*. Methods Enzymol, 2009. **467**: p. 461–497.

Xu, Y., et al., *Neuropilin-2 mediates VEGF-C-induced lymphatic sprouting together with VEGFR3*. J Cell Biol, 2010. **188**(1): p. 115–30.

Yang, J.C., et al., *A randomized trial of bevacizumab, an anti-vascular endothelial growth factor antibody, for metastatic renal cancer*. N Engl J Med, 2003. **349**(5): p. 427–34.

Youssoufian, H., D.J. Hicklin, and E.K. Rowinsky, *Review: monoclonal antibodies to the vascular endothelial growth factor receptor-2 in cancer therapy*. Clin Cancer Res, 2007. **13**(18 Pt 2): p. 5544s–5548s.

Zhang, F., et al., *VEGF-B is dispensable for blood vessel growth but critical for their survival, and VEGF-B targeting inhibits pathological angiogenesis*. Proc Natl Acad Sci U S A, 2009. **106**(15): p. 6152–7.

Chapter 3
Linking Endothelial Cell Stimulation to Tumor Growth and Vascular Density: The VEGF – Bcl-2 – CXCL8 Pathway

Harsh V. Jain and Trachette L. Jackson

1 Introduction

The growth of solid tumors can be characterized as having three distinct stages. The first is typically an avascular stage where tumors begin as avascular spheroids, and rely on diffusion for the supply of oxygen and nutrients from neighboring vessels. As these spheroids grow, their interiors become progressively oxygen-deprived (hypoxic) and nutrient-starved (hypoglycemic) resulting in the formation of a necrotic core of dead cells. Most avascular tumors reach a steady state size of 1–3 mm in diameter (Kerbel 2000; Mantzaris et al. 2004). Any further growth requires an adequate supply of nutrients, and an effective means of waste disposal, which can be met by the establishment of a blood supply. Tumor cells may accomplish this in a variety of ways, such as vessel co-option, in which the tumor grows around and takes over an existing blood vessel (Auguste et al. 2005); vascular mimicry, in which extra-cellular matrix-rich vascular channels lacking endothelial cells develop (Roskoski 2007); vasculogenesis, where circulating endothelial cell precursors derived from the bone marrow contribute to vessel formation; and angiogenesis, during which the tumor stimulates new blood vessel growth from existing vasculature, and is most frequently observed (Papetti and Herman 2002). Thus, during the second stage of growth, the tumor has established a dedicated vascular network, which, in addition to being a source of nutrients and means for waste removal, is also a route for the tumor cells to spread to other parts of

H.V. Jain (✉)
Mathematical Biosciences Institute, The Ohio State University, 364 Jennings Hall, 1735 Neil Avenue, Columbus, OH 43210, USA
e-mail: hjain@mbi.osu.edu

T.L. Jackson
Department of Mathematics, University of Michigan, Ann Arbor, MI 48109, USA
e-mail: tjacks@umich.edu

T.L. Jackson (ed.), *Modeling Tumor Vasculature: Molecular, Cellular, and Tissue Level Aspects and Implications*, DOI 10.1007/978-1-4614-0052-3_3,

the body in a process known as metastasis (Mantzaris et al. 2004). This may be regarded as the final stage of tumor development, where its growth is no longer diffusion-limited.

From this picture, it is clear that angiogenesis is a crucial step in the progression of cancer, and a better understanding of the processes that govern it is vital for the development of effective antitumor therapy targeted against vascular development. A number of mathematical models have been developed studying various aspects of tumor-induced angiogenesis, and a review of all of these is not possible here. Instead, in this chapter, we will develop a multi-scale model of angiogenesis geared toward the investigation of the therapeutic potential of a promising new class of drugs that are currently in various stages of clinical testing for a variety of cancers. The model will connect relevant intracellular signal transduction pathways with cell behavior and ultimately translate this into tissue-level behavior. We will present our model development in Sects. 2.2–2.8, simulations and predictions in Sects. 2.9–2.11, and conclude with a summary of our work, and future directions in Sect. 2.12.

Tumor-induced angiogenesis is a highly complex process operating on several time and length scales. It involves an intricate interplay between biochemical and biomechanical processes. At the biochemical level, there is transcription and release of pro-angiogenic factors by the tumor cells in response to hypoxia. These factors diffuse from the tumor to nearby vessels and are taken up by vascular endothelial cells lining them, resulting in the activation of cell surface receptors and the myriad downstream signaling pathways initiated as a result. These translate into specific cellular behavior, such as proliferation, migration, differentiation, gene transcription, and the further release of factors that regulate angiogenesis. Biomechanical mechanisms such as cell–cell interactions, cell–matrix interactions, result in cooperative interactions of the cells with their micro-environments and play a key role in regulating angiogenesis. However, these will not be considered here.

Of interest to us are a series of experiments conducted by Nör et al. (1999, 2001a,b), who have developed a novel approach to study the in vivo growth of human blood vessels within a mouse model system (Fig. 3.1a). Briefly, human dermal microvascular endothelial cells (HDMECs) along with oral squamous carcinoma cells (OSCCs) were transplanted into severe combined immunodeficient mice on biodegradable polymer matrices. HDMECs transplanted in this way differentiated into functional human microvessels that eventually anastomosed with existing mouse vasculature, thus generating human tumors vascularized with human microvessels (Nör et al. 2001b). In the course of their experiments, Nör et al. (1999, 2001a) observed that the primary pro-angiogenic chemokine being secreted by the tumor cells was vascular endothelial growth factor (VEGF), which in addition to inducing HDMEC proliferation and differentiation, mediated a strong survival signal by up-regulating the expression of the antiapoptotic intracellular protein Bcl-2. Further, it was observed that Bcl-2 in turn up-regulated the expression of the chemokine CXCL8 (Interleukin-8) by the HDMECs, which further induced cell proliferation and differentiation. Figure 3.1b shows a schematic of this pathway.

This newly discovered pathway suggests the possibility of therapeutic intervention targeting either Bcl-2 or CXCL8, in order to control the process of

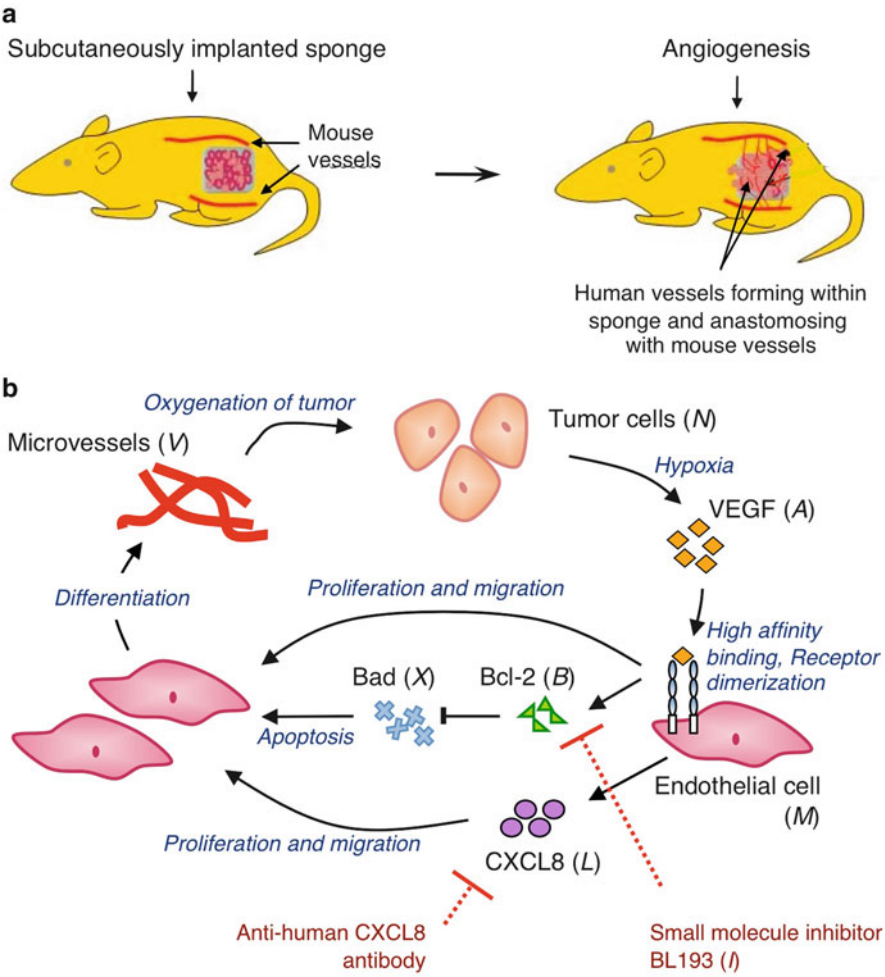

Fig. 3.1 The VEGF – Bcl-2 – CXCL8 pathway in tumor-induced angiogenesis. (**a**) HDMECs along with OSCC-3 or SLK cells are transplanted subcutaneously in the flank region of immunodeficient mice. These implants eventually develop into human tumors, populated with human microvessels. (**b**) Tumor cells produce VEGF under conditions of hypoxia, which binds to VEGFR-2 on endothelial cell surfaces, resulting in receptor dimerization and activation. In addition to inducing a proliferative and chemotactic response from them, this causes over-expression of the intracellular protein Bcl-2, which inhibits the effect of the pro-apoptotic protein Bad. Additionally, Bcl-2 also up-regulates production of CXCL8 production by the cells. CXCL8 further elicits a proliferative and chemotactic response from the endothelial cells. These now begin to aggregate and differentiate into microvessels, that eventually fuse with mouse vessels and become blood borne, resulting in oxygenation of the tumor. Shown also are two therapeutic strategies targeting CXCL8 and Bcl-2 that are investigated with our model. Figure adapted from Jain et al. (2009)

angiogenesis. The model presented here is formulated on the experiments of Nör et al., with the aim of investigating the relative potential of these strategies, in order to aid drug-design and development, and is based on recently published work (Dong et al. 2007; Jain et al. 2008, 2009). We will build the model in stages, beginning with the effects of oxygen and blood-bearing vessels on growing tumor cells, followed by the molecular events associated with the chemical mediators as well as the endothelial cell response to these chemokines, and end with microvessel formation, and maintenance. Any such modeling initiative of biological phenomena must begin with an in-depth understanding of the relevant biology, followed by identification and translation of the key steps of interest into mathematical equations, and we shall use this as our guiding principle in model formulation. The principle components of our model shall be tumor cell density $N(t)$, HDMEC density $M(t)$, free VEGF concentration $A(t)$, intracellular Bcl-2 concentration $B(t)$, intracellular Bad concentration $X(t)$, free CXCL8 concentration $L(t)$, and microvessel density $V(t)$. In addition, we will track the dynamics of cell-surface VEGF receptors $R_a(t)$, and CXCL8 receptors $R_l(t)$ as they associate with their respective ligands.

2 Tumor Cell Growth

Tumor development is mediated by the availability of oxygen and nutrients; that is, cells will proliferate and undergo apoptosis at rates dependent on the local oxygen concentration C. In fact, Ward and King (1999) followed by Gammack and Byrne (2001) have already developed a model for tumor cell growth (3.1) which is based on empirical data, and we will adapt this for our purposes.

$$\frac{\mathrm{d}N}{\mathrm{d}t} = r_1 \frac{C^2}{C_1^2 + C^2} N - r_2 \left(1 - \sigma \frac{C^2}{C_2^2 + C^2}\right) N^2 \tag{3.1}$$

The first term in (3.1) describes the rate of cell proliferation – as oxygen concentration increases the rate of tumor cell proliferation increases until it reaches a maximum value. Likewise, the second term describes the rate of cell apoptosis, which decreases to a minimum level with an increase in oxygen concentration. The N-squared term in the cell death rate reflects the limited carrying capacity of the environment, which here is a function of the local oxygen tension. Thus, the tumor cells grow in a logistic manner.

Oxygen (and nutrients) are supplied to the tumor implant by the microvessels that have an established blood flow; therefore, we can simplify this model slightly by treating oxygen concentration C as a function of blood-bearing vessel density V. The exact form relating C and V is taken from Nagy (2004), and is given in (3.2).

$$C = C(V) = C_{\mathrm{m}} \frac{V_0 + V}{k + V_0 + V}. \tag{3.2}$$

Here, C_m is the maximum oxygen concentration, under normoxia (20% oxygen Gammack and Byrne 2001). As mouse vessels surround the tumor implant, some oxygen may diffuse through to the tumor cells from these. Therefore, a fixed minimum vessel density V_0 is assumed in the region of the implant.

3 Vascular Endothelial Growth Factor

VEGF is one of the most crucial regulators of angiogenesis and is highly up-regulated in most human cancers (Papetti and Herman 2002; Ferrara et al. 2003; Roskoski 2007). It is expressed by tumor cells under conditions of hypoxia, during which there is a build up of the transcription factor hypoxia-inducible factor (HIF-1α). This initiates the transcription of target genes that promote the formation of blood vessels, including the VEGF gene (Ferrara et al. 2003; Roskoski 2007). Therefore, we assume that VEGF is produced by tumor cells under conditions of hypoxia, which occurs when the density of the microvessels is very low. Specifically, the production of VEGF is "switched on" when the microvessel density falls below a threshold level V_{char}, and "switched off" when the density exceeds this value. It should be noted that this angiogenic switch causes the microvessel density to stabilize at a maximum level, at around V_{char}. Following Pettet et al. (1996), the rate of VEGF production by tumor cells is taken to be proportional to $\left(1 + \tanh\left(\frac{V_{\text{char}} - (V + V_0)}{\epsilon}\right)\right) N$. Here, ϵ is a measure of the sensitivity of tumor cells to the critical value V_{char}.

3.1 VEGF Uptake by Cell-Surface Receptors

VEGF diffuses from the tumor to nearby vessels and binds to receptors selectively expressed on the surface of the vascular endothelial cells. These are transmembrane receptor tyrosine kinases (RTKs) including VEGFR1 (flt-1) and VEGFR2 (KDR/flk-1), which are activated through ligand binding. This facilitates receptor dimerization and autophosphorylation of tyrosine residues in the cytoplasmic portion. The phosphotyrosine residues provide docking sites for downstream signaling proteins resulting in a number of downstream effects of VEGF (McMahon 2000). As VEGFR2 is considered to be the principal mediator of the angiogenic effects of VEGF, while VEGFR1 is largely presumed to be a decoy receptor (Ferrara et al. 2003; Roskoski 2007), we will only consider the activation and dimerization of VEGFR2 by VEGF.

A review of the modeling literature shows that most existing models of intratumoral and wound healing angiogenesis which incorporate the effects of pro-angiogenic chemokines such as VEGF, continue to ignore ligand-induced receptor dimerization. Instead, a variety of biologically unrealistic uptake forms for VEGF

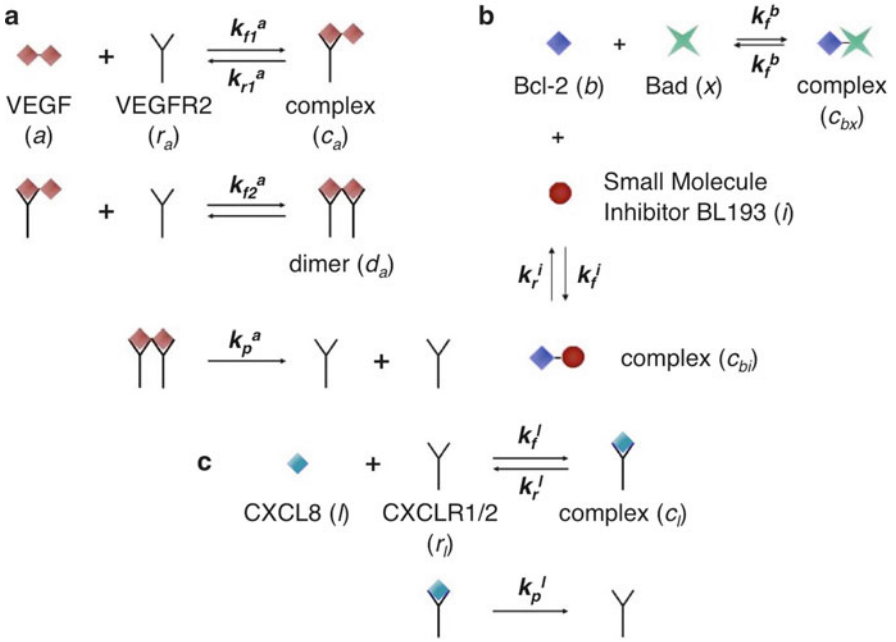

Fig. 3.2 Biochemical reaction networks. (**a**) Cell-surface VEGF–VEGFR2 interactions. VEGF binds to and dimerizes its cell surface receptor VEGFR2. The activated receptor–ligand complex is subsequently internalized, and free receptors recycled. (**b**) Bcl-2-Bad, Bcl-2-BL193 interactions. Bcl-2 heterodimerizes with Bad in the cell cytoplasm. This reaction is inhibited by a small molecule inhibitor, BL193. Figure adapted from Jain et al. (2009). (**c**) Cell-surface CXCL8-CXCL8R1/2 interactions. CXCL8 binds to and activates its cell surface receptors CXCL1/2. The activated receptor–ligand complex is subsequently internalized, and free receptors recycled

by endothelial cells (constant rate, and Michaelis-Menten like terms) are common in the cases where this uptake is not ignored altogether. However, choosing the correct form for VEGF-VEGFR-2 interaction can have a big impact on chemokine dynamics, and consequently model predictions. To this end, we develop a detailed molecular level model of VEGF binding and activating cell surface receptors, as shown in Fig. 3.2a.

Lower case letters are used to represent individual molecules and upper case letters are used to represent their concentration (in moles per liter), so that $A = [a]$ is VEGF concentration, $R_a = [r_a]$ is VEGFR2 concentration, $C_a = [c_a]$ is VEGFR2-VEGF monomer complex concentration, and $D_a = [d_a]$ is VEGFR2-VEGF-VEGFR2 dimer complex concentration. Following the general approach of Levine et al. (2000), the above reaction diagram can be converted to the following system of equations using the law of mass action.

$$\frac{\mathrm{d}A}{\mathrm{d}t} = -2\,\eta_1^a\,k_{f1}^a\,A\,R_a + \eta_2^a\,k_{r1}^a\,C_a + r_3\,N\left(1+\tanh\left(\frac{V_{\mathrm{char}}-(V+V_0)}{\epsilon}\right)\right) - \lambda_a\,A \tag{3.3}$$

$$\frac{\mathrm{d}R_a}{\mathrm{d}t} = -2k^a_{f1}AR_a + \eta^a_3 k^a_{r1} C_a - k^a_{f2} C_a R_a + 2\,\eta^a_4 k^a_{r2} D_a + 2\,\eta^a_4 k^a_p D_a \quad (3.4)$$

$$\frac{\mathrm{d}C_a}{\mathrm{d}t} = 2\,\eta^a_5 k^a_{f1} A R_a - k^a_{r1} C_a - \eta^a_5 k^a_{f2} C_a R_a + 2\,\eta^a_6 k^a_{r2} D_a \quad (3.5)$$

$$\frac{\mathrm{d}D_a}{\mathrm{d}t} = \eta^a_7 k^a_{f2} C_a R_a - 2k^a_{r2} D_a - k^a_p D_a\,, \quad (3.6)$$

where $k^a_{f1,2}$ are association rate constants, $k^a_{r1,2}$ dissociation rate constants and k^a_p is the rate of receptor internalization/recycling. The multiplicative factor of 2 in some of the equations accounts for the possibility that there may be two ways for that product to form. For example, in (3.4), there are two ways for a VEGF dimer molecule to bind to a single receptor molecule, because there are two binding sites on the VEGF molecule. In experimental assays, the weights of chemokines are often measured in picograms or nanograms. Further, the length scale of experiments of interest to us is in millimeters. Thus, the above equations are scaled to units of pg/mm^3 by appropriate constants (η^a_i), which represent ratios of molecular weights of the species involved. Included in the equation describing free VEGF concentration dynamics (3.3), is production by tumor cells, and natural decay, at a rate λ_a. Note that we could have reduced complexity by assuming Michaelis-Menten-like kinetics; however these are not valid when VEGF concentration is low in comparison to its receptor density (Segel and Slemrod 1989), a situation which is to be expected when vessel density is near it threshold V_{char}, and VEGF production by the tumor is "switched-off."

3.2 Endothelial Cell Response to VEGF

VEGF exerts a number of different effects on EC, including inducing changes in EC morphology, cytoskeleton alteration, and stimulation of EC migration. VEGF is also a highly specific mitogen for vascular endothelial cells and stimulates their proliferation (Hicklin and Ellis 2005). In contrast to other models which assume that endothelial cell proliferation depends on extra-cellular growth factor concentrations, we will take HDMEC proliferation to be directly proportional to the amount of dimerized and hence activated receptors on cell surfaces. The rate of change of the free HDMEC population is represented in (3.7). The units of endothelial cell ($M(t)$) and vessel ($V(t)$) densities are number per mm^3. Note that "a microvessel" denotes one segment of a vessel between adjacent branching points that can fit into a cube of side one millimeter.

$$\frac{\mathrm{d}M}{\mathrm{d}t} = (\mu_a\,\phi_a - \lambda_m(X))\;M\left(1 - \frac{M + \alpha_1 V}{M_0}\right), \quad (3.7)$$

where

$$\phi_a = \phi_a(D_a, M, V) = \frac{D_a}{M + \alpha_1 V}. \quad (3.8)$$

The HDMECs are assumed to grow logistically, as the carrying capacity M_0 of this experimental environment is limited. The endothelial cells lining the microvessels also compete with the free endothelial cells for space and nutrients and are therefore incorporated into the logistic term. Here, α_1 is the average number of cells per microvessel. The first term in (3.7) represents cell proliferation rate as a function of activated VEGFR2 density *per cell* (ϕ_a). The second term in (3.7), λ_m is the natural death rate of endothelial cells, which we shall take to be mediated by the Bcl-family of proteins, as discussed in the next section.

4 The Bcl-Family of Proteins

The intracellular Bcl-family of proteins have been identified as crucial mediators of apoptosis. This is a form of cell death in which a programmed sequence of events leads to the disintegration of cells without releasing harmful substances into the surrounding tissue. The Bcl-family may be broadly divided into two categories, the antiapoptotic proteins including Bcl-2, Bcl-x_L, and Mcl-1, and their pro-apoptotic counterparts including Bax, Bad, Bak, and Bid. It is the interaction among these molecules that determines cellular response to apoptotic signals (Adams 2003). Briefly, antiapoptotic proteins like Bcl-2 bind to, and thereby keep in check the pro-apoptotic proteins like Bax and Bak. Bax and Bak build up leads to mitochondrial outer wall permeability, resulting in the release of cytochrome c (cyt c) into the cytoplasm. Once cyt c is released into the cell, it complexes with Apaf 1, and subsequently activates caspase 9. Caspase 9 belongs to a family of proteases that form the core component of cellular apoptotic machinery. Its activation is an irreversible step toward cell death (Adams and Cory 2007).

In order to describe Bcl-2-regulated cell death, we continue our model development at the level of a single endothelial cell. The intracellular concentration, in femtograms per cell of Bcl-2, and a single pro-apoptotic representative of the Bcl family, Bad, will be tracked in time. Single representatives of the pro- and antiapoptotic family members are chosen so as to avoid involving a number of intracellular binding parameters for which there is no experimental data. The particular choice of the representative proteins was made for the following reasons: it is intracellular levels of Bcl-2 that are up-regulated in response to a VEGF stimulus (Nör et al. 2001a); Bad binds to Bcl-2 with a higher affinity than the other Bcl proteins (Wang et al. 2003); and Bad acts upstream of the Bax-like members of the Bcl family.

4.1 Bcl Protein Interactions Within a Single Cell

It is known that Bcl-2 and Bad interact with each other within the endothelial cell to form heterodimers. This balance between pro- and antiapoptotic proteins regulates cell death rate. Figure 3.2b shows the reaction between Bcl-2 and Bad

molecules. As before, the law of mass action is applied to translate this into a system of differential equations (3.9)–(3.11) that govern the temporal changes in the intracellular concentrations of these proteins. Following the same notation as in Sect. 4, upper case letters represent chemical concentrations so that B is unbound Bcl-2 protein per cell, X is unbound Bad protein per cell, C_{bx} is the quantity per cell of the heterodimer formed when one molecule of Bcl-2 binds to one molecule of Bad, η_i^b are appropriate scaling constants, and k_f^b and k_r^b are association and dissociation rate constants, respectively.

$$\frac{\mathrm{d}B}{\mathrm{d}t} = -k_f^b\, B\, X + \eta_1^b\, k_r^b\, C_{bx} + \beta_a \frac{\mathrm{d}}{\mathrm{d}t}\,(\phi_a) \tag{3.9}$$

$$\frac{\mathrm{d}X}{\mathrm{d}t} = -\eta_2^b\, k_f^b\, B\, X + \eta_3^b\, k_r^b\, C_{bx} \tag{3.10}$$

$$\frac{\mathrm{d}C_{bx}}{\mathrm{d}t} = \eta_4^b\, k_f^b\, B\, X - k_r^b\, C_{bx}. \tag{3.11}$$

As mentioned earlier, VEGF also acts as a survival factor for HDMECs by activating the PI3K-Akt (Phosphoinositide 3-kinase/protein kinase B) pathway. This results in the up-regulation of antiapoptotic proteins such as Bcl-2 (Nör et al. 2001a). In order to capture this effect, we postulate that the amount of Bcl-2 produced is directly proportional to the number of active VEGF-receptor dimer complexes per cell (and hence the rate of change of Bcl-2 concentration per cell is proportional to the rate of change of active VEGF-receptor dimer complexes). A corresponding source term for Bcl-2 is included in (3.9). The constant β_a is a measure of the level of this up-regulation.

4.2 Apoptosis Regulation at the Population Level

As it is the pro-apoptotic members of the Bcl family that are directly responsible for regulating caspase activation within the cells (Adams and Cory 2007), the amount of unbound protein Bad (X) is assumed to determine HDMEC death rate λ_m (see (3.7)). In this way, the intracellular signaling dynamics modeled in the previous section are used to determine the response of a population of cells to their microenvironment. Based on (indirect) experimental evidence for the fact that cells are highly sensitive to pro-apoptotic signals, which are normally tightly controlled and balanced by antiapoptotic proteins like Bcl-2, λ_m is taken to be an exponential function of X.

$$\lambda_m(X) = a_d\, e^{b_d\, X}. \tag{3.12}$$

5 CXCL8

We conclude our biochemistry survey by looking at CXCL8. It belongs to a class of small cytokines produced by, among others, endothelial cells. It has a strong mitogenic and chemotactic effect on these cells, because of which its production is tightly regulated, and its constitutive levels in normal tissue are very low (Brat et al. 2005). CXCL8 is also a potent mediator of tumor angiogenesis. Its expression is found to be up-regulated in certain cancers, such as nonsmall cell lung cancer, and melanoma (Papetti and Herman 2002). Further, it has been shown that VEGF is able to induce over-expression of CXCL8 mRNA in HDMECs, via the PI3K/Akt signaling pathway (Nör et al. 1999; Brat et al. 2005). CXCL8 mediates its biological functions by interacting with specific G-protein-coupled CXC chemokine receptors CXCR1 and CXCR2. These are expressed on a variety of cell types including endothelial cells (Brat et al. 2005). Because of its potent pro-angiogenic effects, CXCL8 and its receptors are incorporated explicitly in our model of tumoral angiogenesis.

The reaction diagram for CXCL8 interaction with CXCR1/2 is shown in Fig. 3.2c. For simplicity, CXCR1 and CXCR2 are not distinguished between in the model. Further, in the absence of conclusive evidence that two CXCL8 molecules are required to internalize the activated receptor–ligand complex. It is assumed that one molecule of CXCL8 is sufficient to activate its receptors. As before, the law of mass action can be used to derive the system of (3.13)–(3.15) that describe CXCL8 uptake by its receptors. Upper case letters represent chemical concentrations, so that L is free CXCL8 concentration, R_l is CXCL8 receptor density, C_l is CXCL8-receptor complex density, η_i^l are scaling constants as before, k_f^l and k_r^l are the association and dissociation rate constants, respectively, and k_p^l is the rate of receptor internalization/recycling. A natural decay rate λ_l of CXCL8 in tissue is included in (3.13).

$$\frac{\mathrm{d}L}{\mathrm{d}t} = -\eta_1^l\, k_f^l\, L\, R_l + \eta_2^l\, k_r^l\, C_l - \lambda_l\, L + \beta_l(B)\, M \tag{3.13}$$

$$\frac{\mathrm{d}R_l}{\mathrm{d}t} = -k_f^l\, L\, R_l + \eta_3^l\, k_r^l\, C_l + \eta_3^l\, k_p^l\, C_l \tag{3.14}$$

$$\frac{\mathrm{d}C_l}{\mathrm{d}t} = \eta_4^l\, k_f^l\, L\, R_l - k_r^l\, C_l - k_p^l\, C_l \tag{3.15}$$

5.1 Bcl-2-Mediated Up-regulation of CXCL8

HDMECs are known to maintain a basic concentration of CXCL8. Further, it has experimentally been shown that Bcl-2 up-regulates this expression of CXCL8 through its ability to activate the NF-κB signaling pathway (Karl et al. 2005).

Therefore, we include in (3.13) a production term β_l for CXCL8 by HDMECs, which is taken to be dependent on intracellular Bcl-2 concentration B. In the absence of experimental data that may be used to find the precise form of this function, we make the biologically reasonable assumptions that CXCL8 production rate by HDMECs increases to a maximum level, as intracellular Bcl-2 concentration increases, under the effect of VEGF. We also allow for the possibility that CXCL8 could be produced by endothelial cells independent of Bcl-2. The following function satisfies these conditions.

$$\beta_l(B) = \beta_m + a_p\,(1 - e^{-b_p\,B}). \tag{3.16}$$

6 Endothelial Cell Growth Revisited

Now that we have derived equations for the production and uptake of CXCL8, we need to modify our HDMEC growth equation (3.7) to reflect the proliferative and chemotactic effect of CXCL8 on endothelial cells as follows.

$$\begin{aligned}\frac{\mathrm{d}M}{\mathrm{d}t} &= (\mu_a\,\phi_a + \mu_l\,\phi_l - \lambda_m(X))\;M\left(1 - \frac{M + \alpha_1 V}{M_0}\right)\\ &\quad - \alpha_1\;(\alpha_2\,\phi_a + \alpha_3\,\phi_l)\;M(t-\tau),\end{aligned} \tag{3.17}$$

$$\text{where}\quad \phi_l = \phi_l(C_l, M, V) = \frac{C_l}{M + \alpha_1 V}.$$

Included in (3.18) is a proliferation rate for HDMCEs, dependent on the activated CXCL8 receptors *per cell*, (ϕ_l), in addition to VEGF-mediated proliferation. While there is no explicit experimental evidence that effects of VEGF and CXCL8 on HDMECs are additive, this is a reasonable assumption in the absence of data to the contrary. In addition, both VEGF and CXCL8 have been shown to be potent mitogenic (and chemokinetic) factors for endothelial cells, with VEGF eliciting a stronger response than CXCL8 alone (Nör et al. 1999). Also included in (3.18) is a term that represents cell migration and differentiation into functional microvessels in response to chemical cues from VEGF and CXCL8. This is explained in further detail in the next section.

7 Microvessel Formation and Degradation

As endothelial cells grow in number, they begin to come together and arrange themselves into microvessels in the process of vascular inclusion. While classical models of tumor angiogenesis or wound healing angiogenesis typically address blood vessel formation that results from pre-existing vasculature, due to the nature of our experimental setup, we need to model the process of microvessel formation

via alignment and differentiation of individual endothelial cells. Equation (3.18) gives the rate of change of microvessel density.

$$\frac{\mathrm{d}V}{\mathrm{d}t} = (\alpha_2\,\phi_a + \alpha_3\,\phi_l)\;M(t-\tau) - \alpha_4\;(\lambda_m(X))\;\alpha_1\,V \tag{3.18}$$

VEGF and CXCL8 are both strong chemoattractants for the HDMECs, so that the cells align and form microvessels at a rate dependent on activated receptor densities ϕ_a and ϕ_l. This process of vascular inclusion results in a corresponding decrease in the free endothelial cell density, and is therefore subtracted from the endothelial cell equation 3.7. Recall that α_1 is the average number of endothelial cells per microvessel. Vessel maturation is not incorporated in this model. Therefore, when cells lining an immature vessel die, it becomes dysfunctional at rate, α_4. As in the case of free HDMECs, the death rate of differentiated HDMECS is also taken to be a function of intracellular Bcl-2. In the absence of conclusive evidence that budding and anastomosis significantly affect microvessel densities within the implant, for the sake of simplicity, these processes have not been included in this model.

An important feature of our model is the incorporation of a delay τ in the vessel formation rate. This accounts for the experimentally observed time delay between an endothelial cell receiving a signal in the form of activated cell surface receptors and differentiating to form mature, blood-bearing microvessels. In the experiments of Nör et al. (2001a), this delay is reported to be about 5 days. The principle steps leading to the formation of microvessels via the processes of vasculogenesis and angiogenesis are described in Patan (2000). Briefly, upon receiving a chemical stimulus cells may proliferate or migrate toward this signal in a process known as chemotaxis. As the cells begin to align together, they abandon their invasive phenotype, and begin forming cell–cell or cell-extracellular matrix adhesions, via cell surface molecules such as integrins. This is followed by stretching and thinning of the cells, and vacuole and lumen formation. As more and more cells come together intracellular vacuoles fuse, and the lumens enlarge to generate tubular structures. Finally, specialized cells such as pericytes and smooth muscle cells stabilize these structures by forming basement membrane, resulting in a microvessel capable of carrying blood. In a partial differential equation model, chemotaxis may account for some of the time taken in these steps. However, as we are developing an ordinary differential equation model independent of space, we include a delay in vessel formation to account for the steps involved in capillary formation. Time delays in vessel formation/regression terms have been used previously in ODE models of tumor induced angiogenesis (Daugulis et al. 2004).

8 Receptor Conservation Laws

In our model, HDMECs are assumed to express a fixed number of VEGFR2 (R_t^a) and CXCLR1/2 (R_t^l) per cell. As the endothelial cell number and microvessel density will change with time, we need to ensure that cell-surface receptor numbers are conserved. Mathematically, this means that the sum of the total free and

bound receptor densities must equal the product of the level of receptor expression per cell and the total (free + differentiated) endothelial cell density. That is, the following conditions must be satisfied.

$$R_a + \eta_3^a\, C_a + 2\,\eta_4^a\, D_a = R_t^a\,(M + \alpha_1\, V) \tag{3.19}$$

$$R_l + \eta_3^l\, C_l = R_t^l\,(M + \alpha_1\, V). \tag{3.20}$$

These conservation laws introduce production and loss terms corresponding to changes in HDMEC density in the equations representing VEGFR2 activation ((3.4)–(3.6)) and the equations representing CXCR1/2 activation ((3.14)–(3.15)). For instance, taking the time-derivative of (3.20), we get

$$\frac{\mathrm{d}R_l}{\mathrm{d}t} + \eta_3^l\,\frac{\mathrm{d}C_l}{\mathrm{d}t} = R_t^l\left(\frac{\mathrm{d}M}{\mathrm{d}t} + \alpha_1\,\frac{\mathrm{d}V}{\mathrm{d}t}\right) \tag{3.21}$$

The rates of change of free (M) and differentiated (V) endothelial cells given by (3.18) and (3.18) may be written as the difference of their respective production and death rates. That is, taking

$$\mathrm{Prod}(M,V) = (\mu_a\,\phi_a + \mu_l\,\phi_l)\;M\left(1 - \frac{M + \alpha_1 V}{M_0}\right) \tag{3.22}$$

$$\mathrm{Death}(M,V) = \lambda_m(X)\,M\left(1 - \frac{M + \alpha_1 V}{M_0}\right) + (\alpha_1)^2\,\alpha_4\,\lambda_m(X)\,V, \tag{3.23}$$

we have that

$$\frac{\mathrm{d}M}{\mathrm{d}t} + \alpha_1\,\frac{\mathrm{d}V}{\mathrm{d}t} = \mathrm{Prod}(M,V) - \mathrm{Death}(M,V). \tag{3.24}$$

Substituting this in (3.21), we get

$$\frac{\mathrm{d}R_l}{\mathrm{d}t} + \eta_3^l\,\frac{\mathrm{d}C_l}{\mathrm{d}t} = R_t^l\,(\mathrm{Prod}(M,V) - \mathrm{Death}(M,V)). \tag{3.25}$$

Note that when a cell dies, any free and activated receptors on its surface are lost. However, when a cell is born, it will only have free receptors on its surface. Thus, we split the "Death" term in the above equation as follows.

$$\frac{\mathrm{d}R_l}{\mathrm{d}t} + \eta_3^l\,\frac{\mathrm{d}C_l}{\mathrm{d}t} = R_t^l\,\mathrm{Prod}(M,V) - \left(\frac{R_l}{R_l + \eta_3^l\,C_l} + \eta_3^l\,\frac{C_l}{R_l + \eta_3^l\,C_l}\right) R_t^l\,\mathrm{Death}(M,V). \tag{3.26}$$

We can now modify the equations governing CXCL8 receptor activation by adding the first two terms on the right-hand side in the equation above to the rate of change of free CXCL8 receptors (3.13), and adding the last term on the right-hand

side in the equation above to the rate of change of activated CXCL8 receptors (3.15) to get the following.

$$\frac{\mathrm{d}R_l}{\mathrm{d}t} = -k_f^l\, L\, R_l + \eta_3^l\, k_r^l\, C_l + \eta_3^l\, k_p^l\, C_l + R_t^l\, \mathrm{Prod}(M,V) - \frac{R_l}{R_l + \eta_3^l\, C_l}\, R_t^l\, \mathrm{Death}(M,V) \tag{3.27}$$

$$\frac{\mathrm{d}C_l}{\mathrm{d}t} = \eta_4^l\, k_f^l\, L\, R_l - k_r^l\, C_l - k_p^l\, C_l - \frac{C_l}{R_l + \eta_3^l\, C_l}\, R_t^l\, \mathrm{Death}(M,V). \tag{3.28}$$

The equations representing VEGFR2 activation ((3.4)–(3.6)) can be modified in a similar way, this is left as an exercise for the reader.

9 Vascular Tumor Growth

The model developed in the previous sections has a number of unknown parameters, that must be obtained from a literature survey, or fitted to experimental data. To present a complete parameter estimation is beyond the scope of this chapter, and the reader is directed to the two publications concerning this model (Jain et al. 2008, 2009), where details regarding the choice of parameters are provided. The complete model governing the development of a vascular tumor consists of at least 13 equations (we shall add more in the therapy sections), operating on multiple time-scales – tumor growth and vascular development occurring over a period of weeks; cell death and proliferation occurring on the order of hours; and biochemical reactions occurring over a period of a few minutes. Additionally, the equations governing endothelial cell dynamics are delayed. Solving such a stiff system of delayed differential equations can be challenging, and is a topic of research in itself. We use a numerical package that implements RADAU IIA methods adapted to solve delay differential equations, called RADAR5 Version 2.1 (Guglielmi and Hairer 2001). This package is available freely online, and is coded in Fortran.

We begin with simulations of the model in the absence of antiangiogenic or any other anticancer therapies to illustrate vascular tumor growth dynamics. With parameters at their baseline values, the tumor cell density reaches it's maximum level (1.149×10^4 cells per mm^3) about 28 days after implantation (Fig. 3.3a). The first blood-bearing vessels are seen 5 days after implantation in which period the scaffold is hypoxic. This leads to a transient decrease in tumor cell density that may be attributed to necrosis (Fig. 3.3a, inset). The microvessels reach their steady state of about 53 vessels per mm^3, a further 19 days later (Fig. 3.3b).

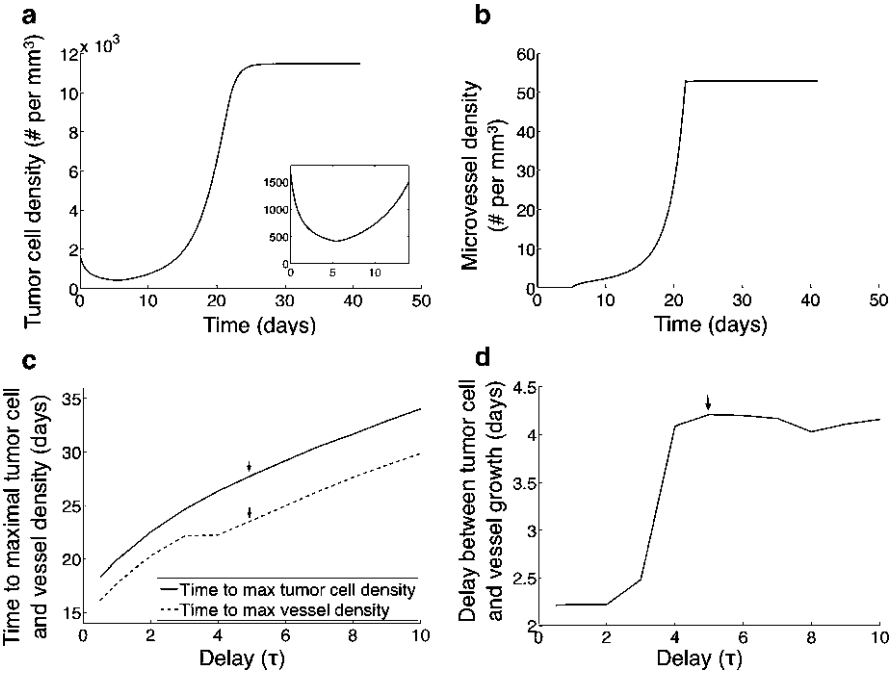

Fig. 3.3 Vascular tumor growth in the absence of therapeutic intervention. (**a**) Tumor cell density reaches its steady state of 1.149×10^4 cells per mm^3 about 4 weeks postimplantation. A transient decrease in cell density is observed due to hypoxic conditions within the implant for the first week (inset). (**b**) Blood borne vessels are first seen 5 days after implantation, and reach their steady state of 53 vessels per mm^3 about 24 days postimplantation. (**c**) As the delay is varied between biologically realistic values of 0.5–10 days, the time taken to maximal tumor cell and vessel densities increases by 88–89%. (**d**) For τ between 0.5 days and 3 days, the delay between tumor cell and vessel development is about 2 days, but for τ greater than 4 days, this delay increases to 4 days. *Arrows* indicate baseline value of $\tau = 5$ days. Figures adapted from Jain et al. (2008)

9.1 Effect of the Discrete Time Delay, τ

Recall that we introduced a delay in the microvessel formation term to account for the time it takes for a free endothelial cell to differentiate into a component of a blood bearing vessel, and we estimated the value of this delay, based on experimental observations, to be 5 days. In order to get an idea of the importance of this delay we study the effect its length has on two key indicators of tumor development – the times taken to reach maximal steady state values of tumor cell and vessel densities. The delay is varied between biologically realistic values of 0.5–10 days. As can be seen from Fig. 3.3c, the time taken to maximal tumor cell density increases from 18 days to 34 days – a change of 89%. Correspondingly, the time taken to reach maximal vessel density also increases by about 88% from 16 days to 30 days. Interestingly, for τ greater than 4 days, the delay between tumor

cell and vessel development is about 4 days, while for τ between 0.5 and 3 days, this delay is only 2 days (Fig. 3.3d). In other words, the longer tumor cells have to wait for their own blood supply, the longer their proliferation will lag behind the developing vasculature. Therapeutically, this could indicate a small window of opportunity for the administration of antiangiogenic treatment, in the cases where a tumor is detected early. Finally, it should be mentioned that the effect of introducing a delay in a system of differential equations is typically the emergence of oscillatory behavior. However, various numerical experiments carried out to test the stability of steady states of the model did not produce any such behavior.

10 Anti-CXCL8 Therapy

We now turn our attention to using this model to investigate the therapeutic potential of targeting the two molecules that are up-regulated downstream of VEGF in the VEGF – Bcl-2 – CXCL8 pathway. First, the model is used to simulate the effect that inhibiting CXCL8 production by HDMECs has on tumor progression. In experiments described in Nör et al. (2001a), polyclonal antihuman CXCL8 antibody was delivered locally, by incorporation into the scaffolds implanted in the mice. These were sacrificed after 21 days and vascular densities noted. The vasculature in treated tumors was reported to have a density of around 20 vessels per mm^3 as opposed to the control case, in which the density was double this value, at around 42 vessels per mm^3 (Fig. 3.4a). In order to model this therapeutic strategy, the equation governing free CXCL8 dynamics (3.13) must be altered to reflect the effect that the anti-CXCL8 antibody has on free CXCL8 concentration. This antibody binds to free CXCL8, effectively reducing its bio-availability for endothelial cells. In modeling terms, this can be thought of as equivalent to a reduction in the production rate of CXCL8, which would mean lower levels of free CXCL8 available to the endothelial cells. We therefore introduce a parameter ϵ_l, which is a measure of therapeutic efficacy and modulates the CXCL8 production term in (3.13). Therapeutic efficacy varies between 1, in which case production of CXCL8 is normal and reflects no application of therapy, and 0, in which case the reproduction of CXCL8 is completely blocked and reflects 100% efficacious therapy. This changes (3.13) as follows.

$$\frac{\mathrm{d}L}{\mathrm{d}t} = -\eta_1^l\, k_f^l\, L\, R_l + \eta_2^l\, k_r^l\, C_l - \lambda_l\, L + \epsilon_l\, \beta_l(B)\, M. \tag{3.29}$$

Numerical simulations show that as ϵ_l is decreased from 1 to 0, the vessel density after 21 days decreases correspondingly from 42 to 12 vessels per mm^3. In particular, $\epsilon_l = 0.589$ (41.1% effective therapy) corresponds to a vascular density of 20 vessels per mm^3 (Fig. 3.4a), the in vivo therapy result as reported in Nör et al. (2001a). Including the error bars from the experimental data allows us to calculate that the efficacy of in vivo therapy must lie between 20% and 100% (ϵ_l between 0.8 and 0). It is also important to determine the effect of varying

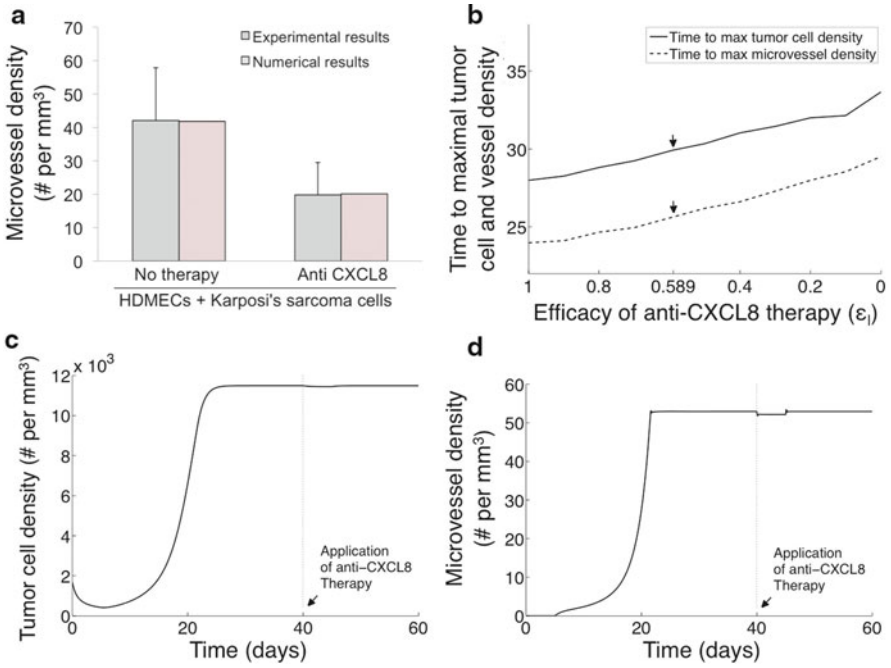

Fig. 3.4 Effect of anti-CXCL8 therapy on vascular tumor growth. (**a**) Comparison of experimental and numerical predictions of microvessel densities (vessels per mm^3) after 21 days of exposure to anti-CXCL8 therapy, in the form of polyclonal antihuman CXCL8 antibody delivered by incorporation into scaffolds implants in the mice, as described in Nör et al. (2001a). (**b**) Maximum delay in tumor progression measured in terms of time to maximal tumor cell and vessel densities is predicted to be 6 days for a 100% efficacious therapy level, as opposed to the no therapy case. $\epsilon_l = 0.589$ corresponds to the in vivo therapy in Nör et al. (2001a). (**c,d**) Anti-CXCL8 therapy is predicted to have a limited impact when applied to a fully developed tumor, with only transient decreases in tumor cell (**c**) and microvessel density (**d**). The anti-CXCL8 therapy is applied on the 40th day, once the tumor has reached its maximal tumor cell and vessel densities. Figures adapted from Jain et al. (2008)

CXCL8 therapy levels on delay in tumor development. As can be seen from Fig. 3.4b, the time taken to reach maximal tumor cell and vessel densities appears to vary linearly with ϵ_l. A 100% efficacious therapy level is predicted to delay tumor development by only 6 days, while the delay is only 2 days corresponding to the in vivo therapy in Nör et al. (2001a) ($\epsilon_l = 0.589$). Note that in Fig. 3.4b, ϵ_l varies from 1 to 0 on the abscissa, which should be interpreted as level of therapy increasing from 0% to 100%. Thus, anti-CXCL8 therapy is predicted only to delay and not regress tumor growth. This can be explained by observing that CXCL8 induces cell proliferation and migration. Hence, reducing CXCL8 levels at an early stage in tumor growth can be expected to produce a delay in vascular development, which correspondingly affects tumor cell proliferation. However, this delay is not very

large, possibly because CXCL8 is not directly related to enhanced endothelial cell survival, and VEGF is also a potent chemoattractant and mitogen.

In the above simulations, anti-CXCL8 therapy was applied from the time of implantation of the scaffold in the mice. However, in order to truly investigate the potential of any anticancer therapy, it is important to predict its effect on a fully formed tumor, which represents a more realistic scenario for clinical application. To this end, we allow the tumor to reach maximal tumor and vessel densities prior to application of anti-CXCL8 therapy (Fig. 3.4c,d). The model predicts that anti-CXCL8 treatment has little or no effect on the tumor when applied at this late stage. The vessel density is seen to decrease transiently, but the tumor cells compensate for this decrease in vascular density by increasing VEGF production, which in turn restores the vessel density to its pretreatment level. We now have an important prediction of the model; that anti-CXCL8 therapy has limited impact on tumor development by itself, and is largely ineffective when applied to fully formed tumors.

11 Anti-Bcl-2 Therapy

The Bcl family proteins have been shown to play a key role in tumor development and progression. A majority of human cancers including prostrate, breast, head and neck cancers, lymphomas, and melanoma are known to over-express Bcl-2, or Bcl-x_L, or both. In addition to promoting cell survival, this protects cancer cells from chemo- and radiotherapy, as these directly or indirectly induce apoptosis (Wang et al. 2003). Further, as we have seen, in some cases such as head and neck cancers, cancer cells are able to extend this protective effect to the endothelial cells lining the blood vessels in the vicinity of the tumor, thus enhancing intratumoral angiogenesis. This has resulted in the identification of Bcl-2 and Bcl-x_L as attractive targets for the development of anticancer drugs. In fact, several forms of therapy targeting Bcl-2/Bcl-X_L are under development, the most promising of which are nonpeptidic, cell-permeable small molecule inhibitors. Better bio-availability and stability, low antigenicity and cost, and ease of molecular modification make these the developmental drugs of choice (Wang et al. 2003). These inhibitor molecules act as antagonists of Bcl-2/Bcl-X_L by competing with pro-apoptotic members such as Bax, Bad, Bak to bind with Bcl-2/Bcl-X_L, leading to increased concentrations of Bax, which eventually results in cell death, as discussed in Sect. 2.5. In this section, we will use our model to investigate the therapeutic potential of targeting the VEGF-Bcl-2-CXCL8 pathway with these inhibitors.

11.1 The Small Molecule Inhibitor BL193

In particular, we will concentrate on the antiangiogenic potential the small molecule inhibitor BL193, which has been shown to induce a marked decrease in the angiogenic potential of endothelial cells (Karl et al. 2005; Zeitlin et al. 2006). As we are using Bcl-2 as a representative of the antiapoptotic members of the Bcl family, and given that BL193 has similar inhibition constants for both Bcl-2 and Bcl-X_L, means that we can easily include the mechanism of action of BL193 in our model. The reaction diagram in Fig. 3.2b describes the inhibition of Bcl-2 by BL193. Let I be the amount of BL193 per cell, and C_{bi} be the quantity per cell in femtograms of the complex formed when one molecule of Bcl-2 binds to one molecule of BL193. Then, the equation governing Bcl-2 dynamics (3.9) as formulated in Sect. 2.5.1 changes as follows, and two additional equations governing BL193 and BL193-Bcl-2 complex dynamics must be added to our model.

$$\frac{\mathrm{d}B}{\mathrm{d}t} = -k_f^b\, B\, X + k_r^b\, C_{bx} - k_f^i\, B\, I + k_r^i\, C_{bi} + \beta_a \frac{\mathrm{d}}{\mathrm{d}t}\,(\phi_a) \tag{3.30}$$

$$\frac{\mathrm{d}I}{\mathrm{d}t} = -k_f^i\, B\, I + k_r^i\, C_{bi} + D_i\,\,(I_0 - I) \tag{3.31}$$

$$\frac{\mathrm{d}C_{bi}}{\mathrm{d}t} = k_f^i\, B\, I - k_r^i\, C_{bi}\,. \tag{3.32}$$

It is assumed that upon application of therapy, the inhibitor molecules diffuse into the endothelial cell across the cell membrane. This is consistent with the design strategy behind these drugs. Thus, there is a source term in (3.31), where the rate of entry of the inhibitor molecules into an endothelial cell is proportional to the difference of extracellular (I_0) and intracellular BL193 concentrations. I_0 is a parameter that varies as the dosage level of therapy changes, and is fit to match such experiments. There are also two key parameters that affect the efficacy of BL193 – the constant D_i with units of 1/day, which is a measure of cell wall permeability to BL193 and governs how quickly it may be internalized into a cell; and the inhibition constant K_{Di}, which is given by the ratio of k_r^i to k_f^i.

11.2 Therapy Simulations

Given the complexity and scale of our model, it is important to validate it by direct comparison of model predictions of treatment by BL193, with experimental observations. Such data is in fact available to us in the form of capillary sprouting assays described in Karl et al. (2005). In these experiments, HDMECs were exposed to 50 ng/mL VEGF and starting on day 5, to 0–5 μM BL193. The number of sprouts were counted daily. Our model can easily be modified to represent this experimental system by removing the tumor cell equation, and keeping the free

VEGF concentration fixed at 50 ng/ml. The amount of drug administered I_0 is the only parameter varied, and a representative simulation is shown in Fig. 3.5a. This corresponds to 0.5 μM of therapy. The model predictions of microvessel densities are seen to match the experimental observations well. The effect of therapy on intracellular protein levels can be seen in Fig. 3.5b, which plots the amounts of Bcl-2, Bad, and BL193 per cell vs. time.

Having validated our model by comparison to in vitro experimental results, we are now in a position to investigate the effect of BL193 on in vivo tumor growth dynamics when applied at an early or late stage of tumor development. Figure 3.5c, d shows the effect of early stage therapy on tumor cell and microvessel densities. As can be seen, increasing doses of BL193 from 0.05 μM to 0.5 μM delays tumor development from 7 to about 17 days, when compared to the no therapy case. A dosage level of 5 μM BL193 appears to be enough to cause the tumor to regress, suggesting that antiangiogenic therapies in the form of small molecule inhibitors of Bcl-2 are highly efficacious when administered at an early stage in tumor development.

Next, we investigate the effect of application of BL193 to a fully developed tumor (Fig. 3.5e,f). Therapy is applied continuously from day 60 of implantation. The model predicts that administering 5 μM of BL193 induces a sharp decrease in microvessel density (Fig. 3.5f), leading to a corresponding decrease in tumor cell density (Fig. 3.5e). However, the tumor cells compensate for this loss of blood supply by increasing VEGF production, resulting in an equally rapid recovery of the tumor. In fact, the model predicts the existence of a threshold amount of therapy (approximately 24.5 mM), needed to induce tumor regression. In this case, the fall in microvessel density is too high for the tumor to recover from.

11.3 Sensitivity to Drug Design Parameters

There are two important considerations behind the design strategy of small molecule inhibitors of Bcl-2 such as BL193. The first is to maximize the inhibition of Bcl-2 by the molecule. We therefore carry out a sensitivity analysis on the inhibition constant K_{Di} of BL193, for the case when the drug is administered to a fully developed tumor. Numerical simulations predict that decreasing K_{Di}, results in an exponential decrease in the amount of drug required to affect a cure (Fig. 3.6a). For instance, reducing K_{Di} from its baseline value by 25% decreases the least amount of therapy required from 27.26 mM to 0.52 mM.

The second factor that underlies the design strategy of drugs such as BL193 is their bio-availability. In particular, it is important to maximize the cell-permeability of the molecule. This is done by varying the rate of diffusion D_i of BL193 across the cell wall. While increasing D_i reduces the amount of therapy required to affect a cure on a fully developed tumor (Fig. 3.6b), the gains are limited when compared to finding an even moderately better inhibitor of Bcl-2. For instance, even a tenfold increase in D_i is predicted to reduce the minimum drug dosage needed for a cure by a factor of only 53%, and any increase in D_i beyond this has no further impact.

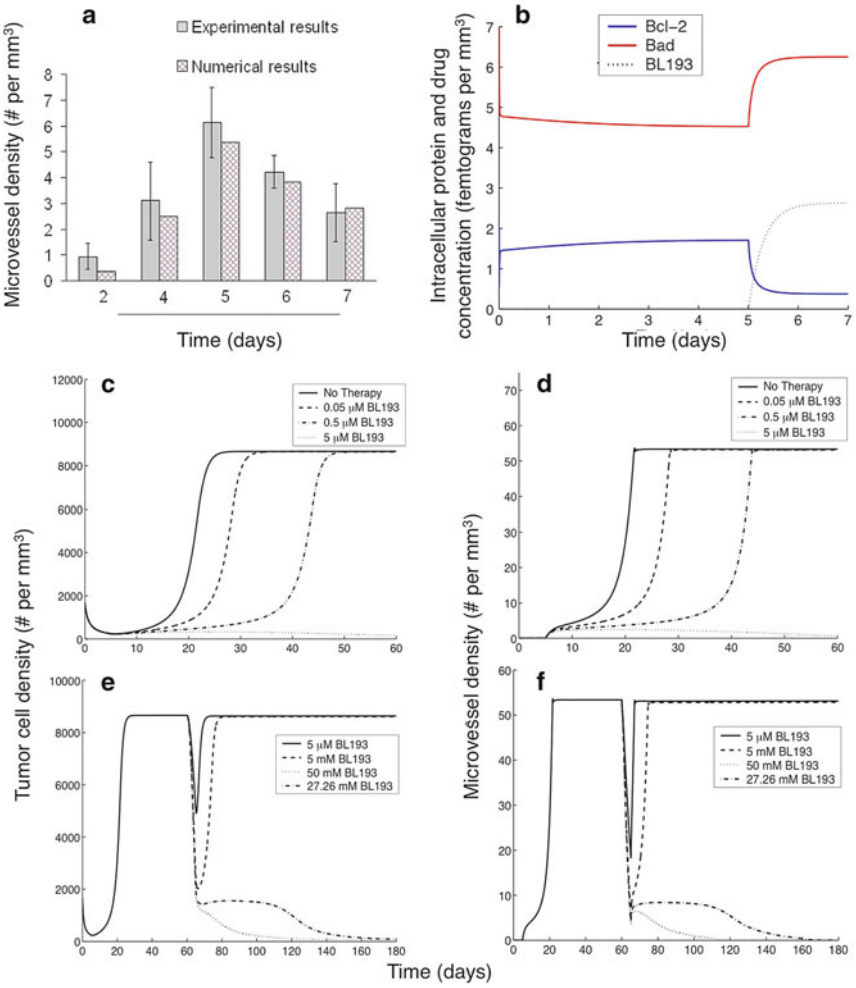

Fig. 3.5 Effect of anti-Bcl-2 therapy on endothelial cell angiogenic potential. (**a**) In capillary sprouting assays described in Karl et al. (2005), HDMECs were cultured in the presence of 50 ng per ml VEGF. Starting on day 5, 0.5 μM BL193 was administered and the number of sprouts counted daily. Numerical simulations of our model are seen to be in good agreement with experimental data. (**b**) Numerical predictions of intracellular protein and drug levels. Upon application of BL193 on Day 5, its levels within a cell begin to increase, causing a decrease in unbound Bcl-2 protein, and a corresponding increase in unbound Bad protein. (**c**) To simulate in vivo therapy, BL193 is administered in tumor cell and HDMEC-containing scaffolds starting from the day of implantation and continuing thereafter. As therapy levels increase from 0 to 0.5 μM, time taken to reach maximal tumor cell density increases by 25% and 89%, respectively. (**d**) The corresponding increase in time taken to reach maximal vessel density is 37% and 121%, respectively. About 5 μM of BL193 appears to be enough to effect a cure. (**e,f**) BL193 is administered to a fully developed tumor, starting from Day 60 of implantation and continuing thereafter. About 5 μM of BL193 is insufficient to effect a cure, inducing only a temporary reduction in tumor cell (**e**), and vessel densities (**f**). The minimum amount of therapy required in order to cause tumor regression is predicted to be 27.26 mM. Figures adapted from Jain et al. (2009)

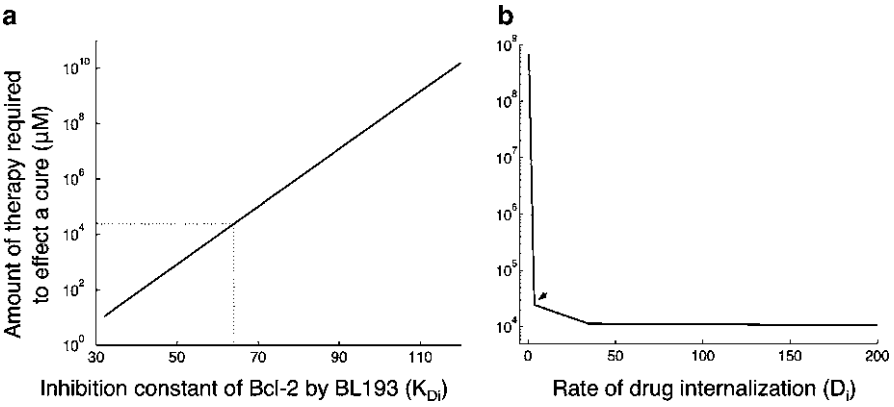

Fig. 3.6 Simulations of anti-Bcl-2 therapy applied to a tumor growing in vivo. (**a**) Minimum amount of therapy required to induce tumor regression is observed to vary exponentially with the 50% inhibition constant K_{Di} of BL193 for Bcl-2. (**b**) As the rate of diffusion D_i of BL193 into the cell is increased, the least amount of efficacious therapy reduces by a maximum amount of 56%, compared to baseline values for D_i. Figures adapted from Jain et al. (2009)

12 Conclusions

Despite advanced efforts in early diagnosis, aggressive surgical treatment and application of additional nonoperative modalities, the prognosis for many cancers is still dismal. This emphasizes the necessity to develop new strategies for its treatment. In this chapter, we investigated the antiangiogenic potential of targeting the VEGF-Bcl-2-CXCL8 pathway by developing a multiscale model quantifying the molecular events associated with VEGF dimerization and subsequent intracellular survival signaling in endothelial cells and for connecting these molecular processes to the temporal changes in tumor cell and microvessel density. We considered behavior starting from subcellular processes and moving to interactions among several cells, while simultaneously modeling tissue dynamics using a macroscopic level of description.

Our focus here has been on the role that endothelial cell stimulation, resulting from tumor cell-secreted factors, plays in tumor angiogenesis. However, this constitutes only part of the story. Emerging evidence indicates that endothelial cells themselves function as initiators of molecular crosstalks that can in fact feedback to the tumor and promote an increasingly aggressive phenotype in cancer cells (Dong and Nör 2009; Neiva et al. 2009). For instance, VEGF can also be secreted by endothelial cells, and induces a mitogenic response in tumor cells. Likewise, CXCL8 secreted by endothelial cells in response to Bcl-2 up-regulation has been shown to mediate tumor cell survival and migration. In fact, mounting evidence has demonstrated that the pro-survival protein Bcl-2, constitutes a unique and important therapeutic target for cancer. Bcl-2 clearly plays a role in the survival of tumor cells and resistance to therapy. It may be up-regulated constitutively, or in response

to VEGF signaling, in tumor cells. A great strength of the modeling approach discussed here lies in the flexibility of its framework; it can easily be modified to incorporate mechanisms such as these in order to test with greater confidence clinically relevant hypotheses regarding cancer growth inhibition resulting from therapies targeted against tumor and endothelial cell cross-talk.

The mathematical model developed here consists of delay differential equations that track temporal changes in the various species of interest. A major assumption underlying such models is that all variables are "well-mixed," that is, they are spatially homogeneous. As the experimental data on which we based the model are mostly density vs. time plots, this approach is the natural first choice. However, the tumor environment is very heterogeneous. In particular, tumor vasculature is highly disorganized and chaotic. Therefore, a natural extension of the model would be to include spatial variations in cell densities, chemical concentrations, and vascular development. Hybrid models, where cells and vessels are tracked individually, while chemokines and nutrient concentrations are treated with partial differential equations (reaction–diffusion), are fast becoming a popular choice to investigate interactions between a tumor and its vasculature. The incorporation of detailed subcellular signal transduction pathways such as the VEGF-Bcl-2-CXCL8 pathway in these models is an interesting problem.

Our goal of developing cell-specific computational models of cancer growth and therapy is increasingly becoming possible due to an explosion in the understanding of the strongly linked, multiple scale processes that drive the advancement of cancer, coupled with an exponential increase in computing power. At the same time, it is important to keep in mind that the eventual clinical application of such efforts necessitates the accurate estimation of a number of variables in a defined experimental setting. In order to fine tune the models we develop, a constant interaction with experimentalists is of vital importance, with an emphasis on model-driven experimentation, to calibrate and train our models. It is through this type of integrative strategy that rapid and significant progress in experimental therapeutics can be achieved.

References

Adams JM (2003) Ways of dying: multiple pathways to apoptosis. Genes Dev 17:2481-2495

Adams JM, Cory S (2007) The Bcl-2 apoptotic switch in cancer development and therapy. Oncogene 26:1324-1337

Auguste P, Lemiere S, Larrieu-Lahargue F, Bikfalvi A (2005) Molecular mechanisms of tumor vascularization. Crit Rev Oncol Hematol 54:53-61

Brat DJ, Bellail AC, Van Meir EG (2005) The role of interleukin-8 and its receptors in gliomagenesis and tumoral angiogenesis. Neuro Oncol 7:122-133

Daugulis P, Arakelyan L, Ginosar Y, Agur Z (2004) Hopf point analysis for angiogenesis models. Discret Contin Dyn S - Series B 4:29-38

Dong Z, Nör JE (2009) Transcriptional targeting of tumor endothelial cells for gene therapy. Adv Drug Deliv Rev 61:542-553

Dong Z, Zeitlin BD, Song W, et al. (2007) Level of endothelial cell apoptosis required for a significant decrease in microvessel density. Exp Cell Res 313:3645-3657

Ferrara N, Gerber HP, LeCouter J (2003) The biology of VEGF and its receptors. Nat Med 9:669-676

Gammack D, Byrne HM (2001) Estimating the selective advantage of mutant p53 tumour cells to repeated rounds of hypoxia. Bull Math Biol 63:135-166

Guglielmi N, Hairer E (2001) Implementing Radau IIA methods for stiff delay differential equations. Computing 67:1-12

Hicklin DJ, Ellis LM (2005) Role of the vascular endothelial growth factor pathway in tumor growth and angiogenesis. J Clin Oncol 23:1011-1027

Jain HV, Nör JE, Jackson TL (2008) Modeling the VEGF-Bcl-2-CXCL8 pathway in intratumoral agiogenesis. Bull Math Biol 70:89-117

Jain HV, Nör JE, Jackson TL (2009) Quantification of endothelial cell-targeted anti-Bcl-2 therapy and its suppression of tumor growth and vascularization. Mol Cancer Ther 8:2926-2936

Karl E, Warner K, Zeitlin B, et al. (2005) Bcl-2 acts in a proangiogenic signaling pathway through nuclear factor-kappaB and CXC chemokines. Cancer Res 65:5063-5069

Kerbel RS (2000) Tumor angiogenesis: past, present and the near future. Carcinogenesis 21:505-515

Levine HA, Sleeman BD, Nilsen-Hamilton M (2000) A mathematical model for the roles of pericytes and macrophages in the initiation of angiogenesis. I. The role of protease inhibitors in preventing angiogenesis. Math Biosci 168:77-115

Mantzaris NV, Webb S, Othmer HG (2004) Mathematical modeling of tumor-induced angiogenesis. J Math Biol 49:111-187

McMahon G (2000) VEGF Receptor Signalling in Tumor Angiogenesis. Oncologist 5:3-10

Nagy JD (2004) Competition and natural selection in a mathematical model of cancer. Bull Math Biol 66:663-687

Neiva KG, Zhang Z, Miyazawa M et al. (2009) Cross talk initiated by endothelial cells enhances migration and inhibits anoikis of squamous cell carcinoma cells through STAT3/Akt/ERK signaling. Neoplasia 11:583-593

Nör JE, Christensen J, Mooney DJ, Polverini PJ (1999) Vascular endothelial growth factor (VEGF)-mediated angiogenesis is associated with enhanced endothelial cell survival and induction of Bcl-2 expression. Am J Pathol 154:375-384

Nör JE, Christensen J, Liu J et al. (2001) Up-Regulation of Bcl-2 in microvascular endothelial cells enhances intratumoral angiogenesis and accelerates tumor growth. Cancer Res 61:2183-2188

Nör JE, Peters MC, Christensen JB et al. (2001) Engineering and characterization of functional human microvessels in immunodeficient mice. Lab Invest 81:453-463

Papetti M, Herman IM (2002) Mechanisms of normal and tumor-derived angiogenesis. Am J Physiol Cell Physiol 282:C947-C970

Patan S (2000) Vasculogenesis and angiogenesis as mechanisms of vascular network formation, growth and remodeling. J Neurooncol 50:1-15

Pettet GJ, Byrne HM, McElwain DL, Norbury J (1996) A model of wound-healing angiogenesis in soft tissue. Math Biosci 136:35-63

Roskoski R Jr (2007) Vascular endothelial growth factor (VEGF) signaling in tumor progression. Crit Rev Oncol Hematol 62:179-213

Segel LA, Slemrod M (1989) The Quasi-Steady-State Assumption: A Case Study in Perturbation. SIAM Review 31:446-77

Wang S, Yang D, Lippman ME (2003) Targeting Bcl-2 and Bcl-X_L with nonpeptidic small-molecule antagonists. Semin Oncol 30:133-142

Ward JP, King JR (1999) Mathematical modeling of avascular-tumour growth. II: Modeling growth saturation. IMA J Math Appl Med Biol 16:171-211

Zeitlin BD, Joo E, Dong Z, et al. (2006) Antiangiogenic Effect of TW37, a Small-Molecule Inhibitor of Bcl-2. Cancer Res 66:8698-8706

Chapter 4
Investigating the Role of Cross-Talk Between Chemical and Stromal Factors in Endothelial Cell Phenotype Determination

Amy L. Bauer and Thimo Rohlf

1 Introduction

The existence of vast amounts of postgenomic data facilitated by the development of high-throughput technologies poses a challenge in systems biology. Most of these data come from molecular perturbations of individual signaling pathways that are connected to other pathways and regulatory systems. Computational modeling is a necessary tool to synthesize, interpret, and understand these data within the larger, cellular regulatory network to which they belong. Computational models incorporating multiple pathways into a network structure can reveal features not observed from analysis of isolated pathways (Bhalla and Iyengar 1999; Bauer et al. 2010). Understanding the mechanisms governing the functions of signalling networks will enable the identification of controlling factors that are potential targets for pharmacological interventions in the treatment of cancer and other angiogenesis-dependent diseases.

In this chapter, we briefly describe the key receptors involved in regulating tumor angiogenesis to provide context for the computational models presented. We review the computational approaches available to model signal transduction and demonstrate the use of discrete and stochastic Boolean logic in a model of receptor cross-talk during angiogenesis. We then present a Boolean hybrid model and compare the results obtained using these different formulations.

A.L. Bauer (✉)
Los Alamos National Laboratory, Theoretical Biology and Biophysics Group, Theoretical Division, Mail Stop T-082, Los Alamos, NM 87545, USA
e-mail: albauer@lanl.gov

T. Rohlf
Epigenomics Project, Genopole, Evry and MPI-MIS, ISSB, Genopole Campus 1, Genavenir 6, 5 rue Henri Desbrueres, F-91030 EVRY cedex, France
e-mail: rohlf@mis.mpg.de

T.L. Jackson (ed.), *Modeling Tumor Vasculature: Molecular, Cellular, and Tissue Level Aspects and Implications*, DOI 10.1007/978-1-4614-0052-3_4,

1.1 Receptor Signaling During Tumor Vascularization

The cellular processes that occur during tumor angiogenesis are tightly coordinated and regulated by signaling molecules. Signal transduction is the mechanism through which cells translate molecular stimuli to activate intracellular response mechanisms. In angiogenesis, signaling molecules activate endothelial cell surface receptors and initiate intracellular signaling cascades. Intracellular signal transduction leads to gene transcription, the production of enzymes and angiogenic factors, increased cell survival, migration, and proliferation (Hicklin and Ellis 2005). Such cellular processes are orchestrated by a cell–cell communication system to generate new blood vessel growth, which ultimately leads to successful tumor vascularization. For a more detailed description of the processes involved in angiogenesis, there are comprehensive reviews available (Paweletz and Knierim 1989; Mantzaris et al. 2004; Folkman 2006).

Endothelial cells are key constituents of the interior lining of all blood and lymphatic vessels, and are the targets of biochemical agents that stimulate cell growth and motility, thereby making them the primary players in angiogenesis. Endothelial cells are equipped with a class of proteins called cell-surface receptors that act as sensory detectors and signal transducers and enable the cell to respond to external stimuli. Transmembrane receptors bind extracellular molecules stimulating a biochemical response across the cell membrane to activate internal signaling cascades. Examples of transmembrane receptors crucial to angiogenesis are receptor tyrosine kinases (RTK), integrins (ITG), and cadherins, which we briefly describe later.

Many growth factors and inhibitors have been discovered to regulate angiogenesis (Folkman 2006). Amongst those vascular endothelial growth factor A (VEGFA) plays a major role in regulating endothelial cell migration, proliferation, and survival (Gerhardt et al. 2003). Endothelial cells are activated by VEGF via two receptor tyrosine kinases, fms-like tyrosine kinase-1 and fetal liver kinase-1, which are often referred to as VEGFR1 and VEGFR2, respectively (Yancopoulos et al. 2000). VEGF binds to these receptors triggering intracellular signaling pathways. For example, the VEGF-Bcl2-CXCL8 signaling pathway mediates pro-angiogenic and pro-survival phenotypes in endothelial cells (Nör et al. 1999). Integrins control the adhesion of cells to extracellular molecules and are crucial components for signal transduction from the extracellular matrix (ECM). Integrin binding to the ECM regulates the expression of cyclin-dependent kinases and activation of the MAPK signal transduction pathway, which control cell cycle progression and growth (Huang and Ingber 1999). Endothelial cells can attach directly to collagen fibers in the ECM through the $\alpha_1\beta_1$ and $\alpha_1\beta_2$ integrin receptors (Silver et al. 2003). These receptors initiate intracellular signaling pathways that regulate cell survival, growth, and motility (Chen et al. 1998; Davis and Senger 2005). Additionally, cells form tight junctions with each other to maintain a barrier between the blood in the blood vessel and the extracellular space and to form cohesive multicellular structures and tissues. The mechanism for endothelial cell–cell adhesion is through

a receptor called VE-cadherin. Inside the cell, cadherins associate with the protein β-catenin to regulate the actin cytoskeleton (Lilien and Balsamo 2005). Externally, cadherins form homodimers with cadherin proteins present on adjacent cells, which provides a mechanism for intercellular communication.

During signal transduction, signaling molecules are often involved in and affect multiple signal transduction pathways. This phenomena is called cross-talk. The KEGG Pathway Database (KEGG 1995–2007) synthesizes a vast amount of disjoint data taken from multitudes of different experimental laboratories using different cell lines to construct signaling pathways. Using KEGG, one can see that the RTK, ITG, and cadherin signaling pathways are highly connected and provide regulatory feedback to each other. As examples, in response to VEGF, endothelial cells upregulate the expression of ITG receptors (Mantzaris et al. 2004; Somanath et al. 2000) and Hutchings et al. (2003) found that integrins can additionally serve as receptors for immobilized $VEGF_{165}$ and $VEGF_{189}$ (VEGFA isoforms) present in the ECM. Through RTK receptors, VEGF activates the MAPK signal transduction pathway stimulating proliferation and cell survival. Cell survival and proliferation, however, critically depend on adherence to the ECM, because even in the presence of stimulating concentrations of growth factor, loss of anchorage to the ECM results in cell cycle cessation and apoptosis (Chen et al. 1998; Huang and Ingber 1999). Another example of receptor cross-talk in angiogenesis occurs through cadherin activation. Cadherins induce signals that mitigate growth factor activation and repress cell proliferation (Zanetti et al. 2002) in a process termed contact inhibition (Gottardi et al. 2001).

1.2 Computational Approaches to Modeling Signal Transduction

A number of different modeling techniques may be employed to model signal transduction systems, including rule-based modeling, differential equations, agent-based models (ABM), semantic networks, molecular dynamics, and Boolean logic (Blinov et al. 2006b; Jain et al. 2008; Dong et al. 2010; Hsing and Cherkasov 2006; Zhang et al. 2009; Bauer et al. 2010). Which computational approach is used depends on the level of detail needed to investigate the scientific hypotheses driving the study and on the availability of empirical data to inform parameter values. In addition, different approaches can be combined to complement each other. We briefly review computational approaches to modeling signal transduction pathways below, but more comprehensive reviews are available (Eungdamrong and Iyengar 2004; Kholodenko 2006; Aldridge et al. 2006; Hsing and Cherkasov 2006; Bauer et al. 2009).

A major bottleneck in the development of signal transduction models is the combinatorial explosion in the number of phosphorylation states and complexes that arises from the multi-domain structure of signaling molecules and the fact that many proteins participate in multiple simultaneous interactions (Hlavacek et al. 2003). In developing a detailed model of a biochemical system using the conventional

manual approach, the modeler must make ad hoc choices to limit the complexity of the resulting network, which otherwise grows rapidly to an intractable size. The modeler must either limit the description of the molecular components to allow only a small subset of possible interactions or must limit the scope of the model to a subset of the molecules known to participate in the specified process. Either of these choices introduces a component of arbitrariness into the model building process and potentially limits the predictive capability of the model. As a result, there are no comprehensive mass action kinetic models of signaling networks capable of predicting the full range of perturbations that can be applied to a signaling network using either molecular genetic or pharmacological tools. For example, current models of the VEGF signaling pathways consider events only at the receptor level (Mac Gabhann and Popel 2007) or use a highly abstracted representation of the intracellular signaling pathways (Jain et al. 2008; Levine et al. 2002).

1.2.1 Rule-Based Modeling

Rule-based modeling, which involves the representation of molecules as structured objects and molecular interactions as rules for transforming the attributes of these objects, provides an alternative approach to modeling signal transduction and other biochemical networks that does not require the tradeoffs just described. The combinatorial complexity of proteins and protein–protein interactions poses a significant barrier to the development of mechanistic models of cellular regulatory systems, as the large number of possible nonisomorphic protein states that can arise from protein interactions overloads conventional methods used to model dynamical systems. The high cost of simulating large-scale reaction networks via numerical integration of differential equations or stochastic simulation limits the ability to parameterize, validate, and analyze models for cellular regulatory systems that account for site-specific details of protein–protein interactions. The BioNetGen Language (BNGL), a model-specification language, and rule-based modeling software tools, such as BioNetGen, GetBonNie, DYNSTOC, NFsim, Rule Monkey, etc. (Blinov et al. 2006a; Hu et al. 2009; Colvin et al. 2009), enable the specification and simulation of large-scale models of cellular regulatory systems.

In a rule-based model, molecular species can represent proteins and other molecular elements of the signaling network that have multiple functional elements (e.g., phospholipids). Covalent modifications and other conformational or chemical states (e.g., phosphorylation status) may be represented as internal states. Rules describe both a chemical transformation and the requirements the reactants must meet to undergo the transformation. Additionally, rules specify the rate at which the transformation is to be applied. Thus, kinetic parameters for the reactions being modeled must be known or estimated. One disadvantage to a rule-based method is that kinetic parameters are often unavailable. On the other hand, the main advantage of using rules to describe molecular interactions, rather than conventional reactions, is that rules may apply to a broad range of different reactant species that share a common set of properties. Thus, a large reaction network may be specified by a

small number of rules that depend only on the local properties of the reactants. BioNetGen has been applied to study a number of biochemical systems (Barua et al. 2007, 2008; Blinov et al. 2006b; Mu et al. 2007; Rubenstein et al. 2007).

1.2.2 Continuum Models

Continuum models are based on the laws of mass action and use differential equations to describe each molecular species and the participation of each species in biochemical reactions. When the number of molecules per species is large, continuum models provide a reasonable approximation to the average molecular concentrations in the system. There are two types of continuum models widely used to model signal transduction: reaction-network models and reaction-diffusion models. Reaction-network models assume each molecular species is uniformly distributed inside the cell and are formulated using ordinary differential equations (ODEs) (Kholodenko 2000; Levine et al. 2002; Jain et al. 2008). In a reaction-network model, there is one ODE for each molecular species that describes every chemical reaction in which that species participates. Numerical methods for solving a coupled system of ODEs are well-developed and can be used to solve for the average concentration of each species in time. To account for both temporal and spatial distributions of molecular species when describing their participation in chemical reactions, a reaction-diffusion model is used (von Dassow et al. 2000; von Dassow and Odell 2002; Smith et al. 2002). Reaction-diffusion models are composed of partial differential equations (PDEs), which provide a more realistic depiction of signaling dynamics, but also require more parameter specification (e.g., diffusion coefficients and boundary conditions) and computational resources to solve numerically. On the other hand, when the number of molecules per species is small, stochastic effects become important. ODE and PDE models can be simulated using stochastic algorithms, for example, the Gillespie algorithm (Gillespie 1976) can be used to simulate systems of ODEs. A disadvantage of continuum models of signal transduction systems is that they require detailed specification of all the interactions that occur between the species and all the rates at which the reactions occur. As with a rule-based model, the kinetic parameters required by a continuum modeling approach are often not known or are insufficiently known. For any significant level of detail, the number of parameters required to specify all the different reactions is large. For a system consisting of only 20 molecular species, each of which is involved in two reactions, the minimum number of parameters is 40. If the reactions are reversible or the number of species or reactions increases, the number of necessary parameters escalates.

1.2.3 ABM

In recent years, ABM have been used to model and simulate signal transduction (Pogson et al. 2008; Miller et al. 2010; Dong et al. 2010). Agent-based modeling

is a stochastic approach used to describe a population of interacting agents, where agents behave according to a set of rules that represent the vital features of a system. In signal transduction systems, examples of agents could be receptors, proteins, complexes, and other signaling molecules, such as kinases. In contrast to ODEs, ABM are useful when the effects of spatial heterogeneity and local interactions are important because agents are programmed to independently respond to changing environmental cues. An advantage of an ABM is that the rules directly map to physical behaviors, making the model and its results easy to understand and interpret and therefore accessible to a broader audience. In addition, complex behavior and patterns often emerge that would not otherwise have been obvious from the simple set of governing rules (Wolfram 1984). One disadvantage, however, is that ABM may require even more parameters than differential equation models.

1.2.4 Semantic Network Models

A semantic network (SN) is a computational approach based on ideas from artificial intelligence and, although traditionally used in computer science applications, has also been applied to model signaling systems (Hsing et al. 2004; Hsing and Cherkasov 2006). A SN organizes information, such as the conformational changes of proteins, graphically using nodes and edges. Nodes represent individual concepts and edges represent relationships between concepts. For example, a protein that catalyzes a chemical reaction would be a node in a SN. The fact that the protein is a catalyst for the reaction would be represented by an arrow going from the protein to the chemical reaction, another node in the network. Dynamic SN, such as Petri nets (Petri 2009), incorporate procedural nodes that manipulate data (e.g., add or delete nodes and alter relationships) resulting in a network that changes dynamically. Thus, not only can a SN be used to characterize local relationships in a signaling network, but also it can be used to characterize global system behaviors. The main advantage of using a SN is that hierarchical and cause-effect information can be captured, clustered, and retrieved in an efficient manner, which is especially useful for handling large amounts of genomic and proteomic data.

1.2.5 Molecular Dynamics Models

Molecular dynamics (MD) models are based on statistical mechanics concepts and specify the equations of motion for atomic particles in the system being modeled. A potential energy function is defined that governs the short- and/or long-range interaction forces of the atoms and molecules. MD models resolve molecular interactions in both space and time and often rely on the assumption that statistical ensemble averages are equal to the time averages of the system. Simulations of MD models are used for systems of molecules because, in general, analytic solutions are impossible to construct. Molecular models and molecular dynamics simulations of signaling events are useful for understanding how molecules interact at the

atomic level and have led to insights into protein–protein interactions (Vaiana and Sanbonmatsu 2009; Zhang et al. 2009). However, with present numerical techniques, the computing power needed to sufficiently sample all possible collision events for just one protein–protein interaction is onerous. For example, 15 ms of aggregate sampling of drug–ribosome interactions took 4 months on 400 processors (Vaiana and Sanbonmatsu 2009). Thus, MD models are not yet a viable option for larger signaling networks.

1.2.6 Boolean Network Models

Boolean networks (BN) have a long standing tradition as idealized models of genetic regulatory dynamics in cells. A BN model consists of N binary state variables $X_1, X_2, \ldots, X_N$ called nodes. Each node can take the values 1 and 0 corresponding to an on-off idealization of regulatory dynamics, for example whether or not a particular gene is expressed, or the presence or absence of a sufficient number of signaling molecules in the cell cytoplasm. For a detailed description of BN dynamics, the reader is referred to Sect. 2.1.

A random Boolean network (RBN) is a BN with randomly assigned interactions and logical functions. Given the fragmented knowledge of gene regulation circuits at the transcription level in the 1960s, Stuart Kauffman originally introduced the notion of RBN to study the dynamical properties of gene regulation networks from a global perspective (Kauffman 1969, 1993). In RBN, f_i is chosen at random from the ensemble of all possible 2^k Boolean functions with k inputs. For any initial configuration of the N state variables, it takes the network a maximum of $2^N - 1$ time steps to settle to a periodic attractor of self-repeating states (Kauffman 1993). Two distinct dynamical phases exist in RBN: an ordered phase, characterized by a small number of attractors with short periods and a vanishing sensitivity to perturbations, and a chaotic phase where both the number and average period of attractors grow exponentially with N and perturbations (damage) propagate through the whole network (Kauffman 1993; Derrida and Pomeau 1986). Of special interest are critical RBN, which lie at the boundary between the ordered and the chaotic phases (Kauffman 1993; Derrida and Pomeau 1986), because these models exhibit the most biologically realistic dynamical properties with respect to robustness and adaptive flexibility (Kauffman 1993; Aldana et al. 2007). In this context, Kauffman's original idea was to identify attractors of BN dynamics near criticality with cell phenotypes. In particular, periodic attractors are reminiscent of periodic cellular dynamics (e.g., cell cycles), and early studies suggested that the average number of different attractors for RBN near the critical transition scaled as $\sim \sqrt{N}$, similar to the number of cell types in metazoa as a function of the number of genes (Kauffman 1969, 1993). More recent studies, however, challenged this idea and predicted a much larger number of attractors in critical RBN (Samuelsson and Troein 2003).

In most studies, RBN dynamics are modeled using synchronous deterministic updates. As in real biological networks stochastic events at the molecular scale are ubiquitous, asynchronous, and stochastic updating schemes attract considerable

attention from researchers. In randomly generated networks, dynamical attractors are often destroyed by asynchronous updates (Gershenson 2004). However, in models of biological networks treated as Boolean systems, attractors are often insensitive to these perturbations. This indicates that evolution might have selected network topologies such that the dynamics are robust against both noise and different time scales of regulatory events (Albert and Othmer 2003; Braunewell and Bornholdt 2007). Furthermore, there is evidence that delays in information propagation contribute significantly to synchronization and thereby stabilize dynamical attractors (Klemm and Bornholdt 2003, 2005). In general, however, discrete Boolean approaches tend to overestimate the impact of stochastic events, because neither smoothing effects from molecular dynamics (with molecule numbers usually much larger than one) nor time scale separations between input signals and phenotypic response found in biological systems can be considered adequately. These problems motivated the development of hybrid BN models, which is introduced in Sect. 2.2.

RBN have been applied in a number of theoretical studies to gain insight into the shaping of biological regulation networks by evolutionary processes, with emphasis on robustness of expression patterns against mutations of regulatory wiring (Bornholdt and Sneppen 1998), evolution of homeostatic regulation near percolation criticality (Bornholdt and Rohlf 2000), and application to problems in morphogenesis (Jackson et al. 1986; Rohlf and Bornholdt 2005). BN models have also been successfully applied to model and predict the regulatory dynamics of several biological organisms, including *Drososphila melanogaster* (Albert and Othmer 2003), integrating known experimental data about the topology of the corresponding cellular networks. Confirming earlier results about the extreme robustness of the developmental BN model of *Drososphila melanogaster* against variations of kinetic constants over orders of magnitude (von Dassow et al. 2000), dynamical attractors in this system are insensitive to large variations of time scales in the Boolean update scheme (e.g., synchronous deterministic vs. asynchronous stochastic updates, Chaves et al. 2005). Similar results were established in BN models of the yeast cell cycle network in the presence of biochemical stochasticity (Braunewell and Bornholdt 2007; Davidich and Bornholdt 2007).

In most signal transduction systems, quantitative information on the speed and duration of biochemical reactions, the initial or resting state of internal nodes, and signal transduction noise is scarce. A Boolean network model of signal transduction in plant guard cells is validated as a theoretical tool that is useful in the absence of quantitative information (Li et al. 2006). Analysis shows that the topology, not the kinetics, of the signaling network determines the dynamic behavior of the system. This model was used to examine the relationship between signal and cell function and to make predictions about unknown or incompletely understood biochemical relationships in the network. A Boolean network approach can be employed to describe signal transduction networks in other biological systems where mostly qualitative data are available. In this chapter, we use several BN approaches to model and analyze the signaling pathways believed to be critical to cellular regulation and function during angiogenesis.

2 Methods

2.1 Discrete Boolean Network Model

2.1.1 Deterministic Dynamics

A Boolean network (BN) is a discrete dynamical system composed of N nodes indexed by $i = 1, \ldots, N$. A Boolean variable $X_i \in \{0, 1\}$ is associated with each node i, and the dynamics is such that

$$\mathbf{F} : \{0, 1\}^N \mapsto \{0, 1\}^N, \tag{4.1}$$

where $\mathbf{F} = (f_1, ..., f_i, ..., f_N)$, and each f_i is represented by a look-up table of k_i inputs from other nodes. For an example, see Fig. 4.1. A node's state $X_i(t) \in \{0, 1\}$ is updated using its corresponding Boolean function:

$$X_i(t + 1) = f_i(X_{i_1}(t), X_{i_2}(t), ..., X_{i_{k_i}}(t)). \tag{4.2}$$

The N nodes are updated synchronously at each time step t, leading to a new system state $\mathbf{X} := (X_1, ..., X_N)$:

$$\mathbf{X}(t + 1) = \mathbf{F}(\mathbf{X}(t)) \tag{4.3}$$

at time $t + 1$.

Given the binary state $X_i(t)$ of each node i at time $t - 1$ and update dynamics as defined earlier, a state vector $\mathbf{X}(t) = (X_1(t), ..., X_N(t))$ is assigned to the network at each discrete time step t. As the dynamics is deterministic and the phase space of the system is finite for finite N, all dynamical trajectories eventually become periodic. When we start a simulation from a randomly assigned initial state, the trajectory will pass through Θ transient states before it starts to repeat itself, forming limit cycles given by:

$$\mathbf{X}(t) = \mathbf{X}(t + \Gamma). \tag{4.4}$$

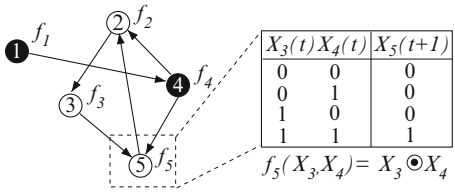

Fig. 4.1 *Left panel*: example of an interaction graph structure for a RBN of size $N = 5$; f_i are Boolean functions assigned to each node $i = 1, \ldots, 5$, *black circles* indicate $X_i = 1$, *white circles* indicate $X_i = 0$. *Right panel*: example of a Boolean update table for site five using the AND function for the site's inputs

The periodic part of the trajectory is the attractor of the dynamics, and the minimum $\Gamma \geq 1$ that satisfies (4.4) is the period of the attractor. Of critical importance is that (4.3) regulates updates in a clock-like synchronous manner for all network nodes at the same time, which constitutes a core feature of BN dynamics. A criticism of BN is that synchronous updates are unrealistic for most dynamical systems occurring in nature, where typically no central clock or pacemaker is present. To overcome this restriction, several types of asynchronous BN update schemes have been developed (cf. e.g., Gershenson 2002). For example, in the following stochastic update scheme:

$$X_i(t+1) = \begin{cases} f_i(X_{i_1}(t), X_{i_2}(t), ..., X_{i_{k_i}}(t)) & \text{with probability } p \\ X_i(t) & \text{else} \end{cases} \tag{4.5}$$

each node updates its state with probability p according to its Boolean function, and otherwise keeps its previous state, leading to a stochastic distribution of update intervals for each node. One can show that asynchronous updates always preserve fixed points of BN dynamics, while attractors of synchronous BN dynamics with $\Gamma \geq 2$ usually do not persist (Gershenson 2002). However, it was shown that delays in signal transmission can recover stable periodic attractors under asynchronous BN updates (Klemm and Bornholdt 2003).

2.1.2 Stochastic Dynamics: Errors in Boolean Updates

Besides stochasticity in the timing of dynamical updates, a second type of noise inevitably arises in real networks: errors in the updates of the dynamical states themselves. Molecular interactions in signaling networks rely on stochastic reactions, such as, protein–protein interactions, binding of transcription factors to DNA, and chemical reactions. Even if all necessary reaction partners are present, interactions take place only with finite probability. To account for this, we generalize (4.2) to a stochastic Boolean rule (Peixoto and Drossel 2009) and keep synchronous updates:

$$X_i(t+1) = \begin{cases} f_i(X_{i_1}(t), X_{i_2}(t), ..., X_{i_{k_i}}(t)) & \text{with probability } 1-p \\ |1 - f_i(X_{i_1}(t), X_{i_2}(t), ..., X_{i_{k_i}}(t))| & \text{with probability } p. \end{cases} \tag{4.6}$$

Equation (4.6) introduces errors by inverting the output state determined by f_i with probability p. From a physics perspective, (4.6) introduces a temperature, or thermal noise, into the system. Thermal noise has an even stronger impact on the phase space of the system than asynchronous timing, as discussed earlier. In the large N limit, arbitrarily low noise is sufficient for transitions between attractors, i.e., the system becomes ergodic (Miranda and Parga 1989), with a sharp first-order transition for the divergence of initially close trajectories at $p = 0$ for BNs with $k \geq 2$ inputs per node (Peixoto and Drossel 2009). From a biological perspective, this behavior is problematic. Instead of fixed attractors (phenotypes),

one now has probability distributions over the entire phase space in asymptotic dynamics. However, since phenotypes of living cells usually are highly reliable and reproducible, the discrete stochastic BN model obviously overestimates the effect of thermal noise in regulatory networks. This can easily be understood from the fact that, as the model is discrete, there is only one instance of each molecular species, while concentrations of signalling molecules in real cells are sometimes small, but usually large enough to smooth out molecular fluctuations to some extent. To overcome the evident limitations of the discrete model, we shall now generalize the model to a hybrid, continuous-time Boolean network.

2.2 Hybrid Boolean Network Model

2.2.1 Overcoming Discrete Boolean Network Model Limitations

Discrete Boolean models have obvious limitations, such as, for example, their sensitivity with respect to different update schemes (e.g., synchronous or asynchronous updates), and the strong impact of thermal noise on asymptotic dynamics. In this section, we introduce a stochastic, continuous-time Boolean network model that overcomes these limitations, while retaining the advantages of BN models. Our approach is based on continuous-time switching networks, which were originally introduced by Glass as a differential equation model of gene expression dynamics (Glass 1973, 1975). Glass' model consists of piecewise linear differential equations that are coupled through a Boolean interaction matrix. This model is more realistic in that it allows for asynchronous switching and smooth transitions, however, it still neglects noise in molecular interactions. We extend Glass' model by introducing molecular noise and discuss limiting cases that relate the model to the discrete models discussed in Sects. 2.1 and 2.1.2.

2.2.2 Stochastic, Continuous-time Boolean Network Model

In this section, we briefly derive the basic notions of our generalized, continuous-time Boolean network model of signal transduction. The concentration $c_i(t)$ of a chemical species i is determined by its production and decay rates. We make the ansatz

$$\frac{\mathrm{d}c_i}{\mathrm{d}t} = f_i(c_1, ..., c_N) - \alpha c_i(t), \tag{4.7}$$

where f_i is the production function of species i, which may depend on the concentrations of other chemical species in the reaction network, and $\alpha \in \mathscr{R}$ is the decay constant, which, for simplicity, is assumed to be the same for all species.

Setting $x_i \equiv \alpha c_i(t)$ and specifying f_i as the Boolean update function in (4.2), we can rewrite (4.7) as:

$$\frac{\mathrm{d}x_i}{\mathrm{d}t} = \alpha \left[f_i(X_{i_1}(t), X_{i_2}(t), ..., X_{i_{k_i}}(t)) - x_i(t) \right]. \tag{4.8}$$

The quantity x_i is normalized on the interval $[0, 1]$ and a Boolean state $X_i(t)$ is associated with each species via a concentration-based threshold switching mechanism:

$$X_i(t+1) = \begin{cases} 0 & \text{if } x_i(t) < 1/2 \\ 1 & \text{if } x_i(t) \geq 1/2. \end{cases} \tag{4.9}$$

Setting f_i to its maximum value $f_{\max} = 1$, taking $\mathrm{d}c_i/\mathrm{d}t = 0$ in (4.7), and assuming that all species can achieve a maximal concentration $c_{\max}$, we have that

$$\alpha = c_{\max}^{-1}. \tag{4.10}$$

Equation (4.8) is still purely deterministic; for a more realistic model, one has to account for stochastic fluctuations, which typically characterize biological systems. Two types of fluctuations are considered here: (1) noise in chemical reactions, i.e., deviations from the (average) production and decay rates and (2) random delays in reactions. This leads to the generalized system

$$\frac{\mathrm{d}x_i}{\mathrm{d}t} = \alpha \left[\left(f_i(X_{i_1}(t-\tau), X_{i_2}(t-\tau), ..., X_{i_{k_i}}(t-\tau)) - \delta(t) \right) - x_i(t) + \varepsilon(t) \right], \tag{4.11}$$

where τ is a time delay, δ a stochastic variable that accounts for fluctuations in the production rate and ε captures stochasticity in decay rates. Here, we focus on fluctuations in the production rate only, and set $\tau = \varepsilon = 0$. Further, we define

$$\delta(t) = \begin{cases} 1 & \text{with probability } p \\ 0 & \text{with probability } 1-p, \end{cases} \tag{4.12}$$

where $p \in [0, 1/2]$. Notice that for $p = 0$, the dynamics are completely deterministic, whereas $p = 1/2$ corresponds to a complete randomization of the production rate function, i.e., making it a random switch. In between, $0 < p < 1/2$, the Boolean update executes with an error rate p, because when $\delta(t) = 1$, the output determined by f_i is always inverted.

Let us briefly comment on the relationship between the stochastic, continuous-time model defined by (4.11) (with $\tau = \epsilon = 0$) and the deterministic, discrete time Boolean network model, as defined in (4.2). If we replace the differentials in (4.11) with finite differences Δx_i and Δt and set $\Delta t = 1$ without loss of generality (since scaling of integration step size is already provided by α), it follows that

$$x_i(t+1) = x_i(t) + \Delta x_i$$
$$= x_i(t) + \alpha\left[\left(f_i(X_{i_1}(t), X_{i_2}(t), ..., X_{i_{k_i}}(t)) - \delta(t)\right) - x_i(t)\right]. \quad (4.13)$$

For $p = 0$ and $\alpha = 1$, (4.13) reduces to (4.2), i.e., to a deterministic Boolean network with discrete time and discrete states. For $p > 0$ and $\alpha = 1$, the system is a BN that updates binary states with error rate p, as introduced in (4.6).

3 Application to a Signal Transduction System in Angiogenesis

We construct a Boolean network model to study the role of cross-talk between chemical and stromal factors in endothelial cell phenotype determination during angiogenesis because reaction rates for most of the kinetic interactions are not available in the experimental literature. Figure 4.2 graphically represents the signal transduction network we have implemented for this study. Empirical data show three

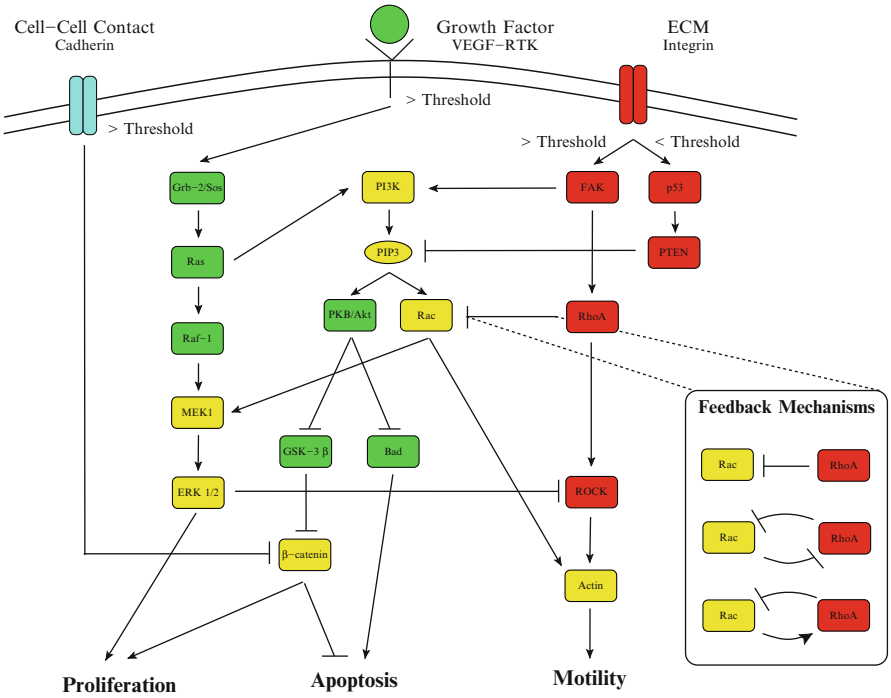

Fig. 4.2 Sparsest network of cross-talk between VEGF-RTK, ITG, and cadherin receptors consistent with empirical observations of cell behavior during tumor angiogenesis. *Arrows* indicate activation and hammerheads indicate inhibition. *Green, red and blue* represent nodes involved in the VEGF-RTK, ITG, and cadherin pathways, respectively. Nodes involved in cross-talk are colored *yellow*. Figure taken from Bauer et al. (2010) with permission

possible feedback schemes between Rac and RhoA: (1) RhoA inhibits Rac, which forms the baseline (BL) model, (2) RhoA inhibits Rac and Rac inhibits RhoA, which we refer to as positive feedback (PF), and (3) RhoA inhibits Rac but Rac activates RhoA, which we refer to as mixed feedback (MF). Arrows indicate activation and hammerheads indicate inhibition. This network was developed by synthesizing empirical data available for endothelial cell signal transduction during angiogenic processes using the sparsest graph consistent with all experimental observations. This BN model enables us to explicitly derive an input/output table linking key environmental cues to cell phenotype during angiogenesis. We systematically analyze the dynamical stability of a deterministic, stochastic, and a hybrid BN model and find that the output states (i.e., cell phenotypes) are insensitive to initial configurations and transient perturbations of internal nodes. However, in the discrete stochastic BN model, thermal noise in the node updates, a more diverse distribution of phenotypes is found. In the more realistic hybrid model, we observed that network dynamics is stable under internal noise, indicating that the network architecture is selected for high reliability of response in a fluctuating environment.

3.1 Discrete Boolean Network Model with Deterministic Dynamics

3.1.1 Prediction of Cell Phenotypes: Construction of an Input/Output Map

Boolean network dynamics of cross-talk in angiogenesis (Fig. 4.2) was simulated with deterministic, discrete updates (cf. Sect. 2.1). Space–time plots of dynamics given random initialization of internal nodes, external signals ITG and VEGF-RTK activated, no contact inhibition, and Rac inactive are shown in Fig. 4.3 for the (a) baseline network and the (b) network with mixed feedback. Time runs from top to bottom. Column colors correspond to the molecular nodes in Fig. 4.2 and black indicates that the corresponding node is inactive. From left to right, the three leftmost columns are the external inputs: cadherin, VEGF-RTK, and ITG. The outputs proliferation, apoptosis, and motility are shown in orange in the three rightmost columns, respectively. After transient signalling cacades propagate through the network, dynamics settles down to fixed point attractors. The network exhibits five critical and distinct cell phenotypes: apoptotic, proliferating, migrating, quiescent, and both proliferating and migrating indicated, respectively, by black, green, red, white, and bicolor red–green. Different Rac and RhoA feedback schemes result in different phenotypes. The BL and PF schemes predict proliferation (Fig. 4.3a), whereas the mixed feedback scheme leads to proliferation with intermittent (oscillatory) motility (10ω) (Fig. 4.3b). For all other input configurations, the BL, PF, and MF schemes lead to the same phenotypes. These results are summarized in the input/output table shown in Fig. 4.3c. For example, in Fig. 4.3c, [10] denotes VEGF-RTK activation only and output (100) indicates proliferation.

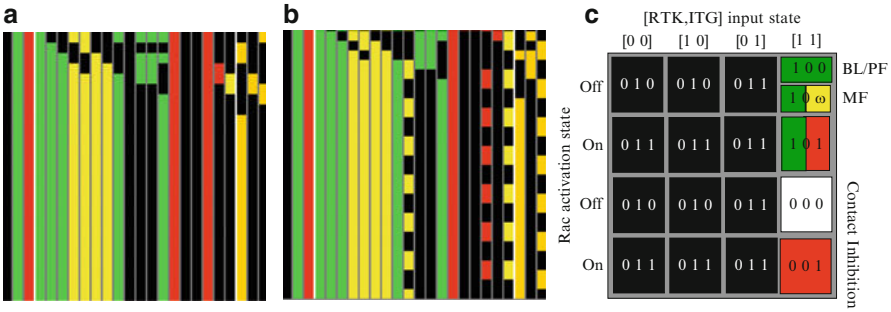

Fig. 4.3 Space–time plots for discrete Boolean network dynamics with inputs: ITG and VEGF-RTK activated, no contact inhibition, and Rac inactive. Time runs from top to bottom. *Colors* correspond to nodes in Fig. 4.2 and *black* indicates the node is off. From left to right, columns correspond to the inputs (cadherin, VEGF-RTK, ITG), internal nodes, and the outputs (proliferation, apoptosis, motility), which are shown in *orange*. (**a**) the resulting phenotype for the BL network is proliferation; (**b**) MF between RhoA and Rac leads to proliferation and intermittent motility (*yellow*). (**c**) Input/output table summarizing cell phenotype predictions by the BN for all input configurations. Cell phenotypes: apoptotic, proliferating, migrating, quiescent, proliferating and migrating are indicated, respectively, by *black, green, red, white, and bicolor red–green*

3.1.2 Phenotypes are Unique and Depend Crucially on Cross-talk

An important question is whether the derived input/output map shown in Fig. 4.3c contains complete information about the phase space of asymptotic dynamics, i.e., whether the predicted phenotypes are unique and depend only on external inputs. To answer this question, we simulated dynamics for all possible 2^{19} initial states of the internal nodes, and for all 16 distinct input configurations. In all cases, dynamics converged to the same set of fixed point attractors as shown in Fig. 4.3c, thereby proving the uniqueness of the predicted phenotypes. The essential role of cross-talk is immediately evident from the phenotype map: the presence of both ITG and VEGF-RTK signals is required for cell viability. Consistent with experimental observation (Ruoslahti and Reed 1994; Hutchings et al. 2003), if either receptor is inactive, apoptosis is induced, and is indicated by the 12 black phenotypes.

3.2 Discrete Boolean Network Model with Stochastic Dynamics

3.2.1 Distribution of Phenotypes Differs Under External and Internal Noise

We now generalize the discrete BN model to allow for stochastic errors in updates according to (4.6). This model still has discrete states and time and clockwise, parallel node updates. As, in the discrete model, no mechanism for smoothing update errors is present, stochasticity has a considerable impact on dynamics.

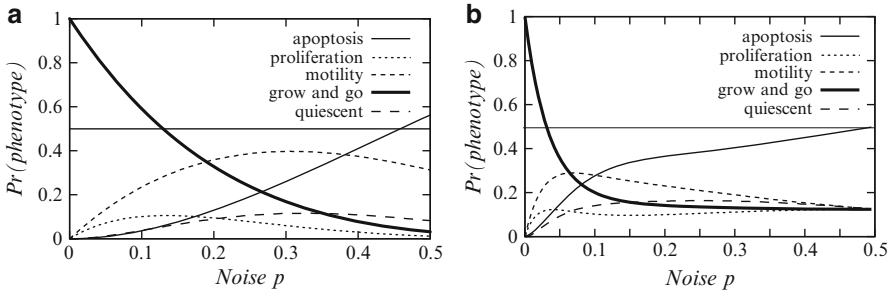

Fig. 4.4 Probability distribution of observed phenotypes with discrete, stochastic Boolean dynamics. (**a**) p denotes the probability of errors (thermal noise) in external signals. Input signals: ITG and VEGF-RTK activated, no contact inhibition and Rac active. (**b**) The same input configuration with update errors occurring in internal nodes with probability p

A deterministic inout/output map of phenotypes no longer exists, but instead, a probability distribution of phenotypes can be constructed, with stochastic transitions between the different phenoytypes.

The effect of varying the noise level p is shown in Fig. 4.4 for noise in (a) external inputs and (b) internal nodes' states. In this example, ITG and VEGF-RTK are activated, there is no contact inhibition, and Rac is activated. This configuration leads to the "go and grow" phenotype predicted by the deterministic model. Under both internal and external noise, for small p, the "go and grow" phenotype is predominant, however, as p increases, the "go and grow" phenotype occurs less frequently. In addition, as noise increases, so does the frequency of a motile phenotype, suggesting that a cell tries to escape an environment that induces too much noise. If it cannot escape, apoptosis becomes the prevalent phenotype. Interestingly, phenotype distributions as a function of p are different depending on whether noise is applied to the external signals (Fig. 4.4a) or to the states of internal network nodes (Fig. 4.4b). Figure 4.4a shows that, for $p \approx 0.3$ noise in external inputs, motility is maximized. The motility phenotype occurs with $\sim$40% probability. Whereas, when there is noise in the internal states, the motility phenotype maximum occurs earlier ($p \approx 0.05$) and the phenotype frequency decreases with increasing p (Fig. 4.4b). A possible explanation for this observation is that motility is only a valid escape mechanism for external noise, which implies that a cell can differentiate between internal and external noise. In addition, apoptosis occurs more frequently at lower internal p suggesting that a cell is more sensitive to internal noise. Differences are also found for the other phenotypes. For example, in the limit of large noise $p \to 0.5$, the probability for apoptosis approaches 0.5 for internal noise and the other four phenotypes become equally distributed with probability 0.125 (Fig. 4.4b); for external noise, however, apoptosis exceeds 50% probability and the remaining phenotypes are not equally probable – motility is most frequently observed (Fig. 4.4a). While there is not much difference between the quiescent phenotype distributions under internal and external

noise, the distributions for proliferation are notably different. Under external noise, proliferative phenotypes vanish with increasing p, suggesting that a cell needs a stable external environment to divide. Whereas, the proliferating phenotype is robust to internal noise.

3.3 Hybrid Boolean Network Model

3.3.1 Reliable Switching Between Phenotypes Below Critical Noise Rate

We apply the hybrid model, introduced in Sect. 2.2, to address the question of the reliability of switching between different phenotypes. Intuitively, one expects that noise in the production function of (4.11) (with $\tau = \varepsilon = 0$) should have a considerable impact on both the asymptotic phenotypes and the delays in network response to changes in external signals. However, below a critical noise rate p_c, it turns out that phenotypes are stable and response delays are independent of p (Fig. 4.5, left panel). This observation can be explained by analyzing the stability of the asymptotic, average dynamics of single nodes. We assume that x_i is close to the stationary state, which implies that f_i is constant, i.e. $f_i = f_i^*$. Hence, fluctuations in the production rate are solely due to the stochastic variable $\delta(t)$ and, on average, occur with probability p. Now, we can represent changes in the average concentration as

$$\left\langle \frac{\mathrm{d}x_i}{\mathrm{d}t} \right\rangle = \alpha \left(|f_i^* - p| - x_i(t) \right). \tag{4.14}$$

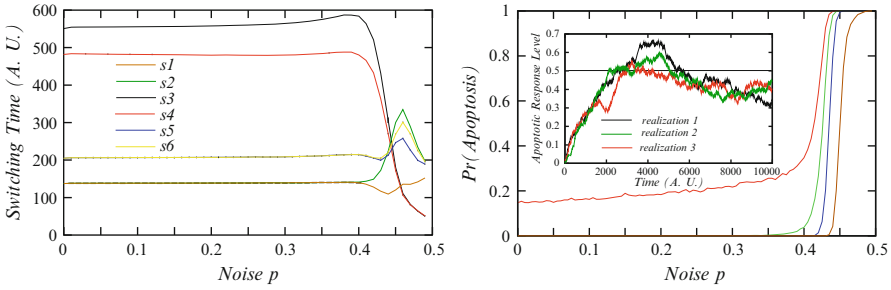

Fig. 4.5 *Left panel:* Time in arbitrary units (A.U.) as a function of update noise p needed for switching between phenotypes using hybrid BN model with $\alpha = 0.01$ given a change in external signals or in Rac activation: (s1) without contact inhibition, (s2) with contact inhibition, (s3) ITG signal is lost, (s4) VEGF-RTK signal is lost, (s5) Rac becomes active, and (s6) Rac becomes inactive. Each data point represents an average over 1,000 switching events. *Right panel:* Dynamics induced by randomization of internal concentrations and states (stress). A stochastic, transient apoptotic response occurs (inset, for three realizations). The probability that apoptosis is induced depends on p and the duration d of the response above the 0.5 threshold: $d = 25$ (*red*), $d = 100$ (*green*), $d = 500$ (*blue*) and $d = 1{,}000$ (*brown*)

Setting the left-hand side of (4.14) to zero, we recognize that the system has two fixed points:

$$x_i^* = \begin{cases} 1-p & \text{if } f_i^* = 1 \\ p & \text{if } f_i^* = 0. \end{cases} \tag{4.15}$$

Extending this result to the whole network implies that, below a critical noise rate p_c, phenotypes are stable and do not depend on noise.

Let us now assume that a switch between the stationary states occurs. For small p, this requires a transition in f_i^*. For the case $f_i^* = 0 \rightarrow f_i^* = 1$ at time $t = 0$, integrating (4.14) results in

$$\langle x_i \rangle(t) = (2p-1)\exp[-\alpha\, t] + (1-p). \tag{4.16}$$

The average time T_s needed for switching is the time required to cross the threshold $x_i = 1/2$. Evaluating (4.16) at T_s yields

$$T_s = \alpha^{-1} \ln 2, \tag{4.17}$$

i.e., T_s is independent of p. Notice, however, that this result only holds below a critical noise rate p_c. Above p_c, the variance of x_i around the mean $x_i^*(p)$ is large enough to induce random transitions of the threshold, thereby decreasing T_s on average. In the regime $p > p_c$, dynamics is completely fluctuation-driven, and hence no stable stationary states exist.

3.3.2 Mixed Feedback Loop Leads to Erratic Motility for Arbitrarily Low Noise

A main result from our study is that the hybrid BN model reliably reproduces the phenotypes predicted with the discrete, deterministic model for noise p below a critical value p_c. Above p_c, dynamics is dominated by fluctuations that cause phenotypes to deviate from those predicted in Fig. 4.3c with increasing probability. There is, however, one important exception. In Sect. 3.1, we found that the discrete, deterministic Boolean model with mixed feedback between RhoA and Rac predicts a phenotype with both proliferation and oscillatory motility present. Simulations using the hybrid model indicate that this phenotype is unstable for arbitrarily low noise, leading to an erratic, noise-driven pattern of on-off motility without any apparent periodicity (Bauer et al. 2010). This result suggested that angiogenesis may be inhibited by engineering the mixed feedback scheme to impose erratic motility in cells. Since robustness against fluctuations of molecular concentrations is a key requirement for living cells, we predicted that either the mixed feedback scheme is not realized in healthy cells or the current model does not capture all relevant regulatory interactions.

3.3.3 Noise-Dependent Apoptotic Response to Cellular Stress

Understanding how to induce conditions for which cells would initiate apoptosis could lead to novel ideas for pro- and anti-angiogenic therapies. As an example, we investigated how cells respond to a sudden, transient increase in stress (a "shock"). Starting with a healthy cell that perceives both ITG and VEGF-RTK signals, i.e., there is no external pressure to enter apoptosis, stress is simulated by suddenly randomizing internal molecular concentration levels. As is apparent in the inset of the right panel of Fig. 4.5, stress leads to a transient increase in the apoptotic response. However, in the presence of noise ($p > 0$), there is a strong stochastic component in the apoptotic response. In particular, whether the threshold ($x_i = 1/2$) to induce apoptosis is crossed is a stochastic process that depends both on noise p and the initial randomization of the internal states. However, the general trend in the switching curve is that the probability to cross the threshold and, hence, induce apoptosis, increases with noise p. The precise form of the switching curve depends on the duration d the response is above the threshold needed to induce apoptosis. As shown in the right panel of Fig. 4.5, as d increases, the switching curve becomes a steep threshold function around p_c. If we interpret p as the amount of stress already present in the system, where low p indicates a healthy state and high reliability of signal processing and high p indicates an unhealthy state, then this observation implies that stressed cells are more likely to undergo apoptosis the less healthy they are.

4 Discussion

BN models are a useful computational tool for describing signal transduction systems that consist of up to hundreds of elements, in particular when many of the kinetic parameters are not available or time resolution is not critical. As an example, we applied Boolean dynamics to model receptor cross-talk in signal transduction during angiogenesis. We showed that a discrete, deterministic BN model is already sufficient for correct prediction of experimentally established cell phenotypes, depending on cadherin-mediated cell–cell contact, ECM integrin binding and growth factor receptor (VEGF-RTK) activation. Our findings confirm the results established by other studies that attractors (phenotypes) in many biological networks primarily depend on the logical structure and wiring of network interactions and that these networks show considerable robustness against variation in kinetic parameters (von Dassow et al. 2000; Braunewell and Bornholdt 2007). A disadvantage of this class of discrete BN models, however, is their sensitivity to thermal noise and desynchronized update schemes. To overcome this limitation, we introduced a hybrid BN model that combines Boolean interactions with concentration dynamics described by piece-wise linear, stochastic differential equations. This generalized BN model leads to a time-scale separation between signal inputs and individual switching events, and exhibits signal transduction

robustness in the presence of thermal noise in molecular interactions. At the same time, the hybrid model preserves essential properties of the discrete BN model, namely the derived phenotype map, demonstrating the high versatility of this generalized class of BN models. We showed that the hybrid model also leads to interesting predictions that may be relevant for novel (anti-)angiogenic therapies: for example, a transient apoptotic response can be induced by external stress. Our model predicts that the probability that apoptosis is induced depends sensitively on the level of internal noise, potentially revealing a route to therapeutic strategies based on selective induction of apoptosis. Another useful application of our BN models is the extensive in-silico study of mutants, e.g., due to knockouts (Bauer et al. 2010) or rewiring of interactions, that generates predictions that can be tested experimentally.

References

R. Albert and H. G. Othmer. The topology of the regulatory interactions predicts the expression pattern of the segment polarity genes in drosophila melanogaster. *J. Theor. Biol.*, 223(1):1–18, 2003.

M. Aldana, E. Balleza, S. Kauffman, and O. Resendiz. Robustness and evolvability in genetic regulatory networks. *J. Theor. Biol.*, 245:433–448, 2007.

B. B. Aldridge, J. M. Burke, D. A. Lauffenburger, and P. K. Sorger. Physicochemical modeling of cell signaling pathways. *Nat. Cell Biol.*, 8:1195–1203, 2006.

D. Barua, J. R. Faeder, and J. M. Haugh. Structure-based kinetic models of modular signaling protein function: Focus on Shp2. *Biophys. J.*, 92:2290–2300, 2007.

D. Barua, J. R. Faeder, and J. M. Haugh. Computational models of tandem src homology 2 domain interactions and application to phosphoinositide 3-kinase. *J. Biol. Chem.*, 283:7738–7745, 2008.

A. L. Bauer, C. A. A. Beauchemin, and A. S. Perelson. Agent-based modeling of host-pathogen systems: The successes and challenges. *Information Sciences*, 179(10):1379–1389, 2009.

A. L. Bauer, T. L. Jackson, Y. Jiang, and T. Rohlf. Receptor cross-talk in angiogenesis: Mapping environmental cues to cell phenotype using a stochastic, boolean signaling network model. *J. Theor. Biol.*, 286:838–846, 2010.

U. S. Bhalla and R. Iyengar. Emergent properties of networks of biological signaling pathways. *Science*, 284:92–96, 1999.

M. L. Blinov, J. R. Faeder, B. Goldstein, and W. S. Hlavacek. Bionetgen: software for rule-based modeling of signal transduction based on the interactions of molecular domains. *Bioinformatics*, 83:3289–3291, 2006.

M. L. Blinov, J. R. Faeder, B. Goldstein, and W. S. Hlavacek. A network model of early events in epidermal growth factor receptor signaling that accounts for combinatorial complexity. *Biosystems*, 83:136–151, 2006.

S. Bornholdt and T. Rohlf. Topological evolution of dynamical networks: Global criticality from local dynamics. *Phys. Rev. Lett.*, 84:6114–6117, 2000.

S. Bornholdt and K. Sneppen. Neutral mutations and punctuated equilibrium in evolving genetic networks. *Phys. Rev. Lett.*, 81:236–239, 1998.

S. Braunewell and S. Bornholdt. Superstability of the yeast cell-cycle dynamics: Ensuring causality in the presence of biochemical stochasticity. *J. Theor. Biol.*, 245(4):638–643, 2007.

M. Chaves, R. Albert, and E. D. Sontag. Robustness and fragility of Boolean models for genetic regulatory networks. *J. Theor. Biol.*, 235:431–449, 2005.

C. S. Chen, M. Mrksich, S. Huang, G. M. Whitesides, and D. E. Ingber. Micropatterned surfaces for control of cell shape, position, and function. *Biotechnol. Prog.*, 14:356–363, 1998.

J. Colvin, M. I. Monine, J. R. Faeder, W. S. Hlavacek, D. D. Von Hoff, and R. G. Posner. Simulation of large-scale rule-based models. *Bioinformatics*, 25:910–917, 2009.

M. I. Davidich and S. Bornholdt. Boolean network model predicts cell cycle sequence of fission yeast. *arXiv: q-bio*, page 1313440, 2007.

G. E. Davis and D. R. Senger. Endothelial extracellular matrix: Biosynthesis, remodeling, and functions during vascular morphogenesis and neovessel stabilization. *Circ. Res.*, 97:1093 – 1107, 2005.

B. Derrida and Y. Pomeau. Random networks of automata: A simple annealed approximation. *Europhys. Lett.*, 1(2):45–49, 1986.

X. Dong, P. T. Foteinou, S. E. Calvano, S. F. Lowry, and I. P. Androulakis. Agent-based modeling of endotoxin-induced acute inflammatory response in human blood leukocytes. *PLoS ONE*, 5(2):e9249, 2010.

N. J. Eungdamrong and R. Iyengar. Modeling cell signaling networks. *Biol. Cell*, 96:355–362, 2004.

J. Folkman. Angiogenesis. *Annu. Rev. Med.*, 57:1–18, 2006.

F. Mac Gabhann and A. S. Popel. Dimerization of VEGF receptors and implications for signal transduction: a computational study. *Biophys. Chem.*, 128:125–139, 2007.

H. Gerhardt, M. Golding, M. Fruttiger, C. Ruhrberg, A. Lundkvist, A. Abramsson, M. Jeltsch, C. Mitchell, K. Alitalo, D. Shima, and C. Betsholtz. VEGF guides angiogenic sprouting utilizing endothelial tip cell filopodia. *J. Cell Biol.*, 161:1163–1177, 2003.

C. Gershenson. Classification of random boolean networks. In R. K. Standish, M. A. Bedau, and H. A. Abbass, editors, *Artificial Life VIII:Proceedings of the Eight International Conference on Artificial Life*, pages 1–8, 2002.

C. Gershenson. Updating schemes in random Boolean networks: Do they really matter? In *ARTIFICIAL LIFE IX*, pages 238–243. M I T PRESS, 2004.

D. T. Gillespie. A general method for numerically simulating the stochastic time evolution of coupled reaction equations. *J. Comp. Phys.*, 22:403–434, 1976.

L. Glass. The logical analysis of continuous, non-linear biochemical control networks. *J. Theor. Biol.*, 39:103–129, 1973.

L. Glass. Classification of biological networks by their qualitative dynamics. *J. Theor. Biol.*, 54:85–107, 1975.

C. J. Gottardi, E. Wong, and B. M. Gumbiner. E-cadherin suppresses cellular transformation by inhibiting beta-catenin signaling in an adhesion-independent manner. *J. Cell Biol.*, 153(5):1049–1060, 2001.

D. J. Hicklin and L. M. Ellis. Role of the vascular endothelial growth factor pathway in tumor growth and angiogenesis. *J. Clin. Onc.*, 23(5):1011–1027, 2005.

W. S. Hlavacek, J. R. Faeder, M. L. Blinov, A. S. Perelson, and B. Goldstein. The complexity of complexes in signal transduction. *Biotechnol. Bioeng.*, 84:861–876, 2003.

M. Hsing, J. L. Bellenson, C. Shankey, and A. Cherkasov. Modeling of cell signaling pathways in macrophages by semantic networks. *BMC Bioinformatics*, 5:156–169, 2004.

M. Hsing and A. Cherkasov. Integration of biological data with semantic networks. *Curr. Bioinform.*, 1(3):273–290, 2006.

B. Hu, G. M. Fricke, J. R. Faeder, R. G. Posner, and W. S. Hlavacek. Getbonnie for building, analyzing and sharing rule-based models. *Bioinformatics*, 25:1457–1460, 2009.

S. Huang and D. E. Ingber. The structural and mechanical complexity of cell-growth control. *Nat. Cell Biol.*, 1(5):E131–E138, 1999.

H. Hutchings, N. Ortega, and J. Plouet. Extracellular matrix-bound vascular endothelial growth factor promotes endothelial cell adhesion, migration, and survival through integrin ligation. *FASEB J.*, 17(11):1520–1522, 2003.

E. R. Jackson, D. Johnson, and W. G. Nash. Gene networks in development. *J. Theor. Biol.*, 119(4):379–396, 1986.

H. V Jain, J. E. Nor, and T. L. Jackson. Modeling the VEGF-Bcl2-CXCL8 pathway in intratumoral angiogenesis. *Bull. Math. Biol.*, 70(1):89–117, 2008.

S. A. Kauffman. Metabolic stability and epigenesis in randomly constructed genetic nets. *J. Theor. Biol.*, 22:437–467, 1969.

S. A. Kauffman. *The origins of order: Self-organization and selection in evolution*. Oxford University Press, first edition, 1993.

B. N. Kholodenko. Negative feedback and ultrasensitivity can bring about oscillations in the mitogen-activated protein kinase cascades. *Eur. J. Biochem.*, 267:1583–1588, 2000.

B. N. Kholodenko. Cell-signalling dynamics in time and space. *Nat. Rev. Mol. Cell Biol.*, 7:165–176, 2006.

K. Klemm and S. Bornholdt. Robust gene regulation: Deterministic dynamics from asynchronous networks with delay. *arXiv: q-bio*, page 0309013, 2003.

K. Klemm and S. Bornholdt. Stable and unstable attractors in Boolean networks. *Phys. Rev. E*, 72:055101(R), 2005.

H. A. Levine, A. L. Tucker, and M. Nilsen-Hamilton. A mathematical model for the role of cell signal transduction in the initiation and inhibition of angiogenesis. *Growth Factors*, 20(4):155–175, 2002.

S. Li, S. M. Assmann, and R. Albert. Predicting essential components of signal transduction networks: A dynamic model of guard cell abscisic acid signaling. *PLoS Biology*, 4(10):1732– 1748, 2006.

J. Lilien and J. Balsamo. The regulation of cadherin-mediated adhesion by tyrosine phosphorylation/deposphorylation of β-catenin. *Curr. Opin. Cell Biol.*, 17:459–465, 2005.

N. V. Mantzaris, S. Webb, and H. G. Othmer. Mathematical modeling of tumor-induced angiogenesis. *J. Math. Biol.*, 49:111–187, 2004.

J. Miller, M. Parker, R B. Bourret, and M. C. Giddings. An agent-based model of signal transduction in bacterial chemotaxis. *PLoS ONE*, 5(5):e9454, 2010.

E. N. Miranda and N. Parga. Noise effects in the kauffman model. *Europhys. Lett.*, 10:293, 1989.

F. Mu, R. F. Williams, C. J. Unkefer, P. J. Unkefer, J. R. Faeder, and W. S. Hlavacek. Carbon fate maps for metabolic reactions. *Bioinformatics*, 23:3193–3199, 2007.

J. E. Nör, J. Christensen, D. J. Mooney, and P. J. Polverini. Vascular endothelial growth factor (VEGF)-mediated angiogenesis is associated with enhanced endothelial cell survival and induction of bcl-2 expression. *Am. J. Path.*, 154(2):375–384, 1999.

KEGG: Kyoto Encyclopedia of Genes and Genomes, 1995–2007.

N. Paweletz and M. Knierim. Tumor related angiogenesis. *Crit. Rev. Oncol. Hematol.*, 9:197–242, 1989.

T. P. Peixoto and B. Drossel. Noise in random boolean networks. *Phys. Rev. E*, 79(3):036108, Mar 2009.

C. A. Petri. Nets, time and space. *Theoret. Comp. Sci.*, 153:3–48, 2009.

M. Pogson, M. Holcombe, R. Smallwood, and E. Qwarnstrom. Introducing spatial information into predictive nf-κb modeling – an agent-based approach. *PLoS ONE*, 3(6):e2367, 2008.

T. Rohlf and S. Bornholdt. Self-organized pattern formation and noise-induced control based on particle computations. *JSTAT*, L12001:379–396, 2005.

R. Rubenstein, P. C. Gray, T. J. Cleland, M. S. Piltch, W. S. Hlavacek, R. M. Roberts, J. Ambrosiano, and J.-I. Kim. Dynamics of the nucleated polymerization model of prion replication. *Biophys. Chem.*, 125:360–367, 2007.

E. Ruoslahti and J. C. Reed. Anchorage dependence, integrins, and apoptosis. *Cell*, 77:477–478, 1994.

B. Samuelsson and C. Troein. Superpolynomial growth in the number of attractors in kauffman networks. *Phys. Rev. Lett*, 90:098701, 2003.

A. C. Vaiana and K. Y. Sanbonmatsu. Stochastic gating and drugribosome interactions. *J. Mol. Biol.*, 386(3):648–661, 2009.

F. H. Silver, J. W. Freeman, and G. P. Seehra. Collagen self-assembly and the development of tendon mechanical properties. *J. Biomech.*, 36:1529–1553, 2003.

A. E. Smith, B. M. Slepchenko, J. C. Schaff, L. M. Loew, and I. G. Macara. Systems analysis of Ran transport. *Science*, 295:488–491, 2002.

P. R. Somanath, A. Ciocea, and T. V. Byzova. Integrin and growth factor receptor alliance in angiogenesis. *Cell Biochem. Biophys.*, 53(2):53–64, 2009.

G. von Dassow, E. Meir, E. M. Munro, and G. M. Odell. The segment polarity network is a robust developmental module. *Nature*, 406:188–192, 2000.

G. von Dassow and G. M. Odell. Design and constraints of the drosophila segment polarity module: robust spatial patterning emerges from intertwined cell state switches. *J. Exp. Zool.*, 294:179–215, 2002.

S. Wolfram. Cellular automata as models of complexity. *Nature*, 311(5985):419–424, 1984.

G. D. Yancopoulos, S. Davis, N. W. Gale, J. S. Rudge, S. J. Wiegand, and J. Holash. Vascular-specific growth factors and blood vessel formation. *Nature*, 407:242–248, 2000.

A. Zanetti, M. G. Lampugnani, G. Balconi, F. Breviario, M. Corada, L. Lanfrancone, and E. Dejana. Vascular endothelial growth factor induces shc association with vascular endothelial cadherin: A potential feedback mechanism to control vascular endothelial growth factor receptor-2 signaling. *Arterioscler. Thromb. Vasc. Biol.*, 22:617–622, 2002.

Q. Zhang, H. H. Petersen, H. Ostergaard, W. Ruf, and A. J. Olson. Molecular dynamics simulations and functional characterization of the interactions of the PAR2 ectodomain with factor viia. *Proteins*, 77(3):559–569, 2009.

Part II
Angiogenesis

Chapter 5
A Hybrid Discrete-Continuum Model of Tumour Induced Angiogenesis

Alexander R.A. Anderson, Mark A.J. Chaplain, and Stephen McDougall

1 Biology

1.1 Angiogenesis

Angiogenesis, the formation of blood vessels from a pre-existing vasculature, is a crucial component of many mammalian growth processes. For example, it occurs in early embryogenesis during the formation of the placenta, after implantation of the blastocyst in the uterine wall (Graham and Lala 1992) it occurs in adult mammals during tissue-repair and wound healing (Arnold and West 1991). Although these are examples of controlled angiogenesis, by contrast, uncontrolled or excessive blood-vessel formation, is essential for tumourigenesis and is also observed in inflammatory diseases such as arthritis, abnormal neovascularisation of the eye, duodenal ulcers and following myocardial infarction (Folkman and Klagsbrun 1987; Folkman 1985, 1995). These instances may all be considered as pathological examples of angiogenesis (Folkman and Brem 1992). In each case, however, the well-ordered sequence of events characterising angiogenesis is the same, beginning with the rearrangement and migration of endothelial cells from a pre-existing vasculature and culminating in the formation of an extensive branched, connected network of new capillaries (Madri and Pratt 1986; Paweletz and Knierim 1989).

A.R.A. Anderson (✉)
H. Lee Moffitt Cancer Center and Research Institute, Tampa, FL 33612, USA
e-mail: Alexander.Anderson@moffitt.org

M.A.J. Chaplain
University of Dundee, Dundee, DD1 4HN, Scotland
e-mail: Chaplain@maths.dundee.ac.uk

S. McDougall
Heriot-Watt University, Edinburgh, EH14 4AS, Scotland
e-mail: Steve.McDougall@pet.hw.ac.uk

T.L. Jackson (ed.), *Modeling Tumor Vasculature: Molecular, Cellular, and Tissue Level Aspects and Implications*, DOI 10.1007/978-1-4614-0052-3_5,

In this chapter, we focus our attention on the original hybrid discrete-continuum mathematical model of tumour induced angiogenesis (Anderson and Chaplain 1998).

1.2 Tumour Induced Angiogenesis

Folkman (1971) made the crucial link between angiogenesis and tumour invasion and metastasis, realising that preventing new vessels forming could be a simple way to inhibit further tumour growth. Although it was in fact Shubi (1968) 2 years earlier who actually coined the term *tumour angiogenesis*. It is generally accepted that the initiation of tumour-induced angiogenesis involves the tumour secreting a number of soluble chemicals, collectively known as tumour angiogenic factors, or TAF [5], into the surrounding tissue. Folkman's hypothesis was the defining first step, but it took over 10 years until the discovery of the first angiogenic factor (bFGF) by Shing et al. (1984) before real biological interest was triggered. This then led to the discovery of perhaps the most studied growth factor, Vascular endothelial growth factor (VEGF) by Klagsbrun and Soker (1993). Key to our current understanding of angiogenesis is the role that such growth factors play in promoting/inhibiting new vessel production, so called pro-angiogenic and anti-angiogenic factors (Carmeliet and Jain 2000).

Tumours are thought to secrete both pro- and anti-angiogenesis factors and it has been postulated that while a balance between the growth factors and the inhibitory factors exists, angiogenesis does not occur. However, if the level of growth factor exceeds the level of inhibitor then angiogenesis can be initiated (Folkman 1995; Hanahan and Weinberg 2000). The discovery of such anti-angiogenic factors and their use as therapeutic agents has been the subject of intense biological study for the last two decades and has led to many drugs being used in clinical trials. Factors such as angiostatin (O'Reilly et al. 1994), enodstatin (O'Reilly et al. 1997) and VEGI (Zhai et al. 1999) held great promise as a means of tumour control. However, whilst results in rodents have been successful, results in humans have been less predictable and sometimes with toxic side effects (Kerbel 2000).

In any case, the angiogenic factors, once secreted by the tumour, diffuse through the tissue creating a chemical gradient between the tumour and any existing vasculature. Upon reaching any neighbouring blood vessels, endothelial cells (EC) lining these vessels are first induced to degrade the parent venule basement membranes and then migrate through the disrupted membrane towards the tumour through the extra cellular matrix (ECM) (Paku and Paweletz 1991). The initial response of the EC to the TAF concentration gradient is a chemotactic one, i.e. a directed migration towards higher concentrations of TAF (Bowersox and Sorgente 1982; Quigley et al. 1983; Terranova et al. 1985; Albini et al. 1987; Paweletz and Knierim 1989). Interactions between the EC and certain components of the ECM (e.g. fibronectin,

laminin) have been shown to enhance cell adhesion to the matrix. In particular, cultured EC are known to synthesise and secrete cellular fibronectin and respond haptotactically to gradients of fibronectin, i.e. directed migration towards higher concentrations of bound matrix macromolecules present within the extracellular matrix (Carter 1965, 1967; Schor et al. 1981; Lacovara et al. 1984; McCarthy et al. 1984; Hynes 1990). In addition to the initial recruitment from the parent vessel and subsequent migration, EC proliferation near the tip of the new capillary sprout permits further extension of the capillary (Sholley et al. 1984; Ausprunk and Folkman 1977). After the new capillary sprouts have reached a certain distance from the parent vessel, they tend to incline towards each other leading to the formation of many loops (anastomosis) (Paweletz and Knierim 1989). From these loops new sprouts emerge (branching) repeating the angiogenic sequence of events and providing for further extension of the capillary network. In the case of tumour-induced angiogenesis the whole process continues unchecked until the tumour is vascularised.

The precise sequence of events involved in angiogenesis is now well known thanks largely to the development and use of a wide range of angiogenesis assays, both *in vivo* and *in vitro* (Paweletz and Knierim 1989). These assays include the chick chorioallantoic membrane (CAM), animal corneal models, transparent chamber assays (e.g. ear chambers, dorsal skin, cranial windows, cheek pouches) and various polymer gel assays. The sequence of events is shown schematically in Fig. 5.1: (1) EC migration; (2) Sprout formation (Fig. 5.1a); (3) EC proliferation near sprout tips; (4) Branching and anastomosis (Fig. 5.1b); (5) Repeat (1)–(4) (Fig. 5.1c); (6) Vascularisation of tumour (Fig. 5.1d). An illustration of the results of an animal cornea experiment is given in Fig. 5.2.

Tumour-induced angiogenesis provides the crucial link between the avascular phase of solid tumour growth and the more harmful vascular phase, wherein the tumour invades the surrounding host tissue and blood system. Once invasion has occurred, the possibility of the cancer spreading to other parts of the body (metastasis) becomes a reality and is far more difficult to treat clinically. In developing mathematical models of angiogenesis we hope to be able to provide a deeper insight into the interplay between the underlying mechanisms which cause the process. But, perhaps more crucially, mathematical models can give both insight and direction as to specific treatment stratagies. It is therefore essential that mathematical models are developed which are capable of producing the precise, quantitative *morphological features* of developing blood vessels. As a first step towards this goal we treated the vascular network as a complex connected hollow structure (Anderson and Chaplain 1998). Subsequent development of this model resulted in true *growing, flowing, adapting networks* that can be used to predict blood/drug delivery to the tumour (McDougall et al. 2002; Stephanou et al. 2005a,b; McDougall et al. 2006; Chaplain et al. 2006; Macklin et al. 2009).

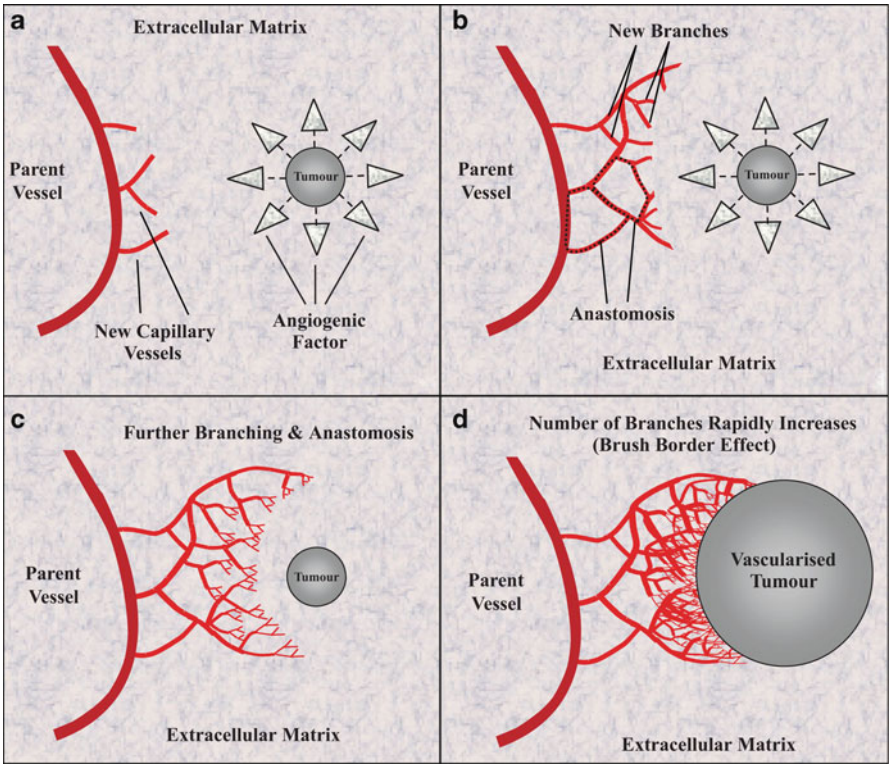

Fig. 5.1 Schematic diagram illustrating the key processes involved in tumour-induced angiogenesis

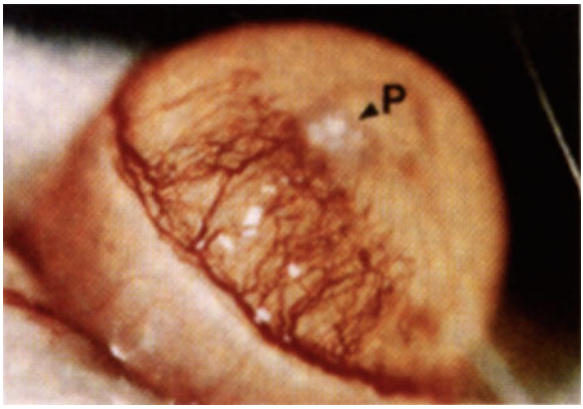

Fig. 5.2 Capillary network formation in a mouse cornea experiment six days after a small pellet soaked with an angiogenic factor (bFGF) is implanted at location P. This results in the growth of new blood vessels from the parent limbal vessel. Taken from O'Reilly et al. (1996)

2 Continuous Models of Angiogenesis

The scientific study of networks and their function can be traced back as far as Leonardo da Vinci with his beautifully detailed and intricate sketches of human lungs. Perhaps the first mathematical analysis of networks can be found in the classic work of Thompson (1917) where he studies *"... a number of interesting points in connection with the form and structure of the blood-vessels....."*. In more recent years several mathematical models, using a variety of applied mathematical techniques, have been developed to describe some of the key features of tumour-induced angiogenesis.

Whilst this chapter is not intended to be an extensive review of mathematical models of angiogenesis, it is worth noting that there are number of purely continuum models of angiogenesis that primarily emerged from the work Chaplain and colleagues. Most of these use the mathematical technique of partial differential equations, and have been able to examine the distribution in space and time of variables such as endothelial cell density, capillary tip and branch density and angiogenic factor concentration. Models in one space dimension include those of (Zawicki et al. 1981; Balding and McElwain 1985; Chaplain and Stuart 1993; Byrne and Chaplain 1995; Orme and Chaplain 1996; Anderson and Chaplain 1997). These models deal both with tumour-induced angiogenesis and angiogenesis in wound healing. Although these models are capable of capturing some features of angiogenesis at a "macroscale", such as average sprout density and network expansion rates, they are unable to provide more detailed information at the "microscale" concerning the actual structure and morphology of the capillary network and as such were of limited predictive value.

More realistic partial differential equation models of angiogenesis in two space dimensions have also been considered (Chaplain 1995; Orme and Chaplain 1996; Olsen et al. 1997; Chaplain and Orme 1998; Levine et al. 2001). The results of these models permit a more detailed qualitative comparison with in vivo observations concerning the spatio-temporal distribution of capillary sprouts within the network. However, even with these models, it is not possible to capture certain important events such as repeated sprout branching and, hence, the overall dendritic structure of the network. Other two-dimensional models deal with the role of mechanical forces on the developing capillary network (Mannoussaki et al. 1996; Murray et al. 1998; Murray and Swanson 1999; Holmes and Sleeman 2000). Finally, other models have been developed to examine strategies of anti-angiogenesis (Orme and Chaplain 1997; Anderson et al. 2000a,b). Although somewhat dated now an excellent and comprehensive overview of the continuum mathematical modeling done in this area can be found in the review paper of Mantzaris et al. (2004), also consider the reviews by Plank and Sleeman (2003a); Chaplain et al. (2006).

3 Discrete Models of Angiogenesis

In contrast to these deterministic, continuum models, several different types of discrete models, such as coupled map lattice models, fractal models, diffusion limited aggregation models and L-systems, have been used to model the branching morphology of capillary network formation and angiogenesis (Kiani and Hudetz 1991; Landini and Misson 1993; Nekka et al. 1996). One of the key initial models in this area was developed by Stokes and Lauffenburger (1991) and used a discrete probabilistic framework in two-space dimensions, based on stochastic differential equations. This approach had the advantage of enabling the motion of *individual endothelial cells* to be followed. Realistic capillary network structures were generated by incorporating rules for sprout branching and anastomosis. As parameters were estimated, as far as possible, from available experimental data, this permitted both qualitative and quantitative comparisons with in vivo networks to be made. Most of these discrete models are lattice-based where the angiogenic network is restricted by the lattice geometry, Plank and Sleeman (2003a,b) developed and off-lattice discrete model based on a reinforced random walk. This model produced aesthetically better vascular structures than Anderson and Chaplain (1998), subsequently Plank and Sleeman (2004) directly compared their off-lattice model with the lattice-based model of Anderson and Chaplain (1998) and concluded that they produced qualitatively similar results. More recently the cellular potts model (Bauer et al. 2007; Merks and Glazier 2006; Merks et al. 2008) has been used, as well as other discrete approaches (Bentley et al. 2009).

The most rapidly developing area that utilizes discrete models of angiogenesis is in multiscale models of cancer development, because angiogenesis is a key step in tumour progression, any model that hopes to capture the whole process of cancer development must also include angiogenesis. The works of Lowengrub and Cristini (Zheng et al. 2005; Frieboes et al. 2007; Macklin et al. 2009), Maini and Byrne (Alarcon et al. 2005, 2006; Owen et al. 2009; Perfahl et al. 2011), Popel (Qutub et al. 2009) and colleagues have all utilized discrete models of angiogenesis within a larger multiscale framework. However, the focus of this chapter is primarily on the hybrid discrete-continuum (HDC) model of angiogenesis by Anderson and Chaplain (1998). It is worth noting that since its publication in 1998 this paper has received over 400 citations and is currently the 2nd most highly cited paper in the history of the Bulletin of Mathematical Biology.

4 The Hybrid Discrete-Continnum Model of Angiogenesis

The HDC model is classified as “Hybrid”, because a continuum deterministic model (based on a system of reaction-diffusion-chemotaxis equations) controls the chemical/ECM dynamics and a discrete cellular automata like model (based on a biased random-walk model) controls cell migration and interactions. This approach was initially developed for modeling nematode movement through heterogeneous

microenvironments (Anderson et al. 1997), and was subsequently adapted for angiogenesis via inspiration from the stochastic model of Stokes and Lauffenburger (1991) and the continuum models of Chaplain (Chaplain and Stuart 1993; Byrne and Chaplain 1995; Chaplain 1996; Orme and Chaplain 1997; Chaplain and Orme 1998).

Initially, we define a system of coupled nonlinear partial differential equations to model tumour angiogenesis. Focussing on how the interactions between 3 key variables, (i) Endothelial cells (EC); (ii) Angiogenic factors (AF); (iii) Extracellular matrix (ECM), drive tumour angiogenesis. We then discretise this system of equations using finite differences and solve the AF/ECM equations numerically whereas the partial differential equation governing endothelial cell migration is used as the basis for the movement rules of individual EC. A key assumption in this approach is that the individual EC we are modeling are in fact located at the tip of a capillary sprout and govern the motion of the whole sprout. This is not unreasonable because EC lining the sprout-wall are contiguous (Paweletz and Knierim 1989; Stokes and Lauffenburger 1991). As we are modeling individual cells we can now more accurately model processes such as proliferation, branching, anastomosis and production/degradation at the individual cell level. The crucial point of this technique is that it allows cells to be treated as discrete individuals and the cell processes to be modeled at the cell level whilst allowing the AF/ECM to be treated as continuous. A detailed discussion on the types of system that this technique is applicable to is given in Anderson (2003). Other applications of the technique can be found in Anderson et al. (2000a,b), Anderson and Pitcairn (2003), Anderson (2005), Anderson et al. (2006), Gerlee and Anderson (2007, 2008, 2009), and Basanta et al. (2009).

4.1 The Continuum Model

In this section we briefly describe the continuum equations that subsequently drive discrete equations which form the basis for our HDC technique. In order to simplify the mathematical modeling, we assume first of all that there is a net excess of angiogenic factors being produced (angiogenic inhibitors may easily be considered in a modified model). We also assume that the motion of the EC is influenced by three main factors: random motility (analogous to diffusion); chemotaxis, i.e. directed motion in response to gradients of soluble angiogenic factors (Stokes and Lauffenburger 1991) and haptotaxis, i.e. directed motion in response to gradients of bound molecules within the ECM (e.g. fibronectin, McCarthy et al. 1984). We consider a generic angiogenic factor (AF) and a generic matrix macromolecule (MM). We denote the EC density per unit volume by n, the AF concentration by c and the MM concentration by f.

The derivation of the complete system can be found in Anderson and Chaplain (1998) and results in the following system of partial differential equations describing the spatio-temporal evolution of AF, MM concentration and EC density:

$$\begin{aligned}
\frac{\partial n}{\partial t} &= \overbrace{D_n \nabla^2 n}^{\text{random motility}} - \overbrace{\nabla \cdot (\chi(c) n \nabla c)}^{\text{chemotaxis}} - \overbrace{\nabla \cdot (\rho(f) n \nabla f)}^{\text{haptotaxis}}, \\
\frac{\partial f}{\partial t} &= \overbrace{\omega n}^{\text{production}} - \overbrace{\mu n f}^{\text{uptake}}, \\
\frac{\partial c}{\partial t} &= - \overbrace{\lambda n c}^{\text{uptake}},
\end{aligned} \tag{5.1}$$

where D_n is the EC random motility coefficient, $\chi(c)$ and $\rho(f)$ the chemotaxis and haptotaxtis functions, respectively, and ω, μ, and λ are positive constants (see Anderson and Chaplain 1998 for full details).

We non-dimensionalise (5.1) by rescaling distance with the parent vessel to tumour distance of L, time with $\tau = L^2/D_c$ (where D_c is the AF diffusion coefficient), endothelial cell density with n_0, and AF and MM concentration with c_0 and f_0, respectively (where n_0, c_0, f_0 are appropriate reference variables). We shall also assume that the chemotactic function $\chi(c) = \chi_0/(1 + \alpha c)$ and the haptotactic function $\rho(f) = \rho_0$, where χ_0, α and ρ_0 are positive constants. Therefore setting

$$\tilde{c} = \frac{c}{c_0}, \ \tilde{f} = \frac{f}{f_0}, \ \tilde{n} = \frac{n}{n_0}, \ \tilde{t} = \frac{t}{\tau}$$

and dropping the tildes for clarity, we obtain the non-dimensional system,

$$\begin{aligned}
\frac{\partial n}{\partial t} &= D \nabla^2 n - \nabla \cdot (\chi(c) n \nabla c) - \nabla \cdot (\rho n \nabla f), \\
\frac{\partial f}{\partial t} &= \beta n - \gamma n f, \\
\frac{\partial c}{\partial t} &= -\eta n c,
\end{aligned} \tag{5.2}$$

where

$$\begin{aligned}
D = \frac{D_n}{D_c}, \chi = \frac{\chi_0 c_0}{D_c}, \alpha = \frac{c_0}{k_1}, \rho = \frac{\rho_0 f_0}{D_c}, \\
\beta = \frac{\omega L^2 n_0}{f_0 D_c}, \gamma = \frac{\mu L^2 n_0}{D_c}, \eta = \frac{\lambda L^2 n_0}{D_c},
\end{aligned}$$

and subject to the no-flux conditions,

$$\underline{\zeta} \cdot \left(-D \nabla n + n \left(\frac{\chi}{1 + \alpha c} \nabla c + \rho \nabla f \right) \right) = 0 \tag{5.3}$$

on the boundaries of the unit square in 2D and unit cube in 3D.

The above system of equations can be used to model two- and three-dimensional angiogenesis (e.g. corneal assays, collagen gel assays). In two-dimensions the system is considered to hold on a square of tissue side 2 mm, while in three-dimensions it holds on a cube of side 2 mm. The parent vessels (e.g. limbal vessels) are placed at appropriate locations on the boundary of the domain, and the tumour (i.e. source of angiogenic factor) is placed either on the boundary (in two-dimensions) or in the centre (in three-dimensions). We shall assume that the EC, AF and MM all remain within the domain of tissue throughout the simulations and therefore impose no-flux boundary conditions on n, c and f.

4.2 Discretisation and EC Movement Rules

After defining the continuous system we next discretize it using standard Euler central finite difference approximations (Mitchell and Griffiths 1980), using a grid of discrete points (mesh size h), at discrete time intervals k. This process can be done in two or three dimensions but for the sake of completeness and ease of reproducibility we will define the discrete systems fully in both 2 and 3 spatial dimensions.

4.2.1 2D Discretisation

In two spatial dimensions the system of partial differential equations (5.2) becomes the following system after discretisation:

$$\begin{aligned} n_{l,m}^{q+1} &= n_{l,m}^{q} P_0 + n_{l+1,m}^{q} P_1 + n_{l-1,m}^{q} P_2 + n_{l,m+1}^{q} P_3 + n_{l,m-1}^{q} P_4, \\ f_{l,m}^{q+1} &= f_{l,m}^{q} \left[1 - k\gamma n_{l,m}^{q}\right] + k\beta n_{l,m}^{q}, \\ c_{l,m}^{q+1} &= c_{l,m}^{q} \left[1 - k\eta n_{l,m}^{q}\right], \end{aligned} \tag{5.4}$$

with $x = lh$, $y = mh$ and $t = qk$.

In order to generate a realistic capillary network structure we assume that the motion of an individual EC located at the tip of a capillary vessel governs the growth of the whole vessel (in terms of its direction). Under this assumption, the coefficient P_0, which is proportional to the probability of no movement, has the form,

$$\begin{aligned} P_0 = 1 &- \frac{4kD}{h^2} + \frac{k\alpha\chi(c_{l,m}^{q})}{4h^2(1+\alpha c_{l,m}^{q})}\left[\left(c_{l+1,m}^{q} - c_{l-1,m}^{q}\right)^2 + \left(c_{l,m+1}^{q} - c_{l,m-1}^{q}\right)^2\right] \\ &- \frac{k\chi(c_{l,m}^{q})}{h^2}\left(c_{l+1,m}^{q} + c_{l-1,m}^{q} - 4c_{l,m}^{q} + c_{l,m+1}^{q} + c_{l,m-1}^{q}\right) \\ &- \frac{k\rho}{h^2}\left(f_{l+1,m}^{q} + f_{l-1,m}^{q} - 4f_{l,m}^{q} + f_{l,m+1}^{q} + f_{l,m-1}^{q}\right), \end{aligned}$$

and the coefficients P_1, P_2, P_3 and P_4, which are proportional to the probabilities of moving left, right, up and down, respectively, have the forms,

$$P_1 = \frac{kD}{h^2} - \frac{k}{4h^2}\left[\chi(c^q_{l,m})\left(c^q_{l+1,m} - c^q_{l-1,m}\right) + \rho\left(f^q_{l+1,m} - f^q_{l-1,m}\right)\right],$$

$$P_2 = \frac{kD}{h^2} + \frac{k}{4h^2}\left[\chi(c^q_{l,m})\left(c^q_{l+1,m} - c^q_{l-1,m}\right) + \rho\left(f^q_{l+1,m} - f^q_{l-1,m}\right)\right],$$

$$P_3 = \frac{kD}{h^2} - \frac{k}{4h^2}\left[\chi(c^q_{l,m})\left(c^q_{l,m+1} - c^q_{l,m-1}\right) + \rho\left(f^q_{l,m+1} - f^q_{l,m-1}\right)\right],$$

$$P_4 = \frac{kD}{h^2} + \frac{k}{4h^2}\left[\chi(c^q_{l,m})\left(c^q_{l,m+1} - c^q_{l,m-1}\right) + \rho\left(f^q_{l,m+1} - f^q_{l,m-1}\right)\right].$$

When there is no AF or MM in the same region as an endothelial cell, P_1 to P_4 are equal because the values of c and f are 0. Also when there is an equal amount of AF and MM on either side of an endothelial cell (i.e. no gradient), the values $(c, f)_{l,m-1}$ and $(c, f)_{l,m+1}$ cancel each other out as do $(c, f)_{l-1,m}$ and $(c, f)_{l+1,m}$ and thus P_1 to P_4 are equal. Therefore, in both these circumstances unbiased random movements will be produced. However, if there is more AF (MM) on one side of the endothelial cell than the other, the probabilities (P_1 to P_4) will no longer be equal and hence directed movement, towards the higher concentration of AF (MM), will result. If both AF and fibronectin gradients exist then the probabilities will be biased by both gradients, and weighted depending on the coefficients χ and ρ.

4.2.2 3D Discretisation

In three spatial dimensions the system of partial differential equations (5.2) becomes the following system after discretisation:

$$\begin{aligned} n^{q+1}_{l,m,w} &= n^q_{l,m,w}P_0 + n^q_{l+1,m,w}P_1 + n^q_{l-1,m,w}P_2 + n^q_{l,m+1,w}P_3 \\ &\quad + n^q_{l,m-1,w}P_4 + n^q_{l,m,w+1}P_5 + n^q_{l,m,w-1}P_6, \\ f^{q+1}_{l,m,w} &= f^q_{l,m,w}\left[1 - k\gamma n^q_{l,m,w}\right] + k\beta n^q_{l,m,w}, \\ c^{q+1}_{l,m,w} &= c^q_{l,m,w}\left[1 - k\eta n^q_{l,m,w}\right], \end{aligned} \tag{5.5}$$

where the subscripts specify the location on the grid and the superscripts the time steps. That is $x = lh$, $y = mh$, $z = wh$ and $t = qk$ where l, m, w, k, q and h are positive parameters.

Focussing on the discrete EC equation, as above, we use the seven coefficients P_0 to P_6 to generate the motion of an individual EC at the tip of a capillary vessel. These coefficients can be thought of as being proportional to the probabilities of the EC being stationary (P_0) or moving west (P_1), east (P_2), north (P_3), south (P_4), up (P_5), or down (P_6), i.e. the movement probabilities for an EC biased random walk.

The coefficient P_0, which is proportional to the probability of no movement, has the form,

$$\begin{aligned}P_0 = 1 - \frac{4kD}{h^2} + \frac{k\alpha\chi(c^q_{l,m,w})}{4h^2(1+\alpha c^q_{l,m,w})}\Big[\Big(c^q_{l+1,m,w} - c^q_{l-1,m,w}\Big)^2 \\ + \Big(c^q_{l,m+1,w} - c^q_{l,m-1,w}\Big)^2 + \Big(c^q_{l,m,w+1} - c^q_{l,m,w-1}\Big)^2\Big] \\ - \frac{k\chi(c^q_{l,m,w})}{h^2}\Big(c^q_{l+1,m,w} + c^q_{l-1,m,w} + c^q_{l,m,w+1} + c^q_{l,m,w-1} - 6c^q_{l,m,w} + c^q_{l,m+1,w} \\ + c^q_{l,m-1,w}\Big) - \frac{k\rho}{h^2}\Big(f^q_{l+1,m,w} + f^q_{l-1,m,w} + f^q_{l,m,w+1} + f^q_{l,m,w-1} - 6f^q_{l,m,w} \\ + f^q_{l,m+1,w} + f^q_{l,m-1,w}\Big),\end{aligned}$$

and the coefficients P_1, P_2, P_3, P_4, P_5 and P_6 which are proportional to the probabilities of moving west, east, north, south, up, and down, respectively, have the forms,

$$P_1 = \frac{kD}{h^2} - \frac{k}{4h^2}\Big[\chi(c^q_{l,m,w})\Big(c^q_{l+1,m,w} - c^q_{l-1,m,w}\Big) + \rho\Big(f^q_{l+1,m,w} - f^q_{l-1,m,w}\Big)\Big],$$

$$P_2 = \frac{kD}{h^2} + \frac{k}{4h^2}\Big[\chi(c^q_{l,m,w})\Big(c^q_{l+1,m,w} - c^q_{l-1,m,w}\Big) + \rho\Big(f^q_{l+1,m,w} - f^q_{l-1,m,w}\Big)\Big],$$

$$P_3 = \frac{kD}{h^2} - \frac{k}{4h^2}\Big[\chi(c^q_{l,m,w})\Big(c^q_{l,m+1,w} - c^q_{l,m-1,w}\Big) + \rho\Big(f^q_{l,m+1,w} - f^q_{l,m-1,w}\Big)\Big],$$

$$P_4 = \frac{kD}{h^2} + \frac{k}{4h^2}\Big[\chi(c^q_{l,m,w})\Big(c^q_{l,m+1,w} - c^q_{l,m-1,w}\Big) + \rho\Big(f^q_{l,m+1,w} - f^q_{l,m-1,w}\Big)\Big],$$

$$P_5 = \frac{kD}{h^2} - \frac{k}{4h^2}\Big[\chi(c^q_{l,m,w})\Big(c^q_{l,m,w+1} - c^q_{l,m,w-1}\Big) + \rho\Big(f^q_{l,m,w+1} - f^q_{l,m,w-1}\Big)\Big],$$

$$P_6 = \frac{kD}{h^2} + \frac{k}{4h^2}\Big[\chi(c^q_{l,m,w})\Big(c^q_{l,m,w+1} - c^q_{l,m,w-1}\Big) + \rho\Big(f^q_{l,m,w+1} - f^q_{l,m,w-1}\Big)\Big].$$

As in the 2D case, when there is no AF or MM in the same region as an EC, P_1 to P_6 are equal because the values of c and f are 0. Also when there is an equal amount of AF and MM on either side of an EC (i.e. no gradient) then P_1 to P_6 are equal. Therefore, in both these circumstances unbiased random movements will be produced. However, if there is more AF (MM) on one side of the EC than the other, the probabilities (P_1 to P_6) will no longer be equal and hence directed movement, towards the higher concentration of AF (MM), will result. If both AF and MM gradients exist then the probabilities will be biased by both gradients, depending on the coefficients χ and ρ.

In the 2D case the five coefficients P_0 to P_4 and in the and 3D case the seven coefficients P_0 to P_6 are proportional to the probabilities of an individual EC being stationary or moving to one of the neighbouring grid points. Each coefficient is

actually a function of the local AF and MM concentrations, and therefore, the motion of an individual cell at the vessel-tip is governed by its interactions with angiogenic factors and matrix macromolecules in its local environment. In fact each of the movement coefficients (i.e. not P_0) in both the 2D and 3D cases consists of three components,

$$P_n = \text{Random movement} + \text{Chemotactic} + \text{Haptotactic}, \tag{5.6}$$

thus showing how the discrete EC movements are linked to the continuous EC equation in system (5.1).

4.3 Individual-Based Processes

As we are considering migration at the cellular level, we can incorporate micro-scale processes such as EC proliferation, the generation of new capillary vessels (branching) and the fusion of two vessels (anastomosis), explicitly into the model. Although there is a good deal of information regarding the actual events of the generation of new sprouts (sprout branching) and the formation of loops (anastomosis), there is no explanation as to the precise mechanisms which cause them (Paweletz and Knierim 1989). Figure 5.1 gives a schematic illustration of the processes which we will model explicitly using the HDC technique.

4.3.1 Branching

We will assume that the generation of new sprouts (branching) occurs only from existing sprout-tips and only when sufficient space exists. It is also reasonable to assume that the newly formed sprouts are unlikely to branch immediately. From these assumptions we obtain the following two conditions, which must be satisfied before a capillary sprout can branch at its tip and generate a new sprout: (1) The age of the current sprout is greater than some threshold branching age ψ, i.e. new sprouts must mature for a length of time at least equal to ψ before being able to branch. (2) There is sufficient space locally for a new sprout to form, i.e. branching into a space occupied by another sprout is not possible. Given that each of the above two conditions are satisfied, we assume that each sprout-tip has a probability, P_b, of generating a new sprout (branching) and that this probability directly proportional to the local AF concentration (see Anderson and Chaplain 1998 for further details). Therefore very little branching occurs initially (near the parent vessel where the AF concentration is low), but as the endothelial cells migrate closer to the tumour (the AF concentration slowly increases) the number of new sprouts slowly increases. A short distance from the tumour the frequency of branching dramatically increases

(as does the AF concentration) creating the "brush border" effect (Muthukkaruppan et al. 1982), i.e. a very dense network of interconnected vessels at the leading edge.

4.3.2 Anastomosis

The formation of loops by capillary sprouts is another very important feature of angiogenesis, which can be captured explicitly by the HDC technique. As the sprouts progress towards the tumour, driven by the movement probabilities defined above, at each time step of the simulation, the endothelial cells at the sprout-tips can move to any of their orthogonal neighbours on the discrete grid. If upon one of these moves another sprout is encountered then anastomosis can occur (see Fig. 5.1b). For simplicity, we assume that as a result of the anastomosis, only one of the original sprouts continues to grow (the choice of which is purely random).

4.3.3 Proliferation

During angiogenesis EC are initially recruited from the parent vessel and migrate towards the tumour without proliferation. Approximately $36-48$ h into the process, cell mitosis is observed (Paweletz and Knierim 1989; Sholley et al. 1984) and is confined to a region just behind the sprout-tip. Endothelial cell doubling time has been estimated at 18 h (Williams 1987) and we model the process of cell division in the discrete model by assuming that some of the cells behind the sprout-tip divide (into two daughter cells) every 18 h. We assume that this has the effect of increasing the length of a sprout by approximately one cell length every 18 h. In terms of the HDC model, this is equivalent to the sprout length being increased by one grid point every half time unit. As the age of each EC at a sprout-tip is known we can easily determine when proliferation should occur. Owing to the inherent randomness of the HDC technique, proliferation will occur asynchronously in separate sprouts, as is observed experimentally (Paweletz and Knierim 1989).

4.3.4 Production/Degradation

As we are modeling individual tumour cells we must consider production of AF and degradation of MM at the level of a single cell. In the continuum model (5.2) we have these rates as being proportional to the tumour cell density. However, in the discrete form of the PDE model (5.4,5.5) these terms will only be active at a specific lattice point if a tumour cell is occupying that point (i.e. we take $n = 1$) otherwise they will be zero (i.e. we take $n = 0$), additionally we must scale the rates appropriately for individual cells.

4.4 Simulation Process for the Hybrid Discrete-Continuum Model

Having a fully discrete system of equations and a collection of individual-based processes gives us the key ingredients to begin simulating our HDC model of angiogenesis. However, we must first normalise the movement coefficients, in order to define appropriate movement probability ranges. Then within an appropriately initialised spatial domain, and set of parameters, we can simulate distinct angiogenic responses in two and three spatial dimensions.

4.4.1 Normalisation and Probability Ranges

Each time step of the simulation process involves solving either the 2D-discrete system (5.4) or 3D-discrete system (5.5) numerically to generate the new AF, MM concentrations as well as the movement coefficients P_n for all the EC tip cells we are considering.

An important step that was accidentally omitted in the original paper (Anderson and Chaplain 1998) was the need to normalise these coefficients such that they sum to unity. This highlights another issue, that throughout the years we have been asked about many times – what do you do if one of the coefficients becomes negative? This can happen, in part due to the fact that these movement coefficients are derived from a finite difference discretisation of a PDE but also because the gradients in MM or AF can become sufficiently steep as to create a negative coefficient. If the coefficient is negative it effectively means that movement in that direction should never happen. The solution to this problem is simple, merely set any negative coefficient to zero before normalisation, this will ensure that movement is not chosen and leads to a rescaling of the other coefficients in a proportional manner. Assuming all coefficients are positive (or zero), a normalised coefficient, Q_n can formally be defined as a summed scaling of the coefficient as follows: $Q_n = P_n / \sum_{i=0}^{j} P_i$, where $j = 4$ in 2D and $j = 6$ in 3D and n represents a placeholder for all coefficients.

Now that we have a set of normalised coefficients we can compute probability ranges from them by summing these coefficients to produce five ranges in 2D or seven ranges in 3D, $R_0 = 0$ to Q_0 and $R_j = \sum_{i=0}^{j-1} Q_i$ to $\sum_{i=0}^{j} Q_i$, where $j = 1 - 4$ in 2D and $j = 1 - 6$ in 3D. We then generate a random number between 0 and 1, and depending on the range which this number falls in, the current individual endothelial cell under consideration will remain stationary (R_0) or move left (R_1), right (R_2), up (R_3) or down (R_4) in 2D or move west (R_1), east (R_2), north (R_3), south (R_4), up (R_5) or down (R_6) in 3D. The larger a particular range, the greater the probability that the corresponding coefficient will be selected. Each endothelial cell is therefore restricted to move to one of its orthogonal neighbouring grid points or remain stationary at each time step. It is worth noting that even if there is a probability of an EC moving back to a grid point it previously occupied we do

not allow this to occur, since by definition we assume that these are EC tip cells that lead the way for the rest of the EC to follow in a contiguous fashion creating a sprout. So effectively in 2D there are only three possible movements and five possible movements in 3D, remaining stationary always being a possibility in both.

4.4.2 Initialisation

All the 2D simulations of the HDC model were carried out on a 200×200 grid, which is a discretization of a the unit square, $[0, 1] \times [0, 1]$, with a space step of $h = 0.005$. Given that our unit of length is 2 mm, this means that h is equivalent to a dimensional length of $10\,\mu$m, i.e. approximately the length of one or two endothelial cells (Paku and Paweletz 1991). A discrete form of the no flux boundary condition (5.3) was imposed on the square grid, restricting the endothelial cells to within the grid. Similarly, 3D simulations were carried out on a $100 \times 100 \times 100$ grid, which is a discretization of a the unit cube, $[0, 1] \times [0, 1] \times [0, 1]$, with a space step of $h = 0.01$.

The first event of tumour-induced angiogenesis is the secretion of AF by the tumour cells. The AF then diffuses into the extracellular matrix and a concentration gradient is established between the tumour and parent vessel. If we consider the tumour as approximately circular and assume AF diffuses and decays then an approximation of the steady-state (Chaplain 1995, 1996) has a concentration field of the form,

$$c(x, y, 0) = \begin{cases} 1, & 0 \leq r \leq 0.1, \\ \dfrac{(\nu - r)^2}{(\nu - 0.1)^2}, & 0.1 \leq r \leq 1, \end{cases} \tag{5.7}$$

where ν ia a positive constant and r is given by,

$$r = \sqrt{(x - 1)^2 + \left(y - \frac{1}{2}\right)^2}, \tag{5.8}$$

assuming that the tumour is centred on $(1, \frac{1}{2})$, with a radius of 0.1. Taking (5.7) as the initial conditions for the AF concentration profile might then be a reasonable description of the actual concentration field arising from a small circular tumour implant. To approximate a row of tumour cells (or a larger circular implant) we also consider an initial AF concentration field of the form,

$$c(x, y, 0) = e^{-\frac{(1-x)^2}{\epsilon_1}}, \quad (x, y) \in [0, 1] \times [0, 1], \tag{5.9}$$

where ϵ_1 is a positive constant. For similicity we assume a uniform initial concentration of fibronectin throughout the domain, i.e.

$$f(x, y, 0) = 1, \quad (x, y) \in [0, 1] \times [0, 1], \tag{5.10}$$

In the simulations that follow using initial condition (5.9) emphasises that any lateral motion of the endothelial cells is due to the interactions with AF and fibronectin and is not dependent on the underlying geometry of the system.

The 2D initial conditions are given by discrete forms of the AF (5.7) and fibronectin (5.10) equations. We assume that there are five capillary sprouts initiated by five EC located at the sprout-tips, starting at $y = 0.17,\ 0.3,\ 0.5,\ 0.65,\ 0.84$ all at $x = 0$. The 3D initial conditions take a similar form but instead of placing the tumour on the boundary of the domain we place it in the centre and modify the AF (5.7) and fibronectin (5.10) equations as appropriate. We assume that there are 15 capillary sprouts initiated by 15 EC located at the sprout-tips, with three equally spaced on five faces of the units cube (initial EC positions can be seen in the first panel of Fig. 5.4).

4.4.3 Parameterisation

Wherever possible parameter values have been estimated from available experimental data (see Anderson and Chaplain 1998 for a full justification as well as Rupnick et al. 1988; Bray 1992; Williams 1987). The non-dimensional parameter values used in the following simulations are $D = 0.00035$, $\alpha = 0.6$, $\chi_0 = 0.38$, $\rho = 0.34$, $\beta = 0.05$, $\gamma = 0.1$ and $\eta = 0.1$. Through trial and error it was found that a threshold branching age of $\psi = 0.5$ (equivalent to a dimensional time of 0.75 days) produced simulated networks which were qualitatively similar in morphology to those networks observed in vivo. Note that the estimates for $L = 2\,\text{mm}$ and $D_c = 2.9 \times 10^{-7}\text{cm}^2\text{s}^{-1}$ give the timescale $\tau = L^2/D_c$ as 1.5 days. For a complete list of parameters and how they were chosen see Anderson and Chaplain (1998).

4.5 Hybrid Model Simulation Results

We simulate the HDC model to predict the growth of a capillary network in two different experimental assays, i.e. (1) a two-dimensional experiment, that is equivalent to the animal corneal implant (Gimbrone et al. 1974; Muthukkaruppan et al. 1982) and (2) a three-dimensional experiment, that of a small implant in a collagen gel assay or modeling the actual in vivo scenario of the capillary response to a solid tumour.

Figure 5.3 shows two sets of results from simulations of the model in a square domain of length 2 mm, at times $t = 7$ days (left figures) and $t = 15$ days (right figures) days. Both simulations have the parent vessel located along the left hand

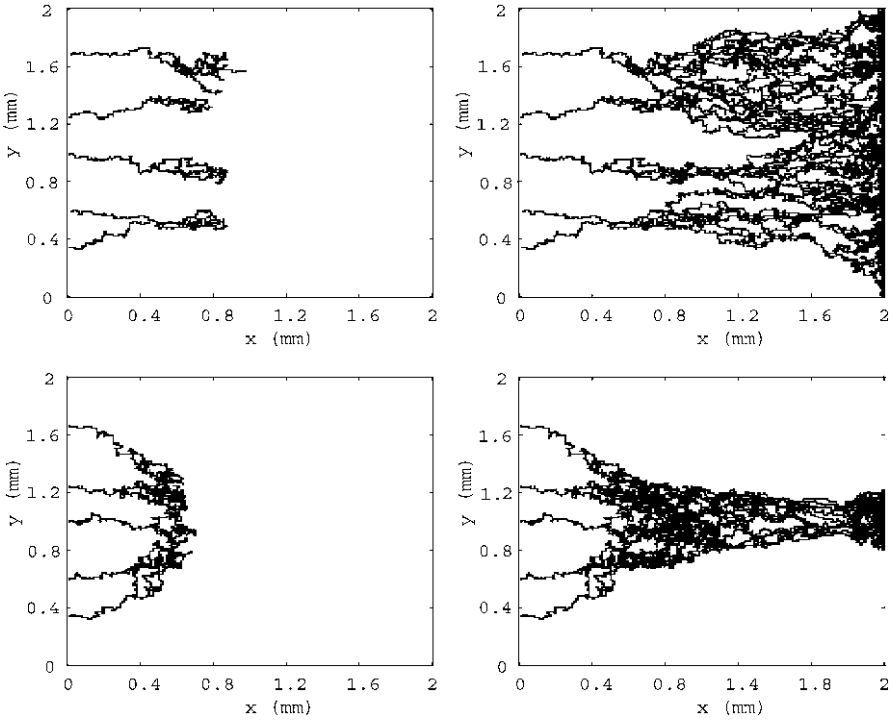

Fig. 5.3 Figure showing the theoretically generated capillary networks from the HDC model using AF boundary conditions, (5.9) *upper panels* and (5.7) *lower panels*. The figures show the evolution of the network towards a large tumour (*upper two figures*) and a smaller circular tumour (*lower figures*) at times 7 days (*left*) and 15 days (*right*)

edge of the domain ($x = 0$), while the tumour is located along all of the right hand edge for one simulation (representing a large tumour, upper figures) and in the centre of the right hand edge for the other (representing a small circular tumour, lower figures). Initially, we assume there are five sprouts; uniform fibronectin distribution; high AF at tumour, low at parent vessel.

At $t = 7$ days, both simulations have a similar initial outgrowth of sprouts, but in the case of the circular tumour simulation, we clearly have more anastomosis occurring. By $t = 15$ days both networks have developed into highly branched, connected structures which have vascularised the tumours. In the case of the small circular tumour the resulting network is more focussed than that of a large tumour. The latter has produced a broader network which has more anastomosis occurring closer to the tumour replicating the brush border effect (Gimbrone et al. 1974; Muthukkaruppan et al. 1982), compare with Fig. 5.2.

Whilst the results of the two-dimensional simulations are in excellent qualitative agreement with the experimental results carried out in animal corneal models (Gimbrone et al. 1974; Muthukkaruppan et al. 1982), we know that generally in

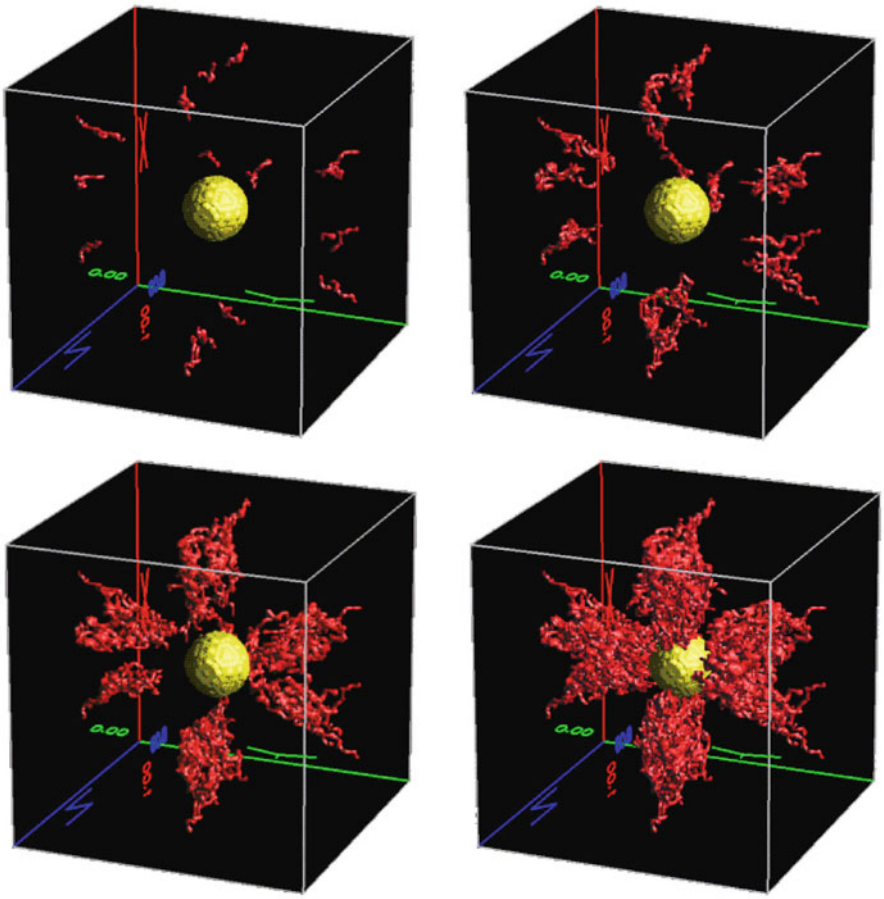

Fig. 5.4 Figure showing the theoretically generated 3-dimensional capillary network of the mathematical model. The figure shows the evolution of the network (*red capillaries*) towards a *solid spherical* tumour implant (*yellow spheroid*) located in the centre of the cube for the times $t = 1, 3, 7, 10$ days

vivo angiogenesis is a fully three-dimensional process. Hence, we also simulate the three-dimensional (theoretical) response to a small tumour implant in a collagen gel assay. In the simulation results shown in Fig. 5.4 a spherical tumour is positioned at the centre of a 2mm cube of tissue with the resulting TAF concentration field assumed to be radially symmetric. Three capillary sprouts are initiated on five of the six faces of the cube and an initial uniform (homogeneous) fibronectin distribution is assumed throughout the whole cube.

From these results we see that at $t = 1$ day the initial vessels have grown a short distance towards the tumour, but have only branched a little. As time progresses ($t = 3$ days) the vessels begin to branch more and migrate further towards the tumour.

By $t = 7$ days there is a reasonable number of branches, which are sufficiently close to one another, for some anastomosis to occur which will lead to a better connected vasculature. Finally, at $t = 10$ days we have connection with tumour and the completion of the angiogenic process. The number of branches rapidly increases between $t = 7$ and $t = 10$ days creating a dense vasculature which almost engulfs the tumour.

4.6 Quantitative Analysis of Network Structures

An important aspect not considered in the original 1998 paper was how to quantify the networks the HDC model produces and how sensitive these networks would be to parameter changes. Using the HDC model, it is possible to calculate the following quantities from our simulations: vascular length, surface area of network, volume of network, number of vessels in network; "fractal" dimension; EC migration rate; EC proliferation rate. Moreover, we can examine the sensitivity of the model/assay to variations in the parameters, e.g. chemotaxis and haptotaxis coefficients. The following figures show calculations of some of these quantities as well as the effect of varying specific parameters. The data for these figures were easily obtained from running multiple implementations of the HDC model with various parameter sets. This is far quicker, easier, cheaper and more humane than doing the equivalent experimental implementation.

Anderson and Chaplain (1998) estimated a majority of the parameter values from experimental data, this gives us the following base or control parameter set: $\gamma = 0.05, \beta = 0.1, \eta = 0.1, \chi = 0.3, \rho = 0.3$, domain size 2 mm $\times$ 2 mm, proliferation rate 18 h and cell size 10μ m. In the following simulations we investigate the effect of varying the parameters on quantitative measures of the vascular structure. In particular we shall focus on the average number of vessels vs. time as our main quantitative measure and calculate the average over ten simulations. We define the number of vessels to be the total number of individual branches within the network at a given time, e.g. in Fig. 5.3 there are four initial vessels (excluding the parent vessel). Other quantitative measurements such as vessel length distribution and growth rate of the network are also considered.

Figure 5.5 shows the average number of vessels vs. time for our base case model (shown in black) and how this changes by increasing each individual parameter as follows, with all other parameters as in the base case, $\gamma = 0.5$ (dark blue), $\beta = 1$ (red), $\chi = 0.6$ (green) and $\rho = 0.6$ (light blue). Variations in η (results not shown) had little or no effect on network structure (as measured by any quantitative analysis). We also performed a range of other more systematic simulations (results not shown) examining the sensitivity of the network structure to changes in the kinetic parameters (γ, β) and found little difference in comparison to the base case. Clearly from Fig. 5.5, χ is the most sensitive parameter, as little variation from the base case is seen with the other parameters. Therefore, we shall examine further the effects of varying the chemotaxis parameter, χ, in more detail.

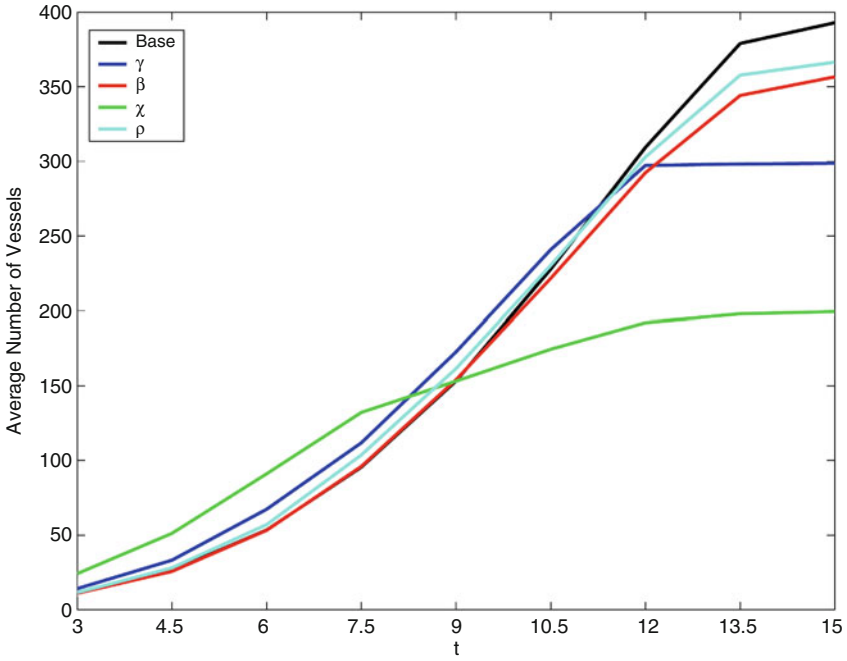

Fig. 5.5 Calculated average total number of vessels in the capillary networks generated with varying model parameters for times $t = 1 - 15$. The base case is calculated from the upper panels of Fig. 5.3 (*black*) and compared with results from varying the model parameters, $\gamma = 0.5$ (*dark blue*), $\beta = 1$ (*red*), $\chi = 0.6$ (*green*) and $\rho = 0.6$ (*light blue*)

Figure 5.6 (upper panel) shows the results of varying χ from 0.1 to 0.6 with all other parameters as in the base case for a range of time. Initially, the curves follow an intuitive distribution, i.e. the higher values of χ produce more vessels. However, as time evolves there is a switch in the behaviour, i.e. the highest value of χ produces the least number of vessels. This can be explained by the fact that as we increase χ the time taken to reach the tumour implant decreases and, therefore, the time available to form the network (i.e. branching and anastomosis) decreases. This implies an optimal speed of growth for the formation of a fully connected network, i.e. an optimal value of χ. Figure 5.6 (lower panel) shows the distribution of the average number of vessels at $t = 12$ for the same range of values of $\chi = 0.1$–0.6. This indicates that a value of $\chi = 0.3$ produces the maximum number of vessels at this time for this given set of parameters. Later times give a similar distribution.

Figure 5.7 shows the results of varying the two taxis parameters and how this affects the speed of network growth. This is defined in relation to the time taken for the first vessel to reach the tumour (located at the right hand boundary of the 2 mm

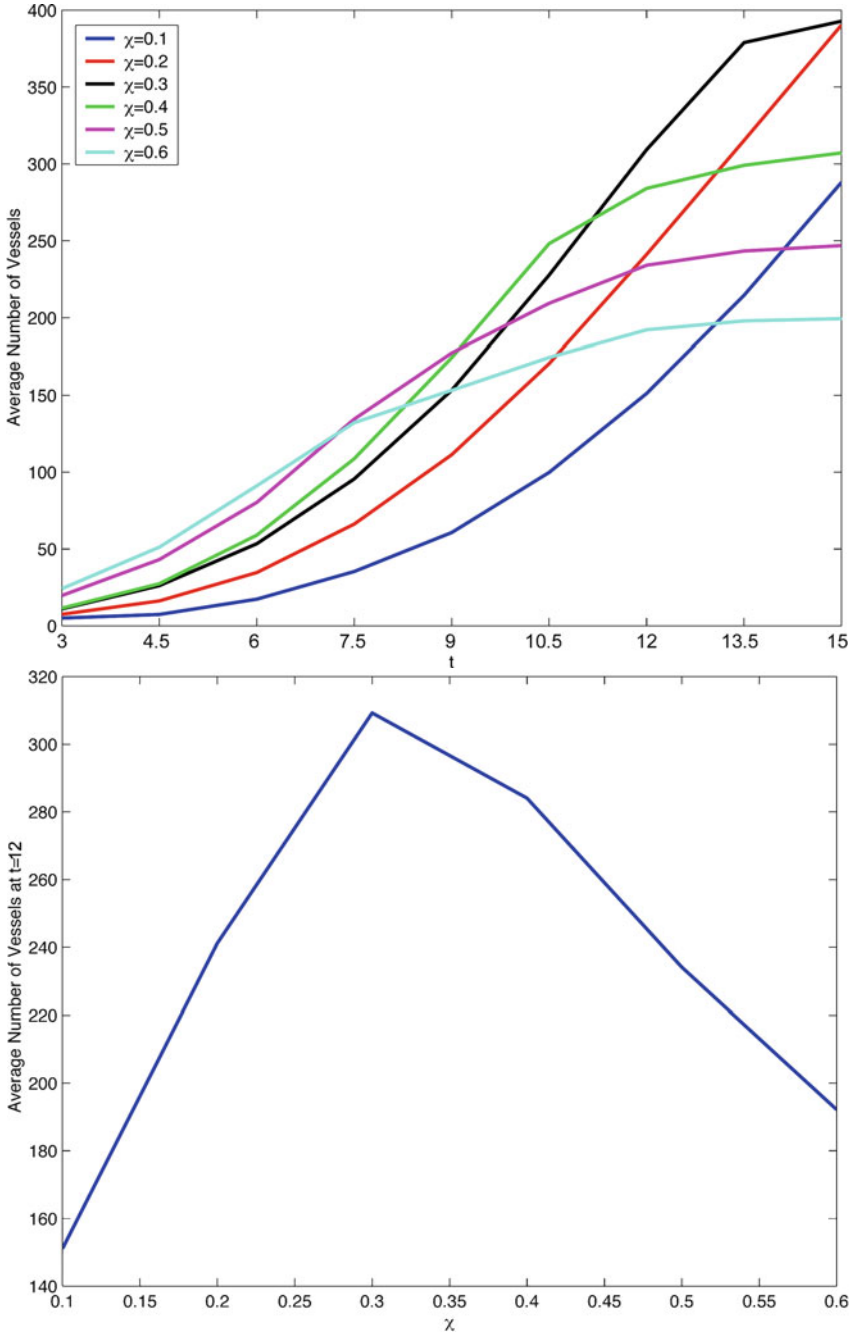

Fig. 5.6 Calculated average total number of vessels in capillary networks generated with different chemotactic parameters ($\chi = 0.1 - 06$). *Upper panel*: Shows how the average changes over time, $t = 1 - 15$. *Lower panel*: Shows how the average changes for a fixed time, $t = 12$

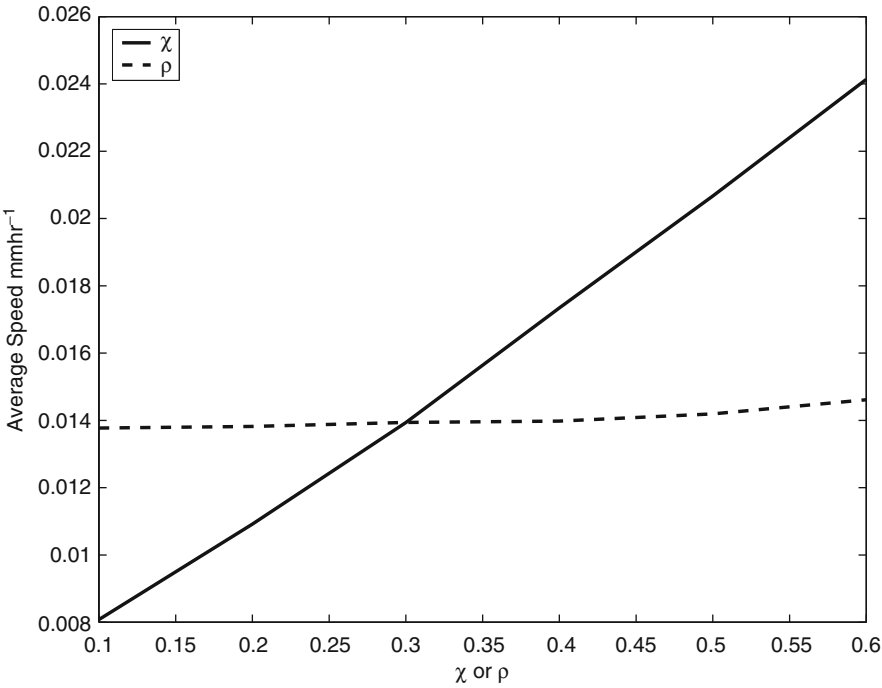

Fig. 5.7 Calculated average migration speed as function of changing the chemotaxis parameter ($\chi = 0.1 - 0.6$, *solid line*) and haptotaxis parameter ($\rho = 0.1 - 0.6$, *dashed line*) independently. All other parameters are the same as the base set

domain). As can be seen, the rate of EC migration is linearly proportional to the chemotaxis and haptotaxis coefficients, however, the effect of increasing χ is much greater than that of increasing ρ.

Figure 5.8 shows the frequency distribution of individual capillary sprout lengths at time $t = 15$ days calculated from the theoretical networks of Fig. 5.3. This is measured by the distance between branch points, calculated from the number of individual EC that make up each capillary branch (because our spatial length scale gives one grid point to equal one EC length, $10\mu m$, the number of spatial grid points is equivalent to the number of EC) . The results here show a skewed distribution with a greater proportion of smaller (shorter) vessels in the network than larger (longer) vessels. We note that there is a greater number of longer sprouts for the large tumour than for the smaller circular tumour. These results are in good qualitative agreement with similar measurements made in actual experiments (Norrby 1998; Moore et al. 1998).

In addition to vessel area and number, using standard techniques (e.g. box-counting, Falconer, 1990), it is straightforward to calculate a fractal dimension for our networks (Kirchner et al. 1996; Parsons-Wingerter et al. 1998). We have calculated the fractal dimension of a number of two and three dimensional networks

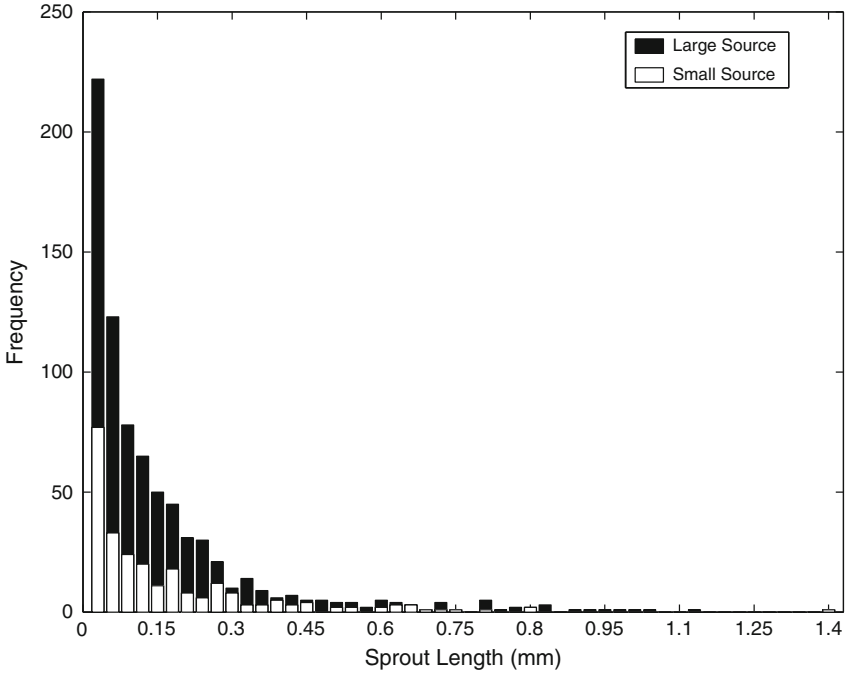

Fig. 5.8 Calculated frequency distribution of the individual capillary sprout lengths in each of the two final networks in Fig. 5.3 (*upper panel – black histogram and lower panel – white histogram*) at time $t = 15$ days. Large AF source is given by the boundary condition, (5.9) and the small circular AF source is given by (5.7)

generated by our model, and this ranges from 1.4−1.8 (two-dimensional case) 2.2−2.6 (three-dimensional case) depending upon the specific time of measurement and the underlying AF concentration profile (e.g. earlier times, smaller tumours, fewer initial sprouts have a lower fractal dimension).

Finally, other data such as canalization rate, blood flow rate and vascular permeability could in principle be obtained from a slightly more developed model.

5 Discussion and Conclusions

The HDC model of tumour angiogenesis is a novel blend of continuum, deterministic modeling and discrete, stochastic modeling in both two and three space dimensions. The results it produces not only replicate existing experimental protocols (animal cornea models) but also provide an new alternative, non-invasive, predictive three-dimensional "assay". The model results are in good qualitative agreement with experimental data where parameter values for the model (in particular the length scale L, the cell random motility coefficient D_n, the TAF

diffusion constant D_e, the chemotactic coefficient χ_0 and the endothelial cell proliferation rate) have been estimated, as far as possible, from independent experimental measurements, thus grounding the results in a realistic framework. In addition to quantitative estimates relating to cell migration and network expansion, we can also provide quantitative data relating to the actual network structure itself.

Although the model has incorporated several key mechanisms involved in the angiogenic process, extensions of the model are of course possible. For example, one might consider explicitly modeling more than one angiogenic factor (it is known that some factors induce a mitogenic response while others induce a migratory response). The effect of angiogenic inhibitors may also be considered, as well as more than one matrix macromolecule (e.g. laminin, collagen). However, we believe that these possible extensions are unlikely to provide much more information than is already present (rather they may be considered as "fine tuning"). Perhaps a more fruitful direction for the modeling to take is to turn attention to the events occurring at the molecular level. For example, several angiogenic factors, e.g. vascular endothelial growth factor (VEGF), acidic and basic fibroblast growth factor (aFGF, bFGF), angiogenin and others, have been isolated (Folkman 1985; Folkman and Klagsbrun 1987) and endothelial cell receptors for these proteins have been discovered (Hanahan 1997). Indeed, there is now clear experimental evidence that disrupting these receptors has a direct effect on the final structure of the capillary network (Hanahan 1997).

Other important aspects of angiogenesis which can and have been added to the model (as can be seen in subsequent chapters) include incorporating blood flow through the capillary network, with direct application to drug delivery and optimisation of chemotherapy regimes; the role of oxygen gradients and oxygen concentration and the role of macrophages and pericytes (McDougall et al. 2002; Stephanou et al. 2005a,b; McDougall et al. 2006; Chaplain et al. 2006; Macklin et al. 2009). These aspects are also very important for angiogenesis in wound healing.

Notwithstanding these additions, the model already gives more than an glimpse of the potential of a mathematical model of angiogenesis. Indeed a paper by Jain and co-workers (Jain et al. 1997) discusses the merits and demerits of various angiogenesis assays currently in use both in vivo and in vitro, e.g. chronic transparent chambers; exteriorised tissue preparations; in situ preparations; vascularisation into matrix implants; excised tissues; Boyden chamber migration assays; collagen gel assays and proliferation assays. In deciding how effective, efficient and accurate a particular angiogenesis assay is, Jain et al. (1997) identified nine criteria for comparison with an "ideal assay". Specifically, an ideal assay should: (1) provide a knowledge of the release rate and spatio-temporal concentration distribution of angiogenic factors and inhibitors; (2) make use of genetically well-defined neoplastic cells; (3) provide quantitative measurement of the structure of the new vasculature (vascular length, surface area, volume, vessel number, fractal dimension, extent of basement membrane, etc.); (4) provide quantitative measurement of the function of the vasculature (i.e. endothelial cell migration rate, proliferation rate, canalisation rate, blood flow rate and vascular permeability); (5) be able to distinguish between

newly formed and pre-existing vasculature/vessels; (6) avoid tissue damage; (7) be able to confirm any in vitro response in vivo; (8) ensure the provision of long-term and non-invasive monitoring; (9) be cost-effective, rapid, easy-to-use, reproducible and reliable.

Comparing our HDC angiogenesis model against this list of criteria we find that vessel quantification is highly accurate and easy to do, there is no invasive procedure and no difficulty in "setting up the experiment", there is very little preparation time, and it costs almost nothing as all work is done in silico. Experimental replication is easy, as is changing the experimental design, e.g. the tumour size and geometry, the amount of angiogenic factor and/or matrix macromolecules in the system. The mathematical model we have presented and developed also enables one to carry out a quantitative analysis of vascular structures and provides both quantitative structural data (such as vascular length, network surface area, network volume, number of vessels in network, "fractal" dimension) and also quantitative functional data (such as endothelial cell migration rate and proliferation rate). This naive comparison highlights just how well our model compares with real angiogenesis assays but we are aware of the over simplifying assumptions it is based upon and the limitations they impose.

Finally, it is worth noting that mathematical modeling of angiogenesis now stretches back decades and as new mathematical and computational tools and techniques have developed so has the complexity and predictive power of the models. However, one must be acutely aware of the trade-off between complexity and understanding. A major advantage of the HDC model of angiogensis is that it utilized a minimal set of variables (EC, AF, MM), parameters, and cell-based processes to generate complex branched networks. This minimal modeling approach does oversimplify but crucially it allows us to understand the key drivers of the outcomes it can produce and therefore naturally leads to experimentally testable hypotheses.

References

Alarcon, T., Byrne, H. M., Maini, P. K. (2005). A multiple scale model for tumor growth. *Multiscale Model Simul.* **3**, 440–475.

Alarcon T, Owen MR, Byrne HM, Maini PK (2006) Multiscale modeling of tumour growth and therapy: the influence of vessel normalisation on chemotherapy. Comput Math Method M 7: 85119.

Albini A, Allavena G, Melchiori A, Giancotti F, Richter H, Comoglio PM, Parodi S, Martin GR, Tarone G. Chemotaxis of 3T3 and SV3T3 cells to fibronectin is mediated through the cell-attachment site in fibronectin and fibronectin cell surface receptor. *J. Cell Biol.* 1987; **105:** 1867–1872.

Anderson, A. R. A., Sleeman, B.D., Young, I.M. & Griffiths, B.S. (1997) Nematode movement along a chemical gradient in a structurally heterogeneous environment: II. Theory. *Fundam. appl. Nematol.*, **20**, 165–172.

Anderson ARA, Chaplain MAJ. Continuous and discrete mathematical models of tumor-induced angiogenesis. *Bull. Math. Biol.* 1998; **60:** 857–899.

Anderson ARA, Chaplain MAJ. A mathematical model for capillary network formation in the absence of endothelial cell proliferation. *Appl. Math. Letters* 1997; **11:** 109–114.

Anderson ARA, Chaplain MAJ, Garcia-Reimbert C, Vargas CA. A Gradient-Driven Mathematical Model of Anti-Angiogenesis. *Math. Comp. Mod.* 2000; **32:** 1141–1152.

Anderson, A. R. A., Chaplain, M. A. J., Newman, E. L., Steele, R. J. C. & Thompson, A. M. (2000) Mathematical Modeling of Tumour Invasion and Metastasis. *J. Theoret. Med.*, **2**, 129–154.

Anderson, A. R. A. A Hybrid Discrete-Continuum Technique for Individual Based Migration Models in *Polymer and Cell Dynamics*, eds. W. Alt, M. Chaplain, M. Griebel, J. Lenz, 2003, Birkhauser.

Anderson, A. R. A. & Pitcairn, A. Application of the Hybrid Discrete-Continuum Technique in *Polymer and Cell Dynamics*, eds. W. Alt, M. Chaplain, M. Griebel, J. Lenz, 2003, Birkhauser.

Anderson, A. R. A. (2005) A hybrid mathematical model of solid tumour invasion: The importance of cell adhesion. *IMA J. Math. Med. and Biol.*, **22**, 163–186.

Anderson, A. R. A, Weaver A.M., Cummings P.T. & Quaranta V. (2006) Tumor Morphology and Phenotypic Evolution Driven by Selective Pressure from the Microenvironment. *Cell*, **127**, 111.

Arnold F, West DC. Angiogenesis in wound healing. *Pharmac. Ther.* 1991; **52:** 407–422.

Ausprunk DH, Folkman J. Migration and proliferation of endothelial cells in preformed and newly formed blood vessels during tumour angiogenesis. *Microvasc. Res.* 1977; **14:** 53–65.

Bowersox JC, Sorgente N. Chemotaxis of aortic endothelial cells in response to fibronectin. *Cancer Res.* 1982; **42:** 2547–2551.

Balding D, McElwain DLS. A mathematical model of tumour-induced capillary growth. *J. theor. Biol.* 1985 **114:** 53–73.

Basanta D, Strand DW, Lukner RB, Franco OE, Cliffel DE, Ayala GE, Hayward SW, Anderson AR. The role of transforming growth factor-beta-mediated tumor-stroma interactions in prostate cancer progression: an integrative approach. Cancer Res. 2009 Sep 1;69(17):7111–20.

Bauer AL, Jackson TL, Jiang Y. A cell-based model exhibiting branching and anastomosis during tumor-induced angiogenesis. Biophys J. 2007 May 1;92(9):3105–21. Epub 2007 Feb 2.

Bentley, K., Mariggi, G., Gerhardt, H. and Bates, P. A. (2009) Tipping the balance: Robustness of Tip Cell Selection, Migration and Fusion in Angiogenesis. PLoS Computational Biology 5(10): e1000549.

Bowersox JC, Sorgente N. Chemotaxis of aortic endothelial cells in response to fibronectin. *Cancer Res.* 1982; **42:** 2547–2551.

Bray D: Cell Movements. Garland Publishing, New York, 1992

Byrne HM, Chaplain MAJ. Mathematical models for tumour angiogenesis: numerical simulations and nonlinear wave solutions. *Bull. Math. Biol.* 1995 **57:** 461–486.

Carmeliet P, Jain RK. Angiogenesis in cancer and other diseases. Nature. 2000 Sep 14;407(6801):249–57.

Carter SB. Principles of cell motility: The direction of cell movement and cancer invasion. *Nature* 1965; **208:** 1183–1187.

Carter SB. Haptotaxis and the mechanism of cell motility. *Nature* 1967; **213:** 256–260.

Chaplain MAJ, Stuart AM. A model mechanism for the chemotactic response of endothelial cells to tumour angiogenesis factor. *IMA J. Math. Appl. Med. Biol.* 1993 **10:** 149–168.

Chaplain MAJ. The mathematical modeling of tumour angiogenesis and invasion. *Acta Biotheor.* 1995; **43:** 387–402.

Chaplain MAJ. Avascular growth, angiogenesis and vascular growth in solid tumours: the mathematical modeling of the stages of tumour development. *Math. Comput. Modeling* 1996; **23:** 47–87.

Chaplain MAJ, Anderson ARA. The mathematical modeling, simulation and prediction of tumour-induced angiogenesis. *Invas. Metast.* 1997; **16:** 222–234.

Chaplain MAJ, Orme ME: Mathematical modeling of tumor-induced angiogenesis. In: Little CD, Mironov V, Sage EH (eds) Vascular morphogenesis: In vivo, in vitro, in mente. Birkhäuser, Boston, 1998, pp 205–240.

Chaplain MA, McDougall SR, Anderson AR. Mathematical modeling of tumor-induced angiogenesis. Annu Rev Biomed Eng. 2006;8:233–57.

Folkman J (1971) Tumour angiogenesis therapeutic implications. New Engl J Med 285: 11821186.
Folkman J: Tumor angiogenesis. *Adv. Cancer Res.* 1985; **43:** 175–203.
Folkman J, Klagsbrun M. Angiogenic factors. *Science* 1987; **235:** 442–447.
Folkman J, Brem H: Angiogenesis and inflammation. In: Inflammation: Basic Principles and Clinical Correlates Second Edition. (eds. JI Gallin, IM Goldstein and R Snyderman). New York:Raven Press, 1992
Folkman J: Angiogenesis in cancer, vascular, rheumatoid and other disease. *Nature Medicine* 1995; **1:** 21–31.
Frieboes HB, Lowengrub JS, Wise S, Zheng X, Macklin P, et al. (2007) Computer simulation of glioma growth and morphology. Neuroimage 37(S1): 5970.
Gerlee P, Anderson AR. An evolutionary hybrid cellular automaton model of solid tumour growth. J Theor Biol. 2007 Jun 21;246(4):583–603. Epub 2007 Feb 12.
Gerlee P, Anderson AR. A hybrid cellular automaton model of clonal evolution in cancer: the emergence of the glycolytic phenotype. J Theor Biol. 2008 Feb 21;250(4):705–22.
Gerlee P, Anderson AR. Evolution of cell motility in an individual-based model of tumour growth. J Theor Biol. 2009 Jul 7;259(1):67–83.
Gimbrone MA, Cotran RS, Leapman SB, Folkman J. Tumor growth and neovascularization: An experimental model using the rabbit cornea. *J. Natn. Cancer Inst.* 1974; **52:** 413–427.
Graham CH, Lala PK. Mechanisms of placental invasion of the uterus and their control. *Biochem. Cell Biol.* 1992; **70:** 867–874.
Hanahan D. Signaling vascular morphogenesis and maintenance. *Science* 1997; **227:** 48–50.
Hanahan D, Weinberg RA. The hallmarks of cancer. Cell. 2000 Jan 7;100(1):57–70.
Hynes RO: Fibronectins. New York. Springer-Verlag, 1990
Holmes MJ, Sleeman BD. A mathematical model of tumour angiogenesis incorporating cellular traction and viscoelastic effects *J. Theor. Biol.* 2000; **202:** 95–112.
Jain RK, Schlenger K, Höckel M, Yuan F: Quantitative angiogenesis assays: Progress and problems. Nature Med. 1997; **3:** 1203–1208.
Kerbel RS. Tumor angiogenesis: past, present and the near future. Carcinogenesis. 2000 Mar;21(3):505–15.
Kiani M, Hudetz A. Computer simulation of growth of anastomosing microvascular networks. *J. theor. Biol.* 1991; **150:** 547–560.
Kirchner LM, Schmidt SP, Gruber BS. 1996. Quantitation of angiogenesis in the chick chorioallantoic membrane model using fractal analysis. Microvasc. Res. 51:2–14.
Klagsbrun M, Soker S. VEGF/VPF: the angiogenesis factor found? Curr Biol. 1993 Oct 1;3(10):699–702.
Lacovara J, Cramer EB, Quigley JP. Fibronectin enhancement of directed migration of B16 melanoma cells. *Cancer Res.* 1984; **44:** 1657–1663.
Landini G, Misson G. Simulation of corneal neo-vascularization by inverted diffusion limited aggregation. *Invest. Opthamol. Visual Sci.* 1993; **34:** 1872–1875.
Levine HA, Sleeman BD, Nilsen-Hamilto M. Mathematical modeling of the onset of a capillary formation initiating angiogenesis. *J. Math. Biol.* 2001;**42:**195–238.
Macklin P, McDougall S, Anderson AR, Chaplain MAJ, Cristini V, et al. (2009) Multiscale modeling and nonlinear simulation of vascular tumour growth. J Math Biol 58: 765798.
Madri JA, Pratt BM. Endothelial cell-matrix interactions: in vitro models of angiogenesis. *J. Histochem. Cytochem.* 1986; **34:** 85–91.
Mannoussaki D, Lubkin SL, Vernon RB, Murray JD. A mechanical model for the formation of vascular networks in vitro. *Acta Biotheor.* 1996; **44:** 271–282.
Mantzaris N, Webb SD, Othmer HG (2004) Mathematical modeling of tumour angiogenesis: A review. J Math Biol 49: 111187.
McCarthy JB, Furcht LT. Laminin and fibronectin promote the directed migration of B16 melanoma cells in vitro. *J. Cell Biol.* 1984; **98:** 1474–1480.
McDougall SR, Anderson ARA, Chaplain MAJ, and Sherratt JA (2002) Mathematical modeling of flow through vascular networks: implications for tumour-induced angiogenesis and chemotherapy strategies. Bull. Math. Biol. 64(4), 673–702.

McDougall SR, Anderson ARA, Chaplain MAJ (2006) Mathematical modeling of dynamic adaptive tumour-induced angiogenesis: Clinical implications and therapeutic targeting strategies. J Theor Biol 241: 56489.

Merks RMH and Glazier JA. 2006. Dynamic mechanisms of blood vessel growth. Nonlinearity, 19, C1–C10.

Merks RMH, Erica D. Perryn, Abbas Shirinifard and James A. Glazier. 2008. Contact-inhibited chemotactic motility in de novo and sprouting blood vessel growth. PLoS Computational Biology 4(9): e1000163, 2008.

Mitchell, A. R. and D. F. Griffiths (1980). *The Finite Difference Method in Partial Differential Equations*, Chichester: Wiley.

Moore A, Marecos E, Simonova M, *et al.* Novel gliosarcoma cell line expressing green fluorescent protein: A model for quantitative assessment of angiogenesis. *Microvasc. Res.* 1998; **56:** 145–153.

Murray JD, Mannoussaki D, Lubkin SL, Vernon RB: A mechanical theory of in vitro vascular network formation. In: Little CD, Mironov V, Sage EH (eds) Vascular morphogenesis: In vivo, in vitro, in mente. Birkhäuser, Boston, 1998, pp 173–188

Murray JD, Swanson KR: On the mechanochemical theory of biological pattern formation with applications to wound healing and angiogenesis. In: Chaplain MAJ, Singh GD, McLachlan JC (eds) On Growth and Form: Spatio-temporal Pattern Formation in Biology. Wiley, Chichester, 1999, pp 251–285

Muthukkaruppan VR, Kubai L, Auerbach R: Tumor-induced neovascularization in the mouse eye. J. Natn. Cancer Inst. 69: 699–705, 1982

Nekka F, Kyriacos S, Kerrigan C, Cartilier L. A model of growing vascular structures. *Bull. Math. Biol.* 1996; **58:** 409–424.

Norrby K. Microvascular density in terms of number and length of microvessel segments per unit tissue volume in mammalian angiogenesis. *Microvasc. Res.* 1998; **55:** 43–53.

Olsen L, Sherratt JA, Maini PK, Arnold, F. A mathematical model for the capillary endothelial cell-extracellular matrix interactions in wound-healing angiogenesis. *IMA J. Math. Appl. Med. Biol.* 1997; **14:** 261–281.

O'Reilly MS, Holmgren L, Shing Y, Chen C, Rosenthal RA, Moses M, Lane WS, Cao Y, Sage EH, Folkman J. Angiostatin: a novel angiogenesis inhibitor that mediates the suppression of metastases by a Lewis lung carcinoma. *Cell* 1994; **79:** 315–328.

O'Reilly MS, Holmgren L, Chen C, Folkman J. Angiostatin induces and sustains dormancy of human primary tumours in mice. *Nature Med.* 1996; **2:** 689–692.

O'Reilly MS, Boehm T, Shing Y, Fukai N, Vasios G, Lane WS, Flynn E, Birkhead JR, Olsen BR, Folkman J. Endostatin: an endogenous inhibitor of angiogenesis and tumor growth. Cell. 1997 Jan 24;88(2):277–85.

Orme ME, Chaplain MAJ. A Mathematical model of the First Steps of Tumour-Related Angiogenesis: Capillary Sprout Formation and Secondary Branching. *IMA J. Math. App. Med. Biol.* 1996; **13:** 73–98.

Orme ME, Chaplain MAJ. Two-dimensional models of tumour angiogenesis and anti-angiogenesis strategies. *IMA J. Math. App. Med. and Biol.* 1997; **14:** 189–205.

Owen MR, Alarcn T, Maini PK, Byrne HM (2009) Angiogenesis and vascular remodelling in normal and cancerous tissues. J Math Biol 58: 689721.

Paku S, Paweletz N. First steps of tumor-related angiogenesis. *Lab. Invest.* 1991; **65:** 334–346.

Parsons-Wingerter P, Lwai B, Yang MC, Elliott KE, Milaninia A, Redlitz A, Clark JI, Sage EH. 1998. A novel assay of angiogenesis in the quail chorioallantoic membrane: stimulation by bFGF and inhibition by angiostatin according to fractal dimension and grid intersection. Microvasc. Res. 55:201–214.

Paweletz N, Knierim M. Tumor-related angiogenesis. *Crit. Rev. Oncol. Hematol.* 1989; **9:** 197–242.

Perfahl H, Byrne HM, Chen T, Estrella V, Alarcn T, et al. 2011 Multiscale Modeling of Vascular Tumour Growth in 3D: The Roles of Domain Size and Boundary Conditions. PLoS ONE 6(4): e14790.

Plank, M. J. and Sleeman, B. D. (2003). Tumour-induced angiogenesis: a review. J. Theor. Med. 5, 137–153.

Plank, M. J. and Sleeman, B. D. (2003). A reinforced random walk model of tumour angiogenesis and anti-angiogenic strategies. Math. Med. Biol. 20, 135–181.

Plank, M. J. and Sleeman, B. D. (2004). Lattice and non-lattice models of tumour angiogenesis. Bull. Math. Biol. 66, 1785–1819.

Quigley JP, Lacovara J, Cramer EB. The directed migration of B-16 melanoma-cells in response to a haptotactic chemotactic gradient of fibronectin. *J. Cell Biol.* 1983; **97:** A450–451.

Qutub AA, F. Mac Gabhann, E.D. Karagiannis; P. Vempati, A.S. Popel, Multiscale models of angiogenesis. Engineering in Medicine and Biology Magazine, IEEE, 28(2):14–31 2009

Rupnick MA, Stokes CL, Williams SK, Lauffenburger, DA. Quantitative analysis of human microvessel endothelial cells using a linear under-agarose assay. *Lab. Invest.* 1988; **59:** 363–372.

Schor SL, Schor AM, Brazill GW. The effects of fibronectin on the migration of human foreskin fibroblasts and syrian hamster melanoma cells into three-dimensional gels of lattice collagen fibres. *J. Cell Sci.* 1981; **48:** 301–314.

Shing Y, Folkman J, Sullivan R, Butterfield C, Murray J, Klagsbrun M. Heparin affinity: purification of a tumor-derived capillary endothelial cell growth factor. Science. 1984 Mar 23;223(4642):1296–9.

Sholley MM, Ferguson GP, Seibel HR, Montour JL, Wilson JD. Mechanisms of neovascularization. Vascular sprouting can occur without proliferation of endothelial cells. *Lab. Invest.* 1984; **51:** 624–634.

Stephanou A, McDougall SR, Anderson ARA, Chaplain MAJ (2005a) Mathematical modeling of flow in 2d and 3d vascular networks: Applications to anti-angiogenic and chemotherapeutic drug strategies. Math Comp Modeling 41: 1137–1156.

Stephanou A, McDougall SR, Anderson ARA, Chaplain (2005b) Mathematical modeling of the influence of blood rheological properties upon adaptive tumour- induced angiogenesis. Math. Comp. Model. 44, 96–123.

Stokes CL, Lauffenburger DA, Williams SK. Migration of individual microvessel endothelial cells: stochastic model and parameter measurement. *J. Cell Sci.* 1991; **99:** 419–430.

Stokes CL, Lauffenburger DA. Analysis of the roles of microvessel endothelial cell random motility and chemotaxis in angiogenesis. *J. theor. Biol.* 1991; **152:** 377–403.

Terranova VP, Diflorio R, Lyall RM, Hic S, Friesel R, Maciag T. Human endothelial cells are chemotactic to endothelial cell growth factor and heparin. *J. Cell Biol.* 1985; **101:** 2330–2334.

Thompson DW. On Growth and Form, Cambridge University Press, Cambridge, 1917

Williams SK: Isolation and culture of microvessel and large-vessel endothelial cells; their use in transport and clinical studies. In: McDonagh P (ed) Microvascular Perfusion and Transport in Health and Disease. Karger, Basel, pp 204–245, 1987

Zawicki DF, Jain RK, Schmid-Schoenbein GW, Chien S. Dynamics of neovascularization in normal tissue. *Microvasc. Res.* 1981; **21:** 27–47.

Zhai Y, Ni J, Jiang GW, Lu J, Xing L, Lincoln C, Carter KC, Janat F, Kozak D, Xu S, Rojas L, Aggarwal BB, Ruben S, Li LY, Gentz R, Yu GL. VEGI, a novel cytokine of the tumor necrosis factor family, is an angiogenesis inhibitor that suppresses the growth of colon carcinomas in vivo. FASEB J. 1999 Jan;13(1):181–9.

Zheng X, Wise SM, Cristini V (2005) Nonlinear simulation of tumor necrosis, neo-vascularization and tissue invasion via an adaptive finite-element/level set method. Bull Math Biol 67(2): 211–259.

Chapter 6
Cell-Based Models of Tumor Angiogenesis

Yi Jiang, Amy L. Bauer, and Trachette L. Jackson

1 Introduction

Angiogenesis, the growth of new blood vessels from existing ones, is an important step in tumor development. Tumor cells in hypoxic microenvironments upregulate their production and secretion of angiogenic factors, the key players of which include the vascular endothelial growth factor family (VEGFs). The formation of vascular networks is a finely tuned and complex process controlled by the signaling balance among integrins, angiopoietins, chemokines, adhesion molecules, oxygen sensors, endogenous inhibitors and many others (Carmeliet 2003). A detailed description of the molecular mechanisms of angiogenesis has been offered in several excellent review articles (Folkman and D'Amore 1996; Carmeliet 2000; Carmeliet and Jain 2000; Adams and Alitalo 2007).

At the onset of angiogenesis, endothelial cells activated by angiogenic factors are stimulated to proliferate, suppress cell death, and produce a number of proteolytic enzymes that degrade specific ECM proteins including the basement membrane of the blood vessel (Iruela-Arispe et al. 1991; Iruela-Arispe et al. 1991). After basement membrane degradation, endothelial cells migrate into the extracellular matrix (ECM) of the stroma in response to chemical gradients of VEGF and other angiogenic factors. The ECM plays a central role in cellular migration, cell shape,

Y. Jiang (✉)
Theoretical Division, MS B284, Los Alamos National Laboratory, Los Alamos, NM 87545, USA
e-mail: jiang@lanl.gov; yijianglanl@gmail.com

A.L. Bauer
Los Alamos National Laboratory, Theoretical Biology and Biophysics Group,
Theoretical Division, Mail Stop T-082, Los Alamos, NM 87545, USA
e-mail: albauer@lanl.gov

T.L. Jackson
Department of Mathematics, University of Michigan, Ann Arbor, MI 48109, USA
e-mail: tjacks@umich.edu

T.L. Jackson (ed.), *Modeling Tumor Vasculature: Molecular, Cellular, and Tissue Level Aspects and Implications*, DOI 10.1007/978-1-4614-0052-3_6,

and orientation (Huang and Ingber 1999). To reach the tumor, endothelial cells must navigate the stroma. Activated endothelial cells also upregulate integrins, which regulate cellular adhesion to matrix molecules (Senger et al. 1997), as well as vascular cadherins, which regulate adhesion between endothelial cells.

In addition to cell-ECM attachment, cellular adhesion to other cells plays a crucial role in the formation and stabilization of nascent blood vessels (Wallez and Huber 2008). Formation of cell–cell adhesion junctions via VE-cadherin inhibits the chemotactic response of endothelial cells to VEGF-A at the cell-contact boundaries, also termed contact-inhibited chemotaxis, and increases the stability of those boundaries (Perryn et al. 2008). Moreover, the growth rate of cultured endothelial cells decreases as the area of VE-cadherin junctions increases, also termed contact-inhibited growth (Lampugnani et al. 2003).

1.1 Mathematical Models of Angiogenesis

Mathematical models of angiogenesis date from the 1970s, and their numbers continue to grow rapidly. From continuous PDEs to cell-based models to sophisticated multiscale models, each has brought new insight to understanding the mechanisms underlying the angiogenesis process. The goal of this chapter is to provide a brief overview of cell-based models of angiogenesis.

Cell-based models start from phenomenological representations of individual cells, and simulate how the collective behavior of multiple simplified cells drives tissue-level processes. In contrast to continuous modeling approaches, which are described in other chapters, cell-based models offer several unique advantages. First, the cell provides "a natural level of abstraction for mathematical and computational modeling" (Merks and Glazier 2005). Describing cells as individual entities that follow certain behavioral rules is not only mathematically and computationally desirable but also makes biological sense. Under most circumstances, cells act like functional units with input/output relationships between the environmental signals and a finite list of cell behavioral changes. Although continuum models are computationally efficient for describing noncellular materials like diffusing chemicals, they are limited when the tissue level properties depend on the dynamics at the cellular level. At the same time, many cell-based models reproduce experimental observations missing from continuum models. For example, Merks et al. (2006) showed with their cell-based model that cell elongation is essential for vasculogenesis and remodeling, and that chemotaxis parameters assumed by previous continuous models (Ambrosi et al. 2004) could not produce stable vasculature.

Cell-based models have been called by many names, including cellular automata models (Anderson and Chaplain 1998; Peirce et al. 2004; Gatenby et al. 2005; Anderson et al. 2006), agent-based models (Drasdo and Hohme 2003; Rejniak 2007; Zhang et al. 2007; Yin et al. 2008; Macklin et al. 2009; Qutub and Popel 2009; Jackson and Zheng 2010), and several variations of cellular Potts models (Turner and Sherratt 2002; Jiang et al. 2005; Merks and Glazier 2005; Merks et al. 2006;

Merks and Glazier 2006; Bauer et al. 2007; Szabo et al. 2008; Bauer et al. 2009; Merks and Koolwijk 2009). Cellular automata models describe cells as point-like objects that live on a lattice and follow a set of rules. In agent-based models, cells may have extended bodies and follow equations of motion in addition to rules, but do not necessarily live on a lattice. Many of these models are hybrid models; they couple the advantages of discrete cell representation to continuous reaction–diffusion models that better represent environmental variables, such as growth factors.

2 Building a Cell-Based Model

In this chapter, we introduce a general three-step procedure for building a cell-based model in the context of tumor angiogenesis. A similar description has been published in the nice overview paper by Merks and Glazier (2005). We offer a more detailed introduction emphasizing model validation and using angiogenesis as an example.

2.1 Assemble a Cell Behavior List

Step 1 is to assemble a cell behavior list. We start from experimental data and prioritize a list of "important and relevant" individual cell behaviors that we need to consider in the model. Table 6.1 provides a short list of examples for cellular behavior/properties and typical experimental means to obtain the corresponding parameters. Most of these data are available in the literature, albeit often from very different experimental settings. Care should be taken to distinguish the usefulness of such parameters. Some measures, e.g., endothelial cell proliferation rate, differ drastically depending on the experimental setup; while other measures, e.g., cell size, vary within a narrow range independent of the experimental design. In some cases, to inform parameter choices, additional experiments may be needed to obtain more quantitative data on cell behavior.

2.2 Develop a Computational Model

Step 2 is to develop a computational model of cell behaviors. Once we identify the cell behaviors, we can describe them in a conceptual model, which we then translate into a mathematical model and implement computationally. A cell-based computational description represents individual cells phenomenologically, which does not itself offer explanation or insight beyond a description of empirical observations. The value of such a model lies in tissue level simulations, where many individual cells interact with each other and with their environment, and give

Table 6.1 Sample list of cell properties for a cell-based model and typical experimental techniques to obtain the parameters

Cell property	Experimental method
Proliferation rate	Cell staining and flow cytomety
Cell cycle duration (arrest)	Cell number count in time, cell cycle fraction
Death rate (apoptosis, autophagic, necrosis)	TUNEL, biomarkers
Cell–cell adhesion	Cadherin level GFP
Cell–matrix adhesion	Integrin level GFP
Cell mechanics (rigidity)	Nano-indentation, shearing
Migration (random walk, chemotaxis, haptotaxis)	Cell tracking
Metabolic rates (consumption, production)	Tracer techniques, autoradiography, positron computed tomography (metabolite dependent)
Respond to signals	Signal dependent
Secrete signal	Fluorescent labeling, GFP (signal dependent)
Membrane integrity	Molecular biology
Size and shape	Confocal microscopy, flow cytometry

rise to multicellular morphology and dynamics, which are often emergent. Using simulations, we can study the mechanisms by which single-cell phenomenology directs multicellular morphogenesis and physiology (Merks and Koolwijk 2009). We can also use simulations to determine whether a single-cell level description is sufficient to generate tissue level patterns and functions observed in experiments (Merks and Glazier 2005).

2.3 Model Validation

Step 3 is model validation. Model validation provides a means to assess whether the computational model corresponds to reality. We consider model validation an integral part of model development and propose a three step systematic process for model validation.

First, we specify and rank-order characteristic experimental attributes, both qualitative and quantitative. Examples include (1) endothelial cell proliferation rate as a function of time, (2) endothelial shapes in the sprout, (3) number of sprout tips in a given area, (4) sprout extension speed, (5) sprout branching probability, (6) location of proliferating cells in sprout, (7) VEGF concentration, (8) lacunae size distribution, etc. Note this list ought to be different from the one used as input to build the model. Ranking depends on the goal of the modeling effort. If the goal is to explain the assembly of cells into network patterns, such as those found in in vitro cell culture experiments (Merks et al. 2006), then attributes related to network patterns are more important. On the other hand, if the goal is to study the initiation of angiogenesis and growth of sprout then attributes related to sprout specifics are more important. The comparisons between quantitative measures are

straightforward, whereas those between qualitative data can be somewhat arbitrary. Hunt et al. (2006) have proposed a systematic approach to compare between in silico and in vitro (in vivo) experiments according to prespecifed similarity measures (Tang et al. 2007).

Second, we tune the adjustable parameters and rules in the computational model until it exhibits the targeted attributes, which completes one cycle of model refinement. We then start a new cycle: expand the targeted attribute set until an addition falsifies the current model. The expanded list becomes the new, targeted list, and we repeat the above process to refine the model. As long as the results do not match, we continue to refine the model until they match. It can sometimes be very difficult to determine if the mismatch is due to incorrect model assumptions, inaccurate parameters, or imprecise computational implementation of conceptually correct models. Each of these aspects has to be examined to refine the model. Merks and Koolwijk (2009) emphasized the necessity of developing quantitative in vitro experiments for model development. In some cases, identifying the mechanisms of simulation failure can reveal new and significant effects. For example, if our model reproduce all targeted attributes on Day 1 through Day 4 in retinal vasculogenesis in vivo, but fails to do so on Day 5, it may suggest that new or additional mechanisms appear by Day 5 in vivo that have not been included in the model. A mismatch requires that we go back to examine the experimental data, and possibly conduct additional experiments, to unveil the cause of simulation failure and to improve the model. We repeat these steps until there are no mismatches. When the results match, we have validated the model.

The third and final step of validation is to perturb both the computational and the experimental models. For example, change VEGF from a diffusible isoform to a matrix bound isoform (Bauer et al. 2007) and compare the results with experiments where VEGF isoforms are perturbed (Lee et al. 2005). The comparison and validation process repeats until we converge on a validated model.

In addition, we should perform sensitivity analysis to gauge the limitations and regions of validity of the model and its predictions. Sensitivity analysis can also help to assess the importance and impact of each parameter and to inform decisions on how to allocate experimental resources, for example, which estimated parameters, if any, are most critical to measure experimentally. Sensitivity analysis involves systematically perturbing each model parameter or sets of parameters and qualitatively or quantitatively apportioning any differences in the model's outputs to the changes in the perturbed parameters. Methods for implementing sensitivity analysis include: derivative methods, such as automated differentiation (Grievank 2000), and sampling-based methods (Helton et al. 2006) such as Latin hypercube sampling (Marino et al. 2008). The former are appropriate for continuum models, while the latter are suitable for stochastic and agent (cell)-based models.

3 Cell-Based Models of Angiogenesis

There are many possible ways to implement a cell-based model. Several detailed reviews on this topic have been published, including Drasdo (2003), Hatzikirou et al. (2005), Byrne et al. (2006), and in particular, Merks and Glazier (2005), Anderson et al. (2007), Lowengrub et al. (2010). Here we briefly review a few most recent cell-based models of tumor angiogenesis.

Merks and co-workers (Merks et al. 2006, 2008; Merks and Glazier 2006) implemented the cellular Potts model (CPM) to investigate the cell behaviors necessary for in vitro vasculature formation, such as in human umbilical–vein endothelial–cell (HUVEC) cultures. They focused on the effects of cell–cell adhesion, cell elongation, and migration due to autocrine VEGF on the vascular network patterns (Fig. 6.1a). Bauer et al. (2007) added an explicit representation of ECM to the CPM, which allowed direct investigation of stromal heterogeneity on sprout branching (Fig. 6.1b), VEGF diffusivity on sprout morphology, as well as the effects of ECM topography on sprout development (Bauer et al. 2009). Szabo et al. (2008) modified the CPM to include a bias for motile cells to contact elongated cells, in order to test the hypothesis that multicellular patterning results from cells' preferential-attachment to elongated cells. Shirinifard et al. (2009) extended these efforts and simulated tumor induced angiogenesis as well as the resulting vascular tumor growth in three dimensions (Fig. 6.1c).

In addition to a cohort of efforts based on the CPM approach, other cell-based methods brought different insights. Yin et al. (2008) used an agent-based model to test the hypothesis of ECM-based signaling for angiogenesis. They allowed endothelial cells to deposit collagen when migrating, providing new ECM-based cues for themselves and neighboring cells. Stochastic fluctuations in the directional guidance by these collagen trails led to sprout branching and the formation of a progressively branched vascular pattern (Fig. 6.1d). (Qutub and Popel 2009) developed a model where cells are connected segments of tubes that follow behavioral rules, and studied sprouting and the total vessel growth as a function of VEGF concentration and Delta-Notch binding (Fig. 6.1e).

Jackson and Zheng (2010) developed another rather unique cell-based model that uses discrete spatial points to track cells where each point represents the front of a cell, and a continuous representation of cell mass and maturity. Instead of rules, this model relied entirely on differential equations to control cell processes as well as the reaction-diffusion dynamics of growth factors. The cell processes modeled included a mechanical model of elongation and a biochemical model of cell phenotype variation regulated by angiopoietins within a developing sprout. They studied the relative roles of endothelial cell migration, proliferation, and maturation in corneal angiogenesis experiments (Fig. 6.1f).

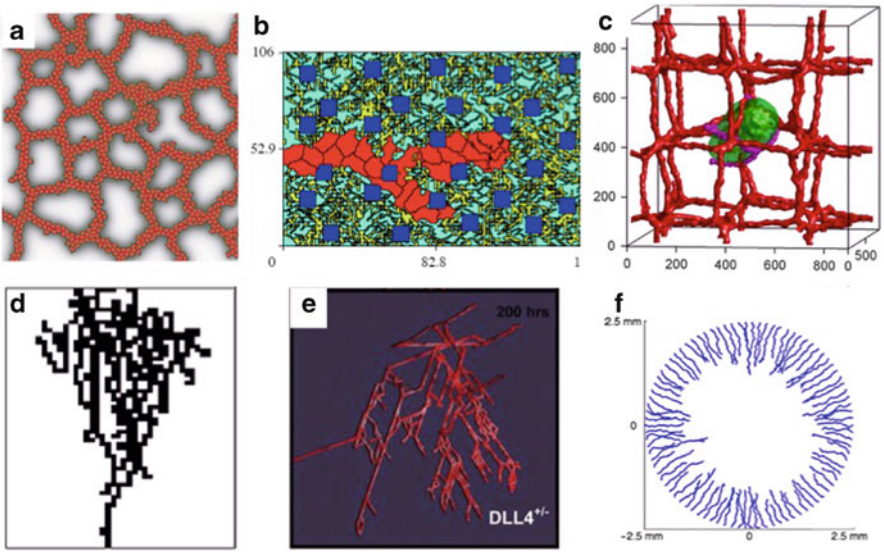

Fig. 6.1 Selected cell-based model of angiogenesis. (**a**) Aggregation of endothelial cells from initial random distribution into a vascular network pattern in 2D. Courtesy of Merks from Merks et al. (2008). (**b**) A branching sprout from an existing blood vessel into the stroma in tumor induced angiogenesis in 2D. From Bauer et al. (2007) with permission. (**c**) Tumor angiogenesis and vascular tumor growth in 3D. Courtesy of Shirinifard from Shirinifard et al. (2009). (**d**) Branching vascular pattern based on ECM-directional guidance (2D). Courtesy of Levchenko from Yin et al. (2008). (**e**) Vasculature development in 3D due to VEGF and Notch signaling. From Qutub and Popel (2009) with permission. (**f**) Vasculature pattern mimicking angiogenesis in cornea in 2D. From Jackson and Zheng (2010) with permission

4 Cellular Potts Model for Tumor Angiogenesis

Here we illustrate the three-step model building procedure outlined above for tumor angiogenesis using the cellular Potts model. The modeling goal is to focus on the underlying biophysical mechanisms of nascent sprout development during tumor-induced angiogenesis.

Step 1: we first identify a list of endothelial cell behaviors and the relevant stromal environment properties based on the literature:

1. VEGF secreted by hypoxic tumor cells activates endothelial cells in preexisting blood vessels (Yancopoulos et al. 2000).
2. VEGF diffuses, decays, and is taken up by endothelial cells (Anderson and Chaplain 1998).
3. Stroma consists of heterogeneously distributed ECM and stromal cells (Kass et al. 2007).
4. Activated endothelial cells upregulate proliferation, migration, and downregulate apoptosis (Hicklin and Ellis 2005).

5. Two distinct types of endothelial cells: tip cells that form filopodia and migrate toward sources of VEGF, and nonmigrating stalk cells that proliferate but do not form filopodia (Gerhardt 2008; Phng and Gerhardt 2009).
6. Endothelial cells migrate along positive gradients of VEGF (chemotaxis) (Gerhardt et al. 2003).
7. Endothelial cells migrate along positive gradients of ECM adhesion sites that are present in the ECM, commonly known as haptotaxis (Lamalice et al. 2007).
8. Endothelial cells elongate as they migrate and form sprouts (Drake et al. 2002).

Step 2: computational model. Because most angiogenesis data exist in two dimensions (2D), including the cell culture in dish (Merks et al. 2006), chick chorioallantoic membrane (Brooks et al. 1994), retinal (Lu et al. 1999) and cornea vasculature (Sholley et al. 1984) development, we start from a 2D cell model. Although the importance of cell–matrix interactions in regulating cell migration and morphogenesis has long been recognized, the detailed understanding of the mechanics of cell–matrix interactions in 3D is still lacking (Rangarajan and Zaman 2008). Working in 2D greatly simplifies the modeling because the cells move on top of the ECM rather than through it.

The CPM (Graner and Glazier 1992; Glazier and Graner 1993) is a lattice-based Monte Carlo approach that describes biological cells as spatially extended clusters of identical lattice indices.[1] Intercellular junctions and cell junctions to the ECM determine adhesive (or binding) energies. On a 2D square lattice, cells are patches of identical lattice numbers $S(i, j)$, where each number labels a single biological cell. Connections between neighboring lattice sites of unlike numbers $S(i, j) = S(i', j')$ represent membrane bonds, where the bond energy is $J_{S,S'}$, assuming that the types and number of adhesive cell-surface proteins determine the value of J. To model the development of vessel sprouts into the stroma, Bauer et al. (2007) considered endothelial cells (ECs), matrix fibers, tissue cells, and interstitial fluid (see Fig. 6.1b), denoted by type τ(E, M, T, F), respectively. Matrix fibers and interstitial fluid are collectively identified by 1s and 0s, respectively, and are treated as generalized cells. Using this representation, each cell and generalized cell has a finite volume, a deformable shape, and competes for space. Cellular dynamics are characterized by an equation for total energy given by:

$$E = \sum_{\text{lattice sites}} J_{\tau(s_1)\tau(s_2)}[1 - \delta(S_1, S_2)] + \sum_{\text{cells}} \gamma \cdot (v - V^T)^2 + \sum_{\text{EC}} \mu C + \sum_{\text{cells}} \gamma'[1 - \delta(v, v')]. \tag{6.1}$$

[1]Recently, it is also called Glazier-Graner-Hogeweg model, or GGH (Glazier et al. 2007; Swat et al. 2009). A CPM open source modeling environment named CompuCell3D is available online at http://www.compucell3d.org (Swat et al. 2009).

In (6.1), the first term is the contribution to total energy resulting from cell adhesion at cell surfaces. The adhesion bond energy depends on the cell types involved. The second term takes into account the fact that cell growth and deformation require energy, where v denotes the current volume of cell S and V^{T} is a designated "target" volume. We assume that the target volume of an endothelial cell undergoing mitosis is the volume that it would grow to in the absence of external forces and given sufficient nutrition, and is set as twice its initial volume. Note that other growth functions have been used, e.g., in Shirinifard et al. (2009) the target volume of the proliferating endothelial cell is set to be a function of local VEGF concentration. Detailed quantitative comparisons with experimental data are required to evaluate the validity of using one growth function over another. The third term describes the chemotactic potential of active endothelial cells. The parameter $\mu < 0$, is the effective chemical potential, describing the strength of chemotaxis relative to other forces in the model; C is the concentration of VEGF. Phenomenologically, VEGF concentration gradients induce endothelial cells to move in the direction of increasing concentration with a speed proportional to the VEGF gradient. Because cells must move through the highly viscous ECM, their motion is over-damped and the force required for motion is proportional to velocity. Consequently, force is proportional to the chemical gradient, and we can construct an effective chemotaxis potential that is proportional to the local chemical gradient. The last term is a continuity constraint applied to endothelial cells, where v and v' are the current volume and the measured volume from a continuous cell domain. This constraint prevents un-biological fragmentation of migrating cells.

The CPM evolves in time using a modified Metropolis algorithm. Procedurally, a lattice site, (i, j), is selected at random and assigned the S from one of its unlike nearest neighbors, (i', j'), which has also been randomly selected. The total energy of the system is computed before and after the proposed update. If the total energy of the system is reduced as a result of the update, the change is accepted. If the update increases the energy of the system, we accept the change with a Boltzmann probability. The probability of accepting an update is given by:

$$p = \begin{cases} 1, & \text{if } \Delta E < 0 \\ e^{-\Delta E/k_{\mathrm{b}}T}, & \text{if } \Delta E \geq 0 \end{cases}, \tag{6.2}$$

where ΔE is the change in total energy of the system as a result of the update, k_{b} the Boltzmann constant, and T is the effective temperature that corresponds to the amplitude of cell membrane fluctuations. A total of n proposed updates, where n is the number of sites on the lattice, constitutes one Monte Carlo step and is the unit of time used in the model. Through such a Monte Carlo update, the CPM naturally represents the stochastic, exploratory behavior of migrating cells, modeling it as the biased extension and retraction of pseudopods, instead of a biologically implausible single force acting on a cells' center of mass or on the tip cell as in some other cell-based models (Merks et al. 2008).

Following Bauer et al. (2007), lattice updates are coupled to the diffusion-reaction dynamics of VEGF, which is described by a partial differential equation:

$$\frac{\partial C}{\partial t} = D\nabla^2 C - \lambda C - B, \tag{6.3}$$

where D, λ, B are the diffusion coefficient, decay rate, and uptake function of VEGF, respectively. The number of VEGF receptors available on the cell surface limits the uptake of VEGF by endothelial cells. For simplicity, we assume cells have a constant number of uniformly distributed receptors and bind available VEGF molecules until all the VEGF receptors are bound. The uptake function is:

$$B = \begin{cases} \beta, & \text{if} \quad \beta \leq V; \\ V, & \text{if} \quad 0 \leq V \leq \beta. \end{cases} \tag{6.4}$$

Where V is the number of VEGF molecules at the cell surface. Because the diffusion and decay processes for VEGF occur much faster than the cellular uptake, we can solve for the steady-state solution to (6.3) to obtain the initial VEGF concentration profile. Within the CPM, each endothelial cell responds to the local VEGF concentration by deciding whether the VEGF level is above its activation threshold level. An activated endothelial cell further decides whether it is a tip cell that will migrate and degrade the ECM, or if it is a proliferating stalk cell that will grow and divide, or if it is a quiescent stalk cell. After the CPM evolves one Monte Carlo step, the VEGF uptake function B is rederived based on the new distribution of endothelial cells on the lattice. Solving (6.3) using the updated uptake function provides a new VEGF concentration field, which is fed into the CPM for another round of endothelial cell decision-making. This iterative feed-back between the VEGF dynamics and the CPM allows each endothelial cell to respond to its changing environment.

Step 3: model validation. As Savill and Merks (2007) nicely put it, performing tissue level simulations is like "releasing hundreds of such cellular Potts endothelial cells into an in silico Petri dish," to study how cell-level phenomenology drives tissue-level morphogenesis. Using their in silico experiment, Bauer et al. (2007) showed that guided by a VEGF signal from the tumor and contact guidance from the ECM, endothelial cells organize into a sprout pattern that exhibits vessel merging and branching (Fig. 6.1b) naturally without prescribed branching rules. As part of the model validation, they perturbed the VEGF profile, from a smooth profile with a shallow gradient resulting from the fast diffusion of VEGF to a steep gradient due to cell uptake of a matrix bound VEGF isoform (Fig. 6.2). To model matrix bound VEGF, after the initial diffusion of VEGF into the stroma and binding to ECM, only degradation of matrix by tip endothelial cells releases the VEGF molecules, which are then uptaken by the cells. Figure 6.2a shows that a matrix bound VEGF profile results in strong chemotaxis guidance for the tip cell, which produces a fast extending sprout that is narrow. Figure 6.2b shows that the smooth profile of

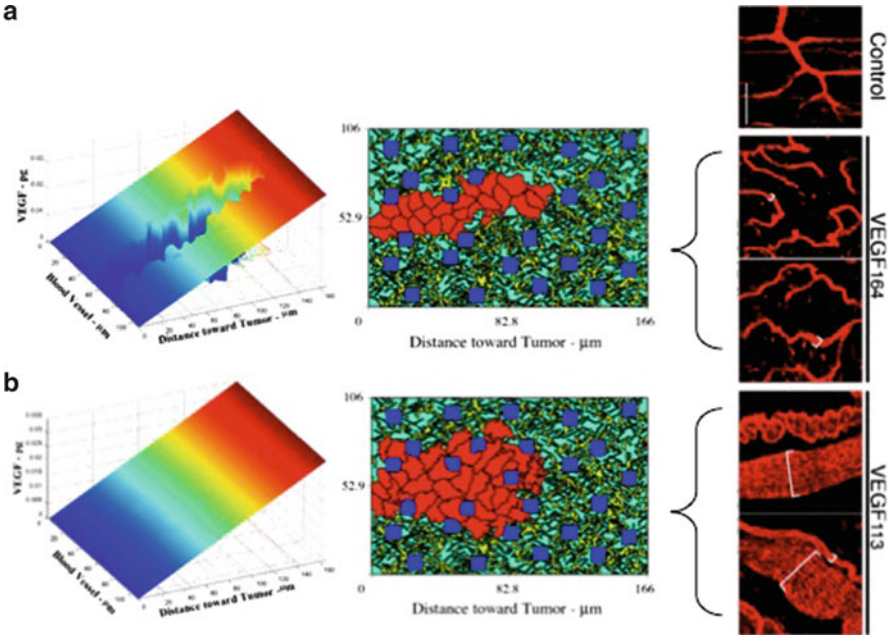

Fig. 6.2 The markedly different capillary sprout morphologies that result from steep (**a**) vs. shallow (**b**) VEGF gradients. Swollen, invasive sprouts result from shallow VEGF gradients that develop when freely soluble VEGF is expressed, whereas when matrix-bound VEGF isoforms are assumed, steep gradients develop and result in narrower capillary sprouts. Both results concur with the experimental observations of Lee et al. (2005). From Bauer et al. (2007) and Lee et al. (2005) with permission

diffusible VEGF results in a swollen sprout as the tip cell migrates slower and is less directed with a weaker VEGF gradient. These observations agree with two separate experimental results. Gerhardt et al. (2003) showed tip cell filopodia lost their polarity and excessive filopodia extend from stalk cells in response to shallow gradients of VEGF in transgenic mice expressing only $VEGF_{120}$. Moreover, Lee et al. (2005) demonstrated in tumor angiogenesis in vivo that soluble VEGF induced significant cell proliferation and broad invasion of the stroma (vessel diameter of 109 µm), whereas matrix-bound isoforms resulted in filopodia extension, limited stromal invasion, and cell–cell associations consistent with sprouting angiogenesis (vessel diameter of 15 µm).

In addition, Bauer et al. (2009) perturbed the stromal structure with ECM and stromal cell distribution, and observed that the stromal heterogeneity alone can cause sprout branching and anastomosis. These studies indicate that anisotropic ECM distribution strongly influences the direction and morphology of the migrating capillary sprout. Using the in silico angiogenesis model, they further investigated the topography of ECM, including density and alignment, on sprout morphogenesis. Figure 6.3 shows the effect of ECM density on the vessel sprout development: very

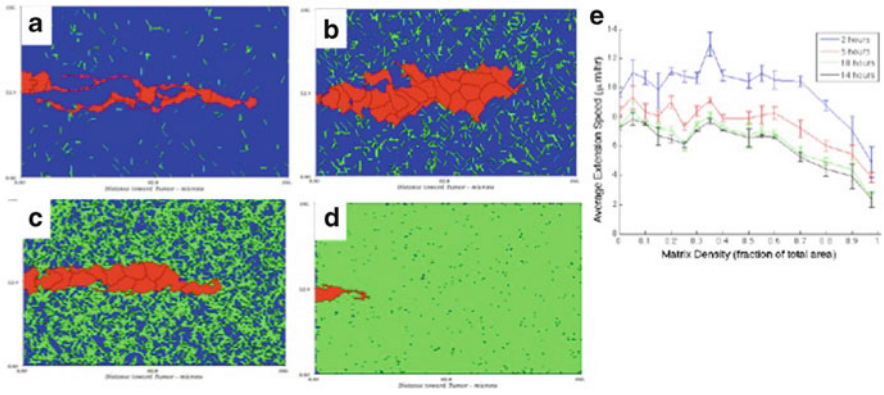

Fig. 6.3 The effect of the ECM density on sprout morphology and viability

low ECM density generates nonviable sprouts, very high ECM density prohibits sprout extension, whereas for intermediate ECM densities (corresponding to physiological ranges) the sprout develops normally.

5 Discussion

Cell-based models are increasingly becoming the method of choice for modeling biological and biomedical problems at the tissue level, partly because of their visual appeal, and partly because such models allow for a natural description and easy examination of emergent collective behaviors. Computational advances have made it possible for cell-based models to describe systems from bacterial colonies to developmental biology and cancer dynamics. Here we provide an introduction on how to develop a cell-based model with an emphasis on model validation, survey a limited set of the latest developments in cell-based models in the field of angiogenesis, and illustrate a model of tumor angiogenesis using the cellular Potts model.

The CPM is but one of many possible ways to implement a cell-based modeling technique. The extended cell body representation of the CPM allows for detailed description of a cell's contact energy with surrounding cells and the ECM, which determine the cell's shape. The surface area over which two cells adhere or a cell adheres to the ECM determines the forces needed to separate them. Another advantage of the CPM is its clear distinction between long-range (e.g., chemotaxis) and short-range (e.g., cell adhesion) interactions.

To make the models more closely related to modern molecular cell biology experiments and eventually therapeutic goals, additional molecular-level details will need to be added to this framework. Dynamically regulated receptor levels on the cell surface, and intracellular regulations (Jiang et al. 2005) or signaling pathways

(Qutub and Popel 2009; Bauer et al. 2010) are a few obvious candidate choices to expand the model and incorporate subcellular time and length scales. The first part of this book highlights the state of the art in this area. At the other end of the spectrum, one might also consider organ or system level environmental or anatomical descriptions and dynamics. For example, breast duct structure (Macklin et al. 2009) for breast tumor development, and incorporation of immune response (de Pillis et al. 2005). This type of multiscale model effort faces many challenges, particularly in terms of multiple scale and multiple model integration, as discussed in the third part of this book.

In a more general sense, cell-based models are a convenient way to scale up the observations from a limited number of cells to a predicted behavior of multicellular ensembles and tissues. In the process, we can determine whether the limited set of cell behavior and cellular interactions is sufficient to explain tissue level behavior, or whether further assumptions describing multicell interactions are needed. Validated cell-based models are handy "in silico Petri dishes" for testing and generating hypotheses, and suggesting new experiments to test model predictions. Attention is shifting from traditional oncology research and practice to "out of the box" ideas of applying mathematical tools for new cancer strategies of cancer therapy (Anderson and Quaranta 2008; Gatenby 2009; Wolkenhauer et al. 2010). Cell-based models help to distill key elements from the complexity of cell and tissue level phenomena and to define their mechanistic principles. In addition, cell-based models are a modeling platform for integrating multiple scales, from molecule to tissue and organ. In the future, we expect that integrated models can provide unexpected insights into the underlying mechanisms controlling angiogenesis and can generate novel hypotheses for experimentation.

References

Adams RH and Alitalo K(2007) Molecular regulation of angiogenesis and lymphangiogenesis Nat Rev Mol Cell Biol 8: 464–478.

Ambrosi D, Gamba A and Serini G(2004) Cell directional persistence and chemotaxis in vascular morphogenesis Bull Math Biol 66: 1851–1873.

Anderson AR and Chaplain MA(1998) Continuous and discrete mathematical models of tumor-induced angiogenesis Bull Math Biol 60: 857–899.

Anderson AR, Weaver AM, Cummings PT, et al. (2006) Tumor morphology and phenotypic evolution driven by selective pressure from the microenvironment Cell 127: 905–915.

Anderson AR, Chaplain MA and Rejniak KA(2007). Single-Cell Based Models in Biology and Medicine, Birkhauser.

Anderson AR and Quaranta V(2008) Integrative mathematical oncology Nat Rev Cancer 8: 227–234.

Bauer AL, Jackson TL and Jiang Y(2007) A cell-based model exhibiting branching and anastomosis during tumor-induced angiogenesis Biophys J 92: 3105–3121.

Bauer AL, Jackson TL and Jiang Y(2009) Topography of extracellular matrix mediates vascular morphogenesis and migration speeds in angiogenesis PLoS Comput Biol 5: e1000445.

Bauer AL, Jackson TL, Jiang Y, et al. (2010) Receptor cross-talk in angiogenesis: mapping environmental cues to cell phenotype using a stochastic, Boolean signaling network model J Theor Biol 264: 838–846.

Brooks PC, Clark RA and Cheresh DA(1994) Requirement of vascular integrin alpha v beta 3 for angiogenesis Science 264: 569–571.
Byrne HM, Alarcon T, Owen MR, et al. (2006) Modeling aspects of cancer dynamics: A review Phi. Trans. R. Soc. A 364: 1563–1578.
Carmeliet P(2000) Mechanisms of angiogenesis and arteriogenesis Nat Med 6: 389–395.
Carmeliet P and Jain RK(2000) Angiogenesis in cancer and other diseases Nature 407: 249–257.
Carmeliet P(2003) Angiogenesis in health and disease Nat Med 9: 653–660.
de Pillis LG, Radunskaya AE and Wiseman CL (2005) A validated mathematical model of cell-mediated immune response to tumor growth Cancer Res 65: 7950–7958.
Drake CJ, LaRue A, Ferrara N, et al. (2002) VEGF regulates cell behavior during vasculogenesis Dev Biol 224: 178–188.
Drasdo D(2003). On selected individual-based approaches to the dynamics of multicellular systems.In: Alt W. Multiscale Modeling.Basel, Birkhauser.
Drasdo D and Hohme S(2003) Individual-based approaches to birth and death in avascular tumors Math. Comput. Modeling 37: 1163.
Folkman J and D'Amore PA (1996) Blood vessel formation: what is its molecular basis? Cell 87: 1153–1155.
Gatenby RA, Gawlinski ET, Alarcon T, et al. (2005) A multiple scale model for tumor growth Multiscale Modeling Simulation 3: 440–475.
Gatenby RA(2009) A change of strategy in the war on cancer Nature 459: 508–509.
Gerhardt H, Golding M, Fruttiger M, et al. (2003) VEGF guides angiogenic sprouting utilizing endothelial tip cell filopodia J Cell Biol 161: 1163–1177.
Gerhardt H(2008) VEGF and endothelial guidance in angiogenic sprouting Organogenesis 4: 241–246.
Glazier JA and Graner F(1993) Simulation of the differential adhesion driven rearrangement of biological cells Phys Rev E Stat Phys Plasmas Fluids Relat Interdiscip Topics 47: 2128–2154.
Glazier JA, Balter A and Poplawski NJ(2007). Magnetization to morphogenesis: a brief history of the Glazier-Graner-Hogeweg model.In: Anderson ARA, Chaplain MAJ and Rejniak KA. Single-Cell Based Models in Biology and Medicine, Birkhauser: 346.
Graner F and Glazier JA(1992) Simulation of biological cell sorting using a two-dimensional extended Potts model Phys Rev Lett 69: 2013–2016.
Lampugnani GM, Zanetti A, Corada M, et al. (2003) Contact inhibition of VEGF-induced proliferation requires vascular endothelial cadherin, beta-catenin, and the phosphatase DEP-1/CD148 J Cell Biol 161: 793–804.
Grievank A(2000). Evaluating derivatives, Principles and techniques of algorithmic differentiation., SIAM publisher.
Hatzikirou H, Deutsch A, Schaller C, et al. (2005) Mathematical modeling of glioblastoma tumour development: A review Math. Models Methods Appl. Sci. 15: 1779–1794.
Helton JC, Johnson JD, Salaberry CJ, et al. (2006) Survey of sampling based methods for uncertainty and sensitivity analysis. Reliability Engineering and System Safety Reliability Engineering and System Safety 91: 1175–1209.
Hicklin DJ and Ellis LM(2005) Role of the vascular endothelial growth factor pathway in tumor growth and angiogenesis J Clin Oncol 23: 1011–1027.
Huang S and Ingber DE(1999) The structural and mechanical complexity of cell-growth control Nat Cell Biol 1: E131–138.
Hunt CA, Ropella GEP, Yan L, et al. (2006) Physiologically based synthetic models of hepatic disposition J Pharmacok Pharmacodyn 33: 737–772.
Iruela-Arispe ML, Diglio CA and Sage EH (1991) Modulation of extracellular matrix proteins by endothelial cells undergoing angiogenesis in vitro Arterioscler Thromb 11: 805–815.
Iruela-Arispe ML, Hasselaar P and Sage H (1991) Differential expression of extracellular proteins is correlated with angiogenesis in vitro Lab Invest 64: 174–186.
Jackson T and Zheng X(2010) A cell-based model of endothelial cell migration, proliferation and maturation during corneal angiogenesis Bull Math Biol 72: 830–868.

Jiang Y, Pjesivac-Grbovic J, Cantrell C, et al. (2005) A multiscale model for avascular tumor growth Biophys J 89: 3884–3894.
Kass L, Erler JT, Dembo M, et al. (2007) Mammary epithelial cell: Influence of extracellular matrix composition and organization during development and tumorigenesis International Journal of Biochemistry & Cell Biology 39: 1987–1994.
Lamalice L, Le Boeuf F and Huot J (2007) Endothelial cell migration during angiogenesis Circ Res 100: 782–794.
Lee S, Jilani SM, Nikolova GV, et al. (2005) Processing of VEGF-A by matrix metalloproteinases regulates bioavailability and vascular patterning in tumors J Cell Biol 169: 681–691.
Lowengrub JS, Frieboes HB, Jin F, et al. (2010) Nonlinear modeling of cancer: bridging the gap between cells and tumours Nonlinearity 23: R1–R91.
Lu M, Amano S, Miyamoto K, et al. (1999) Insulin-induced vascular endothelial growth factor expression in retina Invest Ophthalmol Vis Sci 40: 3281–3286.
Macklin P, Kim J, Tomaiuolo G, et al. (2009). Agent-Based Modeling of Ductal Carcinoma In Situ: Application to Patient-Specific Breast Cancer Modeling In: Pham T. Computational Biology Issues and Applications in Oncology New York, Springer: 77–111.
Marino S, Hogue I, Ray CJ, et al. (2008) A methodology for performing global uncertainty and sensitivity analysis in systems biology J Theor Biol 254: 178–196.
Merks RM and Glazier JA(2005) A cell-centered approach to developmental biology Physica A 352: 113–130.
Merks RM, Brodsky SV, Goligorksy MS, et al. (2006) Cell elongation is key to in silico replication of in vitro vasculogenesis and subsequent remodeling Dev Biol 289: 44–54.
Merks RM and Glazier JA(2006) Dynamic mechanisms of blood vessel growth Nonlinearity 19: C1-C10.
Merks RM, Perryn ED, Shirinifard A, et al. (2008) Contact-inhibited chemotaxis in de novo and sprouting blood-vessel growth PLoS Comput Biol 4: e1000163.
Merks RM and Koolwijk P(2009) Modeling Morphogenesis in silico and in vitro: Towards Quantitative, Predictive, Cell-based Modeling Math. Model. Nat. Phenom. 4: 149–171.
Peirce SM, Van Gieson EJ and Skalak TC (2004) Multicellular simulation predicts microvascular patterning and in silico tissue assembly FASEB J 18: 731–733.
Perryn ED, Czirok A and Little CD(2008) Vascular sprout formation entails tissue deformations and VE-cadherin-dependent cell-autonomous motility Dev Biol 313: 545–555.
Phng LK and Gerhardt H(2009) Angiogenesis: a team effort coordinated by notch Dev Cell 16: 196–208.
Qutub AA and Popel AS(2009) Elongation, proliferation & migration differentiate endothelial cell phenotypes and determine capillary sprouting BMC Syst Biol 3: 13.
Rangarajan R and Zaman MH(2008) Modeling cell migration in 3D: Status and challenges Cell Adh Migr 2: 106–109.
Rejniak KA(2007) An immersed boundary framework for modeling the growth of individual cells: an application to the early tumour development J Theor Biol 247: 186–204.
Savill NJ and Merks RMH(2007). The Cellular Potts Model in Biomedicine.In: Anderson ARA, Chaplain MAJ and Rejniak KA. Single-Cell Based Models in Biology and Medicine, Birkhauser: 346.
Senger DR, Claffey KP, Benes JE, et al. (1997) Angiogenesis promoted by vascular endothelial growth factor: regulation through alpha1beta1 and alpha2beta1 integrins Proc Natl Acad Sci USA 94: 13612–13617.
Shirinifard A, Gens JS, Zaitlen BL, et al. (2009) 3D multi-cell simulation of tumor growth and angiogenesis PLoS One 4: e7190.
Sholley MM, Ferguson GP, Seibel HR, et al. (1984) Mechanisms of neovascularization. Vascular sprouting can occur without proliferation of endothelial cells Lab Invest 51: 624–634.
Swat MH, Hester SD, Balter AI, et al. (2009) Multicell simulations of development and disease using the CompuCell3D simulation environment Methods Mol Biol 500: 361–428.
Szabo A, Mehes E, Kosa E, et al. (2008) Multicellular sprouting in vitro Biophys J 95: 2702–2710.

Tang J, Ley KF and Hunt CA(2007) Dynamics of in silico leukocyte rolling, activation, and adhesion BMC Syst Biol 1: e14.

Turner S and Sherratt JA(2002) Intercellular adhesion and cancer invasion: a discrete simulation using the extended Potts model J Theor Biol 216: 85–100.

Wallez Y and Huber P(2008) Endothelial adherens and tight junctions in vascular homeostasis, inflammation and angiogenesis Biochim Biophys Acta 1778: 794–809.

Wolkenhauer O, Auffray C, Baltrusch S, et al. (2010) Systems biologists seek fuller integration of systems biology approaches in new cancer research programs Cancer Res 70: 12–13.

Yancopoulos GD, Davis S, Gale NW, et al. (2000) Vascular-specific growth factors and blood vessel formation Nature 407: 242–248.

Yin Z, Noren D, Wang CJ, et al. (2008) Analysis of pairwise cell interactions using an integrated dielectrophoretic-microfluidic system Mol Syst Biol 4: 232.

Zhang L, Athale CA and Deisboeck TS(2007) Development of a three-dimensional multiscale agent-based tumor model: simulating gene-protein interaction profiles, cell phenotypes and multicellular patterns in brain cancer J Theor Biol 244: 96–107.

Chapter 7
A Cell-Based Model of Endothelial Cell Migration, Proliferation, and Maturation in Corneal Angiogenesis

Trachette L. Jackson and Xiaoming Zheng

1 Introduction

The corneal angiogenesis system is one of the most experimentally studied models of blood vessel growth, due to its accessibility and high visibility of the in vivo environment. In corneal angiogenesis experiments, either a tissue injury (Sholley et al. 1984; Thompson et al. 2003) or an implanted tumor (Ausprunk and Folkman 1977) is created in the center of the cornea. The tissue/tumor cells release angiogenic stimulaters such as VEGF. When ECs that line the blood vessels in the limbus become activated by vascular endothelial growth factor (VEGF), they degrade the basement membrane and migrate through the extracellular matrix (ECM) toward the cornea center. Neovascularization is clearly the result of many complex processes that culminate in the proliferation and migration of ECs, via their interaction with the ECM, sprout lumen formation, and the maturation of newly formed sprouts.

There have been many mathematical models for angiogenesis, including continuous models (Balding and McElwain 1985; Byrne and Chaplain 1995, 1996; Anderson and Chaplain 1998a,b; Levine et al. 2001; Sleeman and Wallis 2002; Plank and Sleeman 2003, 2004; Plank et al. 2004; Levine and Nilsen-Hamilton 2006), discrete models (Anderson and Chaplain 1998b; Plank and Sleeman 2003, 2004; Stokes and Lauffenburger 1991; Tong and Yuan 2001; Sun et al. 2005; Gevertz and Torquato 2006; Milde et al. 2008), and cell-based models (Peirce et al. 2004; Bauer et al. 2007; Qutub and Popel 2009). However, none of these

T.L. Jackson
Department of Mathematics, University of Michigan, Ann Arbor, MI 48109, USA
e-mail: tjacks@umich.edu

X. Zheng (✉)
Department of Mathematics, Central Michigan University, Mount Pleasant, MI 48859, USA
e-mail: xzheng@cmich.edu

T.L. Jackson (ed.), *Modeling Tumor Vasculature: Molecular, Cellular, and Tissue Level Aspects and Implications*, DOI 10.1007/978-1-4614-0052-3_7,

mathematical approaches has correctly captured the mechanisms underlying two critical experimental observations (Sholley et al. 1984): first, without proliferation, only a restricted sprout network that never reaches the source of chemoattractant, is formed; second, proliferation mainly occurs at the leading edge of developing sprouts. A detailed review of advantages and disadvantages of these models is provided in Mantzaris et al. (2004) and Jackson and Zheng (2010).

The key to modeling the angiogenesis process is to understand the relationships among migration, proliferation, and maturation of ECs that constitute developing vessels.

Both proliferation and migration are important for the extension of capillary sprouts. A widely accepted theory is that migration is the primary event of and plays a leading role in capillary extension, while proliferation is secondary but provides the necessary material resources for capillary extension (Sholley et al. 1984; Ausprunk and Folkman 1977; Semino et al. 2006). In growing sprouts, specialized tip ECs migrate and lead sprout extension (Gerhardt et al. 2003; De Smet et al. 2009), while the proliferation happen anywhere in the stalk except at the sprout tip (Gerhardt et al. 2003). However, the proliferative activities are not uniform along the vessel: ECs at the leading edge exhibit a higher rate of proliferation (Sholley et al. 1984).

In developing vessels, ECs depend on VEGF for survival (Benjamin et al. 1999), and later recruit pericytes to form a stabilizing and protective coating (Griffioen and Molema 2000). This stabilization process is regulated by another important family of angiogenic proteins, angiopoietins, among which Ang1 and Ang2 are best studied. Both Ang1 (Davis et al. 1996) and Ang2 (Maisonpierre et al. 1997) are ligands for one EC-specific receptor tyrosine kinase, Tie2. It is believed that Ang1 is an activator of Tie2, while Ang2 is known to antagonize the binding of Ang1 to Tie2 (Augustin et al. 2009). It is established that Ang1 enhances the interaction between ECs and pericytes and other support cells (Witzenbichler et al. 1998; Scharpfenecker et al. 2005), and the tight contact between ECs and support cells inhibits EC proliferation (Ashara et al. 1998). Therefore, Ang1 can repress EC proliferation and render them quiescent. In contrast, Ang2 destabilizes vessels by loosening the EC/pericyte contacts and drives EC sensitive to other chemokine signals. More biological properties of angiopoietins can be found in the review (Augustin et al. 2009).

Taken together, the information we glean from the current biological understanding of angiogenesis suggests that mathematical models of these processes will have to cut across several levels of biological organization. In the next sections, we build a computational framework that operates at three levels: molecular, cellular, and tissue. At the molecular level, we consider the diffusion, decay, and interactions with cells of VEGF, Ang1, and Ang2. At the cellular level, we consider the EC migration, proliferation, and maturation. At the tissue level, we model the extension of capillary sprouts in the tissue of the length scale 2 mm. The variables of the model are: displacement, mass, and maturity level assigned to each EC, and global concentrations of VEGF, Ang1, and Ang2. In Sects. 2–4, we derive equations for each variable and then simulate the full model in Sect. 5. The conclusion is given in Sect. 6.

2 Molecular Level Models

2.1 Corneal Angiogenesis Domain

The rat cornea has a thickness of about $0.2 \sim 0.3$ mm, and the part bordered by limbus has a diameter of $4 \sim 5$ mm (Sholley et al. 1984); therefore, it is justifiable to simplify to a two-dimensional flat tissue plane. The computational domain Ω is chosen as the square $[-2.5, 2.5]^2$ mm^2, as shown in Fig. 7.1, in order to simplify the generation of meshes and the finite difference schemes used in this work. The limbus is a circle with radius 2.5 mm from the center. The lesion Ω_T is a disc centered at $(0, 0)$ with radius $r = 0.5$ mm, and the region inside Ω excluding Ω_T is denoted as Ω_C, i.e., $\Omega_C = \Omega / \Omega_T$. Any spatial point in Ω is denoted as $\mathbf{x} = (x, y)$.

2.2 VEGF Equation

VEGF is produced by the injured cornea cells, and it diffuses in the tissue with natural decay. In the vicinity of ECs, VEGF is captured by the receptor VEGFR2 to form a complex VEGF/VEGFR2, which is converted to some product to modulate cell behaviors.

Denote c as the VEGF concentration, r_0 as the free VEGFR2 concentration, r_v as the VEGF/VEGRFR2 complex concentration, then the VEGF/VEGFR2 kinetics can be described as:

$$\text{VEGF } (c) + \text{Receptor } (r_0) \underset{k_{\text{off}}}{\overset{k_{\text{on}}}{\rightleftarrows}} \text{Complex } (r_v), \tag{7.1}$$

$$\text{Complex } (r_v) \xrightarrow{k_p} \text{Product} + \text{Receptor}(r_0), \tag{7.2}$$

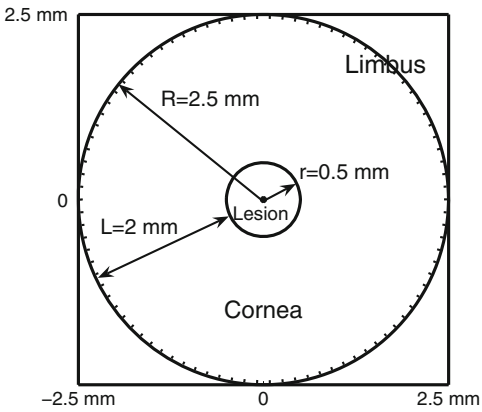

Fig. 7.1 The computational domain $\Omega = [-2.5, 2.5]^2$ mm^2, and the lesion Ω_T is the center disc with radius $r = 0.5$ mm. New sprouts will grow from the limbus toward the lesion

where k_{on}, k_{off}, k_p are kinetic constants. Based on these reactions, the governing equations are written as:

$$\frac{\mathrm{d}c}{\mathrm{d}t} = -k_{\text{on}} c\, r_0 + k_{\text{off}} r_v, \tag{7.3}$$

$$\frac{\mathrm{d}r_0}{\mathrm{d}t} = -k_{\text{on}} c\, r_0 + k_{\text{off}} r_v + k_p r_v, \tag{7.4}$$

$$\frac{\mathrm{d}r_v}{\mathrm{d}t} = k_{\text{on}} c\, r_0 - k_{\text{off}} r_v - k_p r_v. \tag{7.5}$$

By summing up (7.4) and (7.5) it is easy to tell that $r_0 + r_v$ is a constant, which is the concentration of total receptors and will be denoted as T.

Assuming the kinetics occur far faster than the diffusion so that, for any given VEGF value c, the receptor and complex immediately reach steady state values. That is, both $\frac{\mathrm{d}r_0}{\mathrm{d}t}$ and $\frac{\mathrm{d}r_v}{\mathrm{d}t}$ are equal to zero in (7.4) and (7.5). Some algebras lead to the steady state value

$$r_v = \frac{Tc}{k_n + c}, \tag{7.6}$$

where $k_n = \frac{k_{\text{off}} + k_p}{k_{\text{on}}}$. Plugging this r_v value and $r_0 = T - r_v$ into (7.3), we obtain

$$\frac{\mathrm{d}c}{\mathrm{d}t} = -\frac{k_{\max} c}{k_n + c}, \tag{7.7}$$

where $k_{\max} = T k_p$. The constant $k_{\max}$ is called the maximum uptake rate, and k_n is the half-saturation constant. This equation is the standard Michaelis-Menten kinetics or the quasi steady state approximation (c.f. Edelstein-Keshet 1998).

With the spatial diffusion and the natural decay, the equation for VEGF $c(\mathbf{x}, t)$ is

$$\frac{\partial c}{\partial t} = D_c \nabla^2 c - \mu_c c - \frac{k_{\max} c}{k_n + c} \chi_e(\mathbf{x}), \text{ in } \Omega_C, \tag{7.8}$$

where D_c is the diffusion constant, μ_c is the natural decay rate. The function $\chi_e(\mathbf{x})$ is the EC indicator function, taking value one where ECs are located and zero otherwise. In numerical simulations, χ_e is smoothed away from blood vessel curves to the whole tissue domain.

In the corneal angiogenesis model, we assume VEGF is produced on the lesion boundary where its value is a constant, that is, $c|_{\partial\Omega_C} = c_0$. Inside the lesion Ω_T, VEGF is simply assumed to be c_0. On the outer boundary $\partial\Omega$, we impose the no-flux condition: $\frac{\partial c}{\partial n}|_{\partial\Omega} = 0$.

2.3 Angiopoietin Equations

There are very few mathematical models of angiopoietins due to the paucity of experimental data, and our current model is based on Plank et al. (2004). From experiments we know that Ang1 is mainly expressed by pericytes. We assume the pericyte density to be proportional to that of mature cells; therefore, the production of Ang1 is associated with mature ECs. Ang1 has a uniform background value a_0. Ang2 is released by immature ECs. Denote the Ang1 and Ang2 concentrations as $a_1(\mathbf{x}, t)$ and $a_2(\mathbf{x}, t)$, respectively. The equations of Ang1 and Ang2 are

$$\frac{\partial a_1}{\partial t} = D_{a_1}\nabla^2 a_1 + b_{a_1} m \chi_e + \mu_{a_1}(a_0 - a_1), \tag{7.9}$$

$$\frac{\partial a_2}{\partial t} = D_{a_2}\nabla^2 a_2 + b_{a_2}(1-m)\chi_e - \mu_{a_2} a_2, \tag{7.10}$$

where D_{a_1} and D_{a_2} are diffusion constants, b_{a_1} and b_{a_2} the production rates, and μ_{a_1} and μ_{a_2} are decay rates. We impose the initial conditions $a_1(\mathbf{x}, 0) = a_0$, $a_2(\mathbf{x}, 0) = 0$, and no-flux boundary conditions $\frac{\partial a_1}{\partial n}|_{\partial\Omega} = 0$, $\frac{\partial a_2}{\partial n}|_{\partial\Omega} = 0$.

By far, we have mathematically described the chemokines that mediate cell fate; in the next section, we turn to cellular behaviors.

3 Cellular Level Models

ECs in a growing sprout exhibit different phenotypes: according to Gerhardt et al. (2003) and De Smet et al. (2009), the tip EC owns the migratory phenotype and leads the sprout extension, but does not proliferate; while the stalks cells behind the tip have the proliferative phenotype, but they are passively dragged by the tip EC. Therefore, in this section, we first develop the tip EC migration model, then describe the stalk cell maturation and proliferation models.

3.1 Tip EC Migration Model: One-dimensional Case

In this subsection, we develop a viscoelastic spring model of EC migration. Models of cell movement are abundant in the literature, for example, Anderson et al. (2007). We take the approach of Larripa and Mogilner (2006) and regard the tip EC and ECM as a spring-dash pot system. A typical spring-dash pot system with the displacement u can be described as

$$m\frac{\mathrm{d}^2 u}{\mathrm{d}t^2} + c\frac{\mathrm{d}u}{\mathrm{d}t} + ku = F, \tag{7.11}$$

where m is the EC mass, k accounts for the elasticity of the spring, c responsible for the resistance from the dash pot, and F is the external force. In the case of slow motion such as the EC migration, the second derivative term is small compared with other terms and will be neglected.

The physical parameters describing the tip EC are the Young's modulus E, viscosity μ, and friction β between EC and ECM. Lamellipodia, formed by the cytoskeletal protein actin projections on the leading edge of EC, generate a protrusion force F, so that the elongation of the cell body u satisfies the force balance equation

$$\frac{EA_0}{L_0}u + \frac{\mu A_0}{L_0}\frac{\mathrm{d}u}{\mathrm{d}t} + \beta A_1 \frac{\mathrm{d}u}{\mathrm{d}t} = F, \tag{7.12}$$

where A_0 is the cross-section area, L_0 the initial length, and A_1 is the contact area of lamellipodia with ECM. The first term is the elastic force generated by the stress fibers in the EC body. The second term is the viscous friction produced by the cytoplasma, internal fluid inside the EC. The third term is the friction or drag on the contact surface with the ECM. The last term F is the protrusion force. This equation has the unit picoNewton (pN) and can be rigorously derived from the viscoelastic model with small deformation (for details, see Jackson and Zheng 2010).

If all the parameters and the force F are constants then the solution of (7.12) with the initial condition $u(0) = 0$ is

$$u = \frac{FL_0}{EA_0}(1 - e^{-t/T_0}), \tag{7.13}$$

where $T_0 = \frac{\mu}{E} + \frac{\beta A_1 L_0}{EA_0}$. T_0 is the typical relaxation time, and $u_s = \frac{FL_0}{EA_0}$ is the steady state (or resting) length of the cell.

The Young's modulus for ECs is chosen as $2 \times 10^3 \frac{pN}{\mu m^2}$ (Costa et al. 2006). The viscosity μ is not available for ECs, so we replace it with the value for fibroblasts (Thoumine and Ott 1997): $\mu = 10^4 \frac{pN \cdot s}{\mu m^2}$. The estimate of β will be highly dependent on the material, and we use the value $\beta = 10^3 \frac{pN \cdot s}{\mu m^3}$ from Larripa and Mogilner (2006). The protrusion force is about $2 \times 10^4 pN$ according to Prass et al. (2006). An unstretched EC is roughly $10\,\mu m$ long, $10\,\mu m$ wide, and $1\,\mu m$ thick (Levine et al. 2001), thus $L_0 = 10\,\mu m$ and $A_0 = 10\,\mu m^2$. The length of lamellipodia L_1 is assumed to be $10\,\mu m$, so its area $A_1 = 100\,\mu m^2$. With these values, the relaxation time is $T_0 = 50$ s, and the steady state is $u = 10\,\mu m$, and the total length of EC is $L_0 + u + L_1 = 30\,\mu m$, which is a reasonable estimate (c.f. Gerhardt et al. 2003).

Note the time scale T_0 is far smaller than the angiogenesis time scale, 1 day. Thus, at any instant, we assume the ECs extend to a steady state in numerical simulations.

We have described the elongation scalar in one-dimensional case, and next we turn to the multidimensional case, where the elongation becomes a vector.

3.2 Tip EC Migration Model: Multidimensional Case

We assume the protrusion force F obeys the receptor law (e.g., Othmer and Stevens 1997). That is, the EC lamellipodia generates the force according to the spatial gradient of VEGF that the EC detects. The VEGF level the EC can detect is the VEGF/VEGFR2 complex concentration. We further assume it is the steady state value r_v given in (7.6). Thus, the force is proportional to the gradient of r_v, i.e.,

$$F = \gamma \nabla r_v = k_c \frac{\alpha_1}{(c+\alpha_1)^2} \nabla c, \tag{7.14}$$

where γ is the proportion constant, $k_c = \gamma T$, and $\alpha_1 = k_n$. Therefore, the steady state of EC elongation becomes

$$u_s = k_e \frac{\alpha_1}{(c+\alpha_1)^2} \nabla c, \tag{7.15}$$

where $k_e = \frac{k_c L_0}{E A_0}$.

ECs are observed to migrate along ECM fibers, a phenomenon called "contact guidance" (Guido and Tranquillo 1993). We adopt the conductivity tensor $\mathbf{K}$ from Sun et al. (2005) and modify the protrusion force to be $\mathbf{K} \circ F$, then the elongation of a tip cell becomes

$$u_s = k_e \frac{\alpha_1}{(c+\alpha_1)^2} \mathbf{K} \circ \nabla c. \tag{7.16}$$

As in Sun et al. (2005), $\mathbf{K}$ is assumed to be a second-order symmetric tensor, and in two-dimensional space it has the form:

$$\mathbf{K} = k_{\text{cond}} \begin{pmatrix} a_x^2 & a_x a_y \\ a_y a_x & a_y^2 \end{pmatrix} + \frac{k_{\text{cond}}}{k_a} \begin{pmatrix} a_y^2 & -a_x a_y \\ -a_y a_x & a_x^2 \end{pmatrix}. \tag{7.17}$$

The parameter $k_{\text{cond}} > 0$ stands for the mechanical response of fibers to the pulling force exerted by the cell. The parameter $k_a \geq 1$ stands for the directional anisotropy of fibers. If $k_a = 1$ then $\mathbf{K}$ becomes $k_{\text{cond}}\mathbf{I}$, where $\mathbf{I}$ is the identity matrix, so it is isotropic at this point. As $k_a \to \infty$, $\mathbf{K}$ tends to be $k_{\text{cond}}\mathbf{a} \otimes \mathbf{a}$. Both k_a and k_{cond} are chosen as random numbers to represent the heterogeneity of the contact guidance. The unit vector $\mathbf{a} = (a_x, a_y)$ is in the direction of the fiber at (x, y) in the ECM, and it is a random variable in space to represent the random orientation of fibers in ECM. Denoting $\mathbf{a}$'s orthogonal vector as $\mathbf{a}^\perp = (-a_y, a_x)$, then (7.17) can be rewritten with tensor products as

$$\mathbf{K} = k_{\text{cond}}\mathbf{a} \otimes \mathbf{a} + \frac{k_{\text{cond}}}{k_a}\mathbf{a}^\perp \otimes \mathbf{a}^\perp, \tag{7.18}$$

which is the generic form in a multidimensional case.

3.3 Stalk EC Maturation Equation

Cells of the developing sprouts have differential properties including proliferative potential. At the beginning stage of angiogenesis, ECs are actively proliferating and migrating. While at later stages, ECs associate tightly with pericytes and thus turn to proliferatively quiescent and form stabilized blood vessels, which is called the maturation process. The maturation process is essential for the efficient and sustained blood transfer (Mantzaris et al. 2004).

For each EC, we assign a quiescent/maturity level, denoted as m, which is defined as the volume fraction of quiescent cells in a well-defined neighborhood of this cell. The value of m is between 0 and 1, and $m = 0$ corresponds to proliferative cells, while $m = 1$ implies quiescent/mature cells. The equation of m is

$$\frac{\partial m}{\partial t} = b_m(1-m)\frac{a_1}{a_1+\alpha_2}\frac{c}{c+\alpha_3} - \mu_m m a_2 H(a_2 - \lambda a_1). \tag{7.19}$$

The first term on the right models the transition from immature to mature state, where the dependence on Ang1 and VEGF is modeled by receptor laws. The second term measures the transition from mature to immature state, where the Heaviside function $H(a_2 - \lambda a_1)$ dictates that ECs are activated only when Ang2 is more than λ-fold of Ang1, where λ is a parameter ranging from 4 to 8.

3.4 Stalk EC Proliferation Equation

We assume only the immature ECs with mass $(1-m)e$ have significant proliferative activity, then

$$\frac{\partial e}{\partial t} = \beta_e(1-m)eH(c-c_p)\frac{c}{c+\alpha_4} - \mu_e(1-m)e, \tag{7.20}$$

with initial value $e(0) = e_0$, the normal cell mass in nonproliferative vessels. Cell proliferation depends on VEGF, and we assume a receptor law $\frac{c}{c+\alpha_4}$. We further assume the proliferation occurs only when VEGF is higher than a threshold value c_p.

4 Tissue Level Model

In this section, we integrate the molecular and cellular models developed in the previous two sections to describe the sprout extension in tissues.

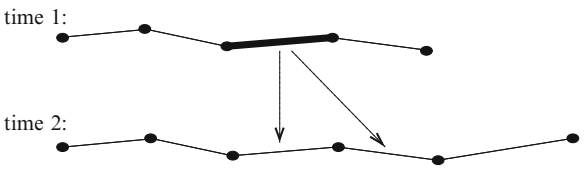

Fig. 7.2 A schematic of sprout extension and EC division. The sprout extends to the right. One EC doubles its mass (*thicker line*) at time 1 and divides to two daughter ECs (*arrows*) at time 2. *Black dots* denote the front and rear endpoints of ECs

Each EC is identified by a line segment with two endpoints, each of which represents the front or the rear of the cell. Within a sprout, every two neighboring cells are tightly connected by adhesions, so they have one endpoint in common. Therefore, a sprout is represented by an array of discrete points, which form an irregular line in space due to contact guidance (see Fig. 7.2). Each EC is assigned the time dependent variables: position vector u_s, mass e, and maturity level m. The concentrations of VEGF (c), Ang1 (a_1), and Ang2 (a_2) are defined in the entire space Ω.

The entire migration and mitosis process can be described as follows:

- *Molecular variables*: VEGF, Ang1, and Ang2 are solved from (7.8), (7.9), and (7.10), respectively.
- *tip EC Migration*: The tip cell of each sprout elongates with displacement given by u_s (7.16).
- *stalk EC proliferation and maturation*: The maturation (7.19) and proliferation (7.20) are solved for each stalk EC.
- *stalk EC divisions and sprout extension*: If the mass of an EC in the stalk doubles then this cell divides into two new cells, and each of them starts with mass and quiescent level equal to half that of their mother cell. One of these new cells takes the position of the old cell, and the other new cell occupies the position of the cell in front. Every cell in front of the dividing cell is dragged to replace the cell directly ahead of it, and the tip cell elongate again. A schematic of these processes is shown in Fig. 7.2.

The sprout extension in anastomosis and branching are also considered (Jackson and Zheng 2010). For the numerical schemes to solve all these differential equations, please refer to Jackson and Zheng (2010).

5 Simulation of Rat Corneal Angiogenesis

In this section, we use the numerical simulation to study the angiogenesis induced by a lesion in the center of the rat cornea (Fig. 7.1). Initially, 90 sprout buds are uniformly distributed along the limbus, and each sprout is of length 0.1 mm. The values of all parameters used in these simulations are given in Table 7.1.

Table 7.1 Dimensional parameters and their values

Parameters	Values
EC reference density, e_0	$3.32 \times 10^{-8} \mu$M
VEGF reference concentration, c_0	$3.33 \times 10^{-3} \mu$M
Angiopoietin reference concentration, a_0	10^{-3} μM
VEGF diffusion constant, D_c	50.88 mm^2 per day
VEGF decay rate, μ_c	15.60 per day
VEGF maximum uptake rate, $k_{\max}$	3.68×10^6 per day
VEGF half-saturation constant, k_n	$8.85 \times 10^{-4} \mu$M
Ang1 diffusion constant, D_{a_1}	1.67×10^{-5} mm^2/h
Ang2 diffusion constant, D_{a_2}	1.67×10^{-6} mm^2/h
Ang1 production rate, b_{a_1}	3×10^4 per day
Ang1 decay rate, μ_{a_1}	0.1 per day
Ang2 production rate, b_{a_2}	1.2×10^6 per day
Ang2 decay rate, μ_{a_2}	4.0 per day
EC proliferation rate, β_e	0.96 per day
EC death rate, μ_e	0.005 per day
EC maturation rate, b_m	0.4 per day
EC activation rate, μ_m	$9.0 \times 10^{-5} \mu\ M$ per day
EC maturation parameter, λ	4
EC elongation parameter, k_e	2.66×10^{-3}mm $\cdot\ \mu$M
VEGF threshold value for EC proliferation, c_p	$3.33 \times 10^{-4} \mu$M
EC elongation parameter, α_1	$8.85 \times 10^{-4} \mu$M
EC maturation parameter, α_2	$10^{-3} \mu$M
EC maturation parameter, α_3	$3.33 \times 10^{-4} \mu$M
EC proliferation parameter, α_4	$3.33 \times 10^{-5} \mu$M
ECM conductivity parameter, k_{cond}	$^* N(1, 0.1)$
ECM anisotropy parameter, k_a	$^* U(1, 20)$

$N(p, q)$ means normal random variable with mean p and variance q.
$U(p, q)$ means uniform random variable between p and q

The results of the simulation are shown in Figs. 7.3–7.5. The vasculature extends halfway at Day 4 (Fig. 7.3a), reaches the lesion at Day 7 (Fig. 7.3b), and gives rise to the brush-border effect. The EC maturity is higher at the roots than that at the tips on both Days 4 and 7, which is the same as the distribution of Ang1, but opposite to Ang2. Note that the spatial distributions of Ang1 and Ang2 in Fig. 7.4 agree with the patterns of Ang1 and Ang2 transcripts in the vascular remodeling of rat ovary (Maisonpierre et al. 1997), respectively.

Figure 7.5 shows the evolution of these quantities on one specific sprout. At Day 4, the sprout reaches a length of 1.08 mm, and all the cells have a relatively low and uniform quiescent level and Ang1 concentration, but have a very high Ang2 concentration, thus, they are actively proliferating. At Day 7, the sprout reaches the lesion and the cells near the limbus are of high quiescent level (close to 1), consistent with the high value of Ang1 and low value of Ang2. But the cells in the front still maintain low values of quiescence and Ang1 but high level of Ang2, thus proliferate actively.

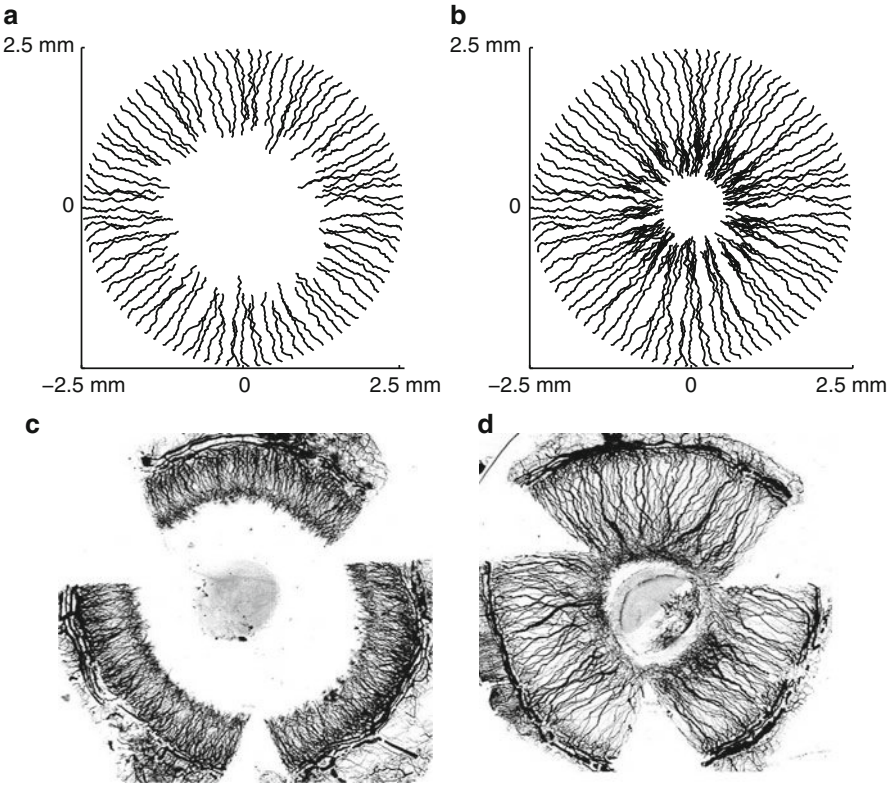

Fig. 7.3 Corneal angiogenesis (Reproduced from Jackson and Zheng (2010) with permission from Springer). *Left column*: Day 4. *Right column*: Day 7. (**a**) At Day 4, 90 sprouts with average length 1.06 mm. (**b**) At Day 7,336 sprouts with average length 1.84 mm. (**c**)&(**d**): experimental results (Reproduced from Thompson et al. (2003) with permission from Wiley–VCH Verlag GmbH & Co. KgaA.)

6 Conclusion

Correctly understanding the endothelial cell migration, proliferation, and maturation mechanisms is prerequisite to battling against angiogenesis-related diseases, including cancer. This is a big challenge because these mechanisms are regulated by a large amount of different growth factor families and various cell species.

In this chapter, we met this challenge by presenting a cell-based angiogenesis model, which has two prominent features. The first is a viscoelastic model of ECs, which are tightly connected by cell–cell adhesions, in a developing sprout. Thus, the whole vasculature is regarded as a spring network. The tip cell generates the protrusion force that drags the trailing sprout, but only a limited distance dictated by elasticity. Therefore, without new cells added by proliferation, sprouts can only extend to a limited length. The second main feature is the introduction of

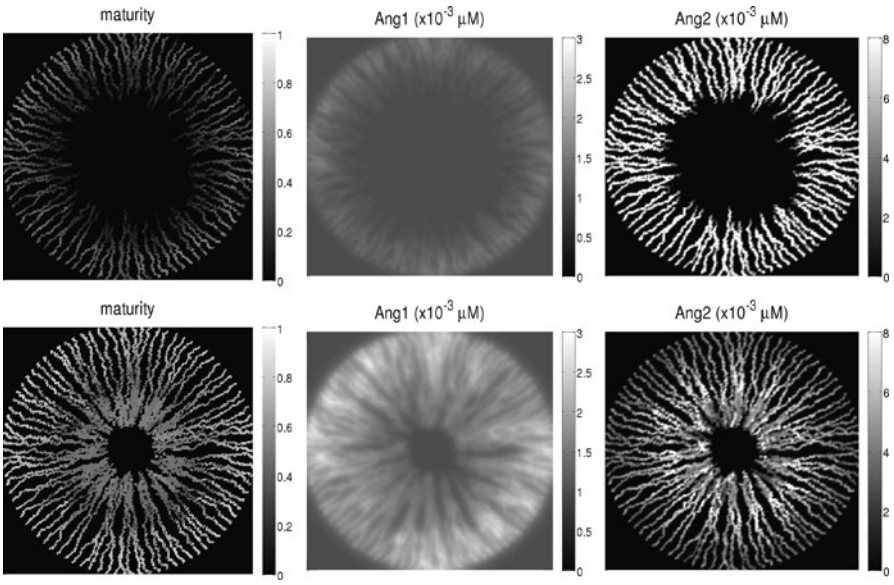

Fig. 7.4 Corneal angiogenesis (Reproduced from Jackson and Zheng (2010) with permission from Springer). *First row*: Day 4. *Second row*: Day 7. *First column*: maturity level. *Second column*: Ang1 concentration. *Third column*: Ang2 concentration

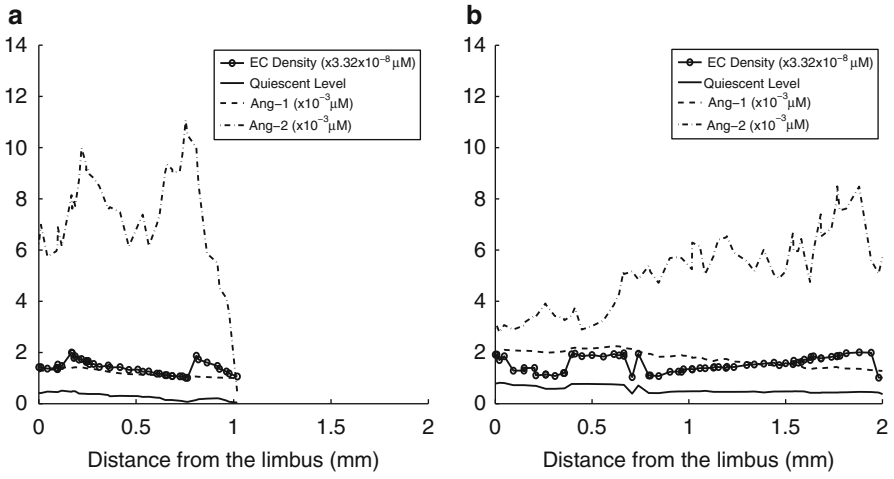

Fig. 7.5 Quantities on a sprout at Day 4 (**a**) and Day 7 (**b**): EC density (*circled line*), quiescent level (*solid line*), Ang1 (*dashed line*) and Ang2 (*dashdot line*). Reproduced from Jackson and Zheng (2010) with permission from Springer

the maturation process modulated by angiopoietins. Our results indicate that the maturation process can explain why the endothelial cells at the leading edge of vasculature are more proliferatively active than those at the rear. Therefore, this model provides biophysically and biochemically reasonable interpretations to the two critical experimental observations in Sholley et al. (1984), which are mentioned at the beginning of this chapter.

References

M.M. Sholley, G.P. Ferguson, H.R. Seibel, J.L. Montour, and J.D. Wilson. Mechanisms of neovascularization. Vascular sprouting can occur without proliferation of endothelial cells. *Lab. Invest.*, 51:624–634, 1984.

L.J. Thompson, F. Wang, A.D. Proia, K.G. Peters, B. Jarrold, and K.D. Greis. Proteome analysis of the rat cornea during angiogenesis. *Proteomics*, 3:2258–2266, 2003.

D.H. Ausprunk and J. Folkman. Migration and proliferation of endothelial cells in preformed and newly-formed blood vessels during tumor angiogenesis. *Microvasc. Res.*, 14:53–65, 1977.

D. Balding and D.L.S. McElwain. A mathematical model of tumor-induced capillary growth. *J. Theor. Biol.*, 114:53–73, 1985.

H.M. Byrne and M.A.J. Chaplain. Mathematical models for tumour angiogenesis: Numerical simulations and nonlinear wave solutions. *Bull. Math. Biol.*, 57:461–486, 1995.

H.M. Byrne and M.A.J. Chaplain. Explicit solutions of a simplified model of capillary sprout growth during tumor angiogenesis. *Appl. Math. Lett.*, 9:69–74, 1996.

A.R.A. Anderson and M.A.J. Chaplain. A mathematical model for capillary network formation in the absence of endothelial cell proliferation. *Appl. Math. Lett.*, 11:109–114, 1998.

A.R.A. Anderson and M.A.J. Chaplain. Continuous and discrete mathematical models of tumor-induced angiogenesis. *Bull. Math. Biol.*, 60:857–900, 1998.

H.A. Levine, S. Pamuk, B.D. Sleeman, and M. Nilsen-Hamilton. Mathematical modeling of capillary formation and development in tumor angiogenesis: Penetration into the stroma. *Bull. Math. Biol.*, 63:801–863, 2001.

B.D. Sleeman and I.P. Wallis. Tumour induced angiogenesis as a reinforced random walk: modeling capillary network formation without endothelial cell proliferation. *J. Math. Comp. Modeling*, 36:339–358, 2002.

M.J. Plank and B.D. Sleeman. A reinforced random walk model of tumor angiogenesis and anti-angiogenesis strategies. *IMA J. Math. Med. Biol.*, 20:135–181, 2003.

M.J. Plank and B.D. Sleeman. Lattice and non-lattice models of tumour angiogenesis. *Bull. Math. Biol.*, 66:1785–1819, 2004.

M.J. Plank, B.D. Sleeman, and P.F. Jones. A mathematical model of tumour angiogenesis, regulated by vascular endothelial growth factor and the angiopoietins. *J. Theor. Biol.*, 229:435–454, 2004.

H.A. Levine and M. Nilsen-Hamilton. Angiogenesis-A Biochemial/Mathematical Perspective. In Aver Friedman, editor, *Tutorials in Mathematical Biosciences III*, number 1872 in Lecture Notes in Mathematics, chapter 2, page 65. Springer, 2006.

C.L. Stokes and D.A. Lauffenburger. Analysis of the roles of microvessel endothelial cell random mobility and chemotaxis in angiogenesis. *J. Theor. Biol.*, 152:377–403, 1991.

S. Tong and F. Yuan. Numerical simulations of angiogenesis in the cornea. *Microvasc. Res.*, 61:14–27, 2001.

S. Sun, M.F. Wheeler, M. Obeyesekere, and C. Patrick. A deterministic model of growth factor-induced angiogenesis. *Bull. Math. Biol.*, 67:313–337, 2005.

J.L. Gevertz and S. Torquato. Modeling the effects of vasculature evolution on early brain tumor growth. *J. Theor. Biol.*, 243:517–531, 2006.

F. Milde, M. Bergdorf, and P. Koumoutsakos. A hybrid model for three-dimensional simulations of sprouting angiogenesis. *Biophysical Journal*, 95:3146–3160, 2008.

S.M. Peirce, E.J. Van Gieson, and T.C. Skalak. Multicellular simulation predicts microvascular patterning and in silico tissue assembly. *The FASEB Journal*, Feb 2004.

A. Bauer, T. Jackson, and Y. Jiang. A cell-based model exhibiting branching and anastomosis during tumor-induced angiogenesis. *Biophysical Journal*, 92:3105, 2007.

A. Qutub and A. Popel. Elongation, proliferation & migration differentiate endothelial cell phenotypes and determine capillary sprouting. *BMC Systems Biology*, 3(1):13, 2009.

N. Mantzaris, S. Webb, and H.G. Othmer. Mathematical modeling of tumor-induced angiogenesis. *J. Math Biol.*, 49:111–187, 2004.

T. Jackson and X. Zheng. A cell-based model of endothelial cell migration, proliferation and maturation during corneal angiogenesis. *Bull. Math. Biol.*, 72:830–868, 2010.

C.E. Semino, R.D. Kamm, and D.A. Lauffenburger. Autocrine EGF receptor activation mediates endothelial cell migration and vascular morphogenesis induced by VEGF under interstitial flow. *Exp. Cell Res.*, 312:289–298, 2006.

H. Gerhardt, M. Golding, M. Fruttiger, C. Ruhrberg, A. Lundkvist, A. Abramsson, M. Jeltsch, C. Mitchell, K. Alitalo, D. Shima, and C. Betsholtz. VEGF guides angiogenic sprouting utilizing endothelial tip cell filopodia. *J Cell Biol.*, 162, 2003.

F. De Smet, I. Segura, K. De Bock, P.J. Hohensinner, and P. Carmeliet. Mechanisms of vessel branching: Filopodia on endothelial tip cells lead the way. *Arterioscler Thromb Vasc Biol*, 29(5):639–649, 2009.

L.E. Benjamin, D. Golijanin, A. Itin, D. Pode, and E. Keshet. Selective ablation of immature blood vessels in established human tumors follows vascular endothelial growth factor withdrawal. *J. Clin. Invest.*, 103(2):159–165, 1999.

A.W. Griffioen and J. Molema. Angiogenesis: Potentials for pharmacologic intervention in the treatment of cancer, cardiovascular diseases, and chronic inflammation. *Pharmacol.Rev.*, 52(2):237–268, 2000.

S. Davis, T.H. Aldrich, P.F. Jones, A. Acheson, D.L. Compton, V. Jain, T.E. Ryan, J. Bruno, C. Radziejewski, P.C. Maisonpierre, and G.D. Yancopoulos. Isolation of angiopoietin-1, a ligand for the Tie2 receptor, by secretion-trap expression cloning. *Cell*, 87(7):1161–1169, 1996.

P.C. Maisonpierre, C. Suri, P.F. Jones, S. Bartunkova, S.J. Wiegand, C. Radziejewski, D. Compton, J. McClain, T.H. Aldrich, N. Papadopoulos, T.J. Daly, S. Davis, T.N. Sato, and G.D. Yancopoulos. Angiopoietin-2, a natural antagonist for Tie2 that disrupts in vivo angiogenesis. *Science*, 277:55–60, 1997.

H.G. Augustin, G. Young Koh, G. Thurston, and K. Alitalo. Control of vascular morphogenesis and homeostasis through the angiopoietin-tie system. *Nat Rev Mol Cell Biol*, 10(3):165–177, 2009.

B. Witzenbichler, P.C. Maisonpierre, P. Jones, G.D. Yancopoulos, and J.M. Isner. Chemotactic properties of angiopoietin-1 and -2, ligands for the endothelial-specific receptor tyrosine kinase Tie-2. *J. Biol. Chem.*, 273:18514–18521, 1998.

M. Scharpfenecker, U. Fiedler, Y. Reiss, and H.G. Augustin. The Tie-2 ligand Angiopoietin-2 destabilizes quiescent endothelium through an internal autocrine loop mechanism. *J. Cell Sci.*, 118:771–780, 2005.

T. Ashara, D. Chen, T. Takahashi, K. Fujikawa, M. Kearney, M. Magner, G.D. Yancopoulos, and J.M. Isner. Tie-2 receptor ligands, angiopoietin-1 and angiopoietin-2, modulate VEGF-induced postnatal neovascularisation. *Circ. Res.*, 83:233–240, 1998.

L. Edelstein-Keshet. *Mathematical Models In Biology*. McGraw-Hill Companies, 1998.

A.R.A. Anderson, M.A.J. Chaplain, and K.A. Rejniak, editors. Mathematics and Biosciences in Interaction. Birkhauser Verlag Basel/Switzerland, 2007.

K. Larripa and A. Mogilner. Transport of a 1d viscoelastic actin-myosin strip of gel as a model of a crawling cell. *Physica A*, 372:113–123, 2006.

K.D. Costa, A.J. Sim, and F.C. Yin. Non-hertzian approach to analyzing mechanical properties of endothelial cells probed by atomic force microscopy. *Journal of Biomechanical Engineering*, 128(2):176–184, 2006.

O. Thoumine and A. Ott. Time scale dependent viscoelastic and contractile regimes in fibroblasts probed by microplate manipulation. *J. Cell Sci.*, 110:2109–2116, 1997.

M. Prass, K. Jacobson, A. Mogilner, and M. Radmacher. Direct measurement of the lamellipodial protrusive force in a migrating cell. *J. Cell Biol.*, 174(6):767–772, 2006.

H. Othmer and A. Stevens. Aggregation, blowup, and collapse: The ABC's of taxis in reinforced random walks. *SIAM J. Appl. Math.*, 57:1044–1081, 1997.

S. Guido and R.T. Tranquillo. A methodology for the systematic and quantitative study of cell contact guidance in oriented collagen gels. *J. Cell Sci.*, 105, 1993.

Chapter 8
Blood Flow and Tumour-Induced Angiogenesis: Dynamically Adapting Vascular Networks

Mark A.J. Chaplain, Steven R. McDougall, and Alexander R.A. Anderson

1 Introduction

Uncontrolled or excessive blood-vessel formation is an essential accompaniment to solid tumour growth, beginning with the rearrangement and migration of endothelial cells from a pre-existing vasculature and culminating in the formation of an extensive network, or bed, of new capillaries (Madri and Pratt 1986). Although the precise molecular cascades associated with a given instance of angiogenesis may differ from case to case, a common sequence of events associated with tumour-induced angiogenesis has been broadly identified and well-documented.

The process begins when the oxygen demands of cancerous cells within a solid tumour are unable to be adequately met via diffusion from nearby capillaries. These cells consequently become hypoxic and this is assumed to trigger cellular release of tumour angiogenic factors (TAFs) (Folkman and Klagsbrun 1987), which start to diffuse into the surrounding tissue and approach the endothelial cells of nearby blood vessels. These endothelial cells subsequently respond to the TAF concentration gradient by releasing a number of matrix degrading enzymes (including matrix metalloproteinases), which degrade the surrounding tissue leading to the formation of new capillary sprouts. These then migrate towards the tumour (Schoefl 1963; Ausprunk and Folkman 1977; Sholley et al. 1984) and the resulting vascular connection subsequently provides all the nutrients and oxygen required

M.A.J. Chaplain (✉)
University of Dundee, Dundee, DD1 4HN, Scotland
e-mail: Chaplain@maths.dundee.ac.uk

S.R. McDougall
Heriot-Watt University, Edinburgh, EH14 4AS, Scotland
e-mail: Steve.McDougall@pet.hw.ac.uk

A.R.A. Anderson
H. Lee Moffitt Cancer Center and Research Institute, Tampa, FL 33612, USA
e-mail: Alexander.Anderson@moffitt.org

T.L. Jackson (ed.), *Modeling Tumor Vasculature: Molecular, Cellular, and Tissue Level Aspects and Implications*, DOI 10.1007/978-1-4614-0052-3_8,

for continued tumour growth. Once the finger-like capillary sprouts have reached a certain distance from the parent vessel, they are seen to incline towards each other (Paweletz and Knierim 1989), leading to numerous tip-to-tip and tip-to-sprout fusions known as anastomoses. Such anastomoses result in the fusing of the finger-like sprouts into a network of poorly perfused loops or arcades. Following this process of anastomosis, the first signs of circulation can be recognised and from the primary loops, new buds and sprouts emerge repeating the angiogenic sequence of events and providing for the further extension of the new capillary bed.

Most modeling studies dealing with the process of angiogenesis have tended to concentrate upon the way in which the new capillary bed is initiated and migrates in response to various chemical stimuli and mechanical forces affiliated with the tumour and host tissue. However, relatively few studies have examined the important role played by blood perfusion during angiogenesis and fewer still have explored the ways in which a dynamically evolving bed architecture can affect the distribution of flow within it. This is clearly an important feature of angiogenesis, as capillary size and bed architecture are key determinants of not only oxygen delivery to the tumour during growth but also chemotherapy delivery during treatment. It is reasonable to assume that an aberrant tumour vasculature will hinder uniform delivery of therapeutic compounds to the tumour tissue.

Although there have been a number of theoretical models developed to try to better understand vascular architecture in general (Secomb 1995; Gödde and Kurz 2001; Krenz and Dawson 2002) and to examine clinical implications in a broader sense (Baish et al. 1996; El-Kareh and Secomb 1997; Jackson et al. 1999; Quarteroni et al. 2000), there have only been a small number of theoretical studies examining blood flow in tumour-induced (micro) capillary networks (McDougall et al. 2002; Alarcon et al. 2003; Stéphanou et al. 2005a,b; McDougall et al. 2006). Any therapeutic applications described in these studies have tended to focus upon the impact of bed topology on the delivery of a cytotoxic drug to a tumour and have largely neglected the important possibility of disrupting the vascular network itself. The fact that new treatments are being tailored to specifically target vascular endothelium suggests that it would be of some benefit to understand the coupling between vascular structure and perfusion more fully in this new context.

Genetically, vascular cells are more stable than tumour cells. The latter tend to mutate during chemotherapy, leading to increased levels of resistance to infused cytotoxic compounds (Munn 2003), and it is the relative genetic stability of endothelial cells that makes them ideal candidates for treatment. The vast majority of solid tumours depend upon a local blood supply for continued expansion, and so one naïve standpoint to the issue of cancer treatment may be to simply search for the most effective “capillary killer”. There are a number of difficulties with this approach, however. Firstly, tumour-induced vasculature is often composed of several different cell types – not only endothelial cells but also fibroblasts, pericytes, and even tumour cells themselves. In addition, the relative proportions of each cell type in the cellular mosaic tends to vary from tissue to tissue. Secondly, different vascular disrupting agents (VDAs) attack vascular networks in different ways. For example, combrestatins act as tubulin depolymerisation

agents and primarily attack only proliferating endothelial cells (Tozer et al. 2005), whilst other compounds act as angiogenesis inhibitors by blocking the signalling pathways associated with various growth factors (Brekken and Thorpe 2001; Izumi et al. 2002). Additional VDAs currently under investigation include compounds that affect the down-regulation of integrin activity (Kumar 2000) and the recruitment of circulating endothelial precursor cells (Rafil et al. 2002).

The fact that different VDAs target different elements of the vascular network suggests that it is not too surprising that the overall effectiveness of any one drug would be case-specific. Moreover, the wider implications of targeting only certain elements of the capillary bed are not immediately clear. However, it appears that there is one characteristic of a developing capillary network that may be correlated with VDA efficacy – namely, pericyte coverage. First described by Rouget in 1873, the pericyte is a perivascular cell that is recruited by migrating capillaries, helping to stabilise the network structure by wrapping finger-like extensions around the developing vessels. Although its ontogeny remains somewhat controversial, it is clear that the pericyte plays a vital role during angiogenesis and there is growing evidence that disrupting pericyte–endothelium interactions may inhibit tumour growth (Gee et al. 2003; Bagley et al. 2006). Moreover, it appears that VDAs that target only endothelial cells may leave behind an intact skeleton of pericytes that could act as a template for revascularisation at a later time (Mancuso et al. 2006).

In light of these issues, it is clear that the time is ripe for the development of a modeling framework that incorporates not only important feedback mechanisms associated with blood flow through evolving vascular networks but also the recruitment of pericytes during vessel maturation. This paper accordingly describes the development of such a framework and presents a range of two- and three-dimensional numerical simulations that are used to identify the main criteria required of a tumour-induced vascular network for optimised delivery of cytotoxic, anti-angiogenic, and/or anti-vascular agents. The ultimate aim of the approach is to identify a VDA-specific "plasticity window" (a time period corresponding to low pericyte density), within which a given VDA would be most effective.

The next section briefly outlines the capillary growth model used throughout this work, the precise details of which are summarised in Appendix 1. The model is an extension of that proposed earlier by Anderson and Chaplain (1998) and incorporates the important feature of matrix degrading enzyme (MDE) secretion by migrating endothelial cells. This discussion is then followed by a short précis describing the introduction of blood perfusion and vessel dilation/constriction into the model. A fuller description, including details of the algorithms used to capture the effects of blood rheology, vessel remodeling, and shear-induced vessel branching, is presented in Appendix 2. Capillary beds corresponding to different stages in the development of the fully dynamic adaptive tumour-induced angiogenesis (DATIA) model are presented. The results show the evolution of the model and demonstrate the impact of dynamic remodeling and shear-induced vessel branching upon global network architecture.

Having summarised the angiogenesis model itself, attention is next focussed upon the utilisation of the model for the simulation of various chemotherapy treatment protocols. Two- and three-dimensional results relating to the delivery of chemotherapeutic agents to the tumour surface are presented in Sect. 3: firstly via a static, uniform bed of rigid capillaries, then via a dynamically adaptive bed. Results from even the simple static model show the importance of tumour geometry and anastomosis density in determining treatment efficacy, whilst results from the full DATIA model demonstrate the impact of vessel heterogeneity within a given network. These simulations highlight the need for incorporating vessel adaptations into any angiogenesis model involving transport issues, such as chemotherapeutic intervention, and also show that three-dimensional modeling is required if quantitative predictions are to be made.

Section 4 considers the effects of anti-angiogenic and anti-vascular therapies – i.e. therapies that are specifically aimed at disrupting the vascular bed itself. These are initially modeled by means of simple "capillary pruning" algorithms that are used to approximate the key mechanisms associated with different treatments. The pruning algorithms are seen to modify the network connectivity in a number of different ways and the impact of each upon subsequent chemotherapy delivery is discussed. Finally, a model for pericyte recruitment to migrating capillaries is described and the spatial distribution of pericyte density is investigated in both two and three dimensions under a number of different model assumptions, including cases where pericyte coverage (i.e. vessel maturity) determines the degree of vessel remodeling. Results suggest that it may indeed be possible to identify a "plasticity window" that would maximise the effectiveness of a given VDA.

The chapter concludes with a discussion section summarising all the main results and offering directions for future model development and study.

2 DATIA

This section begins by briefly describing the salient features of the extended angiogenesis model (including the effects of matrix degrading enzymes) used to migrate capillary sprouts from a nearby parent vessel. This is followed by a short summary describing the way in which blood perfusion and vessel dilation/constriction mechanisms have been incorporated into the model. These extensions result in a more realistic model of the angiogenesis process that is both adaptive and dynamic, with the resulting vascular network evolving both temporally and spatially in response to a number of migratory and transport-related cues. Results are presented that they demonstrate the importance of these processes in determining global network architecture.

2.1 Capillary Migration in the Absence of Flow

The dynamic capillary migration model presented in this paper explicitly takes into account the important function of matrix degrading enzymes (such as matrix metalloproteinases, MMPs; urokinase plasminogen activators, uPAs) during angiogenesis in the absence of flow (Levine et al. 2001). Mediation in vessel growth via extracellular matrix proteolysis by specific enzymes produced by endothelial cells is also included. A number of recent publications have demonstrated the importance of enzymes from the MMP family and their involvement in the regulation of the various stages of the angiogenic process (Davis et al. 2000; Yan et al. 2000; Hidalgo and Eckhardt 2001; Sternlicht and Werb 2001). These MMPs are involved in the migration of endothelial cells within the extracellular matrix, the endothelial cell proliferation, and the remodeling of the basement membrane of newly formed vessels. Their importance is such that these proteinases and their regulation form new targets for cancer treatment. As our ultimate goal is to propose a global modeling framework within which to further investigate new treatments, it is important to incorporate the MMP effect into the modeling.

All of the vasculatures presented in this paper were generated using a hybrid discrete-continuum model inspired by the tumour-induced angiogenesis model proposed by Anderson and Chaplain (1998). It should be noted that the vasculatures shown throughout this chapter correspond to *additional* vessels generated in response to tumour hypoxia: we assume that a pre-existing background vascular network has existed prior to the angiogenic response and that this has already provided sufficient nutrients and oxygen for the tumour to have grown to a pre-vascularised size. The model assumes that endothelial cells at the tips of the new capillary sprouts (vessels) migrate through (1) random motility, (2) chemotaxis in response to tumour angiogenic factors (TAF) released by the tumour and (3) haptotaxis in response to fibronectin (FN) gradients in the extracellular matrix. A (non-dimensional) equation describing endothelial cell (n) conservation is used to produce movement weightings for discrete tip cells as they leave the parent vessel (see Appendix 1 and Fig. 8.23). The equation is given by:

$$\frac{\partial n}{\partial t} = \overbrace{D\nabla^2 n}^{\text{random}} - \overbrace{\nabla\cdot(\chi(c)n\nabla c)}^{\text{chemotaxis}} - \overbrace{\rho\nabla\cdot(n\nabla f)}^{\text{haptotaxis}}. \tag{8.1}$$

In addition to an equation for endothelial cell density, the model also requires equations governing the evolution of angiogenic factor (c), MDE (m) and the matrix-bound protein associated with the haptotactic response (fibronectin in this case, denoted by f). For the TAF, it is assumed that a (quasi) steady state distribution already exists in the matrix, the TAF having initially been secreted by the tumour cells. As the endothelial cells migrate through the tissue, there is some binding of the TAF to the cells and this is modeled with a simple uptake term that is switched on locally in the presence of a migrating tip cell. Fibronectin exists in the matrix in bound form and therefore there is no diffusion term for fibronectin.

Endothelial cells are known to produce fibronectin as they migrate and also to degrade the matrix as they progress. Consequently, simple production and loss terms in the fibronectin equation are switched on wherever an endothelial tip cell exists to reflect these facts. Tumour angiogenesis factors and fibronectin are known to bind to specific membrane receptors on endothelial cells and subsequently trigger molecular cascades inside the ECs, activating cell migratory machinery. One consequence of this activation process is the production by the cells of a MDE, which enhances the attachment of the cells to fibronectin contained in the extracellular matrix. The endothelial cells are consequently able to exert the traction forces required to propel themselves during migration. This mechanism is included in the modeling by allowing individual tip cells to produce MDE locally, which then diffuses and degrades within the host tissue. With these modeling assumptions the full (non-dimensional) system of equations can be defined as:

$$\begin{aligned}
\frac{\partial c}{\partial t} &= -\eta\, n_k\, c, \\
\frac{\partial f}{\partial t} &= \beta\, n_k - \gamma\, m\, f, \\
\frac{\partial m}{\partial t} &= \alpha\, n_k + \varepsilon \nabla^2 m - \nu\, m,
\end{aligned} \tag{8.2}$$

where c represents the TAF concentration, f the FN concentration, m the MDE density and n_k a Boolean value (1 or 0) that indicates the presence or absence of an endothelial cell at a given position. Details of other parameters, together with a brief explanation of the hybrid modeling approach and algorithms for sprout branching and anastomosis are given in Appendix 1.

2.2 Capillary Migration Incorporating Flow

Having extended the migration model to account for the key biochemical interactions characterising the angiogenesis process, attention next turns to the incorporation of perfusion-related mechanisms. Previous approaches examining flow through tumour-induced networks by McDougall et al. (2002) and Stéphanou et al. (2005a) had made the rather limiting assumptions of constant capillary radius and invariant blood viscosity, whereas, in reality, biological structures tend to exhibit some degree of compliance and blood is non-Newtonian. This earlier formulation must be therefore extended to account for variable blood viscosity and evolving capillary vessels that may either dilate or constrict both spatially and temporally. The details of how this has been achieved, including a discussion related to the different timescales associated with endothelial cell migration and capillary flow processes, are available in McDougall et al. (2006) and will only be briefly summarised here.

2.2.1 Blood Rheology

Because of its biphasic nature, blood does not behave as a continuum and the viscosity measured while flowing at different rates in microvessels is not constant. Moreover, direct measurement of blood viscosity in living microvessels is very difficult to achieve with any degree of accuracy. Pries et al. (1996) have proposed an alternative approach, which involves "history matching" the flow distribution in a numerical network (generated by a mathematical model) with similar experimental systems. The relationship which was found to offer the best fit with the experimental data at the microvascular scale, is given by:

$$\mu_{\mathrm{rel}}(R, H_{\mathrm{D}}) = \left[1 + (\mu_{0.45} - 1) f(H_{\mathrm{D}}) \left(\frac{2R}{2R - 1.1}\right)^2\right] \left(\frac{2R}{2R - 1.1}\right)^2, \quad (8.3)$$

where $\mu_{0.45}$ is the viscosity corresponding to the normal average value of the discharge haematocrit ($H_{\mathrm{D}} = 0.45$), R the vessel radius and $f(H_{\mathrm{D}})$ a function of the haematocrit. The various terms appearing in (8.3) are defined as follows:

$$\begin{aligned} \mu_{0.45} &= 6e^{-0.17R} + 3.2 - 2.44e^{-0.06(2R)^{0.645}}, \\ f(H_{\mathrm{D}}) &= \frac{(1 - H_{\mathrm{D}})^C - 1}{(1 - 0.45)^C - 1}, \\ C &= (0.8 + e^{-0.15R}) \left(-1 + \frac{1}{1 + 10^{-11}(2R)^{12}}\right) + \left(\frac{1}{1 + 10^{-11}(2R)^{12}}\right). \end{aligned} \quad (8.4)$$

The relative viscosity defined by (8.3) and (8.3) has been used in an extended form of Poiseuille's law at the scale of a single capillary. Of course, this is only one particular formulation of relative viscosity and any well-founded local flow/pressure-drop relationship could easily be incorporated into the model if alternatives emerge from future experimental studies. The methodology used to model perfusion within a developing network is described more fully in McDougall et al. (2002) and summarised in Appendix 2.

2.2.2 Vessel Adaptation

Blood rheological properties and microvascular network remodeling are interrelated issues, as blood flow creates stresses on the vascular wall (shear stress, pressure, tensile stress) which lead to adaptation of the vascular diameters via either vasodilatation or constriction. In turn, blood rheology (viscosity, haematocrit, etc.) is affected by the new network architecture – consequently, adaptive angiogenesis should be expected to be a highly dynamic process. In this paper, vessel adaptation follows the treatment of Pries et al. (1995, 1998, 2001a) and considers a number

of stimuli affecting vessel diameter that account for the influence of the wall shear stress (S_{wss}), the intravascular pressure (S_{p}), and a metabolic mechanism depending on the blood haematocrit (S_{m}). These stimuli form a basic set of requirements in order to obtain stable network structures with realistic distributions of vessels diameters and flow velocities. The equation used for radial variation as a function of these stimuli is as follows:

$$\Delta R = \left[\underbrace{\log\left(\tau_w + \tau_{\text{ref}}\right)}_{S_{\text{wss}}} - \underbrace{k_p \log \tau_e(P)}_{S_{\text{p}}} + \underbrace{k_m \log\left(\frac{Q_{\text{ref}}}{QH_D} + 1\right)}_{S_{\text{m}}} - k_s \right] R \Delta t. \quad (8.5)$$

The various terms used in (8.3) are described more fully in McDougall et al. (2006) and a brief summary is supplied in Appendix 2, along with details of a modified branching algorithm that accounts for vessel branching in areas of heightened wall shear stress.

2.3 *Vascular Network Comparisons*

A comparison of the final vasculatures resulting from the different stages of the model development is shown in Fig. 8.1 (2D) and Fig. 8.2 (3D). Figure 8.1a shows a 2D network resulting from the simple migration model, without any flow-related remodeling, whilst Fig. 8.1b demonstrates the effect of dynamic remodeling after growth. Although the overall architectures from the static and a posteriori remodeled approaches are similar, the dilated backbone apparent in the remodeled network will clearly play a dominant role in determining drug delivery to the tumour surface (as will be shown in the next section). Hence, it seems reasonable to infer that the effect of capillary remodeling should be incorporated into angiogenesis models at this scale if transport issues are to be addressed.

Of course, restricting the remodeling of a capillary bed until after migration is complete is rather artificial, as blood perfusion begins soon after the first capillary arcade has formed. In reality, bed remodeling and capillary dilation/constriction occur as immediate consequences of primary anastomosis and the network resulting from this approach is shown in Fig. 8.1c. The effect of increased vessel branching in areas of high wall shear stress modifies the bed topology, leading to the formation of dilated arcades closer to the parent vessel accompanied by an overall increase in capillary density. The implications for therapeutic delivery of coupling capillary growth and radial adaptation will be discussed in the following section.

In addition to radial adaptation, the dimensionality of the capillary network itself will also be shown to have a large impact upon treatment delivery. The architecture comparison shown in Fig. 8.2 suggests that drug bypassing could be even more of an issue in three dimensions, with the dilated backbone (Fig. 8.2c) branching into many

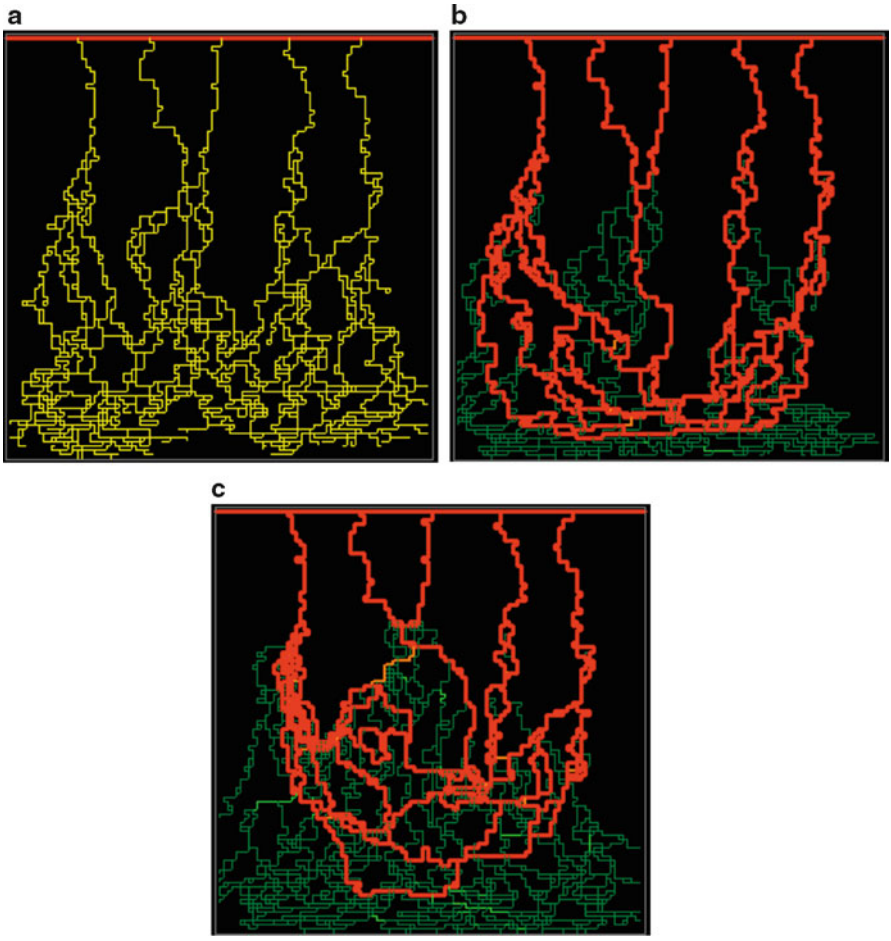

Fig. 8.1 2D capillary networks formed as endothelial sprouts migrate from a parent vessel at the upper boundary of the domain through the extracellular matrix in response to gradients in TAF (chemotaxis) and FN (haptotaxis). Growth complete after approximately 16 days. (**a**) Simple migration model without flow-induced remodeling of the capillaries; (**b**) a posteriori remodeling after growth; (**c**) full DATIA model, including shear-stress-induced branching. Radii vary from 12 μm (*red*) to 6 μm (*yellow*) to 2 μm (*green*)

alternative directions and forming a dense brush border as the tumour periphery is approached. It would be reasonable to anticipate that delivery using 2D models would overestimate delivery considerably and that 3D models should be used for quantitative comparisons with experiment.

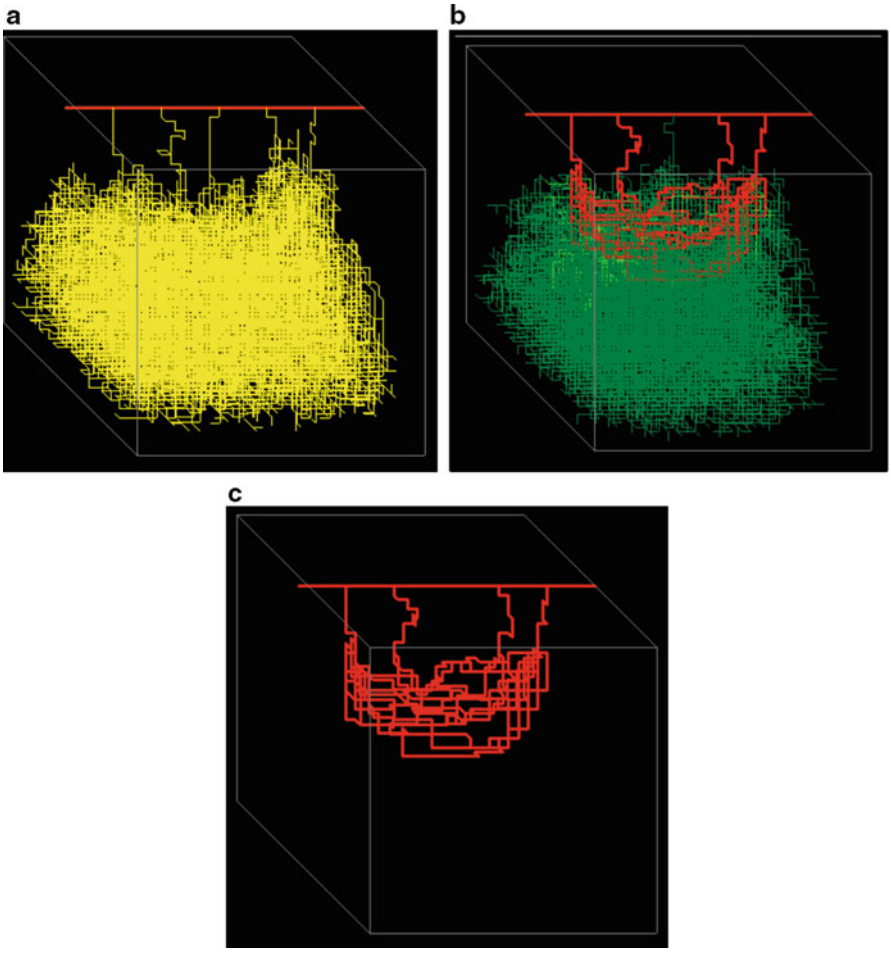

Fig. 8.2 3D capillary networks formed as endothelial sprouts migrate from a parent vessel at the upper face of the domain through the extracellular matrix. (**a**) Simple migration model without flow-induced remodeling of the capillaries; (**b**) full DATIA model, including shear-stress-induced branching; (**c**) the dilated backbone isolated from (**b**). Radii vary from 12 μm (*red*) to 6 μm (*yellow*) to 2 μm (*green*)

3 Chemotherapy Delivery to the Tumour Periphery

As a first attempt towards modeling the flow of chemotherapy drugs through tumour-induced vascular networks, an algorithm was developed to track concentration profiles of a generic tracer (drug) injected into the upstream end of the parent vessel. Initially, a constant viscosity was assumed for the circulating fluid, although this assumption was later relaxed when blood rheological properties were taken into account. In both instances, however, tracer concentrations were updated as follows.

Firstly, nodal pressures and elemental flows were calculated within the tortuous network structure as described in Appendix 2. At each timestep, the following procedure was adopted:

1. The total amount of drug flowing into each node was calculated.
2. Perfect mixing was assumed at each node and new drug concentrations were calculated for all outflow vessels based upon the updated nodal values.

It should be noted that the time-step required when dealing with calculations involving convective transport within a network must be less than or equal to the minimum time required for the least efficient capillary element in the network to empty; i.e. $\Delta t = \text{MIN}(V_{\text{cap}}/Q_{\text{cap}})$, where V_{cap} and Q_{cap} correspond to the volume and flow of a capillary element. This procedure ensures that mass is conserved during a simulation. In the simulations described later, the lower edge of the domain is taken to represent the tumour periphery and it is assumed that any drug reaching this lower boundary is effectively delivered to the tumour mass itself. Of course, this is not strictly correct, as the pressure distribution within the tumour (as well as the resident vasculature network) will determine the actual degree of drug uptake. Hence, even the low uptake values shown later should be considered as maximum achievable cytotoxic doses.

The investigation of chemotherapeutic delivery to the tumour periphery begins with flow simulations on a static capillary bed comprising identical, rigid cylindrical vessels.

3.1 Chemotherapy Delivery via Static Capillary Beds

The chemotherapy simulations presented in this section were undertaken using only a static, non-adaptive capillary bed and Newtonian fluid. The first set of results corresponds to continuous drug infusion into a 2D vascular network, which was generated by a linear source of TAF lying along the lower boundary of the domain. A chemotherapy drug of concentration C_{max} was fed into the left-hand side of the parent vessel at $t = 0$ and sequential drug concentration profiles for the base case simulation are shown in Fig. 8.3. It is clear that, instead of supplying drug to the tumour, some branches actually *remove* drug from the capillary network (Fig. 8.3c), thereby reducing its efficacy. Indeed, for this set of input data, 16,800 s (4–5 h) of continuous infusion is required for a drug concentration of 0.1% C_{max} to reach the tumour.

The effect of blood viscosity upon drug delivery and uptake is evident from the results shown in Fig. 8.4a. The drug reaches the tumour sooner when the blood viscosity is decreased, as may be inferred from the inverse relationship between elemental flow and fluid viscosity, coupled with the linear nature of the pressure equations. Next, by decreasing the mean capillary radius, the effect of narrowing the capillaries on drug delivery was examined. Figure 8.4b shows the results of drug delivery into capillaries with a mean radius of 2 μm, 3 μm and 4 μm

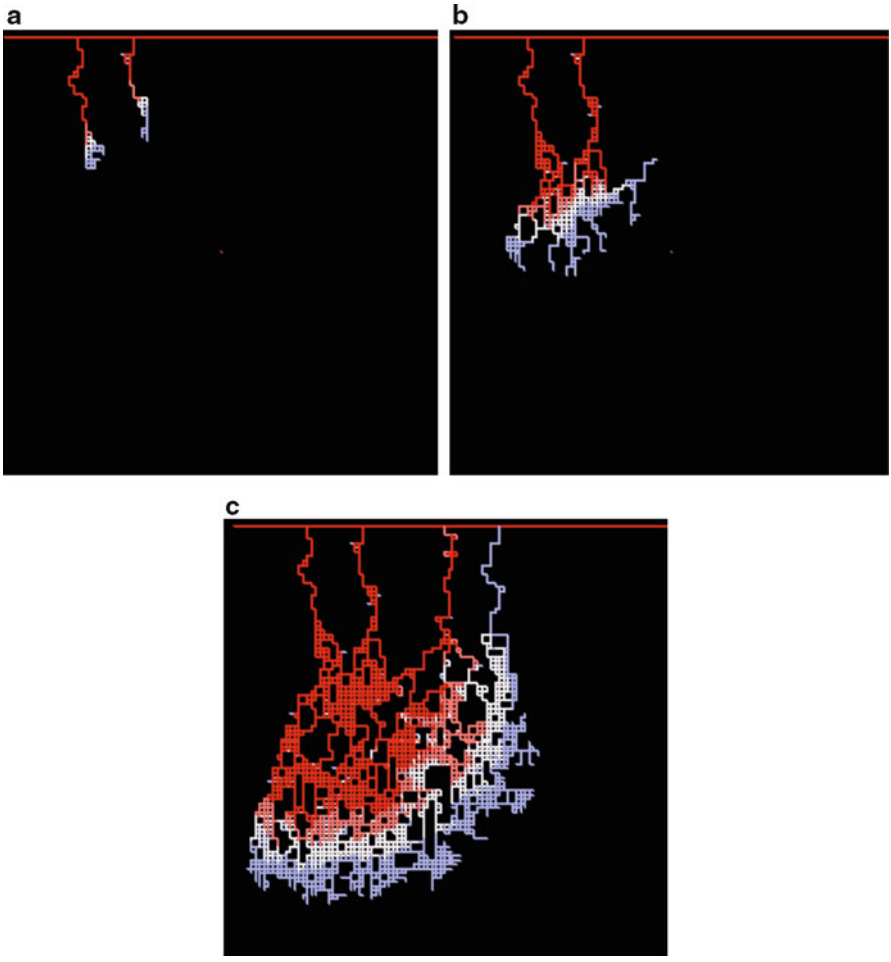

Fig. 8.3 Concentration contours for continuous infusion into a vasculature formed from a linear TAF source. 100 × 100 domain size. (**a**) $t = 240$ s, (**b**) $t = 1{,}200$ s, (**c**) $t = 7{,}200$ s. *Red* corresponds to high concentration and *blue* to low concentration

(used in the base case). As the radius decreases the flow rate and consequently drug uptake by the tumour decreases. Hence for narrower capillaries infusion would have to continue for many hours/days before significant tumour uptake could occur. The second set of results using the simple static network corresponds to a 30-s bolus injection of drug into a network formed in response to a more focussed semicircular TAF source. The rather striking drug evolution snapshots are shown in Fig. 8.5. The large number of interconnections between capillaries – even quite far from the tumour – means that there is very little flow in the lower part of the network, and the bolus of drug essentially bypasses the tumour.

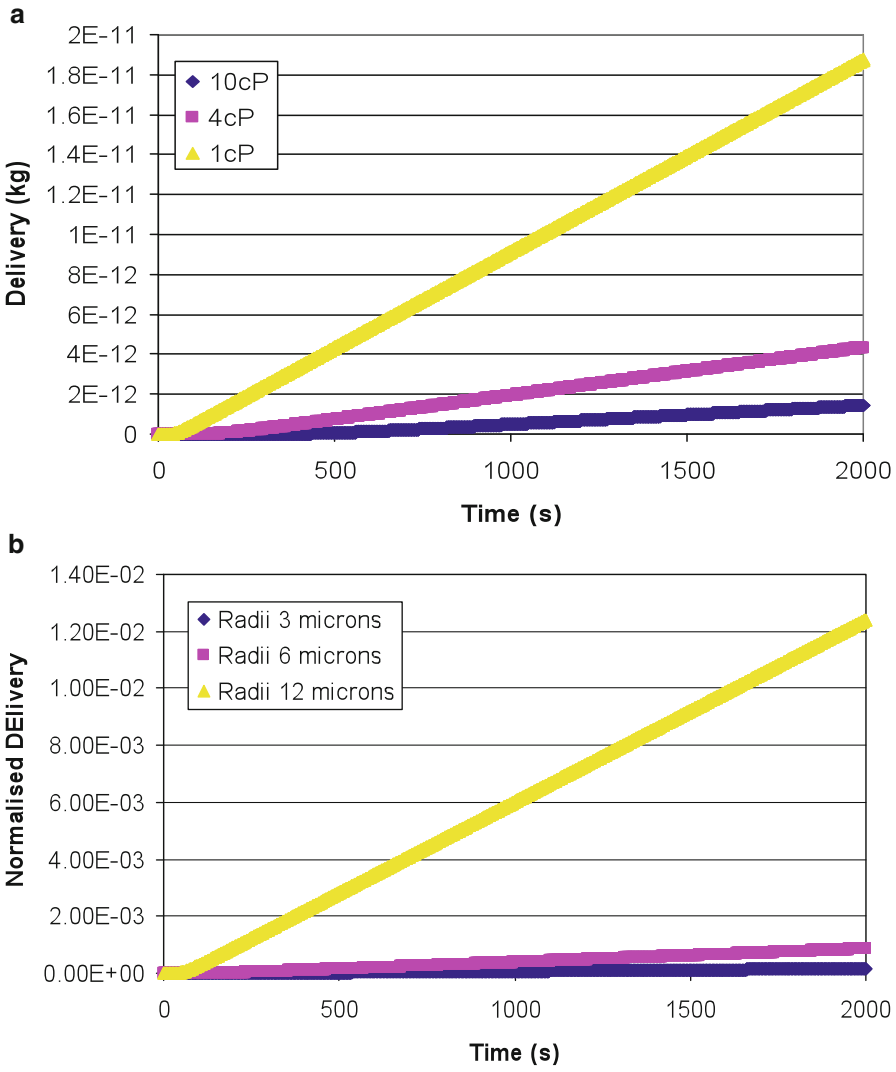

Fig. 8.4 Effect of (**a**) viscosity and (**b**) mean capillary radius, upon drug delivery – continuous infusion into a 30×30 vasculature formed from a linear TAF source. Delivery has been normalised in (**a**) to the total mass of drug injected into the parent vessel over 2,000 s

Of course, in vivo tumour-induced vasculatures grow in three dimensions, and so it is important to ascertain whether the same bypassing issues apply. The snapshots shown in Fig. 8.6 suggest that they do and a direct comparison between deliveries in a 2D and 3D system confirm this (Fig. 8.7). Delivery is two orders of magnitude lower in the 3D case. This will be revisited in the context of a fully adaptive network in the next section.

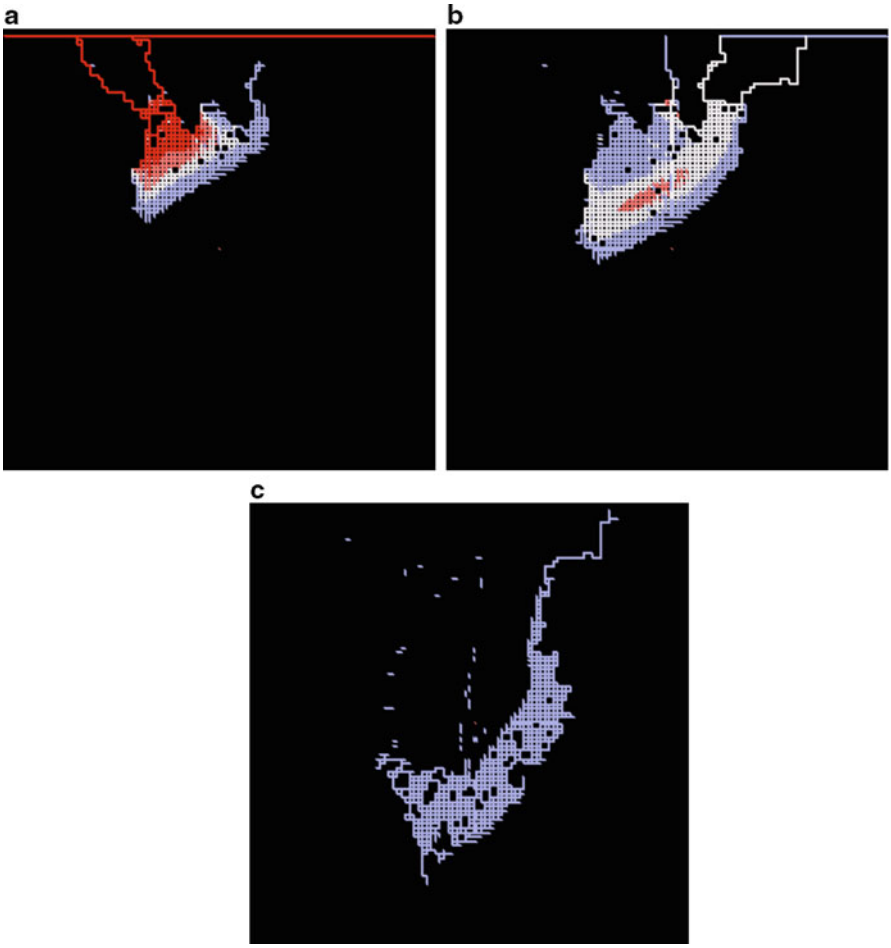

Fig. 8.5 Concentration contours for bolus injection into a vasculature formed from a semicircular TAF source at the lower domain boundary. 100×100 domain size. (**a**) $t = 1{,}200$ s, (**b**) $t = 3{,}600$ s, (**c**) $t = 62{,}400$ s. *Red* corresponds to high concentration and *blue* to low concentration

3.2 Chemotherapy Delivery via Dynamically Adaptive Capillary Beds

Results presented in this section will show the impact of dynamic remodeling and shear-induced vessel branching upon global network architecture and chemotherapeutic treatment delivery – these highlight a number of new therapeutic targets for tumour management. The initial focus will be on two-dimensional capillary beds, as results are far easier to visualise and interpret. However, quantitative analysis requires the third dimension and so some drug delivery comparisons from 3D simulations will be presented at the end of the section.

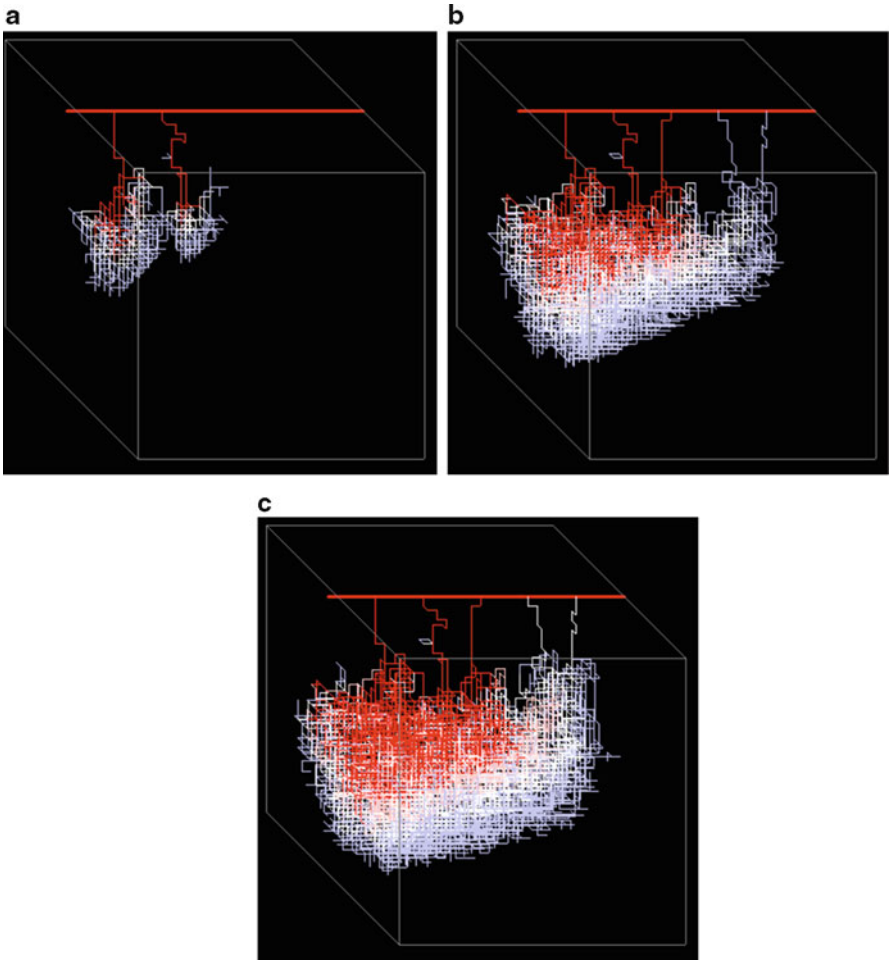

Fig. 8.6 Concentration contours for continuous infusion into a 3D vasculature formed from a linear TAF source. $30 \times 30 \times 30$ domain size. (**a**) $t = 50$ s, (**b**) $t = 500$ s, (**c**) $t = 1{,}000$ s. *Red* corresponds to high concentration and *blue* to low concentration

An example of the changes seen in bed topology due to dynamic radial adaptation was presented earlier in Fig. 8.1. The most important aspect of this example was that it demonstrated how shear-induced branching could lead to earlier formation of dilated anastomoses close to the parent vessel. However, this example is only one of many – by varying a number of physical and biochemical parameters in the model, a wide range of network heterogeneity is predicted (Fig. 8.8). Consequently, by quantifying the efficiency of these different networks in carrying blood-borne material to the tumour, it is hoped that some insights can be offered into the precise fate of chemotherapeutic agents in the vasculature during treatment and, moreover,

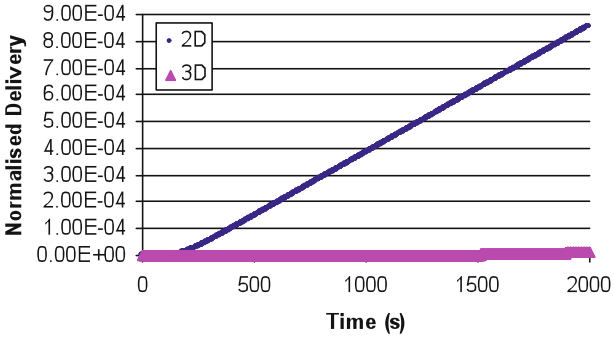

Fig. 8.7 Normalised drug delivery comparison between a 30 × 30 static 2D vascular bed and a 30 × 30 × 30 static 3D vascular bed. Delivery has been normalised to the total mass of drug injected into the parent vessel over 2,000 s

that this could lead to the identification of a number of new therapeutic targets and strategies for tumour management (for example, drug-induced normalization of tumour blood vessels, to be addressed later in Sect. 4)

In order to assess transport efficacy within a given adapted vessel network, a drug at concentration $C_{\max}$ was continuously infused into the inlet of the parent vessel for 500 s. The base-case simulation for transport utilised the vasculature shown in Fig. 8.1c. Figure 8.9 shows the tracer-drug evolution through the capillary network at a number of different times (in seconds). It is immediately clear that the bulk (in fact, almost all) of the injected tracer-drug flows through the highly conductive dilated backbone, largely by-passing the tumour and recirculating to the parent vessel. In excess of 250 s of continuous infusion is required before any tracer-drug reaches the tumour surface, and only then in very small concentrations. Figure 8.10 shows plots of the total drug mass in the system (parent vessel and capillary network) and delivery to the tumour surface as functions of time. It should be noted that all masses have been normalised to the total mass injected into the parent vessel over the course of the simulation. Only around 1.5% of the infused tracer-drug even enters the capillary network and, although the total mass in the network reaches a plateau after approximately 50 s (transport being essentially governed by steady-state flow through the dilated backbone), it takes another 200–250 s before uptake commences. This is because capillaries forming part of the brush border close to the tumour surface are narrow and poorly perfused – consequently, only a very small fraction of the injected treatment actually reaches the target. As an aside, it should be noted that, although convective transport through the vessels of the network would be a rather poor delivery mechanism for large molecules (i.e. cytotoxic treatments), the dilated network is sufficiently well-developed within a few hundred microns of the tumour surface that diffusion of nutrients (oxygen, glucose) would be relatively efficient over the timescale of tumour growth.

Figure 8.11a shows the uptake using an identical network architecture but with all capillary radii set permanently to 6 μm (the default value given at vessel birth in the

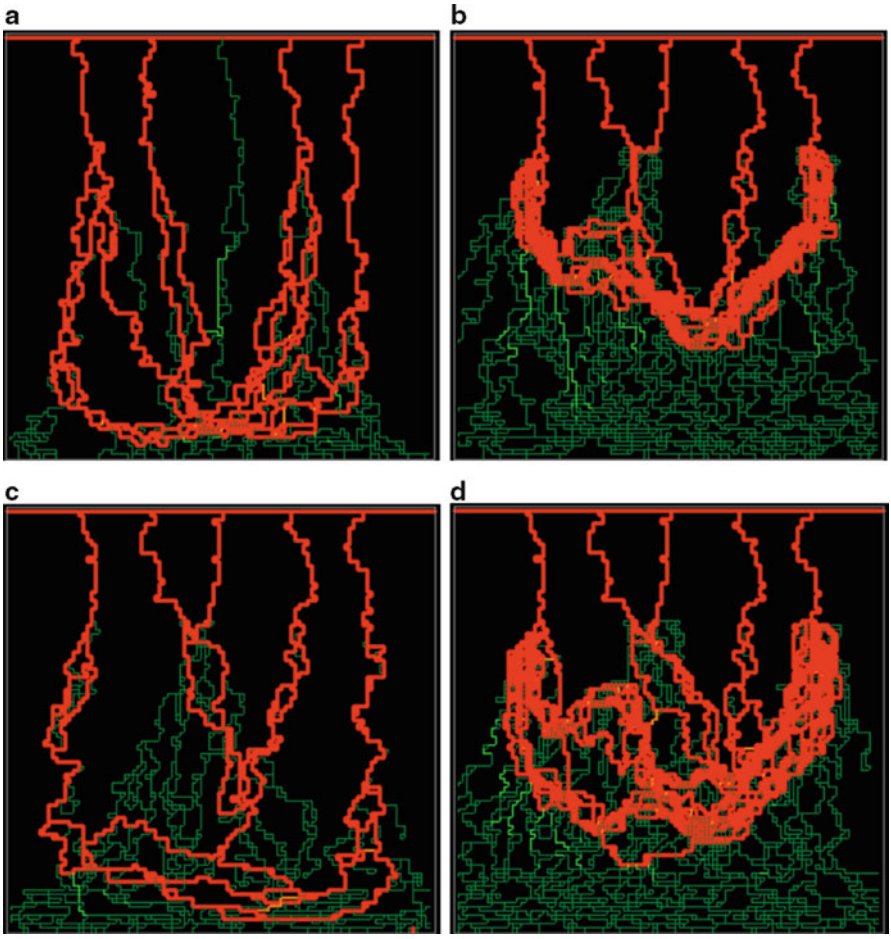

Fig. 8.8 Plots showing the different steady-state capillary network structures which have evolved after 48 days due to changes in model parameters. (**a**) reduced haptotactic coefficient $r = 0.16$; (**b**) reduced input haematocrit $H_D = 0.225$; (**c**) reduced inlet blood pressure ($P_{in} = 2{,}960$ Pa, $P_{out} = 2{,}060$ Pa); (**d**) reduced outlet blood pressure ($P_{in} = 3{,}260$ Pa, $P_{out} = 1{,}760$ Pa). Compare with the base case in Fig. 8.1c

model) – uptake values are approximately three orders of magnitude larger that those obtained from the remodeled vasculature. These results clearly demonstrate the impact of network heterogeneity upon treatment efficacy and highlight the need for incorporating vessel adaptations (dilation/constriction) into any angiogenesis model involving transport issues, such as chemotherapeutic intervention. In the absence of vessel size variation, delivery is greatly overestimated.

A possible therapeutic target identified from the simulation is the manipulation of the haptotactic response of the migrating endothelial cells during angiogenesis, characterised by reduced lateral migration of the vessels and reduced shear-induced branching (Fig. 8.8a). The tracer-drug evolution through this vessel network

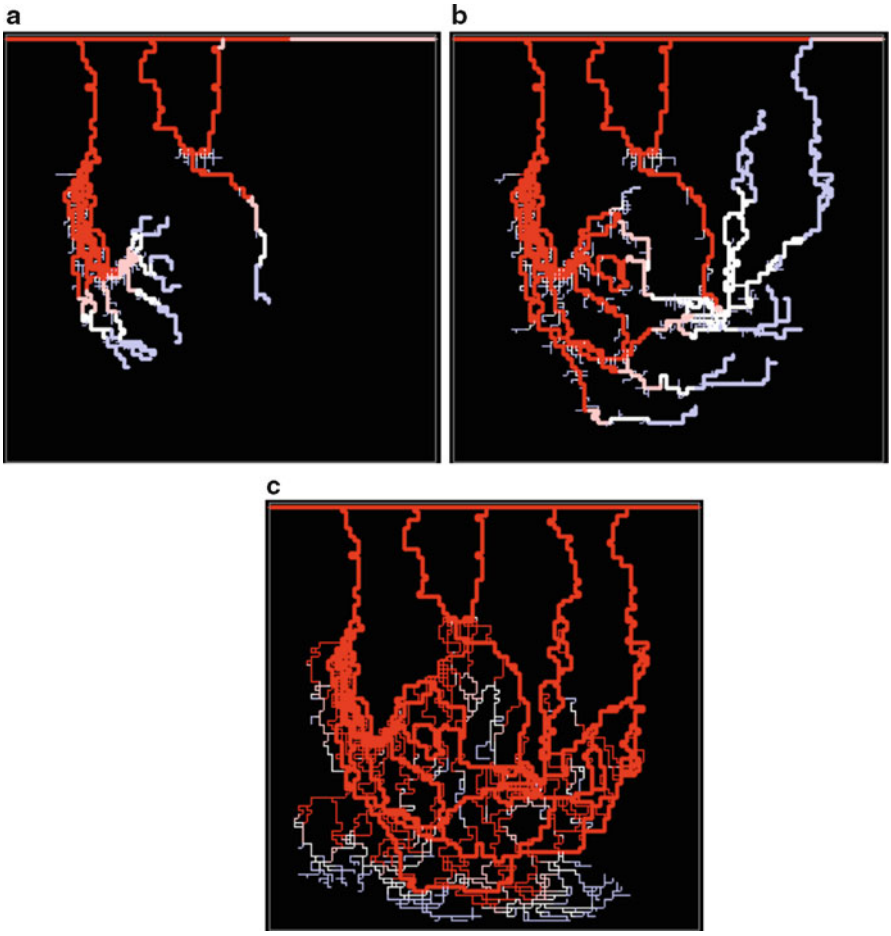

Fig. 8.9 Plots of the tracer-drug concentration distribution in the network shown in Fig. 8.1c at different times. *Red* corresponds to high concentration and *blue* to low concentration

suggests that tumours supplied by this type of vasculature would be well-supplied with nutrients and could be expected to grow rapidly. Paradoxically, however, such tumours would also be highly susceptible to infused treatments, with far more cytotoxic agent reaching the tumour than observed in previous cases. This conjecture is supported by the uptake results from the infusion simulation shown in Fig. 8.11b. Whilst the total mass of tracer-drug entering the supplying vasculature is almost identical to that observed in the base case simulation ($\rho = 0.28$, not shown), the drug uptake by the tumour *is 50 times greater* when lateral migration and vessel branching are reduced.

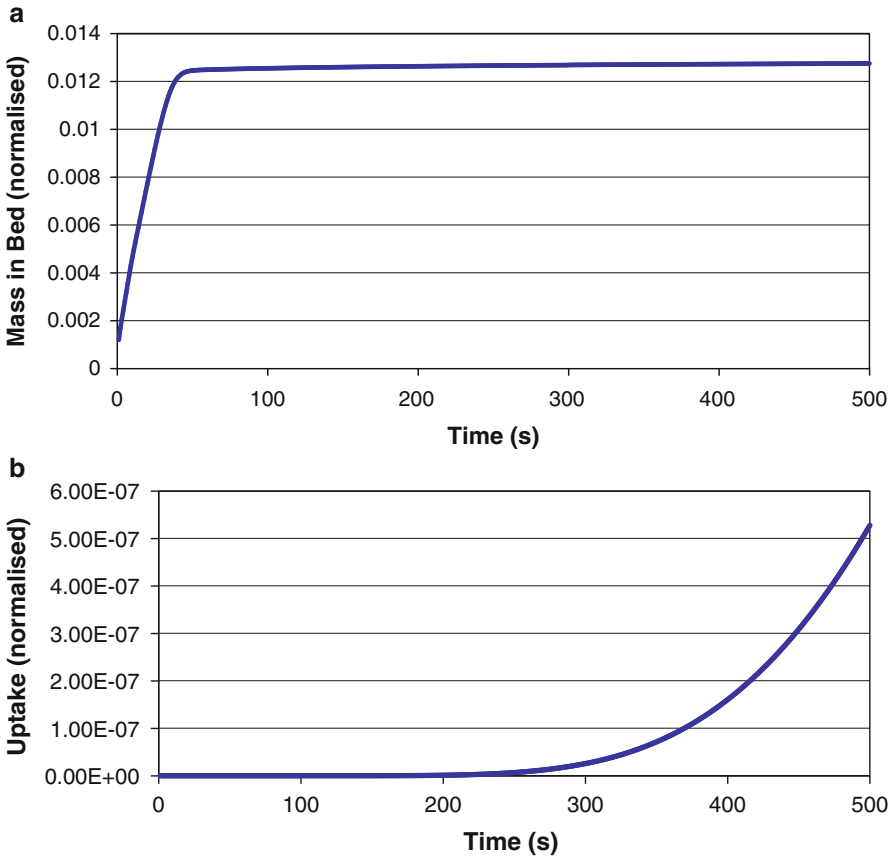

Fig. 8.10 Plots of (**a**) normalised total drug mass in parent vessel and network over time and (**b**) normalised delivery reaching the tumour

The network shown in Fig. 8.8b suggests that a depressed haematocrit can be expected to lead to the formation of highly dilated arcades close to the parent vessel and Fig. 8.11c shows the therapeutic implications of this phenomenon – more drug enters the capillary network than entered in the base-case simulation but drug delivery to the tumour *is reduced by more than three orders of magnitude*. In the context of nutrient supply to the tumour, this suggests that that a decreased local haematocrit could generate vasculatures that are detrimental to tumour growth.

Figure 8.11d shows the impact upon drug delivery of lowering the pressure at the inlet of the parent vessel by 300Pa (2.25 mmHg) prior to angiogenesis, whilst keeping the outlet pressure unchanged. Delivery is dramatically *increased* – by more than three orders of magnitude – and tumours characterised by similar vascular architectures are consequently highly likely to be vulnerable to chemotherapeutic in-

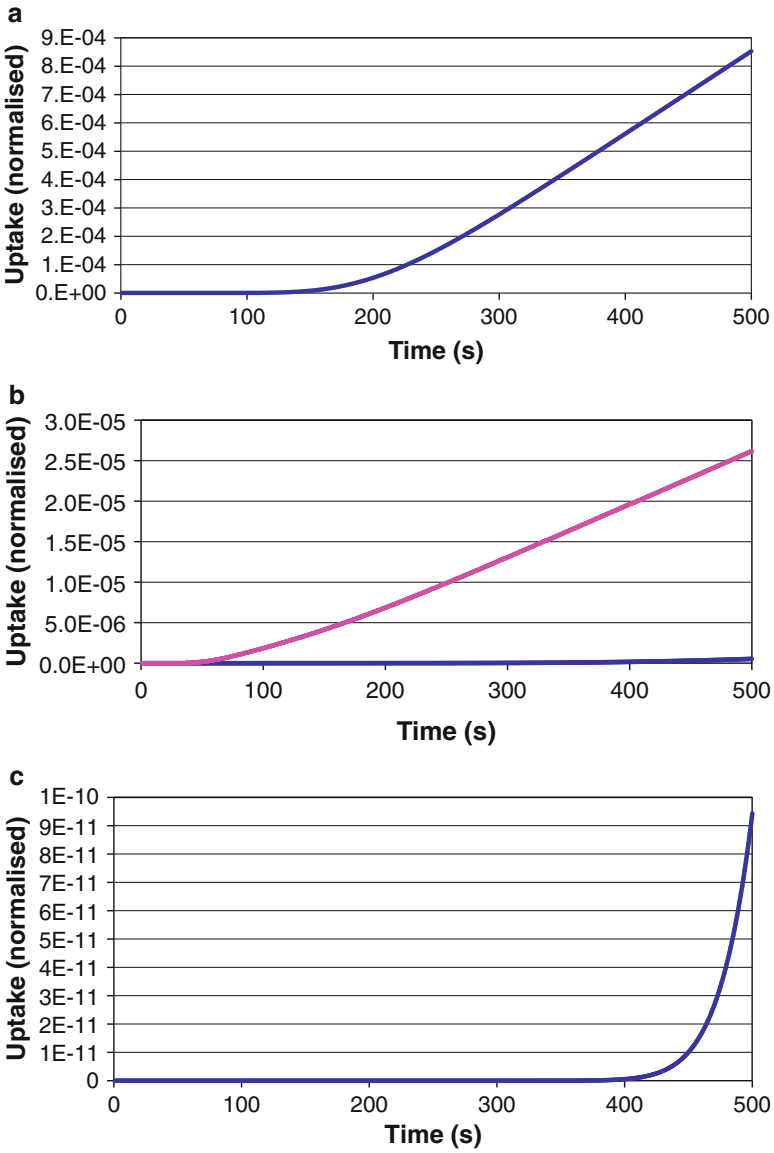

Fig. 8.11 Plot showing the amount of drug reaching the tumour over time under various model assumptions. (**a**) A network where all vessels have a fixed radius of 6 μm. Note the difference in scale compared to that of Fig. 8.10b. (**b**) The effect of varying haptotactic sensitivity (*dashed line* corresponds to $r = 0.16$, *solid line* corresponds to $r = 0.16$), (**c**) the effect of reduced input haematocrit $H_D = 0.225$, (**d**) lower pressure at inlet of parent vessel, (**e**) lower pressure at outlet of parent vessel

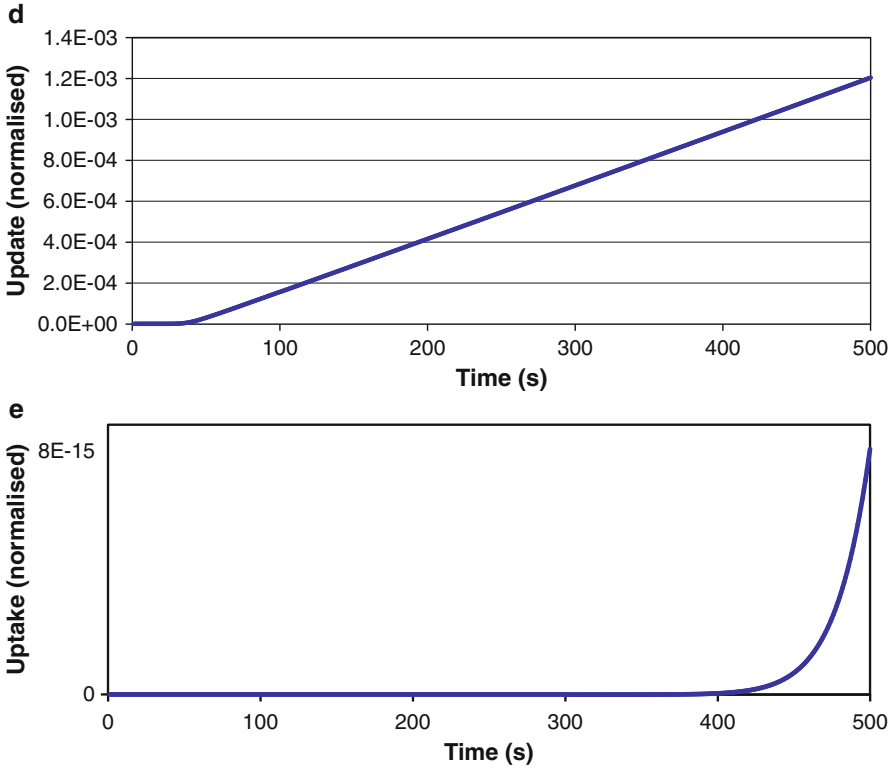

Fig. 8.11 (continued)

fusions. Finally, Fig. 8.11e shows the uptake by the tumour supplied by the network in Fig. 8.8d, where the pressure *gradient* across the parent vessel was increased by 300Pa (2.25 mmHg) prior to angiogenesis. Uptake is extremely poor, which is not too surprising given the presence of highly dilated loops close to the parent vessel. Hence, intravenous/intra-arterial treatments would be expected to prove ineffective in this case.

Having examined the role played by vessel adaptation on drug delivery qualitatively in two-dimensions, attention next turns towards quantitative simulations in three dimensions. Snapshots of the drug evolution through the 3D adaptive bed are shown in Fig. 8.12 and once again demonstrate the dominant role played by the dilated backbone in determining drug bypassing. As expected, bypassing begins earlier in the adaptive network, with the backbone effectively at maximum concentration after approximately 100 s. Delivery comparisons between 3D adaptive and

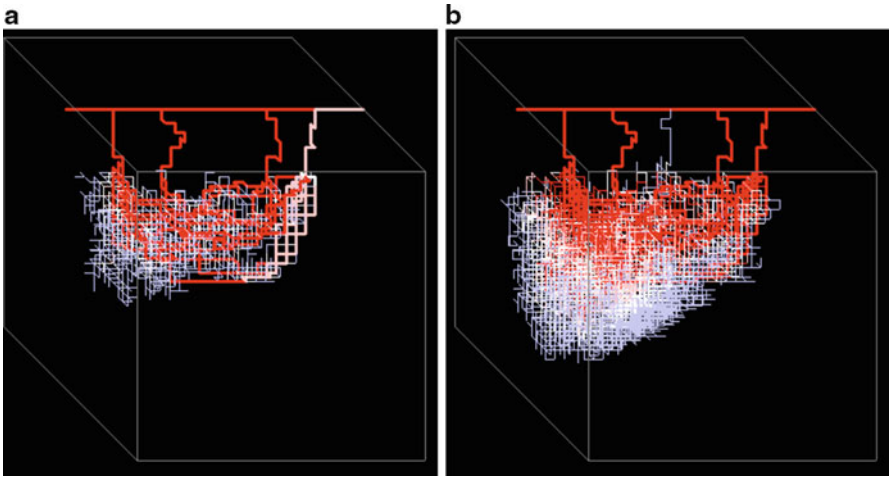

Fig. 8.12 Concentration contours for continuous infusion into an adaptive 3D vasculature formed from a linear TAF source. $30 \times 30 \times 30$ domain size. (**a**) $t = 50$ s, (**b**) $t = 500$ s. *Red* corresponds to high concentration and *blue* to low concentration

non-adaptive networks and between 2D and 3D adaptive networks are presented in Fig. 8.13. Increased dimensionality and vessel adaptation each reduce delivery by over an order of magnitude. The importance of the third dimension and the inclusion of adaptive architecture in providing quantitative predictions for comparison with in vivo results is clear.

4 Anti-angiogenic and Anti-vascular Treatment Simulations

The previous section described the delivery of chemotherapeutic agents from parent vessel to tumour boundary and did not discuss the possibility of certain drugs modifying the capillary architecture itself. In this section, several models are presented to examine precisely this issue – i.e. the effects of anti-angiogenic and anti-vascular therapies that are specifically aimed at disrupting the vascular bed. These therapies are initially modeled by means of simple "capillary pruning" algorithms that are used to approximate the key mechanisms thought to pertain to different treatments. Attention is restricted to 2D vasculatures for ease of presentation and interpretation, although similar qualitative conclusions can be immediately inferred for three dimensions.

The capillary pruning approach could be considered as being somewhat naïve, however, in that the underlying biological principles of how a certain therapy operates is subsumed into a very basic vessel removal algorithm. Hence, in order to study the effects of different anti-vascular and anti-angiogenic therapies from a more rigorous modeling standpoint, a new model is described that explicitly

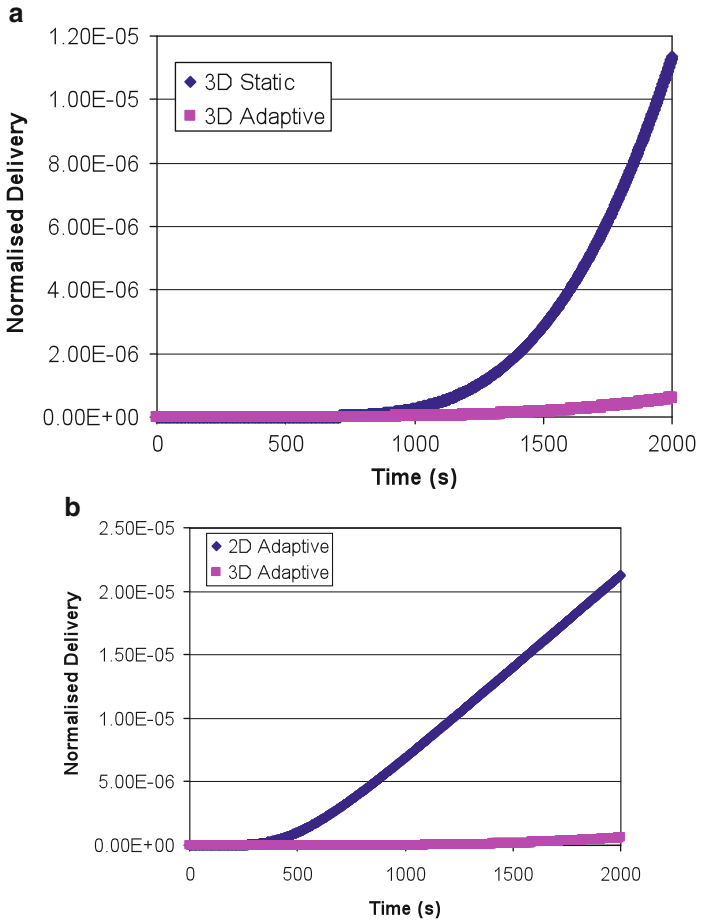

Fig. 8.13 Normalised drug delivery comparisons. (**a**) $30 \times 30 \times 30$ static 3D bed vs. $30 \times 30 \times 30$ adaptive 3D bed, (**b**) 30×30 2D adaptive bed vs. $30 \times 30 \times 30$ 3D adaptive bed. Delivery has been normalised to the total mass of drug injected into the parent vessel over 2,000 s

incorporates pericyte recruitment to migrating capillaries. The spatial distribution of pericyte density is investigated in both 2D and 3D under a number of different model assumptions and the implications for anti-angiogenic and anti-vascular treatments are discussed.

4.1 Capillary Pruning

In this section, the effect of various modifications to the network connectivity upon the efficiency of drug delivery to the tumour is investigated. The motivation for this

comes from the possibility of targeting particular areas of a growing vasculature with anti-angiogenic and anti-vascular drugs. This section focuses upon a posteriori capillary pruning (i.e. capillary removal from a static pre-existing capillary bed) of a vasculature similar to that shown in Fig. 8.1a. Modifications are achieved by removing a fraction of vessels in the lower part of the vasculature.

Three pruning algorithms have been considered: (1) vessels removed in a totally random fashion; (2) vessels removed if their flow lies below a given threshold; (3) vessels removed if their flow exceeds a given threshold. These three approaches seek to broadly cover the spectrum of possible targeting strategies for anti-angiogenic and anti-vascular treatments – the first relates to a broad-based indiscriminate anti-vascular drug, the second relates to an anti-angiogenic drug that preferentially targets immature, poorly perfused capillaries, and the third relates to the possible targeting of capillaries characterized by high wall stresses. In all simulations, a bolus injection at concentration $C_{\max}$ and duration $t = 375$ s was considered.

4.1.1 Random Vessel Removal

Figure 8.14 presents the variation in drug uptake at time $t = 2{,}500$ s as the fraction (f) of vessels randomly removed from the initial vasculature is increased. Note, that $t = 2{,}500$ s corresponds to the time at which drug uptake via the unpruned vasculature (i.e. $f = 0.0$) ceased. It can be seen in Fig. 8.14 that the total amount of drug uptake increases to a maximum for $f = 0.06$. A sharp decrease is then observed, corresponding to poorly connected architectures that are unable deliver drug effectively.

Visualization of the flow distribution in the optimized vasculature shows an increase in flow in the distal part of the capillary bed (close to the tumour) and this redistribution increases the efficacy of drug delivery to the tumour by approximately 130% (Fig. 8.15). These simulations clearly show that drug delivery to a tumour becomes optimized when (1) highly interconnected regions of the vasculature are removed and (2) a high capillary density can be preserved close to the tumour surface. If an anti-angiogenic treatment could achieve this architecture then the efficacy of subsequent chemotherapy treatments would be much improved. However, we should also point out that if an anti-angiogenic agent were to be used in isolation (i.e. without chemotherapeutic follow-up) then the effect may be to simply optimize nutrient supply and this could actually encourage tumour growth.

4.1.2 Flow-Dependent Vessel Removal: Low Flow Rate Threshold

As shown earlier, the process of random removal of vessels can lead to drastic changes in drug delivery to a tumour and these variations can be either positive or negative. In this section, motivated by the possibility of targeting drugs at poorly perfused areas of the vasculature, some of the vessels are selectively removed if their flow falls below a given threshold value.

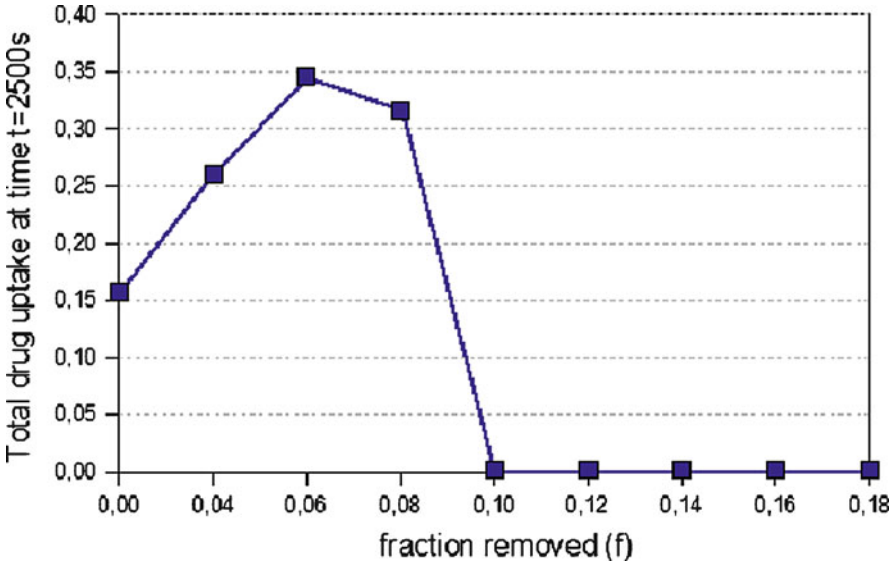

Fig. 8.14 Plot of the total amount of drug received by the tumour at $t = 2{,}500$ s vs. fraction of vessels randomly removed from the capillary bed (the fraction removed, FR, is varied from 0.0 to 0.18)

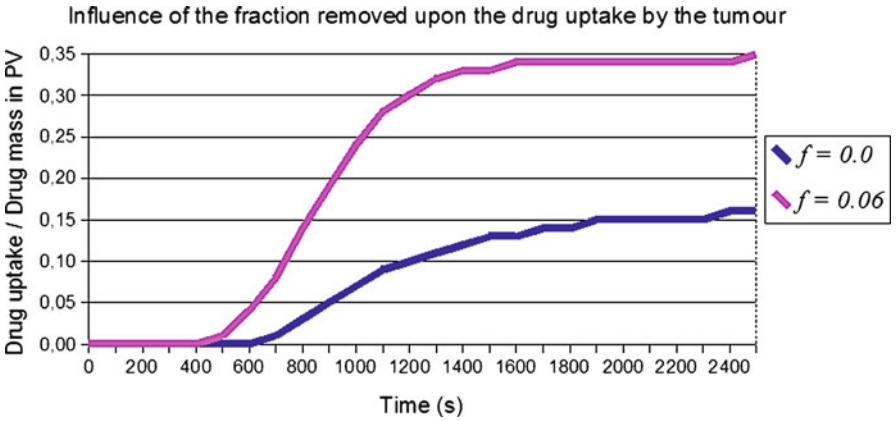

Fig. 8.15 Plot showing the comparison of the drug uptake between the $f = 0.06$ vasculature and the original $f = 0.0$ case

The next simulation focussed on a case where vessels having flow less than 1% of the maximum capillary flow ($Q_{\max}$) were removed – the fraction removed actually represents 40% of the total capillary bed. It is found that the flow distribution remains essentially unchanged when compared with the unmodified vasculature and a comparison of drug uptake in the two systems shows that maximum

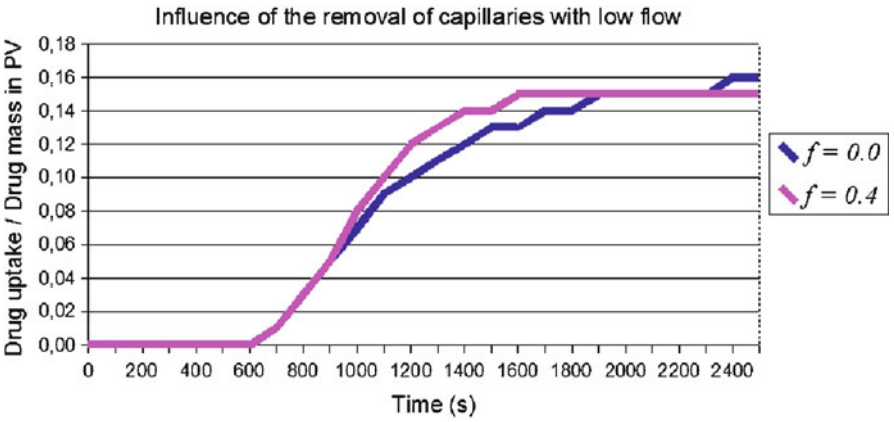

Fig. 8.16 Plot showing the comparison of the drug uptake between the $f = 0.4$ vasculature and the original $f = 0.0$ case

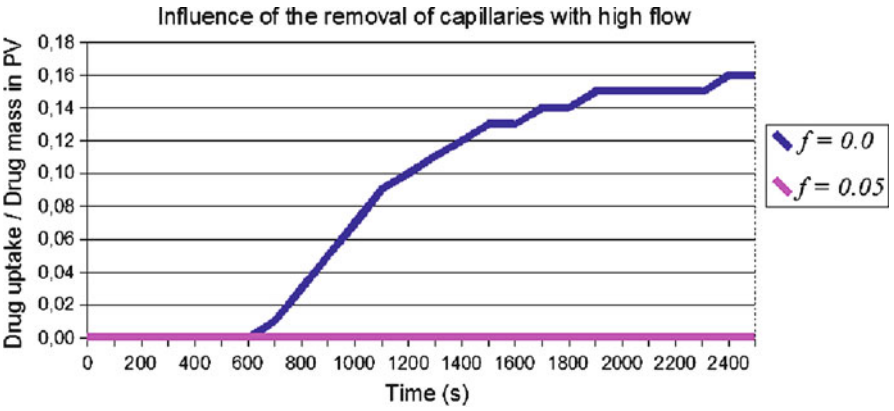

Fig. 8.17 Plot showing the comparison of the drug uptake between the $f = 0.05$ vasculature and the original $f = 0.0$ case

uptakes are also similar (Fig. 8.16). It should be noted, however, that the modified network initially delivers the drug more quickly: the "treated" vasculature has been optimized and drug delivery is accelerated by approximately 30%.

4.1.3 Flow-Dependent Vessel Removal: High Flow Rate Threshold

The final approach to capillary pruning relates to the possible targeting of "bottleneck" capillaries characterized by high wall stresses. In this scenario, capillaries with flow exceeding 95% of the maximum network value were removed – this corresponded to a removed fraction $f = 0.05$. Figure 8.17 shows the resulting

delivery profile. It can be seen that the network has essentially shut down in this case, with no drug delivery to the tumour. Hence, if an anti-vascular treatment could be developed to target these fast-flowing "bottleneck" capillaries, it would be a highly efficient way of slowing tumour growth.

4.2 Pericyte Recruitment and "Plasticity Window" Identification

Having discussed a number of broad approximations to modeling the effects of anti-vascular and anti-angiogenic drugs, a more rigorous basis for vascular disruption is now sought. It is clear from the recent literature that the stability of a developing capillary network – and therefore the efficacy of a vascular disrupting agent (VDA) – is closely linked to the corresponding pericyte coverage of the constituent capillaries. Moreover, pericytes are a prime target for new VDAs currently in clinical trials, and so any modeling framework aimed at capturing the main features of anti-vascular and anti-angiogenic treatments should somehow acknowledge pericyte–endothelium interactions during angiogenesis. It is hoped that the current approach could ultimately be used to identify a VDA-specific "plasticity window" (i.e. a time period corresponding to low pericyte density), within which a given VDA would be most effective.

This section consequently begins by describing a simple model for pericyte recruitment during vessel maturation, whereby developing capillaries recruit stabilising pericytes from the surrounding tissue. Under physiological conditions, four main recruitment pathways have so far been identified (Chantrain et al. 2006; Jain 2003): (1) latent TGF-β1 secreted by endothelial cells, activated by proteases during angiogenesis, and bound to ALK5 receptors on neighbouring pericytes; (2) sphingosine 1-phosphate (S1P) signalling from mast cells and platelets to receptor EDG-1 on endothelial cells, promoting N-cadherin trafficking and strengthening pericyte contacts; (3) the Ang-1/Tie2 signalling loop, whereby Tie2 expressed by endothelium forms a complex with its agonistic ligand Ang-1 expressed by perivascular cells; (4) PDGF-B/PDGFR-β signalling between sprouting endothelial cells and mural cells. The precise details of these various signalling cascades are only now being uncovered and some pathways appear to be interdependent. The most salient features of these mechanisms, however, can initially be distilled into a relatively small number of modeling assumptions.

As a first attempt towards capturing the process of pericyte recruitment, a simple logistic law is assigned to all capillary elements, allowing pericyte coverage to increase with time towards some limiting carrying capacity. The following relationship is used:

$$\frac{\mathrm{d}p}{\mathrm{d}t} = \beta \cdot K(R) \cdot p \left(1 - \frac{p}{K(R)}\right), \tag{8.6}$$

where $p(t)$ denotes the total number of pericytes covering a vessel at time t, β is a constant related to the degree of contact inhibition among pericytes, and $K(R)$

is the carrying capacity of the vessel segment. The term $\beta.K(R)$ is equivalent to an intrinsic recruitment rate for pericytes. Note that, in the base-case scenario, the carrying capacity is taken to depend upon vessel radius, more specifically:

$$K(R) = \frac{\text{Surface Area of Vessel Segment}}{\text{Surface Area of Pericyte}}, \tag{8.7}$$

where the surface area of a pericyte is taken to be πR_{pc}^2 with $R_{\text{pc}} = 20\,\mu\text{m}$. This, in effect, means that smaller capillaries have a smaller carrying capacity and recruit pericytes at a slower rate (due to fewer receptors/ligands being available on the vessel wall and a reduced surface area for expression of signalling molecules). Although the simplifying assumption has been made here that the entire capillary wall could become covered with pericytes (whereas, in reality, fenestrations between elongated mural cells are often in evidence), this could easily be modified by means of a constant in the equation defining $K(R)$. However, this can be expected to have little effect upon the pericyte *densities* shown later. In all of the following simulations, the fully dynamic DATIA angiogenesis model was used to grow and remodel the capillary bed. Once again, only 2D results will be presented initially for ease of interpretation, with a few 3D comparisons shown at the end for completeness.

The base-case simulation is presented in Fig. 8.18 and shows both the developing capillary bed and the evolution of pericyte density (normalised to the carrying capacity of each capillary). Experimentally, the pericyte recruitment process occurs on the same timescale as the angiogenesis process but appears to lag the migration of endothelial cells by several days (Benjamin et al. 1998). This is reproduced by the model over a wide range of β values (0.0075, 0.075), with substantial pericyte coverage only occurring after approximately $\tau = 4$ ($t = 6.4$ days). In the base-case simulation, only flowing vessels were allowed to recruit pericytes, resulting in a highly heterogeneous spatial distribution of stabilised capillaries that corresponds broadly to the main flowing backbone of the vasculature. Notice however, that between times $\tau = 11$ and $\tau = 15$ some vessels dilate (branch 4 leaving the parent vessel, for example), whilst others constrict, and this impacts upon the *density* of the pericyte coating of these vessels – dilation of a vessel without additional recruitment effectively reduces its pericyte density (and stability), whilst a constricting vessel becomes more stable. Hence, although a vessel may initially appear functionally stable at some point during angiogenesis, subsequent flow-induced dilation may reveal a window of instability that would help VDA treatment. The results suggest that the plasticity window for this particular network is $\tau < 11 (t < 18$ days), as high pericyte densities are restricted to regions proximal to the parent vessel up to this point. Moreover, it is clear that treating this capillary bed at a later time with a VDA specific to endothelial cells (i.e. the blue regions) would be of only temporary benefit, as the main skeleton of enveloping pericytes would remain as a template for future endothelial migration. Conversely, the simulation shows that a VDA targeted

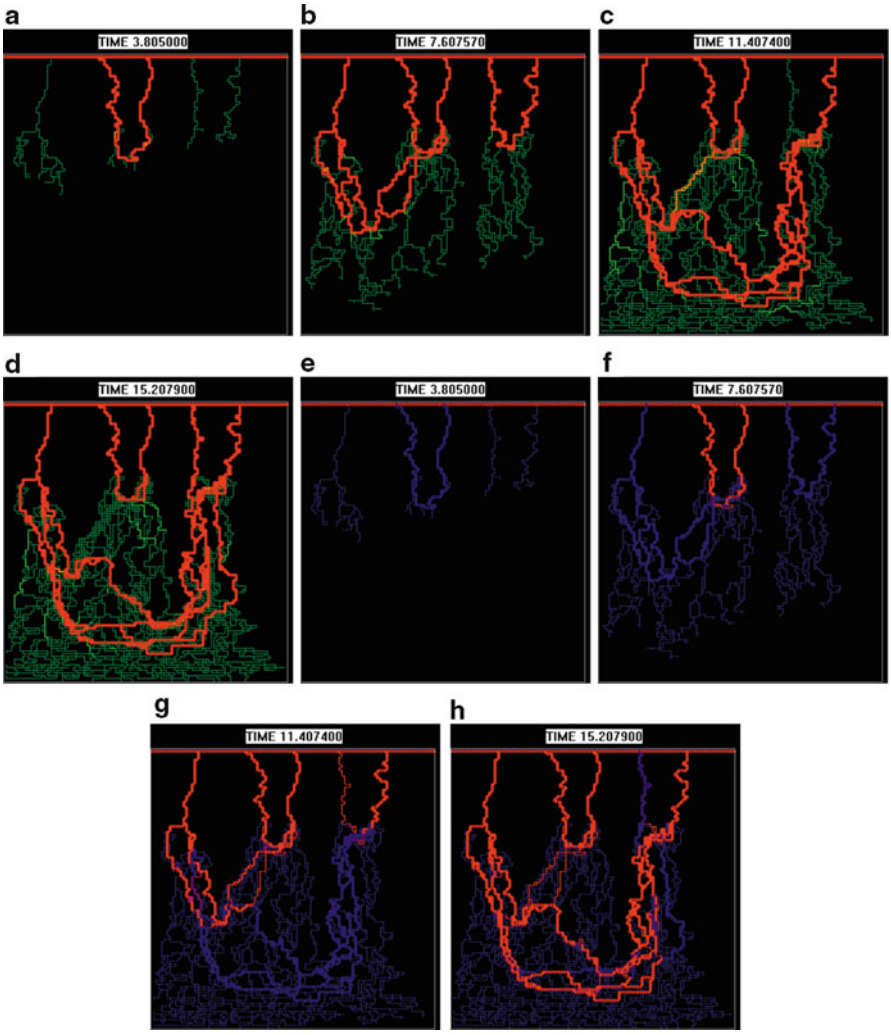

Fig. 8.18 Snapshots of the developing capillary bed (*top*) and pericyte density (*bottom*) at different dimensionless times ($\tau = t$(days)/1.6). Only flowing vessels recruit pericytes and the recruitment parameter $\beta = 0.0075$. For the pericyte figures, blue corresponds to low pericyte density and *red* corresponds to high pericyte density

at disrupting pericyte–endothelium adhesion could be more effective, starving the tumour of an efficient nutrient supply by removing the main flowing backbone of the network.

The second simulation, shown in Fig. 8.19, corresponds to a tenfold increase in intrinsic recruitment rate ($\beta = 0.075$). Pericyte recruitment again lags endothelial cell migration by several days and the pericyte density distribution up to

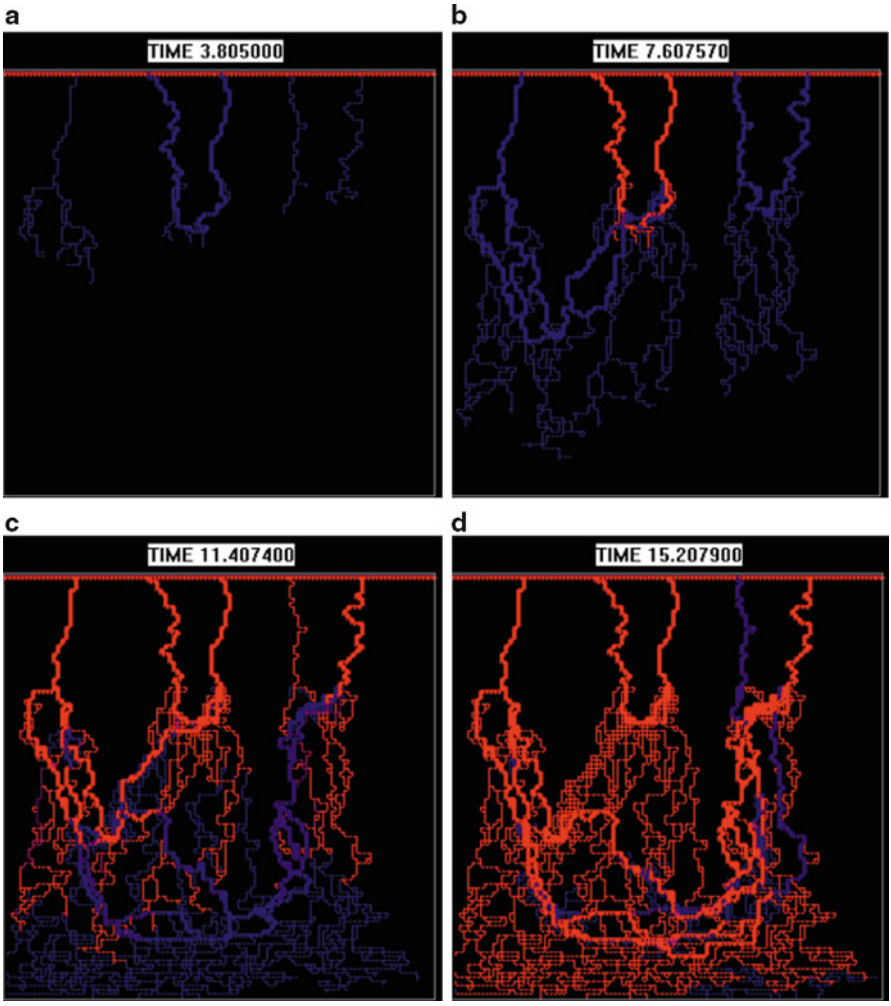

Fig. 8.19 Snapshots of the pericyte density evolution at different dimensionless times ($\tau = t$ (days)/1.6). Again, only flowing vessels recruit pericytes but the recruitment parameter is increased tenfold ($\beta = 0.075$). *Blue* corresponds to low pericyte density and *red* corresponds to high pericyte density

approximately $\tau = 7$ is the same as that observed in the base case. However, increased recruitment ultimately results in a more stable network after approximately 18 days ($\tau = 11$). Furthermore, the increased pericyte coverage of even small capillaries means that this network would be difficult to eradicate even with a combination of endothelium-specific and pericyte-specific VDAs – although the high concentrations of VDA convicted through the main backbone would expedite its removal, a widespread template of low-flow pericyte-covered capillaries

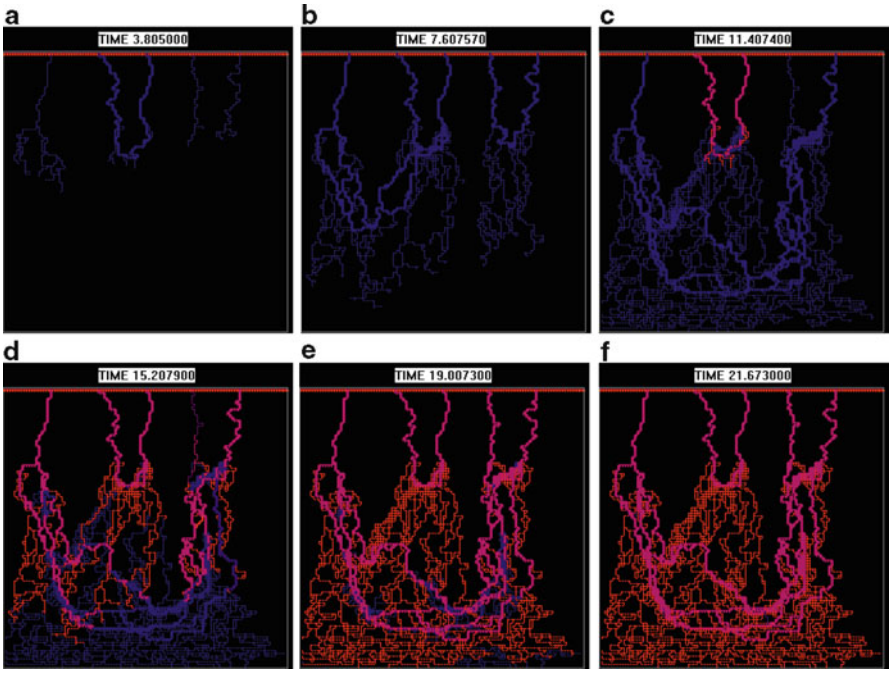

Fig. 8.20 Snapshots of the pericyte density evolution at different dimensionless times ($\tau = t$ (days)/1.6). Again, only flowing vessels recruit pericytes but the carrying capacity is fixed at some average value (see text). $\beta = 0.0075$. *Blue* corresponds to low pericyte density, *magenta* to intermediate density and *red* to high density

would probably remain (relying on diffusion-driven mass transport from dilated vessels for treatment). This suggests that the treatment efficacy of any infused drug would generally depend upon a local combination of convective, diffusive, and reactive transport mechanisms (quantifiable in terms of local Peclet and Damköhler numbers).

The results of the previous two simulations highlight the importance of pericyte recruitment rate in determining the treatment potential of a given tumour-induced capillary bed. They demonstrate how the model can be used to suggest additional experimental studies in order to help justify or refute various model assumptions. One of the main assumptions of the modeling approach thus far has been the radius-dependency of the pericyte carrying capacity and Fig. 8.20 shows the impact of relaxing this by setting the carrying capacity of all vessels to be constant (taken to be that corresponding to a vessel of average radius, 7 μm). It is immediately clear that this has the effect of lengthening the treatment window considerably, as pericyte recruitment lags capillary migration by approximately 16 days and subsequent vessel dilation results in a low pericyte density around the main flowing backbone of the bed. Indeed, the low pericyte density is sustained indefinitely in

these regions due to the limit imposed upon pericyte carrying capacity. Note also that the distribution of small, stable capillaries lies somewhere between those shown earlier when a varying carrying capacity was used (compare snapshots at $\tau = 15$, for example, in Figs. 8.18–8.20). In the case of a fixed (average) carrying capacity, it would therefore appear that the main flowing backbone would remain highly susceptible to a VDA targeting pericytes for some considerable time. Although a considerable number of small pericyte-coated capillaries would again remain after treatment, these would be efficiently disconnected from the main parent vessel. Furthermore, if anti-endothelial treatment were supplied within the $\tau < 15$ plasticity window then these capillaries would also remain disconnected from the tumour surface and the surviving pericyte template would remain relatively ineffectual.

Finally, two sensitivities are presented that include feedback between pericytes and endothelium by means of an explicit interdependency between vessel remodeling potential and local pericyte density. In these cases, vessels could only remodel if their pericyte coverage was below $0.5K_{\max}(R)$, where $K_{\max}(R)$ corresponds to the radius-dependent maximum carrying capacity of a given vessel. This implies a correlation between network stability and pericyte coverage, which is thought to be the case physiologically (Hughes et al. 2006). Figure 8.21a shows the pericyte coverage after approximately 24 days of migration and recruitment ($\tau = 15$) when only flowing vessels are able to recruit. The figure is similar to that shown for the base-case simulation with a few minor, but important, differences. The regression of two dilated vessels in the base-case (circled in Fig. 8.21c) is no longer possible when the potential for capillary remodeling is coupled to pericyte density – the high pericyte coverage of these vessels at an earlier time means that they remain dilated for the remainder of the simulation. Note also, that the increased stability of the backbone in this area perturbs subsequent reinforcement of the network elsewhere, leading to a different downstream architecture (observe also that branch 4 (arrowed in Fig. 8.21c is unable to dilate in response to remodeling cues, unlike the base-case). Such minor changes in bed architecture can have a significant impact upon transport issues, causing increased bypassing of injected chemotherapy treatments. The modeling results suggest that it is important to determine the degree to which vascular remodeling can occur as a function of pericyte density in order to optimise such therapies.

The final simulation was undertaken to test the earlier assumption that only flowing vessels recruit pericytes. This assumption was based on experimental observations that show higher pericyte densities associated with more mature capillary structures in flowing retinal vasculature. However, reliable fate mapping of pericytes in vivo is not possible at present (Armulik et al. 2005) and pericyte recruitment by tumour-induced vasculatures is not well understood. In light of these uncertainties, a simulation was run assuming that *all* nascent capillaries could recruit pericytes from the surrounding tissue, *whether flowing or not*. Once again, vessels could only remodel if their pericyte coverage was below $0.5K_{\max}(R)$. The result is shown in Fig. 8.21b, and shows a very different structure from those seen previously. In this case, only the primary anastomosis has had time to dilate before pericyte density restricts all subsequent remodeling throughout the migrating

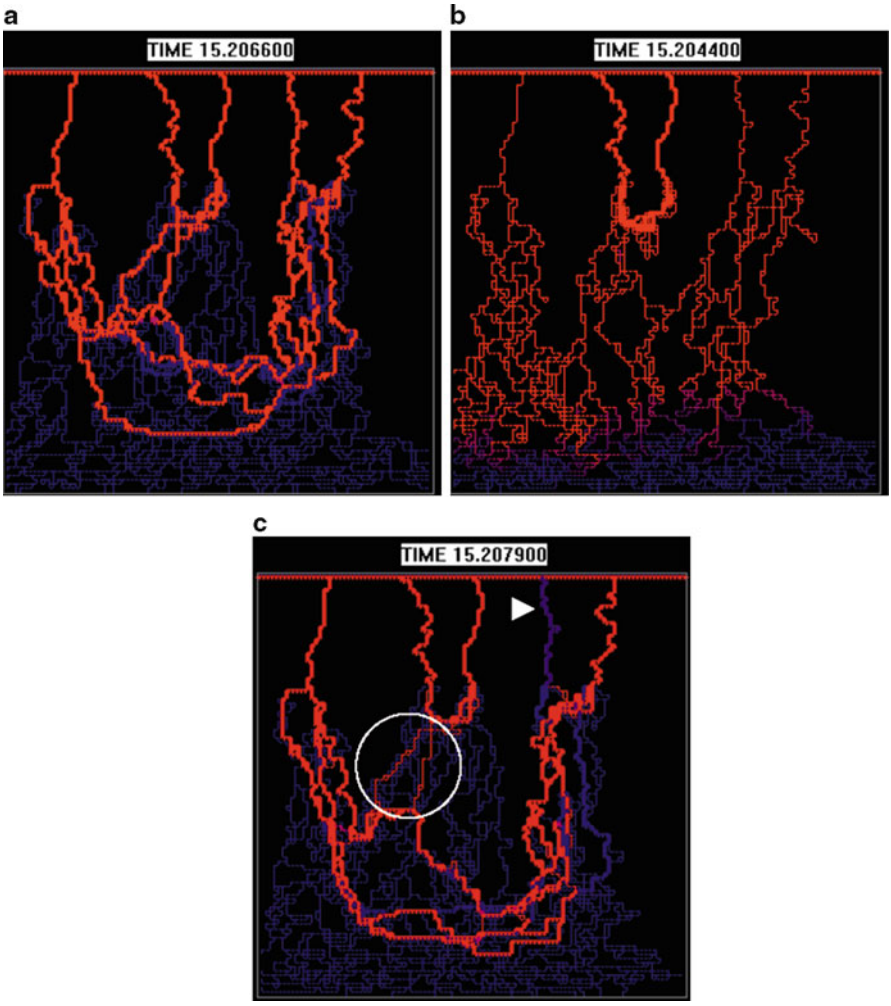

Fig. 8.21 Snapshots of the pericyte density evolution at different dimensionless times ($\tau = t$ (days)/1.6) where vessels can only remodel if pericyte coverage is less than $0.5K_{\max}(R)$. (**a**) only flowing vessels recruit; (**b**) all vessels recruit; (**c**) base case simulation for comparison. $\beta = 0.0075$. Blue corresponds to low pericyte density, magenta to intermediate density and red to high density

bed. This type of bed would be a worst case scenario for VDA treatment, as numerous small, low-flow capillaries would need to be accessed by the injected drug. Most of the treatment would simply be recirculated to the parent vessel, however, by way of the single dilated arcade.

All of the pericyte recruitment simulations shown thus far have been undertaken in two dimensions in order to aid interpretation. However, it has already been shown

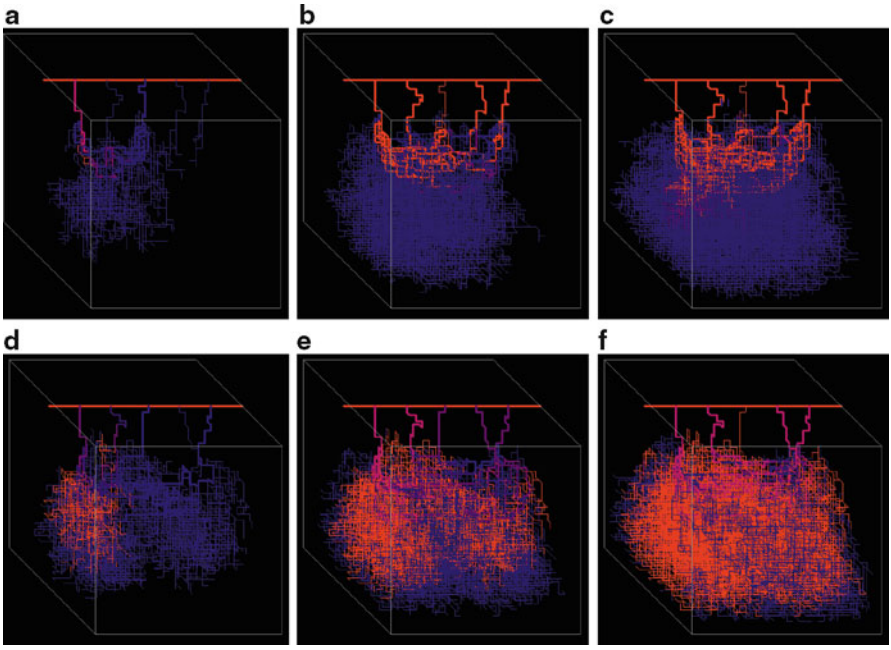

Fig. 8.22 Snapshots of the 3D pericyte density evolution at different dimensionless times ($\tau = t$ (days)/1.6). (**a**–**c**) base case simulation at $\tau = 7$, $\tau = 10$, $\tau = 12$ (see text); (**d**–**f**) fixed average carrying capacity at $\tau = 8$ $\tau = 10$ $\tau = 12$ $\beta = 0.0075$ *Blue* corresponds to low pericyte density, *magenta* to intermediate density and *red* to high density

that quantitative predictions of flow-related delivery require 3D networks. As the future aim of the modeling framework developed here will be to compare numerical results with experimental VDA delivery data, it is important to extend the pericyte work into the third dimension. Hence, this section concludes by presenting two fully adaptive, three-dimensional angiogenesis simulations that incorporate pericyte recruitment. Figure 8.22a–c shows the three-dimensional equivalent of the base-case simulation in Fig. 8.18, whilst Fig. 8.22d–f shows the case when a fixed carrying capacity is assumed for all vessels. Heterogeneity in pericyte coverage is evident in both cases and pericyte coverage again lags endothelial migration by several days. These figures clearly highlight the difficulties faced by researchers in developing generic VDAs aimed at disrupting such heterogeneous aberrant vasculatures.

Of course, many more sensitivities could be examined using the modeling framework described here but the main purpose has been to demonstrate the need for additional experimental observations to clarify the main mechanisms affecting pericyte recruitment and distribution. Armed with this knowledge, it should be possible to optimise the potential of anti-angiogenic and anti-vascular drugs by coupling modeling and experiment.

5 Discussion and Conclusions

This paper has presented a number of results primarily related to convective transport through tumour-induced angiogenic capillary beds. Whilst there have been many modeling studies reported in the literature dealing with the process of angiogenesis itself – i.e. the way in which the new capillary bed is initiated and migrates – there have been relatively few studies examining the important role played by blood perfusion during migration and fewer still examining the delivery of chemotherapeutic compounds through aberrant tumour vasculature. In response to the paucity of transport models in this area, a new framework has been developed within which a wide range of therapeutic interventions can be studied.

Although the salient features of the extended angiogenesis model have been described, including the effects of matrix degrading enzymes and perfusion-related capillary remodeling, the main aim of the paper has been to study the way in which bed architecture and spatial heterogeneity affect the evolution of intravenous/intra-arterial drug treatments. Initially, two- and three-dimensional simulations of chemotherapeutic delivery to the tumour periphery via both static and dynamically adaptive networks were compared. It was demonstrated that, instead of supplying drug to the tumour, some branches of the induced vasculature actually *remove* drug from the network, thereby reducing its efficacy. Indeed, results from a 30-s bolus injection simulation into a network formed in response to a focussed semicircular TAF source highlighted the possibility of the treatment bypassing the tumour altogether.

Simulations using the adaptive model under different parameter regimes highlighted a number of new therapeutic targets for tumour management. For example, reduction of the haptotactic response of the migrating endothelial cells during angiogenesis was shown to reduce lateral migration of the vessels and reduce shear-induced branching. Subsequent evolution of blood perfusion through this network suggested that tumours supplied by this type of vasculature would be well-supplied with nutrients and could be expected to grow rapidly. However, such tumours would also be highly susceptible to infused treatments, with cytotoxic agents reaching the tumour surface in higher concentrations than the base-case simulation. A second set of simulations suggested that a depressed haematocrit could be expected to lead to the formation of highly dilated arcades close to the parent vessel. Although this had the positive effect of causing more drug to enter the capillary network than entered in the base-case simulation, delivery to the tumour was reduced by more than three orders of magnitude. Whilst this is a somewhat negative result in the context of infused treatment, it also suggests that decreasing local haematocrit could be a possible mechanism for remodeling vasculatures that are detrimental to further tumour growth.

The therapeutic applications described in the earlier part of the paper focussed upon the impact of bed topology on the delivery of a cytotoxic drug from parent vessel to tumour periphery. However, these simulations largely neglected the

important possibility of disrupting the vascular network itself. As new treatments are being tailored to specifically target vascular endothelium, it was decided to examine the effects of anti-angiogenic and anti-vascular therapies specifically aimed at disrupting the vascular bed. These therapies were initially modeled by means of simple "capillary pruning" algorithms that were used to modify the network connectivity in a number of different ways. It was found that random removal of vessels (approximating the action of anti-vascular drugs) led to a significant increase in the amount of drug delivered to the tumour, whilst selective removal of vessels characterised by low flow (used to mimic anti-angiogenic treatment) was seen to accelerate delivery by approximately 30%. The possibility of targeting "bottleneck" capillaries, characterized by high wall stresses, was also investigated and the network was essentially shut down in this case. Hence, if a treatment could be developed to target these fast-flowing "bottleneck" capillaries, it would be a highly efficient way of slowing tumour growth.

This simplistic capillary pruning approach is rather unsophisticated and a number of the underlying biological principles have been subsumed into very basic algorithms. Although the approach broadly captured the effects of vascular disrupting agents (VDAs), it is clear from the recent literature that the stability of a developing capillary network – and therefore the efficacy of a VDA – is closely linked to the corresponding pericyte coverage of the constituent capillaries. Hence, in order to study the effects of different anti-vascular and anti-angiogenic therapies more rigorously, a new model was required that explicitly incorporated the important mechanism of pericyte recruitment. As a first step towards capturing this process, a simple logistic law was assigned to all capillary elements, allowing pericyte coverage to increase with time towards some limiting carrying capacity. The spatial distribution of pericyte density was investigated in both 2D and 3D under a number of different model assumptions and the implications for anti-angiogenic and anti-vascular treatments were discussed. It was found that the recruitment of pericytes lagged the migration of endothelial cells by several days over a wide range of intrinsic recruitment rates $(0.0075, 0.075)$, in agreement with experimental observations (Benjamin et al. 1998). Moreover, it was shown that, although a vessel may initially appear functionally stable at some point during angiogenesis, subsequent flow-induced dilation may reveal a window of instability that would help VDA treatment. However, although high concentrations of VDA were observed flowing through the main backbone of all capillary networks studied (thereby expediting its removal), a widespread template of low-flow pericyte-covered capillaries was left behind and treatment of this pericyte template would rely on diffusion-driven mass transport from dilated vessels – this suggests that the treatment efficacy of any infused drug would generally depend upon a local combination of convective, diffusive and reactive transport mechanisms (quantifiable in terms of local Peclet and Damköhler numbers). A more detailed study of this issue will form the basis of future simulation work and it is hoped that the modeling framework could ultimately be used to identify a VDA-specific "plasticity window" (i.e. a time period corresponding to low pericyte density), within which a given VDA would be most effective.

Throughout this chapter, both two- and three-dimensional simulation results have been presented and it has been shown that extending the model to three dimensions reduces chemotherapy delivery to a tumour periphery by an order of magnitude. These results clearly demonstrated that, although two-dimensional studies are valuable in a qualitative sense, three-dimensional angiogenesis modeling appears to be a necessary prerequisite for quantitative prediction for comparison with in vivo results. Of course, many more sensitivities could be examined but our main aim has been to demonstrate the need for additional experimental observations to clarify a number of outstanding issues. For example, the key mechanisms governing pericyte recruitment and drug uptake require additional research, as do the metabolic stimuli affecting blood vessel dynamics.

Armed with this additional knowledge, it should be possible to refine the model still further, perhaps by including discrete pericyte migration and improved dose-response algorithms. Moreover, by closely coupling an improved mathematical framework with corresponding laboratory experiments, it should prove possible to increase the potential of a range of anti-angiogenic and anti-vascular drugs in the future.

Acknowledgement MAJC and SMcD gratefully acknowledge the support of BBSRC Grant BBF0022541 "Guidance cues and pattern prediction in the developing retinal vasculature: a combined experimental and theoretical modeling approach".

Appendix 1: Vascular Network Modeling

In the earlier model of Anderson and Chaplain (1998), endothelial cell densities and their global influence on TAF and FN concentrations were considered in a continuous formulation. Here, the focus is on local effects and so the influence of each individual cell on its local environment is considered. In order to achieve this, the displacement of each individual endothelial cell, located at the tips of growing sprouts, is given by the discretised form of the endothelial cell mass conservation equation (8.1).

The chemotactic migration is characterised by the function $\chi(c) = \chi/(1+\delta c)$ which reflects the decrease in chemotactic sensitivity with increased TAF concentration. The coefficients D, χ and ρ characterise the random, chemotactic and haptotactic cell migration, respectively (full details of the non-dimensionalisation can be found in Anderson and Chaplain 1998). The migration of each cell in 2D is consequently determined by a set of normalized coefficients emerging from this equation (Fig. 8.23), which relate to the likelihood of the cell remaining stationary (P_0) or moving left (P_1), right (P_2), up (P_3) or down (P_4):

$$n_{l,m}^{q+1} = n_{l,m}^{q} P_0 + n_{l+1,m}^{q} p_1 + n_{l-1,m}^{q} p_2 + n_{l,m+1}^{q} P_3 + n_{l,m-1}^{q} P_4, \tag{8.8}$$

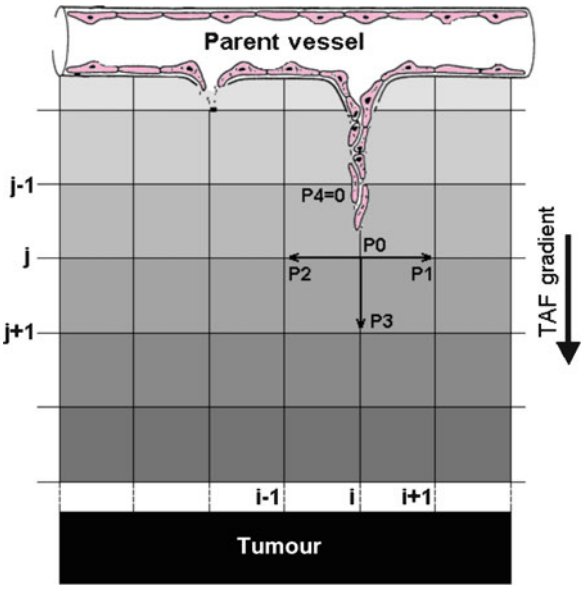

Fig. 8.23 Schematic diagram of a section of the 2D-grid used in the numerical computation procedure illustrating how the process of the migration of tip endothelial cells, and hence capillary sprout growth, is taken into account in the simulations. At each node, the sprout tip can grow in three possible directions in 2D (and five possible directions in 3D)

where l and m are positive parameters which specify the position of the endothelial cell on the 2D spatial grid, i.e. $x = l\Delta x$ and $y = l\Delta y$ and time discretisation is represented by $t = q\Delta t$. These coefficients P_0–P_4 incorporate the effects of random, chemotactic and haptotactic movement and depend upon the local chemical environment (FN and TAF concentrations). In 3D, the discretised endothelial equation has the form:

$$n_{l,m,w}^{q+1} = n_{l,m,w}^{q} P_0 + n_{l+1,m,w}^{q} P_1 + n_{l-1,m,w}^{q} P_2 + n_{l,m+1,w}^{q} P_3 + n_{l,m-1,w}^{q} P_4 + n_{l,m,w+1}^{q} P_5 + n_{l,m,w-1}^{q} P_6. \tag{8.9}$$

With additional movement coefficients: in (P_5) or out (P_6). The model is then given by the following set of equations:

$$\frac{\partial n}{\partial t} = \overbrace{D\nabla^2 n}^{\text{random}} - \overbrace{\nabla \cdot (\chi(c) n \nabla c)}^{\text{chemotaxis}} - \overbrace{\rho \nabla \cdot (n \nabla f)}^{\text{haptotaxis}}, \tag{8.10}$$

$$\frac{\partial c}{\partial t} = -\eta\, n_k\, c,$$

Table 8.1 Sprout tip branching probabilities as a function of the local TAF concentration

TAF concentration	Sprout tip branching probability
<0.3	0.0
] 0.3 – 0.5]	0.2
] 0.5 – 0.7]	0.3
] 0.7 – 0.8]	0.4
>0.8	1.0

$$\frac{\partial f}{\partial t} = \beta\, n_k - \gamma\, m\, f,$$

$$\frac{\partial m}{\partial t} = \alpha\, n_k + \varepsilon \nabla^2 m - \nu\, m, \tag{8.11}$$

where c represents the TAF concentration, f the FN concentration, m the MDE density and n_k a Boolean value (1 or 0) that indicates the presence or absence of an endothelial cell at a given position. The parameters β and α characterise the production rate by an individual endothelial cell of FN and MDE, respectively, and η its TAF consumption rate. The major difference with the earlier model is that degradation of fibronectin f, characterised by the coefficient γ, no longer depends directly on the endothelial cell density n. This now depends upon the MDE density m produced by each individual endothelial cell n_k at rate α. The MDF once produced, diffuses locally with diffusion coefficient ε, and is spontaneously degraded at a rate ν.

Tip and Vessel Branching Probabilities

In earlier work (Anderson and Chaplain 1998; McDougall et al. 2002; Stéphanou et al. 2005a, b), branching at the capillary tips was assumed to depend only upon the local TAF concentration. This formulation has been used again here and the corresponding tip branching probabilities are shown in Table 8.1. In addition to tip branching, however, the physiologically significant process of vessel branching is also modeled as part of the current study. In order to implement this effect in the model, we assume that branching along a vessel (i.e. the generation of a new vessel which branches out at some point along an existing vessel wall as distinct from the vessel tip) depends both on the TAF concentration and on the wall shear stress (WSS). Table 8.2 shows the dependence of vessel branching probability as a function of the combined effects of local wall shear stress and local TAF concentration.

One additional constraint on vessel branching is the age of the vessel itself. The time interval within which a vessel can branch has been fixed at [4–8] days

Table 8.2 Vessel branching probabilities as functions of the local TAF concentration and the magnitude of the local wall shear stress

WSS/τ_{max}						
$[TAF]/TAF_{max}$		[0.0,0.2[	[0.2,0.4[	[0.4,0.6[	[0.6,0.8[	[0.8,1.0[
	[0,0,0.3[	0.00	0.00	0.00	0.00	0.00
	[0.3,0.5[	0.00	0.0.2	0.04	0.06	0.08
	[0.5,0.7[	0.00	0.03	0.06	0.09	0.12
	[0.7,0.8[	0.00	0.04	0.08	0.12	0.16
	[0.8,1.0[	0.00	0.10	0.20	0.30	0.40

TAF_{max} is the maximum TAF concentration at $t = 0$ and $t_{max} = 2\,\text{Pa}$ ($20\,\text{dynes/cm}^2$), the maximum shear stress derived from preliminary flow simulations

in the simulations (i.e. from $\tilde{\tau} = 2.66$ to $\tilde{\tau} = 5.33$). In this interval, the vessel is sufficiently mature for branching to occur yet young enough to ensure that no basal lamina has had time to form (which would contribute considerably to the stabilization of the network; Benjamin et al. 1998; Morikawa et al. 2002).

Initial Conditions

The domain considered for the computational simulation studies is a square of length $L = 2\,\text{mm}$ (2D) or a cube of edge length 0.6 mm (3D) and the parent vessel from which the vascular network grows is located at the upper edge/face of the domain. The tumour surface is located along the lower domain boundary. We assume that the capillary sprouts, TAF and MDE remain confined within the domain and so no-flux boundary conditions are imposed on the boundaries. Initial TAF and fibronectin profiles are the same as those used in McDougall et al. (2002), there is initially no MDE present and vascular growth is initialised by distributing five sprouts at regular intervals along the parent vessel.

Cell Migration Parameters

Unless otherwise indicated, the dimensionless parameter values used for the simulations presented in this paper were as follows (Anderson and Chaplain 1998; McDougall et al. 2002; Stéphanou et al. 2005a, b):

$$D = 0.00035 \quad d = 0.6 \quad \chi = 0.38 \quad r = 0.16$$
$$\eta = 0.1 \quad \beta = 0.05 \quad \gamma = 0.1 \quad a = 10e-6 \quad e = 0.01 \quad n = 3.$$

Capillary migration time was scaled as $\tilde{t} = \frac{t}{\tau}$: with $\tau = L^2/D_c$, where $L = 2\,\text{mm}$ (2D) or 0.6 mm (3D) was the length of the domain and $D_c = 2.9 \times 10^{-7}\,\text{cm}^2\text{s}^{-1}$ was

taken as the diffusion coefficient for TAF (Bray 1992). We note that the timescale associated with the capillary growth process is of the order of several days, whereas flow through the parent vessel and capillary network occurs over a timescale of a few seconds to a few minutes. A discussion of how the two timescales are coupled in the full adaptive model is given in McDougall et al. (2006).

Appendix 2: Adaptive Flow Modeling

General Model

In its most general form, the flow model developed here consists of a three-dimensional cubic network of bond elements. These bonds can be thought of as straight cylindrical capillary elements, although the constraint of cylindrical geometry can easily be relaxed. Now, for a single capillary element i of radius R_i and length L_i, the elemental fluid flow rate in the capillary is given by Poiseuille's law:

$$Q_i = \frac{\pi R_i^4 \Delta P_i}{8\mu L_i}, \tag{8.12}$$

where μ is the fluid viscosity and ΔP_i the pressure drop across the element. At each node (junction), six elements meet (in 3D) and (assuming incompressible flow) mass conservation means that the sum of all six flows must add up to zero, i.e.

$$\sum_{i=1}^{i=6} Q_i = 0. \tag{8.13}$$

Consideration of the whole network then leads to a set of linear pressure equations, the solutions to which (using, e.g. Successive Over-Relaxation (SOR), Choleski conjugate gradient method, Lanczos method) can then be used to calculate elemental flows.

Blood Rheology

When dealing with a non-Newtonian fluid, such as blood, the flow-pressure drop relationship can be approximated by the following Poiseuille-like expression:

$$Q = \frac{\pi R^4 \Delta P}{8\mu_{\text{app}}(R, H_D)L}, \tag{8.14}$$

where $\mu_{\text{app}}(R, H_D) = \mu_{\text{rel}} \times \mu_{\text{plasma}}$ is the apparent blood viscosity, which depends upon the local blood haematocrit, the radius of the vessel through which the blood is flowing, and the underlying plasma viscosity, μ_{plasma} (see (8.3) and (8.4) in main text).

Vessel Adaptation

In this paper, vessel adaptation follows the treatment of Pries et al. (1995, 1998, 2001a). The model considers a number of stimuli affecting vessel diameter that account for the influence of the wall shear stress (S_{wss}), the intravascular pressure (S_{p}), and a metabolic mechanism depending on the blood haematocrit (S_{m}). These stimuli form a basic set of requirements in order to obtain stable network structures with realistic distributions of vessels diameters and flow velocities. A brief description of each now follows.

1. *Wall shear stress* – Many studies show that vessels adapt their radius in order to maintain a constant level of wall shear stress (Pries et al. 1998, 2001a, b; Fung 1993). Hence, vessel radius tends to increase with increasing wall shear stress, whilst wall shear stress decreases with increasing radius. The wall shear stress stimulus can be described by a logarithmic law as

$$S_{\text{wss}} = \log(\tau_{\text{w}} + \tau_{\text{ref}}), \tag{8.15}$$

   where τ_{w} is the actual wall shear stress in a vessel segment calculated from

$$\tau_{\text{w}} = \frac{4\mu(R, H_D)}{\pi R^3}|Q| \tag{8.16}$$

   and τ_{ref} is a constant included to avoid singular behaviour at low shear rates (Pries et al. 2001a). Stresses in (B4) and (B5) are in dynes/cm^2. The wall shear stress calculated in the parent vessel of our computational model is of the order 4Pa (40 dynes/cm^2) and capillary values are less than 2Pa (20 dynes/cm^2), in agreement with those measured experimentally in the dog by Kamiya (1984). Adaptation in response to the wall shear stress stimulus alone tends to reinforce a single path in the network composed of a few well-established fully dilated vessels – corresponding to the main flowing "backbone" of the vasculature – whilst simultaneously eliminating the low-flow paths. However, the resulting network is "unstable" in the sense that there is no consistent balance for the radius and flow distribution achieved when S_{wss} is considered in isolation.
2. *Intravascular pressure* – Intravascular pressure is another key stimulus for vascular adaptation. Pries et al. (1995) have experimentally observed on the rat mesentery the dependence of the magnitude of the wall shear stress with the local intravascular pressure (P). They proposed a parametric description of their

experimental data, which exhibits a sigmoidal increase of the wall shear stress with increasing pressure through the following:

$$\tau_e(P) = 100 - 86 \exp\left\{-5{,}000[\log(\log P)]^{5.4}\right\}. \tag{8.17}$$

Pressure is measured in mm of mercury (1 mmHg = 133Pa) and stresses are again given in dynes/cm^2. The sensitivity of the corresponding stimulus to intravascular pressure is then described by:

$$S_{\mathrm{p}} = -k_{\mathrm{P}} \log \tau_e(P), \tag{8.18}$$

where k_{P} is a constant that dictates the relative intensity of the stimulus.

3. *Metabolic haematocrit-related stimulus* – The metabolic stimulus effectively stabilises the adapting network by stimulating vessel growth in areas of the vascular bed exhibiting low flow. The stimulus is once again described by a logarithmic law and takes the form:

$$S_{\mathrm{m}} = k_{\mathrm{m}} \log\left(\frac{Q_{\mathrm{ref}}}{QH_{\mathrm{D}}} + 1\right), \tag{8.19}$$

where Q_{ref} is a reference flow. In our simulations, Q_{ref} corresponds to the flow in the parent vessel. H_{D} represents the discharge haematocrit in the vessels, Q the flow in the vessel under consideration and k_{m} is a constant characterizing the relative intensity of the metabolic stimulus.

Our theoretical model for vessel adaptation assumes that the change in a flowing vessel radius (ΔR) over a time step Δt is proportional to both the global stimulus acting on the vessel and to the initial vessel radius R, i.e.

$$\Delta R = S_{\mathrm{tot}} R \Delta t = (S_{\mathrm{wss}} + S_{\mathrm{p}} + S_{\mathrm{m}}) R \Delta t, \tag{8.20}$$

which leads to (8.5) in the main text. Note that the additional term k_{s} represents the shrinking tendency of a vessel. This term is interpreted by Pries et al. (1998) as reflecting a natural reaction of the basal lamina, which acts to counter any increase in vessel diameter.

Flow Model Parameters

1. *Vessel Properties*: For the a posteriori remodeling simulations presented, the initial radius of each capillary segment was taken to be 6 μm and remodeling of the vessels was permitted within a range, from a minimum radius of 2 μm (essentially eliminating flow) to a maximum radius of 12 μm. During the DATIA simulations, nascent, non-flowing capillaries (i.e. those not yet part of the

connected flowing network) were assigned 6 μm radii and remodeling was again considered in the range (2, 12) μm. In all simulations, the radius of the parent vessel was kept fixed at 14 μm. These values correspond to vessel radii at the capillary level, where the size of the vessels are very close to the size of the red blood cells (Ciofalo et al. 1999).

2. *Adaptation Parameters*: The parameters used for the base case adaptation model presented in (8.5) were taken to be:

$$k_s = 0.35 \quad k_p = 0.1 \quad k_m = 0.07$$

$$t_{ref} = 0.103 \quad Q_{ref} = 1.909e - 11,$$

(after Stéphanou et al. 2005a, b), where Q_{ref} corresponds to the flow in the parent vessel, calculated from (8.3) with $R = 14\,\mu m$, $L = 2\,mm$ and $\Delta P = 1{,}200$ Pa (9 mmHg) (the pressure drop across the parent vessel). The plasma viscosity m_{plasma} is 1.2×10^{-3} Pa s and this parameterisation gives perfusion velocities in the parent vessel of approximately $3\,mm\,s^{-1}$. One of the main determinants of the extent of vascular remodeling is the intravascular pressure (P). In the simulations carried out here, we have chosen inlet and outlet pressures to ensure average intravascular pressures of approximately 20 mmHg, in accordance with physiological values at the capillary scale.

References

Alarcon T, Byrne HM, Maini PK (2003) A cellular automaton model for tumour growth in inhomogeneous environment. J. Theor. Biol. 225(2), 257–274.

Anderson ARA, Chaplain MAJ (1998) Continuous and discrete mathematical models of tumor-induced angiogenesis. Bull. Math. Biol. 60, 857–899.

Armulik A, Abramsson A, Betsholtz C (2005) Endothelial/pericyte interactions. Circulation Research, 97, 512–523.

Ausprunk DH, Folkman J (1977) Migration and proliferationof endothelial cells in preformed and newly formed blood vessels during tumour angiogenesis. Microvasc. Res. 14, 53–65.

Bagley RG, et al. (2006) Pericytes from human non-small cell lung carcinomas: An attractive target for anti-angiogenic therapy. Microvascular Res. 71, 163–174.

Baish JW, Gazit Y, Berk DA, Nozue M, Baxter LT, Jain RK (1996) Role of tumor vascular architecture in nutrient and drug delivery: an invasion percolation-based network model. Microvasc. Res. 51, 327–346.

Benjamin LE, I. Hemo I, Keshet E (1998) A plasticity window for blood vessel remodelling is defined by pericyte coverage of the preformed endothelial network and is regulated by PDGF-B and VEGF. Development 125, 1591–1598.

Bray D (1992) Cell Movements, New-York: Garland Publishing.

Brekken RA, Thorpe PE (2001) Vascular endothelial growth factor and vascular targeting of solid tumors. 21, 4221–4229.

Chantrain CF, Henriet P, Jodele S, Emonard H, Feron O, Courtoy PJ, DeClerck YA, Marbaix E (2006) Mecanisms of pericyte recruitment in tumour angiogenesis: A new role for metalloproteinases. European J. Cancer 42, 310–318.

Davis GE, Pintar Allen KA, Salazar R, Maxwell SA (2000) Matrix metalloproteinase-1 and –9 activation by plasmin regulates a novel endothelial cell-mediated mechanism of collagen gel contraction and capillary tube regression in three-dimensional collagen matrices. J. Cell Sci. 114, 917–930.

El-Kareh AW, Secomb TW (1997) Theoretical models for drug delivery to solid tumours. Crit. Rev. Biomed. Eng. 25(6), 503–571.

Folkman J, Klagsbrun M (1987) Angiogenic factors. Science. 235, 442–447.

Gee MS, Procopio WN, Makonnen S, Feldman MD, Yeilding NW, Lee WMF (2003) Tumor vessel development and maturation impose limits on the effectiveness of anti-vascular therapy. Am. J. Path. 162, 1, 183–193.

Gödde R, Kurz H (2001) Structural and biophysical simulation of angiogenesis and vascular remodelling. Developmental Dynamics 220, 387–401.

Hidalgo M, Eckhardt SG (2001) Development of matrix metalloproteinase inhibitors in cancer therapy. Journal of the National Cancer Institute 93, 178–193.

Hughes S, Gardiner T, Hu P, Baxter L, Rosinova E, Chan-Ling T (2006) Altered pericyte-endothelial relations in the rat retina during aging: Implications for vessel stability. Neurobiology of Aging 27, 1838–1847.

Izumi Y et al. (2002) Tumour biology: herceptin acts as an antiangiogenic cocktail. Nature 416, 279–280.

Jackson TL, Lubkin SR, Murray JD (1999) Theoretical analysis of conjugate localization in two-step cancer chemotherapy. J. Math. Biol. 39, 353–376.

Jain RK (2003) Molecular regulation of vessel maturation. Nat. Med. 9, 685–93.

Krenz GS, Dawson CA (2002) Vessel distensibility and flow distribution in vascular trees. J. Math. Biol. 44, 360–374.

Kumar CC (2000). Targeting integrins avb3 and avb5 for blocking tumour-induced angiogenesis. Adv. Exp. Med. Biol. 476, 169–180.

Levine HA, Pamuk S, Sleeman BD, Nielsen-Hamilton M (2001) Mathematical modeling of the capillary formation and development in tumor angiogenesis: penetration into the stroma. Bull. Math. Biol. 63(5), 801–863.

McDougall SR, Anderson ARA, Chaplain MAJ, and Sherratt JA (2002) Mathematical modeling of flow through vascular networks: implications for tumour-induced angiogenesis and chemotherapy strategies. Bull. Math. Biol. 64(4), 673–702.

McDougall SR, Anderson ARA, Chaplain MAJ (2006) Mathematical modeling of dynamic adaptive tumour-induced angiogenesis: clinical implications and therapeutic targeting strategies. Journal of Theoretical Biology 241, 564–589.

Madri JA, Pratt BM (1986) Endothelial cell-matrix interactions: in vitro models of angiogenesis. J. Histochem. Cytochem. 34, 85–91.

Mancuso MR, et al. (2006) Rapid vascular regrowth in tumors after reversal of VEGF inhibition. J. Clin. Investigation. 116, (10), 2610–2621.

Morikawa S, Baluk P, Kaidoh T, Haskell A, Jain RK, McDonald DM (2002) Abnormalities in pericytes on blood vessels and endothelial sprouts in tumors. Am. J. Path. 160, 985–1000.

Munn LL (2003) Aberrant vascular architecture in tumors and its importance in drug-based therapies. Drug Discovery Today 8, 396–403.

Paweletz N, Knierim M (1989) Tumor-related angiogenesis. Crit. Rev. Oncol. Hematol. 9, 197–242.

Pries AR, Secomb TW, Gaehtgens P (1996) Biophysical aspects of blood flow in the microvasculature. Cardiovasc Res, 32, 654–667.

Pries AR, Secomb TW, Gaehtgens P (1998) Structural adaptation and stability of microvascular netwoks: theory and simulation. Am. J. Physiol. 275 (Heart Circ. Physiol. 44), H349–H360.

Pries AR, Reglin B, Secomb TW (2001a) Structural adaptation of microvascular networks: functional roles of adaptive responses. Am. J. Physiol. Heart Circ. Physiol. 281, H1015–H1025.

Pries AR, Reglin B, Secomb TW (2001b) Structural adaptation of vascular networks: role of the pressure response. Hypertension 38, 1476–1479.

Quarteroni A, Tuveri M, Veneziani A (2000) Computational vascular fluid dynamics: problems, models and methods. Comput. Visual. Sci. 2, 163–197.

Rafil S, et al. (2002) Vascular and haematopoietic stem cells: novel targets for anti-angiogenesis therapy? Nature Reviews Cancer 2, 826–835.

Rouget C (1873) Memoire sur le developpement, la structure et les proprietes physiologiques des capillaires sanguins et lymphatiques. Arch. Physiol. Norm. Pathol. 5: 603–663.

Secomb TW (1995) Mechanics of blood flow in the microcirculation. In "Biological Fluid Dynamics." eds. C.P. Ellington and T.J. Pedley. Company of Biologists, Cambridge, pp. 305–321.

Schoefl GI (1963) Studies of inflammation III. Growing capillaries: Their structure and permeability. Virchows Arch. Path. Anat. 337, 97–141.

Sholley MM, Ferguson GP, Seibel HR, Montour JL, Wilson JD (1984) Mechanisms of neovascularization. Vascular sprouting can occur without proliferation of endothelial cells. Lab. Invest. 51, 624–634.

Stéphanou A, McDougall SR, Anderson ARA, Chaplain MAJ (2005a) Mathematical modeling of flow in 2D and 3D vascular networks: applications to anti-angiogenic and chemotherapeutic drug strategies. Math. Comp. Model. 41, 1137–1156.

Stéphanou A, McDougall SR, Anderson ARA, Chaplain (2005b) Mathematical modeling of the influence of blood rheological properties upon adaptive tumour-induced angiogenesis. Math. Comp. Model. 44, 96–123.

Sternlicht MD, Werb Z (2001) How matrix metalloproteinases regulate cell behavior. Annu Rev Cell Dev Biol 17, 463–516.

Tozer GM, Kanthou C, Baguley BC (2005) Disrupting tumour blood vessels. Nature Reviews Cancer Vol 5 (June 2005), 423–433.

Yan L, Moses MA, Huang S, Ingber D (2000) Adhesion-dependent control of matrix metalloproteinase-2 activation in human capillary endothelial cells. J. Cell Sci. 113, 3979–3987.

Chapter 9
Modeling Structural and Functional Adaptation of Tumor Vessel Networks During Antiangiogenic Therapy

Lance L. Munn, Walid Kamoun, Michael Dupin, and James Alex Tyrrell

1 Introduction

During tissue development or recovery from wounds or ischemia, immature, angiogenic blood vessels respond to blood forces, re-organizing locally to optimize the network globally (Hansen-Smith et al. 1996; Ichioka et al. 1997; Al-Kilani et al. 2008; Hudlicka and Brown 2009; Reglin et al. 2009). In this process of structural adaptation, some segments dilate, while others are pruned. A stable configuration is eventually reached and then supported and maintained by perivascular cells. In contrast, tumor blood vessels are chronically immature, probably due to the high levels of VEGF and other growth factors in the microenvironment. Interestingly, many anti-VEGF therapies can cause maturation and stabilization of tumor blood vessels through a process resembling flow-based adaptive remodeling (Fig. 9.1).

The structural and functional changes observed in tumor vasculature in response to antiangiogneic therapy –collectively known as vascular "normalization" (Jain 2001) – have been shown to improve the efficacy of subsequently administered chemotherapeutics (Willett et al. 2004; Huber et al. 2005; Jain 2005; Vosseler et al. 2005; Nakahara et al. 2006). The predominant effects of anti-VEGF therapies are decreased vessel leakiness (hydraulic conductivity), decreased vessel diameters and pruning of the immature vessel network (Tong et al. 2004; Winkler et al. 2004; Kamoun et al. 2009) (Fig. 9.2). It is thought that each of these can influence perfusion of the vessel network, inducing flow in regions that were previously sluggish or stagnant. Unfortunately, changes induced by anti-VEGF therapies are dynamic and overlapping in time, and it has been difficult to identify a consistent

L.L. Munn (✉) • W. Kamoun • M. Dupin • J.A. Tyrrell
Massachusetts General Hospital and Harvard Medical School, 149 13th Street, room 3409, Charlestown, MA 02129, USA
e-mail: lance@steele.mgh.harvard.edu; walid@steele.mgh.harvard.edu; mdupin@steele.mgh.harvard.edu; james@steele.mgh.harvard.edu

T.L. Jackson (ed.), *Modeling Tumor Vasculature: Molecular, Cellular, and Tissue Level Aspects and Implications*, DOI 10.1007/978-1-4614-0052-3_9,

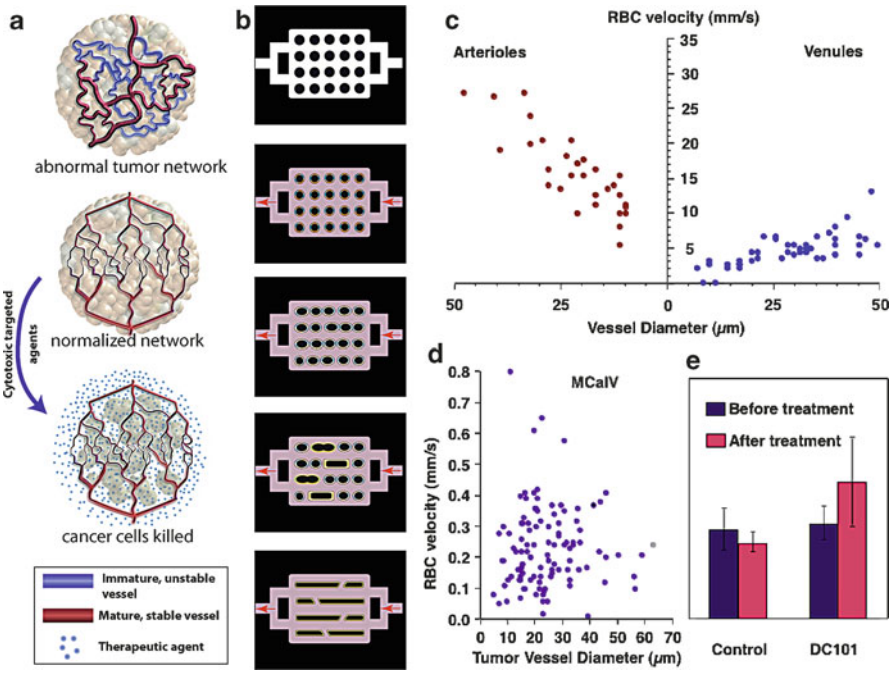

Fig. 9.1 Vascular normalization and adaptive remodeling. (**a**) Antiangiogenic therapies induce structural changes in tumor vessel architecture and increase the efficacy of subsequent chemotherapeutics. (**b**) Schematic illustration of flow-based adaptive remodeling in an idealized network. Flow through the network (*arrows*) results in shear stress gradients on endothelial cells, triggering remodeling. The resulting network is more efficient and offers less resistance to flow. (**c**) Blood flow velocity data from normal pial vessels. There is a positive correlation between velocity and diameter in both arterioles and venules. (**d**) In tumor vessels, there is no correlation between velocity and diameter, indicating that adaptive remodeling is dysfunctional (Yuan et al. 1994). (**e**) The VEGFR-2 blocking antibody, DC101, can increase the average RBC velocity in tumors, a potential mechanism in the restoration of uniform delivery

and predictable normalization "window" during which perfusion and subsequent drug delivery is optimal. This is largely due to the nonlinearity in the system, and the inability to distinguish the effects of decreased vessel leakiness from those due to network structural changes.

Because of its similarities to flow-based adaptation seen in other systems, normalization in tumors may be driven by blood shear forces as well as levels of growth factors such as VEGF. An appropriate mathematical model, which incorporates the necessary elements for predicting the convection and diffusion of nutrients and drugs throughout tumor vessels and tissues, as well as the adaptive remodeling of the network topology is needed to dissect the critical determinants of vessel normalization.

To address this problem, we developed a mathematical model to decouple vascular leakiness and network structural changes; this allows determination of how

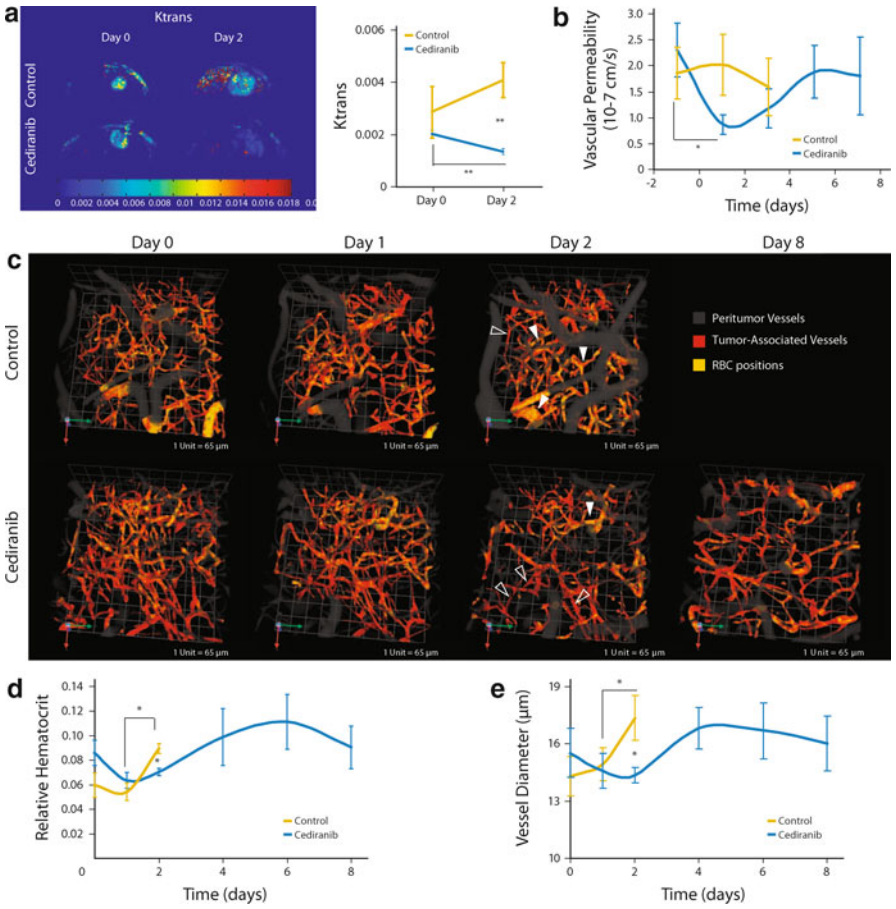

Fig. 9.2 Anti-VEGF treatment normalizes glioma vessel morphology and function. (**a**) Cediranib treatment (6 mg/kg each day) leads to a statistically significant decrease in Ktrans. (**b**) Cediranib significantly decreases vascular permeability measured by intravital microscopy. (**c**) Representative multiphoton laser scanning microscopy (MPLSM) three-dimensional reconstruction of the tumor (*red*) and peritumor vessels (*gray*) superimposed with RBC positions acquired through analysis of injected fluorescently labeled RBC. Control animals have predominantly hemoconcentrated vessels (*closed arrows*). Cediranib-treated animals have predominantly low hematocrit vessels (*open arrows*). (**d**) Mean and SE of tumor vessel relative hematocrit measured by MPLSM. Cediranib significantly decreases relative hematocrit. (**e**) Cediranib transiently but significantly decreases vessel diameter measured by MPLSM

each influences flow patterns and oxygen and drug delivery during antiangiogenic therapy. An understanding of how hydraulic conductivity and network architecture act independently – or in synergy – to enhance delivery of chemotherapeutics will allow rational use of existing drugs, or the design of new ones, to improve chemotherapy.

2 Antiangiogenic Therapies and Tumor Vessel Normalization

Because tumors require production of new vasculature to grow, Folkman proposed that preventing new vasculature would effectively control solid tumors (Folkman 1971). And because VEGF is a major growth factor that supports the growth of new vasculature, it has been the target of many recent therapies (Ferrara et al. 2004; Ferrara and Kerbel 2005; Fischer et al. 2008; Jain 2008).

Unfortunately, the original goal of antiangiogenic therapies – to starve tumors by targeting their blood supply– has been elusive. In most clinical studies, these therapies have had inconsistent effects on tumor physiology, with no long-term inhibition of tumor growth (Ko et al. 2008; Kerbel 2009). Nevertheless, drugs that block angiogenic growth factors such as VEGF often have dramatic effects on the structure and function of the vascular network. Antiangiogenic therapy has been shown to produce "normalization" of tumor blood vessels, improving the efficacy of subsequently administered chemotherapeutics (Figs 9.1a and 9.2) (Jain 2001; Munn 2003). In theory, antiangiogenic drugs targeting endothelial VEGF signaling can improve vessel network structure and function, enhancing the transport of subsequent chemotherapeutics to cancer cells (Ansiaux et al. 2006; Batchelor et al. 2007; Hamzah et al. 2008; Stockmann et al. 2008; Wu et al. 2009). In practice, the effects are unpredictable. The predominant effects of anti-VEGF therapies are decreased vessel leakiness (hydraulic conductivity), decreased vessel diameters and pruning of the immature vessel network (Tong et al. 2004; Winkler et al. 2004; Kamoun et al. 2009) (Fig. 9.2).

Enhanced delivery of subsequent drugs to tumors after vascular normalization might be achieved by affecting vascular architecture or permeability. Tumor vessels have abnormal geometry and connectivity. Therefore, structural and topological changes induced by antiangiogenic therapy (e.g., diameter changes, pruning redundant segments) may result in a network that is more evenly distributed in the tissue. These changes in topology may alter flow patterns by changing the pressures and resistances within the network, thus forcing flow into previously unperfused regions. Changes in vessel permeability to plasma can cause similar changes in network pressure distribution, restoring normal perfusion patterns. Decreased vessel leakiness can also enhance uniform convection through the tissue by restoring the driving force for convection across the vessel into the interstitium (Jain et al. 2007).

The ability of VEGF to modulate vascular permeability has been well-studied, but less is known about its role in structural changes in tumor vasculature, or whether other signals are involved. It is well known that endothelial cells sense shear stress, and through pathways that include nitric oxide signaling, re-organize in the vessel wall to adjust local shear to optimum levels (Pries et al. 1995; Zakrzewicz et al. 2002; Brown and Hudlicka 2003). By contracting or dilating individual segments, overall flow patterns develop that distribute flow evenly through the network. It is therefore possible that VEGF somehow works together with shear stress to remodel immature tumor vessel networks, similar to that observed in wound healing and skeletal muscle (Hansen-Smith et al. 1996; Ichioka et al. 1997;

Hudlicka and Brown 2009; Reglin et al. 2009). Furthermore, there are likely optimal configurations of network architecture and hydraulic conductivity for delivering drugs to tumors.

To understand this complex physiology and distinguish between structural and functional determinants, we have developed a mathematical model that simulates blood flow in complex tumor networks imaged by two-photon microscopy. The model incorporates the necessary components for simulating vascular structure and function during anti-VEGF therapy: (1) lattice-Boltzmann calculations of the full flow field within the vasculature and within the tissue, (2) diffusion and convection of soluble species such as oxygen or drugs within vessels and the tissue domain, (3) distinct and spatially resolved vessel hydraulic conductivities and permeabilities for each species, (4) erythrocyte particles advecting in the flow and delivering oxygen with real oxygen release kinetics, and (5) hypoxia-driven VEGF production, and vi) vascular remodeling driven by VEGF level and shear stress.

3 VEGF Pharmacodynamics

VEGF plays a pervasive and complex role in blood vessel biology. When present at high levels (e.g. when produced by hypoxic cells in wounds or tumors), it is angiogenic, causing endothelial cell proliferation and migration. On the other hand, lack of VEGF can send endothelial cells into senescence, and VEGF is required (at low levels) to maintain a stable vasculature (Baffert et al. 2006; Rudge et al. 2007). Therefore, in the absence of VEGF, blood vessels cannot survive. VEGF also increases permeability of tumor vessels, allowing plasma leakage in regions where VEGF is high (Chien et al. 1988; Senger et al. 1993; Hashizume et al. 2000). This focal leakiness can have a dramatic effect on the blood flow within the vasculature as well as fluid convection through the interstitium.

Figure 9.2 shows typical structural and functional changes in blood vessels exposed to an antiangionic drug. Mice bearing glioma is cranial windows were treated with cediranib, a tyrosine kinase inhibitor that blocks VEGF signaling, and monitored for changes in vessel permeability, hematocrit and vascular architecture (Kamoun et al. 2009). MRI showed that cediranib significantly decreased K_{trans} – a parameter dependent on vascular permeability – in the glioblastoma xenografts (Fig. 9.2a). Furthermore, cediranib significantly decreased tumor vessel permeability and diameter, as well as vascular hemoconcentration (elevated hematocrit, Fig. 9.2b–e).

4 Models of Angiogenesis and Structural Adaptation

A number of elegant theoretical and experimental studies have addressed the issues of tumor angiogenesis and structural adaptation of blood vessels. Lee et al. modeled a growing tumor and a dynamically evolving blood vessel network, reproducing

inhomogeneous tumor-like capillary networks (Lee et al. 2006). This model also reproduced vessel collapse due to reduced blood flow and mechanical compression. Welter and coworkers developed a model to analyze the vascular remodeling process of an arterio-venous vessel network during tumor growth and were able to reproduce complex vascular geometry with necrotic zones and "hot spots" of increased vascular density and blood flow of varying size (Welter et al. 2009). Szczerba and Szekely presented a simple computational model of intussusceptive angiogenesis and remodeling, predicting bifurcation formation and micro-vessel separation in a porous cellular medium (Szczerba and Szekely 2005).

For many years, Pries and Secomb have been at the forefront of the field of angioadaptation in normal physiology and ischemia. Their mathematical models predict vascular patterns that can be compared with vasculature in vivo. An important conclusion from their work is that four parameters are necessary to drive the adaptation to the correct steady state: endothelial wall shear stress, intravascular pressure, a flow-dependent metabolic stimulus, and a stimulus conducted from distal to proximal segments along vascular walls (Pries et al. 1998, 2005; Pries and Secomb 2008). More recently, they proposed that aberrant tumor microcirculation may result from defective structural adaptation (Pries et al. 2009).

Other models have been used to analyze perturbations in blood flow, such as caused by vascular obstructions. Gruionu et al. used morphometric data from vascular casts to simulate the changes in blood flow caused by obstructions, and the subsequent adaptive remodeling. They found that vascular arcades can partially maintain blood flow after vascular blockage and that structural adaptation is important for modifying vessel diameters and controlling flow in this system (Gruionu et al. 2005).

Unfortunately, the existing models generally make simplifying, yet crippling, assumptions about blood flow and the transport of soluble species, or are restricted to two dimensional, artificial networks. Our goal was to build upon these models, adding accurate mechanisms for oxygen delivery and VEGF production to fully resolved advection and convection through actual tumor vessels and tissue.

5 Modeling Tumor Physiology

Our model uses the lattice-Boltzmann approach we have been developing over the past 10 years. Initial applications of this model included studies of interactions between red and white blood cells in dynamic flow (Migliorini et al. 2002; Sun and Munn 2005) and the effects of vessel geometry (Sun et al. 2003) and RBC aggregation (Sun and Munn 2006) on blood rheology. In addition, this approach has allowed us to analyze the relationship among plasma, intravascular hematocrit and blood velocities in simple vessel networks (Sun et al. 2007) and blood forces on digitized vessel walls (Sun and Munn 2008). More recently, we have adapted the model to analyze flowing blood cells with realistic rest shapes and mechanical properties in three dimensions (Dupin et al. 2007 2008a, b; Munn and Dupin 2008).

In other modeling work, we have used deterministic models to analyze fluid convection and pressure distribution in tumors during normalization (Jain et al. 2007). But this approach is limited, not explicitly accounting for blood vessel architecture blood flow or adaptive remodeling. The current model, therefore, extends our lattice-Boltzmann approach to larger domains, and more complicated networks to address questions of heterogeneous perfusion and transport in relatively large volumes of tumor tissue.

5.1 Model Description (Tyrrell et al. in press)

Vascular normalization is still poorly understood, and we cannot predict, in a given tumor, which mechanisms are most important or how they might fail. This makes it difficult to interpret preclinical data or to develop robust, effective clinical strategies. Many mathematical models have been formulated and used to study blood vessel development and function (Chaplain and Anderson 1996, 2004; Gillies et al. 1999; Sun et al. 2005; Jones and Sleeman 2006; Schugart et al. 2008; Kang et al. 2009; Macklin et al. 2009; Pries and Secomb 2009), drug delivery to tumor tissue (Baxter and Jain 1988, 1991a; Baxter et al. 1992; Netti et al. 1996; Baish et al. 1997) or vessel normalization (Jain et al. 2007; Sun et al. 2007). Unfortunately, there is no single comprehensive, predictive mathematical framework for studying the nonlinear relationships between vessel structure and function in real networks.

The minimum requirements for such a mathematical model are (Tyrrell et al. in press):

1. Operate on actual 3D networks obtained from intravital imaging.
2. Solve the pressure-driven flow within the vessel network and throughout the interstitium.
3. Incorporate red blood cells in the flow with accurate oxygen release kinetics and metabolism.
4. Include mechanisms of hypoxia-induced VEGF production.
5. Provide for transvascular and interstitial transport of multiple species, including, for example, oxygen and drugs.
6. Allow the network to re-organize via adaptive remodeling driven by shear stress and growth factors.

5.2 LBM Flow Solver

We use a lattice Boltzmann model (LBM) to solve the flow and transport of blood (Sun et al. 2003, 2007; Sun and Munn 2005; Dupin et al. 2007; Munn and Dupin 2008), oxygen, drugs, and growth factors in the tissue. Being fully

local, LBM offers a distinct advantage over traditional CFD when dealing with complex boundary conditions and highly irregular geometry within the computational domain. Further, coding an LBM solver is rather simple, and the algorithmic complexity is the same in either two- or three-dimensions. In addition, the LBM approach is imminently adaptable to parallel and distributed implementations.

Having its roots in kinetic theory, LBM also offers the advantage of studying the continuum macroscopic properties of a system from its microscopic phenomena. Central to the lattice Boltzmann method is the single-particle distribution function $f(x, \rho, t)$. It describes a fictive particle's state in terms of a statistical ensemble with a measurable probability of being observed with a certain position x and momentum ρ at time t. This distribution function is discretized to have a finite number of velocity components confined to a regular Cartesian lattice (Fig. 9.3a).

The choice of lattice structure is classified according to the DnQm scheme. Here, "D" specifies the dimension and "Q" the number of discrete velocities. In two-dimensions the D2Q9 lattice is preferred, i.e., two-dimensions with 8 velocity components linking nearest-neighbor lattice nodes, plus one velocity reserved for rest particles. However, in three-dimensions, one typically does not need all 26 velocity components linking nearest neighbor lattice nodes, i.e., D3Q27. Instead, the D3Q15 lattice scheme is often preferred.

From the discretized distribution function $f_i(x, t)$, where i indexes the e_i velocity components, one can determine the macroscopic density and velocity as:

$$\rho_f = \sum_i f_i, \mathrm{u} = \frac{1}{\rho_f} \sum_i f_i e_i.$$

Importantly, the ideal gas equation of state in LBM gives the fluid pressure as $P = (1/3)\rho$ and hence the two quantities are often referred to interchangeably as pressure/density.

Determining the distribution function at time t is a two-part process consisting of a *streaming step*, which propagates particles between lattice nodes, followed by a *collision step,* which updates the momentum of the underlying particles as a result of particle–particle interactions. A key development in the application of LBM to systems involving fluid flow is the single-relaxation time Bhatnagar-Gross-Krook (BGK) approximation (Succi 2001):

$$\underbrace{f_i(x + e_i \Delta t, t + \Delta t) = f_i(x, t)}_{\text{streaming}} \quad \underbrace{-1/\tau(f_i(x, t) - f_i^{\mathrm{eq}}(x, t))}_{\text{collision}},$$

where $f_i^{\mathrm{eq}}(\mathrm{x}, t)$ is the equilibrium distribution function defined as:

$$f_i^{\mathrm{eq}}(x, t) = w_i \rho_f (1 + 3e_i \cdot u + 9/2(e_i \cdot u)^2 - 3/2u' \cdot u),$$

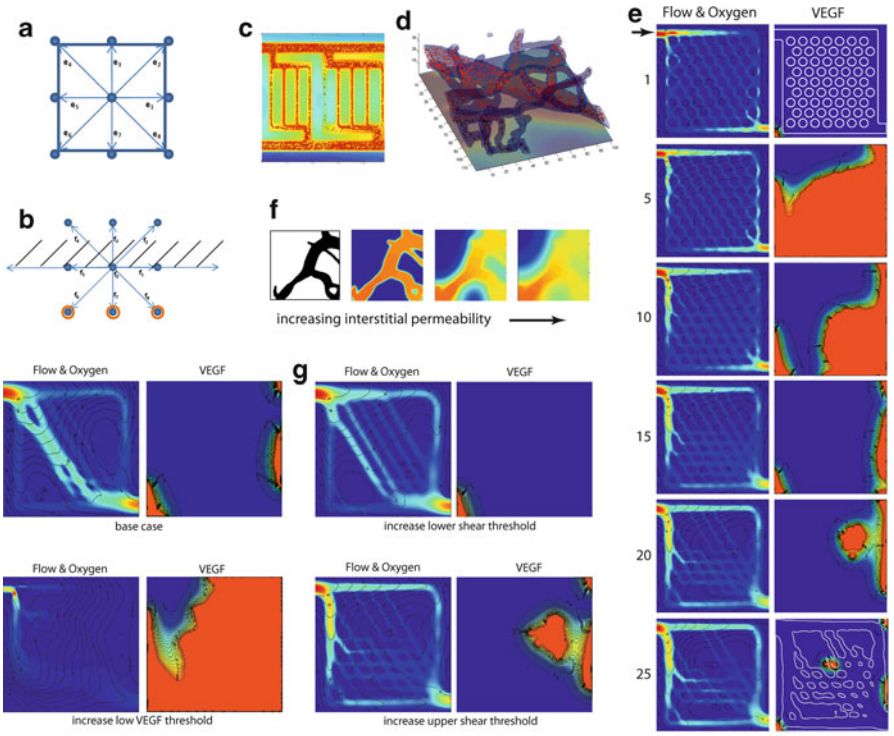

Fig. 9.3 Simulating vessel network dynamics. (**a**) LBM discretized velocities (**b**) Boundary treatment in LBM (**c**) A two-dimensional idealized network with flow from left to right in the top vessel (arteriole), from right to left in the bottom vessel (venule) and from top to bottom through the capillary bed. The particles delivering oxygen are red, and the color map gives the oxygen profile in the tissue. (**d**) Flow and oxygen transport from tumor vasculature in three dimensions. The vasculature of a U87 glioma growing in a mouse was traced using techniques described in Tyrrell et al. (2005). (**e**) Simulation of adaptation in a 2D mesh network over 25 iterations (iteration number is shown at left). Flow velocity is given by the color map; the oxygen contour lines are in *black*. The initial and final network boundaries are shown in *white in the top right and bottom right panels*. Blood flows into the top left and exits the bottom right channel. With this parameter set, there is an initial excess of oxygen metabolism that induces VEGF in the beginning. Vessel dilation and remodeling compensate, relieving the initial hypoxia. Local VEGF production protects vessels from pruning, even if shear is below the lower threshold. (**f**) Simulating intravascular and interstitial transport of drugs with varying diffusivity. A portion of a tumor network was traced and the model simulates flow through the network and interstitial space. By changing the bounce-back conditions at nodes outside the vessel boundary, we can simulate varying levels of interstitial diffusivity. (**g**) Snapshots of simulations in an ideal 2D network. The initial network was the same as that in panel E, *top right*, in all cases. Each simulation was run for 19 remodeling iterations. Increasing the lower shear threshold results in initial contraction of vessels in the lower left part of the domain, which redirects flow to the top right; this drives flow through more of the "capillaries," maintaining them for more iterations compared with the base case. Increasing the lower VEGF threshold subjects vessels to indiscriminate contraction, which closes the upper main feeding arteriole. Thus, this domain is very hypoxic by iteration 19. Finally, increasing the upper shear threshold exposes fewer high-flow vessels to dilation. This effectively maintains vessel diameters in the capillary bed, preventing the dilation/coalescence seen in the base case (Tyrrell et al. in press)

where w_i are lattice weights with $\sum w_i = 1$. The collision operator is defined as a *relaxation toward local equilibrium*. The parameter τ controls the rate of relaxation, and is directly related to the kinematic viscosity of the fluid under study:

$$\nu = \frac{1}{3}\left(\tau - \frac{1}{2}\right)$$

5.3 Boundary Conditions

Complex and irregular boundaries are simple to handle using LBM, making it ideal for modeling vascular networks. There are essentially two important types of boundary conditions: (a) those that involve fluid/solid interfaces at internal lattice nodes and (b) those that involve the domain boundary. To handle the first type, a zero-slip boundary condition is enforced on all fluid/wall interfaces. A particularly simple approach is to omit the collision step above at all solid nodes and instead reflect all incoming fluid packets in the reverse outgoing direction. This is referred to as the mid-plane bounceback rule:

$$f_\alpha^{\text{out}}(x,t) = f_{-\alpha}^{\text{in}}(x,t^-),$$

where $\alpha, -\alpha$ correspond to opposite lattice directions, i.e., $-e_\alpha = e_{-\alpha}$ and the t^- indicates the half-time step just prior to collision. The mid-plane bounceback rule gets its name from the fact that the "wall" is actually situated half-way between adjacent fluid/solid nodes. Note, in practice, the rule works best when $\tau \approx 1$.

When a lattice node lies on the boundary of the domain, one has a problem during the streaming step, as certain fluid packets will be undefined. To illustrate, consider the 2-d example at a north wall interface in Fig. 9.3b. After streaming, the direction specific densities f_6, f_7, f_8 are unknown because the implied off-lattice nodes above the boundary do not contribute during the streaming step. The simplest solution is to invoke periodic boundary conditions where outgoing fluid packets are wrapped around the domain. Additionally, one can specify Dirichlet (pressure) boundaries at the inlet and outlet of a channel. This requires solving for the three unknown fluid packets as well as the macroscopic velocity in the direction normal to the boundary. The solution involves simple algebra. First, from above, we have the equations for pressure (a scalar). This is set to $\rho_0 = \sum f_i$. Next, the equation for velocity is a vector, and gives 2 constraints:

$$0 = f_2 - f_4 + f_1 - f_5 + f_8 - f_6,$$
$$\rho_0 v = f_6 - f_4 + f_7 - f_3 + f_8 - f_2$$

Hence, one more constraint is needed, and is provided by assuming the bounceback condition applies to the normal directions:

$$f_7 - f_7^{\text{eq}} = f_3 - f_3^{\text{eq}}$$

giving a system of four equations with four unknowns. Similarly, one can specify an incoming velocity and outgoing pressure (flux boundaries). Details of the solution in both 2/3-dimensions can be found in (Zou and He 1997).

5.4 Transvascular Convection and Diffusion

Another attractive aspect of the LBM technique is its ability to simulate multicomponent flows including a fluid and gas phase. When a gas species, e.g., oxygen, has a momentum that is negligible compared to blood plasma, it can be considered a *passive solute*, which does not impact the pressure or velocity fields of the advecting fluid. Rather, the solute is simply advected by the background fluid.

The key artifice is to introduce another distribution function that uses a simplified equilibrium distribution function:

$$g_i^{\mathrm{eq}}(\mathrm{x}, t) = w_i C_{\mathrm{g}}(1 + 3\mathrm{e}_i \cdot \mathrm{u}),$$

where C_{g} analogously represents the gas concentration, rather than a fluid density. The macroscopic velocity u is taken directly from the underlying fluid. Constant flux/concentration boundary conditions can be specified in a manner similar to the Dirichlet boundary condition described above (Sukop and Thorne 2007).

An important aspect of LBM solute transport models is that they are known to generally solve the convection-diffusion/dispersion equation under a variety of conditions (Sukop and Thorne 2007). For example, in the case where the fluid has no velocity, LBM can be shown to solve the diffusion equation. Here, the diffusion coefficient of the solute is then analogous to the kinematic viscosity of the underlying fluid (Sukop and Thorne 2007):

$$D = \frac{1}{3}\left(\tau_g - \frac{1}{2}\right)$$

Note that the relaxation rate of the gas solute and underlying fluid are independent, hence the notation τ_g.

5.5 Interstitial Convection and Diffusion

LBM techniques have been applied successfully to the study of complex porous media (Dardis and McCloskey 1998). The idea is to specify a computation domain consisting of open "fluid" nodes bounded by "solid" nodes that represent a porous medium. Though simple and effective, the lattice resolution must be on the order of the smallest pore or conduit in the material being studied. It also implicitly requires

one to know the pore-space geometry, which might be infeasible. Instead, a partial bounce-back (PBB) rule can be employed to simulate a mesoscale permeability (Walsh et al. 2008):

$$f_{\alpha}^{\text{out}}(\mathrm{x},t) = (1-n_s)\, f_{\alpha}(\mathrm{x},t) + n_s\, f_{-\alpha}^{\text{in}}(\mathrm{x},t^{-}).$$

Note, that this revised partial bounceback rule is similar to the mid-plane rule introduced above, except that a fraction n_s of the distribution before collision (note the t^{-}) is added to the distribution after collision. Further, when the solid fraction is unity, the partial bounceback rule actually recovers the original mid-plane boundary condition. Similarly, for a solid fraction of zero, the standard collision rule is in effect.

By utilizing partial bounce-back, the entire computational domain becomes open to both flow and solute transport. Thus, we are able to study interstitial convection and diffusion at the mesoscale level. Further, local spatial modulation of the partial bounce-back is ideal for simulating phenomenon like vessel wall permeability and can be used to independently control diffusion in plasma and the interstitium. Naturally, as each component of the flow has a separate distribution function, permeability can be tailored independently.

5.6 Incorporation of RBC Particles and Oxygen Release (Fig. 9.3c, d)

As presented thus far, the basic LBM approach is unable to capture the physiological effects that red blood cells (RBCs) have on the transport of oxygen in blood. For example, at oxygen partial pressures typical in arterioles (20–60 mmHg), the oxygen content of hemoglobin in a volume of blood at 30% hematocrit, is nearly two orders of magnitude greater than the dissolved oxygen in an equivalent volume of plasma (Waite and Fine 2007). Therefore, to accurately simulate oxygen delivery to tissue, a mechanism to simulate the oxygen content of hemoglobin in blood must be included. A particle suspension is a natural choice.

Our on-going work has focused on highly accurate modeling of the red blood cell membrane, and the interaction among RBCs, leukocytes, platelets, and cell–cell, cell–fluid and cell–wall interactions. For example, important phenomena such as inertial lift forces and RBC aggregation evolve naturally from these complex models based on the underlying physics. In the current simulations, we utilize a simpler particle model and impose the same physics as external constraints. This allows us to focus on the primary problem of interest, oxygen delivery and consumption in the interstitium. Hence, we utilize an approach whereby RBCs simply advect with the underlying fluid. To describe the position of each particle p_i we also include a Brownian motion along with an interparticle and wall repulsion force:

$$\mathrm{p}_i(t+\Delta t) = \mathrm{p}_i(t) + \Delta t \left(u(p_i(t)) + w_{\sigma} + F_{\text{wall}}(p_i(t)) + \sum\nolimits_{i \neq j} F_p(p_i(t), p_j(t)) \right).$$

Here, the underlying fluid velocity $\mathrm{u}(\mathrm{p}_i(t))$ provides the advective component, and w_σ is a Gaussian white-noise process whose integration over time is equivalent to a Brownian motion. The wall force density is a nonlinear function involving the magnitude and gradient of the Euclidean distance map. This map gives the minimum distance between any point in the domain and the nearest wall point. The wall force is tuned to ensure an appropriate cell-free layer. Interparticle forces are defined similarly over a small local neighborhood around each particle.

5.7 Metabolism

Accurately modeling the kinetics of oxygen delivery and consumption are a key aspect of the proposed model. Modeling reactive flows is straightforward using LBM and in its simplest form amounts to a modification of the collision operator to include a change in density/concentration at each time step (Succi 2001; Alemani 2007):

$$f_i(x + e_i \Delta t, t + \Delta t) = f_i(x,t) - 1/\tau(f_i(x,t) - f_i^{eq}(x,t)) + R_i,$$

where $\bar{R} = \sum R_i$ represents the reaction rate. Key parameters like the diffusion rate and solubility of oxygen in blood/tissue, as well as the oxygen consumption rate are reported in Lagerlund and Low (1993), based on studies in a rat model. Data related to the reaction rate of oxygen and hemoglobin are reported in (Staub 1963; Keller 1971; Eaton et al. 1999).

5.8 Simulating VEGF Production and Drug Delivery

Adding a passive reactive solute to the model is straightforward. The difference between VEGF and oxygen is primarily in the incorporation of different boundary conditions and release mechanism. Sources of VEGF are identified as regions deemed sufficiently hypoxic within the interstitium ($<$1 mmHg). The source is added as a local increase in concentration flux of an additional distribution corresponding to VEGF. The transport of VEGF follows the same advection-diffusion through the interstitium as oxygen, but with its own, lower coefficient of diffusion. Drugs are handled in a similar way, but the source is restricted to the inlet vessels, with concentrations varying according to an imposed function. Drugs or particles of various sizes can be included by assigning different vessel permeabilities and different interstitial diffusivities (set via bounce-back rules).

5.9 Vessel Remodeling

The algorithm uses a set of key parameters to control the remodeling process. Specifically, the thresholds on the wall shear stress and local VEGF are not known precisely and must be calibrated. In order to simplify this process, we have focused on shear stress alone in the context of flow-based remodeling of vessel bifurcations. Szczerba and coworkers constructed a basic fluid dynamics model of forces in bifurcations to explain the optimization of bifurcation angles based on flow adaptation (Szczerba and Szekely 2005). As branching angles are well-characterized for many tissues and for various vessel sizes, it was relatively straightforward to tune our vessel dilation and contraction rules to reproduce these structures.

The last phase of the algorithm involves a novel mechanism to control vascular remodeling based on wall shear stress (WSS) and local levels of VEGF. The production of VEGF is directly related to the underlying distribution of oxygen, which then depends on delivery by the underlying flow. Hence, we implement a feedback loop that modifies the vasculature through a process of dilation and/or contraction until WSS, pO2 and VEGF levels have reached a physiologically optimal state.

Note that although it is an important process during tumor growth, we are not explicitly simulating angiogenesis – the formation of new vessels. Thus, although we provide for the possibility that vessels can dilate in response to VEGF, we do not include the additional mechanisms for vessel sprouting to make new segments. This is reasonable, because angiogenesis is not generally observed during anti-VEGF therapy.

5.10 Model Validation and Sensitivity Analysis

Figure 9.3 demonstrates the capabilities of the model. In Fig. 9.3c, an idealized 2D capillary bed is simulated, with a single arteriole and single venule spanning the domain, connected by parallel capillaries. Plasma and RBC particles flow into the network, delivering oxygen based on local oxygen tension. The oxygen then convects and diffuses through the tissue (color map). In Fig. 9.3d, a 3D network was acquired from actual tumor tissue, binarized with our vessel tracing algorithm and perfused with simulated blood. Figure 9.3e shows the time course of adaptation in an example network. Initially the network is a dense mesh (white outline). By iteration 25, the network has adapted in response to shear forces and local VEGF level. After an initial influx of VEGF driven by hypoxia, the vessels dilate to bring in more oxygen, and in the process, the network is subjected to shear-based remodeling. Note that patches of high VEGF, such as seen at iteration 20, effectively protect vessels in hypoxic regions from being pruned. Figure 9.3f demonstrates the ability of the model to simulate varying interstitial permeabilities by adjusting bounce-back conditions for the extra-vascular nodes. In this way, we can simulate delivery of drugs of various sizes.

The most important parameters for the simulations are the thresholds for VEGF and shear stress that determine local contraction or dilation of the vessels. Figure 9.3g illustrates the complex interplay between these parameters. In the base case, adaptation has produced a thinned-out network with a large, central capillary that is carrying much of the flow. Flow is maintained to the corners due to metabolic demand (and VEGF production) in these regions. The resulting network provides adequate perfusion with little hypoxia. Increasing the lower threshold for shear contraction produces the counter-intuitive result shown in the upper right panels. The more uniform network is formed due to an initial contraction of the lower left "arteriole" which redirects flow to the upper right, distributing flow through more of the capillaries. This prevents their contraction and pruning, and leads to better oxygen uniformity. Increasing the lower VEGF threshold, on the other hand, results in a rapid contraction of the upper feeding arteriole and many of the capillaries, causing widespread hypoxia in the domain. And finally, by increasing the upper shear threshold, we can delay the dilation of vessels with high flow. This maintains more of the parallel capillaries and the arteriole segments extending in the corners. The central hypoxia oscillates as the vessels there dilate to bring more oxygen and then contract as VEGF recedes (not shown). In real vasculature, it is likely that structural fortification of vessels by pericytes and smooth muscle cells serves to buffer these types of oscillations.

Vascular remodeling and normalization are a central feature of tumor networks treated with antiangiogenic therapy. As shown in Fig. 9.3, the current model is capable of reproducing the appropriate network dynamics and transport properties of soluble species. With appropriate calibration of the various thresholds for adaptation for individual tumor types, this model will enable detailed, time-resolved analyses of network changes and drug and nutrient delivery to tissue. This will provide a rational framework for the development of new therapeutic strategies or more effect use of existing drugs.

Data acquisition for Boundary and Initial Conditions

To produce useful simulations using this model, we need accurate representations of network architecture and reasonably detailed boundary conditions. We have recently developed methods for the comprehensive analysis of vessel and blood flow dynamics in vivo using laser scanning multiphoton imaging (Tyrrell et al. 2005; Kamoun et al. 2010) (Fig. 9.4). The methodology allows simultaneous analysis of vessel morphology (including vessel diameter, vessel length and location within the network) and fluid dynamics (red blood cell velocity, red blood cell flux and relative hematocrit) at the single vessel level.

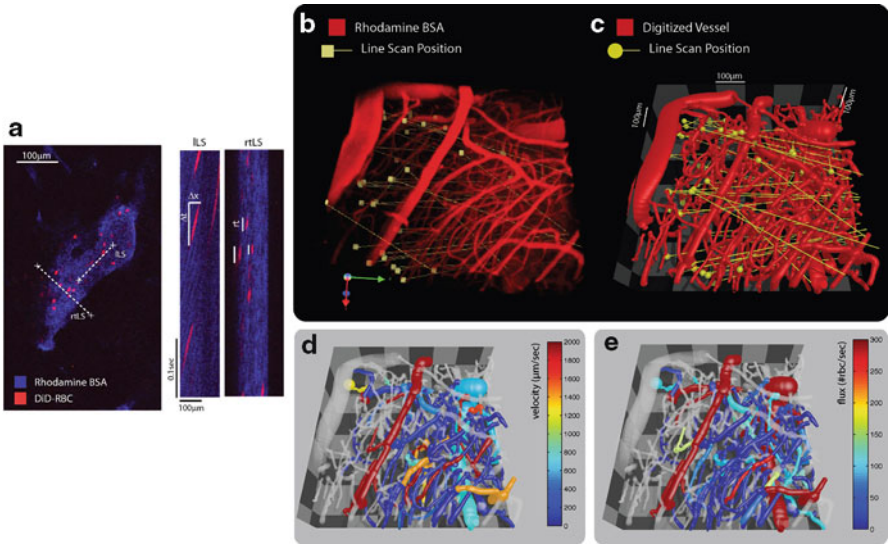

Fig. 9.4 Measuring blood flow velocities at single vessel resolution over a network (Kamoun et al. 2010). (**a**) x vs. t images generated by scanning along the centerline of the vessel (lLS) and perpendicular to the vessel (rtLS). Analysis of flow velocity is based on the slope of the RBC signal ($\Delta x/\Delta t$). (**b**) To analyze large networks, lines intersect multiple vessels and the velocities and fluxes are deconvolved using the structural information (i.e., angles between the vessel and scan line). (**c**) network trace of (**b**), showing the binary representation of the network. (**d** and **e**) Velocity and flux maps, respectively, superimposed on the traced digital network to visualize the relationships between flow and topology. Image size is $630 \times 630 \times 50\,\mu m$

Vessel Morphology (Tyrrell et al. 2007): We implement an algorithm that reliably and accurately traces vessels in 3D with the extraction of structural parameters such as vessel density, vessel diameter, branching angles and vessel segment length (Fig. 9.4c). The robust tracing algorithm uses a cylindroidal super-ellipsoid as the underlying shape descriptor. This model offers an explicit, low-order parameterization, enabling joint estimation of vessel boundary, centerlines and local pose.

Vessel Perfusion: To quantify flow velocity in single vessels over a network, laser lines are scanned across multiple vessel segments; velocities and fluxes of RBCs are deconvolved based on the residence time within the scan and the angles of intersection between the laser and the vessel (extracted from the structural tracings Kamoun et al. 2010). This allows us to measure flow parameters over large networks quickly, with single-vessel resolution (Fig. 9.4a).

Measuring Effective Permeability of Tumor Vessels

The lattice Boltzmann model allows specification of spatiotemporally varying vascular permeabilities. To measure vessel permeabilities, we inject tumor-bearing mice with rhodamine-conjugated dextran and acquire full-field images in the tumor. Images are recorded at various depths in the tissue to capture a volume, with 1 μm z-resolution. Volume data are recorded every 30 s for 30 min as the extravasating tracer accumulates outside the vessels. After incorporating intravascular tracer kinetics and the vessel surface/volume ratio (Brown et al. 2001), the change in intensity with time is translated into a 3D map of effective vessel permeability.

References

Al-Kilani A, Lorthois S, Nguyen TH, Le Noble F, Cornelissen A, Unbekandt M, Boryskina O, Leroy L and Fleury V (2008). During vertebrate development, arteries exert a morphological control over the venous pattern through physical factors. *Phys Rev E Stat Nonlin Soft Matter Phys* 77(5 Pt 1): 051912.

Alemani D (2007). A lattice boltzmann numerical approach for modeling reaction-diffusion processes in chemically and physically heterogeneous environments. Geneva, UNIVERSITÉ DE GENÈVE. PhD.

Ansiaux R, Baudelet C, Jordan BF, Crokart N, Martinive P, DeWever J, Gregoire V, Feron O and Gallez B (2006). Mechanism of reoxygenation after antiangiogenic therapy using su5416 and its importance for guiding combined antitumor therapy. *Cancer Res* 66(19): 9698–704.

Baffert F, Le T, Sennino B, Thurston G, Kuo CJ, Hu-Lowe D and McDonald DM (2006). Cellular changes in normal blood capillaries undergoing regression after inhibition of vegf signaling. *Am J Physiol Heart Circ Physiol* 290(2): H547–59.

Baish JW, Netti PA and Jain RK (1997). Transmural coupling of fluid flow in microcirculatory network and interstitium in tumors. *Microvascular Research* 53: 128–141.

Batchelor TT, Sorensen AG, di Tomaso E, Zhang WT, Duda DG, Cohen KS, Kozak KR, Cahill DP, Chen PJ, Zhu M, Ancukiewicz M, Mrugala MM, Plotkin S, Drappatz J, Louis DN, Ivy P, Scadden DT, Benner T, Loeffler JS, Wen PY and Jain RK (2007). Azd2171, a pan-vegf receptor tyrosine kinase inhibitor, normalizes tumor vasculature and alleviates edema in glioblastoma patients. *Cancer Cell* 11(1): 83–95.

Baxter LT and Jain RK (1988). Vascular permeability and interstitial diffusion in superfused tissues: A two-dimensional model. *Microvascular Research* 36(1): 108–15.

Baxter LT and Jain RK (1991a). Vascular and interstitial transport in tumors. *Tumor blood supply and metabolic microenvironment: Characterization and therapeutic implications*. P. Vaupel and R. K. Jain. Stuttgart, Fischer Publications.

Baxter LT, Yuan F and Jain RK (1992). Pharmacokinetic analysis of the perivascular distribution of bifunctional antibodies and haptens: Comparison with experimental data. *Cancer Research* 52(20): 5838–44.

Brown EB, Campbell RB, Tsuzuki Y, Xu L, Carmeliet P, Fukumura D and Jain RK (2001). In vivo measurement of gene expression, angiogenesis and physiological function in tumors using multiphoton laser scanning microscopy. *Nature Medicine* 7(7): 864–8.

Brown MD and Hudlicka O (2003). Modulation of physiological angiogenesis in skeletal muscle by mechanical forces: Involvement of vegf and metalloproteinases. *Angiogenesis* 6(1): 1–14.

Chaplain M and Anderson A (2004). Mathematical modeling of tumour-induced angiogenesis: Network growth and structure. *Cancer Treat Res* 117: 51–75.

Chaplain MA and Anderson AR (1996). Mathematical modeling, simulation and prediction of tumour-induced angiogenesis. *Invasion Metastasis* 16(4–5): 222–34.

Chien S, Lin SJ, Weinbaum S, Lee MM and Jan KM (1988). The role of arterial endothelial cell mitosis in macromolecular permeability. *Advances in Experimental Medicine & Biology* 242: 59–73.

Dardis O and McCloskey J (1998). Lattice boltzmann scheme with real numbered solid density for the simulation of flow in porous media. *Physical Review E* 57(4): 4834–4837.

Dupin M, Halliday I, Care C and Munn L (2008a). Lattice boltzmann modeling of blood cell dynamics. *Int J Comp Fluid Dynamics* 22(7): 481–492.

Dupin MM, Halliday I, Care CM, Alboul L and Munn LL (2007). Modeling the flow of dense suspensions of deformable particles in three dimensions. *Phys Rev E Stat Nonlin Soft Matter Phys* 75(6 Pt 2): 066707.

Dupin MM, Halliday I, Care CM and Munn LL (2008). Efficiency-oriented, hybrid approach for modeling deformable particles in three dimensions. *Progress in Computational Fluid Dynamics* 8: 109–120.

Eaton WA, Henry ER, Hofrichter J and Mozzarelli A (1999). Is cooperative oxygen binding by hemoglobin really understood? *Nature Structural Biology* 6: 351–358.

Ferrara N, Hillan KJ, Gerber HP and Novotny W (2004). Discovery and development of bevacizumab, an anti-vegf antibody for treating cancer. *Nat Rev Drug Discov* 3(5): 391–400.

Ferrara N and Kerbel RS (2005). Angiogenesis as a therapeutic target. *Nature* 438(7070): 967–74.

Fischer C, Mazzone M, Jonckx B and Carmeliet P (2008). Flt1 and its ligands vegfb and plgf: Drug targets for anti-angiogenic therapy? *Nat Rev Cancer* 8(12): 942–56.

Folkman J (1971). Tumor angiogenesis: Therapeutic implications. *N Engl J Med* 285(21): 1182–6.

Gillies RJ, Schornack PA, Secomb TW and Raghunand N (1999). Causes and effects of heterogeneous perfusion in tumors. *Neoplasia* 1(3): 197–207.

Gruionu G, Hoying JB, Gruionu LG, Laughlin MH and Secomb TW (2005). Structural adaptation increases predicted perfusion capacity after vessel obstruction in arteriolar arcade network of pig skeletal muscle. *Am J Physiol Heart Circ Physiol* 288(6): H2778–84.

Hamzah J, Jugold M, Kiessling F, Rigby P, Manzur M, Marti HH, Rabie T, Kaden S, Grone HJ, Hammerling GJ, Arnold B and Ganss R (2008). Vascular normalization in rgs5-deficient tumours promotes immune destruction. *Nature* 453(7193): 410–4.

Hansen-Smith FM, Hudlicka O and Egginton S (1996). In vivo angiogenesis in adult rat skeletal muscle: Early changes in capillary network architecture and ultrastructure. *Cell & Tissue Research* 286(1): 123–36.

Hashizume H, Baluk P, Morikawa S, McLean JW, Thurston G, Roberge S, Jain RK and McDonald DM (2000). Openings between defective endothelial cells explain tumor vessel leakiness. *Am J Pathol* 156(4): 1363–80.

Huber PE, Bischof M, Jenne J, Heiland S, Peschke P, Saffrich R, Grone HJ, Debus J, Lipson KE and Abdollahi A (2005). Trimodal cancer treatment: Beneficial effects of combined antiangiogenesis, radiation, and chemotherapy. *Cancer Res* 65(9): 3643–55.

Hudlicka O and Brown MD (2009). Adaptation of skeletal muscle microvasculature to increased or decreased blood flow: Role of shear stress, nitric oxide and vascular endothelial growth factor. *J Vasc Res* 46(5): 504–12.

Ichioka S, Shibata M, Kosaki K, Sato Y, Harii K and Kamiya A (1997). Effects of shear stress on wound-healing angiogenesis in the rabbit ear chamber. *J Surg Res* 72(1): 29–35.

Jain RK (2001). Normalizing tumor vasculature with anti-angiogenic therapy: A new paradigm for combination therapy. *Nature Medicine* 7(9): 987–989.

Jain RK (2005). Normalization of tumor vasculature: An emerging concept in antiangiogenic therapy. *Science* 307(5706): 58–62.

Jain RK (2008). Lessons from multidisciplinary translational trials on anti-angiogenic therapy of cancer. *Nat Rev Cancer* 8(4): 309–16.

Jain RK, Tong RT and Munn LL (2007). Effect of vascular normalization by antiangiogenic therapy on interstitial hypertension, peritumor edema, and lymphatic metastasis: Insights from a mathematical model. *Cancer Res* 67(6): 2729–35.

Jones PF and Sleeman BD (2006). Angiogenesis - understanding the mathematical challenge. *Angiogenesis* 9(3): 127–38.

Kamoun WS, Chae SS, Lacorre DA, Tyrrell JA, Mitre M, Gillissen MA, Fukumura D, Jain RK and Munn LL (2010). Simultaneous measurement of rbc velocity, flux, hematocrit and shear rate in vascular networks. *Nat Methods*. 7:655–660.

Kamoun WS, Ley CD, Farrar CT, Duyverman AM, Lahdenranta J, Lacorre DA, Batchelor TT, di Tomaso E, Duda DG, Munn LL, Fukumura D, Sorensen AG and Jain RK (2009). Edema control by cediranib, a vascular endothelial growth factor receptor-targeted kinase inhibitor, prolongs survival despite persistent brain tumor growth in mice. *J Clin Oncol*. 27:2542–52.

Kang Y, Choi M, Lee J, Koh GY, Kwon K and Choi C (2009). Quantitative analysis of peripheral tissue perfusion using spatiotemporal molecular dynamics. *PLoS ONE* 4(1): e4275.

Keller KH (1971). Effect of fluid shear on mass transport in flowing blood. *Federation Proceedings* 30(5): 1591–1599.

Kerbel RS (2009). Issues regarding improving the impact of antiangiogenic drugs for the treatment of breast cancer. *Breast* 18 Suppl 3: S41–7.

Ko AH, Dito E, Schillinger B, Venook AP, Xu Z, Bergsland EK, Wong D, Scott J, Hwang J and Tempero MA (2008). A phase ii study evaluating bevacizumab in combination with fixed-dose rate gemcitabine and low-dose cisplatin for metastatic pancreatic cancer: Is an anti-vegf strategy still applicable? *Invest New Drugs* 26(5): 463–71.

Lagerlund TD and Low PA (1993). Mathematical modeling of time-dependent oxygen transport in rat peripheral nerve. *Comput Biol Med* 23(1): 29–47.

Lee DS, Rieger H and Bartha K (2006). Flow correlated percolation during vascular remodeling in growing tumors. *Phys Rev Lett* 96(5): 058104.

Macklin P, McDougall S, Anderson AR, Chaplain MA, Cristini V and Lowengrub J (2009). Multiscale modeling and nonlinear simulation of vascular tumour growth. *J Math Biol* 58(4–5): 765–98.

Migliorini C, Qian Y, Chen H, Brown E, Jain R and Munn L (2002). Red blood cells augment leukocyte rolling in a virtual blood vessel. *Biophys J*. 83: 1834–41.

Munn LL (2003). Aberrant vascular architecture in tumors and its importance in drug-based therapies. *Drug Discovery Today* 8: 396–403.

Munn LL and Dupin MM (2008). Blood cell interactions and segregation in flow. *Ann Biomed Eng* 36(4): 534–44.

Nakahara T, Norberg SM, Shalinsky DR, Hu-Lowe DD and McDonald DM (2006). Effect of inhibition of vascular endothelial growth factor signaling on distribution of extravasated antibodies in tumors. *Cancer Res* 66(3): 1434–45.

Netti PA, Roberge S, Boucher Y, Baxter LT and Jain RK (1996). Effect of transvascular fluid exchange on arterio-venous pressure relationship: Implication for temporal and spatial heterogeneities in tumor blood flow. *Microvascular Research* 52: 27–46.

Pries AR, Cornelissen AJ, Sloot AA, Hinkeldey M, Dreher MR, Hopfner M, Dewhirst MW and Secomb TW (2009). Structural adaptation and heterogeneity of normal and tumor microvascular networks. *PLoS Comput Biol* 5(5): e1000394.

Pries AR, Reglin B and Secomb TW (2005). Remodeling of blood vessels: Responses of diameter and wall thickness to hemodynamic and metabolic stimuli. *Hypertension* 46(4): 725–31.

Pries AR and Secomb TW (2008). Modeling structural adaptation of microcirculation. *Microcirculation* 15(8): 753–64.

Pries AR and Secomb TW (2009). Origins of heterogeneity in tissue perfusion and metabolism. *Cardiovasc Res* 81(2): 328–35.

Pries AR, Secomb TW and Gaehtgens P (1995). Design principles of vascular beds. *Circ Res* 77(5): 1017–23.

Pries AR, Secomb TW and Gaehtgens P (1998). Structural adaptation and stability of microvascular networks: Theory and simulations. *Am J Physiol* 275(2 Pt 2): H349–60.

Reglin B, Secomb TW and Pries AR (2009). Structural adaptation of microvessel diameters in response to metabolic stimuli: Where are the oxygen sensors? *Am J Physiol Heart Circ Physiol* 297(6): H2206–19.

Rudge JS, Holash J, Hylton D, Russell M, Jiang S, Leidich R, Papadopoulos N, Pyles EA, Torri A, Wiegand SJ, Thurston G, Stahl N and Yancopoulos GD (2007). Inaugural article: Vegf trap complex formation measures production rates of vegf, providing a biomarker for predicting efficacious angiogenic blockade. *Proc Natl Acad Sci U S A* 104(47): 18363–70.

Schugart RC, Friedman A, Zhao R and Sen CK (2008). Wound angiogenesis as a function of tissue oxygen tension: A mathematical model. *Proc Natl Acad Sci U S A* 105(7): 2628–33.

Senger DR, Van de Water L, Brown LF, Nagy JA, Yeo KT, Yeo TK, Berse B, Jackman RW, Dvorak AM and Dvorak HF (1993). Vascular permeability factor (vpf, vegf) in tumor biology. [review]. *Cancer & Metastasis Reviews* 12(3–4): 303–24.

Staub NC (1963). Alveolar-arterial oxygen tension gradient due to diffusion *J. Appl. Physiol*. 18: 673–680.

Stockmann C, Doedens A, Weidemann A, Zhang N, Takeda N, Greenberg JI, Cheresh DA and Johnson RS (2008). Deletion of vascular endothelial growth factor in myeloid cells accelerates tumorigenesis. *Nature* 456(7223): 814–8.

Succi S (2001). *The lattice boltzmann equation for fluid dynamics and beyond. Oxford*, Oxford University Press.

Sukop MC and Thorne DT (2007). *Lattice boltzmann modeling: An introduction for geoscientists and engineers* New York, Springer.

Sun C, Jain RK and Munn LL (2007). Non-uniform plasma leakage affects local hematocrit and blood flow: Implications for inflammation and tumor perfusion. *Ann Biomed Eng* 35(12): 2121–9.

Sun C, Migliorini C and Munn LL (2003). Red blood cells initiate leukocyte rolling in postcapillary expansions: A lattice-boltzmann analysis. *Biophysical Journal* 85: 208–222.

Sun CH and Munn LL (2005). Particulate nature of blood determines macroscopic rheology: A 2-d lattice boltzmann analysis. *Biophysical Journal* 88(3): 1635–1645.

Sun CH and Munn LL (2006). Influence of erythrocyte aggregation on leukocyte margination in postcapillary expansions: A lattice-boltzmann analysis. *Physica A* 362: 191–196.

Sun CH and Munn LL (2008). Lattice boltzmann simulation of blood flow in digitized vessel networks. *Computers & Mathematics with Applications* 55: 1594–1600.

Sun S, Wheeler MF, Obeyesekere M and Patrick CW, Jr. (2005). A deterministic model of growth factor-induced angiogenesis. *Bull Math Biol* 67(2): 313–37.

Szczerba D and Szekely G (2005). Computational model of flow-tissue interactions in intussusceptive angiogenesis. *J Theor Biol* 234(1): 87–97.

Tong RT, Boucher Y, Kozin SV, Winkler F, Hicklin DJ and Jain RK (2004). Vascular normalization by vascular endothelial growth factor receptor 2 blockade induces a pressure gradient across the vasculature and improves drug penetration in tumors. *Cancer Res* 64(11): 3731–6.

Tyrrell JA, Kamoun W and Munn LL (2010). A mathematical framework for predicting oxygen deliver and vessel remodeling. Biomedical Engineering Society Annual Meeting, Austin, TX.

Tyrrell JA, Mahadevan V, Tong RT, Brown EB, Jain RK and Roysam B (2005). A 2-d/3-d model-based method to quantify the complexity of microvasculature imaged by in vivo multiphoton microscopy. *Microvasc Res* 70(3): 165–78.

Tyrrell JA, Tomaso Ed, Fuja D, Tong RT, Kozak KR, Jain RK and Roysam B (2007). Robust 3-d modeling of vasculature imagery using superellipsoids. *IEEE Trans Med Imaging* 26: 223–37.1026.

Vosseler S, Mirancea N, Bohlen P, Mueller MM and Fusenig NE (2005). Angiogenesis inhibition by vascular endothelial growth factor receptor-2 blockade reduces stromal matrix metallopro-

teinase expression, normalizes stromal tissue, and reverts epithelial tumor phenotype in surface heterotransplants. *Cancer Res* 65(4): 1294–305.

Waite L and Fine J (2007). *Applied biofluid mechanics*. New York, McGraw-Hill.

Walsh SDC, Burwinklea H and Saar MO (2008). A new partial-bounceback lattice-boltzmann method for fluid flow through heterogeneous media *Computers and Geosciences*. 35(6):1186–1193.

Welter M, Bartha K and Rieger H (2009). Vascular remodelling of an arterio-venous blood vessel network during solid tumour growth. *J Theor Biol* 259(3): 405–22.

Willett CG, Boucher Y, di Tomaso E, Duda DG, Munn LL, Tong RT, Chung DC, Sahani DV, Kalva SP, Kozin SV, Mino M, Cohen KS, Scadden DT, Hartford AC, Fischman AJ, Clark JW, Ryan DP, Zhu AX, Blaszkowsky LS, Chen HX, Shellito PC, Lauwers GY and Jain RK (2004). Direct evidence that the vegf-specific antibody bevacizumab has antivascular effects in human rectal cancer. *Nat Med* 10(2): 145–7.

Winkler F, Kozin SV, Tong R, Chae S, Booth MF, Garkavtsev I, Xu L, Hicklin DJ, Fukumura D, di Tomaso E, Munn LL and Jain RK (2004). Kinetics of vascular normalization by vegfr2 blockade governs brain tumor response to radiation: Role of oxygenation, angiopoietin-1 and matrix metalloproteinases. *Cancer Cell* 6: 553–563.

Wu J, Long Q, Xu S and Padhani AR (2009). Study of tumor blood perfusion and its variation due to vascular normalization by anti-angiogenic therapy based on 3d angiogenic microvasculature. *J Biomech* 42(6): 712–21.

Yuan F, Salehi HA, Boucher Y, Vasthare US, Tuma RF and Jain RK (1994). Vascular permeability and microcirculation of gliomas and mammary carcinomas transplanted in rat and mouse cranial windows. *Cancer Research* 54(17): 4564–4568.

Zakrzewicz A, Secomb TW and Pries AR (2002). Angioadaptation: Keeping the vascular system in shape. *News Physiol Sci* 17: 197–201.

Zou Q and He X (1997). On pressure and velocity boundary conditions for the lattice boltzmann bgk model. *Phys. Fluids* 9(6): 1493–1858.

Part III
Whole Organ Modeling of Tumor Growth and Vasculature

Chapter 10
Effect of Vascularization on Glioma Tumor Growth

Haralambos Hatzikirou, Arnaud Chauvière, John Lowengrub, J. De Groot, and Vittorio Cristini

1 Introduction

Cancer describes a group of genetic and epigenetic diseases, characterized by uncontrolled proliferation of cells, leading to a variety of pathological consequences and frequently death. Cancer progression can be depicted as a sequence of traits or phenotypes that cells have to acquire if a neoplasm (benign tumor) is to become an invasive and malignant cancer. A phenotype refers to any kind of observed morphology, function or behavior of a living cell. Hanahan and Weinberg (2000) have identified six cancer cell phenotypes: unlimited proliferative potential, environmental independence for growth, evasion of apoptosis, angiogenesis, invasion, and metastasis. The attempt to define a temporal order of tumor cells acquiring new capabilities remains still unclear in general.

H. Hatzikirou • A. Chauvière
Department of Pathology, University of New Mexico, 1 University of New Mexico, Albuquerque, NM 87131, USA
e-mail: hhatzikirou@salud.unm.edu; achauviere@salud.unm.edu

J. Lowengrub
Department of Mathematics, The University of California at Irvine, Irvine, CA, USA
e-mail: lowengrb@math.uci.edu

J. De Groot
Department of Neuro-Oncology, Cancer Medicine, The University of Texas M. D. Anderson Cancer Center, Houston, TX, USA
e-mail: jdegroot@mdanderson.org

V. Cristini (✉)
Department of Pathology and Department of Chemical and Biomedical, Engineering University of New Mexico, 1 University of New Mexico, Albuquerque, NM 87131, USA
e-mail: vcristini@salud.unm.edu

T.L. Jackson (ed.), *Modeling Tumor Vasculature: Molecular, Cellular, and Tissue Level Aspects and Implications*, DOI 10.1007/978-1-4614-0052-3_10,

In this chapter, we aim at understanding how neovascularization is coupled to tumor growth dynamics and focus on brain tumors (glioma) because this type of tumor is one of the most vascularized (Zuelch 1986; Mikkelsen et al. 2003). We base our investigation on an experimental data set published by Lee et al. (2006). These data correspond to in vivo tumor growth of implanted U87 glioma cells and the associated tumor-induced vascularization in nude mice brains. They provide a prototype brain tumor model that allows for measurements of the tumor progression and neovascular development that we will describe in more detail in the next section. We analyze the experimental data by applying and extending a mathematical model of tumor growth considered by Cristini et al. (2003) and address in particular the following questions:

- What is the critical tumor size at which angiogenesis is initiated?
- What is the interplay between vascularization dynamics and glioma growth?
- Why does the tumor radius seem to grow linearly with time (Brù et al. 2003), at later stages of growth, and what are the corresponding consequences?

Even though each of these questions may have been addressed independently in former studies (see below for a short review of tumor-induced angiogenesis models), we will provide a unified approach to answer these questions and explain the connections between them. As an outlook, we will underline what are the implications of our findings in the context of anti-angiogenic treatment and how this may affect the post-treatment tumor dynamics.

There is a rich literature on mathematical modeling of tumor-induced vascularization and angiogenesis. A large part of the literature focuses on the spatio-temporal dynamics of vessel formation and the morphology of the resulting vasculature (e.g., Stokes et al. 1991; Anderson and Chaplain 1998; Plank and Sleeman 2003; Sun et al. 2005; Kevrekidis et al. 2006; Bauer et al. 2007; Milde et al. 2008). The coupling of blood flow and network remodeling has also been studied by various authors (e.g., Pries et al. 1998; McDougall et al. 2002; Stephanou et al. 2005; McDougall et al. 2006; Stephanou et al. 2006; Wu et al. 2007; Zhao et al. 2007; Pries and Secomb 2008; Sun and Munn 2008). Merks and Glazier (2006) describe the initial stage of angiogenesis, which requires the so-called sprouting instability. Vasculogenesis, i.e., de novo formation of vascular networks, has also been studied in Merks et al. (2008) and a review of older papers can be found in Ambrosi et al. (2005).

The first model that (nonlinearly) couples tumor growth and angiogenesis was developed by Zheng et al. (2005). Other more recent models of coupling between vascularization and tumor growth can be found in Frieboes et al. (2007); Welter et al. (2008); Bearer et al. (2009); Macklin et al. (2009); Welter and Rieger (2010). The connection of our work to the earlier papers is that here we consider a simplified model that provides insight into the biophysical problem and help identify key parameters and growth regimes to be used for deeper investigations with more sophisticated models.

In this chapter, our starting point is a set of in vivo glioma mice data that we detail in Sect. 2. In Sect. 3, we briefly introduce the nonlinear mathematical model we use.

We calibrate the parameters of the model in Sect. 4 to reproduce the experimental data. As a result of this process, we gain new insight regarding the vascularization effects on tumor dynamics. Accordingly, we propose in Sect. 5 a scenario to explain the different growth regimes experimentally observed and we extend the original model to explore further this scenario in Sect. 6. We finally summarize our findings and discuss their implications in the context of therapeutical perspectives.

2 Description and Processing of Experimental Data

2.1 Observations of Glioma Xenografts in Mice

Animal models of cancer, including both traditional tumor transplant models and newer genetically engineered mouse models of cancer, have helped the investigation of tumor growth dynamics. Implantation of U87 MG glioma cells into immunodeficient animals produces solid intracerebral tumors where most of the growth characteristics of these tumors are reproducible. For such reasons, U87 MG is one of the most frequently used models for testing therapies for malignant gliomas. In this chapter, we use implanted xenografts of U87 MG in a nude mouse model in order to characterize tumor growth and vascular development of human glioma. We focus, in particular, on experimental data obtained by Lee et al. (2006).

In their study, Lee and coworkers investigated morphological and immunohistochemical features of glioma growth. Here, we mainly exploit the volumetric data of the growth. At eight distinct time points, the authors measured the tumor volume V (Fig. 10.1c) and the microvessel density MVD ρ_v (Fig. 10.1d), which accounts for the number of microvessels and endothelial cells within a given tumor area. MVD data are rarely quantitatively used as they do not contain conclusive information regarding vessel functionality. However, here we use MVD data together with tumor growth data to consider the relative number of endothelial and tumor cells, which displays an interesting and instructive nonmonotone behavior in time.

Immunohistochemical measurements were also performed for a more complete description of the growth of U87 MG intracranial xenografts and the host angiogenic response, which allowed the following observations. Eight hours after cell implantation, the cells were grouped together, and there was no evidence of modifications to surrounding host vessels. At this time, some of the implanted U87 MG cells proliferated actively. Twenty-four hours after cell implantation, the cells were still clustered together as a small mass, but with a center displaying signs of cell death. Discussions with the authors suggest that this may be an artifact resulting from the implantation technique rather than hypoxia induced central necrosis. This is a characteristic of these cell-lines that release vascular endothelial growth factors (VEGF) factors and triggers a fast and strong angiogenic response, avoiding therefore the occurrence of hypoxic regions and potentially resulting necrotic areas.

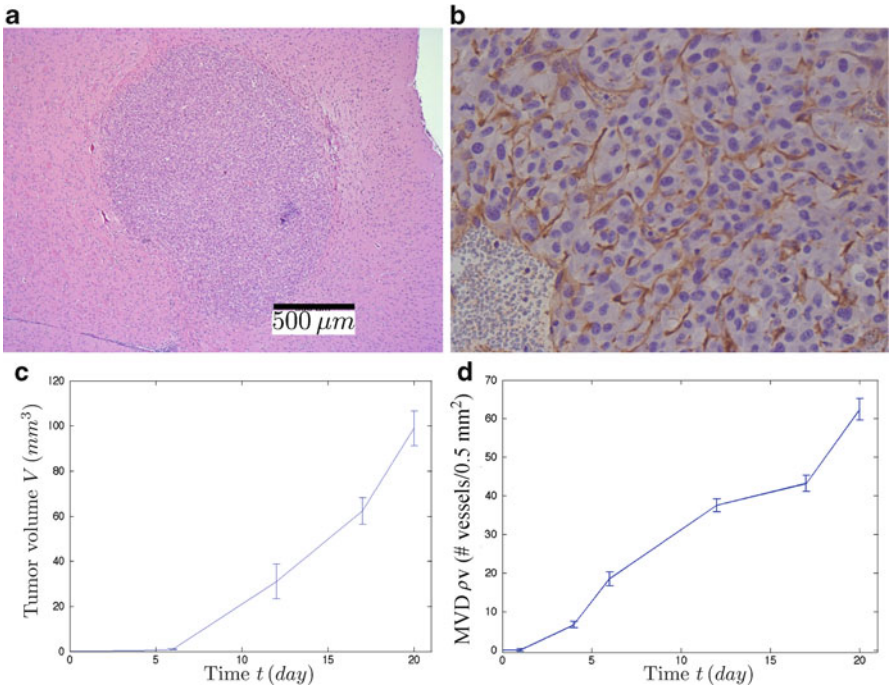

Fig. 10.1 (**a**) H&E staining of a human glioma xenograft U87 MG in a nude mouse model. Illustration of the spheroid morphology. (**b**) Spatial vessel distribution close to the tumor margin. (**c**) Temporal evolution of the experimental tumor volume. (**d**) Temporal evolution of the experimental mean vessel density

At the same time, vessels in the normal parenchyma of mice proximal to the tumor were observed. By Day 4, the tumors had grown to a mean volume $V = 0.37\text{mm}^3$ and contained a small area of dead cells surrounded by a mass of living tumor cells with a very low MVD. The vessels in the host parenchyma surrounding the tumor displayed changes in morphology, including an enlarged diameter and a disorganized structure. Some of the vessels interacted physically with peripheral tumor cells through the process of cooption and/or new branching. On Day 6 after implantation, although the tumors were small ($V \approx 1\text{mm}^3$), the MVD curve profile was within an exponential phase. Twelve days after implantation, the tumors were vascularized sphere-like masses of cells ($V = 31\text{mm}^3$) showing no signs of necrosis. The tumor margin was clearly defined and cancer cells did not exhibit an invasive pattern into host tissues. The tumor volume at Day 20 after implantation approximatively reached $V \approx 100\text{mm}^3$. At this time, the tumors also exhibited a high mean MVD plus a highly proliferative pattern without areas of necrosis. All mice showed signs of toxicity by Day 30, which correlates with the development of an expansive mass, causing extreme brain compression. The time-dependent volumetric characteristics are illustrated in Figs. 10.1c,d.

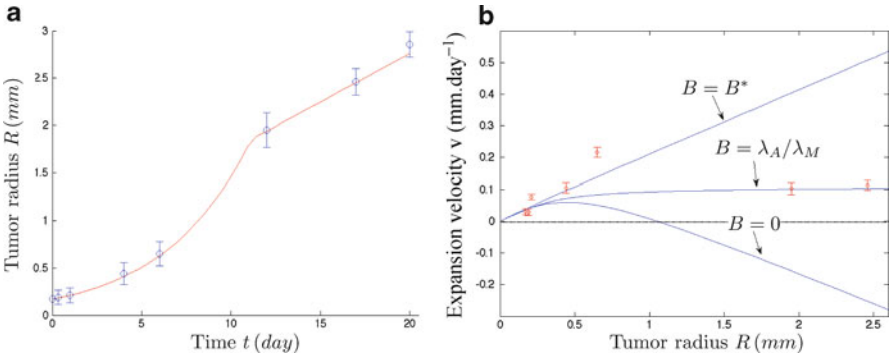

Fig. 10.2 (**a**) Temporal evolution of the tumor radius. The *circles* correspond to the experimental values obtained by data processing. The *solid line* corresponds to the best fit obtained from our model with B as a piecewise constant function of time (see text for details). (**b**) Regimes of tumor growth in the phase plan $(v(R), R)$. The *circles* correspond to the experimental values obtained by data processing. The three *solid curves* result from our model for different uniform values of B (see text for details)

2.2 Data Processing

We have processed the experimental observables of interest and especially the volumetric data. Indeed, the original data consists in the time evolution of the tumor mean volume $\mathbb{E}[V(t)]$ and the corresponding variance $\mathrm{Var}[V(t)]$. We work here under the assumption of radial symmetry, i.e., assuming that the tumor grows as a sphere, which is reasonable with respect to experimental observations (see Fig. 10.1a). We evaluate successively the mean value $\mu_R(t) = \mathbb{E}[R(t)]$ and the standard deviation $\sigma_R(t) = \sqrt{\mathrm{Var}[R(t)]}$ of the tumor radius $R(t)$, and $\mu_v(t) = \mathbb{E}[v(t)]$ and $\sigma_v(t) = \sqrt{\mathrm{Var}[v(t)]}$ of the growth speed $v(t)$, i.e., the time derivative of the tumor radius. The latest will help a better understanding of the growth regimes. The derivation of these quantities is presented in Appendix 1. We show our results in Figs. 10.2a,b.

3 Mathematical Modeling

We briefly introduce the mathematical model we use, which was originally published in Cristini et al. (2003). A more detailed description is provided in Appendix 2 at the end of this chapter. The model originally describes evolution of avascular and vascularized tumors but not the angiogenic transition between the two. Here, we show how to extend the model to describe the angiogenic transition.

The tumor is treated as an incompressible fluid flowing through a porous medium where tissue elasticity is simplified; the tumor–host interface is assumed to be sharp and cell-to-cell adhesive forces are modeled as a surface tension at the tumor–host

interface. The tumor expands as a mass whose growth is governed by a balance between cell birth (mitosis) and death (apoptosis, i.e., programmed cell-death). We focus on a description of nonnecrotic tumors because U87 MG xenografts show only few signs of necrosis during the development.

The mitotic rate within the tumor is assumed to be linearly dependent on the nutrient concentration and is therefore characterized by its maximal value λ_M at the tumor–host interface; we assume that the apoptosis rate λ_A is uniform. The concentration of nutrient obeys a reaction-diffusion equation in the tumor volume, where nutrient is supplied from the functional vasculature blood and consumed by the tumor cells at a uniform consumption rate.

The resulting dimensional problem can be reformulated into two nondimensional decoupled problems for modified variables, i.e., nutrient concentration and pressure within the tumor, respectively. From these problems, one can derive the following evolution equation for the full radius R of the tumor under the assumption that the tumor remains radially symmetric:

$$\frac{\mathrm{d}R}{\mathrm{d}t} = \frac{1}{3}(\lambda_M B - \lambda_A)R + \lambda_M(1-B)L_D\left(\frac{1}{\tanh(R/L_D)} - \frac{L_D}{R}\right), \qquad (10.1)$$

where the nonnegative parameter B represents the net effect of vascularization on the tumor radius evolution and L_D is an intrinsic length scale resulting from the nutrient dynamics, i.e., diffusion, supply, and consumption. This model has been shown in Cristini et al. (2003) to capture various growth regimes that are dictated by the values of the parameters λ_M, λ_A, and B, while the length scale L_D has been estimated in previous studies in the range $[0.1\mathrm{mm}, 0.2\mathrm{mm}]$ (see Ward and King 1997, for example). In particular, these regimes are:

1. *Low vascularization*: $B < \lambda_A/\lambda_M$.
   This regime includes the special case of avascular growth $B = 0$. Evolution is monotone and always leads to a stationary tumor spheroid.
2. *Moderate vascularization*: $\lambda_A/\lambda_M \leq B < 1$.
   Unbounded growth always occurs. The temporal growth of the spheroid radius tends to be exponential for $B > \lambda_A/\lambda_M$ and linear for $B = \lambda_A/\lambda_M$, respectively, at large radii.
3. *High vascularization*: $B \geq 1$.
   In this regime, both unbounded growth and total tumor shrinkage can be obtained, depending on the amount of apoptosis.

We will show in the next section how to calibrate the model parameters with respect to the experimental data from Lee et al. (2006).

4 Parameter Calibration

Our mathematical model predicts different growth regimes that can be better understood in terms of the velocity $v = \mathrm{d}R/\mathrm{d}t$ as a function of the radius R, i.e., the r.h.s. of (10.1). As previously explained, the tumor dynamics is controlled by

the value of B. We present in Fig. 10.2b three cases obtained after a first parameter exploration, together with the experimental velocities extracted from the data. The experimental data exhibit a rapid increase in tumor growth velocity at small radii. Then the velocity decreases to be approximately constant at large radii.

The lower curve is plotted by using $B = 0$ with particular values of λ_A and λ_M that will be later given. We observe that the maximum velocity value of this curve is far below the experimental maximum. This curve corresponds to the avascular case and can only reproduce the early phase of the growth. Indeed, the velocity starts decreasing after approximatively 12 h to reach a null value, which yields a steady spheroid where growth is stopped.

The intermediate curve corresponds to $B = \lambda_A/\lambda_M$, i.e., an asymptotically linear growth regime with constant speed, with the same previous values of λ_A and λ_M. For these values, the early growth phase is again captured by the model, while the late (linear) growth phase is now in excellent agreement with the experimental velocities. The intermediate phase is however poorly captured.

Keeping again the same values of λ_A and λ_M, the upper curve is plotted with $B = B^* > \lambda_A/\lambda_M$. We observe here that this case seems to better represent the intermediate growth phase.

These three examples, when compared to the experimental growth speed, suggests that different regimes occur during tumor growth. In particular, all the examples capture the initial phase, while $B = \lambda_A/\lambda_M$ reproduces the (linear) late phase and $B = B^*$ the intermediate one. We base the calibration of the parameters on this hypothesis and study in more detail each of these phases. We split the tumor growth in three different regimes: (1) early growth phase (Days 0–1 and radius smaller than 0.21mm), (2) transient growth phase (Days 1–12 and corresponding radii 0.21–1.95mm) and (3) late growth phase (Days 12–20 and corresponding radii 1.95–2.87mm).

4.1 Early Tumor Growth Phase (Days 0–1)

For a better understanding of the early growth predicted by our model, we work under the small radius assumption, i.e., we assume $R \ll L_D$ and develop the r.h.s. of (10.1) accordingly. We keep the two first orders and find the approximation

$$\frac{dR}{dt} \simeq \frac{1}{3}(\lambda_M - \lambda_A)R - \frac{\lambda_M(1-B)}{45L_D^2}R^3. \tag{10.2}$$

The first information we can extract is that the very early growth, dictated by the first term of the approximation, is always of exponential nature and does not depend on the parameter B (i.e., the tumor-induced vascularization effect). This first phase depends indeed solely on the net proliferation rate $\lambda_p^e = \lambda_M - \lambda_A$ at the early stage. By using the radius values at early times, we find $\lambda_p^e \approx 0.7\,\text{day}^{-1}$ which provides a good approximation of the experimental data.

The second observation is that the exponential growth is later affected by the vascularization through the parameter B, that starts playing a significant role when the two terms of the r.h.s. of (10.2) have similar orders of magnitude. This occurs around a critical radius R_c that can be evaluated by setting

$$\frac{1}{3}(\lambda_{\mathrm{M}} - \lambda_{\mathrm{A}})R_c \approx \frac{\lambda_{\mathrm{M}}(1-B)}{45L_{\mathrm{D}}^2}R_c^3. \tag{10.3}$$

As we have found $\lambda_{\mathrm{M}} - \lambda_{\mathrm{A}} = \lambda_p^e > 0$, which is necessary for initial growth, (10.3) requires $B < 1$, which is consistent with an initial low vascularization regime. Under this assumption, we evaluate

$$R_c \approx L_{\mathrm{D}}\sqrt{\frac{15(\lambda_{\mathrm{M}} - \lambda_{\mathrm{A}})}{\lambda_{\mathrm{M}}(1-B)}}. \tag{10.4}$$

This provides an estimate of the tumor size at which nonlinearities of the model, involving vascularization processes, start significantly influencing the initial exponential growth.

4.2 Late Tumor Growth Phase (Days 12–20)

From the experimental tumor velocity v at the late stages (see Fig. 10.2b), we assume here that the late tumor growth (after Day 12) evolves linearly, which is consistent with the long-term behavior of tumor growth where linear radial evolution is prominent (Brù et al. 2003). In our model, this assumption is equivalent to assigning $B = \lambda_{\mathrm{A}}/\lambda_{\mathrm{M}}$. For this value of B the (constant) asymptotic value v_∞ (i.e., $R \to \infty$ in (10.1)) of the velocity becomes

$$v_\infty = \left.\frac{\mathrm{d}R}{\mathrm{d}t}\right|_\infty = (\lambda_{\mathrm{M}} - \lambda_{\mathrm{A}})L_{\mathrm{D}}. \tag{10.5}$$

This phase then depends solely on the net proliferation rate $\lambda_p^l = \lambda_{\mathrm{M}} - \lambda_{\mathrm{A}}$ at the late stages, multiplied by the intrinsic length scale L_{D}. In order to minimize errors, we evaluate v_∞ by linearly fitting the experimental values of the radius using the three last time points (at Days 12, 17, and 20). We obtain the best fit using $\lambda_p^l L_{\mathrm{D}} \approx 0.11\,\mathrm{mm\,day^{-1}}$.

Assuming that the net proliferation $\lambda_p = \lambda_{\mathrm{M}} - \lambda_{\mathrm{A}}$ remains time-invariant, we can state that $\lambda_p^l = \lambda_p^e \approx 0.7\,\mathrm{day^{-1}}$, value extracted from the early exponential growth. This yields the value $L_{\mathrm{D}} \approx 0.16\,\mathrm{mm}$, which is consistent with previous studies that have shown that the nutrient diffusion length should be within the range $[0.1\mathrm{mm}, 0.2\mathrm{mm}]$.

To recapitulate, at this stage we have found the relation $\lambda_p = \lambda_M - \lambda_A \approx 0.7\,\text{day}^{-1}$ by focusing on the early phase of tumor growth, and the value $L_D \approx 0.16\,\text{mm}$ by focusing on the late phase. We have also observed that the early growth phase is independent of B, while the late one is accurately described by the particular value of $B = \lambda_A/\lambda_M$. If we assume time-invariant values of the characteristic mitotic rate λ_M and apoptosis rate λ_A and consider the plausible value $\lambda_M = 1\,\text{division}/18\,\text{h} \approx 1.3\,\text{day}^{-1}$, this yields $\lambda_A \approx 0.6\,\text{day}^{-1}$. Moreover, we have calculated an analytical estimate of the critical radius at which tumor-induced angiogenesis may initiate and affect the tumor growth through nonlinearities of our model. In the next section, we conclude the calibration by studying the intermediate growth phase.

4.3 Intermediate Tumor Growth Phase (Days 1–12)

During this transient regime, the growth dynamics is not obvious. As we have previously shown that the late regime is well described by using $B = \lambda_A/\lambda_M$ and that this value can also be taken for the early growth (independent of B), we first study the case of a time-invariant value of B, i.e., $B = \lambda_A/\lambda_M$ at any time of the growth. This yields a simplified version of (10.1) that becomes

$$\frac{dR}{dt} = \lambda_p L_D \left(\frac{1}{\tanh(R/L_D)} - \frac{L_D}{R} \right). \tag{10.6}$$

As we have already evaluated $\lambda_p \approx 0.7\,\text{day}^{-1}$ and $L_D \approx 0.16\,\text{mm}$, we present in Fig. 10.2b the corresponding curve of the velocity function of the radius. It is clear that our model cannot capture the dynamics of the tumor growth with B being constant during the tumor progression. This implies that a value $B^* > \lambda_A/\lambda_M$ is necessary during the intermediate regime of growth. We will use these values of λ_p and L_D together with the understanding of the various growth regimes provided by the parameter calibration to propose an insight into the global growth dynamics.

5 Likely Scenario for Tumor Growth Dynamics

Here, using the insight drawn from the previous section, we propose the most plausible scenario that describes the temporal evolution of the vascularization dynamics. The tumor initially follows an avascular exponential growth ($B = 0$). After the exponential phase and before the slowdown of the radial velocity, angiogenesis is triggered due to VEGF release by tumor cells, and a strong vascularization phase is initiated. The effective vasculature (functional vessels that allow for blood flow) matures, possibly supplying an excess of nutrients through blood flow with respect to the small size of the tumor. This regime has already been identified from

biologists and is characterized as an over-vascularization regime (Brown et al. 1997; Hlatky et al. 2002). This increased vascularization ($B = B^*$) places the tumor in a second exponential regime (slower than the first one) that takes over from the avascular growth (that would have ended up with a finite tumor size). Reaching finally its late stage, tumor growth relaxes to the linear regime ($B = \lambda_A/\lambda_M$) as an adaptation to the minimal requirement for unbounded growth.

We have previously shown that, by considering a time-invariant value of the parameter B in our model, we cannot reproduce the growth features experimentally observed. We propose here the simplest approach with the previously found time-invariant values of the characteristic mitotic rate λ_M and apoptosis rate λ_A and assume that B is a piecewise constant function of time. Each constant value of B is associated with one of the phases we have identified. This temporal variation may be seen as the result of vasculature changes triggered by angiogenesis, e.g., considering a dependence on the MVD ρ_v that is quickly increasing in time (see Fig. 10.1d). Under this assumption, we define B as follows:

- Early tumor growth (exponential regime): $B(t) = 0$ for $t \in [0, 1)$.
  As the early growth does not depend on B, the null value represents the most appropriate choice because no neovascularization is present at this time of the growth.
- Intermediate tumor growth (transient regime): $B(t) = B^* > \lambda_A/\lambda_M$ for $t \in [1, 12)$.
  This value can be seen as an average of B over the transient period because the exact modulation of B cannot be determined by the small number of measurement points.
- Late tumor growth (linear regime): $B(t) = \lambda_A/\lambda_M$ for $t \in [12, 20]$.
  According to the values $\lambda_M \approx 1.3\,\text{day}^{-1}$ and $\lambda_A \approx 0.6\,\text{day}^{-1}$, we find that $B \approx 0.46$ during this phase.

Our parameter exploration yielded the value $B^* \approx 0.9$ that puts the intermediate phase still in a moderate vascularization regime because $B^* < 1$. We show the corresponding simulation result on Fig. 10.2a, which is in excellent agreement with the experimental data.

Our approach, defining B as a piecewise constant function of time, is obviously a model simplification. A more likely scenario using a continuous function $B(t)$ is sketched in Fig. 10.3a, which shows the correlation between tumor growth and vascularization as the result of our data-driven analysis.

An interesting question that arises is how to link the overshooting of B with the experimental data. One piece of the experimental data we have not used so far is the microvessel density MVD ρ_v. It is the only available experimental measurement that could inform us on the evolution of the vasculature. However, it has been shown in the literature that MVD provides only limited information concerning angiogenic and tumor dynamics. In particular, Hlatky et al. (2002) critically discussed the usefulness of MVD and have concluded that MVD mainly contributes as a prognostic indicator, in the sense of metastatic likelihood and assessment of the current stage of the disease. These authors claim that the MVD by itself cannot

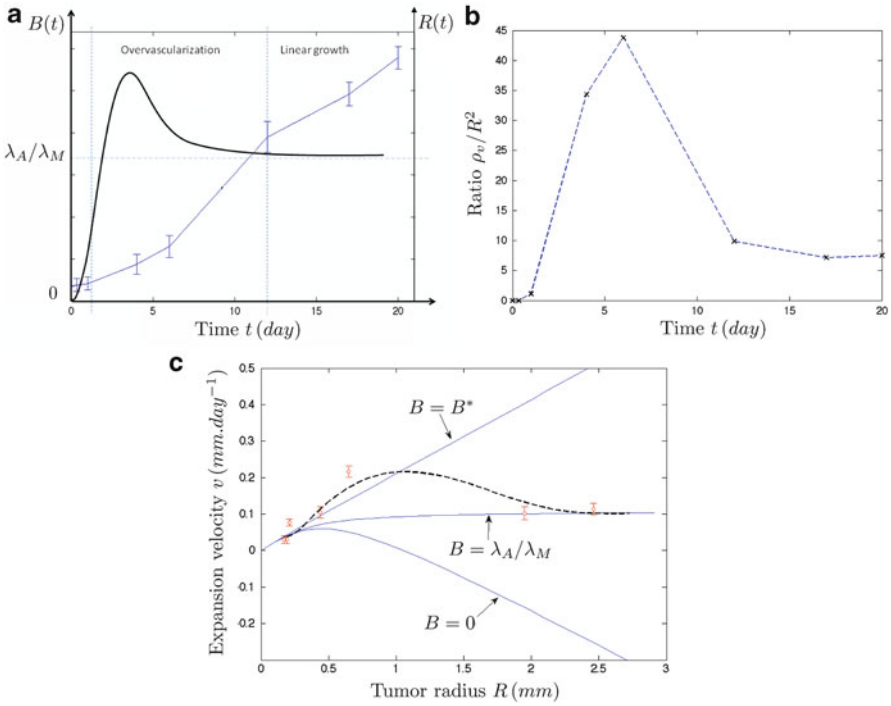

Fig. 10.3 (**a**) Likely scenario of the time-dependent coupling between the vascularization parameter B and the tumor growth regimes (this graph is no simulation result). The *bold curve* is an example of the time evolution of B that allows for the reproduction of the different tumor growth regimes experimentally observed and superimposed in the figure. (**b**) Temporal evolution of the ratio of vessel to tumor cell number $\rho_v(t)/R^2(t)$ evaluated from the experimental data. The nonmonotone behavior coincides with the time evolution of the parameter B. (**c**) Tumor radius velocity versus tumor radius: original model (*solid lines*); data of implanted U87 glioma in nude mice brains (*circles*); modified feedback-loop model (*dashed curve*, see text for details). The tumor dynamics predicted by the modified feedback-loop model is initially characterized by an exponential growth (where $B = 0$); then the velocity increases (due to overvascularization characterized by $B > \lambda_A/\lambda_M$) and reaches a maximum before decreasing and relaxing to a constant value, i.e., linear growth over time characterized by $B = \lambda_A/\lambda_M$

provide information about the dependence of tumor growth on angiogenic activity. However, the association of MDV with a parameter that expresses the influence of neovasculature on the tumor growth dynamics – in the context of our model – could provide another dimension to this measurement.

In the experimental setup used by Lee and coworkers, the MVD is evaluated as a number of vessels N_v^0 (including large microvessels and single brown-stained endothelial cells) within a surface $S_0 = 0.5\text{mm}^2$ in five different fields and averaged accordingly. The MVD is therefore experimentally evaluated as $\rho_v = N_v^0/S_0$ and is a monotonically increasing function of time (see Fig. 10.1d). As ρ_v is obtained as a spatial average, we can assume that the number of vessels N_v^0 within a constant

surface S entirely containing the tumor is $N_{\mathrm{v}}^0(t) = \rho_{\mathrm{v}}(t)S$. We evaluate now the number of tumor cells in S. They all are contained in a disc of radius R, which leads to a number of tumor cells $N_{\mathrm{T}}(t) = \rho_{\mathrm{T}}\pi R^2(t)$ in S, the tumor surface density ρ_{T} being constant. We build now the only dimensionless quantity extractable from the experimental measurement, i.e., the ratio of vessel to tumor cell number (or mass) in S, which yields

$$\frac{N_{\mathrm{v}}^0(t)}{N_{\mathrm{T}}(t)} = \frac{\rho_{\mathrm{v}}(t)S}{\rho_{\mathrm{T}}\pi R^2(t)} \propto \frac{\rho_{\mathrm{v}}(t)}{R^2(t)}. \tag{10.7}$$

Interestingly, this dimensionless quantity behaves in a similar manner to the parameter B, as depicted in Fig. 10.3b. It exhibits a local maximum in time as our predicted parameter B (Fig. 10.3a), and decreases relaxing further to a plateau. Therefore, we suggest that the dynamics of B may be associated with this ratio, which is supported by the scenario we have proposed: In a first stage, vascularization increases faster than the tumor. Then tumor growth accelerates, because supported by new vessels and additional nutrient supply. In the late stage, the number of necessary vessels equilibrates with the number of tumor cells to reach the minimal requirement for unbounded tumor growth.

6 Model Extension

Our data analysis and parameter calibration have provided a deeper insight in the interplay between tumor and vascularization dynamics. Of particular interest is the temporal evolution we have identified for the parameter B. We extend our original model to account for an intrinsic regulation of this parameter.

In tumor biology, angiogenic pathways, typically related to VEGF production, are activated to initiate angiogenic processes. In vivo secretion of VEGF is commonly assumed to depend on tumor hypoxia (Dvorak et al. 1995). VEGF affects endothelial cells of the existing vasculature, which further results in vessel instability, endothelial cell proliferation, and formation of a neovasculature whose vessels mature. When the neovascular network connects the tumor with the existing vasculature, tumor is perfused with blood that provides additional nutrient. This process eventually inhibits VEGF production, which reduces the formation of new capillaries.

In in vivo tumors, VEGFs are typically produced due to the activation of pathways related to reduced oxygen availability. In U87 tumors, histopathology data do not provide evidence of hypoxia. Indeed, U87 cells release VEGF "by default" even under normoxic conditions (Brown et al. 1997; Lucio-Eterovic et al. 2009). Therefore, we do not specify here any mechanism that up- and down-regulates VEGF release. However, due to the vascularization adaptation process (overshooting and relaxation) we believe there still exists a feedback loop between the tumor growth and the VEGF production. In particular, VEGF activation may be down-regulated either (1) by excessive oxygen supply from the new vessels or (2) by VEGF

diffusion through the capillaries. The above-described processes coincide with the definition of an activator–inhibitor system mediated by a negative feedback loop.

Accordingly, we extend our initial model to account for the coupling of VEGF and vascularization dynamics. We introduce the uniform VEGF concentration ρ_{VEGF} as a spatial average over the computational domain. A first-order ordinary differential equation (ODE) is used to model the temporal VEGF evolution. Concerning the dynamics of the vasculature effect B, the shape of the time evolution we have previously identified as a requirement to reproduce the evolution of the tumor radius over time (i.e., the overshooting regime) is typical of an excited damped oscillator. We write then the corresponding generic ODE system as follows:

$$\gamma_{\text{V}} \frac{\mathrm{d}\rho_{\text{VEGF}}}{\mathrm{d}t} + k_{\text{V}} \rho_{\text{VEGF}} = A_{\text{V}}(R,t) - I_{\text{V}}(B,R,t), \tag{10.8}$$

$$m_B \frac{\mathrm{d}^2 B}{\mathrm{d}t^2} + \gamma_B \frac{d\,\mathrm{B}}{\mathrm{d}t} + k_B B = A_B(\rho_{\text{VEGF}}, t). \tag{10.9}$$

In system (10.8)–(10.9), the coefficients γ_i, k_i (for $i = V, B$), and m_B are constant. Equation (10.8) models the evolution of the VEGF concentration: VEGF is produced through the activation term $A_{\text{V}}(R,t)$, diminished due to the vascularization effects through $I_{\text{V}}(B,R,t)$ and decays in time. The second equation (10.9) models the damped oscillating dynamics of B that is driven by the influence of VEGF concentration through $A_B(\rho_{\text{VEGF}}, t)$. VEGF signalling activates the formation of new vessels that requires several intermediate processes (e.g., migration of endothelial cells toward the tumor, vessel maturation), which introduces a delay in the excitation of B. We account for this delay by using the second-order time derivative with "inertia" coefficient m_B, while γ_B is the "damping" coefficient. Finally, the parameter k_B models the "stiffness" (compliance) of the vascularization to any changes of the VEGF production. In our approach, tumor growth is still modeled by (10.1) with B now resulting from (10.9), while the tumor size (the radius R) can influence B through VEGF activation $A_{\text{V}}(R,t)$ and inhibition $I_{\text{V}}(B,R,t)$, respectively.

We aim here at testing if such an approach can capture the dynamics of B and simplify the new model as much as possible. To this end, we suppose that the coupling terms in (10.8) depend only on time and not on the tumor radius R: $A_{\text{V}}(R,t) \equiv c_R(t)$, $I_{\text{V}}(B,R,t) \equiv c_B B(t)$ and $A_B(\rho_{\text{VEGF}}, t) \equiv c_V \rho_{\text{VEGF}}(t)$ where c_B and c_V are constant, while $c_R(t)$ depends on time to reflect VEGF release over time by U87 cells. Indeed, the experimental data suggest that VEGF production by U87 cells is uncontrolled from the beginning of the experiment. This is due to genetic modifications of these cells, which allows them to secret VEGF right after the injection time. We assume that VEGF production factor $c_R(t)$ is initially high and then decreases and relaxes to a constant value at longer times. This can be justified by the fact that the U87 cells release large amount of VEGF from the very beginning of their implantation. The system of (10.8)–(10.9) is decoupled from the tumor evolution although the function $B(t)$ influences the tumor growth through (10.1).

Solving the system of (10.8)–(10.9) and (10.1) and tuning accordingly the parameters, we calculate a potential trajectory of the system in the phase space. We observe that the simulated tumor velocity $v(R)$, the dashed curve in Fig. 10.3c, follows a trajectory similar to the one derived from the experimental observations. In particular, the tumor velocity overshoots and then relaxes to a constant value, recovering the linear growth regime at longer times. Therefore, we conclude that by assuming a feedback mechanism between VEGF release and effective vasculature, we can explain the overvascularization regime and the linear evolution of the tumor radius as a result of an adaptation process between the metabolic needs of the tumor and the vascularization dynamics.

7 Summary and Discussion

In this chapter, we have studied the coupling between tumor growth and tumor-induced neovascularization using a mathematical model informed by data obtained from U87 tumors grown in the brain of immunodeficient mice. Driven by the data analysis, we have used the mathematical model to reproduce the experimental volumetric data. Through this process, we have gained a better understanding of the tumor dynamics to answer the following questions.

What is the critical tumor size where angiogenesis is initiated?

Our model shows that the initial phase of tumor growth is of exponential nature and does not depend on vascularization, i.e., the evolution of the tumor radius is described by the leading term of (10.2):

$$\frac{\mathrm{d}R}{\mathrm{d}t} = \frac{1}{3}(\lambda_{\mathrm{M}} - \lambda_{\mathrm{A}})R\,.$$

This means that there exists a critical radius R_c (hence a critical time) until which angiogenesis – and eventually vascularization represented by the parameter B – confers no evolutionary advantage to tumor growth. We have derived the following expression for this critical radius:

$$R_c \approx L_{\mathrm{D}}\sqrt{\frac{15(\lambda_{\mathrm{M}} - \lambda_{\mathrm{A}})}{\lambda_{\mathrm{M}}(1-B)}}.$$

The above relation provides an approximate tumor radius where the nonlinearities (involving B) of (10.2) become significant. The effect of the nonlinear terms is to saturate the growth, i.e., $\mathrm{d}R/\mathrm{d}t = 0$ when the radius reaches R_c. As only exponential growth is observed for small radii (early phase), we argue that angiogenesis should be activated before the critical tumor radius and suggest that R_c is an upper bound for the development of angiogenic processes.

We can therefore predict the value of the avascular tumor critical radius R_c when knowing the value of the parameters present in the earlier expression. During the parameter calibration, we have found $\lambda_M \approx 1.3\,\text{day}^{-1}$, $\lambda_A \approx 0.6\,\text{day}^{-1}$, and $L_D \approx 0.16\,\text{mm}$. By assuming that the tumor is completely avascular in that early phase, i.e., $B = 0$, we can evaluate the corresponding value $R_c \approx 0.45\,\text{mm}$. This value of the critical radius is in excellent agreement with the experimental observations, since Lee et al. (2006) localize the end of the avascular phase around the first day where the tumor radius is 0.44 mm.

What is the interplay between vascularization dynamics and glioma growth?

The parameter calibration for our mathematical model has revealed further details of the interplay between vascularization and tumor growth dynamics. In particular, we have concluded in a biologically plausible scenario for the temporal evolution of the tumor dynamics (Fig. 10.3a). We claim, with the support of the data, that the tumor initially follows an exponential growth. During this avascular phase, U87 tumor cells initiate angiogenic processes (VEGF release), which results in the formation of a neovasculature. Follows then a highly vascularized phase that places the tumor in an overvascularization regime with an excess of new vessels and, potentially, an increase of blood flow. The increased vascularization boosts the tumor into a second exponential regime (however slower than the first one) that takes over from the avascular growth (that would have ended up in a steady tumor size). Reaching finally its late phase, tumor growth relaxes to a linear regime where the vasculature adapts to the metabolic needs of the tumor (see also next question).

Driven by these results, we have proposed an extension of our initial model to take into account a feedback mechanism between VEGF production and tumor vascularization. We have shown that the modified model, incorporating this self-regulated mechanism, was also capable of reproducing the earlier discussed vascularization and tumor growth dynamics.

Why does linear growth regime occur at the latest phase?

An aspect of interest in tumor growth dynamics is the linear expansion regime. As previously stated, linear growth seems to be a common feature to in vivo human and animal tumors (Brù et al. 2003). The experimental measurements by Lee and coworkers led us to the conclusion that, after a transient regime, the late growth we observe in this model of glioma is also linear. In our model, linear growth is asymptotically realized for the only particular value $B = \lambda_A/\lambda_M$, i.e., when proliferation weighted by vascularization balances cell death. This means that the tumor, in order to sustain unbounded growth, compensates cell death by increasing the tumor cell proliferation rate (which is proportional to the nutrient supply) by means of neovascularization.

At this point, the linear growth regime could be seen as a manifestation of spatio-temporal homeorhesis (*Greek:* stable flow). In biology is well established the concept of homeostasis, that is the tendency of living organisms to maintain (or return to) a stable steady state among its interacting internal components, regardless of the interactions with the external environment. Homeorhesis is a dynamical generalization of homeostasis describing a system that returns to a steady evolution trajectory (*chreod*) under internal and external disturbances (Waddington 1957). Biologically, it can be interpreted as the natural tendency of living organisms to continue their development, albeit being possibly different under different environmental conditions. Therefore, we suggest that tumors sustain a linear growth by returning always to a trajectory of expansion that is defined as the equilibration of the vascularization and metabolism dynamics. Moreover, linear tumor growth can be viewed as a solution to a minimization process of the energy expenditures for creating sufficient new vasculature, i.e., minimal value of B, in order to sustain a constant linear expansion rate.

Anti-angiogenic therapeutical implications and Outlook

Here, we comment on the implications of our study to the use of anti-angiogenic therapies against tumor growth. Our model suggests an explanation for the often disappointing efficacy of anti-angiogenic therapy observed in human clinical trials. Acknowledging the fact that anti-angiogenic treatments aim at depriving the tumor of nutrient through the inhibition of neovascularization processes, we show that a tumor cannot be eradicated (i.e., $R = 0$) by means of nutrient deprivation. This can be understood from the solution of (10.1): if a treatment (modeled by setting $B = 0$) is administrated at the late phase of the growth (at large radii), the tumor radius would initially decrease due to diminished nutrient supply, but would eventually stabilize at a finite size (intersection of the $B = 0$ orbit with the R-axis in Fig. 10.2b).

As stated earlier, the introduction of anti-angiogenic therapy in our model would imply a reduction of the vascularization parameter B. In Cristini et al. (2003) it has been shown that lowering B below a critical value may also affect the tumor morphology. In particular, for low enough values of B the tumor boundary becomes unstable and its morphology deviates from the spherical one. The resulting "fingering" morphology corresponds to in vivo observed tumor invasive patterns (see also Frieboes et al. 2007). The emergence of an invasive tumor cell phenotype would imply that tumor cells tend to "diffuse" away from the tumor bulk to reach better nourished locations, which allows for the creation of new tumor colonies. Therefore, the initiation of tumor invasion, due to treatment-induced hypoxia, could also reduce the efficacy of anti-angiogenic therapy.

Finally, we have shown that a feedback loop between VEGF release and vascularization effect could explain the adaptive behavior of the vascularization dynamics. A straightforward extension of our approach is to consider hypoxia as the cause of VEGF release, thus assuming that low oxygen concentration activates the vascularization dynamics. The neovasculature would increase oxygen supply to the

tumor, i.e., relax the hypoxic conditions, resulting in the inhibition of angiogenic signals. Including this mechanism in the current formulation of our model would improve the description of the biology of in vivo tumors. Assuming that anti-angiogenic treatment inhibits the vascularization effect through B, we could use this model as a basis for optimization of anti-angiogenic therapy protocols.

Acknowledgements HH, AC, and VC acknowledge support from The Cullen Trust for Health Care and the National Institute for Health, Integrative Cancer Biology Program: 1U54CA149196, for the Center for Systematic Modeling of Cancer Development. JL and VC acknowledge support from the National Science Foundation, Division of Mathematical Sciences. VC also acknowledges support from the National Cancer Institute. H. Hatzikirou and A. Chauvière contributed equally to this work.

Appendix 1. Data Processing

We present here the detailed derivation of the results of Sect. 2.2. We start with evaluating the temporal evolution of the tumor radius under the assumption of radial symmetry. We assume that the radii $R(t)$ are random variables (r.v.) – as biological observations include a degree of stochasticity – following the normal distribution $\mathcal{N}(\mu_R(t), \sigma_R(t))$ where $\mu_R(t) = \mathbb{E}[R(t)]$ and $\sigma_R(t) = \sqrt{\text{Var}[R(t)]}$ are the mean value and the standard deviation of $R(t)$, respectively. Therefore, we can assume that the r.v. $\{R(t)\}_{t\in T}$, where T the time of the process (in our case, a discrete time set), are subjected to Gaussian Markov process.[1] As the volume of the tumor is given by

$$V(t) = \frac{4\pi}{3} R^3(t),$$

it is proportional to the third raw moment of the radius. Therefore, we can explicitly write down, at each time point, the relations between the first two central moments (mean and variance) of the volume and the radius. For the sake of simplicity, we drop the time argument to write

$$\mathbb{E}[V] = \mathbb{E}\left[\frac{4\pi}{3} R^3\right] = \frac{4\pi}{3} \int_{\mathbb{R}} r^3 f(r)\mathrm{d}r = \frac{4\pi}{3} \left(\mu_R^2 + 3\mu_R \sigma_R^2\right), \quad (10.10)$$

$$\begin{aligned} \text{Var}[V] &= \mathbb{E}[V^2] - \mathbb{E}[V]^2 = \frac{4\pi}{3} \left[\int_{\mathbb{R}} r^6 f(r)\mathrm{d}r - \left(\int_{\mathbb{R}} r^3 f(r)\mathrm{d}r\right)^2\right] \\ &= 20\pi\sigma_R^2 \left(\mu_R^4 + \frac{36}{15}\mu_R^2 + 1\right), \end{aligned} \quad (10.11)$$

[1] A Gaussian Markov process $X(t)$ is a Markov process whose probability density function is Gaussian.

where $f(r) = \exp\left(-\frac{1}{2}(r-\mu_R)^2/\sigma_R^2\right)$ is the probability density function of the normal distribution. The solution of system (10.10)–(10.11) provides us with the mean μ_R and variance σ_R of the radius R at each time point of the experiment.

A more challenging task is the calculation of the tumor expansion rate (the tumor speed $v(t) = \mathrm{d}R(t)/\mathrm{d}t$), i.e., the radius increase per unit of time. Our approach consists in writing the process that dictates the radius evolution as the stochastic differential equation

$$\mathrm{d}R(t) = M(R,t)\mathrm{d}t + \Sigma(R,t)\mathrm{d}W(t), \tag{10.12}$$

where $M(R,t) = \mu_v(t)$ and $\Sigma^2(R,t) = \sigma_v^2(t) + \mu_v^2(t)$. In particular, the quantity $M(R,t)$, which is called drift, denotes the first moment of the velocity

$$M(R,t) = \lim_{\tau\to 0} \frac{\mathbb{E}[R(t+\tau) - R(t)]}{\tau} = \lim_{\tau\to 0} \frac{\mu_R(t+\tau) - \mu_R(t)}{\tau}, \tag{10.13}$$

where τ is an infinitesimal time step. The quantity $\Sigma(R,t)$, so-called diffusion coefficient, corresponds to the second moment of the velocity, i.e.,

$$\Sigma^2(R,t) = \lim_{\tau\to 0} \frac{\mathbb{E}[(R(t+\tau) - R(t))^2]}{\tau}. \tag{10.14}$$

According to the stochastic differential equations theory, the noise $W(t)$ corresponds to Wiener processes for each time point and $W(t) \sim \mathcal{N}(0,1)$ (property of the Gaussian processes).

Equation (10.14) can be reformulated by using $\mathbb{E}[A+B] = \mathbb{E}[A] + \mathbb{E}[B]$ as

$$\Sigma^2(R,t) = \lim_{\tau\to 0} \frac{1}{\tau}\Big(\mathbb{E}[R^2(t+\tau)] + \mathbb{E}[R^2(t)] - 2\mathbb{E}[R(t+\tau)R(t)]\Big). \tag{10.15}$$

In (10.15), the second moment of $R(t)$ corresponds to $\mathbb{E}[R^2(t)] = \sigma_R^2(t) + \mu_R^2(t)$ for any time t. The quantity $\mathbb{E}[R(t+\tau)R(t)]$ is the autocorrelation function of the process that quantifies how much correlated are two radii at successive times t and $t+\tau$. Under the assumption of a stationary Markovian process (i.e., assuming that the calculation of $R(t+\tau)$ requires only the knowledge of $R(t)$ with the corresponding transition probability being time invariant) the autocorrelation function rewrites

$$\begin{aligned}\mathbb{E}[R(t+\tau)R(t)] &= \sigma_R^2(t)e^{-\beta\tau} + \mathbb{E}[R(t+\tau)]\mathbb{E}[R(t)] \\ &= \sigma_R^2(t)e^{-\beta\tau} + \mu_R(t+\tau)\mu_R(t),\end{aligned} \tag{10.16}$$

where β is the characteristic relaxation rate of the autocorrelation function.

As the experimental observations correspond to a discrete time process $T = \{t_1, ..., t_n\}$, $n = 8$ being the number of experimental measurements, we use the discrete version of the (10.12)

$$R(t_i + \tau_i) - R(t_i) = M(R,t_i)\tau_i + \Sigma(R,t_i)\Delta W(t_i)\sqrt{\tau_i}. \tag{10.17}$$

In (10.17), the set $\{\tau_i\}_{i=1...n-1}$ corresponds to the time intervals between the experimental observations and the noises $\Delta W(t_i) \sim \mathcal{N}(0,1)$ are identically, normally distributed. We use the following discrete form of the stochastic drift:

$$M(R,t_i) \equiv \mu_v(t_i) = \frac{\mu_R(t_i+\tau_i)-\mu_R(t_i)}{\tau_i}. \tag{10.18}$$

We assume that the time between two experimental observations is much larger than the process characteristic time, i.e., $\tau_i \gg 1/\beta$ for $i = 1...n-1$. This assumption corresponds to complete independence between two experimental measurements $R(t_i)$ and $R(t_i+\tau_i)$. Thanks to (10.16) we find $\mathbb{E}[R(t_i+\tau_i)R(t_i)] = \mu_R(t_i+\tau_i)\mu_R(t_i)$. Then the discrete form of the diffusion coefficient writes

$$\Sigma^2(R,t_i) = \frac{1}{\tau_i^2}\Big(\sigma_R^2(t_i+\tau_i)+\mu_R^2(t_i+\tau_i)+\sigma_R^2(t_i)+\mu_R^2(t_i)-2\mu_R(t_i+\tau_i)\mu_R(t_i)\Big), \tag{10.19}$$

which leads to

$$\sigma_v^2(t_i) = \mathrm{Var}[v(t)] = \Sigma^2(R,t_i) - M^2(R,t_i) = \frac{\sigma_R^2(t_i+\tau_i)+\sigma_R^2(t_i)}{\tau_i^2}. \tag{10.20}$$

We can finally conclude that, at each time point t_i, the tumor velocity $v(t_i)$ can be evaluated through the normal distribution $\mathcal{N}\big(\mu_v(t_i),\sigma_v(t_i)\big)$ where μ_v and σ_v are given by (10.18) and (10.20), respectively.

Appendix 2. Details of the Mathematical Model

We consider a nonnecrotic tumor whose volume growth results from a balance between cell mitosis and cell apoptosis, driven by the presence of nutrient (e.g., oxygen or glucose). In the absence of inhibitor chemical species, the spatio-temporal dynamics of the nutrient concentration $\sigma(\mathbf{x},t)$ is modeled by the quasi-steady reaction-diffusion equation

$$0 = D\nabla^2\sigma + \Gamma, \tag{10.21}$$

where D is the diffusion coefficient and Γ is the rate at which nutrient is added to the tumor volume $\Omega(t)$. The quasi-steady assumption is well supported by the observation that the diffusion time scale for oxygen or glucose ($\sim$1 minute) is much lower than the cell doubling time ($\sim$1 day). The rate Γ incorporates all sources and sinks in the tumor volume and is based on the following phenomenological assumptions:

Biological assumption 1: Nutrient is homogeneously supplied by the vasculature at a rate $\Gamma_B = -\lambda_B(\sigma-\sigma_B)$ where σ_B is the uniform nutrient distribution in the blood and λ_B is uniform;

Biological assumption 2: Nutrient is consumed by tumor cells at a rate $\lambda\sigma$ with λ uniform.

This yields a rate Γ given by

$$\Gamma = -\lambda_B (\sigma - \sigma_B) - \lambda\sigma . \tag{10.22}$$

The tumor is modeled as an incompressible fluid whose velocity field $\mathbf{u}$ in Ω satisfies the continuity equation

$$\nabla \cdot \mathbf{u} = \lambda_{\mathrm{P}}, \tag{10.23}$$

where λ_{P} is the net proliferation rate that leads to volume growth (or decrease). This formulation rests on the additional assumptions:

Biological assumption 3: The tumor is modeled as a unique homogeneously distributed phenotype, meaning that all tumor cells behave in the same way;

Biological assumption 4: Tumor expansion depends solely on the net cell proliferation and invasive processes (e.g., cell diffusion) are not explicitly included;

Biological assumption 5: The model assumes that the density of tumor cells is constant and homogeneous within the tumor bulk.

The net cell proliferation rate is chosen as:

$$\lambda_{\mathrm{P}} = \lambda_{\mathrm{M}} \frac{\sigma}{\sigma^{\infty}} - \lambda_{\mathrm{A}}, \tag{10.24}$$

where σ^{∞} is the nutrient concentration outside the tumor volume and

Biological assumption 6: The mitotic and apoptotic rates λ_{M} and λ_{A} are uniform.

The velocity is assumed to obey Darcy's law (porous media flow)

$$\mathbf{u} = -\mu \nabla P, \tag{10.25}$$

where μ is a (constant) cell motility parameter and $P(\mathbf{x}, t)$ is the pressure inside the tumor that is assumed to satisfy the Laplace-Young boundary condition at the interface, which corresponds to

Biological assumption 7: Cell–cell adhesive forces are modeled by a surface tension γ at the tumor boundary.

By introducing the intrinsic length scale $L_{\mathrm{D}} = D^{1/2}/(\lambda_B + \lambda)^{1/2}$, we obtain an intrinsic relaxation time scale $\lambda_R^{-1} = (\mu\gamma)^{-1} L_{\mathrm{D}}^3$. We use these length and time scales to nondimensionalize our model that can be rewritten (using bar-notation for dimensionless quantities) in terms of the modified nutrient concentration $\bar{\sigma}$ and pressure $\bar{p}$ defined by:

$$\sigma = \sigma^{\infty}\big(1 - (1 - B)(1 - \bar{\sigma})\big),$$

$$P = \frac{\gamma}{L_{\mathrm{D}}} \left(\bar{p} + \frac{1}{\lambda_R} \left(\lambda_{\mathrm{M}}(1 - B)(1 - \bar{\sigma}) + (\lambda_{\mathrm{A}} - \lambda_M B) \frac{\bar{\boldsymbol{x}} \cdot \bar{\boldsymbol{x}}}{2d} \right) \right). \tag{10.26}$$

The parameter

$$B = \frac{\sigma_B}{\sigma^\infty}\frac{\lambda_B}{\lambda_B + \lambda} \tag{10.27}$$

represents the effect of vascularization. By using algebraic manipulations, the original dimensional problem can we reformulated in terms of two nondimensional decoupled problems:

$$\begin{aligned} \nabla^2\bar{\sigma} - \bar{\sigma} &= 0, \\ (\bar{\sigma})_\Sigma &= 1; \end{aligned} \tag{10.28}$$

and

$$\begin{aligned} \nabla^2\bar{p} &= 0, \\ (\bar{p})_\Sigma &= \kappa - \frac{1}{\lambda_R}(\lambda_\mathrm{A} - \lambda_M B)\frac{(\bar{\boldsymbol{x}}\cdot\bar{\boldsymbol{x}})_\Sigma}{2d}, \end{aligned} \tag{10.29}$$

in a d-dimensional tumor separated from the host tissue by the interface Σ (of local curvature κ) that evolves with the normal velocity $\bar{v} = \boldsymbol{n}\cdot(\bar{\boldsymbol{u}})_\Sigma$, $\boldsymbol{n}$ being the outward normal to Σ.

When considering evolution of a three-dimensional tumor that remains radially symmetric, problems (10.28) and (10.29) have analytical solutions that lead to the following evolution equation for the dimensionless tumor radius $\bar{R}$:

$$\frac{\mathrm{d}\bar{R}}{\mathrm{d}\bar{t}} = \bar{v} = \frac{1}{\lambda_R}\left(\frac{1}{3}(\lambda_\mathrm{M}B - \lambda_\mathrm{A})\bar{R} + \lambda_\mathrm{M}(1-B)\Big(\frac{1}{\tanh(\bar{R})} - \frac{1}{\bar{R}}\Big)\right). \tag{10.30}$$

We use the dimensional version of this equation for the tumor radius $R = L_\mathrm{D}\bar{R}$ evolving with respect to time $t = \bar{t}/\lambda_R$, which is (10.1) given in Sect. 3.

References

Ambrosi D, Bussolino F, Preziosi L (2005) A review of vasculogenesis models. Comp Math Meth Med 6:1–19

Anderson ARA, Chaplain MAJ (1998) Continuous and discrete mathematical models of tumor-induced angiogenesis. Bull Math Biol 60:857–900

Bauer AL, Jackson TL, Jiang Y (2007) A cell-based model exhibiting branching and anastomosis during tumor-induced angiogenesis. Biophys J 92:3105–3121

Bearer EL, Lowengrub JS, Chuang YL, Frieboes HB, Jin F, Wise SM, Ferrari M, Agus D, Cristini V (2009) Multiparameter computational modeling of tumor invasion. Canc Res 69(10):4493–4501

Brown LF, Detmar M, Claffey K, Nagy JA, Feng D, Dvorak AM, Dvorak HF (1997) Regulation of angiogenesis, Boston (MA): Birkhauser, chap Vascular permeability factor/vascular endothelial growth factor: a multifunctional angiogenic cytokine

Brù A, Albertos S, Subiza JL, Garcia-Asenjo JL, Bru I (2003) The universal dynamics of tumor growth. Bioph J 85:2948–2961

Cristini V, Lowengrub J, Nie Q (2003) Nonlinear simulation of tumor growth. J Math Biol 46:191–224

Dvorak HF, Brown LF, Detmar M, Dvorak AM (1995) Vascular permeability factor/vascular endothelial growth factor, microvascular hyperpermeability, and angiogenesis. Am J Pathol 146(5):1029–1039

Frieboes HB, Lowengrub JS, Wise S, Zheng X, Macklin P, Bearer E, Cristini V (2007) Computer simulation of glioma growth and morphology. NeuroImage 37:59–70

Hanahan D, Weinberg RA (2000) The hallmarks of cancer. Cell 100:57–70

Hlatky L, Hahnfeldt P, Folkman J (2002) Clinical application of antiangiogenic therapy: microvessel density, what it does and doesn't tell us. J Nat Canc Inst 94(12):883–893

Kevrekidis PG, Whitaker N, Good DJ, Herring GJ (2006) Minimal model for tumor angiogenesis. Phys Rev E 73:061,926

Lee O, Fueyo J, Xu J, Yung WK, Lemoine MG, Lang FF, Bekele BN, Zhou X, Alonso MA, Aldape KD, Fuller GN, Gomez-Manzano C (2006) Sustained angiopoietin-2 expression disrupts vessel formation and inhibits glioma growth. Neoplasia 8(5):419–428

Lucio-Eterovic AK, Piao Y, de Groot JF (2009) Mediators of glioblastoma resistance and invasion during antivascular endothelial growth factor therapy. Clin Cancer Res 15(14):4589–4599

Macklin P, McDougall S, Anderson ARA, Chaplain MAJ, Cristini V, Lowengrub J (2009) Multiscale modeling and nonlinear simulation of vascular tumour growth. J Math Biol 58(4-5):765–798

McDougall SR, Anderson ARA, Chaplain MAJ, Sherratt JA (2002) Mathematical modeling of flow through vascular networks: implications for tumour-induced angiogenesis and chemotherapy strategies. Bull Math Biol 64:673–702

McDougall SR, Anderson ARA, Chaplain MAJ (2006) Mathematical modeling of dynamic adaptive tumour-induced angiogenesis: Clinical applications and therapeutic targeting strategies. J Theor Biol 241:564–589

Merks RMH, Glazier JA (2006) Dynamic mechanisms of blood vessel growth. Nonlinearity 19:1–10

Merks RMH, Perrynand ED, Shirinifard A, Glazier JA (2008) Contact-inhibited chemotaxis in de-novo and sprouting blood-vessel growth. PLoS Comput Biol 4:e1000,163

Mikkelsen T, Enam SA, Rosenblum MR (2003) Invasion in malignant glioma, Philadelphia: W. B. Saunders Co., pp 687–713

Milde F, Bergdorf M, Koumoutsakos P (2008) A hybrid model for three-dimensional simulations of sprouting angiogenesis. Biophys J 95:3146–3160

Plank MJ, Sleeman BD (2003) A reinforced random walk model of tumour angiogenesis and anti-angiogenic strategies. Math Med Biol 20:135–181

Pries AR, Secomb TW (2008) Modeling structural adaptation of microcirculation. Microcirculation 15(8):753–764

Pries AR, Secomb TW, Gaehtgens P (1998) Structural adaptation and stability of microvascular networks: theory and simulations. Am J Physiol Heart Cir Physiol 275:349–360

Stephanou A, McDougall SR, Anderson ARA, Chaplain MAJ (2005) Mathematical modeling of flow in 2d and 3d vascular networks: Applications to anti-angiogenic and chemotherapeutic drug strategies. Math Comput Model 41:1137–1156

Stephanou A, McDougall SR, Anderson ARA, Chaplain MAJ (2006) Mathematical modeling of the influence of blood rheological properties upon adaptative tumour-induced angiogenesis. Math Comput Model 44:96–123

Stokes CL, Lauffenburger DA, Williams SK (1991) Migration of individual microvessel endothelial cells: stochastic model and parameter measurement. J Cell Sci 99(2):419–430

Sun C, Munn LL (2008) Lattice-boltzmann simulation of blood flow in digitized vessel networks. Comp Math Appl 55:1594–1600

Sun S, Wheeler MF, Obeyesekere M, Patrick CW Jr (2005) A deterministic model of growth factor-induced angiogenesis. Bull Math Biol 67:313–337

Waddington CH (1957) The Strategy of the Genes. Geo Allen & Unwin, London
Ward JP, King JR (1997) Mathematical modeling of avascular tumour growth. IMA J Math Appl Med Biol 14:36–69
Welter M, Rieger H (2010) Physical determinants of vascular network remodeling during tumor growth. Eur Phys J E Soft Matter 33:149–163
Welter M, Bartha K, Rieger H (2008) Emergent vascular network inhomogenities and resulting blood flow patterns in a growing tumor. J Theor Biol 250:257–280
Wu J, Xu SX, Long Q, Collins MW, Koenig CS, Zhao GP, Jiang YP, Padhani AR (2007) Simulation of microcirculation in solid tumors. In: IEEE/ICME Int. Conf. on Complex Med. Eng., pp 1555–1562
Zhao G, Wu J, Xu S, Collins MW, Long Q, Koenig CS, Jiang Y, Wang J, Padhani AR (2007) Numerical simulation of blood flow and interstitial fluid pressure in solid tumor microcirculation based on tumor-induced angiogenesis. Acta Mech Sinica 23:477–483
Zheng X, Wise SM, Cristini V (2005) Nonlinear simulation of tumor necrosis, neovascularization and tissue invasion via an adaptive finite-element/level-set method. Bull Math Biol 67:211–259
Zuelch KJ (1986) Brain tumors, 3rd edn. Heidelberg: Springer

Chapter 11
Particle Simulations of Growth: Application to Tumorigenesis

Michael Bergdorf, Florian Milde, and Petros Koumoutsakos

1 Computing Growth

Do we have today the capabilities to simulate effectively the growth of organs and living organisms? We understand "growth" as the process of the gain in size or the transformation of a living organism that is accompanied by a change of its shape. Starting at any stage during the growth of an organ can simulations predict the subsequent evolution of shape? We believe that the answer to our question above is "no" with the specification "not today" and possibly not even in the next 10 years. Growth involving processes that span several orders of magnitude in spatial and temporal scales is the core of all development and it assumes its most intricate variety in this context. Organisms of the full range of morphologic complexity are formed through the interplay of biochemical and mechanical forces, orchestrated by genetic regulation and control. The phenomena involved in growth are intimidatingly complex and multiscale, yet the complexity of this process and the capabilities that can be provided by predicting growth under healthy and pathological conditions merit the making of first steps in that direction (Fig. 11.1).

One of the earliest steps in that direction was made by Turing (1952) who developed mathematical models for developmental biology. This work shed light on how simple reaction diffusion systems can give rise to patterns, like colorful stripes or spots on certain fish, and prepatterns, which are chemical patterns to which cells respond such that a spatial structure forms. While the growth of healthy tissues and organs remains a topic of intensive research a parallel line of work involves the study of pathological growth and most importantly a process that involves hundreds of millions of people: cancer. Cancer is one of the most impactive pathological growth processes in humans. Cancerous growth of tissues is caused by alterations in the

M. Bergdorf • F. Milde • P. Koumoutsakos (✉)
Chair of Computational Science, ETH Zurich, CH-8092, Switzerland
e-mail: bergdorf@inf.ethz.ch; mildef@inf.ethz.ch; petros@inf.ethz.ch

T.L. Jackson (ed.), *Modeling Tumor Vasculature: Molecular, Cellular, and Tissue Level Aspects and Implications*, DOI 10.1007/978-1-4614-0052-3_11,

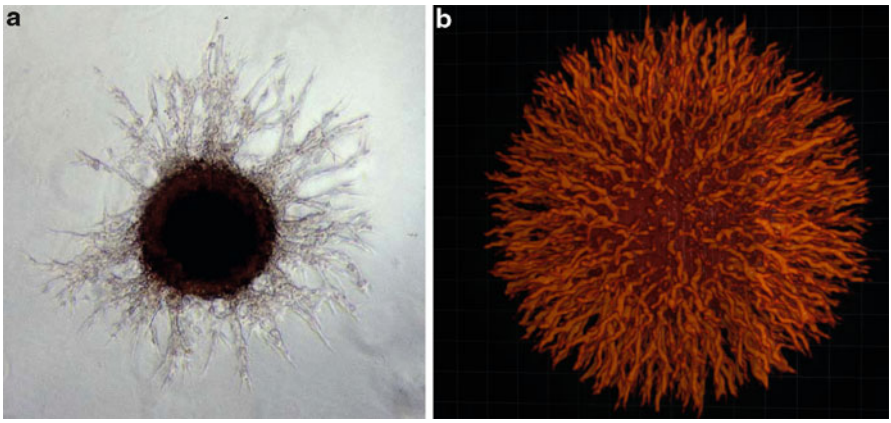

Fig. 11.1 (**a**) A glioblastoma tumor spheroid, with invasive cells shed at its boundary (image from Habib et al. 2003). (**b**) Computer simulation of the shedding of invasive cells (see Chapter Particle Simulations of Growth: Application to Angiogenesis)

cell physiology, which manifest in the cell's self-sufficiency in growth signals, its insensitivity to growth-inhibitory signals, the persistent evasion of cell death and its inexhaustible potential for replication (Hanahan and Weinberg 2000). Recent advances in molecular biology have lead to an incessantly increasing production of oncologic data. Gatenby and Gawlinski (2003) point out that "clinical oncologists and tumor biologists posses virtually no comprehensive theoretical model to serve as a framework for understanding, organizing, and applying these data," and noting the necessity to "[develop] mechanistic models that provide real insights into critical parameters that control system dynamics." Many mathematical models concerning cell dynamics, especially tumor growth and its related biophysical processes have been formulated (see Araujo and McElwain 2004 for a comprehensive review of solid tumor growth modeling). However, only few have reached a maturity which allows to extract quantitative answers and questions from their simulation results. The modeling and simulation of these systems bears several challenges, some of which we address in this work.

In simulation, growing entities need to be distinguished from their surroundings; cells need to be distinguished from the culture they grow on, blood vessels need to be distinguished from other cells and from the extracellular matrix they migrate through, and we need to be able to distinguish between different types of tumor cells and healthy tissue. In this sense, the simulation of these systems is faced with requirements, which are similar to those of multiphase flows, or crystal growth. Continuum approaches for these systems can be classified into *sharp* and *diffuse* interface approaches.

Diffuse interface approaches use scalar functions $\rho_i(\boldsymbol{x}, t)$ to describe the spatial presence of different components $i = 1, 2, \ldots$, e.g., in a two-phase flow, $\rho_1 = 0$ in one phase and $\rho_1 = 1$ in the other phase. Among the two phases there is a smooth

transition from 0 to 1. This diffuse interface has a characteristic size ε, which is chosen such that $\varepsilon \to 0$ as $h \to 0$. Advantages of this approach are that there is no need for interface tracking technology, and that it can manage an arbitrary number of different components, phases, or cell types. This simplicity comes at the expense of numerical difficulties with incorporating surface tension effects into the system, as surface tension appears as a fourth-order nonlinear differential operator and leads to stiff systems. The stiffness makes the involvement of implicit solvers necessary, e.g., nonlinear multigrid methods (Kim et al. 2004). Sharp interface approaches on the other hand are formulated by imposing a sharp boundary between different components. On this interface, boundary conditions need to be formulated and enforced. The interface itself is either represented with an immersed boundary or an immersed interface approach.

In this chapter we address the issues encountered in both the sharp interface and the diffuse interface approach. Within the class of sharp interface models we introduce conservative particle formulations of reactant dynamics on growing and deforming geometries. Furthermore, we present Lagrangian level set methods and apply them to simulations of solid tumor growth, and address the problem of boundary conditions and the scalable solving of surface-tension dynamics. A framework for the class of diffuse interface methods is presented in the chapter Particle Simulation of Growth: Application to Angiogenesis.

2 Particle Methods

Particle methods can be used to simulate systems ranging from water transport in nanotubes to galaxy formation. This unique property of particle methods relies on the formulation of fluid phenomena as interactions between evolving particles. The common algorithmic framework used to describe these interactions enables efficient multiscale simulations in terms of multiresolution and in coupling atomistic and continuum systems. Particle methods for continuum systems, such as Smoothed Particle Hydrodynamics and Vortex Methods, are based on the Lagrangian formulation of the governing equations and quadratures of the corresponding integral equations. Particles interact and adapt according to the flow velocity but the nonuniform distortion of the computational elements prevents the convergence of the method. Hence particles evolve hydrodynamically, albeit inconsistently with the equations they aim to discretize. In order to alleviate this difficulty we have introduced the process of remeshing by reinitializing the particles periodically on grid nodes. Remeshing detracts from the grid free character of particles but enables advances such as multiresolution, the coupling of continuum and atomistic descriptions and last but not least the development of software that seamlessly simulates systems across several scales.

2.1 Function Representation

Particle methods are a natural way of modeling advection dominated problems as the Lagrangian advection is what particles that constitute physical systems actually do; flowing water consists of the motion of water molecules, obeying Newton's laws of motion.

The *Point Particle Approximation* is based on the integral identity

$$q(x) = \int \delta(x-y)\, q(y)\, \mathrm{d}y, \tag{11.1}$$

where δ is the Dirac delta measure. This integral equality is discretized using particles as quadrature points:

$$q^h(x) = \sum_p Q_p\, \delta(x - x_p), \tag{11.2}$$

where Q_p denote the particle weights, e.g., $Q_p = \int_{x_p-h/2}^{x_p+h/2} q(x)\, \mathrm{d}x$, where h is the inter-particle spacing. This simple approximation has the drawback, that q^h cannot be evaluated in-between particle locations. Chorin and Bernard (1973), Leonard and Reynolds (1988), and Raviart (1985) introduced the smooth particle scheme, which starts with the same integral equality (11.1), but then applies a filter to it. In other words, the Dirac delta measure is replaced by an appropriately constructed mollification, yielding:

$$q^\varepsilon(x) = \int \zeta^\varepsilon(x-y)\, q(y)\, \mathrm{d}y, \tag{11.3}$$

where $\zeta^\varepsilon = \varepsilon^d\, \zeta(x)$, for $x \in \mathbb{R}^d$. This approximation introduces an error of size

$$\| q - q^\varepsilon \|_{L^\infty} \leq C\, \varepsilon^r \left\| \frac{\partial^r q}{\partial x^r} \right\|_{L^\infty}, \tag{11.4}$$

given that the mollified kernel satisfies

$$\int \zeta(x)\, x^\alpha\, \mathrm{d}x = 0^\alpha, \qquad 0 \leq \alpha < r, \tag{11.5}$$

and $\| f \|_{L^\infty} = sup\, |f|$.

Discretization is performed in the same way as for the point particle approximation (11.2), by using particles as quadrature weights and quadrature points combinations:

$$q^{\varepsilon,h}(x) = \sum_p Q_p\, \zeta^\varepsilon(x - x_p). \tag{11.6}$$

For a sufficiently smooth ζ the error of this quadrature is given by:

$$\|q^{\varepsilon} - q^{\varepsilon,h}\|_{L^\infty} \leq C \left(\frac{h}{\varepsilon}\right)^m \left\| \frac{\partial^m q}{\partial x^m} \right\|_{L^\infty}, \tag{11.7}$$

where m depends on the smoothness properties of ζ. It is very important to note that for particle methods to work, particle kernels need to be at least in C^0 and smooth particles must overlap, i.e., $\frac{h}{\varepsilon} < 1$. Note however, that ε is only a characteristic kernel size, so either we need to set it to a well-defined size (especially in the case of "small kernels" (Tornberg and Engquist 2004) or we actually need to set $\varepsilon \sim h^\alpha$, with $\alpha < 1$ to ascertain convergence.

2.2 Operator Approximations

In order to solve general transport problems using particle methods, we additionally need a means to evaluate differential operators on the function using particles. A conservative and accurate approximation of the Laplace operator was developed by Degond and Mas-Gallic (1989). In this work, they did not use the paradigm of exact operators but approximate ones; the method of particle strength exchange (PSE), approximates differential operators by suitable integral operators, e.g., the Laplacian:

$$\Delta^{\varepsilon} q = \varepsilon^{-2} \int \big(q(y) - q(x)\big)\, \eta^{\varepsilon}(x - y)\, \mathrm{d}y. \tag{11.8}$$

The accuracy of this approximation can be derived by assuming that η is local, we can expand $q(y)$ at x and find

$$\Delta^{\varepsilon} q = \varepsilon^{-2} \int \sum_{\alpha} (x - y)^{\alpha} \frac{\partial^{\alpha} q}{\partial x^{\alpha}}\, \eta^{\varepsilon}(x - y)\, \mathrm{d}y, \tag{11.9}$$

and with the same argumentation as for the function approximation we obtain an rth order approximation of Δ if

$$\int \eta(x)\, x^{\alpha}\, \mathrm{d}x = 0, \qquad \text{for } \alpha = 1 \text{ and } 2 < \alpha < r + 2, \tag{11.10}$$

and η is scaled such that

$$\int \eta(x)\, x^2\, \mathrm{d}x = 2. \tag{11.11}$$

Analogous to the function approximation using particles, the integral (11.8) is now approximated with particle locations as quadrature points and particle strengths as quadrature weights:

$$\big(\Delta^{\varepsilon,h} q\big)(x_{p'}) = \varepsilon^{-2} \sum_{p} \left(Q_p - Q_{p'} \frac{v_p}{v_{p'}} \right) \eta^{\varepsilon}(x_{p'} - x_p), \tag{11.12}$$

where v_p is the particle volume associated with the particle p. We note here that the PSE particle approximation of diffusion is equivalent to various finite difference schemes for different kernels when the particles find themselves distributed regularly on a grid.

2.3 The Lagrangian Frame and Remeshing

Particle methods have been extensively used to discretize transport equations in the Lagrangian frame. This bypasses the discretization of the convection term, which is associated with stability issues and excessive numerical diffusion for schemes such as finite differences and finite elements. One possible way to derive the equations for the particle quantities is to go back to the original integral form of the transport equations and consider them in the Lagrangian frame, i.e., a frame that moves with the local flow field $\boldsymbol{u}$, i.e., $\mathrm{d}\boldsymbol{x}/\mathrm{d}t = \boldsymbol{u}$. Let us consider the following convection diffusion problem in $\mathbb{R}^d$:

$$\frac{\partial q}{\partial t} + \nabla \cdot (q\,\boldsymbol{u}) = 0. \tag{11.13}$$

(11.13) states that the conserved quantity $\int q\,\mathrm{d}x$ is convected in the flow field $\boldsymbol{u}$, i.e.,

$$\begin{aligned}
\frac{\mathrm{d}}{\mathrm{d}t}\int_{V(t)} q\,\mathrm{d}v &= \int_{V(t)} \frac{\partial q}{\partial t}\,\mathrm{d}v + \oint_{\partial V(t)} q\,\frac{\mathrm{d}\boldsymbol{x}}{\mathrm{d}t}\,\mathrm{d}\boldsymbol{a} \\
&= \int_{V(t)} \frac{\partial q}{\partial t}\,\mathrm{d}v + \oint_{V(t)} q\,\boldsymbol{u}\,\mathrm{d}v \\
&= \int_{V(t)} \frac{\partial q}{\partial t} + \nabla\cdot(q\,\boldsymbol{u})\,\mathrm{d}v \\
&= 0.
\end{aligned} \tag{11.14}$$

So if we initialize particle strengths as $\int_{V_p(t=0)} q(\boldsymbol{x},0)\,\mathrm{d}v$, or simply as $h^d\,q(\boldsymbol{x}_p(t=0))$, and advect the particles with the local flow field, i.e., solve

$$\begin{aligned}
\frac{\mathrm{d}\boldsymbol{x}_p}{\mathrm{d}t} &= \boldsymbol{u}(\boldsymbol{x}_p, t), \\
\frac{\mathrm{d}Q_p}{\mathrm{d}t} &= 0,
\end{aligned} \tag{11.15}$$

then we obtain the solution of (11.13) at $\boldsymbol{x}$ and t by reconstructing $q^{\varepsilon,h}$ as

$$q^{\varepsilon,h}(\boldsymbol{x},t) = \sum_p Q_p(t)\,\zeta^\varepsilon\big(\boldsymbol{x} - \boldsymbol{x}_p(t)\big). \tag{11.16}$$

However, as particles follow the flow field, the locations of the particles can become distorted and the overlapping condition can be violated. The reconstruction (11.16) breaks down because ζ^{ε} is not well-sampled anymore and the method fails to converge.

Many approaches that address this problem of Lagrangian distortion have been formulated (see Cottet and Koumoutsakos 2000, and references therein). The approach that is most efficient and commonly used in the context of smooth particle methods is called "remeshing" and amounts to periodically interpolating particle strengths onto a regular grid and creating a new set of particles at the grid point locations:

$$\tilde{Q}_p = \sum_l Q_l \, M(\tilde{\boldsymbol{x}}_p - \boldsymbol{x}_l); \tag{11.17}$$

the old particles are discarded, and the grid points $\tilde{\boldsymbol{x}}_p$ become the new particles. The interpolation or remeshing kernel M is chosen, such that it conserves the discrete moments of Q_l, i.e., such that

$$\sum_p \tilde{Q}_p \, \tilde{\boldsymbol{x}}_p^{\alpha} = \sum_l Q_l \, \boldsymbol{x}_l^{\alpha} \qquad \text{for } 0 \leq \alpha < \tilde{r}. \tag{11.18}$$

Note that the number of particles is not necessarily the same for the new and old set of particles. In multidimensions M is usually chosen as a tensor product of one-dimensional kernels, i.e.,

$$M(\boldsymbol{x}) = \prod_{i=1}^{d} B(\{\boldsymbol{x}\}_i), \tag{11.19}$$

where $\{\boldsymbol{x}\}_i$ is the ith component of $\boldsymbol{x}$. Examples of $B(x)$ include B-splines and extrapolations thereof (Monaghan 1985). Replacing (11.17) into (11.18), for the 1D case, and $\tilde{x}_p = i\,h$ we obtain:

$$\sum_i \sum_p Q_p \, M(i\,h - x_p)(i\,h)^{\alpha} = \sum_p Q_p \, x_p^{\alpha}. \tag{11.20}$$

Now for simplicity consider $Q_p = \delta_{0\,p}$, then (11.20) becomes

$$\sum_i M(i\,h - x_0)(i\,h)^{\alpha} = x_0^{\alpha}, \tag{11.21}$$

in other words: the requirement for polynomial reproduction.

The remeshing kernel should be chosen based on the nature of the problem that we want to solve, e.g., in Direct Numerical Simulations of turbulent flows, it is crucial to employ a kernel which is interpolating, so that the amount of numerical diffusion that is introduced is minimal, however in compressible flows that feature discontinuities in the density or velocity, such a kernel can lead to spurious shock

waves, and smoothing remeshing kernels should be used. For the application of the smooth particle method to incompressible flow the kernel of choice is usually a tensor product of the M_4' function:

$$M_4'(x) = \begin{cases} \frac{1}{2}(|x|-1)(3|x|^2-2|x|-2) & |x|<1 \\ -\frac{1}{2}(|x|-1)(|x|-2)^2 & 1\le|x|<2 \\ 0 & 2\le|x|. \end{cases} \tag{11.22}$$

This kernel is nominally third-order accurate, is interpolating, and has a support of 4 (Koumoutsakos 1997).

For high-order calculations we employ M_6''' and the M_6^* kernel functions:

$$M_6'''(x) = \begin{cases} -\frac{1}{88}(|x|-1)(60|x|^4-87|x|^3-87|x|^2+88|x|+88) & |x|<1 \\ \frac{1}{176}(|x|-1)(|x|-2)(60|x|^3-261|x|^2+257|x|+68) & 1\le|x|<2 \\ -\frac{3}{176}(|x|-2)(4|x|^2-17|x|+12)(|x|-3)^2 & 2\le|x|<3 \\ 0 & |x|\ge 3. \end{cases} \tag{11.23}$$

The first six moments of this kernel vanish, it is interpolating, it has even parity, and the first derivative is zero at $x = \pm 3$. The M_6^* function is nominally fourth-order accurate and has a support of 6:

$$M_6^*(x) = \begin{cases} -\frac{1}{12}(|x|-1)(25|x|^4-38|x|^3-3|x|^2+12|x|+12) & |x|<1 \\ \frac{1}{24}(|x|-1)(|x|-2)(25|x|^3-114|x|^2+153|x|-48) & 1\le|x|<2 \\ -\frac{1}{24}(|x|-2)(|x|-3)^3(5|x|-8) & 2\le|x|<3 \\ 0 & 3\le|x|. \end{cases} \tag{11.24}$$

This kernel was derived by requiring: $M_6^* \in C^2(\mathbb{R}^3)$, interpolation (or delta-Kronecker property), polynomial reproduction up to fourth order, even parity, and vanishing first and second derivatives at the end points ($x = \pm 3$). The presented methods have recently been extended to a multiresolution Lagrangian particle method with enhanced, wavelet-based adaptivity (Bergdorf and Koumoutsakos 2006).

3 Evolving Geometries

3.1 Representing Complex Geometries

Growth processes involve complex, deforming geometries. In order to be able to tackle the effects introduced by the time dependent geometric complexity of these processes, we need to effectively represent those complex geometries and to formulate the respective differential operators. Thinking particles, the first approach that comes to mind is to represent the surface of the geometry as a set of points in space. This surface can be deformed by simply moving these points with a given velocity. A simple query however, such as deciding whether we are within the geometry or outside calls for a notion of connectivity between the points, requiring that we perform a triangulation of this point set. When the geometry is subject to large deformations, one needs to resort to remeshing techniques, introducing new points in expansion zones, and removing points in compression zones (Lindsay and Krasny 2001). When the geometries undergo topological changes, however, one needs to resort to heuristics. Methods that follow this line are called *interface tracking* or *front tracking* methods, they have been successfully applied to problems as diverse as multiphase flow (Unverdi and Tryggvason 1992), drop breakup dynamics (Cristini et al. 2001), or solidification (Juric and Tryggvason 1996).

The level set method (Osher and A. 1988) is an interface capturing approach, where the geometry Γ is described implicitly as the zero isosurface of a level set function φ, i.e.,

$$\Gamma = \{ \boldsymbol{x} \mid \varphi(\boldsymbol{x}) = 0 \}. \tag{11.25}$$

This level set function is chosen such that it represents a signed-distance function, defined by:

$$|\nabla \varphi| = 1. \tag{11.26}$$

The interface Γ can be moved and deformed by making it subject to a simple advection equation, which is often called the "level set equation":

$$\frac{\partial \varphi}{\partial t} + \boldsymbol{u} \cdot \nabla \varphi = 0. \tag{11.27}$$

Surface properties can be retrieved directly from φ, e.g., the surface normal is given by:

$$\boldsymbol{n} = \nabla \varphi|_{\Gamma}, \tag{11.28}$$

and the mean curvature by

$$\kappa = \nabla \cdot \boldsymbol{n}|_{\Gamma} = \Delta \varphi|_{\Gamma}. \tag{11.29}$$

Level set methods have been successfully applied to a wide range of problems (see the textbook Osher and Fedkiw 2003 and references therein). Most level set methods solve (11.27) in an Eulerian frame using finite-difference discretizations. A drawback of this approach is the inherent numerical diffusion associated with the discretization of the convection term in (11.27). This numerical diffusion leads to the loss of small scale features in the geometry or interface that is represented by the level set. Several remedies have been proposed, most prominently the so called "Particle Level Set Method" introduced by Enright et al. (2002). This formulation employs an Eulerian representation of the level set function on a grid, and additionally uses marker particles, which are scattered around the interface and carry subgrid-scale information to maintain and reconstruct the interface. In Hieber and Koumoutsakos (2005) a truly Lagrangian particle level set method was introduced by Hieber and Koumoutsakos, which enjoys the characteristically small numerical diffusion errors of the Lagrangian particle approach.

Equation (11.27) can be discretized using a particle scheme:

$$\begin{aligned}\frac{\mathrm{d}\varphi_p}{\mathrm{d}t} &= 0,\\ \frac{\mathrm{d}\boldsymbol{x}_p}{\mathrm{d}t} &= \boldsymbol{u}(\boldsymbol{x}_p, t),\\ \frac{\mathrm{d}v_p}{\mathrm{d}t} &= \big(v_p\,\nabla\cdot\boldsymbol{u}\big)(\boldsymbol{x}_p, t),\end{aligned} \tag{11.30}$$

and the function can always be reconstructed as:

$$\varphi(\boldsymbol{x}, t) = \sum_p v_p\,\varphi_p\,M\big(\boldsymbol{x} - \boldsymbol{x}_p(t)\big), \tag{11.31}$$

where v_p denote the particle volumes. Basically, we would have to evolve the particle volumes as well in order to reconstruct φ, this however, is unnecessary if we perform renormalizations of the kernel M as described in Bergdorf (2007), because the renormalization factor is equal to the particle volume: $\sum_p h\,M(x - x_p) = v(x)$.

The signed-distance property (11.26) of the level set has the following advantages: the distance to the interface can always be assessed in $\mathcal{O}(1)$ operations, which can be crucial for immersed interface applications (e.g., Section 5). The property (11.26) is also a condition on the regularity of the gradient, which can be crucial for stable computation of curvature and other higher-order surface properties (note because (11.29) requires $|\nabla\varphi| = 1$, we can easily generalize (11.29) to $\kappa = \nabla\cdot\nabla(\varphi/|\nabla\varphi|)$).

The equation for the evolution of the signed-distance property, $\mathcal{M} \equiv \frac{1}{2}|\nabla\varphi|^2$ can be derived using (11.27) and results in

$$\frac{\partial\mathcal{M}}{\partial t} + \boldsymbol{u}\cdot\nabla\mathcal{M} = -2\mathcal{M}\,\boldsymbol{n}\cdot\big(\nabla\otimes\boldsymbol{u}\big)\boldsymbol{n}, \tag{11.32}$$

so as soon as there is some deformation in the flow in normal direction, $\mathcal{M}$ derails exponentially from unity.

Reinitialization is the periodically applied process of healing this divergence from the signed-distance property. There are many different approaches to this, they can however be classified into two broad categories: fast marching type methods and PDE-based methods.

Fast Marching Type Methods The fast marching method for reinitialization has been introduced by Sethian (1996) (see Sethian 1999 for a comprehensive review). These methods solve the Eikonal equation $|\nabla\varphi| = 1$ by discretizing the ∇ operator using one-sided finite differences and updating grid point by grid point in an iterative fashion. This method has a nominal computational cost of $\mathcal{O}(N\,logN)$, as it requires the grid points to be sorted based on their φ-value. There exist improvements, like the group marching method (Kim 2001), which reduces the operational cost to $\mathcal{O}(N)$. However, the drawbacks of this class are twofold. The first drawback is that solving the Eikonal equation with one-sided differences leads to rough solutions, i.e., the error introduced is not smooth. As a consequence, the computation of operators that involve high-order derivatives leads to rather noisy results – this may necessitate regularized operators, e.g., for curvature-driven flows. The second drawback is that fast marching methods require a "kickoff" procedure: as fast marching methods solve the Eikonal equation grid point by grid point, we require at least two grid points at the interface for which the correct value of φ is known to start off the process. Chopp (2001) presented a kickoff procedure which is designed to provide a signed-distance function in a h neighborhood of the interface. The method relies on a level set function with the sole property of $\varphi(\boldsymbol{x}) > 0$ outside of Γ and $\varphi(\boldsymbol{x}) < 0$ inside. The method then constructs bi/tricubic polynomials in each grid cell which is intersected by the interface (sign change in φ), and computes the distance of every grip point bounding this cell by finding the closest point on Γ using a Newton method.

This method produces layers of grid points $|\varphi(\boldsymbol{x}_i)| \leq h$ with correct signed-distance level set values with second-order accuracy. The method works efficiently in situations where the level set is well-resolved. If the level set is locally under-resolved the Newton method fails to converge and the method breaks down. Under-resolved situations will always arise whenever the interface undergoes topological changes, e.g., drop break-up. We therefore suggest to locally switch to a lower order approximation of the interface in this cases, e.g., from bi/tricubic to bi/trilinear. This switch will introduce the necessary numerical dissipation to regularize the problem.

An alternative to fast marching methods was introduced by Sussman et al. (1994), where the following PDE is solved to steady state:

$$\begin{aligned} \frac{\partial\varphi}{\partial\tau} &= S(\varphi_o)\,(1 - |\nabla\varphi|)\,, \\ \varphi(\boldsymbol{x}, \tau = 0) &= \boldsymbol{x}_o(\boldsymbol{x}), \end{aligned} \tag{11.33}$$

where $S(\varphi)$ is a h-mollified *sign* function. High-order solutions can be obtained by using a WENO scheme in conjunction with TVD RK integrators (Jiang and Peng 2000). Choosing WENO over ENO schemes results in smooth errors which

is desirable if we require to compute high-order derivatives of φ. These methods have the drawback that they are very expensive because (11.33) needs to be solved to steady state. As we shall see later (Section 5.2), the more grave drawback is that in general (11.33) perturbs the interface location. Remedies for the latter have been proposed (Sussman and Fatemi 1999), however, being costly, we have not implemented them in the course of our work.

In the context of particle level set methods Cottet and Maitre (2006) employ the following procedure to ascertain a signed-distance property: when the signed-distance to the zero level set is required, it is obtained by evaluating $\varphi(\boldsymbol{x})/|\nabla\varphi|$ in place of $\varphi(xv)$. Hence

$$\left|\frac{\varphi}{|\nabla\varphi|}\right| = \left|\frac{\nabla\varphi}{|\nabla\varphi|} - \frac{\varphi(\nabla\otimes\nabla\varphi)\nabla\varphi}{|\nabla\varphi|^3}\right|, \tag{11.34}$$

which is equal to 1 at $\varphi(\boldsymbol{x}) = 0$. An other way of expressing this idea is to Taylor expand φ around the interface as:

$$\varphi(\boldsymbol{x}) = \varphi(\boldsymbol{x}_\Gamma) \pm |\boldsymbol{x} - \boldsymbol{x}_\Gamma|\frac{\partial\varphi}{\partial n} + \mathcal{O}(|\boldsymbol{x} - \boldsymbol{x}_\Gamma|^2),$$

and thus

$$\left(\frac{\varphi}{|\nabla\varphi|}\right)(\boldsymbol{x}) = \pm|\boldsymbol{x} - \boldsymbol{x}_\Gamma| + \mathcal{O}(|\varphi|^2).$$

Above reinitialization technique is very simple and very efficient but only accurate very close to the interface (Hieber and Koumoutsakos 2005; Engquist et al. 2004).

As mentioned earlier, the PDE-based approach (11.33) is computationally expensive and if reinitialization is performed at every time step, its heavy use of WENO technology essentially challenges the use of particle methods in the first place, as the biggest part of the computational expense will be spent on reinitialization. Thus we may want to find a reinitialization scheme that inherits the Lagrangian efficiency for advection problems. Revisiting Sussman and Osher reinitialization:

$$\frac{\partial\varphi}{\partial\tau} + sign(\varphi_o)\,(|\nabla\varphi| - 1) = 0.$$

Replacing $|\nabla\varphi|$ by $|\nabla\varphi|^2$ we can rewrite this Hamilton-Jacobi form into

$$\frac{\partial\varphi}{\partial\tau} + \nabla\varphi\,(sign(\varphi_o)\nabla\varphi) = sign(\varphi_o).$$

This equation now consists of an advection and a "reaction" term, and the advection velocity is given as

$$\boldsymbol{u}_{\text{sussman}} = sign(\varphi_o)\nabla\varphi.$$

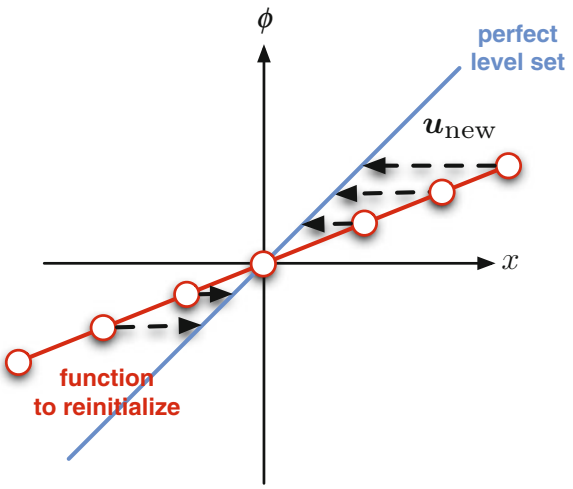

Fig. 11.2 Optimal choice for the reinitialization velocity for a level set function carried by particles

It is noteworthy that we can replace $sign(\varphi_o)$ by an arbitrary odd function, it could be φ for that matter. But in the context of Eulerian discretization of convection the sign choice appears to be the best. As illustrated in Fig. 11.2, there should be a choice for the "reinitialization velocity", that is more pertaining to the Lagrangian frame.

$$\frac{\partial \varphi}{\partial \tau} + \varphi \left(1 - |\nabla \varphi|^{-1}\right) |\nabla \varphi| = 0.$$

What is hidden in this Hamilton-Jacobi form is the following equivalent "advection" form:

$$\frac{\partial \varphi}{\partial \tau} + \left(\varphi - |\nabla \varphi|^{-1} \varphi\right) \boldsymbol{n} \cdot \nabla \varphi = 0.$$

There are no "reaction" terms in this formulation anymore, and the convection velocity is given as

$$\boldsymbol{u}_{\text{new}} = \left(\varphi - |\nabla \varphi|^{-1} \varphi\right) \boldsymbol{n}.$$

This formulation has not been tested yet, and while the accuracy of a WENO discretization may be higher, it may still serve as a good "preconditioner" for (11.33).

3.2 Reaction Diffusion Systems on Complex Stationary Geometries

Bertalmio et al. (2001) introduced a method to perform diffusion calculations on geometries that are represented by level sets in three dimensions. Xu and Zhao

(2003) and Adalsteinsson and Sethian (2003) later independently proposed a level set method for the transport of surface-bound substances on a deforming interface. Both works employed a nonconservative formulation based on level set interface capturing and showed results of passive advection of an interface with an associated surfactant.

A general reaction diffusion system for N_S species on a smooth surface $\Gamma \subset \Omega \subseteq \mathbb{R}^3$ can be written as,

$$\frac{\partial c_s}{\partial t} = F_s(\boldsymbol{c}) + \nabla_\Gamma \left(\underline{\underline{D}}_s \nabla_\Gamma c_s \right), \tag{11.35}$$

where $s = 1, 2, \ldots, N_S$ and $\boldsymbol{c} = (c_1, c_2, \ldots, c_{N_s})$; F_s represents the reaction terms for species s and $\underline{\underline{D}}_s$ denotes the diffusion tensor associated with species s. For simplicity of presentation we will only consider homogeneous isotropic diffusion in the following, i.e.,

$$\underline{\underline{D}}_s = D_s \, \mathbb{1}, \qquad s=1, 2, \ldots, N_S, \tag{11.36}$$

where D_s is a constant. Equation (11.35) then simplifies to

$$\frac{\partial c_s}{\partial t} = F_s(\boldsymbol{c}) + D_s \Delta_\Gamma c_s, \tag{11.37}$$

The operator Δ_Γ is called the Laplace-Beltrami operator on Γ.

We now consider a geometry that changes in time, i.e.,

$$\Gamma(t) = \{ \boldsymbol{x}_\Gamma(t) \}, \tag{11.38}$$

with

$$\frac{\mathrm{d}\boldsymbol{x}_\Gamma}{\mathrm{d}t} = \boldsymbol{u}_n(\boldsymbol{x}, \boldsymbol{c}, \Gamma). \tag{11.39}$$

Using (11.39) we rewrite (11.37) as

$$\frac{\partial c_s}{\partial t} + \nabla_\Gamma \cdot (c_s \, \boldsymbol{u}) = F_s(\boldsymbol{c}) + D_s \, \Delta_\Gamma c_s, \tag{11.40}$$

which can be rewritten as

$$\frac{\partial c_s}{\partial t} + \big((\mathbb{1} - \boldsymbol{n} \otimes \boldsymbol{n}) \, \nabla \big) (c \, \boldsymbol{u}) = F_s(\boldsymbol{c}) + D_s \nabla \cdot ((\mathbb{1} - \boldsymbol{n} \otimes \boldsymbol{n}) \nabla c_s), \tag{11.41}$$

see Stone (1990) for details of the derivation. In order to solve this problem with particle methods it is more suitable to write (11.41) as a conservation law:

$$\frac{\partial c_s}{\partial t} + \nabla \cdot (c_s \, \boldsymbol{u}) = (\boldsymbol{u} \cdot \boldsymbol{n}) \frac{\partial c_s}{\partial n} + c_s \, \boldsymbol{n} \otimes \boldsymbol{n} \nabla \boldsymbol{u} + F_s(\boldsymbol{c}) + D_s \nabla \cdot ((\mathbb{1} - \boldsymbol{n} \otimes \boldsymbol{n}) \nabla c_s). \tag{11.42}$$

The reformulation from (11.41) to (11.42) necessitates the extension of both c_s and $\boldsymbol{u}$ from Γ to Ω. The primary requirement on this extension is that it be differentiable. However, inspecting the first two terms on the right-hand side of (11.42), we realize that if we extend c_s and $\boldsymbol{u}$ such, that

$$\frac{\partial c_s}{\partial n} = 0, \text{ and } \frac{\partial (\boldsymbol{n} \cdot \boldsymbol{u})}{\partial n} = 0, \tag{11.43}$$

we can simplify (11.42) to

$$\frac{\partial c_s}{\partial t} + \nabla \cdot (c_s \, \boldsymbol{u}) = F_s(\boldsymbol{c}) + D_s \nabla \cdot \big((\mathbb{1} - \boldsymbol{n} \otimes \boldsymbol{n}) \nabla c_s \big). \tag{11.44}$$

In other words, ignoring the reaction terms, an extension satisfying (11.43), allows us to view a conservation law on a deforming geometry as a conservation law in the embedding space Ω.

Given that the surface itself is advanced by the level set equation (11.27), the particle discretization of (11.44) leads to the following system of ordinary differential equations:

$$\begin{aligned} \frac{\mathrm{d}\boldsymbol{x}_p}{\mathrm{d}t} &= \boldsymbol{u}(\boldsymbol{x}_p, t), \\ \frac{\mathrm{d}\boldsymbol{C}_p}{\mathrm{d}t} &= v_p \, \boldsymbol{F}(\boldsymbol{c}) + v_p \boldsymbol{D} \nabla^h \cdot \big((\mathbb{1} - \boldsymbol{n} \otimes \boldsymbol{n}) \nabla^h \boldsymbol{c} \big), \\ \frac{\mathrm{d}v_p}{\mathrm{d}t} &= v_p \, \nabla \cdot \boldsymbol{u}. \end{aligned} \tag{11.45}$$

As we are solving the conservation law formulation (11.44) we need to extend both the concentrations $\boldsymbol{c}$ and the velocities $\boldsymbol{u}$ off the interface Γ, requiring that this extension satisfies the requirements (11.43). As we are only interested in the concentrations on Γ it suffices to extend the quantities into a narrow band around the level set, which we define as

$$\Gamma_\mathrm{e} = \big\{ \boldsymbol{x} \;\big|\; |\varphi(\boldsymbol{x})| \leq \gamma \big\}, \tag{11.46}$$

where the narrow band thickness is chosen such that it is greater than the support of the P $\rightarrow$ M kernel employed. All calculations are restricted to this narrow band. We periodically extend the concentrations by solving the following PDEs (Chen et al. 1997; Peng et al. 1999):

$$\begin{aligned} \frac{\partial c_s}{\partial \tau} + sign(\varphi_o) \nabla \varphi \cdot \nabla c_s &= 0, \\ \frac{\partial uv}{\partial \tau} + sign(\varphi_o) \nabla \varphi \cdot \nabla \boldsymbol{u} &= 0, \end{aligned} \tag{11.47}$$

which leads to $\frac{\partial c_s}{\partial n} = 0$ and $\frac{\partial \boldsymbol{u}}{\partial n} = 0$.

3.3 Boundary Conditions on Complex Geometries

In order to be able to calculate transport problems within or around complex geometries, we need to be able to impose boundary conditions on them. In the context of particle methods, several approaches to handle boundary conditions on complex geometries have been introduced (see Ploumhans and Winckelmans 2000; Cottet and Koumoutsakos 2000). Most of these approaches have been devised for the primary application of particle methods at the time, the incompressible Navier-Stokes equations in vorticity form.

Recently, particle methods have been applied to simulation of diffusion processes in complex geometries (Sbalzarini et al. 2005). There a homogenous Neumann boundary condition was imposed on the diffusing function by using the method of images. The order of accuracy attainable with this approach has not been established in general (Ploumhans and Winckelmans 2000), and its application to complex 3D geometries is not straightforward.

An alternative approach is the Immersed Boundary Method as introduced by Peskin (1972). By extending the fluid to a rectangle containing the original domain and its interior, Peskin modeled the boundary conditions as singular forces exerted onto the fluid by the interface. Peskin's key idea was to model these forces by a mollified delta function, such that an appropriate amount of force is spread onto the grid points, thus also confining the corrections to computational elements in a narrow neighborhood of the immersed boundary. The drawbacks of Peskin's mollified delta approach are that it is limited to delta singularities (i.e., continuous solutions), and that it is of relatively low order in accuracy. For more detail we refer to the review of Mittal and Iaccarino (2005), and to Hieber (2007) for its application in the context of particle methods.

The immersed interface method was introduced by Leveque and Li (1994), as a method for solving elliptic equations with discontinuous coefficients or singular sources that are located on a possibly complex interface. Similar to the immersed boundary approach, the interface is "immersed" in a regular grid. In the immersed interface technique, finite difference stencils are modified if they intersect the boundary. The requirements on the geometry representation are therefore different from the immersed boundary method: while we require an explicit representation of the boundary with surface elements in the immersed boundary method, the immersed interface method needs information on the distance of grid points close to the boundary. Although we can envision a purely particle-based immersed boundary method, the immersed interface method relies on grid representations and its design pertains to hybrid particle-mesh methods only. For a thorough introduction to the immersed interface method we refer to the original article (Leveque and Li 1994), and to works inspired by it (Fedkiw et al. 1999; Wiegmann and Bube 2000).

In the following we will illustrate the concepts of the method by considering two simple examples. Assume we wish to evaluate

$$\frac{\mathrm{d}c_p}{\mathrm{d}t} = \left(\Delta^h c\right)(\boldsymbol{x}_p, t),$$

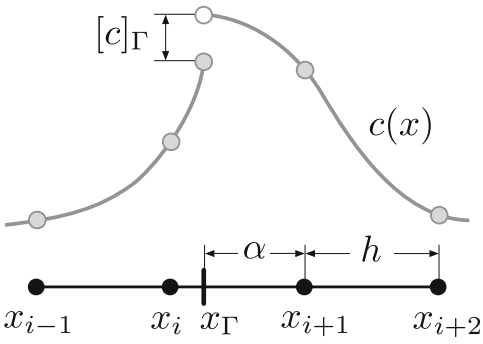

Fig. 11.3 A function c with a jump discontinuity at $x = x_\Gamma$

This involves three steps: P $\rightarrow$ M interpolation, the evaluation of $\Delta^h c$ on the grid, and the interpolation back onto particle locations, M $\rightarrow$ P. The evaluation of $\Delta^h c$ on the grid is done using finite differences, say a standard five-point stencil in 2D. Assume furthermore, that we need to satisfy a Dirichlet boundary condition or a jump condition on an immersed interface Γ represented by a level set function φ. As a five-point stencil only uses directly neighboring grid points, i.e., $\boldsymbol{i} \pm 1$, we can apply the standard stencil for all points $\boldsymbol{i}$ for which $|\varphi_{\boldsymbol{i}}| \geq h$. Stencils at points for which $|\varphi_{\boldsymbol{i}}| < h$ possibly intersect the interface and need to be corrected.

We will limit this exposition to two different cases:

$$c_\Gamma = g, \text{ and} \tag{11.48}$$

$$[c]_\Gamma = J, \tag{11.49}$$

i.e., a Dirichlet condition (11.48) and a jump condition (11.49) across the interface.

For the Dirichlet case we follow Chen et al. (1997): assume the interface intersects the stencil between $\boldsymbol{x}_{i,j}$ and $\boldsymbol{x}_{i+1,j}$. We can determine the intersection point up to second-order accuracy as

$$\alpha = \frac{\varphi_{i,j}}{\varphi_{i.j} - \varphi_{i+1,j}}.$$

Thus, the interface intersects $[\boldsymbol{x}_{i,j}, \boldsymbol{x}_{i+1,j}]$ at $\boldsymbol{x}_{i+\alpha,j}$. Now in order to find the second derivative in x-direction we can construct a second-order polynomial that interpolates $[c_{i-1}, c_i, g]$ at $[\boldsymbol{x}_{i-1,j}, \boldsymbol{x}_{i,j}, \boldsymbol{x}_{i+\alpha,j}]$ and take the second derivative of this polynomial. Other differential operators are adjusted accordingly.

For the case of a known jump discontinuity at Γ, we follow Mayo (1984) and consider a "jump corrected" Taylor expansion of $c(\boldsymbol{x}_{i+1,j})$ around $c(\boldsymbol{x}_{i,j})$ (see Fig. 11.3):

$$c_{i+1,j} = c_{i,j} + h\, c'_{i,j} + \frac{1}{2} h^2\, c''_{i,j} + [c]_\Gamma + (1-\alpha)\, h\, [c']_\Gamma + \frac{1}{2}(1-\alpha)^2\, h^2\, [c'']_\Gamma. \tag{11.50}$$

Let us assume that $[c']_\Gamma = [c'']_\Gamma = 0$. If we construct a standard three-point approximation of Δc at x_i we obtain:

$$\Delta^h c \equiv h^{-2} (c_{i-1} - 2\, c_i + c_{i+1}) = \Delta c + \mathcal{O}(h^2) + h^{-2} [c]_\Gamma, \tag{11.51}$$

and we make a $\mathcal{O}(h^{-2})$ mistake. We therefore need to correct the stencil as

$$\Delta^h_{\text{corr}} c \equiv h^{-2} (c_{i-1} - 2\, c_i + c_{i+1}) - h^{-2}\, J = \Delta\, c + \mathcal{O}(h^2). \tag{11.52}$$

In this way we can also solve Poisson problems with jump conditions using standard fast Poisson solvers (FACR, FFT, MG), because the jump corrections can be precomputed and added to the right-hand side of the Poisson equation (Mayo 1984; Leveque and Li 1994; Wiegmann 1999; Wiegmann and Bube 2000).

4 Reaction Diffusion Systems on Deforming Geometries

As the seminal work of Turing (1952) there have been many works that considered theoretical and computational aspects of pattern-forming reaction diffusion systems. These systems hinge on local autocatalysis and long-range inhibition. The review (Koch and Meinhardt 1994) considered the generation of stripe and spot patterns by activator-inhibitor and activator-substrate systems. Varea et al. (1999) considered a linearized Brusselator system on a sphere. The Schnakenberg system on a sphere has been considered by Chaplain et al. (2001), suggesting that prepattern theory may play a role in solid tumor growth by determination of the distribution of growth promoting factors on the tumor interface. On a different side Harrison and Kolar (1988), Holloway and Harrison (1999) coupled pattern forming reaction diffusion systems to growth algorithms in two dimensions to simulate algal growth. Later, these simulations were extended to three space dimensions in making use of a triangulated representation of the geometry (Harrison et al. 2001). The nodes of this triangulation are then moved according to the local concentration of a morphogen. However, the authors only considered short times and thus presented 3D results with small deformations.

Here we investigate these growth models by employing the conservative formulation of the conservation law for surface-bound reactants as derived in Section 3.2. As we wish to study reaction diffusion systems on deforming geometries, the governing equations are given by a conservation law with reaction terms on the surface Γ:

$$\frac{\partial c_s}{\partial t} = F_s(\boldsymbol{c}) + D_s\, \Delta_\Gamma c_s, \tag{11.53}$$

for chemical species $s = 1, \ldots, N_s$. The surface itself deforms with a prescribed velocity $\boldsymbol{u}(\boldsymbol{x}, t)$, as

$$\frac{\mathrm{d}\boldsymbol{x}_\Gamma}{\mathrm{d}t} = \boldsymbol{u}(\boldsymbol{x}, t).$$

The discretization of (11.53) using particles results in the following system of ODEs:

$$\frac{\partial c_s}{\partial t} + \nabla \cdot (c_s \boldsymbol{u}) = F_s(\boldsymbol{c}) + \nabla \cdot \left((\mathbb{1} - \boldsymbol{n} \otimes \boldsymbol{n}) \nabla c_s\right),$$
$$\frac{\partial \varphi}{\partial t} + \boldsymbol{u} \cdot \nabla \varphi = 0.$$

After discretization with hybrid particle-mesh methods, these yield the following set of ODEs:

$$\begin{aligned}
\frac{\mathrm{d}\boldsymbol{x}_p}{\mathrm{d}t} &= \boldsymbol{u}(\boldsymbol{x}_p, t), \\
\frac{\mathrm{d}\boldsymbol{C}_p}{\mathrm{d}t} &= v_p \boldsymbol{F}(\boldsymbol{c}) + v_p \boldsymbol{D} \nabla^h \cdot \left((\mathbb{1} - \boldsymbol{n} \otimes \boldsymbol{n}) \nabla^h \boldsymbol{c}\right), \\
\frac{\mathrm{d}v_p}{\mathrm{d}t} &= v_p \nabla \cdot \boldsymbol{u}, \\
\frac{\mathrm{d}\varphi_p}{\mathrm{d}t} &= 0.
\end{aligned} \tag{11.54}$$

The reactions that we consider here are a Brusselator and the Koch-Meinhardt activator-substrate system (Koch and Meinhardt 1994). We use a linearized version of the Brusselator (Varea et al. 1999); the concentrations have to be understood as departures from the steady state:

$$\begin{aligned}
\frac{\partial c_1}{\partial t} &= \alpha\, c_1\, (1 - r_1\, {c_2}^2) - c_2\, (1 - r_2\, c_1) + D_1\, \Delta\, c_1, \\
\frac{\partial c_2}{\partial t} &= \beta\, c_2 \left(1 + \frac{\alpha\, r_1}{\beta}\, c_1\, c_2\right) + c_1\, (\gamma - r_2\, c_2) + D_2\, \Delta\, c_2.
\end{aligned} \tag{11.55}$$

The activator-substrate system is given by:

$$\begin{aligned}
\frac{\partial c_1}{\partial t} &= \rho_1 \frac{{c_1}^2\, c_2}{1 + \kappa\, {c_1}^2} - \mu_1\, c_1 + \sigma_1 + D_1\, \Delta_\Gamma\, c_1, \\
\frac{\partial c_2}{\partial t} &= -\rho_2 \frac{{c_1}^2\, c_2}{1 + \kappa\, {c_1}^2} + \sigma_2 + D_2\, \Delta_\Gamma\, c_2.
\end{aligned} \tag{11.56}$$

Simulation results of the system are reported in Fig. 11.4. The anisotropic differential operator in the right-hand side of the equation for the particle weights in (11.54) is discretized using second-order finite differences and second-order approximations of the diffusion tensor, resulting in a $3 \times 3 \times 3$ stencil. The minimal narrow band thickness is, thus, $\gamma = 2\,h$. For our calculations we used $\gamma = 4\,h$, so that the extension (11.47), which is used to enforce $\frac{\partial \boldsymbol{c}}{\partial \boldsymbol{n}} = 0$ and $\frac{\partial \boldsymbol{u}}{\partial \boldsymbol{n}} = 0$, was only performed every third time step. For the results presented herein we used the explicit Euler time integrator, unless stated otherwise.

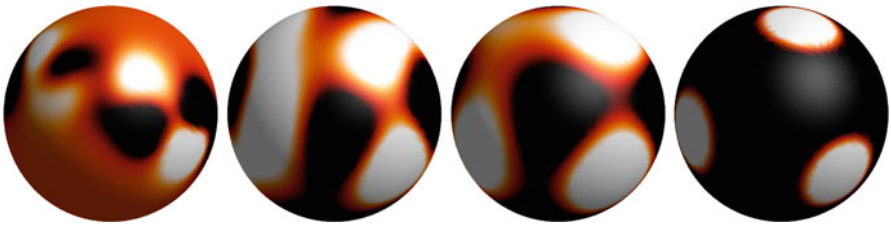

Fig. 11.4 Simulation of the reaction diffusion system (11.55). From *left to right*: distribution of c_1 after iterations 1,000, 10,000, 100,000 and 200,000

4.1 Diffusion on a Sphere

In order to assess the accuracy of the present calculations we perform simulations of diffusion (i.e., $\boldsymbol{F} \equiv 0$, and $\boldsymbol{u} \equiv 0$) on the unit sphere. We consider one species, i.e.,

$$\frac{\partial c}{\partial t} = \Delta_\Gamma c, \tag{11.57}$$

with initial conditions

$$c(\theta, \phi, t = 0) = Y_1^0(\theta, \phi), \tag{11.58}$$

where Y_1^0 is the $(1, 0)$ spherical harmonic. The exact solution is given by:

$$c(\theta, \phi, t) = \mathrm{e}^{-2t}\, Y_1^0(\theta, \phi). \tag{11.59}$$

For the time stepping we employ a TVD RK2 scheme (Shu and Osher 1989) to obtain solutions, which converge with second-order accuracy.

4.2 Growth

In order to assess the accuracy of the presented method in the case of deforming geometries we considered a case without either reaction or diffusion. We initialize a concentration c on the sphere and let the sphere grow with velocity $\boldsymbol{u} = \boldsymbol{n}$. The exact solution for this case is given by a simple rescaling of the initial condition, i.e.,

$$c(\boldsymbol{x}, t) = \left(\frac{R}{|\boldsymbol{x}(t)|}\right)^2 c(\boldsymbol{x}/|\boldsymbol{x}|, 0).$$

The initial condition is again chosen as (11.58). Figure 11.5 displays convergence measurements for this case.

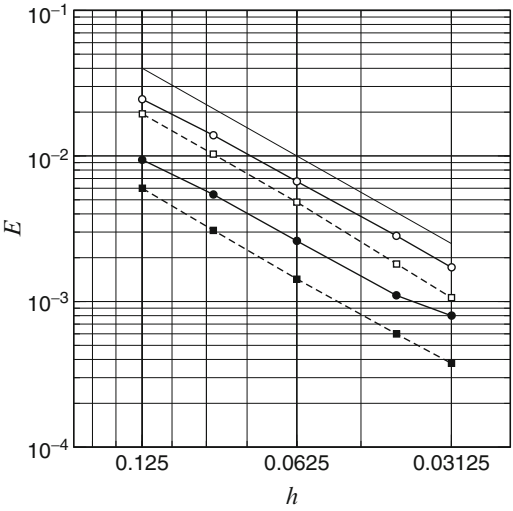

Fig. 11.5 Refinement study for growth only: L_2 and L_∞ error at time $t = 0.4$. Error of concentration – *solid line* with *black circles* (L_2), and *white circles* (L_∞), respectively, and error of the interface location – *dashed line* with *black squares* (L_2), and *white squares* (L_∞), respectively

4.3 Reaction/Diffusion Systems on a Sphere

For the linearized Brusselator (11.55) we use the parameters proposed in Varea et al. (1999): $r_1 = 0.02$, and $r_2 = 0.2$, $D_1 = 0.088$, $D_2 = 0.516$, $\alpha = 0.899$, and $\beta = -0.91$. The initial condition is given by $c_1 = c_2 = 0$ and a uniformly random distribution $[-0.5, 0.5]$ of c_1 and c_2 on a band of width 0.2 centered on the equator. The same six-spot pattern as in the reference (Varea et al. 1999) are obtained. We depict the evolution of the maxima of c_1 and c_2 in Fig. 11.6. After the pattern goes through an initial oscillatory stage in the beginning, the system converges to a stable steady state after 150,000 steps.

The next system we consider is the activator-substrate system (11.56), for which we perform two different parameter sets, $\sigma_1 = 0.0$, $\sigma_2 = 0.02$, $\rho_1 = 0.01$, $\rho_2 = 0.02$, $\mu_1 = 0.01$, $\mu_2 = 0.0$, and $\kappa = 0$ and $\kappa = 0.25$, respectively. The initial condition of the simulation is given as 10% random perturbations from the steady state solution. This parameter choices lead to the evolution of spot patterns and stripe patterns, respectively, on a square lattice in Koch and Meinhardt (1994). We observe similar patterning on the sphere $R = 0.3$. The results are shown in Fig. 11.7 (stripes, $\kappa = 0.25$) and Bergdorf et al. (2010).

Figure 11.8 illustrates that the method can also be applied to more complex geometries.

Reaction Diffusion and Growth We now couple the deformation of the geometry to the reaction diffusion system by calculating the local velocity as:

$$\boldsymbol{u} = \boldsymbol{n}\, c_1. \tag{11.60}$$

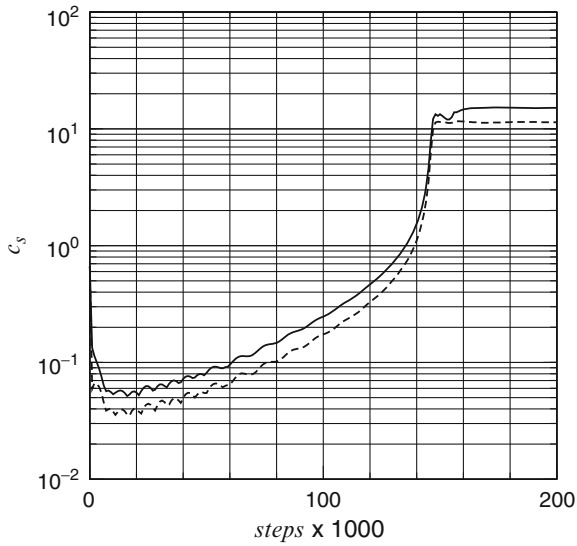

Fig. 11.6 Evolution of the maximum of $|c_1|$ (*solid line*), and $|c_2|$ respectively, for the spot pattern forming system (11.55). The plot illustrates the stiffness of the system and an initial oscillatory phase is apparent during the first 80,000 steps

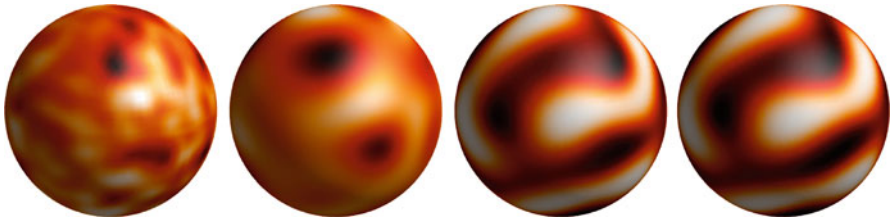

Fig. 11.7 Simulation of the reaction diffusion system (11.56) with $\kappa = 0.25$. From *left to right*: distribution of c_1 after iterations 1,000, 10,000, 40,000 and 140,000

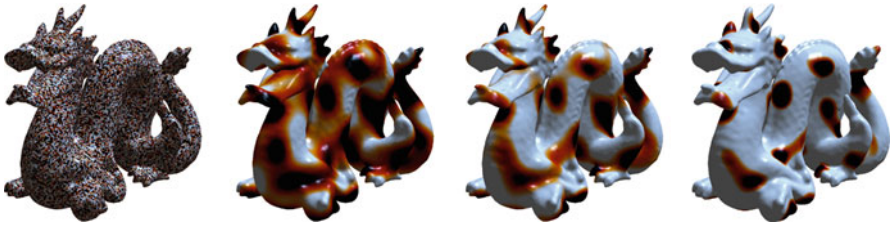

Fig. 11.8 Spot pattern generated by (11.56): iterations 0, 75,000, 150,000, and 290,000

As $c_1 \geq 0$ this will always result in an outward motion of the geometry, and thus it will lead to an increase in surface area. This increase of surface area corresponds to lowering the effective diffusion constants in the reaction diffusion system, as the reactions are generally not dependent on the surface properties; the only direct effect

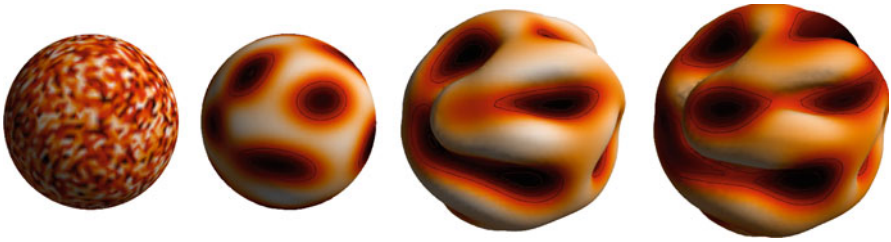

Fig. 11.9 Growth of the stripe pattern of system (11.56). Iterations 0, 50,000, 127,000 and 150,000

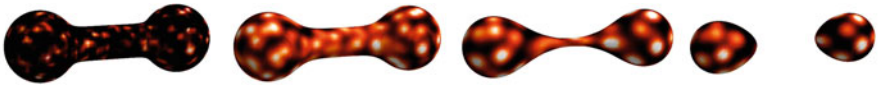

Fig. 11.10 Spot pattern generated by solving (11.56) on a dumbbell shrinking under mean curvature flow

that growth has on the reactions is the decrease of the concentration in the sense of a decay term that depends on the growth velocity. In the next section we will consider a growth model, where reactant concentration and surface deformation are more tightly coupled. Figure 11.9 depict the evolution of these coupled simulations (See also Bergdorf et al. 2010). Figure 11.10 illustrates the robustness of the proposed method with respect to large changes in the morphology.

5 Avascular Tumor Growth

Ever since mathematical modeling has entered the realms of biology and medicine, cancer has been one of the main application domains. If we could predict the evolution of a cancer computationally, this could assist on the understanding of the disease, improve diagnosis, and enable the assessment of new treatments. The biophysical processes at the core of cancer tumor growth are gradually being identified and understood. Here, we model cancer tumor growth, by considering the interplay of a strongly reduced set of such processes. However simple, the framework we put together may serve as a foundation for model studies and refinement.

The model considered herein follows up on the work of Macklin and Lowengrub (2005), and Cristini and Lowengrub (2003). The model is based on a continuum description of a sharp interface that separates cancerous tissue from healthy tissue. The tumor tissue is modeled as an incompressible fluid. All biophysical processes considered here are modeled as continuum phenomena, e.g., cell–cell adhesion is represented as surface tension acting at the tumor boundary, proliferation is modeled as a mass source within the tumor interface. All cells require nutrients for cell viability and reproduction. Here we will only consider one nonspecific

nutrient, which reaches the tumor by diffusion. Depending on the local nutrient concentration within the tumor, cells will die (necrosis), remain quiescent or multiply (proliferation); this situation is reflected by different source or sink terms in the mass balance.

The novelty presented in this work are the extension of a 2D simulation (Macklin and Lowengrub 2005) to a 3D particle simulation, we modify the formulation to allow the application of fast Poisson solvers, which enables large-scale, extended-time, and parallel simulations. Furthermore, by using far-field boundary conditions for the pressure we are able to assess effects of the tumor environment.

5.1 Computational Model

Cells require nutrient supply for cell viability and proliferation. In our model we consider one nutrient, which diffuses from the healthy-tissue region into the tumor and is consumed there. If the nutrient concentration within the tumor interface is sufficient, i.e., greater than a given threshold, tumor cells proliferate which is expressed as mass gain. This mass gain induces a pressure which causes the tumor to grow. However, if the concentration of the nutrient locally drops below a critical level necessary for cell viability, cell necrosis is induced. This is represented by mass loss. In this model, the tumor surface is approximated through a sharp interface separating the cancerous cells from the healthy tissue, dividing the domain into two distinctive regions. The interface is implicitly represented by a level set function.

In the following, (11.61) describes the reaction diffusion system for the nondimensionalized concentration c of the nutrient. If the concentration drops below the critical value N necessary for cell viability, a necrotic core of dead cancer cells is formed. We denote this region by $\Omega_N = \{\boldsymbol{x} \mid c(\boldsymbol{x}) < N\}$ and its boundary by Γ_N. The solution of equation (11.61) is solely dependent on the position of the interface Γ of the living cancer cells and can be calculated without knowing the position of the necrotic core.

The concentration satisfies

$$\begin{aligned} \frac{\partial c}{\partial t} &= \nabla^2 c - c \text{in } \Omega, \\ c|_\Gamma &= 1, \\ c &= 1 \text{ outside } \Omega. \end{aligned} \tag{11.61}$$

The boundary condition $c|_\Gamma = 1$ reflects that the healthy tissue is considered to be an infinite reservoir of nutrient.

5.1.1 Proliferation

As cells proliferate in the tumor, mass is created, and as the tumor is modeled as an incompressible fluid, this added mass leads to a pressure. This nondimensionalized pressure p, depends on the solution of the concentration equation, the curvature κ at the interface Γ, a surface tension coefficient γ and the parameters A, measuring the rate of apoptosis ("preprogrammed" cell death), G, related to the rate of mitosis (cell proliferation), G_N, which measures the rate of volume loss due to necrosis (cell degradation) and N.

The pressure satisfies

$$\begin{aligned} \nabla^2 p &= \begin{cases} -G(c-A) & \text{in } \Omega \text{ if } c \geq N, \\ G G_N & \text{in } \Omega \text{ if } c < N, \end{cases} \\ [p]\,|_\Gamma &= \gamma\,\kappa, \\ \nabla^2 p &= 0 \text{ outside } \Omega. \end{aligned} \tag{11.62}$$

The pressure equation (11.62), poses two difficulties to a numerical solver. First, there is a jump at Γ which has to be taken into account and second, we have to provide boundary conditions for the solver.

The interface Γ is moved by an outward normal velocity given by Darcy's law

$$U|_\Gamma = -\boldsymbol{n} \cdot \nabla p\,|_\Gamma = -\frac{\partial p}{\partial n}\,|_\Gamma, \tag{11.63}$$

where ∇p is the pressure gradient on Γ.

5.2 *Method Outline*

We initialize a level set function φ to define the interface Γ of the tumor. The method follows Algorithm 1.

5.2.1 Discretization

Normal Vector and Curvature The interface normal is given in terms of the level set function as:

$$\boldsymbol{n} = \nabla \varphi, \tag{11.64}$$

and the curvature as:

$$\kappa = \nabla \cdot \boldsymbol{n}. \tag{11.65}$$

Algorithm 1 Algorithm for tumor growth

```
initialize level set φ
for t = 0 to T do
    Reinitialize the level set φ.
    Create particles carrying φ in 𝒟
    Calculate n and κ in a narrow band around interface Γ.
    Solve the reaction diffusion system for the concentration c in Ω.
    Solve the Poisson equation for the pressure p in 𝒟.
    Calculate U.
    Convect the particles.
    t = t + δt.
    Re mesh the particles onto the grid.
end for
```

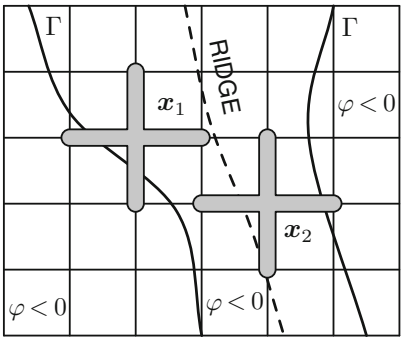

Fig. 11.11 Ridges (*dashed line*) form when two interfaces are close to each other (*solid lines*). The first derivatives of the level set function are not defined on that ridge, and a straight forward application of second-order centered differences at $\boldsymbol{x}_2$ will lead to inaccurate normals and curvature

To compute these surface properties, we interpolate the level set values from the particles onto the grid, where we employ finite-difference approximations of the differential operators in (11.64) and (11.65). The second-order approximations for the derivatives u_x and u_{xx} are computed as:

$$u_x = \frac{1}{2h}\left(u_{i+1} - u_{i-1}\right) + O\left(h^2\right), \tag{11.66}$$

and

$$u_{xx} = \frac{1}{h^2}\left(u_{i-1} - 2u_i + u_{i+1}\right) + O\left(h^2\right). \tag{11.67}$$

With this method, problems arise when two interfaces are close to each other and the derivatives of the level set function are calculated across ridges as illustrated in Fig. 11.11. In order to address this problem, we apply a Weighted Essentially Non-Oscillatory (WENO) Scheme (Jiang and Peng 2000). The WENO detects these ridges as great values in the second derivatives of the level set function around the particle of interest and then approximates the derivatives using a weighted sum of one sided finite differences.

5.2.2 Pressure with Jump Corrections

In our case, where we apply a Poisson solver using finite differences to solve the pressure equations, we have to consider this correction term when constructing the right-hand side. For the pressure, we only have a known jump in the function across the interface. This term is call the Laplace-Young jump condition and is given by:

$$[p]_\Gamma = \gamma\,\kappa,$$

where γ is the constant surface tension coefficient and κ is the local curvature. As the jump is located at Γ, a correction term has to be applied to grid points adjacent to the interface (see (11.52) in Section 3.3). In the present case, the curvature κ is interpolated onto the interface and the term $\frac{\gamma\cdot\kappa}{h^2}$ is subtracted, respectively, added to the right-hand side depending on whether the grid point lies inside or outside Ω.

Boundary Conditions The problem of posing boundary conditions for the pressure equation can be addressed in different ways. If we solve the equation (11.62) in $\mathscr{D}$ with periodic boundary conditions, the tumor is exposed to its own pressure extended across the periodic domain boundaries. The resulting effect is that instead of simulating growth of one tumor into soft tissue, we simulate the growth of many tumors, each influencing its periodic neighbors, thus constraining and corrupting its expansion. In order to reduce the pressure contribution across the boundaries, one could choose $\mathscr{D}$ far bigger than Ω. In a three-dimensional setting, however, the increase in computational time and memory to solve this larger system renders this method impractical. We discuss here two approaches in order to overcome this problem. First, we modified equation (11.62) to $p = 0$ outside Ω and used a GMRES solver (Frayssé et al. 1997) to calculate a correction to the right-hand side, which enforces this condition. We find that this method interferes with the jump correction at the interface. In a second approach, we use a far field solver to solve the pressure equation without jump for particles located on the domain boundary. We then take the solution at these locations as Dirichlet boundary conditions for a finite differences-based Poisson solver and solve the system for all particles in $\mathscr{D}$. In a first variant of this method, we used a Fast Multipole Method solver (Greengard and Rokhlin 1987) to calculate the pressure on the domain boundary, but the solver was far too computationally expensive to satisfy our needs. Finally, an FFT-based approach (Hockney and Eastwood 1988) provided a solution to solve the equation for particles at domain boundary location faster. The advantage of this modification is that we can ensure a free space boundary condition, so that the simulations are independent of the size of the computational domain.

5.2.3 Growth Speed

In order to evaluate equation (11.63), we interpolate ∇p onto Γ, calculate the velocity at the interpolation points and then extend it into $\mathscr{D}$ using the

Hamilton-Jacobi-based extension method (Jiang and Peng 2000; Sussman et al. 1994). In order to attenuate the effect of high-frequency errors in the pressure and curvature approximations on the velocity, a Gauss filter is applied to the velocity as proposed in Macklin and Lowengrub (2005). The 1D form of this filter reads:

$$\hat{U}_I = \frac{1}{S}\frac{1}{M\sqrt{2\pi}}\sum_{i=-3M}^{3M} U_{I-i}\exp\left(-\frac{1}{2}\left(\frac{i}{M}\right)^2\right), \tag{11.68}$$

where S is an appropriately chosen normalization constant and $M = \frac{h}{\sigma}$ where σ is the standard deviation of the filter. In order to save computational time, only particles in a narrow band around the interface are moved. This narrow band demands the application of mollification to the velocity, such that the movement of the particles at the outer region of the narrow band does not abruptly stop, but is gradually reduced. The mollification kernel is calculated as follows:

$$\eta(\boldsymbol{x}) = \begin{cases} 1 & \text{if } \varphi(x) < \beta, \\ (|\varphi(x)| - \gamma)^2 \dfrac{2|\varphi(x)| + \gamma - 3\beta}{(\gamma-\beta)^3} & \text{if } \beta \le \varphi(x) \le \gamma, \\ 0 & \text{if } \varphi(x) > \gamma, \end{cases} \tag{11.69}$$

with the variables γ and β denoting the distances to the interface in between which the mollification is applied. The velocity at particle locations can then be calculated as:

$$\bar{U}(x) = \eta(x)\hat{U}(x). \tag{11.70}$$

5.2.4 Reinitialization

Reinitialization is the process of reinitializing the level set function at particle locations, so that the signed-distance property is restored. As only particles in the proximity of the interface are moved, the level set function carried by particles farther away from the interface has to be recalculated after every convection. In order to reinitialize, we considered two methods. The Group Marching Method (GMM) (Kim 2001) and a PDE-based approach by Jiang and Peng (2000), Sussman et al. (1994), from now on referred to as HAMJAC. We find that, at least in the context of the present particle framework, both of these methods do not accurately reinitialize the level set function.

Computational Details In order to capture the effects of the reinitialization methods on the level set, an initial level set of a sphere is iteratively reinitialized without being moved. Under these conditions, the GMM method does not change the level set, whereas the HAMJAC gradually shrinks the initial level set until it disappears after approximately 1,300 iterations as is illustrated in Fig. 11.12. In terms of speed the GMM method outperforms the HAMJAC method. In order

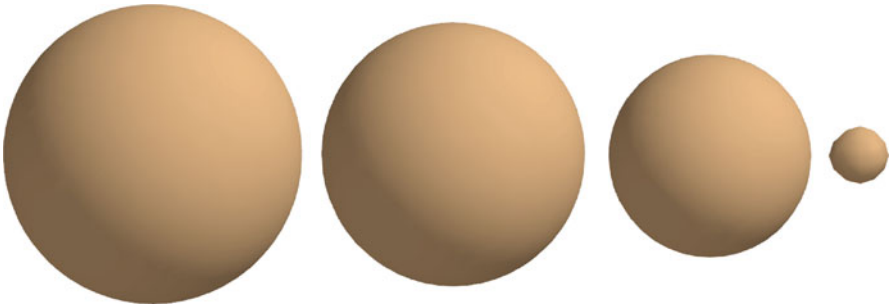

Fig. 11.12 Reinitialization HAMJAC: The figure shows how repeated reinitialization with HAMJAC shrinks the interface. Snapshots are taken at the initial stage, after 500,1000 and 1300 iterations

to reinitialize a sphere with radius $r = 2$ and particle spacing $h = 0.185$ it takes the GMM method 0.48 seconds where the HAMJAC method needs 0.75 seconds. In terms of robustness however, the GMM fails in some cases where the interface exhibits large curvature variations, because the kickoff procedure fails (Bergdorf 2007). In such simulations (Bergdorf 2007) spurious geometries emerge and destroy the level set which causes the simulation to break down. With the HAMJAC method, throughout all the simulations, we have never experienced such deformations of the level set, which may be attributed to the diffusive properties of this method. In order to assess the accuracy of the Poisson solver, we will later use the GMM method, but to grow tumors in 3D, the HAMJAC method will be applied to circumvent the emergence of spurious geometries.

In order to save computational time and memory, we define a narrow band around the interface of the tumor. Curvature and velocity have only to be defined inside this narrow band in the proximity of the level set and only particles within the narrow band will be moved. After one time step, the level set value at particles outside the narrow band will not be correct anymore and has to be reinitialized. The motion of the interface is indirectly a function of the curvature. This coupling heads to a stiff system as described in Hou (1994). Although the stiffness is mollified by the speed-filtering described earlier, it still necessitates a CFL-type Euler step constraint. All simulations are run with CFL $= 0.25$.

5.3 Validation

For validation, we have considered the following tests. The first validation case is the growth of a sphere determined by surface tension dynamics. The second validation case is the evolution of an ellipsoid determined by surface tension dynamics. In a third scenario, we try to reproduce the 2D results from Macklin for the full method and an initial condition of a stretched circle.

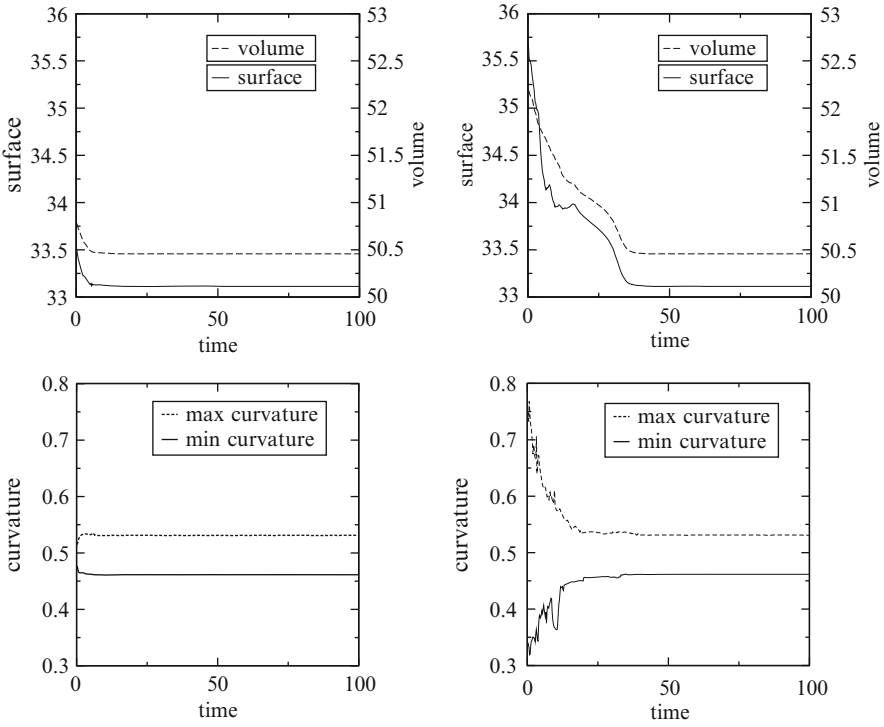

Fig. 11.13 On the *left*, we see the volume/surface and the min/max curvature plots for the evolution of a sphere under surface tension dynamics. On the *right side*, we see the same plots in the case of a *stretched sphere*. One can see how the *stretched circle* evolves back to its original shape with the same volume and surface values as for the sphere

5.3.1 Evolution Under Surface Tension Dynamics

For both scenarios, we define the domain as a cube of volume 12^3 and initialize 65^3 particles throughout the whole domain. This leads to a grid spacing of $h = 0.1875$. The pressure is set to $\nabla^2 p = 0$ in Ω and Ω_0 and $\gamma = 1$. In order to evaluate our results, we capture the interface determined by the level set function together with the minimum and maximum of the curvature on the interface, the surface, and the volume of the sphere at discrete time steps.

Evolution of a Sphere For the evolution of a sphere, the exact solution is given by $r(t) = r_0$, with r_0 being the initial radius of the sphere. We initiate a sphere with radius $r = 2$ at the center of the domain, giving us an initial surface $S = 50.27$ and volume $V = 33.51$. The initial curvature for this scenario is $\kappa = 0.5$. Comparing these numbers to the results in Fig. 11.13, we see that the initial values measured for surface $\hat{S}_0 = 50.50$ and volume $\hat{V}_0 = 33.78$ drop over the first 10 time steps but then stabilize at $\hat{S}_{100} = 50.11$ and $\hat{V}_{100} = 33.45$. The high starting values are due

to the fact that the numerical approximations to the volume and surface for convex shapes are biased. Min and max curvature stabilize around the value of the expected curvature. As Fig. 11.13 shows, the minimum and maximum of the curvature do not converge to the same value, indicating that from a curvature point of view, our level set function does not describe a perfect sphere. On the other hand, as the volume and the surface stabilize under surface tension dynamics, the simulation indicates that the level set describes a perfect sphere from a pressure point of view. This could explain the initial drop in the surface and volume, as the initiated level set is not considered a sphere by the pressure. In order to overcome these differences, the numerical approximations of pressure and curvature should be coordinated.

Evolution of an Ellipsoid As initial condition, we stretch a sphere of radius $r = 2$ located at the origin by a factor $\epsilon = 0.3$, giving us an initial level set defined by:

$$\varphi(\boldsymbol{x}) = \sqrt{(x_1(1+\epsilon))^2 + x_2^2 + (x_3(1-\epsilon))^2} - r. \tag{11.71}$$

As the interface evolves, the stretched circle grows back to its original shape, taking on the same values as measured for the sphere.

5.3.2 Comparison to Macklin and Lowengrub (2005)

In order to compare our solution to the 2D scenario described in Macklin and Lowengrub (2005), we initialize our level set as a stretched cylinder of radius $r = 2$ located at the origin, stretched by a factor $\epsilon = 0.1$:

$$\varphi(x) = \sqrt{(x_1(1+\epsilon))^2 + (x_3(1-\epsilon))^2} - r, \tag{11.72}$$

and consider the cross section. As the boundary conditions have to be periodic in the axis of the cylinder, we cannot solve the pressure equation with the same boundary conditions we use for the normal 3D case. Instead we solve the pressure equation with periodic boundary conditions. In order to reduce the contribution of the pressure across the periodic boundary, we set the computational domain very large (24^3) compared to the diameter of the cylinder. We set $\gamma = 1$ and the parameters determining tumor growth to: $A = 0.5$, $G = 20$, and $N = 0$. The simulation is run twice, once with the GMM and once with the HAMJAC method for reinitialization. The results are illustrated in Fig. 11.15 and Fig. 11.16.

As the figures show, the interfaces evolving under GMM reinitialization resemble the ones presented in (Macklin and Lowengrub, 2005), shown in Fig. 11.14 much better than the ones evolving under HAMJAC reinitialization. The case suggests that simulation with HAMJAC generates more excrescences causing the tumor to gain volume faster than under GMM reinitialization. Pictures of the interface at later times under GMM reinitialization could not be generated, because also in this simulation the GMM method destroyed the level set short after $t = 4$. Therefore, we cannot make further quantitative comparisons.

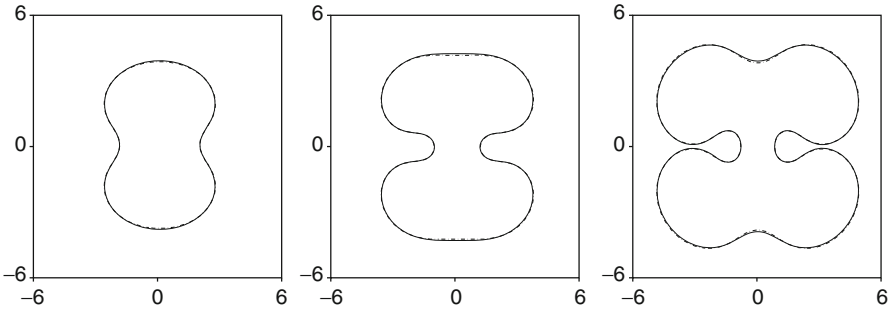

Fig. 11.14 Tumor growth in 2D with ellipse initial condition as shown in Macklin and Lowengrub (2005). Cross sections are cut at time $t = 1.5, 2$, and 2.5

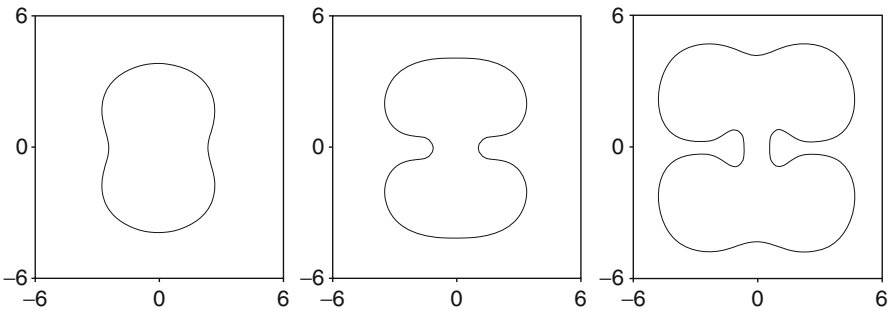

Fig. 11.15 Tumor growth with cylinder initial condition, reinitialized with GMM. Cross sections are cut at time $t = 2, 3$, and 4

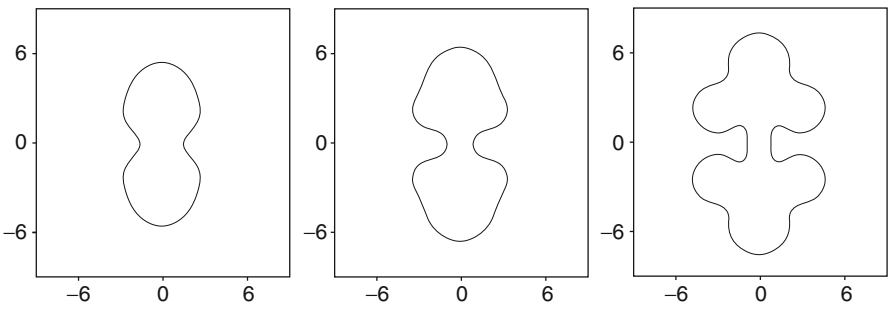

Fig. 11.16 Tumor growth with cylinder initial condition, reinitialized with HAMJAC. Cross sections are cut at time $t = 3, 4$, and 5

5.4 Results

In the following, we will investigate the influence of various factors on tumor growth. Parameters of interest are the size of the domain, the resolution, the necrosis, the surface tension, and the initial condition.

5.4.1 Tumor Growth Without Necrosis

In a first simulation, we initiate an ellipsoid as defined in equation (11.71) with $\epsilon = 0.1$. Further parameters are set to: $A = 0.5$, $G = 20$, $N = 0$, and $\gamma = 1$. The domain is set to a cube of size 24^3 and 129^3 particles are initiated throughout the whole domain. In Fig. 11.17, the interface together with a cross section of the concentration are illustrated at successive time steps. The pressure is mapped onto the interface of the tumor. The figure shows how the tumor grows over a time span of $\delta t = 7$. As healthy tissue is representing an infinite resource of nutrient, the tumor constantly grows and never reaches a steady state or shrinks. We cannot observe approaching interfaces to join, therefore no healthy tissue is completely enclosed by the tumor. Velocity filtering and the pressure approaching interfaces apply on each other prevent the interfaces from closing the gap in between.

In order to examine the effects of the domain size, the initial condition and the parameters are set to the same values as in the previous simulation. One tumor is grown in a cube of size 24^3, the other in a cube of size 48^3. As illustrated in Fig. 11.18, the interfaces evolve the same, even in regions close to the domain boundary. Is the simulation carried on, the tumor in the smaller domain crosses the domain boundary and does not grow according to the tumor in the larger domain. The simulation shows the independence of our pressure solver from the domain size, until the narrow band surrounding the tumor reaches the domain boundary.

In order to illustrate the effects of resolution, we compare three runs in a cubic domain of size 24^3. The initial conditions and parameters are the same as in the previous simulations, the number of particles are set to 65^3, 129^3, and 257^3 leading to grid spacings of size $h = 0.3692, h = 0.1875$, and $h = 0.0938$. Figure 11.19 shows the interfaces for the three simulations at time $t = 4$. As suggested by the figure, the method is very vulnerable to small variations in the level set, here inflicted by the change in resolution. Whether the method converges to a stable simulation under higher resolution cannot be said at this point of time, as the computational costs and memory for higher resolutions increase cubically. However, Fig. 11.15 suggests that the HAMJAC reinitialization method could be the reason for this sensitivity to the level set, as it seems to be the driving force for bumps on the interface. Unfortunately, the case shows that the simulations are determined by the resolution and not representative for the underlying model, prohibiting qualitative, and quantitative statements.

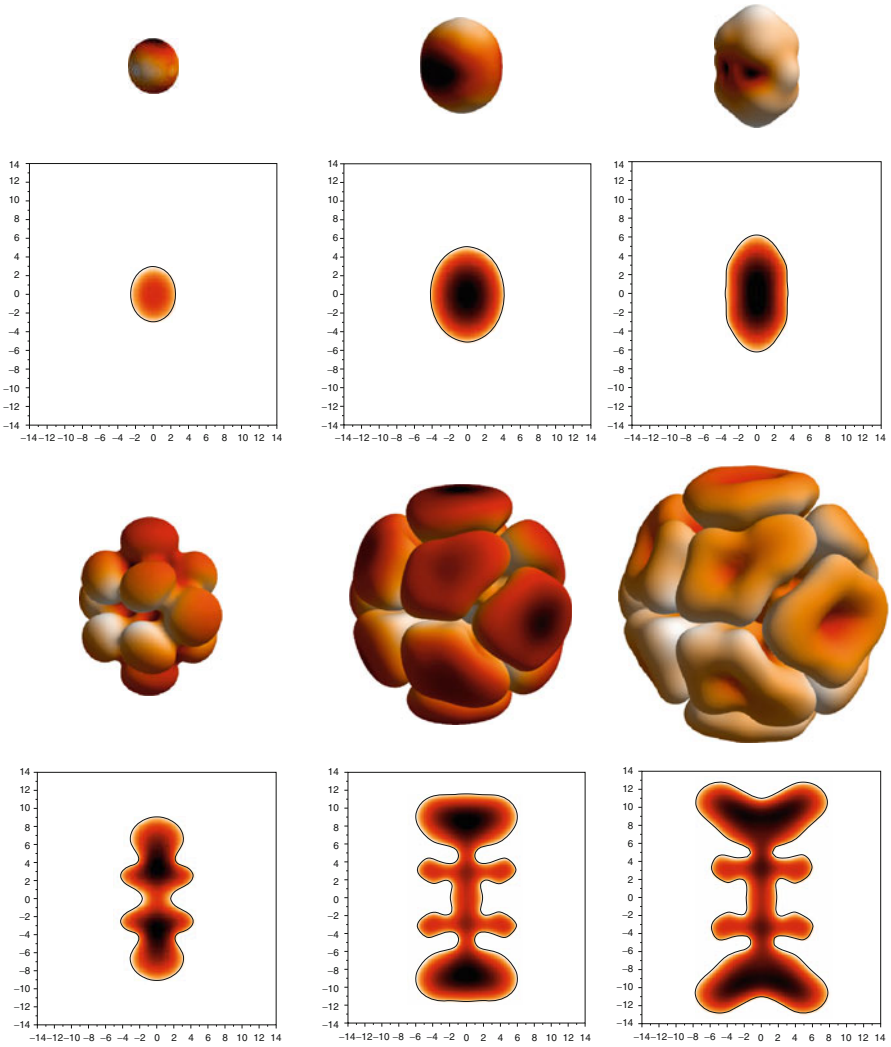

Fig. 11.17 Tumor growth with ellipsoid initial condition. The *color* on the surface indicates the pressure conditions at the interface. Together with the level set, the nutrient concentration throughout the whole domain is shown. Pictures are taken at $t = 0, 1.5, 3, 4.5, 6$, and 7

5.4.2 Effects of Necrosis

In order to capture the effects of necrosis, we run simulations under variation of the parameter N. The initial condition is again the ellipsoid as defined in (11.71) with $\epsilon = 0.1$. The domain is set to a cube of size 24^3, 129^3 particles are initiated equally distributed throughout the whole domain. The parameters determining tumor growth are set to: $A = 0.5$, $G = 20$, and $G_N = 1$ and γ is set to 1. N takes on the values

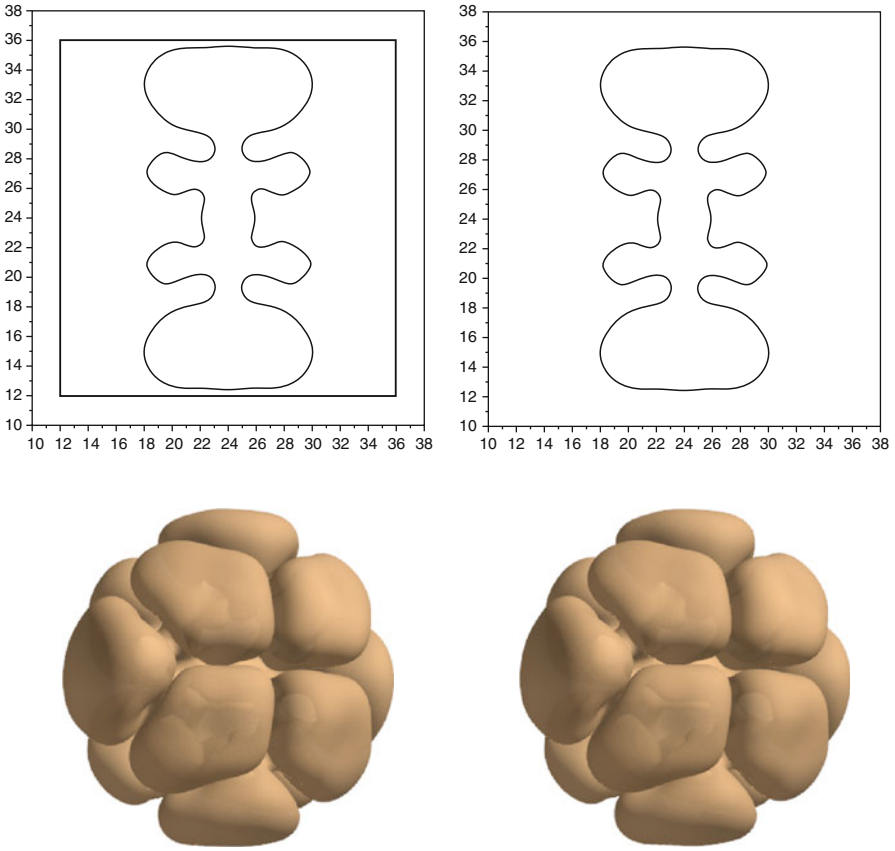

Fig. 11.18 Effects of domain size. Pictures are taken at time $t = 6$. *Left*: Cubic domain of size 24^3, the domain boundary is illustrated as a *black square* in the cross section. *Right*: Cubic domain of size 48^3

0, 0.25, 0.5, and 0.75. The evolution of the interfaces together with the necrotic cores are illustrated in Fig. 11.20. The case with $N = 0$, is illustrated in Fig. 11.17. In order to compare the simulations, the surface and volume of the tumors are recorded (not shown here) (Bergdorf 2007) and indicate that the overall growth is slowed down, when the nutrient level N for cell viability is raised. Even in the case with $N = 0.75$ the over-all growth of the tumor is not limited, as the living tumor tissue is always supplied with nutrient from the healthy tissue outside. The morphology of tumors of the same volume grown with a higher value for N seem to be more diverse than for tumors grown with a lower value for N. The reason for this is that a tumor with larger necrotic core is forced to grow on the outside, whereas tumors without necrotic core will also grow in regions further inside the tumor, causing the cancer to grow faster but inflicting less bumps on the interface.

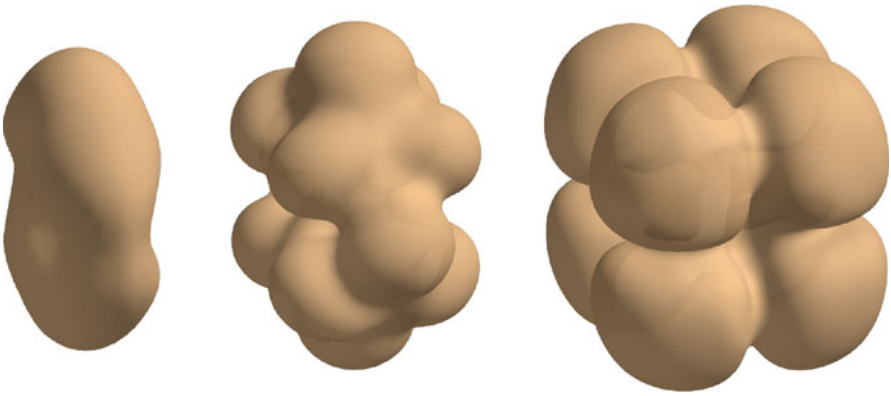

Fig. 11.19 Effects of resolution. The domain is set to a cube of size 24^3. Pictures are taken at time $t = 4$. The number of particles used from *left to right*: 65^3, 129^3, and 257^3

5.4.3 Amorphous Initial Conditions

Tumor growth for amorphous initial conditions is illustrated in Fig. 11.21 and Fig. 11.22 (with necrosis). Parameters determining growth and necrosis are set to $A = 0.5, G = 20, G_N = 1$ and $N = 0$, respectively, $N = 0.5$ for the simulation with necrosis. The domain is set to a cube of size 24^3 and 129^3 particles are initiated. Again, necrosis slows the over-all growth, but does not limit it. Our methods succeed in capturing the diverse morphologies, but as the simulations depend on the resolution, no further statements can be made.

5.4.4 Effects of Surface Tension

Effects of surface tension on tumor growth are investigated by comparing different simulations under variation of parameter γ. The initial condition, parameters and resolution are set to the same values as in the example without necrosis of the previous section, the surface tension coefficient takes on the values $\gamma = 1, 2$ and 5. In Fig. 11.23 we see that the speed of growth is slowed down as γ is increased and a bigger jump seems to have a smoothing effect on the interface. Comparing the cross sections at different times (not shown here) suggests that the shape of the tumor is not significantly disturbed by the surface tension coefficient, similar patterns emerge in all three simulations, sooner for $\gamma = 0$, later for $\gamma = 5$.

5.4.5 Zero Pressure Condition in Ω_0

In a final simulation, we want to compare our 3D results to tumors grown under pressure conditions as suggested in Macklin and Lowengrub (2005). Here, the

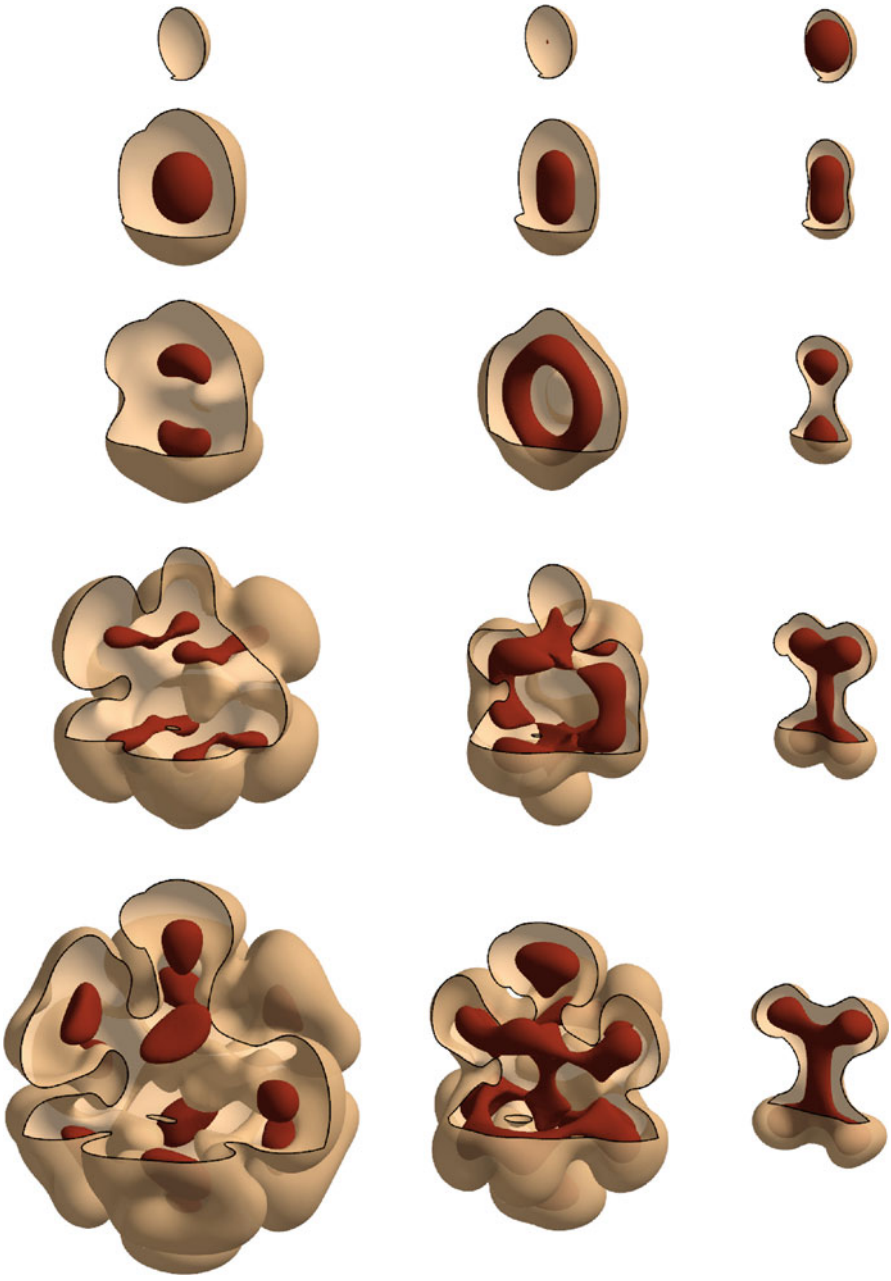

Fig. 11.20 Tumor growth under variation of parameter N. From *left to right*: $N = 0.25, 0.5$, and 0.75. Pictures are taken at $t = 0, 1.5, 3, 4.5$, and 6

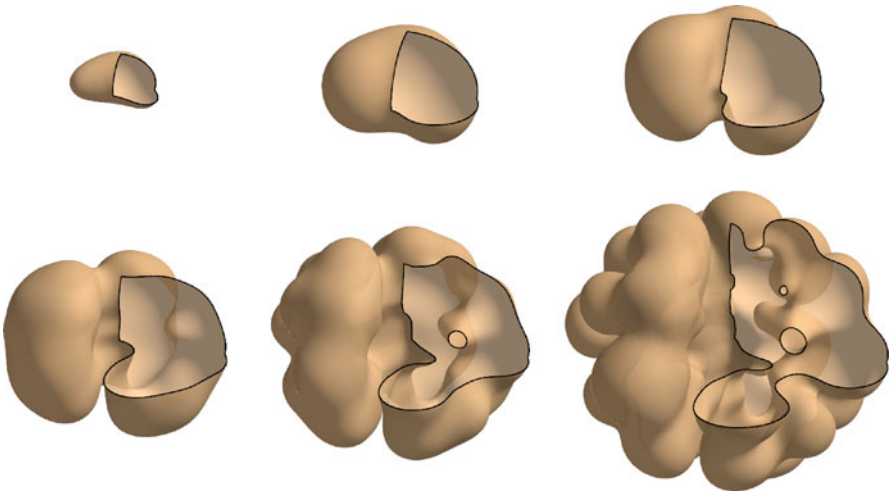

Fig. 11.21 Tumor growth with amorphous initial condition and no necrosis. Pictures are taken at $t = 0, 1, 2, 3, 4$, and 5

equation (11.62) is solved to enforce $p = 0$ outside Ω. The simulation area is set to a cube of size 24^3 and 129^3 particles are used to solve the system. Parameters determining tumor growth are set to $A = 0.5, G = 20, G_N = 1$, and $N = 0.5$. The initial condition is the same as for the other simulations with amorphous initial conditions and γ is set to 1. As illustrated in Fig. 11.24, the zero pressure condition outside the tumor enables approaching interfaces to join and enclose healthy tissue inside the tumor. Comparing Fig. 11.24 to Fig. 11.22 shows that the evolution of the interface under these modified pressure conditions is quite different to the ones observed with the $\nabla^2 p = 0$ outside Ω.

5.5 *Summary*

The model presented here and the methods implementing it have to be considered as a first step towards macroscopic 3D tumor growth simulation. As we have seen from our numerical experiments, the validity of the model hinges on the level set technology its built upon. We have found results to depend very strongly on the level set initialization method used and on the techniques used to extend off the interface values that are defined only in a direct neighborhood of the interface ($|\varphi| \leq h$). Additionally, the development of this framework revealed that interface joining is *not* trivial even though the underlying implicit interface formulation using level sets carries this appraisal. On the other hand, the differences we have found between

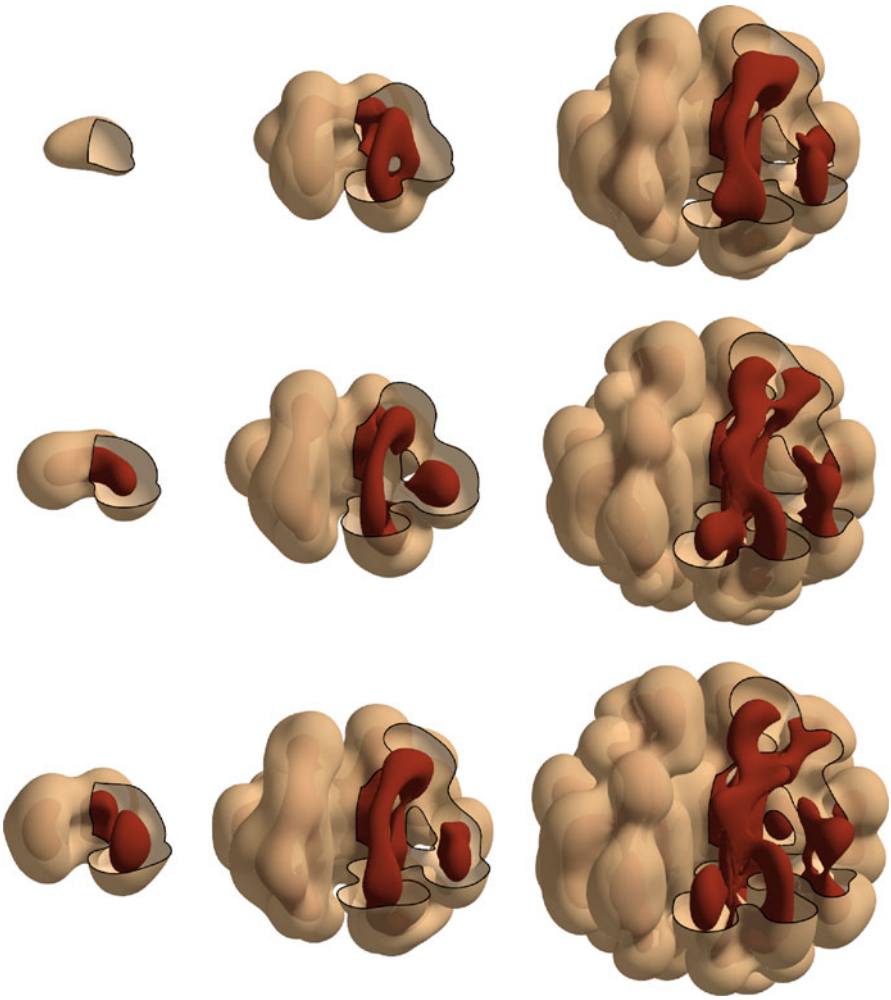

Fig. 11.22 Tumor growth with amorphous initial condition and necrosis ($N = 0.5$). Pictures are taken at $t = 0, 1, 2, 3, 4, 5, 5.5, 6$, and 6.5

$p = 0$ boundary conditions on the tumor, and the free-space formulation employed herein, make a valuable and clear statement: if we aim to develop representative models of tumor growth, the modeling of the tumor microenvironment and thus the healthy tissue is as crucial as appropriate modeling of the tumor itself. This is a fact which to date has largely been neglected in simulations of tumor growth.

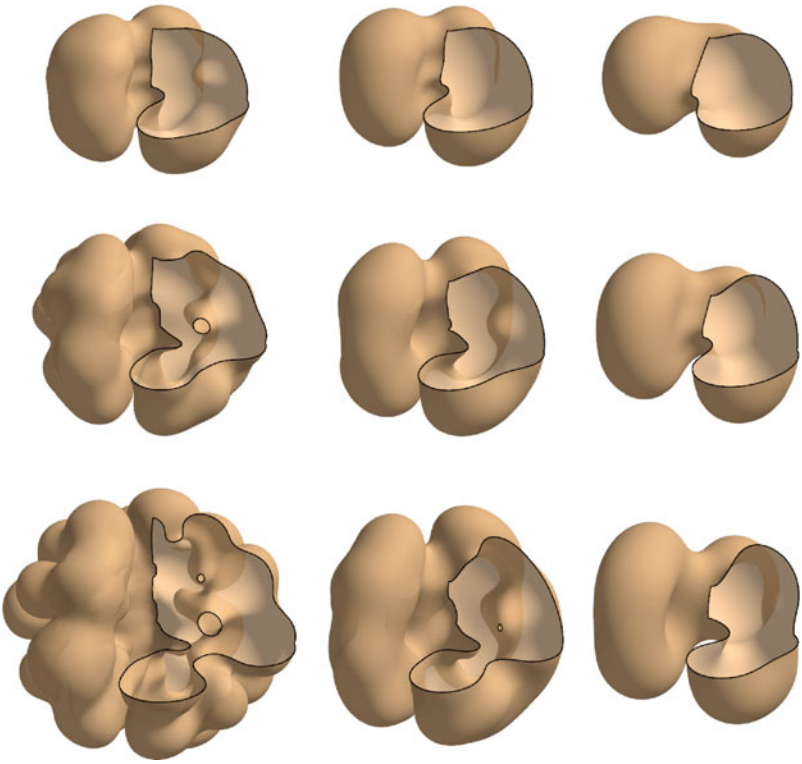

Fig. 11.23 Tumor growth with amorphous initial condition and varying surface tension. From *left to right*, $\gamma = 0, 2$, and 5. Pictures are taken at time $t = 2, 3, 4$, and 5

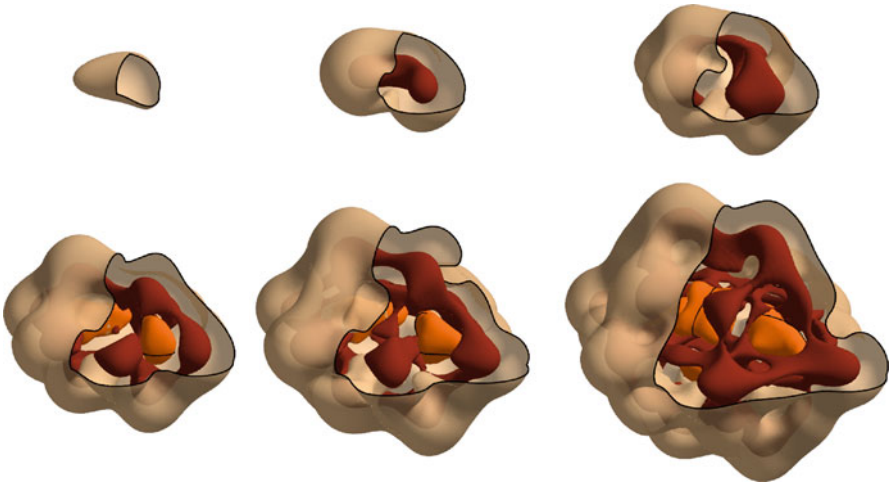

Fig. 11.24 Tumor growth with amorphous initial condition and $p = 0$ in Ω_0. The necrotic core is *colored red*, healthy tissue completely enclosed in the tumor is *colored orange*. Pictures are taken at time $t = 0, 2, 4, 6, 8$, and 10

References

Adalsteinsson D, & Sethian J. A (2003) Transport and diffusion of material quantities on propagating interfaces via level set methods J. Comput. Phys., 185:271–288

Araujo R. P, & McElwain D. L. S (2004) A history of the study of solid tumour growth: the contribution of mathematical modeling Bulletin of Mathematical Biology, 66(5):1039–1091

Bergdorf M (2007) Multireslution Particle Methods for the Simulation of Growth and Flow PhD thesis, ETH Zurich

Bergdorf M, & Koumoutsakos P (2006) A Lagrangian Particle-Wavelet Method Multiscale Model. Simul., 5(3):980–995

Bergdorf M, Sbalzarini I, & Koumoutsakos P (2010-11-01) A Lagrangian particle method for reaction-diffusion systems on deforming surfaces Journal of Mathematical Biology, 61(5):649–663

Bertalmio M, Cheng L.-T, Osher S, & Sapiro G (2001) Variational Problems and Partial Differential Equations on Implicit Surfaces J. Comput. Phys., 174:759–780

Chaplain M. A. J, Ganesh M, & Graham I. G (2001) Spatio-temporal pattern formation on spherical surfaces: numerical simulation and application to solid tumour growth Journal of Mathematical Biology, V42(5):387–423

Chen S, Merriman B, Osher S, & Smereka P (1997) A Simple Level Set Method for Solving Stefan Problems J. Comput. Phys., 135:8–29

Chopp D. L (2001) Some improvements of the fast marching method SIAM J. Sci. Comput., 23:230–244

Chorin A. J, & Bernard P. S (1973) Discretization of a Vortex Sheet, with an Example of Roll-Up J. Comput. Phys., 13:423–429

Cottet G.-H, & Koumoutsakos P. D (2000) Vortex methods: Theory and Practice Cambridge University Press, Cambridge Theory and practice

Cottet G. H, & Maitre E (2006) A level set method for fluid-structure interactions with immersed surfaces Mathematical Models & Methods in Applied Sciences, 16(3):415–438

Cristini V, Blawzdziewicz J, & Loewenberg M (2001) An Adaptive Mesh Algorithm for Evolving Surfaces: Simulations of Drop Breakup and Coalescence J. Comput. Phys., 168(2):445–463

Cristini V, & Lowengrub J (2003) Nonlinear simulation of tumor growth Journal of Mathematical Biology, 46:191–224

Degond P, & Mas-Gallic S (1989) The weighted particle method for convection-diffusion equations. II. The anisotropic case Math. Comp., 53(188):509–525

Engquist B, Tornberg A.-K, & Tsai R (2004) Discretization of Dirac delta functions in level set methods J. Comput. Phys., 207:28–51

Enright D, Fedkiw R, Ferziger J, & Mitchell I (2002) A Hybrid Particle Level Set Method for Improved Interface Capturing J. Comput. Phys., 183(1):83–116

Fedkiw R, Aslam T, Merriman B, & Osher S (1999) A non-oscillatory Eulerian approach to interfaces in multimaterial flows (the ghost fluid method) J. Comput. Phys., 152:457–492

Frayssé V, Giraud E, & Gratton S (1997) A Set of GMRES routines for real and complex arithmetics Technical Report TR/PA/97/49, CERFACS

Gatenby R. A, & Gawlinski E. T (2003) The Glycolytic Phenotype in Carcinogenesis and Tumor Invasion: Insights through Mathematical Models Cancer Research, 63(14):3847–3854

Greengard L, & Rokhlin V (1987) A fast Algorithm for Particle Simulations J. Comput. Phys., 73:325–348

Habib S, Molina-Paris C, & Deisboeck T. S (2003) Complex dynamics of tumors: modeling an emerging brain tumor system with coupled reaction-diffusion equations Physica A: Statistical Mechanics and its Applications, 327(3-4):501–524

Hanahan D, & Weinberg R. A (2000) The Hallmarks of Cancer Cell, 100(1):57–70

Harrison L. G, & Kolar M (1988) Coupling between reaction-diffusion prepattern and expressed morphogenesis, applied to desmids and dasyclads; J. Theoret. Biol., 130(4):493–515

Harrison L. G, Wehner S, & Holloway D. M (2001) Complex morphogenesis of surfaces: theory and experiment on coupling of reaction-diffusion patterning to growth Faraday Discussions, 120:277–294

Hieber S. E (2007) Particle Methods for Flow-Structure Interactions PhD thesis, ETH Zurich

Hieber S. E, & Koumoutsakos P (2005) A Lagrangian Particle level set method J. Comput. Phys., 210(1):342–367

Hockney R. W, & Eastwood J. W (1988) Computer Simulation Using Particles Institute of Physics Publishing, Bristol, PA, USA, 2 edition

Holloway D. M, & Harrison L. G (1999) Algal morphogenesis: modeling interspecific variation in Micrasterias with reaction-diffusion patterned catalysis of cell surface growth Phil. Trans. R. Soc. Lond. B, 354:417–433

Hou T. Y (1994) Why nonconservative schemes converge to wrong solutions: Error analysis Mathematics of Computation, 62(206):497–530

Jiang G.-S, & Peng D (2000) Weighted ENO Schemes for Hamilton-Jacobi Equations SIAM Journal on Scientific Computing, 21(6):2126–2143

Juric D, & Tryggvason G (1996) A Front-Tracking Method for Dendritic Solidification J. Comput. Phys., 123(1):127–148

Kim J, Kang K, & Lowengrub J (2004) Conservative multigrid methods for Cahn-Hilliard fluids J. Comput. Phys., 193(2):511–543

Kim S (2001) An O(N) level set method for eikonal equations SIAM J. Sci. Comput., 22:2178–2193

Koch A. J, & Meinhardt H (1994) Biological pattern formation: from basic mechanisms to complex structures Reviews of Modern Physics, 66(4):1481–1507

Koumoutsakos P (1997) Inviscid Axisymmetrization of an Elliptical Vortex J. Comput. Phys., 138(2):821–857

Leonard A, & Reynolds W. C (1988) Turbulence Research by Numerical Simulation Lecture Notes in Physics, 320:113–142

Leveque R. J, & Li Z (1994) The Immersed Interface Method for elliptic Equations with Discontinuous Coefficients and Singular Sources SIAM J. Numer. Anal., 31(4):1019–1044

Lindsay K, & Krasny R (2001) A particle method and adaptive treecode for vortex sheet motion in three-dimensional flow J. Comput. Phys., 172(2):879–907

Macklin P, & Lowengrub J (2005) Evolving interfaces via gradients of geometry-dependent interior Poisson problems: application to tumor growth J. Comput. Phys., 203:191–220

Mayo A (1984) The Fast Solution of Poisson's and the Biharmonic Equations on Irregular regions SIAM J. Numer. Anal., 21(2):285–299

Mittal R, & Iaccarino G (2005) Immersed boundary methods Annual Review of Fluid Mechanics

Monaghan J. J (1985) Extrapolating B-Splines for Interpolation J. Comput. Phys., 60:253–262

Osher S, & A. S. J (1988) Fronts Propagating with Curvature-dependent Speed – Algorithms based on Hamilton-Jacobi Formulations J. Comput. Phys., 79:12–49

Osher S, & Fedkiw R (2003) Level set methods and dynamic implicit surfaces, volume 153 of *Applied Mathematical Sciences* Springer-Verlag, New York

Peng D, Merriman B, Osher S, Zhao H, & Kang M (1999) A PDE-Based fast local level set method J. Comput. Phys., 155:410–438

Peskin C. S (1972) Flow patterns around heart valves: A numerical method J. Comput. Phys., 10:252–271

Ploumhans P, & Winckelmans G. S (2000) Vortex Methods for High-Resolution Simulations of Viscous Flow Past Bluff Bodies of General Geometry J. Comput. Phys., 165:354–406

Raviart P (1985) An analysis of particle methods Numerical Methods in Fluid Dynamics, pages 243–324

Sbalzarini I. F, Mezzacasa A, Helenius A, & Koumoutsakos P (2005) Effects of Organelle Shape on Fluorescence Recovery after Photobleaching Biophys. J., 89(3):1482–1492

Sethian J. A (1996) A Fast Marching Level Set Method for Monotonically Advancing Fronts Proceedings of the National Academy of Sciences of the United States of America, 93(4):1591–1595

Sethian J. A (1999) Fast Marching Methods SIAM Review, 41(2):199–235
Shu C.-W, & Osher S (1989) Efficient implementation of essentially nonoscillatory shock-capturing schemes. II J. Comput. Phys., 83(1):32–78
Stone H. A (1990) A simple derivation of the time-dependent convective-diffusion equation for surfactant transport along a deforming interface Physics of Fluids A, 2(1):111–112
Sussman M, & Fatemi E (1999) An efficient, interface-preserving level set redistancing algorithm and its application to interfacial incompressible fluid flow SIAM Journal on Scientific Computing, 20(4):1165–1191
Sussman M, Smereka P, & Osher S (1994) A Level Set Approach for Computing Solutions to Incompressible Two-Phase Flow J. Comput. Phys., 114(1):146–159
Tornberg A.-K, & Engquist B (2004) Numerical approximations of singular source terms in differential equations J. Comput. Phys., 200:462–488
Turing A. M (1952) The chemical basis of morphogenesis; Philos. Trans. R. Soc. Lond. Ser. B, 237(1-2):37–72
Unverdi S. O, & Tryggvason G (1992) A front-tracking method for viscous, incompressible, multi-fluid flows J. Comput. Phys., 100(1):25–37
Varea C, Aragon J. L, & Barrio R. A (1999) Turing patterns on a sphere Physical Review E, 60(4):4588–4592
Wiegmann A (1999) The Explicit-Jump Immersed Interface Method and Integral Formulas Technical report, Lawrence Berkeley National Laboratory
Wiegmann A, & Bube K. P (2000) The Explicit-Jump Immersed Interface Method: Finite Difference Methods for PDES with Piecewise Smooth Solutions SIAM J. Numer. Anal., 37(3):827–862
Xu J.-J, & Zhao H (2003) An Eulerian Formulation for Solving Partial Differential Equations along a Moving Interface SIAM J. Sci. Comput., 19(1-3):573–594

Chapter 12
Particle Simulations of Growth: Application to Angiogenesis

Florian Milde, Michael Bergdorf, and Petros Koumoutsakos

1 Tumor Induced Sprouting Angiogenesis

Sprouting angiogenesis describes the process of new capillaries growing from a preexisting vasculature and can be observed in the human body under various conditions. In a physiological context, angiogenesis mainly takes place during embryogenesis and fetal development. Under pathological conditions, angiogenesis can be observed to take place during wound healing, thrombosis and tumor growth (Folkman 2007). Whereas new capillaries grow in a controlled manner during wound healing and thrombosis and stop growing once the pathology has been alleviated, this is not the case for tumor-induced angiogenesis (Folkman 2007).

Angiogenesis as induced by tumors can persist for years, leading to the formation of a disorganized and leaky vasculature (Folkman 2007). Despite the inefficiency of this vasculature, it supplies the tumor with nutrients and growth factors, which allow for increased tumor cell proliferation and growth. In addition, the leaky vasculature enables single cancer cells or cell clusters that detach from the primary tumor to enter the vascular system and metastasize to remote organs.

Anti-angiogenic therapy, although comparatively young, has already been established as the fourth pillar of cancer therapy (Folkman 2006) (next to surgery, radiation and chemotherapy). Regulation of tumor-induced angiogenesis can help establishing more efficient pathways for drug delivery in the naturally leaky and inefficient blood vessels (Saharinen and Alitalo 2003). Inhibition, on the other hand, restrains nutrient supply, decreasing the growth rate of the tumor and reduces the risk of metastasis by preventing cell clusters from entering the vasculature (Folkman 2006). However, complete inhibition of angiogenesis promoting hypoxia (state of

F. Milde • M. Bergdorf • P. Koumoutsakos (✉)
Chair of Computational Science, ETH Zurich, CH-8092, Switzerland
e-mail: mildef@inf.ethz.ch; bergdorf@inf.ethz.ch; petros@inf.ethz.ch

T.L. Jackson (ed.), *Modeling Tumor Vasculature: Molecular, Cellular, and Tissue Level Aspects and Implications*, DOI 10.1007/978-1-4614-0052-3_12,

oxygen shortage) inside the tumor could lead to the occurrence of aggressive migrating tumor cell phenotypes (Axelson et al. 2005; Pennacchietti et al. 2003).

Tumor growth in the avascular stage, e.g. in the absence of a tumor associated vasculature, is restricted to a size of about 1 mm^3 (Folkman 2006). In this case, tumor growth is limited by the shortage of oxygen and nutrient supply transported by means of diffusion from the surrounding tissue. If the tumor grows beyond this size of roughly 1 mm^3, cells in the core of the tumor suffer from oxygen shortage, become hypoxic and eventually die, forming a necrotic region at the core of the tumor. In this avascular state, tumors can remain for a long time (Folkman 2006). However, induced by hypoxia, tumor cells can acquire the ability to secrete angiogenic growth factors (a discrete step (or steps) referred to as "angiogenic switch" (Hanahan and Weinberg 2000)) initiating sprouting angiogenesis at the tumor surrounding vasculature. Different growth factors are involved in the process of angiogenesis.

Vascular Endothelial Growth Factors (VEGF) have been identified to be one of the key components (Ferrara et al. 2003). Upon release by hypoxic tumor cells, VEGF's diffuse through the extracellular matrix(ECM), a fibrous construct occupying the space between the cells and establish a chemical gradient between the tumor and the nearby vessels. Once VEGF binds to specific receptors located on the endothelial cells (EC) lining the blood vessel walls, a cascade of events initiating vessel sprouting is set off.

Initially, ECs stimulated by VEGF start releasing proteases that degrade the basal lamina, a fibril structure supporting the vascular wall, enabling ECs to leave their position in the vessel wall and enter the ECM. Triggered by VEGF, further inter- and intracellular signaling pathways regulate increased EC proliferation and coordinate the selection of migrating tip cells located at the sprouting front. The migrating tip cells extend filopodia in order to probe their environment and migrate guided by the VEGF gradient towards regions of higher VEGF levels, a directed motion referred to as chemotaxis. Increased proliferation of ECs located behind the migrating tip cells leads to an extension of the sprouting blood vessel.

Fibronectin, distributed in the ECM and at the same time released by the migrating tip cells establishes an adhesive gradient guiding endothelial cells that follow behind, a movement referred to as haptotaxis. Next to the chemotactic and haptotactic cues, the fibrous structures present in the ECM influence cell migration by facilitating movement along fiber directions. Anastomosis, the formation of loops in the vascular network is the result of repeated branching and fusion of the tip cells as they migrate through the ECM. Finally, lumen formation within the strands of endothelial cells establishes a network that allows for the circulation of blood.

Maturation, the final stage of angiogenesis, is associated with the rebuilding of a basal lamina and the recruitment of other cell lines such as pericytes and smooth muscle cells that stabilize the vessel walls. The disorganized and leaky vasculature in combination with a growing tumor that exerts pressure on the fragile capillaries and thus suppressing temporal and local blood delivery, induces ever new regions of acute hypoxia. Under these conditions, tumor-induced angiogenesis never comes to a complete stop and full maturation is impaired.

1.1 Vascular Endothelial Growth Factors

Next to the predominant soluble isoform of VEGF, the presence of binding VEGF isoforms has been identified to drastically affect the morphology of capillary network formation (Lee et al. 2005; Ruhrberg et al. 2002). VEGF isoforms expressing a binding site for heparan sulphate proteoglycans found on cell surfaces, in the ECM and in body fluids can establish very localized chemotactic cues. These bound VEGF isoforms can be cleaved from the ECM by matrix metalloproteinases (MMPs) (Lee et al. 2005), attenuating the local gradients. MMPs can be expressed both by tumor cells and migrating ECs. Furthermore, it is noted that tumor cells are not the sole source of VEGF. Cells of the tumor microenvironment such as inflammatory cells stimulated by the tumor can also release VEGF and contribute to the chemotactic cues ECs react to.

1.2 Extracellular Matrix

The extracellular matrix plays an important role in cell migration and growth factor gradient formation. It describes any material that occupies the space between cells in metazoans (including the space between the tumor and the sprouting vasculature). Roughly 30% of the ECM are occupied by fibers such as collagen, laminin and fibrillin coiled up into bundles that serve as a guiding scaffold for migrating cells (Davis and Senger 2005; Friedl and Bröcker 2000). The structure is subject to remodeling by endothelial tip cells (Kirkpatrick et al. 2007). The restructuring greatly facilitates cell migration through the ECM and plays a crucial role in lumen formation. Furthermore, the fibers constituting the ECM present binding sites for molecules such as fibronectin and certain VEGF isoforms that can be cleaved by MMPs.

2 Computational Modeling of Angiogenesis

In computational models of tumor-induced angiogenesis, only a limited number of the involved biological processes is accounted for. The availability of biological data and the understanding of the key processes that account for the phenomena under investigation dictate the choice of model processes. Existing models of angiogenesis can be classified into three broad categories:

1. cell-based models with the aim to capture the behavior of individual biological cells (Bauer et al. 2007),
2. continuum models that model the average, large scale behavior of cell populations (Anderson and Chaplain 1998; Levine et al. 2001)
3. discrete models that capture the explicit vascular networks morphology as determined by the tip cells migration (Chaplain 2000; Sun et al. 2005).

In Bauer et al. (2007), a two-dimensional, Cellular-Potts-based model was developed to study the formation of interconnected networks of endothelial cells. The model explicitly considers migration, division and adhesion of endothelial cells. Two types of EC's are distinguished: migrating tip cells with the capability to degrade the matrix fibers, and proliferating stalk cells located behind the migrating tip cells. Branching and anastomosis of blood vessels can be observed without explicitly defined rules. Two dimensional, continuum models of angiogenesis with a probabilistic modeling of the capillary density have been presented in Anderson and Chaplain (1998). The models have been extended to generate discrete capillaries as masked points on a grid. Branching is modeled as a probabilistic process depending on the sprout age, growth factor concentration levels and the cell density. An extension of the model to three dimensions has been presented in Chaplain (2000). Another discrete two-dimensional model of sprouting angiogenesis has been introduced in Sun et al. (2005). A capillary indicator function is employed to capture the network structure. Branching is modeled to depend on the sprout age and the anisotropy of the ECM. In summary, cell-based models aim to describe angiogenesis at cell level resolution. However, due to their computational cost they are difficult to extend to macroscopic systems exploring large scale network formation processes. On the other hand, continuum-based models bypass these limitations by modeling the evolution of cell densities at the expense of detailed cell–cell interactions.

In this work, we propose two models, following a purely continuum, diffuse interface approach able to capture sprout morphologies and a hybrid particle-continuum-based approach. In both models, endothelial cell migration is considered to be influenced by chemical gradients inducing chemotaxis (VEGF), haptotaxis (Fibronectin) promoting cell–cell and cell–matrix adhesion and the structure of the ECM. VEGF is modeled to appear in a soluble and a matrix bound isoforms. The soluble isoform is released from an implicit tumor source and is subject to diffusion, cellular uptake and decay. The matrix bound VEGF isoform is initially distributed throughout the computational domain and can be cleaved by MMPs released at the sprouting tip (Sect. 1.1). Both soluble and cleaved VEGF isoforms contribute to the migration cues sensed by the ECs (see Fig. 12.1). Most existing models of sprouting angiogenesis account for chemotaxis induced by a soluble VEGF isoform (Anderson and Chaplain 1998; Chaplain 2000; Sun et al. 2005; Bauer et al. 2007). In Bauer et al. (2007) a matrix bound isoform of VEGF has been implicitly accounted for. To the best of our knowledge, the proposed model is the first to include an explicit cleaving mechanism and the presence of both soluble and matrix bound isoforms. Fibronectin is modeled to be released at the sprout tips, building up an adhesive gradient for the EC's (Anderson and Chaplain 1998; Chaplain 2000; Sun et al. 2005; Bauer et al. 2007). In addition, we consider the binding of fibronectin to the ECM localizing the haptotactic cues to a confined area around the sprouts. The ECM is represented by a distribution of randomly oriented fiber bundles. The fiber bundle direction and density modulate the direction and speed of the tip cell's migration. Other models explicitly considering an ECM have been introduced in Bauer et al. (2007) and Sun et al. (2005). In the Former, fiber bundles, structural cells and the interstitial fluid build the constituents of the ECM influencing cell migration

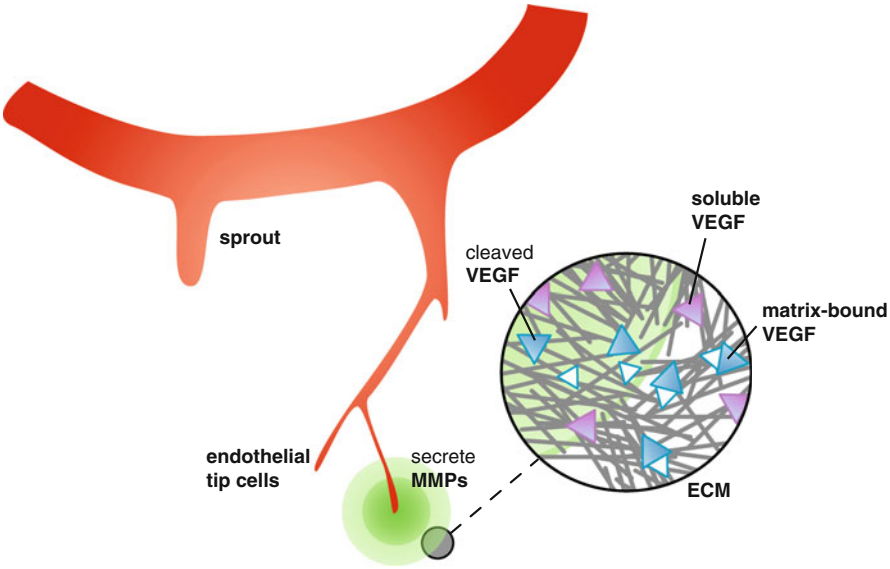

Fig. 12.1 Conceptual sketch of the different VEGF isoforms present in the ECM. Soluble and cleaved VEGF isoforms freely diffuse through the ECM, Matrix-bound VEGF isoforms stick to the fibrous structures composing the ECM and can be cleaved by MMPs secreted by the sprout tips

through adhesive forces. In the latter, a random anisotropic conductivity field accounts for the matrix structure and affects the migration velocity and branching behavior of the sprout tips.

3 A Continuum Modeling Approach

In the following, we propose a continuum, diffuse-interface model for mesenchimal-like cell migration and growth. We investigate on the models capability to reproduce angiogenesis-like growth that in contrast to prior models (except for the approach of Bauer et al. (2007)), does not rely on any probabilistic branching and fusion rules to generate blood vessel morphologies. The presented simulations have been conducted in 2D, as many in vitro experiments are essentially 2D. We note that all the methods described herein have also been extended to 3D. Next to the application of the model to the specific case of sprouting angiogenesis, the study might provide some hints on the relevance of the forces in play at the core of mesenchymal cell cluster migration as observed in organogenesis and infiltrating tumor growth.

3.1 Endothelial Cell Representation

When representing an agglomeration or cluster of cells, similar to the representation of multiphase flow, we can chose to represent the cells by a density function or by

a level set representing the interface between the cell cluster and the extracellular domain. We refer to the former case as "diffuse interface approach" and the later as "sharp interface approach." A prerequisite of the level set approach is the definition of a narrow band of several grid spacings around the interface location. Under these conditions, to represent highly elongated agglomerates of cells as observed in angiogenesis, the level set approach is less favorable as the requirements for the resolution are much more demanding than for a corresponding diffuse interface representation.

3.2 The Extracellular Matrix

The extracellular matrix serves as an adhesive scaffolding in between cells. Migrating cells make use of this fibrous structure to exert forces and propel them selves. So far, the effect of the ECM has rarely ever been explicitly accounted for in continuum simulations of cell migration. We propose to model the extracellular matrix as a collection of randomly distributed bundles that facilitate but also bias migration. The procedure for constructing the matrix is as follows:

We distribute N_F fibers as lines of thickness b_p. The start point $(x_p^{\text{start}}, y_p^{\text{start}})$ is drawn from a uniform distribution inside the computational domain Ω. The endpoint $(x_p^{\text{end}}, y_p^{\text{end}})$ is given as

$$\begin{pmatrix} x_p^{\text{end}} \\ y_p^{\text{end}} \end{pmatrix} = \begin{pmatrix} x_p^{\text{start}} + l_p \, sin(2\,\pi\,\alpha_p) \\ y_p^{\text{start}} + l_p \, cos(2\,\pi\,\alpha_p) \end{pmatrix}, \tag{12.1}$$

with α_p *u.a.r.* $\in [0, 1)$, and l_p is the length of the fiber

$$l_p = l\,2^{m\,z}, \text{ with } z \in \mathcal{N}(0, 1), \tag{12.2}$$

with simulation parameters l and m, and the fiber thickness given as b_p *u.a.r.* $\in [b_{\min}, b_{\max})$. In order to get a smooth, differentiable field, we first discretize the fibers onto the ECM grid e using Bresenham's line rasterization algorithm before we filter e N_{filter}-times with a second-order B-spline kernel.

3.3 Cell–Cell Adhesion

Tissue formation, stability and breakdown, cell sorting and tissue invasion, all these processes are largely influenced and determined by the fundamental biophysical mechanism of cell–cell adhesion. Adhesion of one cell to another, a substrate or the ECM is mediated by specific adhesion molecules on the cell membrane such as integrins and cadherins binding to collagens and fibronection (in the ECM) or

cadherin molecules on other cells, respectively. It is a very local reaction as it is established upon contact. We postulate a set of requirements reflecting the key characteristics of cell adhesion. Cell adhesion is a short-range force that gives rise to a movement towards the entity the cell adheres to. The movement induced by adhesion will decrease as the cell density approaches to the close-packing density. At close-packing density, no residual movement caused by adhesion is accounted for. Given this set of requirements, we model cell adhesion as an autocrine (in the case of cell–cell adhesion), or paracrine signal f (in the case of cell-ECM adhesion). In the absence of other influences, we can formulate the evolution of a cell density ρ subject to cell–cell adhesion as:

$$\begin{aligned}\frac{\partial \rho}{\partial t} &= -\nabla \cdot \left(\boldsymbol{a}^{\mathrm{c/c}}\,\rho\right) + \mathrm{d}\Delta\rho,\\ \boldsymbol{a}^{\mathrm{c/c}} &= \kappa_f\, L(f, \mathrm{d}f)\nabla f,\\ \frac{\partial f}{\partial t} &= -\mu\, f + \alpha\left(1 - \tfrac{f}{f_{\max}}\right)\rho + D_f\,\Delta f.\end{aligned} \tag{12.3}$$

$\boldsymbol{a}^{\mathrm{c/c}}$ denotes the adhesion force, μ, α and D_f the decay, release and diffusion parameters for the adhesion signal f and $f_{\max}$ defines the threshold value for the production of signal f. The cutoff function $L(f, \mathrm{d}f)$ is introduced to keep the magnitude of the gradient bounded by $\mathrm{d}f$ in order to bound the migration velocity of the cells:

$$L(f, \mathrm{d}f) = \mathrm{d}f\,\left(\max(\mathrm{d}f, |\nabla f|)\right)^{-1}. \tag{12.4}$$

The model is easily extended to account for different cell type populations ρ_i

$$\begin{aligned}\frac{\partial \rho_i}{\partial t} &= -\nabla \cdot \left(\sum_j \boldsymbol{a}_{ij}^{c/c}\,\rho_i\right) + d_i\,\Delta\rho_i,\\ \boldsymbol{a}_{ij}^{c/c} &= \kappa_{ij}\, L(f_j, \mathrm{d}f_j)\nabla f_j\\ \frac{\partial f_i}{\partial t} &= -\mu_i\, f_i + \alpha_i\left(1 - \tfrac{f_i}{f_{i,\max}}\right)\rho_i + D_i\,\Delta f_i.\end{aligned} \tag{12.5}$$

Here, κ_{ij} and $\boldsymbol{a}_{ij}^{c/c}$ denote the homotypic $(i = j)$ and heterotypic$(i \neq j)$ adhesion strength and adhesion force.

3.4 Close-Packing Density

So far, the model does not incorporate any repulsive effects that might delimit the local cell density. We introduce such effects by adding the following pressure-like term to the velocity:

$$\boldsymbol{a}^{p} = -\kappa_p\, H\,(\rho - \bar{\rho})\,\nabla\rho\,|\nabla\rho|^{-1}, \tag{12.6}$$

with the overall cell density $\rho \equiv \sum_i \rho_i$, a constant regulating the influence of cell pressure κ_p and the Heaviside function H. We note here that the introduced forcing terms $\boldsymbol{a}^x$ are additive and can be combined to build up a specific model.

3.5 Cell Sorting

In an attempt to explore our model of cell–cell adhesion, we perform a study of cell sorting, testing against the "Differential Adhesion Hypothesis" (see Steinberg 2007; Steinberg and Takeichi 1994 and references therein). The "Differential Adhesion Hypothesis" postulates that cellular sorting is an effect induced by differences in the intercellular adhesion strength amongst different cell populations. In our simulations, we consider two different cell types ρ_1 and ρ_2 which differ in their inter- and intracellular adhesion parameters κ_i, κ_j and κ_{ij}. We observe different sorting behaviors (see Fig. 12.2) such as complete sorting, mixing or engulfment of one population by the other, depending on the choice of the adhesion parameters. Along with the effects of cell–cell adhesion, we explore the influence of the pressure/repulsion effects as introduced earlier (see case b in Fig. 12.2). Despite the fact that we model contact-adhesion via an indirect adhesion signal, the proposed model successfully recovers the different sorting behaviors.

3.6 The ECM, Chemo-, and Haptotaxis

We propose to model the haptotactic influence of the ECM structure on the cell migration velocity as the combinatory effect of the following assumptions. A cell will crawl along fiber bundles that are aligned with the chemotactic cue ($\nabla\phi$) in order to maximize its migration velocity. To propel itself along the scaffold provided by the ECM, cells rely on the presence of fibers. In the absence of fibers ($e = 0$) cell migration is impaired ($e_o \ll 1$). On the other hand, if the fiber density is too high ($e \approx \rho_{\text{cpd}}$), cells have to degrade the matrix fibers before they are able to migrate and are slowed down. These assertions are formulated as:

$$\boldsymbol{a}^{\text{ecm},\phi} = \left[\left(1 - \left|\frac{\nabla e}{|\nabla e|} \cdot \frac{\nabla \phi}{|\nabla \phi|}\right|\right) \nabla e + \nabla \phi\right] (e + e_o)(\rho_{\text{cpd}} - e)\,, \tag{12.7}$$

and illustrated in Fig. 12.3. We note, that the modeling of the chemotactic response as $\boldsymbol{a}^{\text{ecm},\phi}$ is but the most simple one as it ignores many effects such as receptor saturation and activation thresholds.

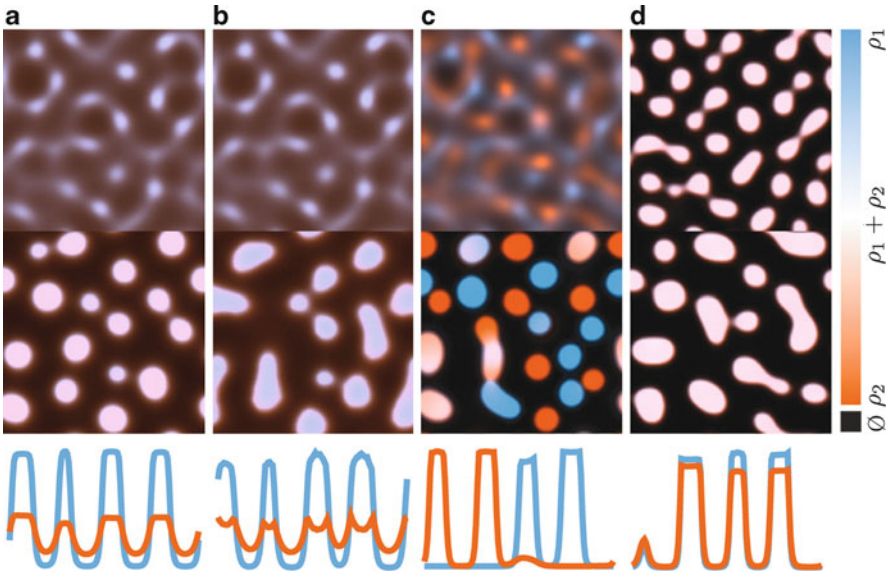

Fig. 12.2 *Top row* depicts solution at $t = 40$, *middle row* at $t = 160$, *bottom row* depicts a cut through the domain at $t = 160$. *Columns*: **a** engulfment, $\kappa_{11} = 0.25$, $\kappa_{22} = 0.025$, and $\kappa_{12} = \kappa_{21} = 0.05$; **b** engulfment with pressure, $\kappa_{11} = 0.25$, $\kappa_{22} = 0.025$, and $\kappa_{12} = \kappa_{21} = 0.05$; **c** sorting, $\kappa_{11} = 0.25$, $\kappa_{22} = 0.25$, and $\kappa_{12} = \kappa_{21} = 0.00$; **d** mixing, $\kappa_{11} = 0.25$, $\kappa_{22} = 0.09$, and $\kappa_{12} = \kappa_{21} = 0.2$

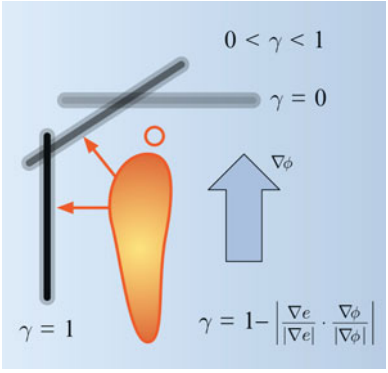

Fig. 12.3 A cell will move "onto" a fiber if the fiber direction is not transverse to the chemotactic gradient, i.e., the gradient of adhesion is not aligned with the chemotactic direction

3.7 Angiogenesis-like Migration

We now combine the models of cell–cell adhesion, cell–matrix adhesion and chemotaxis in order to assemble a system that captures migration of cells through the ECM:

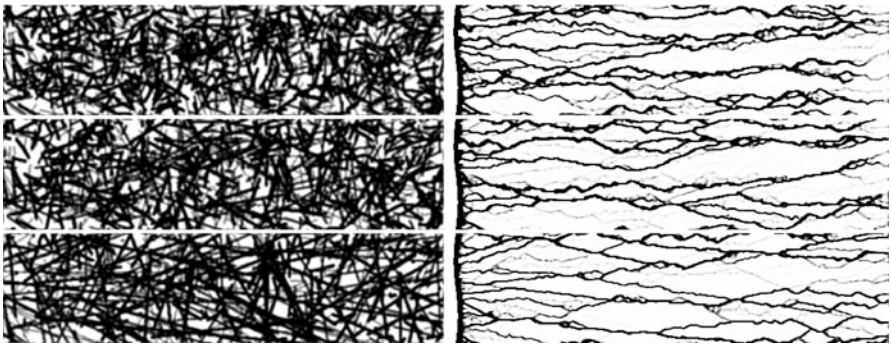

Fig. 12.4 Effect of increasing the length of the fibers (in (12.2)), $m = 0.25$, 1.0, and 4.0

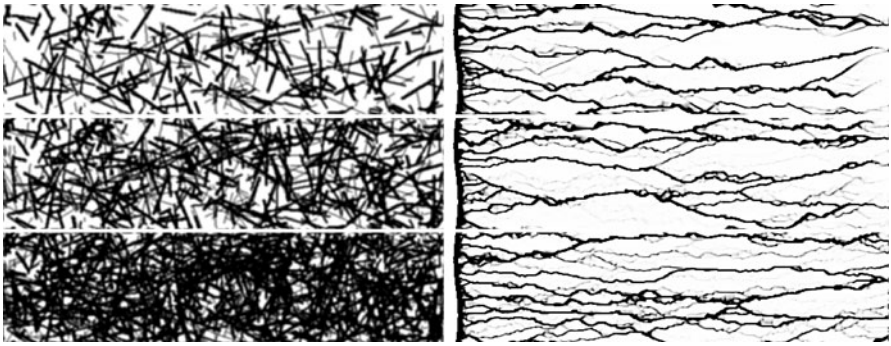

Fig. 12.5 Effect of increasing the matrix density: 31%, 51%, and 75%

$$\begin{aligned}
\frac{\partial f}{\partial t} &= -\mu\, f + \alpha\rho\left(1 - f_{\max}^{-1}\, f\right) + D_f\, \Delta f, \\
\frac{\partial \rho}{\partial t} &= -\nabla \cdot (\boldsymbol{a}\, \rho) + d\, \Delta \rho, \\
\boldsymbol{a} &= \kappa_e \left(1 - \left|\frac{\nabla e}{|\nabla e|} \cdot \frac{\nabla \phi}{|\nabla \phi|}\right|\right) \nabla e + \kappa_\phi \nabla \phi + \kappa_f \nabla_r f_j,
\end{aligned} \tag{12.8}$$

where $\nabla_r x$ denotes the regularized gradient $L(x, dx)$ as defined in (12.4). For greater lucidity we omit here the effects of fiber density that we have introduced in (12.7). Figures 12.4–12.6 illustrate the effects of modifying the model parameters on the resulting vessel morphology. The growth factor concentration ϕ in the reported simulations is kept constant throughout the simulation, linearly increasing towards the right side of the computational domain.

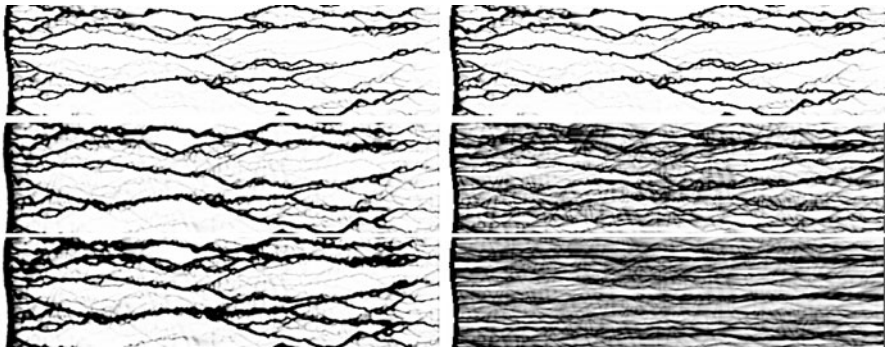

Fig. 12.6 *Left:* Creating thicker vessels by decreasing the close-packing density $\bar{\rho}$. *Right:* Effect of reducing cell adhesion (cell–cell and cell–matrix)

3.8 Matrix-bound Growth Factors

Until now, we have only considered the effect of purely soluble growth factors freely diffusing through the ECM, establishing a global growth factor gradient. It is however known that growth factors can exist in different isoforms, some having the ability to bind to heparine binding sites in the ECM. These isoforms can dynamically bind and unbind to the matrix and do not diffuse freely. Amongst other cell lines, endothelial cells secrete matrix metalloproteinases (MMPs) that have the capability to cleave the matrix binding domain from the rest of the VEGF molecule. The cleaved part of the VEFG molecule becomes diffusible again while retaining its angiogenic signaling potential. We extend our model to account for these processes by distributing small pockets of matrix-bound VEGF at the beginning of the simulation. ECs are modeled to secrete a compound that cleaves the matrix-bound VEGF. Upon cleavage, the bound VEGF become diffusible and adds to the global gradient established by the purely soluble VEGF isoform. Simulation results of such a situation are reported in Fig. 12.7.

Although a setting like this leads to the formation of localized chemotactic cues, we do not observe an increase in branching as observed in both in-vitro and in-vivo models of angiogenesis and vasculogenesis (Ruhrberg et al. 2002; Lee et al. 2005). If we look at the size of the distributed VEGF pockets in the order of a cell diameter, we must realize that the size of the pockets is much larger then what would be found in a real ECM. In the formulation of our continuum model, however it is not possible to explicitly account for localized structures that are of a size of one to two orders in magnitude smaller than cell size without decreasing the computational mesh size drastically. We therefore suggest to introduce a subgrid-scale modeling approach.

From a mesoscopic point of view the effect of localized chemotactic cues that are smaller than the description scale will clearly not propagate into any distinguishable residual localized movement. However, we can expect to see the cumulative effect on one cell, which from a mesoscopic point of view will result in increased random

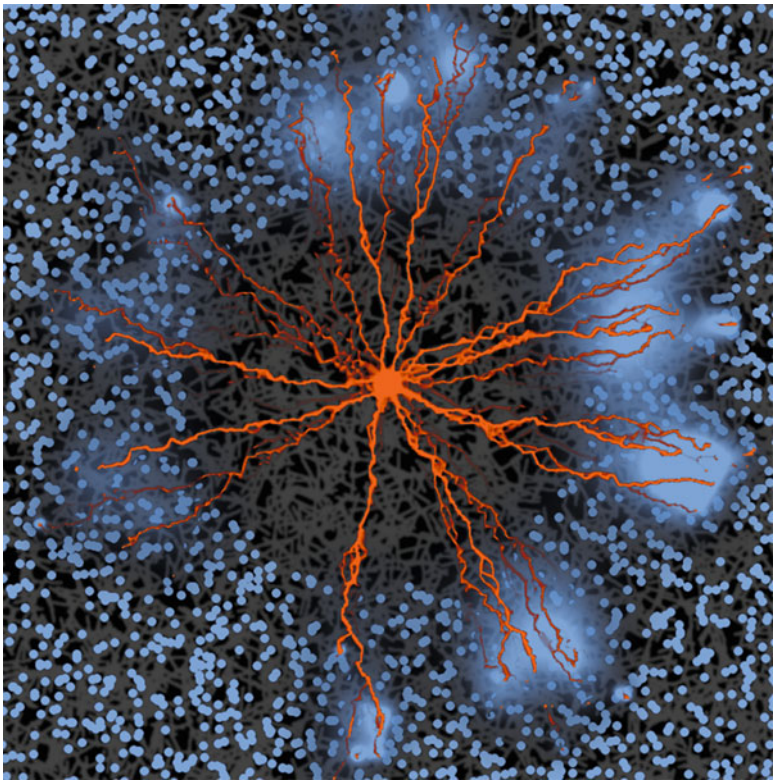

Fig. 12.7 Simulation with matrix-bound growth factors using pockets of matrix-bound VEGF *blue* distributed in the matrix. The endothelial cells *red* release MMPs that cleave the bound growth-factors and make them soluble (diffuse *blue cues*)

motion. It has been shown that microscopic random motion can be modeled as diffusion from a macroscopic view point. We therefore extend the present model to include a spatially varying diffusion term in the equation of EC density, negligible in the absence of matrix-bound VEGF and increasing depending on the local concentration of matrix-bound VEGF. In this model, both release of MMPs and the cleaving of the bound VEGF is modeled implicitly via an increase in EC diffusivity. Results of the modified system showing an increased branching behavior in the presence of matrix-bound VEGF are depicted in Fig. 12.8.

3.9 Summary

The model of sprouting angiogenesis presented in this work relies on a pure continuum, diffuse interface model description. It integrates key aspects of cell

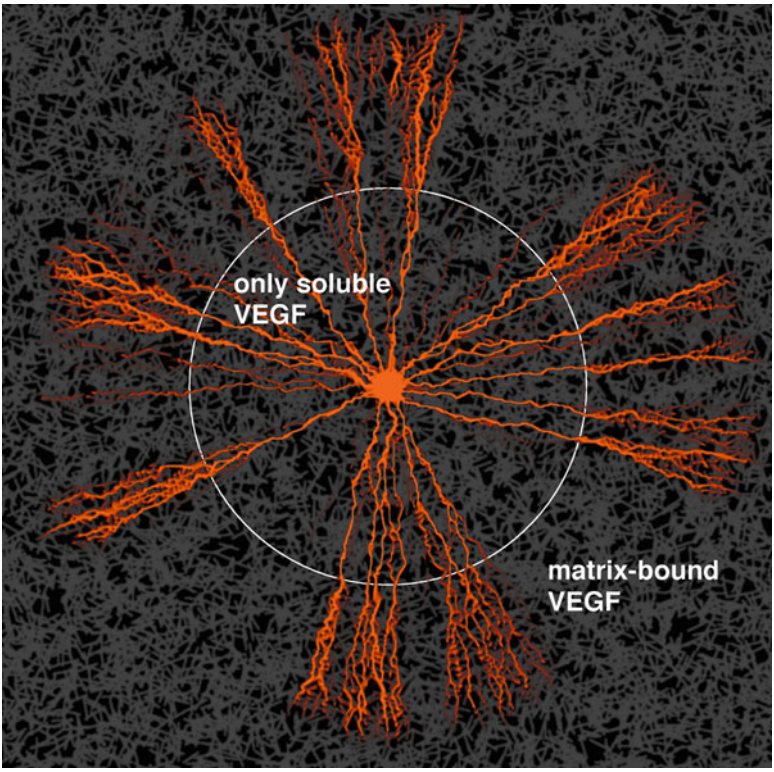

Fig. 12.8 Simulation with matrix-bound growth factors by the "diffusion" model. *Within* the white *circle* there are only soluble growth factors present, *outside of the circle* a constant concentration of growth factors is bound to the matrix. As apparent from the network structure *red*, the matrix-bound growth factors lead to distinctively increased branching

dynamics leading to mesenchymal migration such as cell–cell adhesion, cell density pressure, an explicit description of the ECM, cell–matrix adhesion, chemotaxis, and the effect of matrix-bound growth factors on migrating cells.

We captures cell–cell adhesion effects indirect via the introduction of an artificial autocrine adhesion signal. Despite the simple formulation, the model manages to recover aspects of cell sorting behavior as formulated in the"Differential Adhesion Hypothesis." In comparison to existing continuum models of cell–cell adhesion (Armstrong et al. 2006), the presented model is less intuitive but in turn benefits from an easier and more efficient implementation.

As a result of the explicit matrix representation that exerts an adhesive force on the migrating endothelial cells, the model recovers the branching behavior of migrating endothelial cells. The branching is an output of the model, and does not rely on the formulation of any heuristic branching rules.

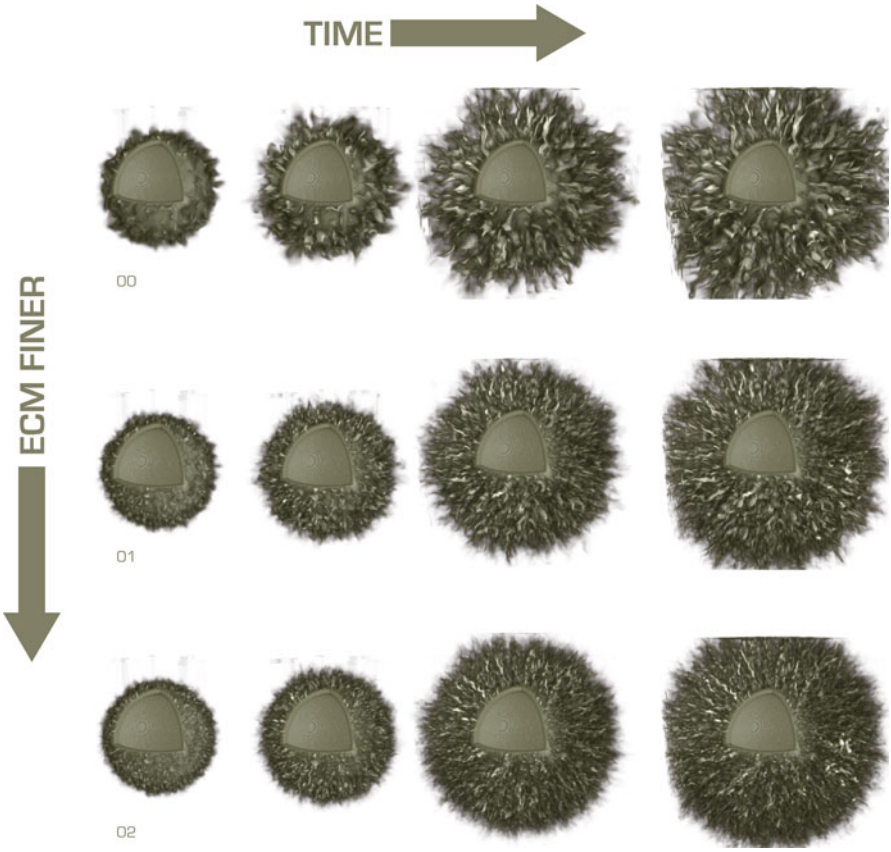

Fig. 12.9 3D simulations of cells shed from the surface a spherical tumor, and their invasion of the surrounding ECM

In addition to soluble chemotactic cues, the model has been extended to also consider matrix-bound cues, modeled using a subgrid-scale approach. The consideration of these localized migration cues leads to an increase in the observed vessel branching, reproducing similar morphological features as observed under experimental conditions.

In its general formulation, the proposed method could easily be adapted to addressed other phenomenons involving mesenchymal cell migration. One further tumor related phenomenon that might be addressed with the proposed model is the infiltrating growth of cancer cells as observed in glioblastoma (see Fig. 12.9).

4 A Hybrid Model of Sprouting Angiogenesis

This chapter is largely based on the work presented in Milde et al. (2008). For a more detailed description, we refer the reader to the original article. The deterministic model of sprouting angiogenesis presented in this section follows a hybrid approach, combining a continuum description of VEGF, MMPs, fibronectin and endothelial stalk cell density with a discrete, agent-based particle representation of the tip cells. We make use of particle-mesh interpolation methods (see Chapter Particle Simulations of Growth: Application to Tumorigenesis, Sect. 2.3) to derive an implicit three-dimensional level-set representation. The level-set description of the capillary sprouts is an extension of the discrete indicator functions considered in existing models. The consideration of particle based, grid-independent tip cell migration was initially proposed by Plank and Sleeman (2004).

The model explicitly considers the presence of both localized matrix-bound and freely diffusing VEGF isoforms. Endothelial tip cells are modeled to release proteases (MMPs) that can cleave the matrix-bound isoforms. We present studies that highlight the effects observable on the vessel geometries.

Further, the model considers the explicit modeling of the ECM to influence EC migration and branching. This approach renders the model completely deterministic in contrast to existing modeling approaches (McDougall et al. 2006; Plank and Sleeman 2004; Chaplain 2000).

In Sun et al. (2005) the ECM was addressed by a heterogeneous and anisotropic description of conductivity. Similar to the work presented in Sun et al. (2005), the ECM model presented herein acts as a tensor on the migration cues established by the chemotactic and haptotactic gradients. Additionally, the present work considers the fibers to offer binding sites for matrix-bound VEGF and fibronectin.

We model tip cell branching events to occur in response to diverging directional cues as mediated by the VEGF and fibronectin gradients as well as the ECM fiber orientation. The local divergence of the migration cues is sensed via the explicit modulation of tip-cell filopodia. We note that no additional branching probabilities need to be introduced (Anderson and Chaplain 1998; Chaplain 2000; Plank and Sleeman 2004). Other models not depending on probabilistic branching rules are presented in Sun et al. (2005); Bauer et al. (2007). An overview of the considered model entities is given in Table 12.1.

4.1 Vascular Endothelial Growth Factors

Of the several growth factors involved in tumor-induced angiogenesis, VEGF has been identified as the key regulator (Ferrara et al. 2003). The release of soluble VEGF (sVEGF) from tumor cells in this model is modeled implicitly via a source term. In addition, a matrix-bound VEGF isoform (bVEGF) is considered. bVEGF is assumed to be locally distributed in the ECM and does not diffuse (Ruhrberg et al. 2002; Taraboletti et al. 2006).

Table 12.1 Molecular species, cells, cell densities and matrix property definitions

Symbol	Description	Equation
[bVEGF]	Concentration of matrix-bound VEGF	(12.9)
[cVEGF]	Concentration of cleaved matrix-bound VEGF	(12.10)
[VEGF]	Concentration of soluble VEGF	(12.11)
[FIB]	Concentration of unbound fibronectin	(12.12)
[bFIB]	Concentration of matrix-bound fibronectin	(12.14)
[MMP]	Concentration of matrix metalloproteinases	(12.15)
[EC]	Endothelial tip cell density	(12.12)(12.15)
ρ	Endothelial cell density lining capillary walls	Sect. 4.7
$\boldsymbol{K}$	Vector field representing the fiber orientation in the ECM	Sect. 4.5
E_ρ	Fiber density in the ECM	Sect. 4.5
E_χ	Fiber indicator function in the ECM	Sect. 4.5

Matrix-Bound VEGF [bVEGF] On initialization, Matrix-bound VEGF is distributed in spherical clusters throughout the computational domain. The pockets of bVEGF are mollified by gaussian filtering and multiplied with the matrix indicator field E_χ to dispose of bVEGF not associated with any matrix fibers. MMPs released from migrating ECs can cleave the bound VEGF (Lee et al. 2005).

The evolution of Matrix-bound VEGF is given by

$$\frac{\partial[\text{bVEGF}]}{\partial t} = -\upsilon_{bV}[\text{MMP}][\text{bVEGF}], \tag{12.9}$$

with cleaving rate υ_{bV}.

Cleaved VEGF [cVEGF] Once cleaved, the released VEGF (cVEGF) diffuses through the ECM. Both cleaved VEGF as well as soluble VEGF are subject to natural decay at a rate given by d_V.

$$\begin{aligned}\frac{\partial[\text{cVEGF}]}{\partial t} &= k_V\nabla^2[\text{cVEGF}] + \upsilon_{bV}[\text{MMP}][\text{bVEGF}] \\ &\quad -\upsilon_V[\text{cVEGF}]\rho - d_V[\text{cVEGF}].\end{aligned} \tag{12.10}$$

Endothelial cells express surface receptors that bind VEGF molecules (Kearney et al. 2004), enabling the cells to sense VEGF gradients in their vicinity and to trigger chemotaxis (Gerhardt et al. 2003). Receptor ligand binding and the internalization of VEGF is captured in the model via VEGF uptake by the ECs at a rate υ_V. The endothelial cell density is given by ρ.

Soluble VEGF [sVEGF] Upon release, the soluble VEGF proteins diffuse through the ECM and are subject to endothelial uptake and decay. The diffusion constant is given by k_V.

$$\frac{\partial[\text{sVEGF}]}{\partial t} = k_V\nabla^2[\text{sVEGF}] - \upsilon_V[\text{sVEGF}]\rho - d_V[\text{sVEGF}]. \tag{12.11}$$

4.2 Fibronectin

Unbound Fibronectin [FIB] Fibronectin is released by the migration ECs depending on its local concentration (Alberts et al. 2002). We consider fibronectin to bind to integrins located at the EC membrane and to ECM fibers, establishing an adhesive interaction force between the fibers in the ECM and the cells (Serini et al. 2006). When not bound, fibronectin diffuses through the ECM with a diffusion rate k_F and decays at a rate given by d_F.

$$\frac{\partial[\mathrm{FIB}]}{\partial t} = k_F \nabla^2[\mathrm{FIB}] + \gamma_F \mathcal{G}\big(F_{th}, [\mathrm{FIB}]\big)[\mathrm{EC}] \\ -\upsilon_{bF}[\mathrm{FIB}]\left(E_\chi bF_{th} - [\mathrm{bFIB}]\right) - d_F[\mathrm{FIB}], \tag{12.12}$$

with creation rate γ_F and creation function

$$\mathcal{G}\big(C_{\mathrm{th}}, [\mathrm{C}]\big) = \frac{C_{\mathrm{th}} - [\mathrm{C}]}{C_{\mathrm{th}}}, \tag{12.13}$$

depending on the creation threshold level F_{th}. The rate of fibronection binding to the ECM is given by υ_{bF}. bF_{th} is a constant introduced to account for binding site saturation in the ECM.

Matrix-Bound Fibronectin [bFIB] Bound to the ECM, fibronectin establishes a haptotactic gradient for the endothelial cells (Paweletz and Knierim 1989). Matrix bound fibronectin does not diffuse, is subject to degradation by MMPs at degradation rate δ_{bF} and decays at a rate given by d_{bF}.

$$\frac{\partial[\mathrm{bFIB}]}{\partial t} = \upsilon_{bF}[\mathrm{FIB}]\left(E_\chi bF_{th} - [\mathrm{bFIB}]\right) - \delta_{bF}[\mathrm{bFIB}][\mathrm{MMP}] - d_{bF}[\mathrm{bFIB}]. \tag{12.14}$$

4.3 Matrix Metalloproteinases (MMPs) [MMP]:

MMPs are proteases involved in the degradation of the ECM, cleaving matrix bound proteins such as bVEGF isoforms from the binding sites in the ECM (Lee et al. 2005). Migrating ECs are assumed to release the MMPs at a rate depending on the local MMP concentration (Iruelaarispe et al. 1991; Mignatti and Rifkin 1993). Upon release, MMPs are assumed to diffuse through the ECM and are subject to natural decay at a rate given by d_M. MMP release is bounded by a predefined threshold level M_{th}. The release and diffusion constants are given by γ_M and k_M, [EC] denotes the endothelial tip cell density. Evolution of the MMP concentration is defined as:

$$\frac{\partial[\mathrm{MMP}]}{\partial t} = k_M \nabla^2[\mathrm{MMP}] + \gamma_M \mathcal{G}\big(M_{th}, [\mathrm{MMP}]\big)[\mathrm{EC}] - d_M[\mathrm{MMP}]. \tag{12.15}$$

4.4 Endothelial Cells

Endothelial cells are the cells lining the interior wall of the blood vessels. Proliferating and migrating into the extracellular space, ECs are actively involved in the formation of new blood vessel sprouts and capillary networks. During angiogenesis, ECs can be observed to occur in three different stats: Quiescent cells lining the vessel walls of the maturated vasculature. Proliferating cells located in a small region behind the sprouting front and migrating tip cells extending filopodia, actively moving into the extracellular space.

Tip Cell Migration While proliferating cells in the sprout stalk provide the cells necessary for capillary growth, the migrating tip cells at the sprout front determine the morphology of the growing capillaries (Gerhardt et al. 2003). Chemotactic and haptotactic cues in the matrix are established via VEGF and fibronectin gradients and determine the migration direction (Gerhardt et al. 2003; Ferrara et al. 2003; Paweletz and Knierim 1989). As the VEGF level increases in the proximity of the tumor, EC surface receptors become occupied, attenuating the cells ability to sense the chemotactic cues (Kearney et al. 2004; Gerhardt et al. 2003). The function $\mathcal{W}$ is introduced to capture the effect of receptor saturation. Tip cell acceleration driving migration is defined as:

$$\boldsymbol{a} = \alpha\left(E_\rho\right)\underline{\boldsymbol{T}}\left(\mathcal{W}\left([\mathrm{VEGF}]\right)\nabla[\mathrm{VEGF}] + w_F\nabla[\mathrm{bFIB}]\right), \tag{12.16}$$

where

$$\mathcal{W}\left([\mathrm{VEGF}]\right) = \frac{w_V}{1 + w_{V2}[\mathrm{VEGF}]}, \tag{12.17}$$

with chemotactic parameters w_V and w_{V2} and

$$[\mathrm{VEGF}] = [\mathrm{sVEGF}] + [\mathrm{bVEGF}] + [\mathrm{cVEGF}]. \tag{12.18}$$

The matrix density has a direct influence on the migration velocity. The presence of fibers (E_ρ) provides a scaffold for migrating tip cells, thus enhancing migration speed of ECs (Friedl and Bröcker 2000). A very dens matrix on the other hand builds up a barrier for migrating ECs that has to be degraded for cells to migrate through, effectively slowing down tip cell migration (Davis and Senger 2005). We capture this effect in the function

$$\alpha\left(E_\rho\right) = \left(E_0 + E_\rho\right)\left(E_1 - E_\rho\right)C_1, \tag{12.19}$$

where a threshold E_0 is introduced to define the migration factor in the complete absence of fibers, E_1 the maximal fiber density completely blocking migration, and C_1 is the ECM migration constant . To model the directional cues the fiber bundles exert on cell migration, a tensor $\underline{\boldsymbol{T}}$ is introduced acting on the migration velocity.

$$\{\underline{\boldsymbol{T}}\}_{ij} = \left(1 - \beta\left(E_\chi\right)\right)\{\mathbb{1}\}_{ij} + \beta\left(E_\chi\right)K_i K_j, \tag{12.20}$$

with

$$\beta\left(E_\chi\right) = \beta_K E_\chi, \tag{12.21}$$

with the ECM strength β_K and $\boldsymbol{K}$ being the vector field the tensor is applied on.

Particle positions $\boldsymbol{x}_p$ are updated according to:

$$\frac{\partial \boldsymbol{x}_p}{\partial t} = \boldsymbol{u}_p, \quad \frac{\partial \boldsymbol{u}_p}{\partial t} = \boldsymbol{a}_p - \lambda \boldsymbol{u}_p, \tag{12.22}$$

with $\boldsymbol{u}_p$ and $\boldsymbol{a}_p$, the velocity and acceleration, respectively, at particle location $\boldsymbol{x}_p$ and λ the drag coefficient.

Branching In this model, we consider branching of tip cells to depend on the presence of diverging migration cues in the ECM (Ruhrberg et al. 2002). Endothelial cells probe their surrounding environment for chemo- and haptotactic cues extending filopodia equipped with cell surface receptors (Gerhardt et al. 2003). Locations of high anisotropy suggesting a locally diverging migration acceleration field $\boldsymbol{V}$ are detected by a curvature measure.

$$k\left(\boldsymbol{x}\right) = \frac{\left|\left|\dot{L}\left(\boldsymbol{x}\right) \times \ddot{L}\left(\boldsymbol{x}\right)\right|\right|}{\left|\left|\dot{L}\right|\right|^3}, \tag{12.23}$$

with $\boldsymbol{V} = (u, v, w)$, $\dot{L}\left(\boldsymbol{x}\right) = \boldsymbol{V}\left(\boldsymbol{x}\right)$ and $\ddot{L} = u\boldsymbol{V}_x + v\boldsymbol{V}_y + w\boldsymbol{V}_z$ (Weinkauf and Theisel 2002).

If a sprout tips age exceeds the threshold level sa_{th} necessary for branching, and the local curvature k is greater then the defined threshold level ai_{th}, branching occurs. In order to determine the exact branching direction in 3D, we introduce a satellite particle-based filopodia model to sense the migration cues in the vicinity of the tip cell. 6 satellite particles are distributed radially around the tip cell in a plane perpendicular to the migration direction (Fig. 12.10). We then measure the velocities at the satellite positions and compute the angle between velocities at opposing satellite points. The branching direction is defined by the location of the two satellite particles with the largest angle between velocities pointing away from the migrating direction. A new tip cell is then created and the particle velocities $\boldsymbol{u}_p$ on the right-hand side of (12.22) are updated

$$\boldsymbol{u}'_p = \frac{\left|\boldsymbol{u}_p\right|}{1+\beta}\left(\frac{\boldsymbol{a}_s}{\left|\boldsymbol{a}_s\right|} + \beta\frac{\boldsymbol{x}_s - \boldsymbol{x}_p}{\left|\boldsymbol{x}_s - \boldsymbol{x}_p\right|}\right), \tag{12.24}$$

where $\boldsymbol{u}_s$ denotes the satellite velocity at satellite position $\boldsymbol{x}_s$ and $\beta = 0.8$. This results in a short acceleration of the two tip cells towards the satellite positions.

Anastomosis The formation of loops in the growing capillary network can be observed after the sprouts have extended some distance into the ECM and branching has taken place (Paweletz and Knierim 1989). We consider two distinct fusion

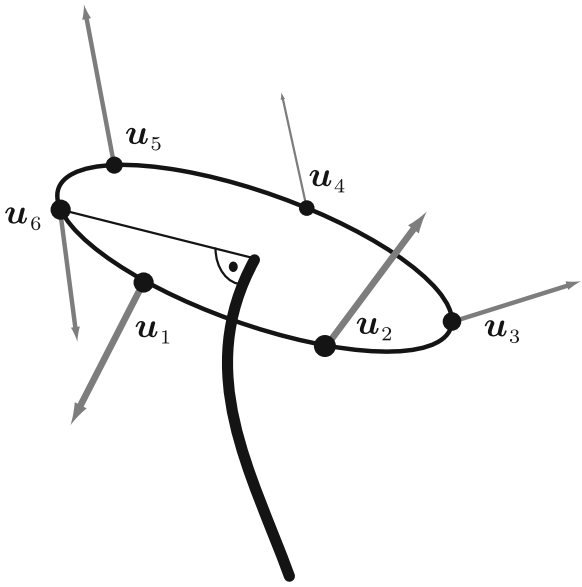

Fig. 12.10 The figure shows satellite particles placed in the plane perpendicular to the sprout migration direction. u_1 through u_6 describe the local migration cues at sprout particle location

events, the fusion of two tip cells and the fusion of a tip cell with an existing sprout. When a fusion event takes place, a loop is closed and migration stops for the fusing sprout tips.

4.5 ECM

We model the ECM as a collection of fiber bundles randomly distributed throughout the computational domain (see also Sect. 3.2). We introduce a three-fold representation of the ECM given by the grid-functions $\boldsymbol{F}$ describing the fiber orientations, E_χ, a smooth indicator function and the fiber density field E_ρ used to regulate the migration speed as defined in (12.17).

The procedure generating the fiber field follows the one described in Sect. 3.2. For the field $\boldsymbol{K}$ the fiber directions are rasterized onto the grid, and for E_χ we tag the grid points at the fiber locations with a value of 1.

$\boldsymbol{K}$ and E_ρ are filtered with a Gaussian filter to obtain a smooth matrix representation. The same is not possible for the vector field E_χ, so the field is constructed using smoothed fibers. For overlapping fibers, the maximum value of the two fibers is retained.

4.6 Methods

We suggest the application of a fractional step algorithm in order to solve the coupled reaction-diffusion system efficiently. In the suggested algorithm the nonlinear

and linear reaction parts of the equations are solved simultaneously using explicit Euler steps. To solve the linear diffusion part of the system, we employ implicit time stepping.

The reaction-diffusion system can be safely decoupled from the tip-cell advection, as EC cell migration occurs on a much larger time scale than molecular diffusion. Steady state can be assumed for the source and sink of the molecular species. Spatial gradients and the curvature measure are calculated on the grid using second order finite differences. We apply Mesh-Particle interpolations using the M_4' kernel (see Chapter Particle Simulations of Growth: Application to Tumorigenesis, Sect. 2.3) in order to approximate the acceleration and curvature at the tip particle location $\boldsymbol{x}_p = (x_p, y_p, z_p)$.

The Particle-Mesh interpolations of the sprout tip density onto the grid are performed using a 4th order B-spline kernel, guaranteeing positive values for [EC] at all grid locations.

4.7 Endothelial Cell Density

Capillary sprouts are defined by the endothelial cell density ρ. We obtain the endothelial cell density by interpolation of the sprout tip cell density Q_p at $\boldsymbol{x}_p$ onto the grid using a 4th order B-spline kernel B_4. The interpolation is done every time step, ρ is updated to the maximum of the interpolated sprout tips and the ρ field at the previous time step.

$$\rho_{ijk}^{n+1} = \max\left(\rho_{ijk}^{n}, \sum_p B_4\left(ih - x_p\right) B_4\left(jh - y_p\right) B_4\left(kh - z_p\right) Q_p\right), \quad (12.25)$$

with particle weight Q_p, and mesh size h. The grid value ρ_{ijk} denotes the cell density at grid point $[i, j, k]$ and n denotes the nth time step.

4.8 Parameters

All model equations are nondimensionalized by scaling the molecular concentrations c with a maximum threshold concentration c_0 of the respective species. The endothelial cell density [EC] is scaled with the close packing cell density $[\mathrm{EC}]_0$. Space and Time variables are scaled with the domain size D_l and D_l^2/k_V, respectively, where k_V is the VEGF diffusion coefficient.

We report the set of initial parameters in the table below. For a detailed description of the parameter values, we refer to Milde et al. (2008) and the works referenced therein.

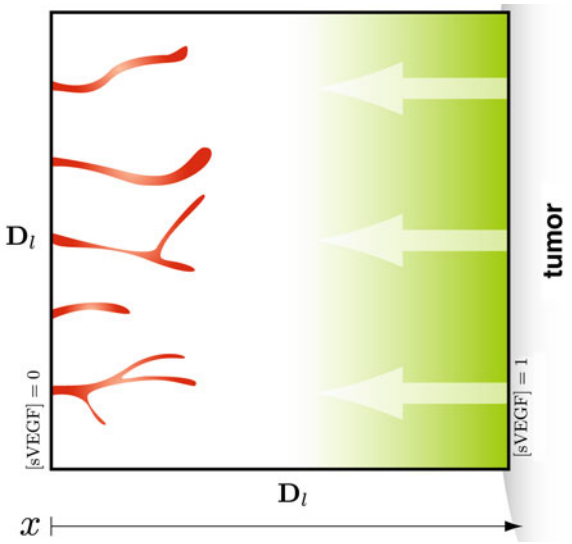

Fig. 12.11 The figure shows a conceptional $x - z$ plane through the computational domain. Five sprout tips are initially placed on the $y - z$ plane lower end of the domain in x direction, a tumor source of soluble VEGF is modeled at the upper end in x direction outside the computational domain

$$
\begin{aligned}
&k_V = 1.0 \quad \upsilon_{bV} = 100.0 \quad \upsilon_V = 0.0 \quad d_V = 0.675 \\
&k_F = 0.05 \quad \gamma_F = 113.0 \quad d_F = 67.5 \\
&\upsilon_{bF} = 1.0 \quad \delta_{bF} = 10.0 \quad d_{bF} = 0.675 \\
&k_M = 0.1 \quad \gamma_M = 113.0 \quad d_M = 0.1 \\
&bF_{th} = 0.5 \quad F_{th} = 0.001 \quad M_{th} = 1.0 \\
&w_V = 0.1 \quad w_{V2} = 0.5 \quad w_F = 0.001 \\
&D_l = 1.0 \quad Fb_l = 10.0 \quad sa_{th} = 5.0 \quad ai_{th} = 15.0 \\
&bV_l = 0.25 \quad bV_r = 0.008 \quad Q_p = 1.0
\end{aligned} \tag{12.26}
$$

Unless indicated along with the specific simulations, the results reported in this section are based on simulations using the above parameter value set.

4.9 Initial and Boundary Conditions

We define the computational domain as a cube of size D_l^3 discretized with a 128^3 uniform grid . At the beginning of the simulation, five vessel sprouts are placed along a line at $z = 0.5$ on the $y-z$ plane at $x = 0.0$, equally distributed in y. The precise locations of the sprouts are at $y = 0.15625, 0.3125, 0.46875, 0.625, 0.78125$ (see Fig. 12.11).

The tumor source of VEGF is modeled via a Dirichlet boundary condition in the x direction, with [sVEGF] $= 1.0$ at $x = 1.0$ and [sVEGF] $= 0.0$ at $x = 0.0$. All other concentrations are subject to homogenous Neuman boundary conditions

in the x direction. In y and z directions we apply periodic boundary conditions for all concentrations and the capillary sprout tips. Matrix bound VEGF pockets are distributed throughout the domain according to the distribution given by

$$\begin{pmatrix} x \\ y \\ z \end{pmatrix} = \begin{pmatrix} 0.1 + 0.9\sqrt{r_1} \\ r_2 \\ r_3 \end{pmatrix} \text{ with } r_1, r_2, r_3 \text{ u.a.r } [0, 1]\,. \tag{12.27}$$

The increase in concentration along the x axis accounts for the tumor source of VEGF. All sprouts leaving the domain in x direction are eliminated from the simulation.

4.10 Results

In the context of large scale parametric studies, we investigate the effects of the structure of the ECM and the distribution of matrix-bound VEGF and present results on the morphology of the generated vessel networks. The presented three-dimensional simulations are novel as they include explicitly soluble and bound growth factors. They account for the structural properties of the ECM and its binding sites and investigate their effects on endothelial cell migration. We quantify the simulation and report statistics on the branching and fusion events in combination with observable measures on the vascular trees such as the branch length distribution. We note that the statistics provide a quantitative, comparative analysis that may guide future experiments and simulations.

Matrix Structure In a first set of simulations, we asses the effect of the ECM density on the generated capillary networks. Different number of fiber bundles are distributed at random to create ECMs of increasing densities: 15,000 fibers resulting in a volume density of 6%, 30,000 fibers (11%), 70,000 fibers (26%), 100,000 fibers (38%), and 200,000 fibers (75%) (see Fig. 12.12). We report the normalized volume density of the matrix as the average density of the fiber density field E_ρ. For each case, we performed 32 simulations with a different random seed for the fiber placement.

Stopping the simulations at time $T = 22$ and comparing the number of branch points found in the computational domain, we find a linear increase of the number of branches for a logarithmic increase in the fiber density up to a threshold density around 40% (Fig. 12.13). After this saturation point, the number of branches can be observed to decrease again. We report examples of vessel network morphologies as observed for different matrix densities in Fig. 12.14. We note that in a low density ECM, branching is largely reduced while in very dense ECMs, branching events can be observed to happen very frequent. In the case of a very high fiber density (75%), we observe that the fiber density is high enough to impair cell migration, leading to shorter capillary networks (Fig. 12.14, E).

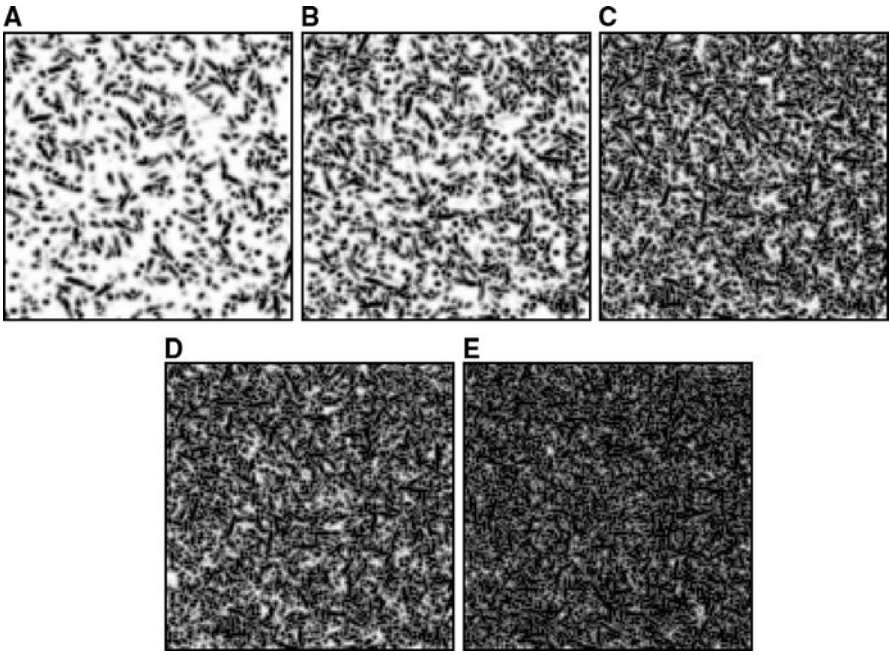

Fig. 12.12 Slice of the [ECM] field for five different densities: A 6%, B 11%, C 26%, D 38%, and E 75%

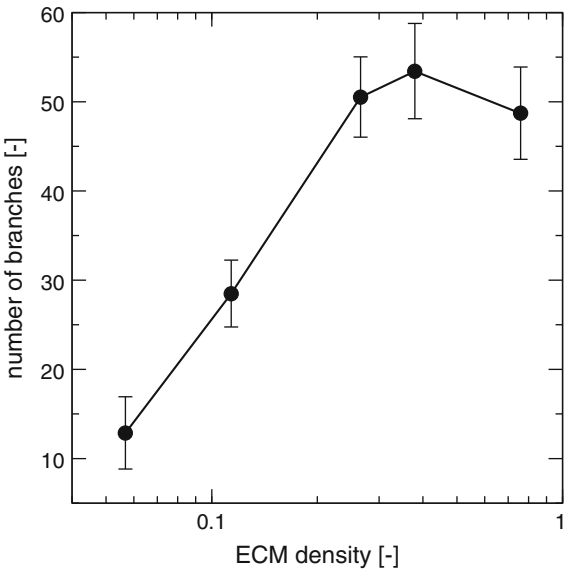

Fig. 12.13 Influence of the matrix density on the number of branches of the vessel network (error bars represent standard deviation of data)

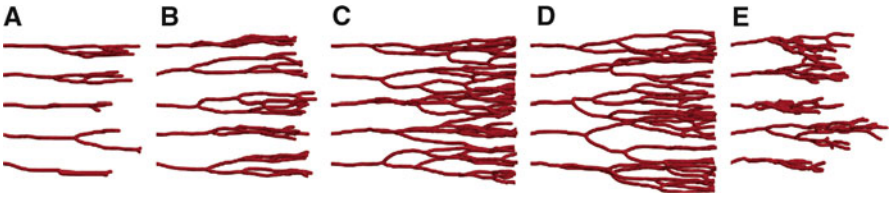

Fig. 12.14 Capillary networks for different ECM densities: 6% (A), 11% (B), 26 % (C), 38% (D), and 75% (E)

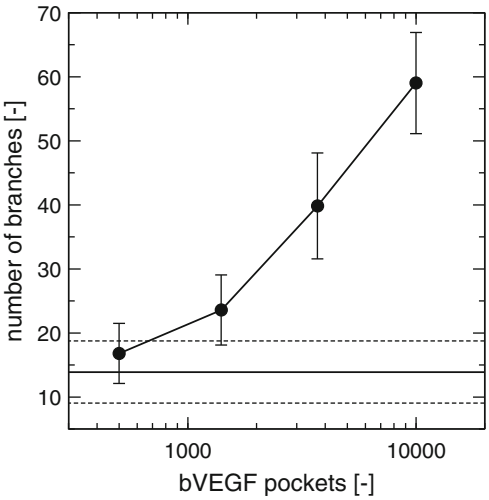

Fig. 12.15 Effect of number of VEGF pockets bV_n on the number of branches (error bars indicate standard deviation of the data). The horizontal line denotes the average number of branches for the case of no bound-VEGF, the dashed lines represent the standard deviation for that case

Matrix-Bound VEGF Focussing on the effect of matrix-bound VEGF pockets, we vary the amount of matrix-bound VEGF, by increasing the number of pockets, distributing 500, 1,400, 3,700 and 10,000 pockets holding a VEGF level of $bV_l = 0.25$. Investigating the effect of matrix-bound VEGF we decrease the threshold age for branching $sa_{th} = 4$ and increased the branching threshold level of anisotropy $ai_{th} = 45$ in all simulation. The parameters governing MMP evolution are set to: $k_M = 0.01$, $\gamma_M = 250$ and $d_M = 100$. In order to focus on the effects induced by matrix-bound VEGF, haptotaxis is completely switched off: $w_F = 0.0$. We observe that an increase in the number of pockets leads to an increase in the number of branching events (see Fig. 12.15).

The pockets induce strong local gradients (Fig. 12.16), increasing the measured curvature k at the pocket location. For high pocket densities, the probability for cells to hit a pocket location is increased, consequently leading to an increase in branching. The presence of a higher pocket density, the probability of a sprout tip hitting a pocket is amplified, consequently leading to an increase in branching.

In a second set of simulations, we varied the VEGF level, comparing runs with constant number of 3,700 pockets containing a VEGF level of $bV_l = 0.01, 0.03, 0.09$ and 0.25 (not shown here) (Milde et al. 2008). Again, we

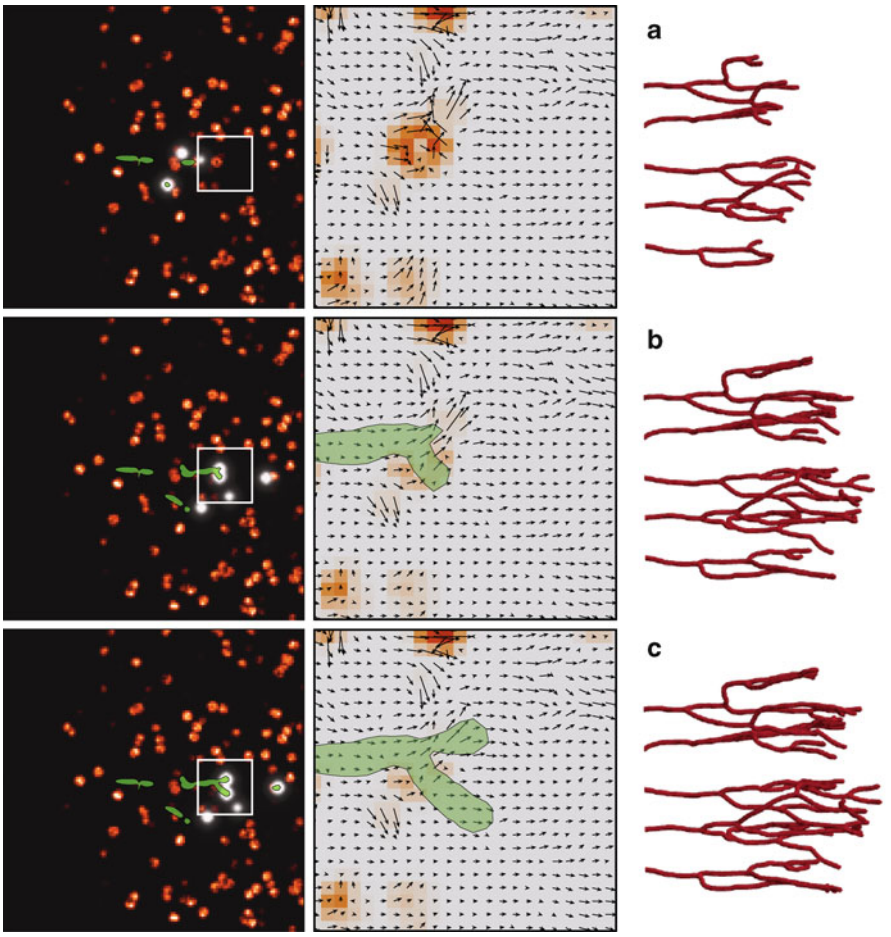

Fig. 12.16 Effect of MMPs cleaving matrix-bound VEGF on chemotactic cues and anisotropy at pocket location for bV_n =3,700 and bV_l = 0.25: t = 13.21 (A), t = 16.89 (B) and t = 20.63 (C). The *white clouds* in the *left figure* denote the MMP concentration, the *orange dots* indicate pockets of matrix-bound VEGF. The figure in the *middle shows* the evolution of the acceleration field at pocket location

observe an increase in branching along with an increase in the VEGF level. The results indicate that not only the density of bound VEGF but also the pocket level has an effect on branching behavior. Here, the effect can not be attributed to the increase in the probability of a sprout tip hitting a pocket but to the MMPs cleaving the matrix-bound VEGF, effectively reducing the chemotactic cues together with the level of anisotropy at pocket location (see Fig. 12.16).

As pockets are being cleaved, their influence on the branching and migration behavior is reduced. In the case of low pocket VEGF concentrations, the cleaving removes most VEGF from the pocket before the sprout tips get there. Thus, the

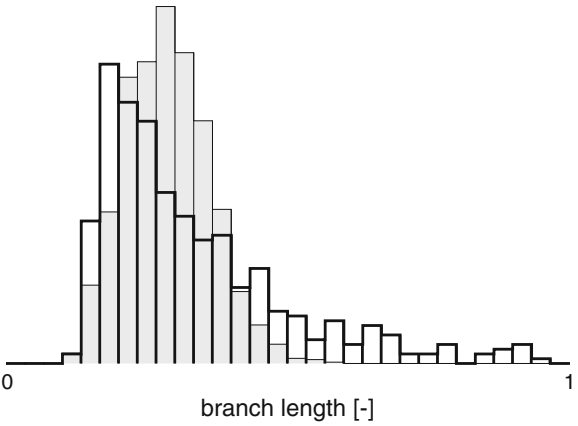

Fig. 12.17 Histogram of branch lengths for no bound VEGF (*white bars*), and 100,000 VEGF pockets (*gray bars*)

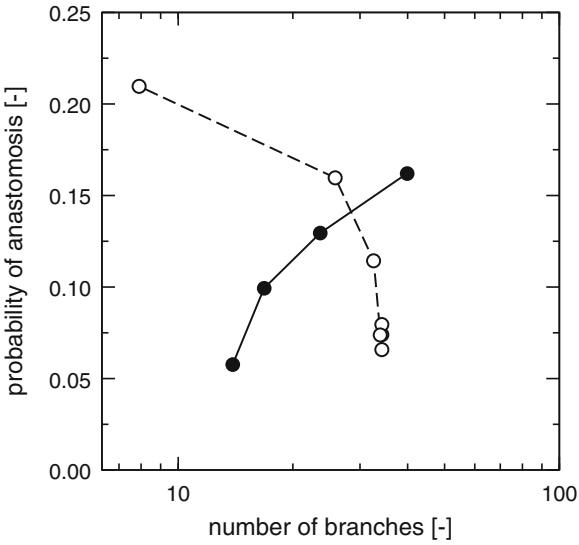

Fig. 12.18 Relationship between the average number of branches and the probability of anastomosis: varying the number of bound-VEGF pockets (*full circles*), and increasing haptotaxis (*white circles*)

influence of bound VEGF levels on the observed branching behavior. As for the branch length distributions in the absence of bound VEGF as compared to the case of 100,000 distributed pockets (see Fig. 12.17), no significant variation is observed in the mean.

However, the distributions for the two cases vary notably, showing a narrower distribution of the branch lengths in the presence of bound VEGF pockets. Concerning the probability of anastomosis, we found that an increase in the number of distributed VEGF pockets leads to an increase in the number of fusion events (not shown here).

A similar effect has been observed for an increase in the weight of haptotactic cues (results reported in Milde et al. (2008)). If however we compare the probability of anastomosis against the number of branches, we find that the two simulation settings having quite a different effects on the fusion probability (see Fig.12.18).

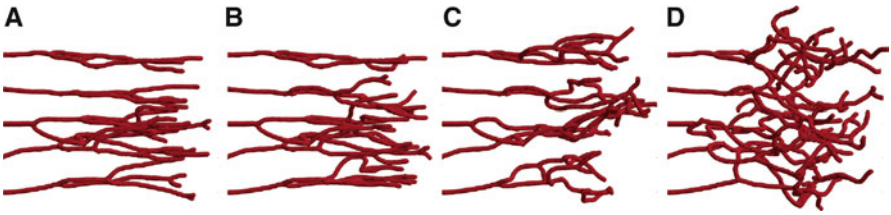

Fig. 12.19 Effect of pocket number of matrix-bound VEGF (bV_n) on the vessel network morphology: $bV_n = 500$ (A), $bV_n = 1{,}400$ (B), $bV_n = 3{,}400$ (C), and $bV_n = 10{,}000$ (D)

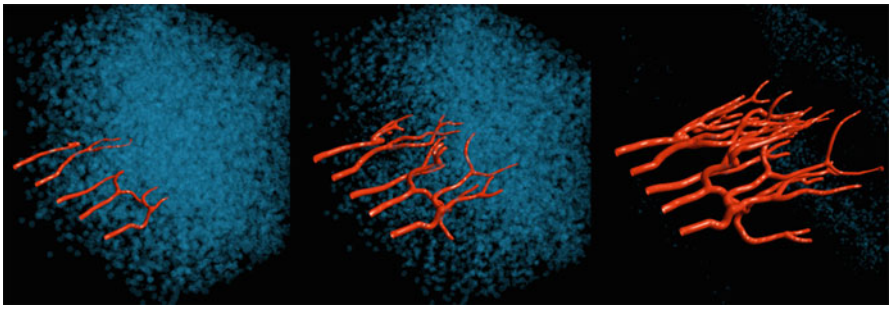

Fig. 12.20 Evolution of angioegenesis (*red*) in the presence of matrix bound VEGF (*blue*). Bound VEGF is cleaved by MMPs (not shown)

The morphology of the vessels (Figs. 12.19, 12.20) suggests that the distributed VEGF pockets attract the migrating sprout tips, leading to a deviation in the migration projectory, whereas the haptotactic cues introduce directed deviation towards existing sprouts (not shown here) (Milde et al. 2008).

4.11 Conclusions

We present a three-dimensional model of sprouting angiogenesis that incorporates the effects of the extracellular matrix structure on the vessel morphology and considers both soluble and matrix-bound growth factor isoforms. Conducted over large scale parametric studies, we report observations on the vessel network morphology as influenced by the structure of the ECM and the distribution of matrix-bound VEGF. The reported results stress the importance of the implicit consideration of an ECM, as its structure and density directly affect the morphology, expansion speed and the branching dynamics of the computationally grown capillary networks. As has been observed experimentally in Friedl and Bröcker (2000); Davis and Senger (2005); Serini et al. (2006), the simulations reflect the strong influence of the ECM composition on the process of angiogenesis. Simulation results on sprout morphology and branching patterns presented for sprouting angiogenesis

in the presence of matrix-bound VEGF isoforms are consistent with the findings made in Lee et al. (2005); Ruhrberg et al. (2002). We would like to stress that with the number of branches depending on the matrix structure and the presence of matrix-bound VEGF isoforms, the model may be easier to tune against experiments compared to branching probabilities that most individual-based methods employ. The grid independent particle representation of migrating tip cells leads to the generation of smooth capillary networks. The coupling of the particle and mesh-based representation is straightforward in the context of Particle to Mesh and Mesh to Particle interpolation schemes. Limitations of the current model are related to the explicit initialization of tip cells at predefined locations. New sprout tips can only emerge at the sprouting tip via branching.

References

Alberts B, Bray D, Lewis J, Raff M, Roberts K, & Watson J. D (2002) Molecular Biology of the Cell Garland Science, New York, 4th edition

Anderson A. R. A, & Chaplain M. A. J (1998) Continuous and Discrete Mathematical Models of Tumor-induced Angiogenesis Bull. Math. Biology, 60:857–900

Armstrong N. J, Painter K. J, & Sherratt J. A (2006) A continuum approach to modeling cell-cell adhesion J. Theor. Biol., 243(1):98–113

Axelson H, Fredlund E, Ovenberger M, Landberg G, & Pahlman S (2005) Hypoxia-induced dedifferentiation of tumor cells - A mechanism behind heterogeneity and aggressiveness of solid tumors; Biology of Hypoxia and Myogenesis and Muscle Disease Seminars in Cell & Developmental Biology, 16(4-5):554–563

Bauer A. L, Jackson T. L, & Jiang Y (2007) A Cell-Based Model Exhibiting Branching and Anastomosis during Tumor-Induced Angiogenesis Biophys. J.,92(9):3105–3121

Chaplain M. A (2000) Mathematical modeling of angiogenesis. J Neurooncol, 50(1-2):37–51

Davis G. E, & Senger D. R (2005) Endothelial Extracellular Matrix: Biosynthesis, Remodeling, and Functions During Vascular Morphogenesis and Neovessel Stabilization Circulation Research, 97(11):1093–1107

Ferrara N, Gerber H.-P, & LeCouter J (2003) The biology of VEGF and its receptors Nat Med, 9:669–676

Folkman J (2006) Angiogenesis Annual Review of Medicine, 57(1):1–18

Folkman J (2007) Angiogenesis: an organizing principle for drug discovery? Nat Rev Drug Discov, 6(4):273–286

Friedl P, & Bröcker E. B(2000) The biology of cell locomotion within three-dimensional extracellular matrix Cellular and Molecular Life Sciences (CMLS), 57(1):41–64

Gerhardt H, Golding M, Fruttiger M, Ruhrberg C, Lundkvist A, Abramsson A, Jeltsch M, Mitchell C, Alitalo K, Shima D, & Betsholtz C (2003) VEGF guides angiogenic sprouting utilizing endothelial tip cell filopodia The Journal of Cell Biology, 161(6):1163–1177

Hanahan D, & Weinberg R. A (2000) The Hallmarks of Cancer Cell, 100(1):57–70

Iruelaarispe M. L, Hasselaar P, & Sage H (1991) Differential expression of extracellular proteins is correlated with angiogenesis invitro Labratory Investigation,64(2):174–186

Kearney J. B, Kappas N. C, Ellerstrom C, DiPaola F. W, & Bautch V. L (2004) The VEGF receptor flt-1 (VEGFR-1) is a positive modulator of vascular sprout formation and branching morphogenesis Blood, 103(12):4527–4535

Kirkpatrick N. D, Andreou S, Hoying J. B, & Utzinger U (2007) Live imaging of collagen remodeling during angiogenesis AJP - Heart and Circulatory Physiology, 292(6):H3298–H3206

Lee S, Jilani S. M, Nikolova G. V, Carpizo D, & Iruela-Arispe M. L (2005) Processing of VEGF-A by matrix metalloproteinases regulates bioavailability and vascular patterning in tumors J. Cell Biol., 169(4):681–691

Levine H. A, Sleeman B. D, & Nilsen-Hamilton M (2001) Mathematical modeling of the onset of capillary formation initiating angiogenesis Journal of Mathematical Biology, V42(3):195–238

McDougall S. R, Anderson A. R. A, & Chaplain M. A. J (2006) Mathematical modeling of dynamic adaptive tumour-induced angiogenesis: Clinical implications and therapeutic targeting strategies Journal of Theoretical Biology, 241(3):564–589

Mignatti P, & Rifkin D. B (1993) Biology and biochemistry of proteinases in tumor invasion Physiological Reviews, 73(1):161–195

Milde F, Bergdorf M, & Koumoutsakos P (2008) A Hybrid Model for Three-Dimensional Simulations of Sprouting Angiogenesis Biophysical Journal, 95(7):3146–3160

Paweletz N, & Knierim M (1989) Tumor-related angiogenesis; Critical Reviews in Oncology/ Hematology, 9(3):197–242

Pennacchietti S, Michieli P, Galluzzo M, Mazzone M, Giordano S, & Comoglio P. M (2003) Hypoxia promotes invasive growth by transcriptional activation of the met protooncogene Cancer Cell, 3:347–361

Plank M, & Sleeman B(2004) Lattice and non-lattice models of tumour angiogenesis Bulletin of Mathematical Biology, 66(6):1785–1819

Ruhrberg C, Gerhardt H, Golding M, Watson R, Ioannidou S, Fujisawa H, Betsholtz C, & Shima D. T(2002) Spatially restricted patterning cues provided by heparin-binding VEGF-A control blood vessel branching morphogenesis Genes Dev., 16(20):2684–2698

Saharinen P, & Alitalo K (2003) Double target for tumor mass destruction Journal of Clinical Investigation, 111(9):1277–1280

Serini G, Valdembri D, & Bussolino F (2006) Integrins and angiogenesis: A sticky business Experimental Cell Research, 312(5):651–658

Steinberg M, & Takeichi M (1994) Experimental Specification of Cell Sorting, Tissue Spreading, and Specific Spatial Patterning by Quantitative Differences in Cadherin Expression Proceedings of the National Academy of Sciences, 91(1):206–209

Steinberg M. S (2007) Differential adhesion in morphogenesis: a modern view Curr. Opin. Genet. Dev., 17(4):281–286

Sun S, Wheeler M. F, Obeyesekere M, & Patrick C. W, Jr. (2005) A deterministic model of growth factor-induced angiogenesis Bulletin of Mathematical Biology, 67:313–337

Taraboletti G, D'Ascenzo S, Dolo V, Giusti I, Marchetti D, Borsotti P, Millimaggi D, Giavazzi R, Pavan A, & Dolo V (February 2006) Bioavailability of VEGF in Tumor-Shed Vesicles Depends on Vesicle Burst Induced by Acidic pH Neoplasia, 8:96–103(8)

Weinkauf T, & Theisel H (2002) Curvature Measures of 3D Vector Fields and their Applications In Skala V (ed), Journal of WSCG, volume 10, pages 507–514

Chapter 13
Blood Vessel Network Remodeling During Tumor Growth

Michael Welter and Heiko Rieger

1 Introduction

Tumor vasculature, the blood vessel network supplying a growing tumor with nutrients like oxygen or glucose, is in many respects different from the hierarchically organized arterio-venous blood vessel network in normal tissues. In order to grow beyond a size of approximately 1–2 mm^3 the tumor has to switch to an angiogenic phenotype and to induce the development of new blood vessels mainly via sprouting angiogenesis, i.e., the formation of new vessels from pre-existing vasculature (Carmeliet and Jain 2000). This process is regulated by a variety of pro- and anti-angiogenic factors and as a consequence the anatomy of a solid, vascularized tumor grown within in a vascularized tissue displays a characteristic compartmentalization into essentially three regions (Holash et al. 1999a,b; Döme et al. 2002, 2007): (1) The highly vascularized tumor perimeter with a microvascular density (MVD) that is substantially higher than the MVD of the surrounding normal tissue. (2) The well vascularized tumor periphery with dilated blood vessels and a tortuous vessel network topology. (3) A poorly vascularized tumor center with large necrotic regions threaded by only a few very thick vessels that are surrounded by a cuff of viable tumor cells.

Several microscopic phenomena on the cellular level have been identified to be involved in this remodeling process: (1) *Angiogenic sprouting:* Up-regulation of pro-angiogenic factors in tumor-cells (like vascular endothelial growth factor, VEGF, and other growth factors) can create additional vessels via sprouting angiogenesis in some regions of the tumor, most frequently in its perimeter (Carmeliet and Jain 2000). (2) *Vessel regression:* The maintenance of incorporated mature microvessels depends on the survival of endothelial cells (ECs) and their

M. Welter • H. Rieger (✉)
Theoretische Physik, Saarland University, PF 151150, 66041 Saarbrucken, Germany
e-mail: mwelter@lusi.uni-sb.de; h.rieger@mx.uni-saarland.de

T.L. Jackson (ed.), *Modeling Tumor Vasculature: Molecular, Cellular, and Tissue Level Aspects and Implications*, DOI 10.1007/978-1-4614-0052-3_13,

survival is intimately tied to their local microenvironment and, in particular, to the presence of pericytes, survival promoting cytokines, and extracellular matrix proteins. The major molecular players that control this process are angiopoietins and VEGF (Holash et al. 1999a,b), and in coopted blood vessels Ang-2 is up-regulated, causing the destabilization of their capillary walls, i.e the detachment of pericytes from the endothelial tube (Holash et al. 1999a,b). Once ECs are separated from pericytes, they become particularly vulnerable resulting in the regression of destabilized vessels. (3) *Vessel dilation:* The vascularization program of the pro-angiogenic phenotype can be switched from sprouting angiogenesis to circumferential growth in the interior of the tumor. This switch is mediated by the guidance molecules EphB4 (and its ligand ephrinB2), both expressed by ECs of malignant brain tumors (Erber et al. 2006), which acts as a negative regulator of blood vessel branching and vascular network formation, and also reduces the permeability of the tumor vascular system via activation of the Ang-1/Tie-2 systems at the endothelium/pericyte interface.

Besides pro- and anti-angiogenic molecular factors physical determinants like mechanical, hydrodynamical, and collective processes are involved in the process that transforms or remodels the original arterio-venous blood vessel network into a tumor specific vasculature. Theoretical modeling can help to quantify the influence of the various factors determining this complex multiscale phenomenon. For recent reviews see Tracqui (2009) and Lowengrub et al. (2010) and references therein. Earlier work focusing on tumor induced angiogenesis can roughly be divided into three categories: (1) continuum models without a proper representation of a blood vessel network and blood flow (Balding and McElwain 1985; Chaplain and Stuart 1993; Chaplain et al. 1995; Byrne and Chaplain 1995; Holmes and Sleeman 2000), (2) hybrid models with a fixed vessel network geometry and a dynamically evolving tumor (Alarcon et al. 2003; Betteridge et al. 2006; Owen et al. 2008; Shirinifard et al. 2009), and (3) hybrid models with a fixed tumor (as a source of a diffusing growth factor) and a dynamically evolving tumor vasculature starting from a single parent vessel far away from the growth factor source (Anderson and Chaplain 1998; McDougall et al. 2002; Stephanou et al. 2005; McDougall, Anderson and Chaplain 2006). The latter models are also denoted as vessel-ingrowth models because the whole tumor vasculature grows from outside toward the tumor surface. Subsequent work was still inspired by these vessel-in-growth models (Zheng et al. 2005; Frieboes et al. 2007; Wise et al. 2008; Macklin et al. 2009): although in these studies the tumor also evolved dynamically, focusing on a detailed analysis of the interactions between tumor and host tissue, all new vessels started to grow from one or more parent vessels in a nonphysiologically far distance from the tumor. The remodeling process that transforms the original arterio-venous vasculature of the host tissue into a tumor specific vessel network has not been addressed with this Ansatz.

Bartha and Rieger (2006) hypothesized that the fundamental characteristics of the remodeling process and the emerging tumor vasculature is predicted by a model that comprises, besides the representation of a growing tumor, a sufficiently dense initial vasculature and three basic dynamical mechanisms – angiogenic

sprouting, blood flow correlated vessel regression and vessel dilation. Indeed, the compartmentalization of the tumor as well other global features, like the time and radius dependencies of average MVD, tumor cell density, vessel radius and blood flow characteristics were predicted in good agreement with experimental data. These predictions were confirmed for varying grids in two space dimensions (2d) (Welter et al. 2008) and three space dimensions (3d) (Lee et al. 2006) as well as for arterio-venous initial vessel networks in 2d (Welter et al. 2009) and 3d (Welter and Rieger 2010). For arterio-venous initial networks even local characteristics like the conditions for the formation of hot spots and spatial heterogeneities could be identified. In this chapter we want to survey these results for the dynamical evolution, final morphology and blood flow properties of tumor blood vessel networks and present a critical comparison of the various model variants.

2 Model Definition

A network which is distributed homogeneously over the system domain serves as the initial vasculature for the model of remodeling by a growing tumor. Configurations based on regular lattices (Bartha and Rieger 2006; Lee et al. 2006) akin to capillary beds as well as hierarchical organizations (Welter et al. 2009) which mimic arterio-venous vasculatures were used. These networks are blood perfused and represent sources of oxygen.

Depending on the local oxygen concentration tumor cells represent the sources of the diffusion determined growth factor (GF) concentration field, which triggers either the generation of tip cells for angiogenic sprouting from existing vessels outside or at the periphery of the tumor, or circumferential growth within the tumor (for potential molecular mechanisms for this switch in the angiogenic program within the tumor see (Erber et al. 2006)). In contrast to vessel in-growth models as in Anderson and Chaplain (1998) tip-cells are not dominantly generated by branching of existing tip-cells but by sprouting from vessels of the original network. Lateral inhibition leads to a minimum spatial distance in a vessel segment between individual tip cell generation events (Bentley et al. 2008).

Tip cells migrate in the direction of a sufficiently large GF gradient (chemotaxis), otherwise randomly. The path they describe is supposed to be filled with stalk cells forming a lumen and finally, once the tip cell hits another vessel (anastomosis), a functional vessel carrying blood flow is formed. Due to the pre-existing vasculature vessels typically migrate only 50–100 μm before the filopodia of the tip-cell extending up to 20–30 μm into the surrounding tissue in all directions (Gerhardt et al. 2003) touch another vessel. Therefore, directional cues are not as important here as in pure vessel in-growth models. Moreover, tip cells which fail to make successful contact with another vessel migrate maximally 100–150 μm and retreat afterward (Nehls et al. 1998).

Inside the tumor, vessels destabilize and regress (for the potential molecular determinants of this destabilization see (Holash et al. 1999a,b)). In our model an increasing contact time of vessels with tumor cells, implying an increasing residence time within the tumor, leads to a higher collapse probability of tumor vessels. The collapse probability is also correlated with the origin of the vessel (artery, vein or capillary) and the shear force exerted by the blood flow upon the vessel walls (Dimmeler and Zeiher 2000).

2.1 Configuration Space

The state of the model is defined by the state of the discrete vessel network and the continuum fields for a nonspecific growth factor concentration g, oxygen concentration o, and tumor-cell density c.

The vessel network can be described as a graph where edges represent vessel segments and nodes represent potential branching points, respectively. This graph is embedded in a regular lattice with the lattice constant Δl, which means that the nodes are located at the lattice sites and edges are coincident with the lattice edges. Edges and Nodes are dynamically created and destroyed over time. In Addition they have attached dynamically varying biophysical properties.

2.2 Blood Flow

In order to determine blood flow, the edges of the network are regarded as ideal pipes with radius r, wall shear stress f and blood flow rate q. Consequently, q is determined by Poiseuille's law $q \propto r^4/\eta\Delta p$, where Δp is the hydrostatic pressure difference between the end points. The viscosity η is radius dependent, following Pries et al. (1994), for simplicity under the assumption of a homogeneous hematocrit of 0.45. Conservation of mass holds, meaning that the sum of all flow rates (with the appropriate sign) at each node must equal zero. With the addition of boundary conditions which in our model consist of prescribing the pressure p at some nodes, one obtains a well defined system of linear equations, which is solved numerically. The selection of these boundary nodes depends on the type of initial network. In arterio-venous networks the top-level root nodes are used (Welter et al. 2009). In regular networks the pressure is prescribed at the system boundary to increase linearly from one corner of the domain to the opposite corner (Bartha and Rieger 2006).

2.3 Tumor Cell Density

In previous work Bartha and Rieger (2006), Lee et al. (2006), and Welter et al. (2009) used a discrete cellular automaton model. There individual tumor cells are represented as sites on a lattice and cell proliferation and tumor expansion are akin to eden growth with the additional constraint that sufficient oxygen must be available at proliferating sites. See the references above for a complete description.

Here and in Welter and Rieger (2010) the model for the tumor is defined based on a continuum approach for the tumor cell density $c(\mathbf{r}, t)$. Under stress-free conditions without cell proliferation and death the tumor cell density is $c^{(norm)}$, which we assume to be $1/10\ \mu\text{m}^3$ reflecting a typical lateral size of tumor cells of $10\ \mu$m. The dynamical evolution of the tumor cell density in the presence of cell proliferation and death is assumed to be given by a reaction-diffusion equation

$$\partial c/\partial t = -\nabla \cdot J + c^+ + c^-, \tag{13.1}$$

where J is the tumor cell flux and c^+ and c^- are source and sink terms describing cell proliferation and death, respectively.

In the following c^+, c^-, and J are defined: We assume that tumor cells need sufficient oxygen to proliferate, which means that the local oxygen concentration o must exceed the threshold $o_{TC}^{(prol)}$, else $c^+ = 0$. Moreover, we assume that a maximum packing density $c^{(max)}$ exists where cells are compressed so that they cannot proliferate further. We use the simplest expression to reflect that:

$$c^+ = 1 \Big/ t_{TC}^{(prol)} c \left(1 - \frac{c}{c^{(max)}}\right) \quad \text{if } o \geq o_{TC}^{(prol)} \quad \text{else } 0, \tag{13.2}$$

where $t_{TC}^{(prol)}$ is the mean proliferation time of unconstrained cells. Furthermore, we assume cells undergo apoptosis with the constant death-rate $1/t_{TC}^{(death)}$ if the local oxygen level o drops below $o_{TC}^{(death)}$. The model includes this by the definition of c^-:

$$c^- = -1 \Big/ t_{TC}^{(death)} c \quad \text{if } o < o_{TC}^{(death)} \quad \text{else } 0. \tag{13.3}$$

For simplicity interaction with the resulting cellular debris is neglected. In the following the cell-flux J is defined. We assume that cells migrate only in response to compression. Therefore, a phenomenological "solid pressure" P is introduced. Its equation of state depends on the cell density c as follows: Below the density $c^{(norm)}$ cells are not compressed, thus feel no forces, thus we set $P = 0$ for $c \leq c^{(norm)}$. Else we define P as linear function which is zero for $c = c^{(norm)}$ and increases to $P = 1$ for $c = c^{(max)}$. In the style of Darcy's law, momentum terms in the equations of motion are neglected so that the cell migration speed is proportional to the driving force, which means that

$$J = -Dc\nabla P, \tag{13.4}$$

where D is an additional mobility constant. The cell density cannot exceed $c^{(max)}$ because there are no external forces and $c^+ \to 0$ for $c \to c^{(max)}$ even though P remains finite.

In the general framework of such a model it would be possible to add cell-cell adhesion. In this case one would consider volume fractions of other species, e.g., normal tissue and necrotic tissue which interact via a free energy potential. See Frieboes et al. (2007, and the references therein). The result is an effective surface tension force. Combined with expansive forces which drive the tumor rim outward it can cause a fingering instability. In our simpler model where we have omitted such forces, tumor cells move diffusively opposed to their density gradient. As tissue oxygenization is homogeneous on a coarse scale this results in approximately spherically growing tumors. Biologically, our model corresponds to a situation where tumor cells adhere to each other as much as to other cells. Also the tumor can expand without significant resistance from the surrounding tissue. We can justify this because (1) not all tumors exhibit fingering instabilities, (2) we consider small tumor of less than 1 cm diameter and (3) pH level changes can happen that kill normal cells.

Later we compare our results with experimental data from melanoma. To accommodate the model to this specific tumor type, which can extend through multiple skin layers from the surface to muscle tissue, it would be straight forward to include inhomogeneous and/or anisotropic environments. We would expect this to trigger a different front shape of the growing tumor. However, we think – as is the case with a "fingering" tumor – that the characteristics of the blood vessel network in which we are interested would be invariant with respect to such additions.

In order to identify necrotic regions, we record the maximum local TC density over time. If the current TC density is zero and there were TCs in the past, we consider the location to be necrotic. On the basis of the rest of our framework, there are no forces that would impose interesting dynamics on the shape of necrotic regions. Thus, we use this crude approximation.

The equations are discretized with a simple explicit finite volume scheme on a cubic grid with 30 μm grid-cell size. We compute the fluxes through the cell faces separately. Knowing the fluxes, $\nabla \cdot J$ in (13.1) is discretized using a convective upwind scheme. To ensure stability, the time step for the integration is 0.1 h, whereas the updates of the rest of the system (see later) are done in 1 h steps.

2.4 Oxygen Concentration Field

The time scale for oxygen diffusion to reach a stationary state is of the order of seconds whereas the times scale for tumor cell proliferation, tip cell migration and endothelial cell proliferation is of the order of hours. Therefore, we use for the oxygen concentration the quasi-static solution o of the diffusion equation, which

adopts instantaneously any change in the source (vessels) and sink (tumor cells) configuration:

$$0 = \nabla^2 o - \gamma_o o + \alpha_o \left(o^{(B)} - o\right), \tag{13.5}$$

where γ_o is a consumption rate coefficient, $o^{(B)}$ the blood oxygen level, and α_o a source coefficient. γ_o is a linear combination of the tissue specific constants $\gamma_o^{(norm)}$, $\gamma_o^{(tum)}$, and $\gamma_o^{(necro)} = 0$, for normal tissue, tumor tissue and necrotic regions, respectively. The definition of the density parameters implies that necrotic areas inside the tumor do not consume oxygen. The factor α_o determines the amount of extravasated oxygen per concentration difference at the vessel wall. It is defined as permeability times wall surface area per concentration and tissue volume. For simplicity, it assumes a constant value for all blood circulated vessels. $o^{(B)}$ is the oxygen concentration in blood plasma, for which local variations are also neglected.

The coefficients γ_o and α_o comprise the diffusion constant and therefore it does not appear in (13.5). We estimate γ_o based on the diffusion range R_o of oxygen around isolated vessels found in tumors. Therefor we use that a delta peak as source distribution generates an exponentially decaying radial profile $\exp(-x\sqrt{\gamma_o})$. Thus, R_g is of the order of $1/\sqrt{\gamma_o}$. The parameter $o^{(B)}$ is determined such that, given γ_o, the concentration in between vessels is ca. 50% of the concentration at the vessel wall.

2.5 Growth Factor Concentration Field

The growth factor concentration g is computed by a Greensfunction-like method. Underoxygenized tumor cells, which means that locally $o < o_{TC}^{(prol)}$, produce growth factor with a constant rate. It diffuses through the tissues and degrades with a constant rate. Therefore, each source cell produces an exponentially decaying distribution. Thus, we can write g as

$$g(\boldsymbol{x}) = \int \mathrm{d}^3\boldsymbol{x}\prime \; G\left(||\boldsymbol{x}\prime - \boldsymbol{x}||\right) \; \theta\left(o_{TC}^{(prol)} - o\left(\boldsymbol{x}\prime\right)\right) \; c\left(\boldsymbol{x}\prime\right), \tag{13.6}$$

where θ is the Heaviside step function. For simplicity we define $G(x) \propto \max(0, 1 - x/R_g)$ as a linearly decaying normalized function which vanishes at $x = R_g$, where R_g is a "diffusion range" and limits the region where angiogenesis is induced.

2.6 Vessel Network Remodeling Dynamics

The evolution of the network is subject to three stochastical processes: sprout initiation, sprout migration and collapse as well as continuous wall degeneration and vessel dilation (Fig. 13.1). The definition of these processes closely follows the

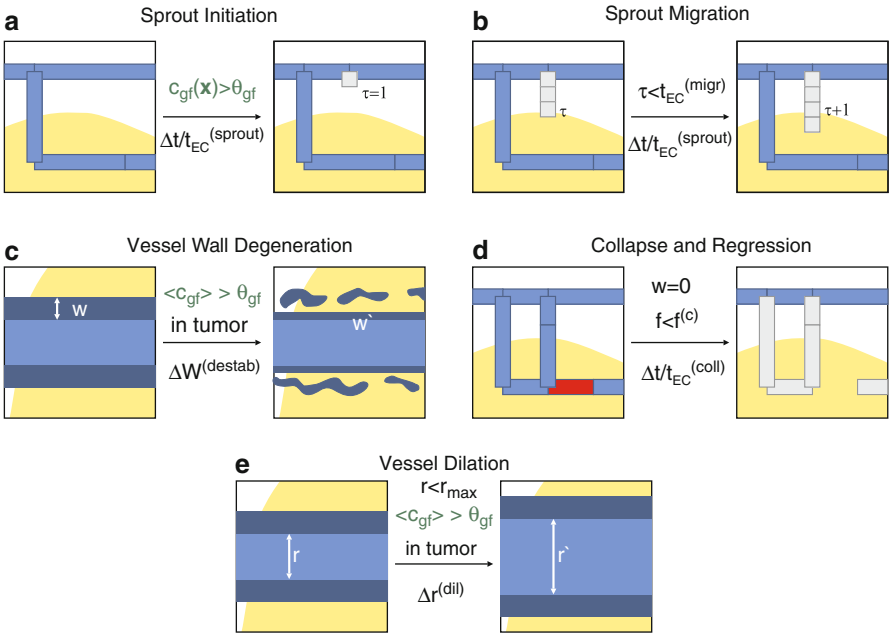

Fig. 13.1 Illustration of the vessel network remodeling processes. The contents of the *boxes* display exemplified states of the vessel network. The vessel segments are shown as *blue boxes* if perfused with blood, else they are in a *gray shade*. The *dark-blue* borders represent vessel walls of varying thickness and detached cells (in **c**). The presence of a tumor is hinted at by a *yellow mass*. The state transitions go from left to right as indicated by the *arrows*, whereby the rate parameter is denoted below- and essential preconditions above the *arrows*. In (**a**) a new sprout is generated by potentially splitting an existing segment, adding a node and adding the new sprout segment. In (**b**) the sprout is extended by adding further segments to its tip. (**c**) Vessel walls degenerate within the tumor due to detachment of support cells. This is modeled by a decreasing maturation parameter and depicted here as decreasing wall strength and surrounding debris. (**d**) Vessel regression is modeled by removal of segments with critically low shear-force (indicated by the *red segment*). This can disrupt blood flow over large sections, leaving many noncirculated vessels, which will also regress within a very short time scale. (**e**) Within the tumor vessels dilate. (See text for details.)

definition in Welter et al. (2009), where 2d networks are considered. Therefore, we only give a brief description here and refer in particular for the biological motivation of the details to Welter et al. (2009).

Sprout initiation: A new vessel segment can be added with probability $\Delta t / t_{EC}^{(sprout)}$ at any location on the network if the local growth factor concentration is nonzero, the distance to the next branching point is less than $l^{(spr)}$ and the time spent within the tumor is less than $t_{EC}^{(switch)}$. "Within" the tumor is defined as $\langle c \rangle > c^{(norm)}/2$ averaged over the segment. The sprout segment occupies an edge on the lattice (length Δl) and points in the direction of the largest growth factor increase.

Sprout migration: These new segments are tagged as sprouts which has the following implications. Segments are appended to the current tip with probability $\Delta t / t_{EC}^{(sprout)}$, extending the original sprout. Sprouts can also spawn sub-sprouts like normal vessels can. But they are excluded from the collapse, degeneration and circumferential growth mechanisms. Sprouts are untagged and become normal vessels if the tip fuses with another vessel such that blood can flow, or if their respective life-time variable τ, which every sprout has attached, reaches its predefined maximum $t_{EC}^{(migr)}$. If the tip fuses with another sprout without creating a conducting branch, the involved segments remain tagged.

Wall degeneration: The structural support provided by the cell layers surrounding the endothelial cells is represented by the wall stability variable w. For new vessels and the original vasculature it is initialized with the wall-thickness of healthy vessels (Welter et al. 2009). For vessels inside the tumor its value decreases at the constant rate Δw until zero.

Vessel collapse: A segment can be removed with probability $\Delta t / t_{EC}^{(coll)}$ if its wall stability variable w is zero and the wall shear stress f is below the threshold $f^{(coll)}$.

Vessel dilation: The vessel radius r increases at the constant rate k_r if $r < r^{(max)}$, the average growth factor concentration over the segment is nonzero and if the time spent within the tumor is larger than $t_{EC}^{(switch)}$.

Per time step ($\Delta t = 1$ h), a Monte-Carlo sweep is done per stochastical process and all continuous variables and fields are advanced in time. The parameter values that we use throughout the paper are given in Table 13.1 (references to physiological data are given in (Bartha and Rieger 2006; Welter et al. 2008, 2009)).

The model is stable with respect to parameters as our observables vary smoothly with parameter deviations. For brevity we omit a analysis here. In previous papers Bartha and Rieger (2006) and Welter et al. (2008) discussed variations for 2d models which are also relevant for the present study.

2.7 Arterio-Veneous Tree Construction

A normal vasculature is hierarchically organized. Arterial and venous trees provide the supply and drainage system for the capillary bed. Vessels in these trees divide into increasingly thinner branches like nearly ideal binary trees, with the exception of occasional anastomosis. Their terminal branches are connected to capillaries, which is where most of the exchange with the surrounding tissue occurs. Capillaries are accordingly thin, permeable and densely and homogeneously distributed. The design goal of such a structure is to provide a sufficient supply of nutrients to all regions of the tissue, while minimizing the energy necessary to maintain the circulation.

We follow Gödde and Kurz (2001) who presented a method to construct representations of vascular trees stochastically according to probabilistic rules that

Table 13.1 List of parameter values used for all simulations

Parameter	Value	Description
N	600	Lattice size
Δl	10 μm	Lattice const.
Δl_V	60 μm	Lattice const. (tree constr.)
D	300 μm^2 / s	TC mobility
$c^{(norm)}$	1 / (10 μm)^3	Normal cell density
$c^{(max)}$	2 / (10 μm)^3	Maximum cell density
$o^{(B)}$	1	Blood oxygen level
α_o	0.004 /μm^2	O_2 source coefficient
$\gamma_o^{(norm)}$	1/(100 μm)^2	O_2 consumption. coeff. by normal cells
$\gamma_o^{(tum)}$	2/(100 μm)^2	O_2 consumption. coeff. by tumor cells
R_g	200 μm	Growth factor diffusion range
$t_{EC}^{(switch)}$	24 h	Sprouting/Dilation switch delay
$t_{EC}^{(sprout)}$	5 h / 10 μm	Sprout extension time
$t_{EC}^{(migr)}$	100 h	Sprout activity duration
$l^{(spr)}$	20 μm	Sprout sites minimum separation
$r^{(sprout)}$	4 μm	Initial sprout vessel radius
k_r	0.4 μm/h	Vessel dilation rate
$r^{(max)}$	25 μm	Maximum dilation radius
$t_{TC}^{(prol)}$	10 h	TC proliferation time
$t_{TC}^{(uo)}$	100 h	Hypoxic TC survival time
$f^{(coll)}$	2 Pa	Critical wall shear-stress
$t_{EC}^{(coll)}$	20 h	Unstable vessel survival time
Δw	0.05 μm/h	Dematuration (w) rate
$o_{TC}^{(death)}$	0.01	TC death O_2 threshold
$o_{TC}^{(prol)}$	0.1	TC hypoxia O_2 threshold

depend on local system properties. The construction of the blood vessel network is based on the stochastic remodeling of a collection of binary trees. Each tree represents either an arterial or a venous branch. Analogous to the definition Sect. 2.1, the tree edges coincide with the edges of a lattice, and have associated hydrodynamic properties.

An initial "guess" for the network is constructed by a random growth process which originates from a prescribed set of arterial and venous "root" vessels or nodes located at the lattice boundaries. Thereby certain elementary structural elements are successively appended at randomly selected leaf nodes until the lattice is filled. The particular element and its direction is also selected randomly. Thereby moves, that would result in overlapping nodes are rejected.

For the study of 2d systems Welter et al. (2009) used different root configurations with long stems positioned randomly within certain ranges. The structural elements comprised a single edge, and a Y-shape of three edges. See the above reference for detailed specifications.

For the 3d systems, single root nodes are uniformly distributed over the system domain faces. Arterial and venous types are selected in alternating order. Configurations are rejected, where the distance between two nodes or between a node and a domain edge is less than 10% of the domain lateral size. The growth pieces are selected from three planar configurations: a single edge, a $\dashv$ shape consisting of three edges, and a $-\ \sqsubset$ shape consisting of five edges. The latter two should approximate the more realistic Y shapes in real vasculatures.

After the initial growth successive optimization sweeps follow until a steady state evolves. Per sweep leafs are removed or extended depending on the wall shear stress in the parent edge. In order to determine a well defined blood flow (Sect. 2.2), and also for the final output, the individual trees are temporarily connected by "capillary" edges between leaf nodes of opposing type (arterial or venous).

While it is highly nontrivial to synthesize vascular networks that are realistic in every way possible, our initial networks exhibit reasonable hierarchical structures, spatial distributions of the capillaries, and agreement with the flow-data in Gödde and Kurz (2001) and the experimental references therein.

3 Temporal Evolution

Figure 13.2 shows snapshots of the temporal evolution of the tumor and the vessel network for a 3d arterio-venous initial vasculature. Independent of the details of the initial vasculature and system dimensionality the emerging global morphologies share the same features. Initially, the tumor oxygen consumption leads to decreased oxygen levels within the nucleus and consequently enables vascular remodeling via growth factor production of the TCs. The sprouting process first creates a dense capillary plexus which provides more oxygen and facilitates tumor growth. Vessel collapses begin after a few days (Fig. 13.2b). Small capillaries collapse immediately under bad perfusion while thicker vessels survive longer due to their stability (large w), independent on blood flow until they become unstable. The network is thus progressively remodeled, predominantly within a thin band around the tumor boundary. The sparse network left in the center remains static except for few collapses of isolated threads.

The resulting network morphologies shown in Fig. 13.3 display the typical high-MVD periphery and low-density center. For the arterio-venous initial vasculatures, the remaining tumor vessels can form well perfused short-cuts between arteries and veins penetrating the tumor boundary. This is a consequence of the dilation that all vessels undergo in the tumor. The short-cuts consist of neovasculature as well as parts of the initial vasculature. For regular initial networks the surviving vessels are predominantly oriented along the global flow direction. This direction is imposed by the flow boundary conditions, dictating a homogeneous flow along the diagonal. Vessels perpendicular to this direction have lower flow rates and shear forces and are thus prone to collapse. Depending on parameters and the initial network configuration, arterio-venous systems can also exhibit such imposed flow

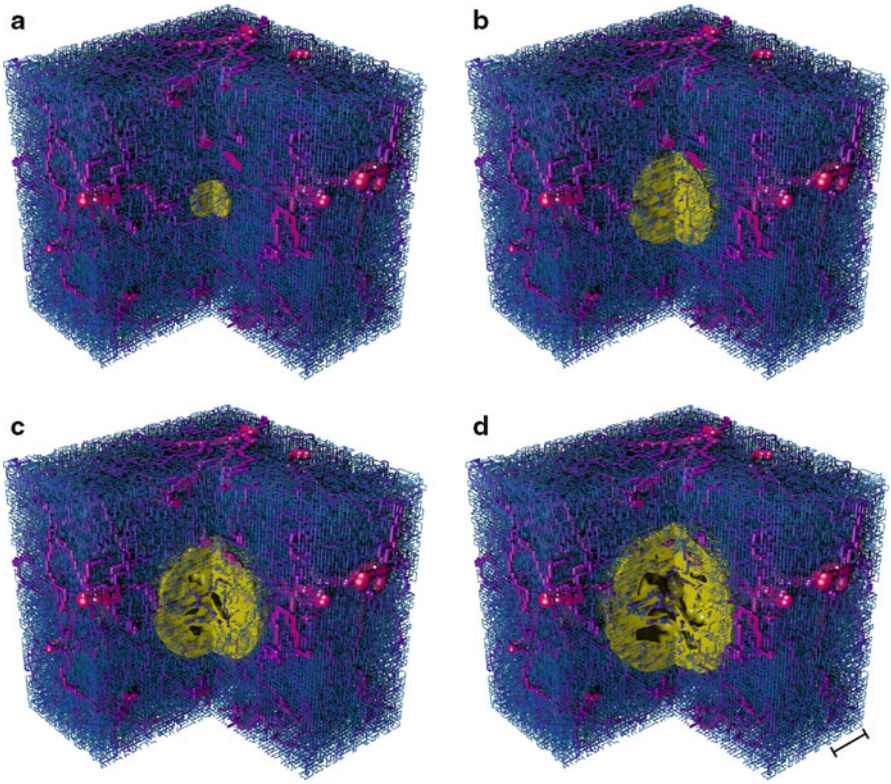

Fig. 13.2 Visualization of 3d vessel network and tumor configurations obtained at times 100 h (**a**), 200 h (**b**), 400 h (**c**), and 500 h (**d**), based on an arterio-venous initial network. A cut through the cubic simulation volume is shown. The scale bar represents approximately 1 mm. The vessels are depicted as *cylinders* which are *color coded* by their blood flow rate q. On a logarithmic scale, it reaches from 1 (*green*) over 10^6 (*blue*) to 10^9 (*red*) in units of $\mu m^3/s$. Noncirculated vessels are shown in *gray shades*. The spheroid in the center shows the iso-surface where the tumor cell density equals 50% of the normal packing density $c^{(norm)}$. Its cutting planes are slightly offset from those of the vessel network in order to make slices of the tumor vasculature visible. Necrotic regions appear in (**c**) and (**d**) as shadowy holes in the viable tumor mass

directions between high-level arteries and veins. However, this is much less apparent due to the hierarchical organization of the network. Starting with different initial arterio-venous networks yields different final configurations (Welter et al. 2009) but their global characteristics, as quantified by the radial distribution functions analyzed in the following do not vary significantly.

The tumor masses grow approximately spherically. After a short initial phase their radius increases linearly because proliferation is predominantly restricted to the boundary where sufficient space and oxygen is available. The cell density profiles c exhibit steep slopes at the invasive edges, dropping from $c^{(norm)}$ to zero. In the tumor interior c fluctuates between zero and $c^{(max)}$ depending on oxygenization.

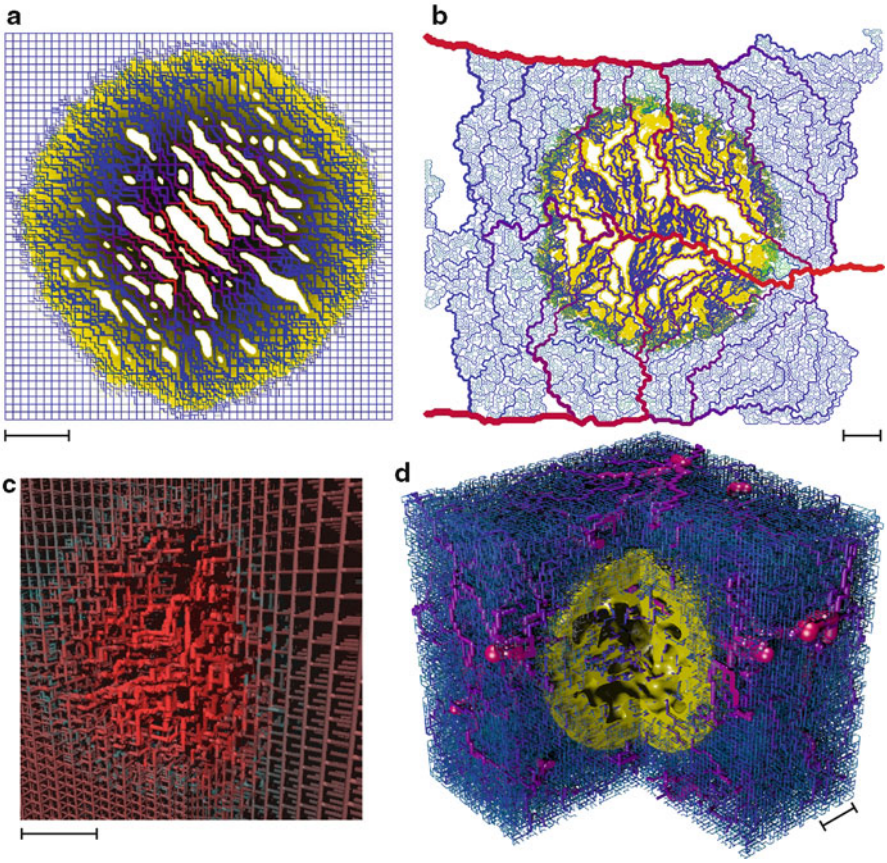

Fig. 13.3 Displays final configurations for (**a**) a 2d system with a regular initial network, at $t = 1{,}000$ h. The lateral size of the simulation domain is 5.1 mm (for details see (Bartha and Rieger 2006)). (**b**) a 2d system with an arterio-venous network based on a hexagonal lattice at $t = 1,200$ h. The domain is 12 mm wide and ca 10 mm high (for details see (Welter et al. 2009)). (**c**) a 3d system with a regular network at $t = 400$ h. The domain size is 4 mm. The tumor is not displayed here. (for details see (Lee et al. 2006)). (**d**) the 3d arterio-venous system emergent at $t = 600$ h from the earlier stages shown in Fig. 13.2. The length of the scale bar represents approximately 1 mm. The tumor is depicted as *yellow* mass except in (**c**). In (**a**) the age of individual tumor cells is indicated by their brightness (*darker* means older). Vessels are depicted as line segments or cylinders with the corresponding width or radius. Their *color* indicates the their flow rate q. The color scale in (**b**) and (**d**) is identical and stated in Fig. 13.2. The flow rate in (**a**) is shown on a linear scale ranging from 0 (*green*) over the value of the flow rate in the undisturbed initial network (which is equal for all initial vessels) (*blue*) to the maximum flow rate (*red*). The color scale in (**c**) ranges from $q = 0$ (*dark-cyan*) to ∞ (*red*)

For the cellular-automaton-based models (Bartha and Rieger 2006; Lee et al. 2006; Welter et al. 2009) the tumor cell density is constant and proliferation is limited to the outer rim by definition and therefore these models also predict a constant

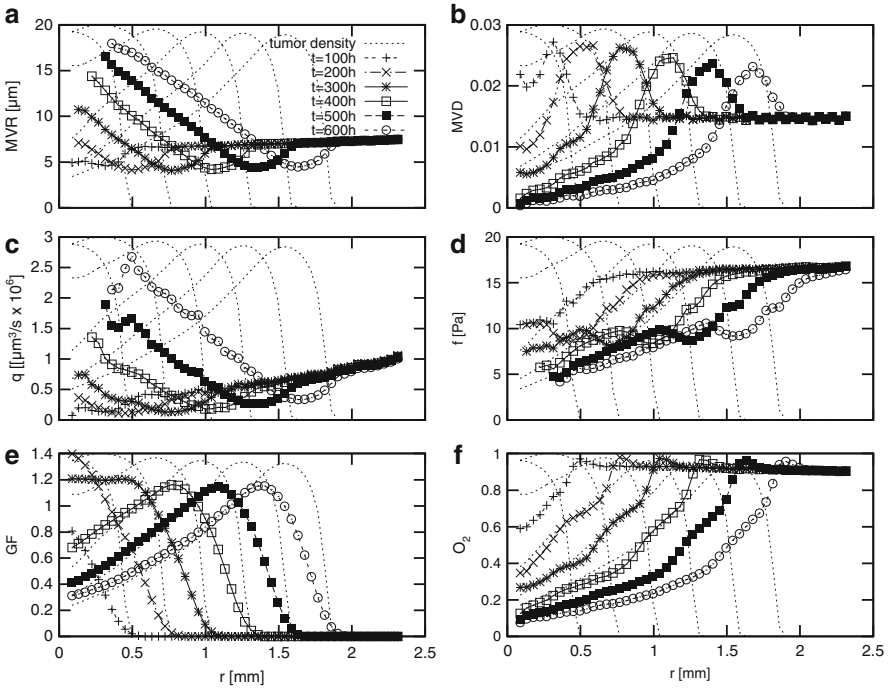

Fig. 13.4 Shows radial distributions obtained from 3d systems with arterio-venous initial vessel networks (Welter and Rieger 2010). Similar data for other systems can be found in Bartha and Rieger (2006), Lee et al. (2006), and Welter et al. (2009). The shown quantities are (**a**) vessel radius (MVR), (**b**) microvascular density (MVD), (**c**) blood flow rate through the vessels, (**d**) vessel wall shear force, (**e**) growth factor concentration, and (**f**) oxygen concentration as a function of the radial distance from the tumor center for different times (legend see top left panel). The *broken lines* indicate the radial tumor density at the times corresponding to the other quantities shown. All curves are averaged over 40 runs and concentric shells of 100 μm width

expansion rate. Until ca. 300 h simulation time, the vessel network is still relatively dens so that all tumor cells are supplied with sufficient oxygen to remain viable ($o > o_{TC}^{(death)}$), but may not be able to proliferate ($o < o_{TC}^{(prol)}$). Further growth and an increasing number of vessel collapses lead to regions where the inter-vascular distance is greater than twice the oxygen diffusion radius. These regions become necrotic due to under-oxygenization and death of tumor cells.

In order to capture morphological and hydrodynamic characteristics quantitatively, we determined the average value of respective quantities in dependence on the radial distance r from the tumor center at different times. An example of these radial distributions is shown in Fig. 13.4 for 3d arterio-venous systems. The data is averaged over 40 simulation runs with different initial networks and over concentric spherical shells centered around the tumor center.

The quantities of interest comprise the following: tumor density (in all panels), microvascular radius (MVR, panel a) microvascular density (MVD, panel b), blood

flow rate through the vessels (q, panel c), vessel wall shear force (f, panel d), growth factor concentration (GF, panel f) and oxygen concentration (O_2, panel c) The microvascular density is defined as volume fraction occupied by the vessels. The quantities associated with vessel segments (MVR, f, q) are averaged over the number of vessel-occupied lattice sites within the respective shells.

The peak in the radial tumor density indicates the boundary of the tumor (stochastic fluctuations within the shells as well from sample to sample cause the finite width of this step). As the individual curves are for equidistant times it is clear from the linear shift of the peak density that the tumor radius grows linearly in time. Behind the peak, at smaller distances r from the center, the tumor density drops monotonously, reflecting the emergence of necrotic zones in the tumor center.

The MVD in panel (b) of Fig. 13.4 has a peak in the peritumoral region, i.e., outside of the tumor at a distance slightly larger than the peak of the tumor density. It is 1.5 to 2-fold higher than the normal MVD (plateau value at large distances). Within the tumor (at small distances) the MVD drops monotonously to zero (at long enough times), again reflecting the emergence of the necrotic core.

Correlated with the peak in the MVD is a small peak in the oxygen concentration (panel f of Fig. 13.4), and a dip in the average vessel radius (panel a), the average flow rate (panel c), and the average shear force (panel d): The peak in the MVD in the peritumoral region reflects the presence of many new capillaries, which increase the oxygen supply but simultaneously decrease the average vessel radius as capillaries have minimum radius. Furthermore, as the average blood flow that is supplied by the arterio-venous network is approximately constant, this flow has to be distributed over 50–100% more microvessels in the tumor perimeter, which induces a reduction in average flow rate and shear force.

Within the tumor (i.e., for distances smaller than the location of the peak of the MVD) the vessel radius increases monotonously with decreasing distance from the tumor center (panel a of Fig. 13.4), which is the effect of the switch from angiogenic sprouting to circumferential growth within the tumor. The axial blood-pressure gradient within the vessels $\mathrm{d}p/\mathrm{d}l$ (not shown here) decreases monotonically with decreasing distance from the tumor center by more than one order of magnitude. Although the pressure gradient decreases, the average blood flow rate (q, panel c) within the vessels increases toward the tumor center because it is proportional to the 4th power of the vessel radius R, $q \propto R^4 \mathrm{d}p/\mathrm{d}l$. The average shear force f is proportional to the 1st power of R, $f \propto R\,\mathrm{d}p/\mathrm{d}l$, therefore it decreases with decreasing distance from the center.

The average oxygen concentration (panel f) decreases rapidly toward the tumor center and drops below the GF production threshold $o_{TC}^{(prol)} = 0.1$ (relative to normal oxygen) at approximately the same distance $r_{\mathrm{low\,oxy}}$, where the growth factor concentration (GF, panel f) displays a peak. This peak is therefore not at the same position as the peak of the tumor density. For distances smaller than the "underoxygenization radius" $r < r_{\mathrm{low\,oxy}}$ all tumor cells produce GF and the shape of the GF concentration versus distance r is identical with the tumor density.

MVD and vessel-radius show the typical compartmentalization that has been observed in melanoma (Döme et al. 2002, 2007) and glioma (Vajkoczy and Menger 2000): For instance Döme et al. (2002) measured the MVD and vessel radius in three distinct regions of human and mouse melanoma: the central region, a 100 μm wide peripheral band just behind the invasive edge, a 200 μm wide peritumoral region outside the invasive edge. In the central region, they found a MVD that was reduced to 25% of the MVD of normal tissue, and increased up to 200% in the peritumoral region. They found that the vessel perimeter grew linearly from 50 μm to a plateau at 200 μm by day 15.

Analogous examinations were realized for 2d / 3d systems with regular initial networks (Bartha and Rieger 2006; Lee et al. 2006) and 2d systems with arterio-venous network (Welter et al. 2009), with qualitative and quantitative good agreement. The precise numbers might be different due to different parameters, minor model variations, and initial networks. However, the global characteristics such as the compartmentalization into regions of different MVD are also apparent.

4 Fractal Dimension and Spatial Inhomogeneities

The topological and geometrical properties of tumor networks are vastly different from normal blood-vessel networks (Baish and Jain 2000). Tumor vessels are tortuous, lack a clear hierarchical organization and are spatially unhomogeneously distributed.

One can characterize and distinguish vessel networks by their are fractal properties. The concept of a fractal dimension is often used for this purpose (Gazit et al. 1995; Baish and Jain 2000). One commonly used method to estimate fractal dimension is box-counting, which is carried out by superimposing boxes of size ϵ arranged as a regular grid on the fractal object and counting the number of boxes N_ϵ which overlap the object. The self-similar nature of true fractal object leads to the power law $N_\epsilon \propto \epsilon^{-D_f}$, where N_ϵ is the number of overlapping boxes. D_f is usually extracted by a linear fit in a log–log plot. However due to the limited size and resolution of the data representation, determination of N_ϵ is limited to ca. two orders of magnitude of ϵ. Furthermore natural objects (or rather photographs thereof) are usually not perfectly fractal, giving rise to deviations from the ideal power law. Therefore, even a small regime of a "good fit" is often considered sufficient to speak of a fractal dimension (or more truthfully named box-counting dimension); see the discussion in Chung and Chung (2001).

The average dimension obtained from tumor networks based on 3d arterio-venous initial networks is $D_f^{av3d} = 2.50 \pm 0.02$. Tumor networks of 3d regular systems were analyzed by Lee et al. (2006), who reported $D_f^{r3d} = 2.52 \pm 0.05$. For 2d arterio-venous systems we obtain $D_f^{av2d} = 1.79 \pm 0.03$ and lastly Bartha and Rieger (2006) reported $D_f^{r2d} = 1.85 \pm 0.05$. For brevity we refer to the references above and Welter and Rieger (2010) for plots and additional data.

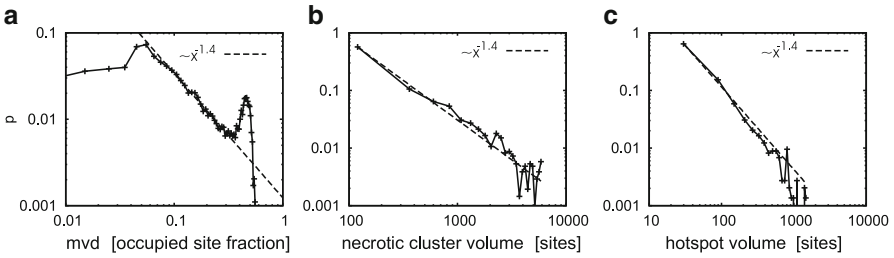

Fig. 13.5 Shows probability distributions for morphological quantities of 2d systems with arterio-venous initial networks. In (**a**) the local MVD, given as the local average over 250 μm wide boxes, (**b**) the volume of necrotic tissue clusters, defined as the number of sites in connected components of dead tissue. (**c**) the volume of vessel hot-spot areas, defined as the connected components of regions where the local MVD exceeds a prescribed threshold (ca. the MVD in the initial vasculature). The curves are generated from data collected from results of 40 simulation runs at $t = 1{,}200$. We note that the distributions show algebraic decay. In this instance in particular with the same exponent with an error of 2%

Bartha and Rieger (2006) and Lee et al. (2006) hypothesized that the fractal properties of the emerging tumor vasculature are independent of the initial (3d) blood vessel network. Our present finding that D_f^{av3d} of the tumor vasculature for a 3d arterio-venous initial network is close to D_f^{r3d} for 3d regular initial networks supports this hypothesis. For two dimensional systems the agreement between D_f^{av2d} and D_f^{r2d} is worse but within the margin of errors. Moreover D_f^{av3d} and D_f^{r3d} agree well with the exactly known value for the conventional critical percolation cluster in 3d $D_f^{\mathrm{perc}3d} = 2.52$ (Stauffer and Aharony 1992). Analogously D_f^{r2d} is very close to the dimension of the percolation cluster in 2d $D_f^{\mathrm{perc}2d} = 1.891$.

For sufficiently large systems such as the tumor networks based on 2d arterio-venous networks Welter et al. (2009) could show that the fractal dimension of the tumor occupied region agrees well with the dimension of the tumor vessel network. The reason for this is that tumor cells survive everywhere in close proximity to vessels, which means that on a scale much larger than the diffusion radius of oxygen the shape of tumor is indistinguishable from the shape of the vessel network.

The basic mechanism responsible for the fractal properties of the tumor vasculature is the stochastic removal of vessels via vessel collapse and regression (Lee et al. 2006; Welter et al. 2008), see also Paul (2009). In conventional percolation a critical cluster only emerges for an exactly tuned bond concentration. In our model the network is dynamically driven into this critical state without such a fine tuning since the removal of vessels is correlated with the blood flow: the collapse of weakly perfused vessels stabilizes the remaining ones due to an increase in blood flow. We propose that this mechanism, and not an underlying invasion percolation process (Baish and Jain 2000; Gazit et al. 1995; Baish and Jain 1998), is also at work in real tumors.

Moreover, spatial inhomogeneities were characterized by probability distribution functions (Fig. 13.5) for (a) local MVD, (b) necrotic region size, and (c) size of regions with high MVD, where “high MVD” is defined as a local MVD which

exceeds a fixed threshold value (ca. the MVD in normal tissue). The local MVD was determined as fraction of occupied sites within cells of a superimposed grid. For the central region of tumor networks emerging in 2d arterio-venous systems (Welter et al. 2009), excluding the strongly vascularized periphery, the resulting distributions for (a),(b), and (c) show an algebraic decay with ca. the same exponent -1.4. The distribution for (a) also show a peak near zero, which is however trivial to due the existence of large necrotic regions. For 3d arterio-venous systems we obtain similar distributions which can also be fit by power laws but with significantly different exponents -0.5 (a), -1.9 (b) and -1.2 (c). These power laws are reminiscent of a self-organized critical state (Jensen 1998), for which the absence of a typical length scale (over which for instance size distributions would decay exponentially) is characteristic, like in a stochastic dilution process at the percolation threshold or a flow-correlated percolation process (Bartha and Rieger 2006).

In the following paragraphs we analyze the occurrence of so called "Hot spots". These hot spots are regions of increased blood flow within the tumor. In clinical imaging of blood flow they can be observed using tomography techniques. See, e.g., Pahernik et al. (2001). As blood flow is directly linked to the existence of blood vessels, it is also important to analyze spatial inhomogeneities of the tumor networks in order to understand "Hot spots". Furthermore the quantity q, defined in Sect. 2.2 as blood flow rate of a vessel segment, is not directly experimentally accessible since it represents the total volume per time transported through a finite sized pipe which might contribute to several voxels in imaging data. The more relevant quantity is therefore the blood flow velocity (magnitude), which can be interpreted as spatially varying field.

For regular initial networks Bartha and Rieger (2006) and Lee et al. (2006) obtained tumor networks which consisted predominantly of isolated strings within the tumor center. It is possible to interpret even one of these strings as "Hot-spot" if there are no other blood perfused vessels in the close vicinity. Depending on parameters the blood flow velocity in these strings may be higher or lower than in the surrounding normal network. This is a consequence of the vessel dilation effect. Although it is the blood pressure which is prescribed via boundary conditions, instead of the blood flow rate, it can be assumed that the flow rate into the tumor is limited by the relatively high flow resistance of the capillary-like surrounding network. Therefore, if the increase in blood capacity is not counterbalanced by sufficient vessel collapses (determined by the critical shear-stress parameter $f^{(coll)}$), the flow velocity in tumor vessel can be lower than in the original vasculature.

Welter et al. (2008) reported the possible emergence of morphological artifacts in systems with regular, hexagonal, and initial networks. Therein surviving vessels converge to a singular point in the center of the tumor. On each side of the central point, perpendicular to the flow direction, a massive region void of vessels emerged. However, it should be stressed that the predicted global properties nonetheless agree with the results from other systems as presented in Sect. 3. Moreover, these artifacts cannot occur in systems based on hierarchical arterio-venous networks due to the fundamentally different blood-flow boundary conditions and network organization.

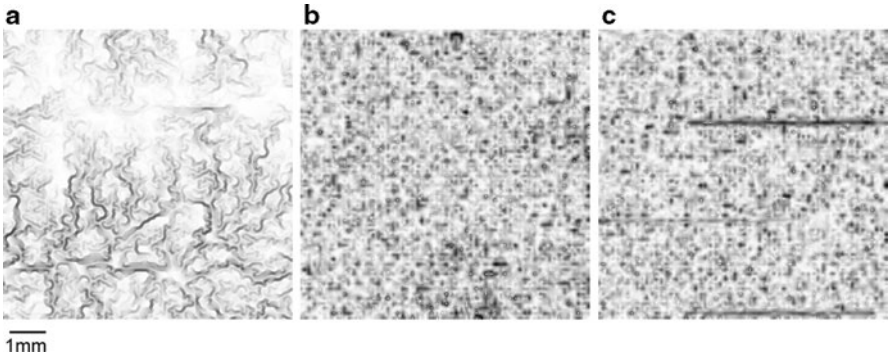

Fig. 13.6 Shows a comparison of the local gradient magnitude $|\nabla p|$ of the continuous field $p(\mathbf{r})$ which interpolates the blood pressure between neighboring vessels of an initial network configuration (see text). $|\nabla p|$ is relevant for the survival of neovasculature because the shear stress within a new connection generated between two original vessels is approximately determined by $|\nabla p|$. Therefore, the fluctuations in p and $|\nabla p|$ can have an impact on the emergence of inhomogeneities in the tumor vasculature. The gray level of the images correspond to the range between the minimum (*white*) and maximum (*black*) $|\nabla p|$ values. (**a**) Shows the result for a 2d arterio-venous obtained by Welter et al. (2009), (**b**) shows a slice through the center of a 3d arterio-venous system and (**c**) also shows a 3d arterio-venous system but with deterministically laid out parent vessels, mimicking the 2d configurations like shown in (**a**) more closely

Welter et al. (2009) quantified and analyzed the spatial distribution of blood flow for 2d initial networks and Welter and Rieger (2010) for 3d networks. In good agreement one could observe that some vessels form short-cuts between high-level arteries and veins penetrating the tumor rim. The dilation effect decreases the flow resistance of the thinnest vessels which would otherwise dominate the resistance of a potential short-cut. Which therefore leads to flow rates and velocities which are orders of magnitudes higher than in a normal capillary beds. The model thus supports the hypothesis raised in Pahernik et al. (2001) that hot spots are due to highly conductive arterio-venous shortcuts. See the references above for plots of flow rate distributions. Also see corresponding figures in the references for an impression of the transport or flow velocities.

Moreover, the model for 2d arterio-venous systems predicts the formation of dense clusters of surviving vessels in the tumor center, accompanying the predominant isolated strings. It could be shown that these clusters are more likely to form in regions with high hydrodynamic pressure differences between neighboring vessels. A spatially varying field $p(\mathbf{r})$ of these pressure differences can be constructed by determining the solution of the Laplace equation for $p(\mathbf{r})$ defined on the space between the vessels with the boundary condition that $p(\mathbf{r})$ is identical to the blood pressure inside the vessel at location $\mathbf{r}$. Thus, the field $p(\mathbf{r})$ interpolates the pressure between vessels (Fig. 13.6). Correlations between the gradient magnitude $|\nabla p|$ of this map for the original vasculatures and the microvascular density in the emerging tumors were determined in two ways (Welter et al. 2009): (1) Globally, where $|\nabla p|$ and the MVD were averaged over the region occupied by the final tumor for 40

different simulation runs. The resulting correlation coefficient is ca. 0.9. (2) Locally, where data points were generated by averaging over several sub-domains of 150 μm radius. Their correlation coefficient varies between 0.2 and 0.4, depending on parameters. As single collapse events lead to long-ranged collapses of adjacent network sections, we think that therefore local measurements show significantly weaker correlations.

In contrast, dense vessel clusters observed in 2d are not apparent in the tumor vasculature emerging within the 3d arterio-venous networks. Concomitantly the pressure (gradient) fields for the 3d initial networks considered here are more homogeneous, except on a very short scale in between neighboring vessels. This is exemplified by Fig. 13.6a in comparison to Fig. 13.6b,c. We think that this is the consequence of the much larger configuration space for 3d initial networks compared to 2d. Vessels can wind around each other, arteries and veins can "cross" each other, which they cannot in 2d, etc. Therefore, using a stochastic algorithm, it seems to be very unlikely to construct a configuration which has the same particular properties as most 2d networks have.

5 Drug Transport

Normal arterio-venous vessel networks are designed to transport a plenitude of substances efficiently to all regions within a tissue. The drastic differences between the architecture of tumor networks to normal networks, i.e., sparsity, tortuosity, lack of a clear hierarchy, etc., raises the question whether the morphological characteristics of tumor networks pose a problem to successful drug delivery. McDougall et al. (2002) first treated this question with the help of a simulation model, where a time-dependent concentration profile c over the vasculature is propagated according to the local blood flow-velocities.

The basis of this model is a network according to the definition in Sects. 2.1 and 2.2. In addition, a mass parameter m is associated with each vessel describing the amount of drug within its blood volume. This mass m is deterministically updated in successive time steps: First the amount flowing out of vessels is determined and added to auxiliary mass variables associated with the network nodes. Under the assumption of perfect mixing, these nodal masses are then redistributed into further downstream vessel. A detailed description can be found in Welter et al. (2008) and McDougall et al. (2002). For simplicity the exchange of drug with extra-vascular space has been neglected up till now.

The results presented by McDougall et al. (2002) and in subsequent papers McDougall, Anderson and Chaplain (2006, and the references therein) are derived from a vascularization model of pure in-growth and are discussed in the context of our results further below.

The transport model was adopted by Welter et al. (2008, 2009); Welter and Rieger (2010) to check whether there are obstacles to successful drug delivery inherent to tumor network which are embedded in a surrounding normal vasculature. The studied systems comprised regular 2d, arterio-venous 2d, and arterio-venous 3d initial networks, respectively.

The simulation starts with a "clean" network without drug. Drug is inserted with a constant dimensionless volume-concentration of value 1 simultaneously through the inlet nodes of the network. In the regular networks, these nodes comprise the boundary nodes of the network pattern where the (negative) pressure gradient imposed by the flow-boundary conditions (see Sect. 2.2) points into the system domain. The resulting drug "front" advances relatively even through the entire network. Within the order of 60 s the front traversed to the out-flow nodes at the opposite corner of the domain, where the domain size is 12 mm and the diameter of the tumor is ca 6 mm. For continuous infusions the network is saturated with the maximum drug concentration after expiration of this time.

The results obtained for arterio-venous initial networks are similar thereto. When drug is inserted through all arterial inlets, it is distributed very rapidly over the whole network. Within the order of several seconds the network is saturated with the maximum drug concentration. To illustrate that, Fig. 13.7 shows a sequence of snapshots over 4 s. At the tumor border, where the MVD is high and the networks contains many loops, there may be tiny regions (ca. 100 μm diameter) that take an order of magnitude longer to fill. Transport through the dilated tumor-internal vessels is as fast as through high-level vessels of the normal vasculature. The outer regions of the system where the network remains normal can also transport drug toward the tumor periphery. Therefore, the tumor vasculature as a whole is well perfused. Qualitatively and quantitatively the results for 3d systems (Welter and Rieger 2010) and 2d systems (Welter et al. 2009) are in good agreement. A notable exception seems to be the robustness of the initial networks with respect to the disruption by the tumor network. With this we mean that in 2d there are larger regions than in 3d ($\gg$100 μm diameter, extending into sections of the original network) with significantly decreased flow velocities. We presume this might be because the initial 2d configurations have fewer pathways to major feeding vessels. Therefore blood flow is more likely to traverse the comparably badly conducting tumor boundary, resulting in low flow rates.

Qualitatively, it was for instance determined how long tumor vessels are exposed to a drug concentration larger than a predefined minimum drug level c_{thres}. Welter and Rieger (2010) report that during a 30 s simulation time over 90% of the vessel network was exposed to at least $c = 0.5$ for at least 25 s, and 99% for at least 15 s. Also by comparing exposure times for different c_{thres} they could conclude that drug advances through the network with a sharp front, exposing vessels "on contact" instantly to high drug concentrations.

Our conclusion is therefore that experimentally observed deficiencies in drug delivery must have other reasons, and these most probably lie within the characteristics of extravasation of drug and interstitial fluid transport within the tumor, which were not included into the present versions of the model.

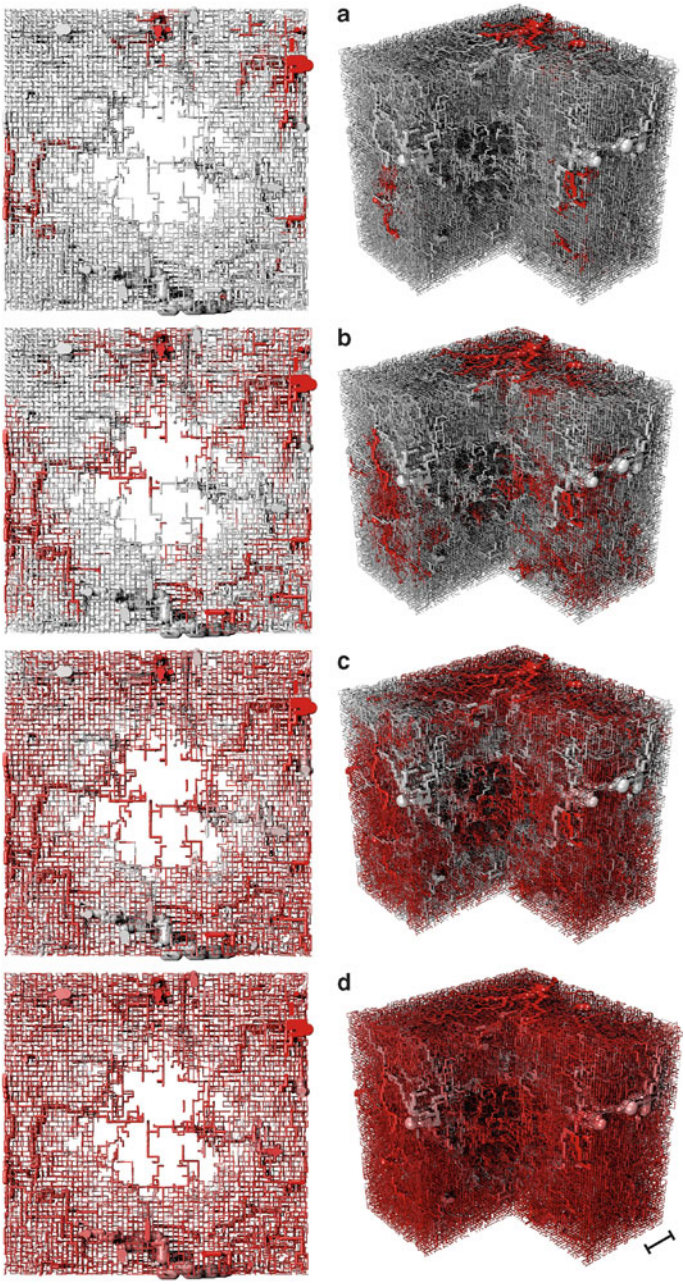

Fig. 13.7 Visualizes the drug concentration c obtained from a flow simulation at times $t = 0.5$ s, 1 s, 2 s and 4 s. The *left column* shows 0.6 mm thick slices through the system center. The *right column* shows perspective views of cuts through the simulation domain. The scale bar represents approximately 1 mm and the size of the simulation domain is 6 mm. The *color* code ranges from 0 (*gray*) to the injected concentration $c = 1$ (*red*). The transport is very effective since already at $t = 4$ s the vasculature is mostly saturated

6 Conclusion

We have demonstrated that realistic morphological properties of vacular remodeling in spherically growing solid tumors are correctly predicted by a mathematical model involving a physiologically relevant initial vasculature and the dynamical processes of angiogentic sprouting in the tumor periphery, circumferential vessel growth and blood flow correlated vessel regression within the tumor. The emerging tumor vasculature is nonhierarchical and compartmentalized into a highly vascularised tumor perimeter, a tumor periphery with large vessels density and dilated vessels and a central region containing necrotic regions with a low microvascular density threaded by extremely dilated vessels.

The incorporation of an arterio-venous initial vasculature is important because it provides a mechanism for short-cuts or "shunts" and concomitantly an increased blood flow through the tumor vasculature (Welter et al. 2009; Welter and Rieger 2010) as observed in experiments (Sahani et al. 2005): Thick arterioles and venules provide a well conducting support structure around the tumor. As the total pressure difference between the tree roots is fixed, the transported blood volume is given by the total flow resistance of entire vascular tree. Dilation of a few vessels forming a path between the tree roots can remove bottlenecks formed by thinner vessels. The creation of new vessels thereby promotes arterio-venous short-cuts, or shunts, through multiple partly disjoint paths. After vessel dilation this leads to a decreased total flow resistance, which implies an increased blood flow through the tumor vasculature when compared with the initial vasculature. This is in contrast to grid-like initial networks, where the total flow resistance is dominated by the network outside the tumor (Bartha and Rieger 2006; Lee et al. 2006; Welter et al. 2008) and the flow cannot not increase via the dilation of tumor internal vessels. Moreover, depending on the details of their construction arterio-venous networks display characteristic spatial inhomogeneities that can, via locally increased pressure gradients (Welter et al. 2009) or simply the presence of major arteries (Welter and Rieger 2010), lead to the formation of hot spots (i.e., regions of increased blood flow) inside the growing tumor.

Vessel dilation via circumferential growth within the tumor is a major physical determinant of the emerging network morphology and blood flow organization: As blood flow through cylindrical vessels increases with the 4th power of its radius a single or a few dilated vessels can carry most of the blood entering a particular region of the tumor thereby destabilizing large parts of the capillary network.

The correlation of vessel regression with the shear force exerted by the blood flow upon the vessel walls is critical for the global geometry of the emerging tumor vasculature as well as for the blood borne drug transport: the basic mechanism responsible for the fractal properties of the tumor vasculature in our model is the stochastic removal of vessels via vessel collapse and regression. In conventional percolation Stauffer and Aharony (1992) a critical cluster only emerges for an exactly tuned bond concentration. In our model the network is dynamically driven into this critical state without such a fine tuning because the removal of vessels is

correlated with the blood flow: the collapse of weakly perfused vessels stabilizes the remaining ones due to an increase in blood flow. In addition the remaining vessels are all well perfused and as a consequence blood borne drug transport through the tumor vasculature is efficient, in contrast to vessel-in-growth models (McDougall et al. 2002; McDougall, Anderson and Chaplain 2006).

This does however not automatically imply that drug reaches all tumor cells because neither drug transport through the tumor tissue nor drug uptake have been addressed (Minchinton and Tannock 2006). The low differences between interstitial fluid pressure (IFP) and microvascular pressure (MVP) due to vessel leakiness (Hassid et al. 2006), causing low convection rates, as well as the low diffusibility of drug molecules through vessel walls, causing lower diffusion ranges for drug than for oxygen, appear to be the key physical determinants preventing successful drug delivery in tumors. Work that incorporates these mechanism in the type of models presented here is in progress.

References

Alarcon T, Byrne H, Maini P (2003) A cellular automaton model for tumour growth in inhomogeneous environment. J. Theor. Biol., 225, 257–274.

Anderson A R A, Chaplain M A J (1998) Continuous and Discrete Mathematical Models of Tumor-induced Angiogenesis. Bull. Math. Biol. 60:857–900.

Baish J W, Jain R K (1998) Cancer, angiogenesis and fractals. Nat. Med. 4:984.

Baish J W, Jain R K (2000) Fractals and cancer. Cancer Res. 60:3683–3688.

Balding D and McElwain D L S (1985) Mathematical modeling of tumour-induced capillary growth. J. Theor. Biol. 114:53–73.

Bartha K, Rieger H (2006) Vascular network remodeling via vessel cooption, regression and growth in tumors. J. Theor. Biol. 241:903–918.

Bentley K, Gerhardt H, Bates P A (2008) Agent-based simulation of notch-mediated tip cell selection in angiogenic sprout initialisation. J. Theor. Biol. 250:25–36.

Betteridge R, Owen M R, Byrne H M, Alarcon T, Maini P K (2006) The impact of cell crowding and active cell movement on vascular tumour growth. Netw. Hetero. Media 1:515–535.

Byrne H M, Chaplain M A J (1995) Mathematical models for tumour angiogenesis: numerical simulations and nonlinear wave solutions. Bull. Math. Biol. 57:461–486.

Carmeliet P, Jain R K (2000) Angiogenesis in cancer and other diseases. Nature 407:249–257.

Chaplain M A J, Stuart A M (1993) A model mechanism for the chemotactic response of endothelial cells to tumour angiogenesis factor. IMA J. Math. Appl. Med. Biol. 10:149–168.

Chaplain M A J, Giles S M, Sleeman B D, Jarvis R J (1995). A mathematical model for tumour angiogenesis. J. Math. Biol. 33:744–770.

Chung H-W, Chung H-J (2001) Correspondence re: Baish J W, Jain R K (2000) Fractals and Cancer. Cancer Res. 60:3683–3688. Cancer Res. 61:8347–8351.

Dimmeler S, Zeiher A M (2000) Endothelial cell apoptosis in angiogenesis and vessel regression. Circ. Res. 87:434–439.

Döme B, Paku S, Somlai B, Tmr J (2002) Vascularization of cutaneous melanoma involves vessel co-option and has clinical significance. J. Path. 197:355–362.

Döme B, Hendrix M, Paku S, Tvri J (2007) Alternative Vascularization Mechanisms in Cancer. Am. J. Path. 170:1–15

Erber R, Eichelsbacher U, Powajbo V, Korn T, Djonov V, Lin J, Hammes H-P, Grobholz R, Ullrich A, Vajkoczy P (2006) EphB4 controls blood vascular morphogenesis during postnatal angiogenesis. EMBO 25:628–641.

Frieboes H B, Lowengrub J S, Wise S, Zheng X, Macklin P, Bearer E, Cristini V (2007) Computer simulation of glioma growth and morphology. NeuroImage. 37:59–70.

Gazit Y, Berk D A, Michael Leunig L T B, Jain R K (1995) Scale-invariant behavior and vascular network formation in normal and tumor tissue. Phys. Rev. Lett. 75:2428–2431.

Gerhardt H, Golding M, Fruttiger M, Ruhrberg C, Lundkvist A, Abramsson A, Jeltsch M, Mitchell C, Alitalo K, Shima D, Betsholtz C (2003) VEGF guides angiogenic sprouting utilizing endothelial tip cell filopodia. J. Cell Biol. 161:1163–1177.

Gödde R, Kurz H (2001) Structural and Biophysical Simulation of Angiogenesis and Vascular Remodeling. Dev. Dyn. 220:387–401.

Hassid Y, Furman-Haran E, Margalit R, Eilam R, Degani H (2006) Noninvasive magnetic resonance imaging of transport and interstitial fluid pressure in ectopic human lung tumors. Cancer Res. 66:4159–4166.

Holash J, Maisonpierre P C, Compton D, Boland P, Alexander C R, Zagzag D, Yancopoulos G D, Wiegand S J (1999a) Vessel Cooption, Regression, and Growth in Tumors Mediated by Angiopoietins and VEGF. Science 284:1994–1998.

Holash J, Wiegand S, Yancopoulos G (1999b) New model of tumor angiogenesis: dynamic balance between vessel regression and growth mediated by angiopoietins and VEGF. Oncogene 18:5356–5362.

Holmes M J, Sleeman B D (2000) A mathematical model of tumour angiogenesis incorporating cellular traction and viscoelastic effects. J. Theor. Biol. 202:95–112.

Jensen H J (1998) Self-Organized Criticality: Emergent Complex Behavior in Physical and Biological Systems. Cambridge University Press, Cambridge.

Lee D S, Bartha K, Rieger H (2006) Flow correlated percolation during vascular remodeling in growing tumors. Phys. Rev. Lett. 96:058104-1–058104-4

Lowengrub J S, Frieboes H B, Jin F, Chuang Y-L, Li X, Macklin P, Wise S M, Cristini V (2010) Nonlinearity 23:R1–R91

Macklin P, McDougall S, Anderson A R A, Chaplain M J, Cristini V, Lowengrub J (2009) Multiscale modeling and nonlinear simulation of vascular tumour growth. J. Math. Biol. 58:765–798

McDougall S R, Anderson A R A, Chaplain M A J, Sherrat J A (2002) Mathematical modeling of flow through vascular networks: implications for tumour-induced angiogenesis and chemotherapy strategies. Bull Math Biol. 64:673–702.

McDougall S R, Anderson A R A, Chaplain M A J (2006) Mathematical Modeling of dynamic adaptive tumour-induced angiogenesis: Clinical implications and therapeutic targeting strategies. J. Theor. Biol. 241:564–589.

Minchinton A I, Tannock I F (2006) Drug penetration in solid tumours. Nat. Rev. Canc. 6:583–592.

Nehls V, Herrmann R, Hhnken M (1998) Guided migration as a novel mechanism of capillary network remodeling is regulated by basic fibroblast growth factor. Histochem. Cell. Biol. 109:319–329.

Owen M R, Alarcon T, Maini P K, Byrne H M (2008) Angiogenesis and vascular remodelling normal and cancerous tissues. J. Math. Biol. 58:689–721.

Pahernik S, Griebel J, Botzlar A, Gneiting T, Brandl M, Dellian M, Goetz A E (2001) Quantitative imaging of tumour blood flow by contrast-enhanced magnetic resonance imaging. Brit. J. Canc. 85:1655–1663.

Paul R (2009) Eurp. Phys. J. E. Flow-correlated dilution of a regular network leads to a percolating network during tumor-induced angiogenesis 30:101–114.

Pries A R, Secomb T W, Gessner T, Sperandio M B, Gross J F, Gaehtgens P (1994) Resistance to blood flow in microvessels in vivo. Circ. Res. 75:904–915.

Sahani D V, Kalva S P, Hamberg L M, Hahn P F, Willett C G, Saini S, Mueller P R, Lee T Y (2005) Assessing tumor perfusion and treatment response in rectal cancer with multisection CT: initial observations. Radiology 234:785–792.

Shirinifard A, Gens J S, Zaitlen B L, Poplawski N J, Swat M, Glazier J A (2009) 3D multi-cell simulation of tumor growth and angiogenesis. PLoS One. 4:e7190.

Stauffer D, Aharony A (1992) Introduction to percolation theory. 2nd ed. Taylor & Francis, London.

Stephanou A, McDougall S R, Anderson A R A, Chaplain M A J (2005) Mathematical modeling of flow in 2D and 3D vascular networks: applications to anti-angiogenic and chemotherapeutic drug strategies. Math. Comput. Model. 41:1137–1156.

Tracqui P (2009) Biophysical models of tumour growth. Rep. Prog. Phys. 72:056701–056731.

Vajkoczy P, Menger M D (2000) Vascular microenvironment in gliomas. J. Neurooncol. 50:99–108.

Welter M, Bartha K, Rieger H (2008) Emergent vascular network inhomogeneities and resulting blood flow patterns in a growing tumor. J. Theor. Biol. 250:257–280.

Welter M, Bartha K, Rieger H (2009) Vascular remodelling of an arterio-venous blood vessel network during solid tumour growth. J. Theor. Biol. 259:405–422.

Welter M, Rieger H (2010) Physical determinants of vascular network remodeling during tumor growth. Eur. Phys. J. E., in press.

Wise S M, Lowengrub J S, Frieboes H B, Cristini V (2008) Three-dimensional multispecis nonlinear tumor growth – I Model and numerical method. J. Theor. Biol. 253:524–543.

Zheng X, Wise S M, Cristini V (2005) Nonlinear simulation of tumor necrosis, neo-vascularization and tissue invasion via an adaptive finite-element/level-set method. Bull. Math. Biol., 67:211–259.

Chapter 14
Blood Perfusion in Solid Tumor with "Normalized" Microvasculature

Jie Wu, Quan Long, and Shi-xiong Xu

Symbol Description

a	AS density perunit area
β	FN production rate
β_d	EC loss rate
β_r	EC proliferation rate
c	TAF concentration
c^*	threshold value of TAF concentration
C_i	solute concentration in interstitial fluid
C_p	solute concentration in plasma
C_max	solute concentration injected into the arteriole parental vessel
D	EC random migration coefficient
D_a	AS diffusion coefficient
D_c	solute diffusion coefficient
e	ES density per unit area
e_0	ES initial concentration
eC_{50}	ES concentration inducing 50% of the maximum inhibiting effect
ε_1	coefficient in FN initial concentration

J. Wu (✉)
School of Naval Architecture, Ocean and Civil Engineering, Shanghai Jiaotong University, 800 Dongchuan Road, Shanghai 200240, People's Republic of China
e-mail: janny_wujie@yahoo.com.cn

Q. Long
Brunel Institute for Bioengineering, Brunel University, Uxbridge, Middlesex, UK
e-mail: quan.long@brunel.ac.uk

S.X. Xu
Department of Mechanics and Engineering Science, Fudan University, Shanghai 200433, People's Republic of China
e-mail: xusx_fd@yahoo.com.cn

T.L. Jackson (ed.), *Modeling Tumor Vasculature: Molecular, Cellular, and Tissue Level Aspects and Implications*, DOI 10.1007/978-1-4614-0052-3_14,

ε_2	coefficient in AS initial concentration
$\varepsilon_{\max}$	maximum inhibiting effect of ES on ECs
f	FN concentration
H,	viscosities (parameters in Fig. 14.11)
K_{e}	drug elimination rate in plasma
K_{T}	hydraulic conductivity of tumor interstitium
$L_{pV,T}$	hydraulic permeability of tumor vessels
$L_{pL}S_L/V$	absorption capacity of lymphatic system
n	EC density per unit area
n_{c}	critical generation of vessel branching
η	TAF rate uptaken by ECs
ρ	EC haptotactic coefficient to ECM
$P_0 \sim P_8$	coefficients relate to the likelihood of EC migration directions
P_{eff}	effective vascular permeability coefficient
P_i	interstitial fluid pressure
$P_{i\,(\mathrm{Center})}$	interstitial fluid pressure in tumor center
$P_{\mathrm{in}}, 1/P_{\mathrm{in}}, 2$	inlet pressure of the parental vessel "1" or "2" (2D model)
$P_{\mathrm{out}}, 1/P_{\mathrm{out}}, 2$	outlet pressure of the parental vessel "1" or "2" (2D model)
P_V	intravascular pressure
$P_{V,A}$	pressure of the arteriole parental vessel (3D model)
$P_{V,V}$	pressure of the venule parental vessel (3D model)
Q_i	interstitial fluid flowrate
Q_t	travascular flowrate
Q_t^+	extravasation flowrate
Q_t^-	intravasation flowrate
r	dimensionless distance from tumor center
γ	rate of FN uptaken by ECs
γ_a	rate of AS uptaken by ECs
γ_c	ES plasma clearance rate
γ_u	coefficient of ES inputs
γ_s	ratio coefficient
R_f	retardation factor
R_{T}	dimensionless tumor radius
U_i	interstitial fluid velocity
$U_{I,\mathrm{ex}}$	exogenous inputs of ES
U_t	travascular fluid velocity
U_V	intravascular blood velocity
v	coefficient in TAF initial concentration
χ	EC chemotactic coefficient to TAF
x, y, z	dimensionless distance along x-, y-, z- axis
σ	coefficient of EC chemotaxis to TAF
ϕ_{s}	solute source term
ξ	EC chemotaxis coefficient to AS
ζ	outward unit normal vector
ζ_1	coefficient in FN initial concentration
ζ_2	coefficient in AS intial concentration

1 Introduction

Antitumor therapies rely on the transport of therapeutic medicines or diagnostic agents to tumor cells via the bloodstream and tumor interstitium. Unlike normal blood vessels, tumor vasculature has abnormal organization, structure, and function. Tumor vessels are leaky and blood flow is heterogeneous and often compromised. Vascular hyperpermeability and the lack of functional lymphatic vessels inside tumors cause elevation of interstitial fluid pressure (IFP) in solid tumors (Boucher et al. 1990; Jain et al. 2007). These characteristics cause abnormal microenvironment in tumors and form a physiological barrier to the delivery of therapeutic agents to tumors. Furthermore, elevated tumor IFP increases fluid flow from the tumor margin into the peri-tumor area and may facilitate peri-tumor lymphatic hyperplasia andmetastasis (Jain et al. 2007; Fukumura et al. 2007).

Tumor vasculature is not just a simple supply line of nutrients to tumors. It governs pathophysiology of solid tumors and thus, tumor growth, invasion, metastasis, and response to various therapies. As its significant roles in tumor development and metastasis, tumor angiogenesis has attracted the attention of investigators in a variety of fields, and become one of the most important areas of active research in the theoretical biology community. In this chapter, the tumor "un-normalized" microvasculatures were generated by the models of tumor angiogensis.

In recent years, tumor vascular-targeted therapies have been extensively studied in both preclinical and clinical settings, including "antiangiogenesis" and "vascular-disrupting" treatments. *Antiangiogenic treatments*, directly targeting angiogenic signaling pathways as well as indirectly modulating angiogenesis, show normalization of tumor vasculature and microenvironment at least transiently in both preclinical and clinical settings (Folkman 2000; Lee et al. 2000; Huber et al. 2005; Jain et al. 2007; Tong et al. 2004; Wildiers et al. 2003; Willett et al. 2004, 2005). Endostatin (ES) has been considered as one of the most important potential antiangiogenic drugs. It can inhibit endothelial cell proliferation, migration, invasion, and tube formation (O'Reilly et al. 1997). Angiostatin (AS), one of antiangiogenic factors, can induce tumor dormancy by inhibiting endothelial cell proliferation (O'Reilly et al. 1994). Although these antiangiogenic drugs have been approved for cancer treatment, it appears that the clinical application of the agents on antiangiogenic therapy is more complex than originally thought (Jain et al. 2006). *Vascular-disrupting treatments* target the established tumor vasculature. Some vascular-disrupting agents have been proven to effectively disrupt or prune vessels in tumor vascular system.

In this chapter, we simulated the tumor "normalized" microvasculatures by the above two treatments – "antiangiogenesis" and "vascular-disrupting." For "antangiogenesis" treatment, we developed a 2D model of tumor antiangiogenesis responding to andostatin and endostatin. For "vascular-disrupting" treatment, four

approaches were designed according to the abnormal characteristics of tumor microvaculature compared with the normal one.

The current understanding of how microenvironmental flow is affected by vascular-targeted therapies is limited because imaging resolution is not adequate to reveal the fine details of tumor microvessel. Numerical simulation plays an important role on study. The majority of the blood flow simulation work aimed to provide data on the vessel adaptation and network remodeling in response to the perfusion-related haemodynamic forces (Alarcon et al. 2003; Stéphanou et al. 2006). Although certain vessel adaptation and remodeling mechanisms were included in these simulation works, only intravascular blood flow was included and assumed as independent from, rather than tightly coupled with, the interstitial flow outside the micro vessels. In another word, no vascular leakage was taken into account. The coupling of the intravascular and interstitial flow still did not appear to be a discussing topic in a recent published review (Chaplain et al. 2006). The problem has only been studied in simplified forms by few groups previously. In the 1990s, Netti et al. incorporated tumor vessel permeability into a single equivalent capillary in a symmetric sphere model. The coupling of flow phenomenon was only partially done in their work by considering either the intravascular with transvascular flow or the transvascular with the interstitial flow, but not combined them simultaneously (Netti et al. 1996, 1997). In this chapter, a coupled flow model is built, combining intravascular, transvascular, and interstitial fluid movements which integrates macro- and microscopic views of the fluid phenomena. The compliance of tumor vessels, blood rheology with hematocritic distribution at branches is also considered.

There are a few mathematical models of tumor antiangiogenesis have been developed so far (Anderson et al. 2000; Levine et al. 2001; Tee and DiStefano III 2004; Zhao et al. 2006). However, neither they use the model to study the normalization of tumor microenvironment nor the effect of tumor vascular-disrupting. Little is known about how tumor blood perfusion is affected by the changes in vasculature structure and transport properties of vessels and interstitium that are associated with vascular-targeted therapies. Particularly, according to a recent literature (Jain et al. 2007), there are no reported measurements of interstitial fluid velocity in tumors, because the experimental data are difficult to obtain.

In this chapter we are going to present our tumor blood perfusion model in which the intravascular, transcappliery, and interstitial fluid flows are closely coupled. We will then use the model to investigate the effects of vasculature normalization caused by difference mechanisms on tumor microenvironment and blood perfusion. The study contains: (1) generation of tumor “un-normalized” microvasculature; (2) generation of tumor “normalized” microvasculature by antiangiogenesis and vascular-disrupting treatments; (3) simulation of tumor blood perfusion on “un-normalized” microvasculature; (4) simulation of tumor blood perfusion on “normalized” microvasculature, and comparison with that on “un-normalized” one.

2 Generation of Tumor "Normalized" Microvasculature

We used the model of tumor angiogenesis to generate the "un-normalized" microvasculatures, including 2D and 3D models. Based on that, we simulated "normalized" microvasculatures, in respond to the (a) antiangiogenesis (2D simulation) and (b) vascular-disrupting (3D simulation) treatments, respectively.

2.1 Tumor Angiogenesis: The Generation of "Un-normalized" Microvasculature

2.1.1 Methods and Models

The angiogenesis model follows that of Anderson and Chaplain (1998) with some exceptions: (a) extending the model from 2D5P to 2D9P and 3D7P, two parental vessels are induced; (b) generating networks able to penetrate into the tumor interior rather than the exterior only; (c) considering branching generations.

Governing Equations

The model assumes that endothelial cells (ECs) migrate through random motility, chemotaxis in response to tumor angiogenesis factors (TAFs) released by the tumor, and haptotaxis in response to fibronectin (FN) gradients in the excellular matrix. We denote the EC density per unit area n, the TAF concentration c, and the FN concentration f. The nondimensional equations describing the vascular growth process is thus given by:

$$\begin{aligned}
\frac{\partial n}{\partial t} &= \overbrace{D\nabla^2 n}^{\text{random motility}} - \overbrace{\nabla\cdot(\chi(c)\, n\nabla c)}^{\text{chemotaxis}} - \overbrace{\nabla\cdot(\rho n\nabla f)}^{\text{haptotaxis}} \\
\frac{\partial f}{\partial t} &= \overbrace{\beta n}^{\text{production}} - \overbrace{\gamma n f}^{\text{uptake}} \\
\frac{\partial c}{\partial t} &= -\overbrace{\eta n c}^{\text{uptake}}.
\end{aligned} \tag{14.1}$$

The chemotactic migration is characterized by the function $\chi(c) = \chi/(1+\sigma c)$, which reflects the decrease in chemotactic sensitivity with increased TAF concentration. The coefficients D, χ, and ρ characterize the random, chemotactic, and haptotactic cell migration, respectively. β, γ, and η are coefficients describing the rates of FN production, FN degradation, and TAF uptake by ECs, respectively.

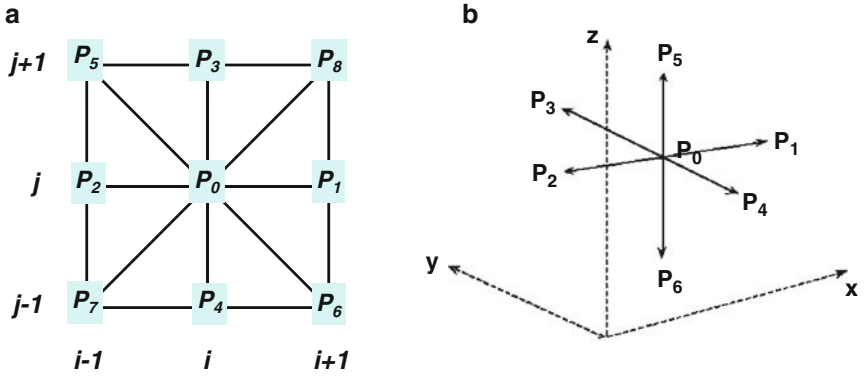

Fig. 14.1 Motion directions of ECs. (**a**) 2D9P model: at each node, the sprout can grow in eight directions or being stationary; (**b**) 3D7P model: at each node, the sprout can grow in six directions or being stationary

Discretization Scheme (2D9P and 3D7P Model)

In order to track the motion of individual endothelial cells located at the sprout tips and the subsequent formation of vessels, the discretized form of the system of partial differential equations is used, obtained by the standard Euler finite difference approximation. Here, we use 2D9P model (Wu et al. 2008a) for the 2D situation. In the 2D9P model, the EC can migrate in eight directions as shown in Fig. 14.1a, and accordingly, the 2D system of equations is discreted using a 9-point finite difference scheme as,

$$\begin{aligned} n_{i,j}^{q+1} &= n_{i,j}^{q} P_0 + n_{i+1,j}^{q} P_1 + n_{i-1,j}^{q} P_2 + n_{i,j+1}^{q} P_3 + n_{i,j-1}^{q} P_4 \\ &\quad + n_{i-1,j+1}^{q} P_5 + n_{i+1,j-1}^{q} P_6 + n_{i-1,j-1}^{q} P_7 + n_{i+1,j+1}^{q} P_8, \\ f_{i,j}^{q+1} &= f_{i,j}^{q}(1 - \Delta t \gamma n_{i,j}^{q}) + k\beta n_{i,j}^{q}, \\ c_{i,j}^{q+1} &= c_{i,j}^{q}(1 - \Delta t \eta n_{i,j}^{q}), \end{aligned} \tag{14.2}$$

where i, j specify the location on the grid and q is for the time step. The spatial distance is $x = i\Delta x$, $y = j\Delta y$, and the time is $t = q\Delta t$. The coefficients $P_0 \sim P_8$ relate to the likelihood of the EC remaining stationary (P_0), or moving along the eight directions controlled by local chemical environment, see Fig. 14.1a. The full expression of $P_0 \sim P_8$ is as follows (in which $\Delta x = \Delta y = h$, $k = \Delta t$),

$$P_0 = 1 - \frac{4kD}{h^2} + \frac{k\sigma\chi}{64h^2(1+\sigma c_{i,j}^{q})^2}(S_1^2 + S_2^2) - \frac{k\chi}{2h^2(1+\sigma c_{i,j}^{q})}S_5 - \frac{k\rho}{2h^2}S_6$$

$$P_1 = \frac{kD}{2h^2} - \frac{k}{32h^2}\left(\frac{\chi}{1+\sigma c_{i,j}^{q}}S_1 + \rho S_3\right) \quad P_5 = \frac{kD}{2h^2} + \frac{k}{64h^2}\left(\frac{\chi}{1+\sigma c_{i,j}^{q}}(S_1 - S_2) + \rho(S_3 - S_4)\right)$$

$$P_2 = \frac{kD}{2h^2} + \frac{k}{32h^2}\left(\frac{\chi}{1+\sigma c_{i,j}^q} S_1 + \rho S_3\right) \quad P_6 = \frac{kD}{2h^2} - \frac{k}{64h^2}\left(\frac{\chi}{1+\sigma c_{i,j}^q}(S_1 - S_2) + \rho(S_3 - S_4)\right)$$

$$P_3 = \frac{kD}{2h^2} - \frac{k}{32h^2}\left(\frac{\chi}{1+\sigma c_{i,j}^q} S_2 + \rho S_4\right) \quad P_7 = \frac{kD}{2h^2} + \frac{k}{64h^2}\left(\frac{\chi}{1+\sigma c_{i,j}^q}(S_1 + S_2) + \rho(S_3 + S_4)\right)$$

$$P_4 = \frac{kD}{2h^2} + \frac{k}{32h^2}\left(\frac{\chi}{1+\sigma c_{i,j}^q} S_2 + \rho S_4\right) \quad P_8 = \frac{kD}{2h^2} - \frac{k}{64h^2}\left(\frac{\chi}{1+\sigma c_{i,j}^q}(S_1 + S_2) + \rho(S_3 + S_4)\right)$$

$$\begin{aligned}
S_1 &= 2(c_{i+1,j}^q - c_{i-1,j}^q) + (c_{i+1,j-1}^q - c_{i-1,j+1}^q) + (c_{i+1,j+1}^q - c_{i-1,j-1}^q)\\
S_2 &= 2(c_{i,j+1}^q - c_{i,j-1}^q) + (c_{i-1,j+1}^q - c_{i+1,j-1}^q) + (c_{i+1,j+1}^q - c_{i-1,j-1}^q)\\
S_3 &= 2(f_{i+1,j}^q - f_{i-1,j}^q) + (f_{i+1,j-1}^q - f_{i-1,j+1}^q) + (f_{i+1,j+1}^q - f_{i-1,j-1}^q)\\
S_4 &= 2(f_{i,j+1}^q - f_{i,j-1}^q) + (f_{i-1,j+1}^q - f_{i+1,j-1}^q) + (f_{i+1,j+1}^q - f_{i-1,j-1}^q)\\
S_5 &= c_{i+1,j+1}^q + c_{i+1,j}^q + c_{i+1,j-1}^q + c_{i,j+1}^q + c_{i,j-1}^q + c_{i-1,j+1}^q + c_{i-1,j}^q + c_{i-1,j-1}^q - 8c_{i,j}^q\\
S_6 &= f_{i+1,j+1}^q + f_{i+1,j}^q + f_{i+1,j-1}^q + f_{i,j+1}^q + f_{i,j-1}^q + f_{i-1,j+1}^q + f_{i-1,j}^q + f_{i-1,j-1}^q - 8f_{i,j}^q.
\end{aligned} \tag{14.3}$$

In 3D7P model, the 3D system of the equations is discreted using a 7-point finite difference approximation,

$$\begin{aligned}
n_{l,m,n}^{q+1} &= n_{l,m,n}{}^q P_0 + n_{l+1,m,n}{}^q P_1 + n_{l-1,m,n}{}^q P_2 + n_{l,m+1,n}{}^q P_3 + n_{l,m-1,n}{}^q P_4\\
&\quad + n_{l,m,n+1}{}^q P_5 + n_{l,m,n-1}{}^q P_6,\\
f_{l,m,n}^{q+1} &= f_{l,m,n}^q (1 - \Delta t \gamma n_{l,m,n}^q) + k\beta n_{l,m,n}^q,\\
c_{l,m,n}^{q+1} &= c_{l,m,n}^q (1 - \Delta t \eta n_{l,m,n}^q),
\end{aligned} \tag{14.4}$$

where l, m, n specify the location on the grid and q is for the time step, i.e., the spatial distance $x = l\Delta x$, $y = m\Delta y$, $z = l\Delta z$ and the time $t = q\Delta t$. Lisewise, $P_0 \sim P_6$ relate to the likelihood of the EC remaining stationary (P_0), or moving along the six directions, as shown in Fig. 14.1b. The full expression of $P_0 \sim P_6$ is as follows (in which $\Delta x = \Delta y = \Delta z = h$, $k = \Delta t$),

$$\begin{aligned}
P_0 = 1 &- \frac{6kD}{h^2} + \frac{k\sigma\chi}{4h^2(1+\sigma c_{l,m,n}^q)^2}\left[\left(c_{l+1,m,n}^q - c_{l-1,m,n}^q\right)^2 + \left(c_{l,m+1,n}^q - c_{l,m-1,n}^q\right)^2\right.\\
&\left. + (c_{l,m,n+1}^q - c_{l,m,n-1}^q)^2\right]\\
&- \frac{k\chi}{h^2(1+\sigma c_{l,m,n}^q)}\left(c_{l+1,m,n}^q + c_{l-1,m,n}^q + c_{l,m+1,n}^q + c_{l,m-1,n}^q + c_{l,m,n+1}^q + c_{l,m,n-1}^q - 6c_{l,m,n}^q\right)\\
&- \frac{k\rho}{h^2}\left(f_{l+1,m,n}^q + f_{l-1,m,n}^q + f_{l,m+1,n}^q + f_{l,m-1,n}^q + f_{l,m,n+1}^q + f_{l,m,n-1}^q - 6f_{l,m,n}^q\right)
\end{aligned}$$

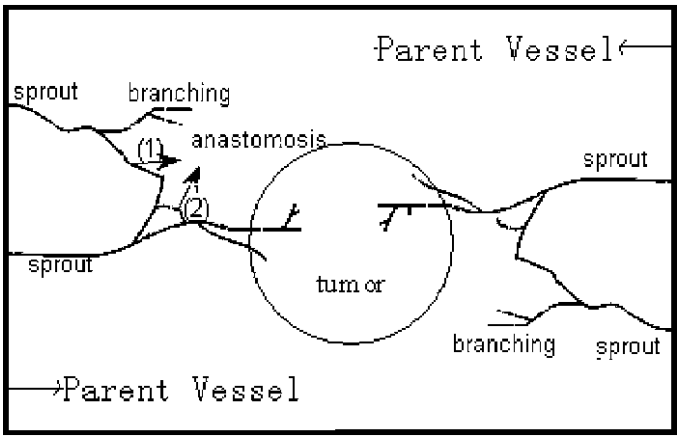

Fig. 14.2 Schematic representation of branching and anastomosis of sprouts

$$
\begin{aligned}
P_1 &= \frac{kD}{h^2} - \frac{k}{4h^2}\left[\frac{\chi}{(1+\sigma c^q_{l,m,n})}\left(c^q_{l+1,m,n} - c^q_{l-1,m,n}\right) + \rho\left(f^q_{l+1,m,n} - f^q_{l-1,m,n}\right)\right];\\
P_2 &= \frac{kD}{h^2} + \frac{k}{4h^2}\left[\frac{\chi}{(1+\sigma c^q_{l,m,n})}\left(c^q_{l+1,m,n} - c^q_{l-1,m,n}\right) + \rho\left(f^q_{l+1,m,n} - f^q_{l-1,m,n}\right)\right]\\
P_3 &= \frac{kD}{h^2} - \frac{k}{4h^2}\left[\frac{\chi}{(1+\sigma c^q_{l,m,n})}\left(c^q_{l,m+1,n} - c^q_{l,m-1,n}\right) + \rho\left(f^q_{l,m+1,n} - f^q_{l,m-1,n}\right)\right];\\
P_4 &= \frac{kD}{h^2} + \frac{k}{4h^2}\left[\frac{\chi}{(1+\sigma c^q_{l,m,n})}\left(c^q_{l,m+1,n} - c^q_{l,m-1,n}\right) + \rho\left(f^q_{l,m+1,n} - f^q_{l,m-1,n}\right)\right]\\
P_5 &= \frac{kD}{h^2} - \frac{k}{4h^2}\left[\frac{\chi}{(1+\sigma c^q_{l,m,n})}\left(c^q_{l,m,n+1} - c^q_{l,m,n-1}\right) + \rho\left(f^q_{l,m,n+1} - f^q_{l,m,n-1}\right)\right];\\
P_6 &= \frac{kD}{h^2} + \frac{k}{4h^2}\left[\frac{\chi}{(1+\sigma c^q_{l,m,n})}\left(c^q_{l,m,n+1} - c^q_{l,m,n-1}\right) + \rho\left(f^q_{l,m,n+1} - f^q_{l,m,n-1}\right)\right]
\end{aligned}
\tag{14.5}
$$

Once the sprouts grow into the tumor, the migration will be adjusted in terms of the mechanical features of the tumor tissues (Gao et al. 2006; Wu et al. 2008a).

Vessel Branching and Anastomosis

The process of branching and anastomosis are assumed as follows (Anderson and Chaplain 1998), see Fig. 14.2.

For branching (formation of new sprouts from existing sprout tips):

1. The likelihood of an existing sprout increases with the local TAF concentration;
2. A sprout vessel must reach a certain level of maturation before it is able to branch.

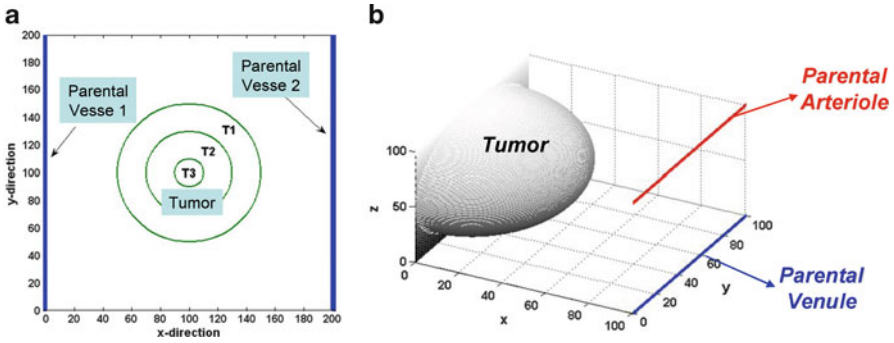

Fig. 14.3 Model scheme of tumor angiogenesis. (**a**) 2D; (**b**) 3D

For anastomosis (formation of loops by fusion of two colliding sprouts):

1. If two sprouts collide as they grow, only one of them is allowed to keep growing (the choice of which is random);
2. If a sprout tip meets another sprout, they fuse to form a loop.

Simulation Region

If the tumor radius is R_T, the tumor is divided into three regions: (a) well vascularized $0.6R_\mathrm{T} \leq r < R_\mathrm{T}$; (b) seminecrotic $0.4R_\mathrm{T} \leq r < 0.6R_\mathrm{T}$; (c) necrotic $r \leq 0.4R_\mathrm{T}$. The simulation regions are 4 mm×4 mm and 2 mm×2 mm×2 mm for the 2D (as shown in Fig. 14.3a) and 3D models (as shown in Fig. 14.3b), respectively. Two parent vessels are located on the side of the tumor.

Boundary and Initial Conditions

Boundary conditions: Zero flux conditions are imposed on the boundaries,

$$\zeta \cdot [-D\nabla n + n\left(\chi\left(c\right)\nabla c + \rho\nabla f\right)] = 0 \tag{14.6}$$

ζ is outward unit normal vector.

Initial conditions: The initial EC density is assumed to be zero in the whole domain except the sprouts on the parent vessel. The initial distribution of FN and TAF concentrations are described by:

$$c(r,0) = \begin{cases} 1 & 0 \leq r \leq 0.3 \\ \dfrac{(v-r)^2}{v-0.4771} & 0.3 \leq r \end{cases} \tag{14.7}$$

$$f(r,0) = \begin{cases} \zeta_1 \left(\exp^{-\frac{x^2}{\varepsilon_1}} + \exp^{-\frac{(x-1)^2}{\varepsilon_1}} \right) & (2D \text{ model}) \\ \zeta_1 \left(\exp^{-\frac{(x-1)^2+(z-1)^2}{\varepsilon_1}} + \exp^{-\frac{(x-1)^2+z^2}{\varepsilon_1}} \right) & (3D \text{ model}) \end{cases}, \quad (14.8)$$

where r is the dimensionless distance from the tumor center and $v = 1.07$, assuming the tumor has a necrotic region with the radius of $0.6R_T$ (corresponding to $r \leq 0.3$, R_T is the tumor radius). Taking (14.7) as the initial conditions for the TAF concentration profile might then be a reasonable description of the actual concentration field arising from a circular tumor implant with a necrotic region. In (14.8), x, z are the dimensionless distance along the x- and z-axis, ζ_1, ε_1 are the positive constants.

Parameter Values

The values of dimensionless parameters imposed in the simulations were: $D = 0.00035$, $\sigma = 0.6$, $\chi = 0.38$, $\rho = 0.22$, $\beta = 0.05$, $\gamma = 0.1$, $\eta = 0.1$, $\zeta_1 = 0.45$, $\varepsilon_1 = 0.75$ (Anderson and Chaplain 1998; Stéphanou et al. 2005). Details of the parameter normalization were given in (Anderson and Chaplain 1998). Time was scaled as $\tilde{t} = t/\tau$ with $\tau = L/D_c$, where L is the length of the domain and $D_c = 2.9 \times 10^{-7}\,\mathrm{cm}^2/\mathrm{s}$ is taken as the diffusion coefficient for TAF (Sherratt and Murray 1990; Bray 1992). In 2D model, the diameters of two parent vessels are 30 μm, in 3D model, the diameters of the parental arteriol and venule were set as 24 μm and 32 μm, respectively, in accordance with the physiological values at microvascular scale. The diameter values of the angiogenic vessels were obtained by the rules described in Wu et al. (2008b, 2009a).

2.1.2 Simulation Results

Seven positions were chosen arbitrarily along the two parent vessels as our initial sprouting sites.

2D Microvasculature

2D network is shown in Fig. 14.4, in which Fig. 14.4a shows the vasculature structure, Fig. 14.4b shows the time evolution of the number of vessels. It took approximately 24 days real time for the growth process to be completed. The simulated network presents the abnormal geometric and morphological features of tumor microvasculature, such as vessel tortuosity, branching and anastomosis, heterogeneous density distribution, and "brush border" phenomenon in well vascularized region. The extensive neovessel bed can supply not only the nutrients for the rapid growth of tumor tissues but also the metastasis pathways for tumor cells.

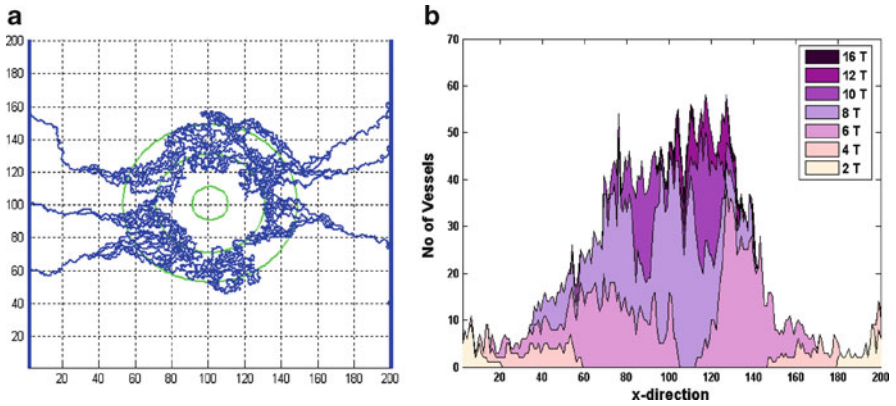

Fig. 14.4 Simulation results of 2D tumor angiogenesis: (**a**) vasculature structure; (**b**) time evolution of the number of vessels (1T = 1.5 day)

3D Microvasculature

Vasculature Architecture

Figure 14.5a shows the angiogenesis result of the 3D vascular architecture. It took approximately $\tilde{t} = 16$ (corresponding to $t = 24$ days) for the growth process to be completed. General morphological features of the network such as the average vascular density; the average vessel branching generation; the average distance of tumor tissue from the nearest blood vessels, are presented in Fig. 14.5b–d, respectively, as a function of dimensionless radial distance to the tumor center. It indicates the vessel branching are more easily to occur in the region of $x \in [30, 60]$, which are approximately corresponding to the well-vascularized and immediate outside area of the tumor (Fig. 14.5c). Likewise, the 3D results could also present the abnormal geometric and morphological features of tumor microvasculature

Vessels Connectivity Analysis and Classification

A postprocessing step of angiogenesis simulation should be carried out to exam the vessel connectivity. The unconnected vessels will be removed to form a functional circulation domain for blood flow. The examination of vessel connectivity is carried out to guarantee the efficiency of blood flow through the network. In real situation, microvessels are classified into different groups of vessels by their structure and function which will be difficult to mimic in the simulation model. In this study, a critical generation n_c is defined to classify the vessels artificially. It is assumed that if the branching generation is beyond nc, the vessels are viewed as capillaries, otherwise are classified as small arterioles or venules according to their original "mother" vessels. Figure 14.6 presents a typical network with the vessels colored by the groups, i.e., red – arterioles, blue – venules and green – capillaries, with

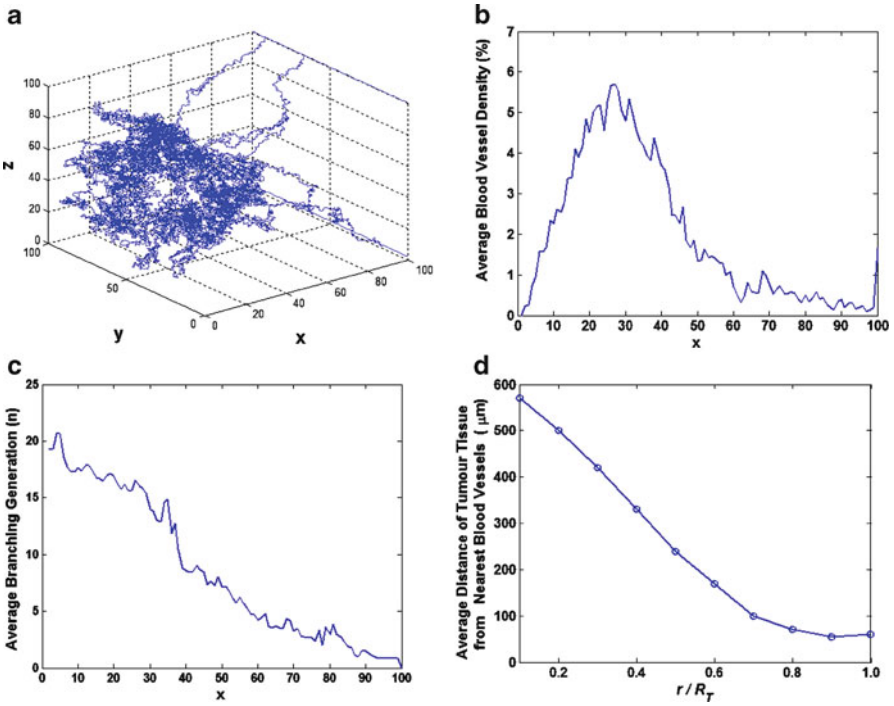

Fig. 14.5 Simulation results of 3D tumor angiogenesis: (**a**) vasculature structure; (**b**) distribution of the average vascular density along *x*-direction; (**c**) distribution of the average vessel diameters along *x*-direction; (**d**) distribution of the average distance of tumor tissue from the nearest blood vessels. (*x*-axis represents the normalized distance from the tumor center to the parent vessels, in Fig. 14.5d R_T is the tumor radius, $r/R_T = 0.0, 1.0$ correspondents to the tumor center and boundary, respectively)

$n_c = 9$. Form the figures, the vessels inside of tumor mostly belong to "capillaries" (Fig. 14.6b), and the diameters of these vessels are nearly 8 μm (Fig. 14.6c). This vessel classification enables us to define the vessel structure such as permeability more accurately.

2.2 "Normalized" Microvasculature 1: Tumor Antiangiogenesis

2.2.1 Methods and Models

Only 2D models of tumor antiangiogenesis, responding to andostatin and endostatin treatments, were developed in this part of study.

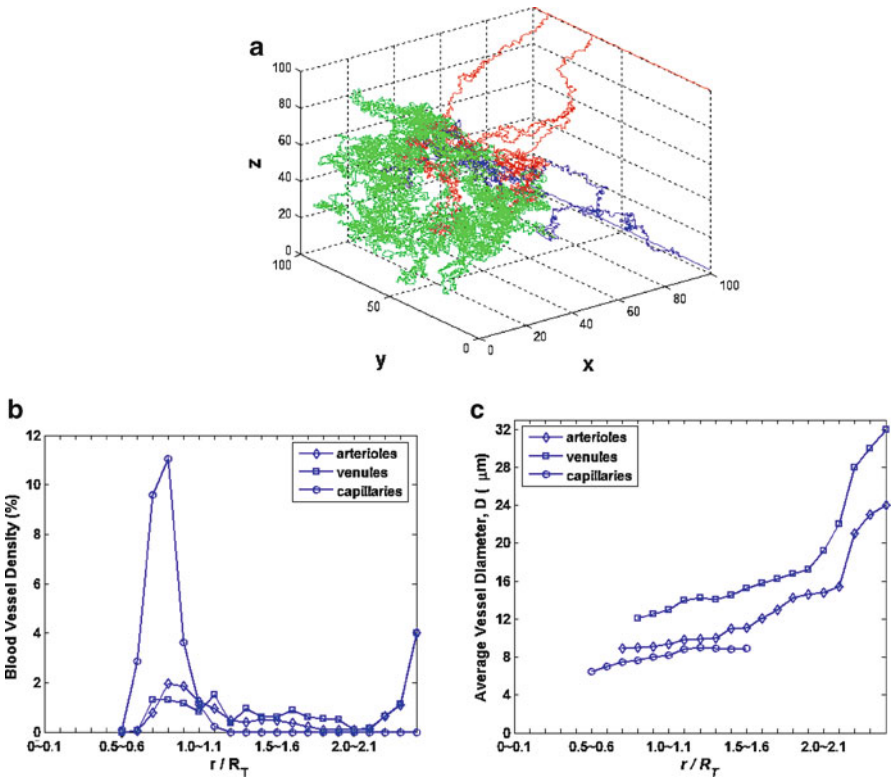

Fig. 14.6 Vessel classification of the 3D angiogenic network: three groups of vessels are presented: *red* – arterioles, *blue* – venules, and *green* – capillaries, according to their branching generations. (**a**) vasculature structure; (**b**) distribution of the average vascular density; (**c**) distribution of the average vessel diameter

Governing Equations

Modified from (14.1), the inhibition of andostatin (AS) and endostatin (ES) on EC proliferation and apoptosis are included in the models in order to simulate the antiangiogenesis effect, the density of AS and ES (represented by "a" and "e," respectively) is also changed by diffusion, absorption (or degeneration), and external injection. The govern equations can be written as the following nondimensional equations (Tee and DiStefano III 2004; Zhao et al. 2006; Wu 2009b),

$$\frac{\partial n}{\partial t} = D\nabla^2 n - \nabla\cdot\left(\frac{\chi}{1+\sigma c}n\nabla c\right) - \nabla\cdot(\xi a n\nabla a) - \nabla\cdot(\rho n\nabla f)$$
$$+\beta_r(1-n)nH(c)\left(1-\frac{\varepsilon_{\max}ee_0}{eC_{50}+ee_0}\right) - \beta_d n$$

$$\begin{aligned}
\frac{\partial f}{\partial t} &= \beta n - \gamma n f \\
\frac{\partial c}{\partial t} &= -\eta n c \\
\frac{\partial a}{\partial t} &= D_a \frac{\partial a^2}{\partial^2 x} - \gamma_a a \\
\frac{\partial e}{\partial t} &= -\gamma_c e + \gamma_u U_{I,\mathrm{ex}},
\end{aligned} \tag{14.9}$$

where D, χ, and ρ are the coefficients of EC diffusion, chemotaxis to TAF and haptotaxis to ECM, respectively. ξ is EC chemotaxis coefficient to AS. β_r is EC proliferation rate. $H(c)$ is an on–off function,

$$H(c) = \begin{cases} 0 & c \le c* \\ c - c^* & c > c* \end{cases}.$$

It means that if c is higher than a threshold value c^*, the EC may proliferate, otherwise it stays dormancy; $\varepsilon_{\max}$ is the maximum inhibiting effect of endostatin on ECs; eC_{50} is ES concentration that induce 50% of the maximum inhibiting effect; e_0 is the initial concentration of ES; β_d is EC loss rate. β is Fn production rate; γ is rate of FN uptaken by ECs. η is TAF rate of uptake by ECs. D_a is AS diffusion coefficient; γ_a is AS rate of uptake by ECs. γ_c is ES plasma clearance rate; $U_{I,\mathrm{ex}}$ is the exogenous inputs of ES; γ_u is the positive coefficient of ES inputs.

The 2D9P discretized form of the system of partial differential equations is used (Wu et al. 2008a),

$$\begin{aligned}
n_{i,j}^{q+1} &= n_{i,j}^q P_0 + n_{i+1,j}^q P_1 + n_{i-1,j}^q P_2 + n_{i,j+1}^q P_3 + n_{i,j-1}^q P_4 \\
&\quad + n_{i-1,j+1}^q P_5 + n_{i+1,j-1}^q P_6 + n_{i-1,j-1}^q P_7 + n_{i+1,j+1}^q P_8 \\
f_{i,j}^{q+1} &= f_{i,j}^q (1 - \Delta t \gamma n_{i,j}^q) + \Delta t \beta n_{i,j}^q \\
c_{i,j}^{q+1} &= c_{i,j}^q (1 - \Delta t \eta n_{i,j}^q) \\
a_{i,j}^{q+1} &= a_{i,j}^q (1 - \Delta t \gamma_a) + \frac{\Delta t D_a}{\Delta x^2} (a_{i+1,j}^q + a_{i-1,j}^q - 2 a_{i,j}^q) \\
e_{i,j}^{q+1} &= e_{i,j}^q (1 - \Delta t \gamma_c) + \Delta t \gamma_u U_{i,\mathrm{ex}},
\end{aligned} \tag{14.10}$$

where i, j specify the location on the grid and q is for the time step, i.e., $x = i\Delta x$, $y = j\Delta y$, and $t = q\Delta t$. The coefficients $P_0 \sim P_8$ incorporate the effects of random, chemotactic, and haptotactic movement and depend upon the local chemical environment (FN and TAF, AS, ES concentrations). The full expression of $P_0 \sim P_8$ is as follows (in which $\Delta x = \Delta y = h$, $k = \Delta t$),

$$P_0 = 1 - \frac{4kD}{h^2} + \frac{k\sigma\chi}{64h^2\left(1+\sigma c_{i,j}^q\right)^2}\left(S_1^2 + S_2^2\right) - \frac{k\chi}{2h^2\left(1+\sigma c_{i,j}^q\right)}S_5 - \frac{k\rho}{2h^2}S_6$$
$$-\frac{k\xi}{4h^2}\left[\left(a_{i+1,j}^q - a_{i-1,j}^q\right)^2 + \left(a_{i,j+1}^q - a_{i,j-1}^q\right)^2\right] - \frac{k\xi}{h^2}a_{i,j}^q S_7$$
$$\beta_r\left(1-n_{i,j}^q\right)H\left(c_{i,j}^q\right)\left(1 - \frac{\varepsilon_{\max}e_{i,j}^q e_0}{e_{i,j}^q C_{50} + e_{i,j}^q e_0}\right) - \beta_d k$$

$$P_1 = \frac{kD}{2h^2} - \frac{k}{32h^2}\left(\frac{\chi}{1+\sigma c_{i,j}^q}S_1 + \rho S_3\right) - \frac{k\xi}{4h^2}a_{i,j}^q\left(a_{i+1,j}^q - a_{i-1,j}^q\right)$$

$$P_2 = \frac{kD}{2h^2} + \frac{k}{32h^2}\left(\frac{\chi}{1+\sigma c_{i,j}^q}S_1 + \rho S_3\right) + \frac{k\xi}{4h^2}a_{i,j}^q\left(a_{i+1,j}^q - a_{i-1,j}^q\right)$$

$$P_3 = \frac{kD}{2h^2} - \frac{k}{32h^2}\left(\frac{\chi}{1+\sigma c_{i,j}^q}S_2 + \rho S_4\right) - \frac{k\xi}{4h^2}a_{i,j}^q\left(a_{i,j+1}^q - a_{i,j-1}^q\right)$$

$$P_4 = \frac{kD}{2h^2} + \frac{k}{32h^2}\left(\frac{\chi}{1+\sigma c_{i,j}^q}S_2 + \rho S_4\right) + \frac{k\xi}{4h^2}a_{i,j}^q\left(a_{i,j+1}^q - a_{i,j-1}^q\right)$$

$$P_5 = \frac{kD}{2h^2} + \frac{k}{64h^2}\left(\frac{\chi}{1+\sigma c_{i,j}^q}\left(S_1 - S_2\right) + \rho\left(S_3 - S_4\right)\right)$$

$$P_6 = \frac{kD}{2h^2} - \frac{k}{64h^2}\left(\frac{\chi}{1+\sigma c_{i,j}^q}\left(S_1 - S_2\right) + \rho\left(S_3 - S_4\right)\right)$$

$$P_7 = \frac{kD}{2h^2} + \frac{k}{64h^2}\left(\frac{\chi}{1+\sigma c_{i,j}^q}\left(S_1 + S_2\right) + \rho\left(S_3 + S_4\right)\right)$$

$$P_8 = \frac{kD}{2h^2} - \frac{k}{64h^2}\left(\frac{\chi}{1+\sigma c_{i,j}^q}\left(S_1 + S_2\right) + \rho\left(S_3 + S_4\right)\right)$$

$$S_1 = 2\left(c_{i+1,j}^q - c_{i-1,j}^q\right) + \left(c_{i+1,j-1}^q - c_{i-1,j+1}^q\right) + \left(c_{i+1,j+1}^q - c_{i-1,j-1}^q\right)$$

$$S_2 = 2\left(c_{i,j+1}^q - c_{i,j-1}^q\right) + \left(c_{i-1,j+1}^q - c_{i+1,j-1}^q\right) + \left(c_{i+1,j+1}^q - c_{i-1,j-1}^q\right)$$

$$S_3 = 2\left(f_{i+1,j}^q - f_{i-1,j}^q\right) + \left(f_{i+1,j-1}^q - f_{i-1,j+1}^q\right) + \left(f_{i+1,j+1}^q - f_{i-1,j-1}^q\right)$$

$$S_4 = 2\left(f_{i,j+1}^q - f_{i,j-1}^q\right) + \left(f_{i-1,j+1}^q - f_{i+1,j-1}^q\right) + \left(f_{i+1,j+1}^q - f_{i-1,j-1}^q\right)$$

$$S_5 = c_{i+1,j+1}^q + c_{i+1,j}^q + c_{i+1,j-1}^q + c_{i,j+1}^q + c_{i,j-1}^q + c_{i-1,j+1}^q + c_{i-1,j}^q$$
$$+c_{i-1,j-1}^q - 8c_{i,j}^q$$

$$S_6 = f^q_{i+1,j+1} + f^q_{i+1,j} + f^q_{i+1,j-1} + f^q_{i,j+1} + f^q_{i,j-1} + f^q_{i-1,j+1} + f^q_{i-1,j} + f^q_{i-1,j-1} - 8f^q_{i,j}$$

$$S_7 = a^q_{i+1,j+1} + a^q_{i+1,j} + a^q_{i+1,j-1} + a^q_{i,j+1} + a^q_{i,j-1} + a^q_{i-1,j+1} + a^q_{i-1,j} + a^q_{i-1,j-1} - 8a^q_{i,j}. \quad (14.11)$$

The rules for vessel branching and anastomosis, the definition of branching generation and vessel diameters are the same as the description in the earlier text.

Boundary and Initial Conditions

The simulation space, boundary and initial conditions were as the same described in the earlier text. In addition, the initial concentration of angiostatin is described by:

$$a(r,0) = \zeta_2 \left(\exp^{-\frac{x^2}{\varepsilon_2}} + \exp^{-\frac{(x-1)^2}{\varepsilon_2}} \right), \quad (14.12)$$

where ζ_2 and ε_2 are the positive constants. The initial concentration of endostatin is $e_0 = 2.0 \times 10^{-9}$mol/L.

Parameter Values

The dimensionless parameter values used for the simulations are (Tee and DiStefano III 2004; Zhao et al. 2006; Wu 2009b): $D = 0.00035, \sigma = 0.6, \chi = 0.38, \rho = 0.22, \beta = 0.05, \gamma = 0.1, \eta = 0.1, \beta_d = 8.3, \varepsilon_{\max} = 1.0, D_a = 0.1, \gamma_a = 6.0, \gamma_c = 8.0, \gamma_u = 15.0, \beta_r = 1.5, \xi = 0.1, U_{I,\text{ex}} = 20\,\text{mg/kg/day}$. Time is scaled as $\tilde{t} = t/\tau$ with $\tau = L/D_c$, where $L = 4\,\text{mm}$ is the length of the domain and $D_c = 2.9 \times 10^{-7}\,\text{cm}^2/\text{s}$ is taken as the diffusion coefficient for TAF.

2.2.2 Antiangiogenesis Simulation Results

In addition to the general EC proliferation, random motility and haptotaxis, four different kinds of models were generated based on the different chemotaxis factors. They are, (1) **AGF** (angiogenesis factor) – the same model as the 2D model in "Sect. 2.1.1" in which AGF is the only chemotaxis factor. It is treated as the control group in this part of study; (2) **AGF_AS** – the chemotaxis factors are AGF and AS; (3) **AGF_ES** – the chemotaxis factors are AGF and ES with an ES infusion of 20 mg/kg/day; (4) **AGF_AS_ES:10, AGF_AS_ES:6, AGF_AS_ES:4** – the chemotaxis factors are AGF, AS, and an ES infusion of 20 mg/kg/day since the 10th, 6th, 4th day from angiogenesis start, respectively. The results of **AGF**only modes are taken as the control group, while the other five are considered the study groups.

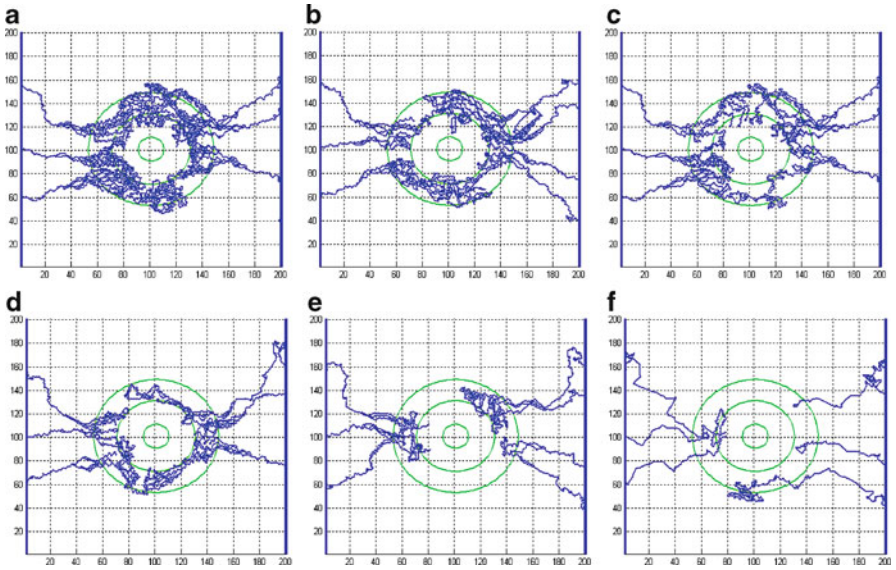

Fig. 14.7 Microvascular networks from the antiangiogenesis simulations. (**a**) **AGF** model (the same as Fig. 14.4a); (**b**) **AGF_AS** model; (**c**) **AGF_ES** model; (**d**) **AGF_AS_ES:10** model; (**e**) **AGF_AS_ES:6** model; (**f**) **AGF_AS_ES:4**

Figure 14.7 shows the microvascular networks from the antiangiogenesis simulations. Figure 14.7a is the result of model **AGF** (the same as Fig. 14.4a), which is considered as the control vasculature. The simulated vasculature of **AGF_AS** model is shown in Fig. 14.7b. Under the inhibition effects of AS, the angiogenic network has become sparser with decreased vessel density, while the growth rates of the capillary sprouts have not been inhibited potently. Figure 14.7c is the simulation result of **AGF_ES** model, compared with Fig. 14.7a, the growth rates and the vessel branching decreased with a reduced vessel density under the inhibiting effects of ES. Figure 14.7d–f represents the networks simulated by considering the chemotaxis of ECs to AGF, AS, and ES since the 10th, 6th, 4th day from angiogenesis start, respectively (**AGF_AS_ES:10, 6, 4**). The figures show that the growth, proliferation, and branching of new vessels are distinctly inhibited, and the extents of vascularization are greatly decreased. Moreover, the earlier ES infusion, the better inhibition effects. Particularly in Fig. 14.7e, f, although a part of sprouts have grown into the tumor, the vessel networks have not matured to supply nutrients for the further development and pathways for the metabolic wastes because of the significant reduction of blood vessel density. It predicts that antiangiogenesis drugs could effectively inhibit the proliferation and migration of ECs on vessel sprouts in earlier period of tumor angiognesis, and as a result inhibit the further growth and metastasis of tuomr (Fig. 14.7d); while in later period of tumor angiogenesis, antiangiogenesis approach could be an assistant treatment combined with other therapies to control tumor growth (Fig. 14.7e, f).

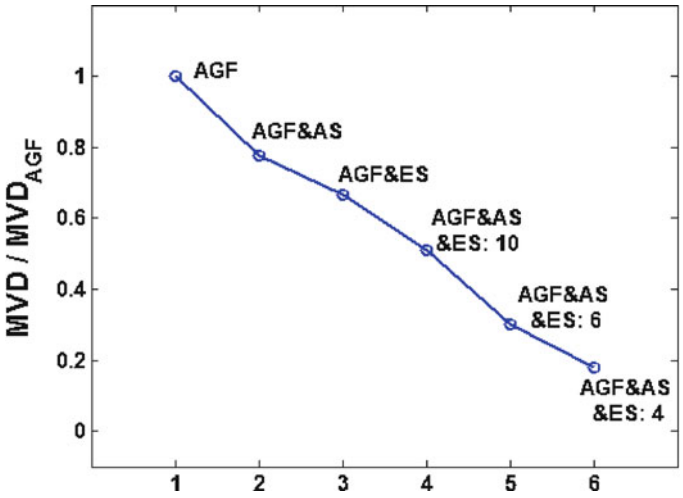

Fig. 14.8 Comparison of MVD values of the six groups

Weidner (1995) indicated that microvessel density (MVD) could be an index for tumor diagnosis. Here, we introduce MVD to compare the antiangiogenic effects of AS and ES to the angiogenesis quantitatively. Due to the simulation randomicities, 50 simulations were carried out for each case to obtain the average MVD, as shown in Fig. 14.8. According to the figure, both single and combination effect of AS and ES can effectively inhibit the process of tumor angiogenesis, especially for the combined model at an earlier stage (e.g., **AGF_AS_ES: 6, 4**). The inhibiting effects show similar feature as the experiment results of using AS and ES to influence the microvessel density as shown in Fig. 14.9 by Eriksson (Eriksson et al. 2003).

2.3 "Normalized" Microvasculature 2: Tumor Vascular-Disrupting

Some vascular-disrupting agents have been proven to effectively disrupt or prune vessels in tumor vascular system. Here, four vascular-disrupting approaches are designed, according to the abnormal characteristics of tumor vasculature. The original network is obtained from the 3D model of tumor angiogenesis in Sect. 2.1.2 as shown in Fig. 14.5a. Based on the original network, four networks with difference disrupting degrees or different disrupting parameters for each disrupting approaches were developed to simulate the disrupting effect. The disrupting approaches and resulted networks can be described as:

- *Disrupting randomly:* Disrupt vessels randomly from the original vascular network, and remove the vessel segments no longer forming loops for effective blood flow. "Network 2(R)," "Network 3(R)," "Network 4(R)" are obtained

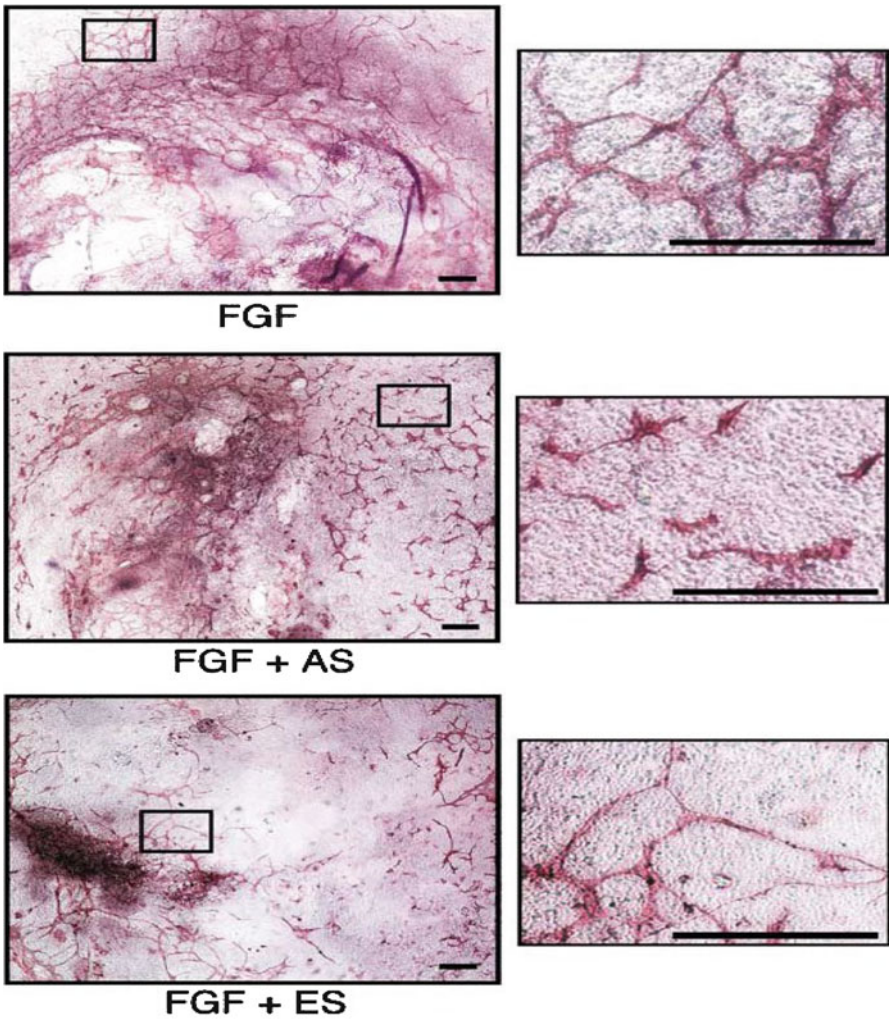

Fig. 14.9 Experimental observation of the inhibiting effects of AS and ES on EC migration. Larger magnifications of specific areas are shown in the right (Eriksson et al. 2003)

by disrupting randomly "Network 1," "Network 2(R)," and "Network 3(R)," respectively.

- *Disrupting according to network structure:* Accordingly, It is believed that trifurcations is a typical network structure abnormality which will influence the blood perfusion in the network (Chang et al. 2000; di Tomaso et al. 2005; McDonald and Choyke 2003). The "normalization" procedure is to cut the trifurcation and remove the residual vessel segments after disrupting. Another abnormality of tumor vasculature structure is vessels being twisted and tangled

with each other, which is pruned and normalized accordingly. "Network 2(S)" is by pruning the vessels having trifurcations branches from "Network 1"; "Network 3(S)" is by disrupting those twisted vessels (more than three that twist together) from "Network 1"; "Network 4(S)" is the result by combining the above two processing.

- *Disrupting according to vessel maturity:* Immature vessels in tumor will not only help local spread of cancer cells but also promote cancer cell infiltration through its own protease partial role. Studies have shown that, the treatment will be more effective than expected if the high proportion of immature vessels inside tumor are destroyed (Liu et al. 2003). Actually, vascular-disrupting agents have been developed for rupturing the rapidly proliferated and immature vascular endothelial cells, thereby block the low mature vessels inside of tumor (Benjamin et al. 1999; Darland and D'Amore 1999). In thischapter, we consider the growing time of vessels as a criterion of its maturity. "Network 2(M)," "Network 3(M)," "Network 4(M)" are obtained from cutting off the vessels in "Network 1" with a growing time less than 5 days, 10 days, and 15 days, respectively. The growing time for a complete network is 24 days.
- *Disrupting according to blood flowrate:* The researches predicated that antitumor drugs can damage some unmature blood vessels, and these vessels are often with lower blood flowrate (Stéphanou et al. 2005). To simulate the effect, we design the fourth approach – disrupting according to blood flowrate. "Network 2(F)," "Network 3(F)," and "Network 4(F)" are obtained by pruning the vessels, in which the blood flowrate is less than 20%, 40%, and 60% of the average blood flowrate throughout the network in "Network 1," respectively.

3 Simulation of Tumor Blood Perfusion with "Normalized" Microvasculature

3.1 Model of Tumor Haemodynamics

The flow model incorporates (a) intravascular blood flow; (b) transvascular leakiness; (c) interstitial fluid movement; (d) blood rheology; (e) vessel compliance; (f) lymphatic absorption, as shown in Fig. 14.10. The detailed description of flow simulation can be found in our recent published article (Wu et al. 2008a, 2009a; Wu 2009b). Briefly, for the intravascular blood flow the basic equation is the flux conservation and incompressible flow at each node. Flow resistance is assumed to follow Poiseuille's law in each vessel; the transvascular flow rate is controlled by starling's law; Darcy's law is used to calculate the interstitial fluid flow. The intravascular and interstitial flow is coupled by the transvascular flow. In addition, blood viscosity is calculated based on the formula developed by Pries et al. (1994), in which bloodviscosity is the function of vessel diameter, local

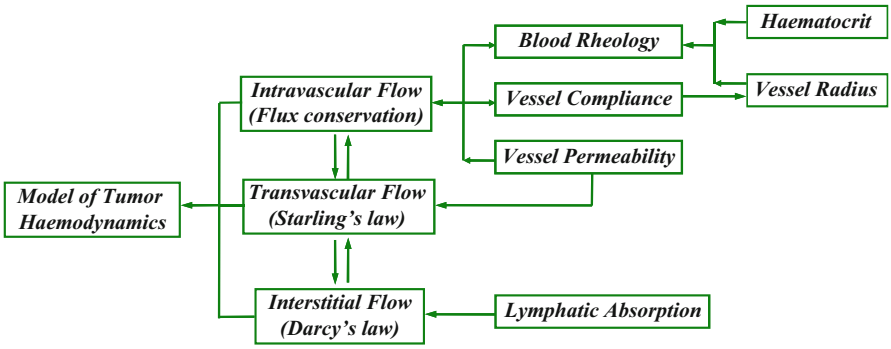

Fig. 14.10 Schematic structure of the flow model

hematocrit, and plasma viscosity. It is assumed that the blood vessels outside the tumor are rigid, the vessel compliance within the tumor is calculated based on the equation of Netti et al. (1996). The distribution of red blood cells (RBCs) at microvascular bifurcations is represented according to the approach proposed by Pries et al. (2005).

A specific coupling procedure is developed in the study to couple the intravascular and interstitial flow. It is based on the iteratively numerical simulation techniques, including local iterations at individual parameter level and one global loop to provide coupling and control of the simulation convergence. The schematic structure of the interactive numerical procedure is shown in Fig. 14.11. For 2D vasculature, the boundary values of the two parental vessels are given $P_{\text{in},1} = P_{\text{in},2} = 25\,\text{mmHg}$, $P_{\text{out},1} = P_{\text{out},2} = 10\,\text{mmHg}$; for 3D vasculature, the pressure of the arteriole and venule parental vessels are given $P_{V,\text{A}} = 25\,\text{mmHg}$, $P_{V,\text{V}} = 10\,\text{mmHg}$. The other parameter values can be found in Wu et al. (2008a, 2009a) and Wu (2009b). The parameter naming system in this part is: subscript provides domain names. Intravascular, transcapillary, and interstitial are represented by ${}^*V$, ${}^*t$, ${}^*i$, respectively. For example, P_V, Q_t, U_i represents intravascular pressure, transcapillary flux and interstitial fluid velocity, respectively. The details can be found in "symbol description" at the end of the chapter.

3.2 Blood Perfusion with "Un-normalized" Microvasculature

3.2.1 Flow in the Vasculature

Figures 14.12a and 14.13a show the change of P_V with the topological and morphological structures of the vasculature for the 2D and 3D simulations, respectively. P_V drops monotonously from the bifurcations of the parent vessels toward the tumor and almost keeps at a constant value in the interior of tumor, where a

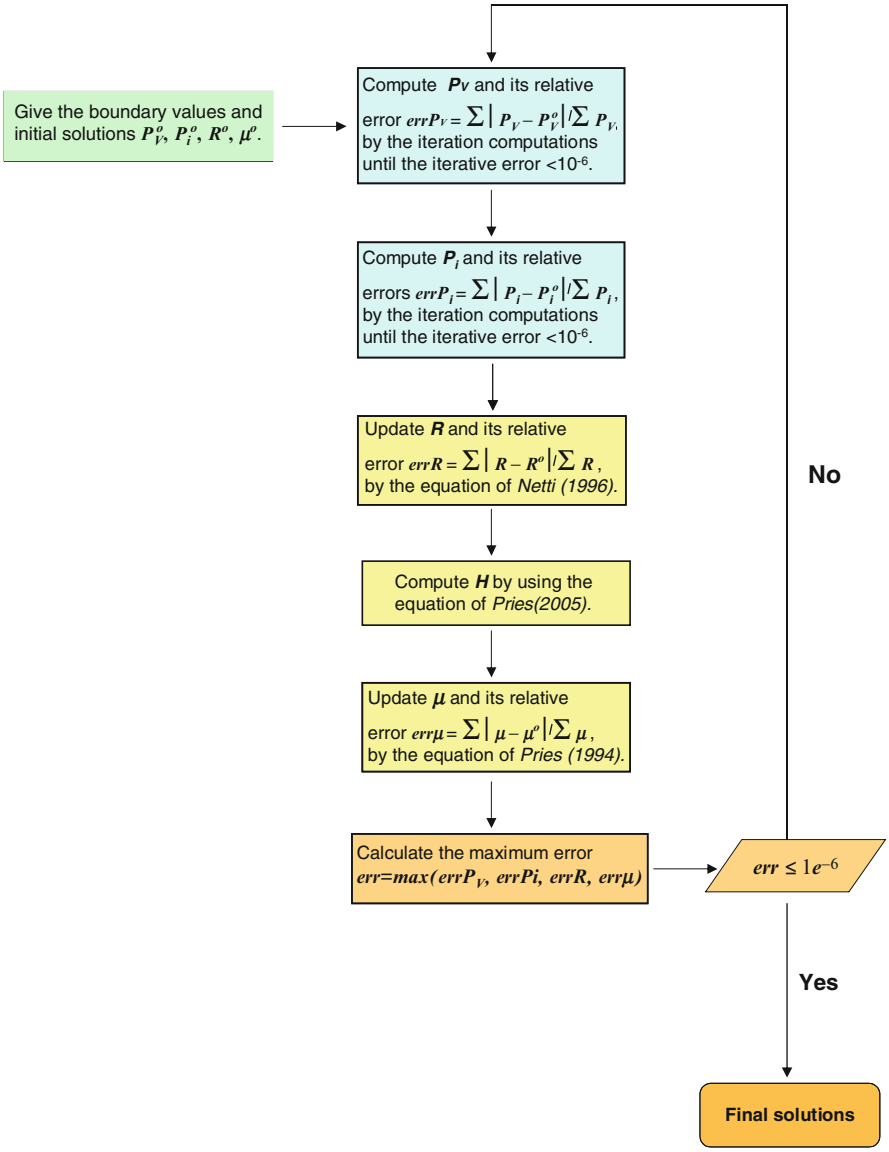

Fig. 14.11 Schematic structure of the interative numerical procedure

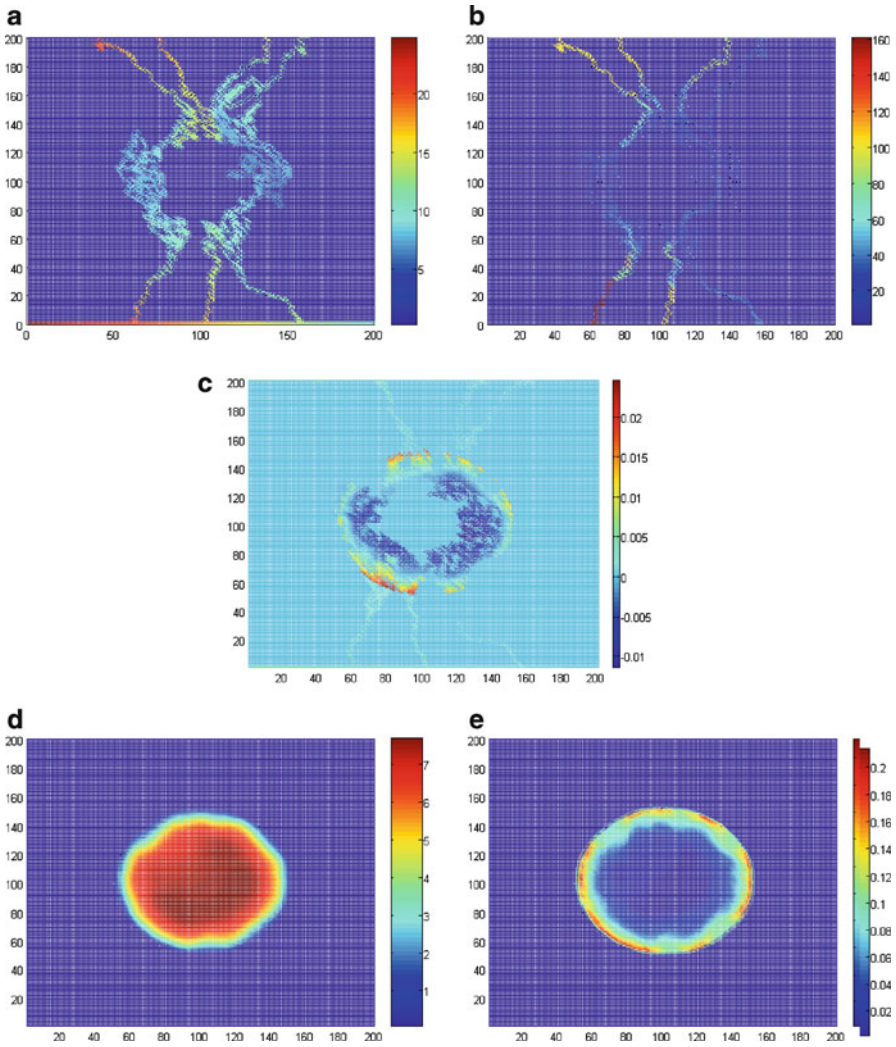

Fig. 14.12 2D flow simulation results of the control group **AGF** (on the network in Fig. 14.4a). The distributions of the (**a**) intravascular pressure P_V (mmHg); (**b**) intravascular velocity U_V (μm/s); (**c**) transvascular velocity U_t (μm/s); (**d**) interstitial pressure P_i (mmHg); (**e**) interstitial flow velocity U_i (μm/s)

more complex vessel structure occurs. The U_V distribution is given in Figs. 14.12b and 14.13b. Blood flows faster at the exterior and the periphery of the tumor than in the core regions. This is consistent with experimental observations (Hamberg et al. 1994; Donnelly et al. 2001; Tozer et al. 2005).

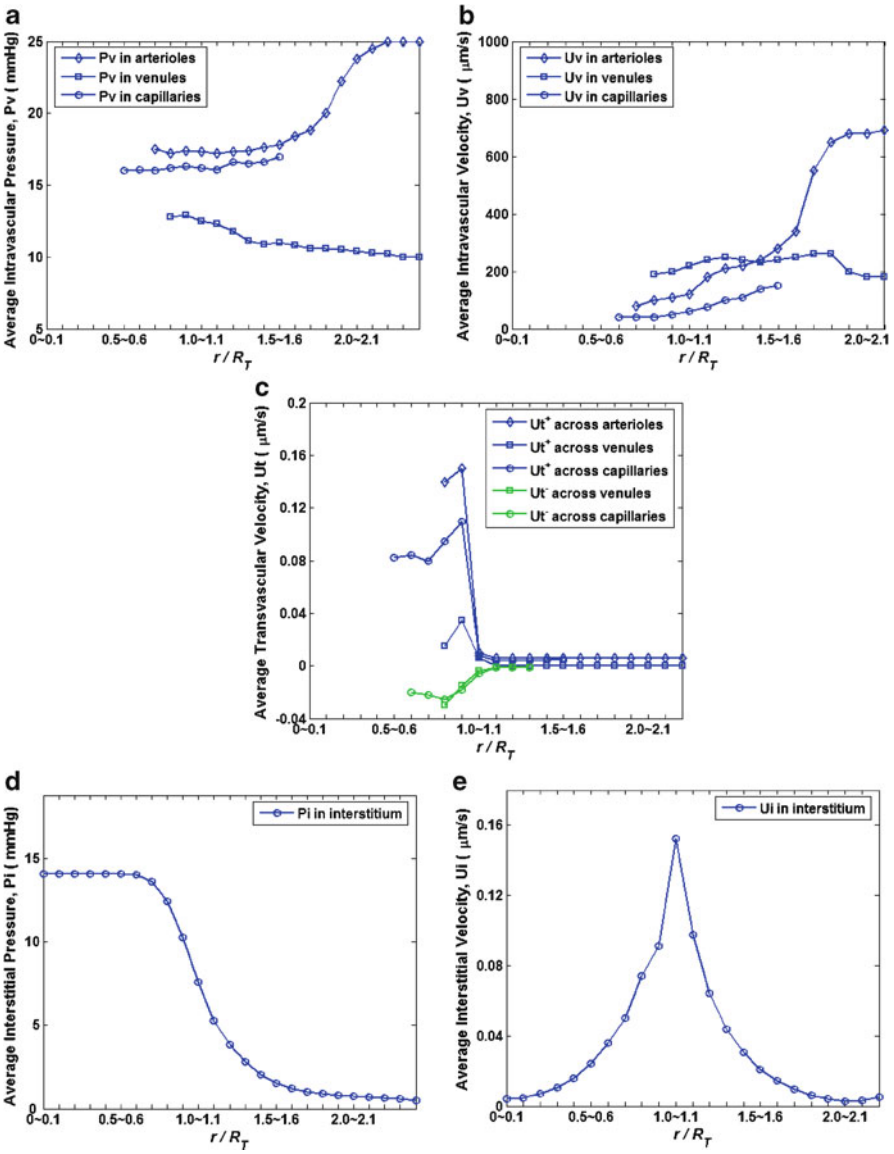

Fig. 14.13 3D flow simulation results of the control group (on the network in Fig. 14.5a). The distributions of the (**a**) intravascular pressure P_V (mmHg); (**b**) intravascular velocity U_V (μm/s); (**c**) transvascular velocity U_t (μm/s); (**d**) interstitial pressure P_i (mmHg); (**e**) interstitial flow velocity U_i (μm/s)

3.2.2 Flow Across the Vasculature

Extravasation flow (or outward flow from capillary) is defined as positive (Q_t^+) while intravasation (or inward flow) as negative (Q_t^-). From Fig. 14.12c, U_t in the host tissue region decreases along the bloodstream due to the decline of P_V, and the direction shifts from positive to negative. In the area of the tumor interior, U_t is mostly negative. In this region, the interstitial fluid is reabsorbed by the capillaries and enters into the bloodstream. Around the internal periphery of the tumor, U_t presents a relatively large positive value, which indicates a great amount of intravascular fluid could infiltrate into the tumor tissue there. Figure 14.13c shows the similar result for 3D analysis.

Comparing Fig. 14.12c with Fig. 14.12b (or Fig. 14.13c with Fig. 14.13b), U_t is two orders of magnitude smaller than U_V, suggesting transvascular flow could be negligible for one single tumor capillary in the microscopic scale. However, the simulation results also show that the total transvascular flux of the induced capillary network ($\sum Q_t$), approaches to 42% of the total inflow of the simulation system. Among the $\sum Q_t$, $\sum Q_t^+ / \sum Q_t^-$ is 80/20. It means that for the entire induced capillary network, nearly 40% of the total fluid participates in the transvascular exchange between the intravascular and the interstitial fluid. Such leakiness not only influences the internal environment of tumors but also provides a carrier for drug delivery as well as metastasis of tumor cells.

3.2.3 Flow Through the Interstitial Space

A plateau of P_i is found in the interior of the tumor, which drops rapidly at the periphery, see Figs. 14.12d and 14.13d. Figures 14.12e and 14.13e show the distribution of U_i (the flow of outward tumor center direction is positive). It is noteworthy that, U_i is very slow inside the tumor due to the low gradient of P_i, which may provide resistance for drug delivery. On the other hand, at the tumor periphery, U_i becomes much larger because of the very high gradient of P_i, so a large amount of interstitial fluid is discharged out of the tumor and enters into the host tissues which may speed the drug to be drained into peritumor lymphatic vessels into the host tissues. Similar blood perfusion features can be found in the 3D network simulations which cannot be presented here in detail due to the space limit.

Both the 2D and 3D simulation results predict the abnormal microcirculation and the resultant hostile microenvironment of tumors, such as poor blood perfusion, large amount of vascular leakiness, elevated interstitial fluid pressure, extremely slow interstitial flow inside tumor, and a rapidly rising convection oozing out from tumor margin into surrounding host tissue, all of which consisted with the corresponding experimental observations reported (Tozer et al. 2005; Jain et al. 2007). These features create a great barrier for drug delivery in tumor therapies.

3.3 Blood Perfusion with "Antiangiogenic" Microvasculature

The antiangiogenic microvasculatures are generated by the tumor antiangiogenesis model described in Sect. 2.2. We used the flow values of **AGF** model as the control group, and made comparisons with the corresponding results obtained from the other five groups (**AGF_AS, AGF_ES, AGF_AS_ES: 10, 6, 4**). In the below figures, each data is the average flow value based on 50 simulated networks of the corresponding antiangiogenesis models to provide a general trend of the flows for each model.

Figure 14.14a shows the comparison of the overall blood perfusion through the vasculature (the total amount of the blood flux through the network), $Q_V / Q_{V(\mathrm{AGF})}$. Q_V of the groups **AGF_ES, AGF_AS_ES: 10, 6, 4** decreased about 16%, 33%, 55%, and 65%, respectively, comparing with control group while the value of **AGF_AS** group is close to the control one $Q_{V(\mathrm{AGF})}$. A predicted 16% reduction of blood flow after one ES treatment is in the similar range with the experimental result by Herbst et al. (2002) in which they predicted a 20–28% tumor blood flow reduction after the first and second treatment cycle, respectively. Other clinical researches also indicated that antiangiogenesis therapy can cut down blood flow inside of tumors, e.g., Willett et al. (2004, 2005) found nearly 30% decrease of tumor blood perfusion determined by functional CT after the antiangiogensis treatment using bevacizumab.

The comparison of the overall transvascular flow is shown in Fig. 14.14b, c. According to Fig. 14.14b, the extravasation flow Q_t^+ increases about 15% and 12% in groups **AGF_AS** and **AGF_ES**, has a decline of 14% and 16% in the groups **AGF_AS_ES: 6, 4** and has similar value to the control model in **AGF_AS_ES:10** group. Due to the greatly decreasing of overall blood perfusion of the study groups, especially in the last three (**AGF_AS_ES:10, 6, 4**), see Fig. 14.14a, Q_t^+ reduces accordingly. There is a remarkable effect on the intravasations by the antiangiogenesis treatments predicted by the present model, as shown in Fig. 14.14c. Q_t^- in the first three study groups (**AGF_AS**, **AGF_ES**, **AGF_AS_ES:10**) decrease 36%, 42%, 94%, respectively, and no intravasation appears in the last two groups (**AGF_AS_ES:6, 4**), which may reduce the chances of metastasis of various growth factors or even tumor cell through the intravasation inside the tumor.

Interstitial hypertension is a reflection of the global pathophysiology of solid tumors and may be used for diagnosis, prognosis, and/or monitoring of treatment responses (Fukumura et al. 2007). Agents such as Bevacizumab, DC101, and SU11657 decrease tumor IFP in breast, colon cancers, and gliomas (Huber et al. 2005; Lee et al. 2000; Tong et al. 2004). Figure 14.14d shows the comparison of the IFP (shown as P_i) in the tumor center. Compared with the control group, P_i of the study groups declined about 17%, 20%, 47%, 60%, 60% for the groups of **AGF_AS, AGF_ES, AGF_AS_ES: 10, 6, 4,** respectively, indicating the plateau

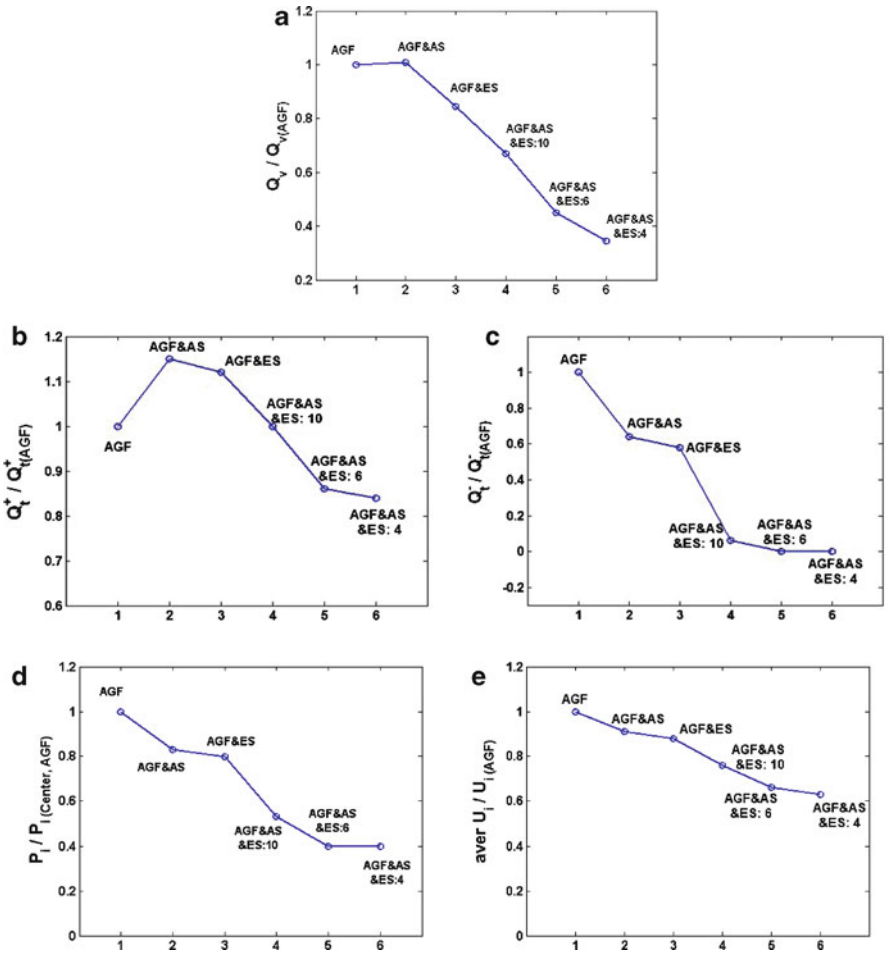

Fig. 14.14 Comparison of the flow values for different antiangiogenesis models. (**a**) the overall Q_v values through the vasculature; (**b**) the overall Q_t^+ values across the vasculature; (**c**) the overall Q_t^- values across the vasculature; (**d**) the Pi values in the tumor center; (**e**) the average U_i values at tumor margin

of tumor IFP is effectively relieved. Accordingly, the velocity of the interstitial fluid at tumor margin declined by 9%, 12%, 23%, 34%, and 37%, as shown in Fig. 14.14e. It reduces the convective flow out of the tumor and may also enhance drug residential time within the tumor.

3.4 *Blood Perfusion with "Vascular-Disrupting" Microvasculature*

In the below figures, each data is the average flow value based on 15 simulated networks of the corresponding disrupting approach to provide a general trend of the flows. We used the flow values before treatment as the baseline value, and made comparisons with the corresponding results on those disrupting networks.

3.4.1 Flows on Microvasculatures of the Four Disrupting Approaches

The comparisons of the flow values on the four disrupting vasculatures are listed in Table 14.1, The results showed that tumor blood perfusion after vascular-disrupting treatments are mostly declining, except the case of "Network 2(F)." Some experimental researches also indicated that vascular-disrupting therapies could either cut down or increase blood perfusion inside of tumors, which depends on the strategy and extent of treatments. For example, the animal experiments predicted that tumor blood perfusion was obviously declined after the vascular-disrupting treatment using the agent CA-4 (Fig. 14.15a) (Tozer et al. 1999). Figure 3.10b predicted that the local blood flow inside of the breast tumor was rising after vascular-disrupting by anti-VEGF TKRi (Fig. 14.15b was provided by Dr A.R. Padhani of Paul Strickland Scanner Centre, UK).

3.4.2 Comparison of Flows of the Four Disrupting Approaches

Because of the different disrupting approaches, the vascular densities among the different groups are not same. As some flow variables (e.g., Q_V, Q_t^+, Q_t^-) are directly related to the vascular density, we did not compare the corresponding values between the groups quantitatively, but adopt the qualitative comparison within the same group. We take the curve of $Q_V/Q_{V(\text{Net.1})}$ as the base line, a good perfusion condition for drug delivery can be the combination of: $Q_t^+/Q_{t(\text{Net.1})}^+ > Q_V/Q_{V(\text{Net.1})}$; $Q_t^-/Q_{t(\text{Net.1})}^- < Q_V/Q_{V(\text{Net.1})}$; and $P_{i(\text{Center})}/P_{i(\text{Center,Net.1})} < Q_V/Q_{V(\text{Net.1})}$. Figure 14.16 shows the qualitative comparison of the flows. According to the above criterion, the flow condition of "vascular-disrupting according to flowrate" group is the best (Fig. 14.16d), especially for the case of "Network 2(F)," not only Q_t^+ has a rising and Q_t^- reduces to zero but also Q_V increases as well, these changes are helpful to drug delivery inside of tumor. Additionally, Q_t^+ value in Fig. 14.16c is generally high, which suggest that disrupting vessels of lower maturity could enhance drug delivery across vasculature. Among the four groups, the effect of "disrupting randomly" group on the flow improvement is relatively poor (Fig. 14.16a). The above analysis told us that disrupting some specific vessels may result in better effects on normalization of tumor microenvironment.

Table 14.1 Comparisons of flows on four disrupting vasculatures

	$Q_V/Q^{a}_{V(\text{Net.1})}$	$Q_t^+/Q^+_{t(\text{Net.1})}$	$Q_t^-/Q^-_{t(\text{Net.1})}$	$P_{i(\text{Center})}/P_{i(\text{Center,Net.1})}$	$Q_i/Q_{i(\text{Net.1})}$
Net. 2(R), 3(R), 4(R)[b]	0.82, 0.52, 0.26	0.66, 0.62, 0.25	0.46, 0.28, 0.02	0.75, 0.68, 0.42	0.72, 0.67, 0.31
Net. 2(S), 3(S), 4(S)	0.90, 0.51, 0.45	1.17, 0.80, 0.56	0.68, 0.21, 0.07	0.86, 0.71, 0.50	0.85, 0.72, 0.44
Net. 2(M), 3(M), 4(M)	0.93, 0.77, 0.57	0.95, 0.85, 0.69	0.72, 0.34, 0.03	0.93, 0.83, 0.65	0.94, 0.83, 0.68
Net. 2(F), 3(F), 4(F)	1.06, 0.65, 0.55	1.22, 0.70, 0.56	0.007, 0.0, 0.0	0.85, 0.64, 0.45	0.82, 0.60, 0.38

[a] $Q_V/Q_{V(\text{Net.1})}$: the overall blood perfusion through the vasculature; $Q_t^+/Q^+_{t(\text{Net.1})}$: the overall extravasation across the vasculature; $Q_t^-/Q^-_{t(\text{Net.1})}$: the overall intravasation across the vasculature; $P_{i(\text{Center})}/P_{i(\text{Center,Net.1})}$: the interstitial pressure in the tumor center; $Q_i/Q_{i(\text{Net.1})}$: the overall interstitial flowrate at the tumor margin

[b] "Net2(R), 3(R), 4(R)" for "disrupting randomly" approach; "Net2(S), 3(S), 4(S)" for "disrupting according to network structure" approach; "Net 2(M), 3(M), 4(M)" for "disrupting according to vessel maturity" approach; "Net 2(F), 3(F), 4(F)" for "disrupting according to blood flowrate" approach

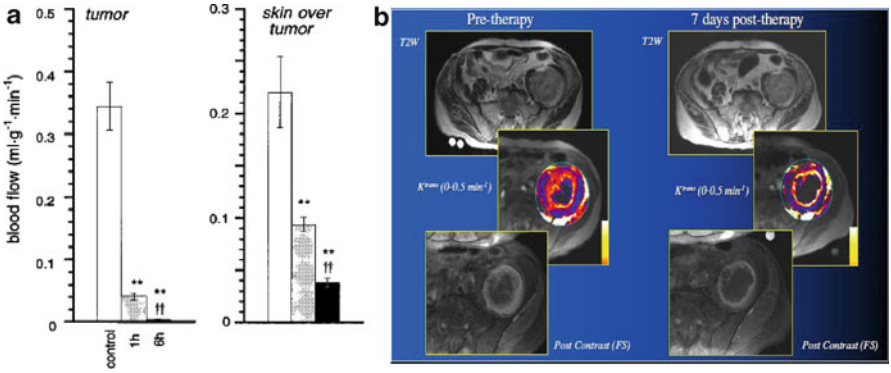

Fig. 14.15 Clinical observations of tumor blood perfusion during the vascular-disrupting treatments. (**a**) from Tozer et al. (1999); (**b**) provided by Dr Padhani AR

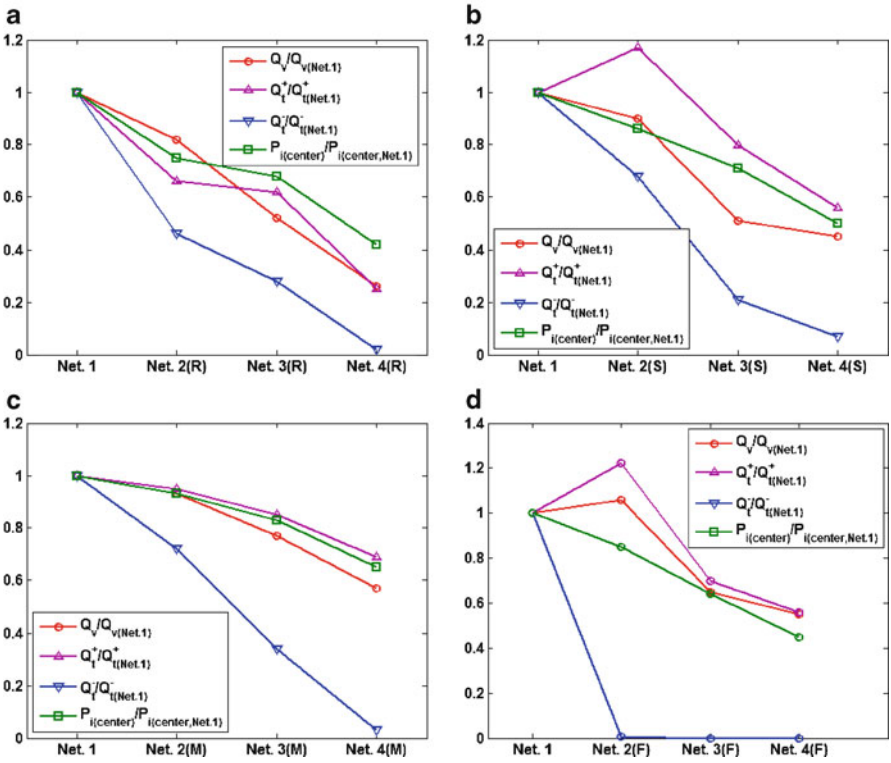

Fig. 14.16 The relative change of the flow variables between the same disrupting group. (**a**) group of disrupting randomly; (**b**) group of disrupting according to network structure; (**c**) group of disrupting according to vessel maturity; (**d**) group of disrupting according to blood flowrate

4 Discussions

4.1 Models of Tumor Haemodynamics

One manifestation of tumor vessel abnormality is a defective and leaky endothelium. Tumor vessel ECs are disorganized and irregularly shaped, and also have loose interconnections and focal intercellular openings. Moreover, the vascular basement membrane has an abnormally loose association with ECs and pericytes and consists of multiple layers. These physical characteristics together with cytokine production (in particular of Vascular Endothelial Growth factor – VEGF) are responsible for elevated macromolecular permeability and also lead to a potential coupling between the intravascular and the interstitial flow. So, contrast to some previous haemodynamic models which neglected vascular leakiness (such as McDougall et al. 2002, 2006; Alarcon et al. 2003, 2006; Stéphanou et al. 2005, 2006), a transvascular flow term was incorporated into this study which links intravascular and interstitial flow together. In addition, the compliance of tumor vessels, blood rheology with hematocritic distribution at branches is also considered. A specific coupling procedure is developed to couple the flows. It is based on the iteratively numerical simulation techniques, including local iterations at individual parameter level and one global loop to provide coupling and simulation convergence. The simulation results not only present the basic features and characteristics of tumor blood perfusion, which agree with the corresponding experimental observations reported, but also predict an intimate relationship between the tumor intravascular and the interstitial flow quantitatively. Among the parameters, the vascular leakiness is a key to govern the systemic flowing pattern, influence the tumor internal environment and contribute to the metastasis of tumor cells. According to our results, more than 40% of the total flux in the flow system is involved in the transvascular exchange. It shows that in a large part of the tumor interior, the interstitial fluid will penetrate to the capillaries and re-enter the blood circulation. In this process, some tumor cells may be transported by these interstitial fluid movements, which facilitate their migration by way of the blood. Furthermore, the continuously perfused blood in the peripheral network is finally absorbed by the lymphatic vessels in the peritumor host tissue through transvascular transport and fluid leakiness via the tumor interface, suggesting the tumor metastasis may transfer from hematogenous spread to lymphatic spread. These results could not be presented by the previous uncoupled flow models.

4.2 Normalization of Tumor Microvasculature and its Microenvironment

In this chapter, we generated two kinds of tumor "normalized" microvasculature by the treatments of (a) "antiangiogenesis" and (b) "vascular-disrupting," and made

the flow simulations on these networks to investigate how normalization of tumor vasculature by vascular-targeted therapies influences its blood perfusion.

For "ant-angiogenesis" case, we developed a 2D model of tumor antiangiogenesis responding to andostatin and endostatin treatments. The results show that the number of microvessels has decreased after using AS and ES, suggesting the inhibiting effects of AS and ES on the proliferation and migration of EC. Additionally, the resultant networks are more efficient with the microenvironment normalization, such as the plateau of tumor interstitial fluid pressure is relieved; the interstitial fluid oozing out from the tumor periphery into the surrounding normal tissue is reduced; the reduction of overall extravasation across vasculature to tumor interstium is much less than the decreased overall blood perfusion; the intravasations is remarkably effected by the change, in some cases there are no intravasation flow appear. However, as tumor angiogenesis is a dynamic process, the normalization of tumor microenvironment by antiangiogenesis can be a transient phenomena.

For "vascular-disrupting" case, four approaches are designed according to the abnormal characteristics of tumor microvaculature compared with normal one. The original network is generated by the tumor angiogenesis model. In regard to the flow analysis, as the vascular density of networks among the different disrupting groups are not same, we did not compare the corresponding flow values among the four groups quantitatively, but adopt the qualitative comparison within the same group. The results predict that the flow condition on the networks with "vascular-disrupting according to flowrate" is the best comparing with other methods. It may provide better result on drug delivery inside of tumor. Moreover, disrupting vessels of lower maturity could effectively enhance fluid transport across vasculature into interstitial space.

4.3 Model Validation: Comparison of the Simulation Results with the Clinical MRI Results

There is no technique available on measuring blood flow in such a complex system to provide direct validation of the simulation result. Dynamic Contrast Enhanced MRI (DCE-MRI) technique is able to provide contrast agent perfusion variation with time in in vivo tumor microvasculature. In similar manor, a low molecular tracer can be injected into the simulation network and the tracer perfusion curve can be calculated in the simulation. The comparison between the two perfusion curves will provide validation information qualitatively.

In doing so, a chemotherapy drug was used as an injected tracer in the systems and the concentration profiles of the drug was traced in the network. The transport of the drug through the vascular network and tumor interstitial space are governed by the convection and convective-diffusion equations, respectively, as follows. Perfect mixing is assumed and no reaction kinetics are considered,

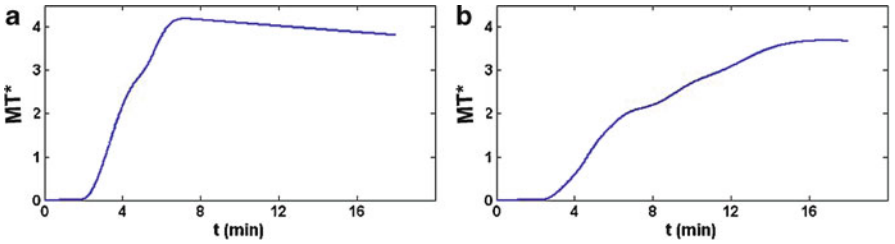

Fig. 14.17 Simulation results of the time-drug mass curve of MT*: (**a**) before treatment (on "Network 1"); (**b**) after treatment (on "Network 2(R)")

$$\frac{\partial C_{\mathrm{p}}}{\partial t} + \nabla \cdot [R_f U_V C_{\mathrm{p}}] = -K_{\mathrm{e}} \cdot C_{\mathrm{p}} - \phi_{\mathrm{s}} \tag{14.13}$$

$$\frac{\partial C_{\mathrm{i}}}{\partial t} + \nabla \cdot [R_f U_i C_{\mathrm{i}}] = \nabla \cdot (D_C \nabla C_{\mathrm{i}}) + \phi_{\mathrm{s}}, \tag{14.14}$$

where C_{p} and C_{i} are the solute concentration in plasma and in interstitial fluid, respectively. U_V and U_i are the fluid velocity in vessels and in interstitial space, respectively. R_f is the retardation factor (the ratio of the solute velocity to the fluid velocity). A correlation from Swabb et al. (1974) yields a value of R_f that is essentially equal to 1.0 for tumor tissue, therefore R_f is assumed to be equal to unity in this analysis. K_{e} is the drug elimination rate in plasma. D_C is the diffusion coefficient, which is assumed as constant here. ϕ_s is the solute source term, obtained using the equation for transcapillary exchange by Kedem and Katchalsky (1958),

$$\phi_{\mathrm{s}}(x, y, t) = \gamma_{\mathrm{s}} P_{\mathrm{eff}} \frac{S}{V} [C_{\mathrm{p}}(x, y, t) - C_{\mathrm{i}}(x, y, t)] \cdot A(x, y), \tag{14.15}$$

where P_{eff} is the effective vascular permeability coefficient and γ_{s} is the ratio coefficient. The other terms are the same as in the flow model.

We choose "Network 1" and "Network 2(R)" as the vasculatures before and after the vascular-disrupting treatment, respectively. The chemotherapy drug at concentration $C_{\max}$ is injected into the arteriole parental vessel, delivered at $t = 0$ and lasting for 120 s. Data are collected corresponding to the total dimensionless mass taken up by the tumor tissue (MT* =total drug mass in the tumor/drug mass injected into the parent vessel in one second).

Figure 14.17a is the time-drug mass curve of MT* before treatment (on "Network 1"). It shows a rapid enhancement in the beginning and gradual washout over a 16-min period. Figure 14.17b is the corresponding result after treatment (on "Network 2(R)"). It shows a much slower accumulation of drug within the tumor and minimal washout over a 16-min period. One of the MRI results is shown in Fig. 14.18, which is the time-contrast agent perfusion curve of MRI on breast cancer before and after treatment (McDonald and Choyke 2003). It presents a similar changing trend as the above simulation result. Due to the differences in

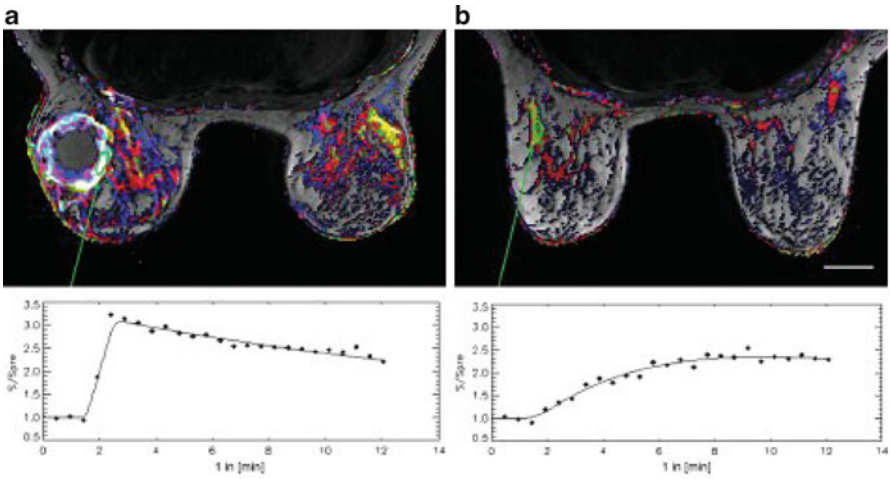

Fig. 14.18 MRI results of the time-contrast agent perfusion curve on breast cancer: (a) before treatment (b) after treatment (McDonald and Choyke 2003)

tumor size and capillary network structures, the time and solute concentration of the two curves (Figs. 14.17 and 14.18) are accordingly different, the similarity is striking.

It is also analysed of the influences to the blood perfusion prediction by changes in transport properties of tumor vessels and tissue such as (a) hydraulic permeability of tumor vessels $L_{pV,T}$; (b) hydraulic conductivity of tumor interstitium K_T; (c) absorption capacity of lymphatic system, $Lp_L S_L / V$. The detailed results cannot be presented in this article due to the space limit. These results indicate that decreasing $L_{pV,T}$ is helpful to relieving the plateau of tumor IFP, reducing the interstitial fluid leakiness into the peri-tumor tissue, which may prevent the tumor cell metastasis through the intravasation inside the tumor. Increasing K_T has positive effects on flattening the tumor IFP plateau, cutting down the chances of tumor cell metastasis, however, it can also lead to the increased convective flow out of tumor, which will reduce the drug residential time within the tumor. There are not remarkable effects on normalizing the tumor microenvironment by the changes in $Lp_L S_L / V$, compared with those by changing $L_{pV,T}$ and K_T.

4.4 Limitations of the Study

Vessel collapse and regression are commonly observed in solid tumors, which is one of the abnormal characteristics of tumor vessels (Fukumura and Jain 2007). Researches showed that the factors leading to vessel collapse in tumors are mechanical stresses generated by the growing tumor itself (pressure)

(Griffon-Etienne et al. 1999) and reduced perfusion of certain vessels (lower wall shear stress) (Milkiewicz et al. 2001). Although the loss of haemodynamic shear stress promotes EC apoptosis at in vivo condition (Meeson et al. 1996), the contribution of EC apoptosis to vessel-like structures collapse is largely unknown (Segura et al. 2002). In the modeling study, Bartha and Rieger (2006) used wall shear stress as a criteria of vessel collapse, based on the experimental evidences showing that the long term reduction of vascular shear stress promotes vessel collapse and regression (Duval et al. 2003). However, further studies about the mechanism and quantitative researches of the influence of WSS on the angiogenesis are required in the future. In the present work we have not included the WSS induced vessel collapse mechanism in angiogenesis. However, vessel compliance was simulated by using a typical constitutive mechanical relation for tumor vessels of Netti et al. (1996). Because lack of feedback mechanism for vessel regression (or collapse), predefined vessel branching probabilities, which is controlled by the tumor location and local chemical–mechanical environment, were used in order to produce a realistic network. When the vessel sprouts grow into the tumor, the migration will be adjusted by the functions. Also, the distribution of TAFs initial concentration was given accordingly, see Sect. 2.1.1. However, these factors are set to be constant during the angiogenesis process, rather than a more realistic dynamic situation. Therefore, the results obtained in this study can only be treated as a snapshot of the tumor microcirculation condition.

Recently, some works considering the dynamic feedback of tumor growth to the angiogenesis have been published. Lowengrub and co-workers described an avascular tumor growth model in the papers Macklin and Lowengrub (2007) and Wise et al. (2008). The growth model incorporated the effects of the interaction between the genetic characteristics of the tumor and its microenvironment on the resulting tumor progression and morphology Rieger et al. made the simulation of transformation of regular normal vasculature into a highly inhomogeneous tumor capillary network by the model they developed which combined a dynamically evolving network in the presence of a dynamically changing tumor (Bartha and Rieger 2006; Welter et al. 2008). In our latest development the tumor growth, vessel regression and blood perfusion are all included in a coupled model. Some of the results will be published soon.

References

Alarcon T, Byrneb HM, Mainia PK (2003) A cellular automaton model for tumor. growth in inhomogeneous environment. J Theor Biol 225, 257–274.

Alarcon T, Owen MR, Byrne HM, Maini PK (2006) Multiscale modeling of tumor growth and therapy: the influence of vessel normalisation on chemotherapy. Computational and Mathematical Methods in Medicine 7, 85–119.

Anderson ARA, Chaplain MAJ (1998) Continuous and discrete mathematical models of tumor-induced angiogenesis. Bulletin of Mathematical Biology 60, 857–900.

Anderson ARA, Chaplain MAJ et al (2000) A gradient-driven mathematical model of anti-angiogenesis. Mathematical and Computer 32, 1141–1152.
Bartha K, Rieger H (2006) Vascular network remodeling via vessel cooption, regression and growth in tumors. J Theor Biol 241, 903–918.
Benjamin LE, et al (1999) Selective ablation of immature blood vessels in established human tumors follows vascular endothelial growth factor with drawal. J Clin Invest, 103(2): 159–165.
Boucher Y, et al (1990) Interstitial pressure gradients in tissue-isolated and subcutaneous tumors: implications for therapy. Cancer Res 50, 4478–4484.
Bray D (1992) Cell Movements. Garland Publishing, New York.
Chaplain MAJ, McDougall SR, Anderson ARA (2006) Mathematical modeling of tumor-induced angiogenesis. Annu Rev Biomed Eng 8, 233–257.
Chang YS et al (2000) Mosaic blood vessels in tumors: frequency of cancer cells in contact with flowing blood. Proc Natl Acad Sci USA, 97: 14608–14613.
Darland DC, D'Amore P (1999) Blood vessel maturation: Vascular development comes of age. J Clin Invest, 103(2): 157–158.
di Tomaso E et al (2005) Mosaic tumor vessels: cellular basis and ultrastructure of focal regions lacking endothelial cell markers. Cancer Res, 65: 5740–5749.
Donnelly EF, Geng L, Wojcicki WE, Fleischer AC, Hallahan DE (2001) Quantified Power Doppler US of Tumor Blood Flow Correlates with Microscopic Quantification of Tumor Blood Vessels. Radiology 219, 166–170.
Duval H, Harris M, Li J et al (2003) New insights into the function and regulation of endothelial cell apoptosis. Angiogenesis 6, 171–183.
Eriksson K, Magnusson P, Dixelius J et al (2003) Angiostatin and endostatin inhibit endothelial cell migration in response to FGF and VEGF without interfering with specific intracellular signal transduction pathways. FEBS Letters 536, 19–24.
Folkman J (2000) Tumor angiogenesis. In: Holland, J.F., et al. (Ed.), Cancer Medicine. B.C. Decker Inc., Ontario, Canada, 132–152.
Fukumura D, Jain RK (2007) Tumor microvasculature and microenvironment: targets for anti-angiogenesis and normalization. Microvas Res 74, 72–84.
Gao H, Xu SX, Cai Y et al (2006) Numerical simulation of tumor-induced angiogenesis in and out of tumor incorporating mechanical effects. Medical Biomechanics, 21(1): 2–7 (in Chinese).
Griffon-Etienne G, Boucher Y, Brekken C et al (1999) Taxane-induced apoptosis decompresses blood vessels and lowers interstitial fluid pressure in solid tumors: clinical implications. Cancer Res 59, 3776–3782.
Hamberg LM, Kristjansen PE, Hunter GJ, Wolf GL, Jain RK (1994) Spatial heterogeneity in tumor perfusion measured with functional computed tomography at 0.05 microliter resolution. Cancer Res 54, 6032–6036.
Herbst RS et al (2002) Development of biologic markers of response and assessment of antiangiogenic activity in a clinical trial of human recombinant endostatin. J Clin Oncol 20, 3804–3814.
Huber PE et al (2005) Trimodal cancer treatment: beneficial effects of combined antiangiogenesis, radiation, and chemotherapy. Cancer Res 65, 3643–3655.
Jain RK et al (2006) Lessons from phase III clinical trials on anti-VEGF therapy for cancer. Nat Clin Pract Oncol 3, 24–40.
Jain RK, Tong RT, Munn LL (2007) Effect of vascular normalization by antiangiogenic therapy on interstitial hypertension, peritumor edema, and lymphatic metastasis: Insights from a mathematical model. Cancer Res 67(6), 2729–2735.
Kedem O, Katchalsky A (1958) Thermodynamic analysis of permeability of biological membranes to non-electrolytes. Biochim Biophs Acta, 27: 229–246.
Lee CG, Heijn M, di Tomaso E et al (2000) Anti-vascular endothelial growth factor treatment augments tumor radiation response under normoxic or hypoxic conditions. Cancer Res 60, 5565–5570.
Levine HA, Pamuk S, Sleeman BD et al (2001) Mathematical modeling of capillary formation and development in tumor angiogenesis: penetration into the stroma. Bull Math Biol 63, 801–863.

Meeson A, Palmer M, Calfon M et al (1996) A relationship between apoptosis and flow during programmed capillary regression is revealed by vital analysis. Development 122, 3929–3938.
Macklin P, Lowengrub J (2007) Nonlinear simulation of the effect of the microenvironment on tumor growth. J Theor Biol 245, 677–704.
McDonald DM, Choyke PL (2003) Imaging of angiogenesis: from microscope to clinic. Nat Med, 9, 713–725.
McDougall SR, Anderson ARA, Chaplain MAJ, Sherratt JA (2002) Mathematical modeling of flow through vascular networks: Implications for tumor-induced angiogenesis and chemotherapy strategies. Bull Math Biol 64, 673–702.
McDougall SR, Anderson ARA, Chaplain MAJ (2006) Mathematical Modeling of Dynamic Adaptive Tumor-Induced Angiogenesis: Clinical Implications and Therapeutic Targeting Strategies. J Theor Biol 241, 564–589.
Milkiewicz M, Brown MD, Egginton S et al (2001) Association between shear stress, angiogenesis, and VEGF in skeletal muscles in vivo. Microcirculation 8, 229–241.
Netti PA, Roberge S, Boucher Y, Baxter LT, Jain RK (1996) Effect of transvascular fluid exchange on pressure–flow relationship in tumors: a proposed mechanism for tumor blood flow heterogeneity. Microvas Res 52, 27–46.
Netti PA, Baxter LT, Boucher Y (1997) Macro- and Microscopic Fluid Transport in Living Tissues: Application to Solid Tumors. AIChE Journal 43(3), 818–834.
O'Reilly MS, Holmgren L, Shing Y et al (1994) Angiostatin: a novel angiogenesis inhibitor that mediates the suppression of metastases by a Lewis lung carcinoma. Cell 79, 315–328.
O'Reilly MS, Boehm T, Shing Y et al (1997) Endostatin: an endogenous inhibitor of angiogenesis and tumor growth. Cell 88, 277–285.
Pries AR, Secomb TW, Gessner T et al (1994) Resistance to blood flow in microvessels in vivo. Circulation Res 75, 904–915.
Segura I, Serrano A, De Buitrago CG et al (2002) Inhibition of programmed cell death impairs in vitro vascular-like structure formation and reduces in vivo angiogenesis. FASEB J 16, 833–841.
Sherratt JA, Murray JD (1990) Models of epidermal wound healing. Proc Roy Soe Lond B241, 29–36.
Stéphanou A, McDougall SR, Anderson ARA, Chaplain MAJ (2005) Mathematical Modeling of Flow in 2D and 3D Vascular Networks: Applications to Anti-angiogenic and Chemotherapeutic Drug Strategies. Math Comput Model 41, 1137–1156.
Stéphanou A, McDougall SR, Anderson, ARA, Chaplain MAJ (2006) Mathematical modeling of the influence of blood rheological properties upon adaptive tumor-induced angiogenesis. Math Comput Model 44, 96–123.
Swabb EA, Wei J, Gullino PM (1974) Fluid and protein fluxes across small and large pores in the microvasculature. Application of two-pore equations. Acta Physiol Scand 131, 441–428.
Tee D, DiStefano III J (2004) Simulation of tumor-induced angiogenesis and its response to anti-angiogenic drug treatment: mode of drug delivery and clearance rate dependencies. J Cancer Res Clin Oncol 130, 15–24.
Tong RT et al (2004) Vascular normalization by vascular endothelial growth factor receptor 2 blockade induces a pressure gradient across the vasculature and improves drug penetration in tumors. Cancer Res 64, 3731–3736.
Tozer GM, Prise VE, Wilson J et al (1999) Combretastatin A-4 Phosphate as a tumor vascular-targeting agent: early effects in tumors and normal tissues. Cancer Res 59, 1626–1634.
Tozer GM, Ameer-Beg SM, Baker J et al (2005) Intravital imaging of tumor vascular networks using multi-photon fluorescence microscopy. Advanced Drug Delivery Reviews 57, 135–152.
Weidner N (1995) Intratumor microvessel density as a prognostic factor in cancer. Am J Pathol 147, 9–19.
Welter M, Bartha K, Rieger H (2008) Emergent vascular network inhomogeneities and resulting blood flow patterns in a growing tumor. J Theor Biol 250, 257.
Wildiers H et al (2003) Effect of antivascular endothelial growth factor treatment on the intratumoral uptake of CPT-11. Br J Cancer 88, 1979–1986.

Willett CG et al (2004) Direct evidence that the anti-VEGF antibody Bevacizumab has anti-vascular effects in human rectal cancer. Nat Med 10, 145–147.

Willett CG et al (2005) Surrogate markers for antiangiogenic therapy and dose-limiting toxicities for Bevacizumab with radiation and chemotherapy: continued experience of a phase I trial in rectal cancer patients. J Clin Oncol 23, 8136–8139.

Wise SM, Lowengrub JS, Frieboes HB, Cristini V (2008) Three-dimensional multispecies nonlinear tumor growth-I. Model and numerical method. J Theor Biol 253, 524–543.

Wu J, Xu SX, Long Q et al (2008a) Coupled modeling of blood perfusion in intravascular, interstitial spaces in tumor microvasculature. J Biomech 41, 996–1004.

Wu J, Xu SX, Long Q et al (2008b) Simulation of 3D Solid Tumor Angiogenesis Including Arteriole, Capillary and Venule. Molecular & Cellular Biomech 5(4), 127–227.

Wu J, Long Q, Xu SX, Padhani AR (2009a) Study of tumor blood perfusion and its variation due to vascular normalization by anti-angiogenic therapy based on 3D angiogenic microvasculature. J Biomech 42, 712–721.

Wu J (2009b) Numerical study of tumor hemodynamics for vascular-targeted therapy. Doctoral Thesis.

Zhao GP, Gao H, Wu J et al (2006) 2D numerical simulation of effect anti-angiogenic factors Angiostatin and Endostatin on tumor-induced angiogenesis. J Med Biomech 21(4), 272279 (in Chinese).

Index

T.L. Jackson (ed.), *Modeling Tumor Vasculature: Molecular, Cellular, and Tissue Level Aspects and Implications*, DOI 10.1007/978-1-4614-0052-3,